



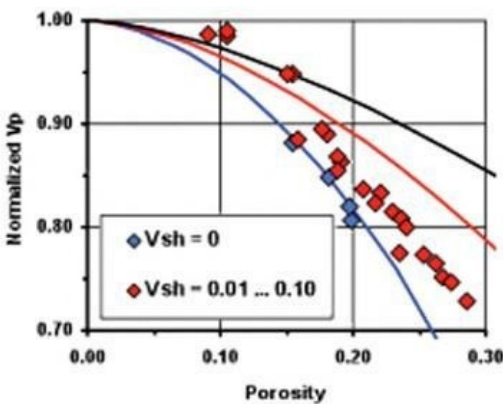
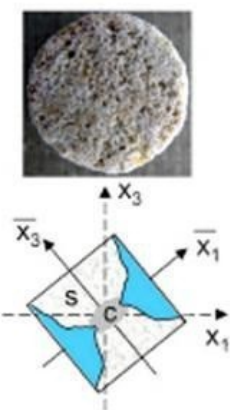
HANDBOOK OF PETROLEUM
EXPLORATION AND PRODUCTION
VOLUME 8

PHYSICAL PROPERTIES OF ROCKS

A WORKBOOK

J.H. Schön

SERIES EDITOR
John Cubitt



Physical Properties of Rocks

*HANDBOOK OF PETROLEUM EXPLORATION
AND PRODUCTION*
8

Series Editor
JOHN CUBITT

Previous volumes in the series:

- Volume 1 Operational Aspects of Oil and Gas Well Testing
- Volume 2 Statistics for Petroleum Engineers and Geoscientists
- Volume 3 Well Test Analysis
- Volume 4 A Generalized Approach to Primary Hydrocarbon Recovery of Petroleum Exploration and Production
- Volume 5 Deep-Water Processes and Facies Models: Implications for Sandstone Petroleum Reservoirs
- Volume 6 Stratigraphic Reservoir Characterization for Petroleum Geologists, Geophysicists, and Engineers
- Volume 7 The Sea of Lost Opportunity

Handbook of Petroleum Exploration and Production, 8

Physical Properties of Rocks

A Workbook

J.H. Schön



ELSEVIER

AMSTERDAM • BOSTON • HEIDELBERG • LONDON
NEW YORK • OXFORD • PARIS • SAN DIEGO
SAN FRANCISCO • SINGAPORE • SYDNEY • TOKYO

Elsevier

The Boulevard, Langford Lane, Kidlington, Oxford, OX5 1GB, UK
Radarweg 29, PO Box 211, 1000 AE Amsterdam, The Netherlands

Copyright © 2011 Elsevier B.V. All rights reserved

No part of this publication may be reproduced, stored in a retrieval system or transmitted in any form or by any means electronic, mechanical, photocopying, recording or otherwise without the prior written permission of the publisher

Permissions may be sought directly from Elsevier's Science & Technology Rights Department in Oxford, UK: phone (+44) (0) 1865 843830; fax (+44) (0) 1865 853333; email: permissions@elsevier.com. Alternatively you can submit your request online by visiting the Elsevier website at <http://elsevier.com/locate/permissions>, and selecting Obtaining permission to use Elsevier material

Notice

No responsibility is assumed by the publisher for any injury and/or damage to persons or property as a matter of products liability, negligence or otherwise, or from any use or operation of any methods, products, instructions or ideas contained in the material herein

British Library Cataloguing-in-Publication Data

A catalogue record for this book is available from the British Library

Library of Congress Cataloging-in-Publication Data

A catalog record for this book is available from the Library of Congress

ISBN: 978-0-444-53796-6

For information on all Elsevier publications
visit our website at elsevierdirect.com

Printed and bound in Great Britain
11 12 13 14 10 9 8 7 6 5 4 3 2 1

Working together to grow
libraries in developing countries

www.elsevier.com | www.bookaid.org | www.sabre.org

ELSEVIER

BOOK AID
International

Sabre Foundation

Contents

Preface	ix
Acknowledgments	xi
1. Rocks—Their Classification and General Properties	
1.1 Introduction	1
1.2 Igneous Rocks	2
1.3 Metamorphic Rocks	3
1.4 Sedimentary Rocks	4
1.5 Physical Properties of Rocks—Some General Characteristics	12
2. Pore Space Properties	
2.1 Overview—Introduction	17
2.2 Porosity	17
2.3 Specific Internal Surface	29
2.4 Fluids in the Pore Space—Saturation and Bulk Volume Fluid	30
2.5 Permeability	32
2.6 Wettability	56
2.7 Fluid Distribution—Capillary Pressure in a Reservoir	59
2.8 Example: Sandstone—Part 1	70
3. Nuclear Magnetic Resonance—Petrophysical Properties	
3.1 Introduction	75
3.2 Physical Origin	76
3.3 The Principle of an NMR Measurement	77
3.4 NMR Relaxation Mechanisms of Fluids in Pores and Fluid-Surface Effects	80
3.5 Applications	90
4. Density	
4.1 Definition and Units	97
4.2 Density of Rock Constituents	98
4.3 Density of Rocks	101

5. Nuclear/Radioactive Properties	
5.1 Fundamentals	107
5.2 Natural Radioactivity	108
5.3 Interactions of Gamma Radiation	126
5.4 Interactions of Neutron Radiation	131
5.5 Application of Nuclear Measurements for a Mineral Analysis	139
5.6 Example: Sandstone—Part 2	146
6. Elastic Properties	
6.1 Fundamentals	149
6.2 Elastic Properties of the Rock Constituents	154
6.3 Velocity of Rocks—Overview	160
6.4 Velocity of Igneous and Metamorphic Rocks	161
6.5 Velocity of Sedimentary Rocks	164
6.6 Anisotropy	181
6.7 Theories	188
6.8 Reservoir Properties from Seismic Parameters	226
6.9 Attenuation of Elastic Waves	232
6.10 Example of Elastic Properties: Sandstone (Gas Bearing)	240
7. Geomechanical Properties	
7.1 Overview, Introduction	245
7.2 Classification Parameters	246
7.3 Fundamental Geomechanical Properties and Processes	249
7.4 Correlation Between Static and Dynamic Moduli	259
7.5 Correlation Between Seismic Velocity and Strength Properties	264
8. Electrical Properties	
8.1 Fundamentals	273
8.2 Electrical Properties of Rock Components	275
8.3 Specific Electrical Resistivity of Rocks	278
8.4 Clean Rocks—Theories and Models	288
8.5 Shaly Rocks, Shaly Sands	296
8.6 Laminated Shaly Sands and Laminated Sands—Macroscopic Anisotropy	304
8.7 Dielectric Properties of Rocks	310
8.8 Complex Resistivity—Spectral-Induced Polarization	324
8.9 Example: Sandstone—Part 3	335
9. Thermal Properties	
9.1 Introduction	337
9.2 Thermal Properties of Minerals and Pore Contents	339
9.3 Thermal Properties of Rocks—Experimental Data	343
9.4 Theories and Models	360

10. Magnetic Properties	
10.1 Fundamentals and Units	373
10.2 Magnetic Properties of Rock Constituents	376
10.3 Magnetic Properties of Rocks	381
11. Relationships Between Some Petrophysical Properties	
11.1 Introduction	393
11.2 Relationships Based on Layered Models—Log Interpretation for Porosity and Mineral Composition Estimate	394
11.3 Relationships Between Thermal Conductivity and Elastic Wave Velocities	403
Appendix A: Physical Properties of Rock-Forming Minerals	415
Appendix B: Some Conversions	423
Appendix C: Files available on the website http://www.elsevierdirect.com/ companion.jsp?ISBN=9780444537966	425
References	433
Index	463

Preface

Petrophysics, beginning with Archie's historical yet evergreen equations, has a key function in all applications of geosciences, petroleum engineering and related technologies. It helps us with understanding the processes and controlling properties, and creates relationships between:

- parameters we can measure as output of the dramatic progress in exploration techniques;
- properties we need for reservoir characterization (hydrocarbons, water, minerals, geothermal energy), but also stability of formations and constructions.

Therefore, there is an increasing interest to understand and manage these relationships.

Petrophysics is complex and multidisciplinary. For the high sophisticated techniques like seismic investigations, nuclear magnetic resonance measurements and spectral methods, excellent textbooks are available. Practical applications and techniques are described in manuals and chartbooks.

Thus, in front of this highly sophisticated, specialized, and detailed world of petrophysical books and literature, my wish is to give a comprehensive presentation of fundamentals from my point of view. To define these topics and contents, I had the valuable help of a long experience working at universities and teaching courses for the industry with colleagues.

As a student, I had a book about "Theoretical Physics" (by Georg Joos) with the preface, "This book should not be a lift carrying the reader without energy on the tops of science. It should be only a simple mountain guide, leading on an elevation, which gives the view on the top of the mountains and acts as a "base camp" for reaching these tops." I have learned to understand this fundamental function of a "base camp" as a location to prepare and to train and to find motivation for the next levels from the real life experiences of our son Peter, when he voyages high on the fascinating summits of mountains in our world.

Over the course of my professional life, I've had the happiness to work on the fascinating subject of "rocks," and as always, as well as with this book, I have the wish to transform and share a little bit this fascination of

studying rocks, to show the pleasure we get from the investigation of the natural rock and its beauty:

*“to see a world in a grain of sand,
and a heaven in a wild flower,
held infinity in the palm of your hand
and eternity in an hour . . .”*

William Blake (1757–1829)

Acknowledgments

I wish to express my deepest gratitude to all my friends, colleagues, and students for their indispensable help, for sharing ideas, and for giving me the motivation to complete this work.

I would like to give special thanks to Erika Guerra for editing the manuscript and for her time and patience spent dealing with my text, the figures, references, and all the details. Many thanks, Erika, you have been more than a “technical writer,” you gave me the foundation for a proper text (that is . . . I hope so).

Over the course of my professional life, I have had the honour and pleasure to work with and to learn from many wonderful people, and to share a common enthusiasm. However, there are too many to name here, and with great regret I can only share a few acknowledgments at this moment. My colleagues and dear friends, Daniel Georgi and Allen Gilchrist, for their long cooperation in teaching petrophysics, as well as in research, and for giving me valuable comments and help . . . especially for the NMR and nuclear section. But most of all, our long cooperation gave me the motivation to try this experiment of writing the fundamentals of our discipline. Frank Börner, one of my first students, and now my friend and colleague, contributed valuable insight and ideas for electrical properties.

The opportunity to teach at universities, particularly Bergakademie Freiberg/Germany, Montanuniversität Leoben, Technical University Graz/Austria, and at the Colorado School of Mines/Golden, laid the foundation for a fruitful teamwork with students—their response to a book like this is of substantial importance. Some of them have followed the “petrophysics way” and helped me mainly with experimental data—one of the rarest components in our science. Nina Gegenhuber made measurements of elastic and thermal properties and I could use these, many thanks.

I could expand teaching beyond the university to training courses for industry—a completely new and valuable experience with the important response of the practice and the fruitful sharing of knowledge and problem analyses. I thank Baker Atlas (Houston) and HOT-Engineering (Leoben) for placing the fundamentals of petrophysics as an integral component of geosciences in their programs and for supporting this work. I was able to acquire much practical experience in my job with Joanneum Research (Graz/Leoben).

I would like to give thanks to various companies and organizations for giving me permission to use their valuable materials—particularly Baker Atlas/Baker Hughes, Schlumberger, AGU, AAPG, EAGE, SEG, SPE, and SPWLA.

Thanks to the staff at Elsevier, in particular Linda Versteeg, Derek Coleman, and Mohana Natarajan, for their constructive cooperation.

Writing a book requires a creative environment and people who can motivate you, focus your energy, and refresh your patience from time to time. My wife, Monika, has done a perfect job in the background and has motivated me many times. Many thanks—now we are ready. Also, our son, Peter, was and is such an energizing factor—his energy and discipline to work for an idea frequently gave me confirmation that we need to use the time we have to do valuable things.

Rocks—Their Classification and General Properties

1.1 INTRODUCTION

Rocks are naturally occurring aggregates of one or more minerals. In the case of porosity or fracturing, they also contain fluid phases.

With respect to their geological genesis and processes, rocks are divided into three major groups:

- igneous rocks (magmatites);
- metamorphic rocks (metamorphites);
- sedimentary rocks (sediments).

Figure 1.1 shows the rock cycle. It starts with the magmatic rocks, formed by crystallization from the magma. Chemical processes and processes of erosion, disintegration, and transportation create sedimentary rocks of different composition and texture. Both types can be transformed into metamorphic rocks through the influence of pressure and temperature; a reworking by melting and recrystallization also occurs.

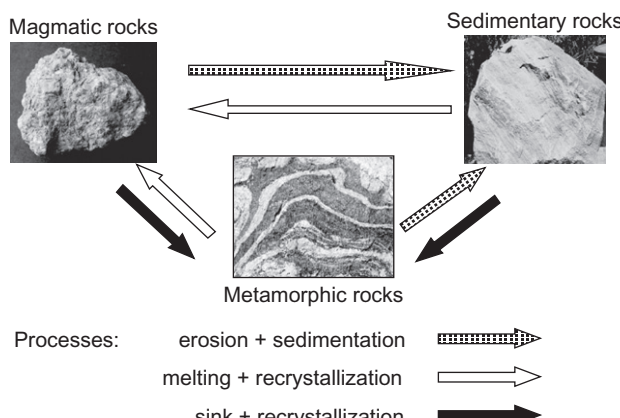


FIGURE 1.1 The rock cycle.

The following sections briefly describe the three rock types. Sedimentary rocks are discussed in more detail with respect to their importance to fluid reservoir exploration (e.g., hydrocarbons, water) and their abundance on the earth's surface. A detailed classification of rocks and their abundances on the earth is given by Best (1995) in *A Handbook of Physical Constants/AGU Reference Shelf 3*.

1.2 IGNEOUS ROCKS

Igneous rocks are formed by crystallization from a molten magma. Three types are characterized by their occurrence and position in the crust:

- plutonic rocks crystallized in great depth and forming large rock bodies;
- volcanic rocks reaching the surface, in many cases forming layers of rocks like a blanket;
- dikes have dominant vertical extension and a horizontal extension in one direction; also, they frequently separate geological units.

Igneous rocks can be classified according to their chemical or mineralogical composition. Chemical classification distinguishes acid, intermediate, basic, and ultrabasic rocks. Mineralogic classification uses the types (Figure 1.2):

- felsic or silicic rocks, for example granite and rhyolite;
- intermediate rocks, for example granodiorite, diorite, dacite, and andesite;
- mafic rocks, for example basalt and gabbro;
- ultramafic rocks, for example peridotite and komatiite.

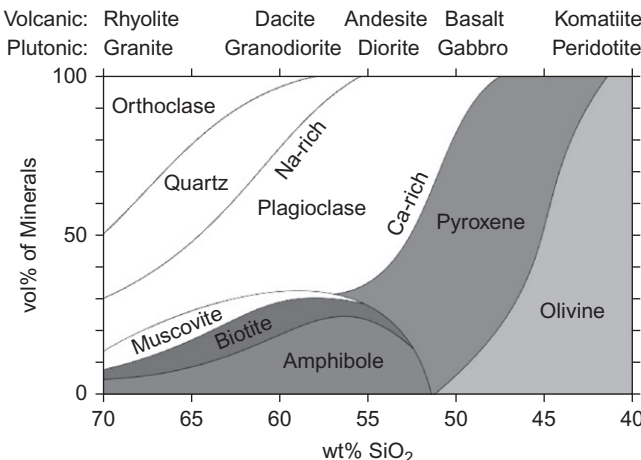


FIGURE 1.2 Mineralogical classification of common magmatic rock types. Modified from http://en.wikipedia.org/wiki/File:Mineralogy_igneous_rocks_EN.svg.

TABLE 1.1 Approximate Average Mineral Composition (Volume Percent) of the Earth's (Upper) Crust and of Major Intrusive Rocks

Mineral	Crust	Granite	Granodiorite	Quartzdiorite	Diorite	Gabbro
Plagioclase	41	30	46	53	63	56
Alkalifeldspar	21	35	15	6	3	
Quartz	21	27	21	22	2	
Amphibole	6	1	13	12	12	1
Biotite	6	5	3	3	5	1
Orthopyroxene	2				3	16
Clinopyroxene	2				8	16
Olivine	0.6					5
Magnetite, Ilmenite	2	2	2	2	3	4
Apatite	0.5	0.5	0.5	0.5	0.8	0.6

After Wedepohl (1969); see also Huckenholz (1982) and Schön (1996).

Mineral composition controls physical properties (e.g., density and seismic velocity increases from felsic to mafic rock types).

Table 1.1 shows the mean mineral composition of magmatic rocks.

1.3 METAMORPHIC ROCKS

“Metamorphic rocks are the result of metamorphism. Metamorphism is the solid-state conversion of igneous and sedimentary rocks under the pressure–temperature regime of the crust” (Huckenholz, 1982). During this process the original mineral assemblages (magmatic or sedimentary) are converted into new assemblages corresponding to the thermodynamic conditions over a geologic time.

Through the different metamorphic processes (regional metamorphism, contact metamorphism, cataclastic metamorphism, etc.), the great variety of original rocks and their composition result in a broad spectrum of metamorphic rock types. Typical members of these metamorphic rock types are phyllites, schists, gneisses, skarns, marbles, felses, quartzites, serpentinites, and amphibolites.

As a result of the metamorphic process, many rocks show a typical structure with parallel-oriented elements like mineral axes and/or fractures and fissures. This results in anisotropy of certain physical properties.

1.4 SEDIMENTARY ROCKS

1.4.1 Overview

Sedimentary rocks are highly important for hydrocarbon exploration; most commercial reservoirs occur in this rock type characterized by its porosity and permeability. Sedimentary rocks cover more than 50% of the earth's surface and are therefore also of fundamental importance in many aspects of our lives, from agriculture to the foundation for buildings, and from ground-water resources to the whole environment.

Sedimentary rocks are formed by a sequence of physical, chemical, and biological processes.

Magmatic, sedimentary, and metamorphic source rocks are disaggregated by weathering to:

- resistant residual particles (e.g., silicate minerals, lithic fragments);
- secondary minerals (e.g., clays);
- water soluble ions of calcium, sodium, potassium, silica, etc.

Weathered material is transported via water, ice, or wind to sites and deposited:

- mineral grains drop to the depositional surface;
- dissolved matter precipitates either inorganically, where sufficiently concentrated, or by organic processes;
- decaying plant and animal residues may also be introduced into the depositional environment.

Lithification (consolidation) occurs when the sedimentary material becomes compacted; aqueous pore solutions interact with the deposited particles to form new, cementing diagenetic (authigenic) minerals (Best, 1995).

We distinguish two major rock classes of sedimentary rocks:

- clastics (siliciclastics);
- carbonates and evaporites.

Siliciclastics are composed of various silicate grains; carbonates consist mainly of only the two minerals dolomite and calcite. Clastic sediments have been transported over long distances, whereas carbonates are formed on-site (mostly marine). Clastic sediments are relatively chemically stable; they form an intergranular pore space. Carbonates on the other hand are chemically unstable; their pore space is very complex and controlled by a variety of influences and pore space geometries.

In addition to the mineral composition for geological characterization of rocks in general and for sedimentary rocks in particular, the term "lithology" is used. The American Geological Institute Glossary of Geology defines lithology as "the

physical character of a rock.” This character is influenced mainly by mineral composition (mineralogy) and texture of the solids (Jorden & Campbell, 1984).

1.4.2 Clastic Rocks

1.4.2.1 Classification

Clastic rocks are formed by:

- erosion, reworking, and transportation of rock components;
- deposition and sedimentation of the material;
- compaction and diagenetic processes.

Typical members of this important group of rocks are conglomerate, sandstone, siltstone, shale, and claystone.¹

The classification in the main types (sandstone, siltstone, and claystone) follows the grain size classification for clastic sediments (Figure 1.3).

The nomenclature of clastic sedimentary rock is given by the following rules:

- Sandstone is composed of >50% sand-sized particles. The mineral composition is dominated by quartz and feldspar.
- Siltstone is composed of >50% silt-sized particles; they are generally less rich in quartz than is sandstone (Jorden & Campbell, 1984).
- Claystone is composed of >50% clay-sized particles; they are generally formed by clay minerals.

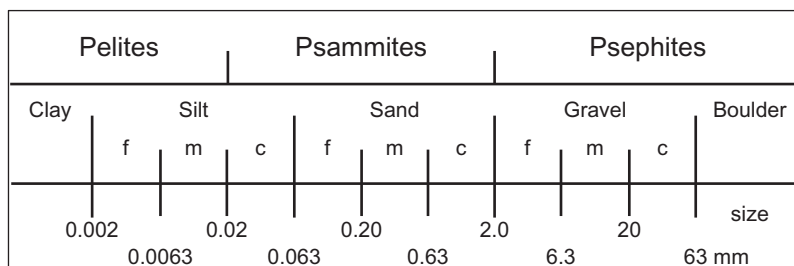


FIGURE 1.3 Classification of clastic sediments according to grain size: f, fine; m, medium; c, coarse. The terms psephites, psammites, and pelites are defined for more than 50% weight of the corresponding grain size range.

¹It may be noted that in addition to this main group of clastics (epiclastics), some specific types also exist as, for example, cataclastics (till) or pyroclastics (tuffs).

The term “shale” describes a sedimentary rock type which is a mixture of clay-sized particles (mainly clay minerals), silt-sized particles (quartz, feldspar, calcite), and perhaps some sand-sized particles as, for example, quartz, occasionally feldspar, calcite (Jorden & Campbell, 1984). Serra (2007) wrote “from a compilation of 10,000 shale analyses made by Yaalon (1962), the average composition of shale is 59% clay minerals, predominantly illite; 20% quartz and chert; 8% feldspar; 7% carbonates; 3% iron oxides; 1% organic material; and others 2%. . . . Mudstone is a rock having the grain size and composition of a shale but lacking its laminations and/or its fissility” As an example, for Pierre shale, Borysenko et al. (2009) gave the following mineral composition: quartz 29%; kaolinite, chlorite 8%; illite, muscovite, smectite 26%; mica 24%; orthoclase, dolomite, albite 13%.

Many properties of shale are controlled by the clay components (e.g., gamma radiation, electrical properties, cation exchange capacity (CEC), neutron response, permeability). For understanding physical properties of sedimentary rocks it is important to distinguish the different terms referred to as shale and clay:

- clay describes a group of minerals (hydrous aluminum silicates, see [Section 1.4.2.3](#));
- clay also defines a particle size ($<0.002\text{ mm}$);
- shale describes a rock type as defined above (“claystone” also refers to a rock type).

The physical properties of clastic sediments are strongly controlled by:

- textural properties (particle dimensions, size, shape, spatial orientation);
- mineral composition, mainly the presence and effect of clay minerals.

1.4.2.2 *Textural Properties—Grain-Size Parameters*

The term texture encompasses particle size and size distribution, and shape and packing of the solid particles in clastic sediments.

Grain size is the classifying and defining parameter for clastic rocks. In general, particles are of nonspherical shape; thus the “grain diameter” depends on the technique of its determination:

- sieve analysis gives an estimate closed to the minimum cross-sectional axis (corresponding to the used mesh size) or a sphere equivalent measure following Stokes’ law (sedimentation analysis);
- image or laser scanned techniques allow the application of numerical algorithms for a representative size description.

Grain size d frequently is given in millimeters or in micrometers ($1\text{ }\mu\text{m} = 1\text{ micron} = 10^{-3}\text{ mm}$). The phi-scale is also used

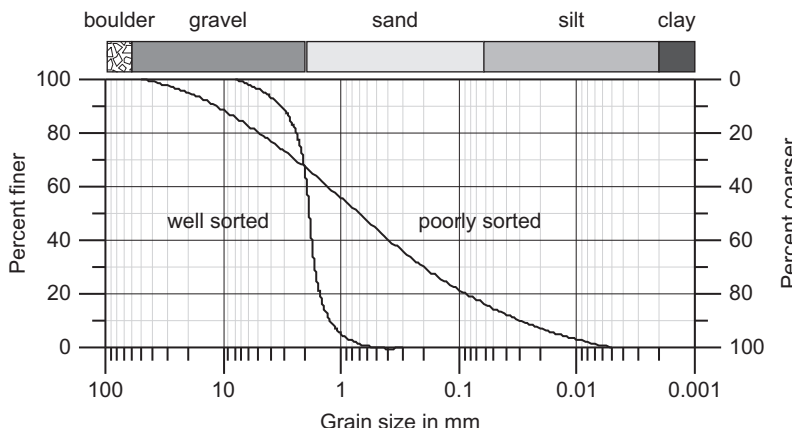


FIGURE 1.4 Grain size distribution curve for two sediments.

$$\text{phi} = -\log_2(d) \quad (1.1)$$

where d is in millimeters.

Rocks show a distribution of grain sizes. This is described normally by a cumulative distribution curve (grain size distribution curve). [Figure 1.4](#) gives an example.

From the grain size distribution various statistical measures or parameters can be derived using defined percentiles referred to as the cumulative weight-percent (weight %):

- Median grain size gives the midpoint of the curve at d_{50} (grain size in millimeters of 50th percentile).
- Grain sorting describes how narrow the distribution is to a single grain size $S_0 = (d_{25}/d_{75})^{0.5}$, where d_{25} is the grain size (mm) of 25th percentile and d_{75} the grain size (mm) of 75th percentile.
- Skewness expresses the symmetry of distribution $S_k = (d_{25} \cdot d_{75} / d_{50}^2)$.

Grain shape (sphericity) describes how nearly a particular grain approaches the shape of a sphere. Grain roundness (angularity) measures the sharpness of edges and corners. Comparison charts are used for both properties.

Grain packing is a measure of the density of the grain aggregates. In terms of physical properties, the spatial arrangement of the individual particles can be defined as internal structure—it controls, for example, anisotropy properties.

1.4.2.3 Some Fundamental Clay Properties

Particularly in logging practices, the terms shale and clay are used interchangeably; the difference was previously discussed in [Section 1.4.2.1](#). Shale is a fine-grained rock; it contains a fraction of clay minerals and silt.

Clay minerals are aluminosilicates with a sheet structure. The principal building elements are two types of sheets or units:

- a tetrahedral unit of a central Si atom and surrounding O atoms;
- an octahedral unit of O atoms and OH groups around a central Al atom.²

Clay minerals (kaolinite, illite, montmorillonite, chlorite) are characterized by different stacking combinations or “architecture” of the two building elements (Figure 1.5). Individual figures always represent one crystal.

Montmorillonite has a water layer between the two units; the amount of water varies so that the size also ranges between $9.7 \cdot 10^{-10}$ and $17.2 \cdot 10^{-10}$ m (9.7 and 17.2 Å). Water trapped between the units or layers influence electrical conductivity (see Section 8.5) and contributes to total porosity (but not to effective porosity).

In the tetrahedral sheet, silica (Si^{+4}) is sometimes partly replaced by aluminum (Al^{+3}); in the octahedral sheet, aluminum (Al^{+3}) can be replaced by magnesium (Mg^{+2}) or other atoms (e.g., iron). Such a replacement by atoms of lower positive valence results in an excess of negative charge. This excess is compensated for by adsorption of cations (Na, Ca, Mg) from the adjacent water and an electric double layer is formed. The compensating cations on the surface layer can be exchanged by other cations. The number of the exchangeable cations is measured by the Cation Exchange Capacity (CEC). Montmorillonite has a high CEC value, but kaolinite and chlorite without interlayer cations have low CEC. Clays with high CEC play a leading role in the electrical conduction of shales and shaly sands (see Section 8.5). The ability of clay minerals to adsorb ions results in case of “radioactive ions” in a contribution to natural radioactivity (see Section 5.2) (Table 1.2).

The effect of clay minerals in the rock depends on the mineral properties and the type of clay distribution. There are three fundamental types:

1. Dispersed: clay is formed within the sediment when clay crystals precipitate from pore fluids.
2. Laminated: clay is of detrital origin, that is, formed outside the sandstone framework.
3. Structural: clay is of diagenetic origin, that is, formed within the sandstone framework as a deposit of clay clasts.

1.4.3 Carbonate and Evaporate Rocks

1.4.3.1 Introduction

The nonclastic carbonate and evaporate rocks are formed mainly by chemical and biochemical precipitation in special environments (typically warm, shallow, clear marine water in low latitudes).

²In some cases also Mg or Fe.

Clay building blocks	
Silica tetrahedral sheet	
Alumina octahedral sheet (Gibbsite, Brucite)	
Montmorillonite $(Ca,Na)_7(Al,Mg,Fe)_4(Si,Al)_8O_{20}(OH)_4$ density = 2.33 g cm^{-3}	 unit layer $9.7 \dots 17.2 * 10^{-10} \text{ m}$ n-H ₂ O & Mg, Na, Ca
Illite $K_{1-1.5}Al_4(Si_{7.0-6.5}Al_{1-1.5}O_{20}(OH)_4$ density = 2.76 g cm^{-3}	 unit layer $10 * 10^{-10} \text{ m}$ K K
Chlorite $(Mg,Al,Fe)_{12}(Si,Al)_8O_{20}(OH)_{16}$ $(Mg,Al,Fe)_6(Si,Al)_{4\circ 10}(OH)_8$ density = 2.77 g cm^{-3}	 unit layer $14 * 10^{-10} \text{ m}$
Kaolinite $Al_4(Si_4O_{10})(OH)_8$ density = 2.69 g cm^{-3}	 unit layer $7.2 * 10^{-10} \text{ m}$

FIGURE 1.5 Clay minerals and some clay mineral properties. Compiled after Jorden and Campbell (1984).

A fundamental description of carbonates and their properties is given in the textbook written by Lucia (1999, 2007). Regarding the need to understand carbonate reservoirs better, a special section on carbonates appears in the May 2005 issue of *The Leading Edge*. For log interpretation problems, Akbar et al. (1995, 2000) gave an overview.

With respect to its abundance and economical importance, it is of interest that “though carbonate rocks make up only 20% of the sedimentary rock record, carbonate reservoirs hold 60% of the world’s petroleum reserves . . .” (Chopra et al., 2005).

TABLE 1.2 Typical Values for Clay Mineral Properties (Ellis & Singer, 2007)

Clay Mineral	Specific Internal Surface in $\text{m}^2 \text{ g}^{-1}$	CEC in meq/100 g	Wet Clay Porosity in p.u.
Smectite/ Montmorillonite	700–800	80–150	40
Illite	113	10–40	15
Chlorite	42	10–40	15
Kaolinite	15–40	3–5	5

Note the trend: with increasing specific surface (see Section 2.3) CEC and wet clay porosity increases. p.u., porosity units.

1.4.3.2 Composition

Carbonates originated autochthonous (formed very close to the depositional site) whereas clastics sandstone and shale are formed of transported sedimentary particles mostly from sources outside the depositional site.

The most abundant carbonatic minerals are calcite (CaCO_3) and dolomite ($\text{CaMg}(\text{CO}_3)_2$). Secondary minerals are anhydrite, chert, and quartz. Accessory minerals are phosphates, glauconite, ankerite, siderite, feldspars, clay minerals, pyrite, etc., depending on the environment of deposition and diagenetic history.

The two main rock types are as follows:

1. Limestone: composed of more than 50% carbonates, of which more than half is calcite.
2. Dolomite: composed of more than 50% carbonates, of which more than half is dolomite. Dolomite can precipitate directly from a solution containing Mg, Ca, and carbonate ions or by chemical alteration of limestone or calcareous mud (dolomitization). Dolomite frequently forms larger crystals than the calcite it replaces (Al-Awadi, 2009) and forms good reservoir properties.

Carbonates are modified by various postdepositional processes such as dissolution, cementation, recrystallization, dolomitization, and replacement by other minerals. Dolomitization is connected with an increase of porosity.

The interaction with meteoric pore fluids can result in a leaching of grains and influence reservoir quality in both directions (new pore space, cementation).

Fracturing as a result of stress and stylolithification are diagenetic processes in carbonates; they can create high-permeability zones and permeability barriers or baffles.

Evaporate sediments are a special type of sedimentary rock that is formed from the concentration of dissolved salts through evaporation (e.g., rock salt/halite).

1.4.3.3 Classification

Carbonates are biologically deposited and contain fossil fragments and other particles with complicated morphology and shape. This results in complex pore structures in general. Dissolution, precipitation, recrystallization, dolomitization, and other processes increase this complexity over scales.

Different types of porosity and complex pore size distributions also result in wide permeability variations for the same total porosity, making it difficult to predict their producibility. Therefore, the analysis of carbonate pore geometries is the key to characterize the reservoir properties of this group of rocks.

For carbonates, two main types of classification have been developed:

1. Textural classification (Dunham, 1962) based on the presence or absence of lime mud and grain support and ranges from:
 - a. grain-supported grainstones, mudstones, and packstones to;
 - b. mud-supported wackestones and mudstones;
 - c. crystalline or boundstones.
2. Fabric selective and nonfabric selective pore type classification (Choquette & Pray, 1970) including:
 - a. fabric selective (interparticle, intraparticle, intercrystal, moldic, fenestral, shelter, and framework);
 - b. nonfabric selective (vug and channel, cavern, and fracture) porosity.

In his fundamental description of carbonatic rocks, Lucia (1983, 1999, 2007) gives the classification as presented in [Figure 1.6](#).

The complex pore system of carbonate reservoirs ranges from microcystalline pores to large vugs or caverns. The petrophysical characteristics are

Classification (Lucia 1983)		
Interparticle	Vuggy	
	Separate	Connecting
Pore types		
Intergrain intercrystal	Moldic Intrafossil Shelter	Cavernous Fracture Solution-enlarged fracture

FIGURE 1.6 Petrophysical classification of carbonate pore types, based on Lucia (1983, 1999, 2007).

controlled by connected networks of interparticle pores (matrix), vuggy pore space, and fractures, where:

- a matrix occupies the major portion of the reservoir, stores most of the fluid volume but has a low permeability;
- fractures (and vugs) occupy a small portion of reservoir volume but have high permeability and control the fluid flow (Iwere et al., 2002).

A classification and description of carbonate pore geometries is also given in Schlumberger's "Carbonate Advisor" (www.slb.com/carbonates) as follows:

- "Micropores, with pore-throat diameters $<0.5\text{ }\mu\text{m}$, usually contain mostly irreducible water and little hydrocarbon.
- Mesopores, with pore-throat diameters between 0.5 and $5\text{ }\mu\text{m}$, may contain significant amounts of oil or gas in pores above the free-water level (FWL).
- Macropores, with throats measuring more than $5\text{ }\mu\text{m}$ in diameter, are responsible for prolific production rates in many carbonate reservoirs, but often provide pathways for early water breakthrough, leaving considerable gas and oil behind in the mesopores above the FWL.
- Vugs are cavities, voids, or large pores in rocks. Vugular porosity is common in rocks prone to dissolution, such as carbonates."

1.4.4 Comparison of Siliciclastic and Carbonate Sediments

In siliciclastic rocks, many physical properties (elastic wave velocity, electrical resistivity, permeability) show a strong correlation to porosity. In carbonate rocks, correlations are controlled or superimposed by the heterogeneous pore distribution, pore type, pore connectivity, and grain size (Westphal et al., 2005).

[Table 1.3](#) compares some prominent properties of the two main groups of reservoir rocks.

1.5 PHYSICAL PROPERTIES OF ROCKS—SOME GENERAL CHARACTERISTICS

The term "petrophysics" was created for physics of reservoir rocks. "Petrophysics" is suggested as the term pertaining to the physics of particular rock types. ... This subject is a study of the physical properties of rock which are related to the pore and fluid distribution ..." (Archie (1950), the

TABLE 1.3 Some Prominent Properties of Siliciclastic and Carbonate Rocks

Clastic Rocks	Carbonate Rocks
	
<i>Origin:</i> Largely inorganic transported material (particles), deposited in dirty water	Largely organic material, accumulated in place, deposited in clean water
<i>Mineral composition:</i> Broad variety Quartz, feldspar, clay minerals; minor diagenetic change	Relatively simple Dominant calcite and dolomite major diagenetic change
<i>Porosity:</i> Relatively simple intergranular pore structure, porosity predictable	Complex interparticle and intercrystal porosity, fractures, vugs, ... porosity difficult to predict
<i>Influences on porosity:</i> With diagenesis and geological processes, a more complicated pore system results; it is influenced and formed by compaction, cementation, solution/dissolution, clay-filling, fracturing	With diagenesis and geological processes, a very complicated pore system results; it includes vugs, channels/caverns; it is influenced and formed by compaction, cementation, solution, grain growth, shrinking (dolomitization), cavity-filling, fracturing

pioneer in the application and quantification of rock physical relations to geosciences and petroleum engineering).

Rocks in most cases are heterogeneous composite materials; only monomineralic rocks like rock salt or anhydrite contain only one mineral type. Heterogeneity becomes more contrasted if pores and fractures, filled

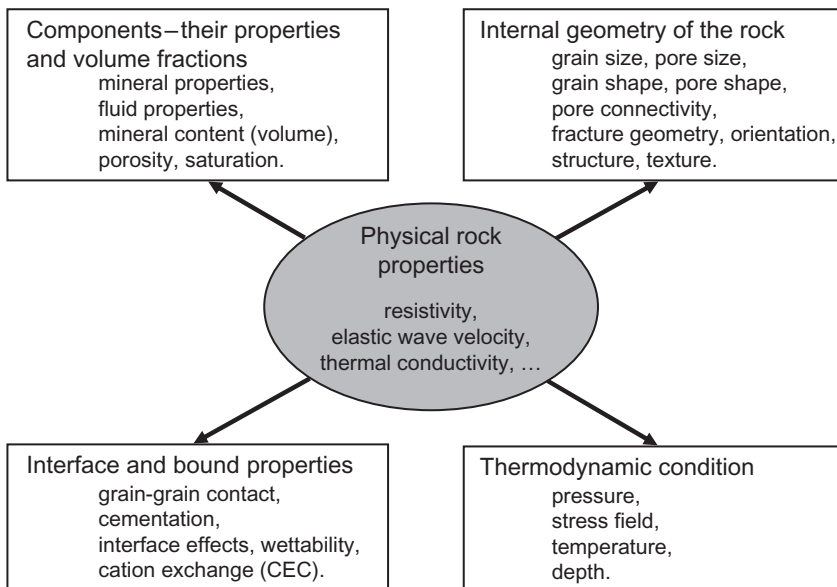


FIGURE 1.7 Rock properties and their main influence parameters and dependencies.

with fluids, are present. Mineral composition, porosity/fracturing, and internal rock structure therefore influence the physical rock properties (Figure 1.7).

On the other hand, physical rock properties (e.g., elastic, electrical, nuclear properties) can be used to characterize rocks with respect to properties and parameters of interest (e.g., reservoir properties, geomechanical properties). This leads to a classification of rock properties into the following two main groups:

- Properties of direct interest for application: reservoir properties (porosity, saturation, permeability), geomechanical properties (deformation, strength), mineralogical characteristics (shale content, fractional mineral composition), content of substances of interest (ore content);
- Properties relevant to the various geophysical methods (elastic/seismic properties, density, electrical properties, nuclear properties, nuclear magnetic resonance (NMR) response).

“Properties of interest” are subjects of interpretation of geophysical data from surface and borehole measurement. This interpretation is a process of transformation of the second type into the first using additional input information. For the transformation, relationships are applied resulting from:

- empirical correlations (e.g., Archie’s equation);

TABLE 1.4 Physical Rock Properties: Classification

Type	Scalar Properties	Tensorial Properties
Properties of direct interest for reservoir and geotechnical application	Porosity Fluid saturation	Permeability Deformation modulus Strength properties
Properties measured by geophysical methods	Density Nuclear cross sections (Gamma–Gamma Density, Neutronlog) Natural Gammalog NMR response	Elastic properties/ wave velocities Electrical properties Thermal properties Magnetic properties

- model-based theories (e.g., Gassmann's equation for fluid substitution, capillary pore channel models); in most cases "theoretical" equations need an empirical modification or calibration with experimental data.

In this book, the most frequently used properties are described. For the physics behind the individual properties, it is important to characterize them with respect to their character as a "scalar property" (given as one value for the property, no directional dependence of the property) or a "tensorial property" (given as a tensor with several components with directional dependence). [Table 1.4](#) gives an overview to the properties.

Tensorial character is relevant for rocks with an anisotropy (originated by lamination, preferred direction of fractures, grain axis or mineral orientation, etc.). The terms isotropy and anisotropy refer to directional dependence of considered (tensorial) properties. Isotropic expresses that a vectorial property has at any point the same magnitude for all directions; if the magnitude shows a directional dependence, then the material is anisotropic.

Another set of terms is important: homogeneity and inhomogeneity. Homogeneity expresses that any property (scalar or vector) is the same at different points (locations) within the volume; if the properties have different values, then the material is inhomogeneous or heterogeneous.

In rocks we find all four combinations as schematically presented in [Figure 1.8](#).

Both anisotropy and heterogeneity are terms connected with the scale of consideration and definition of a property. A small sample size (core, plug)

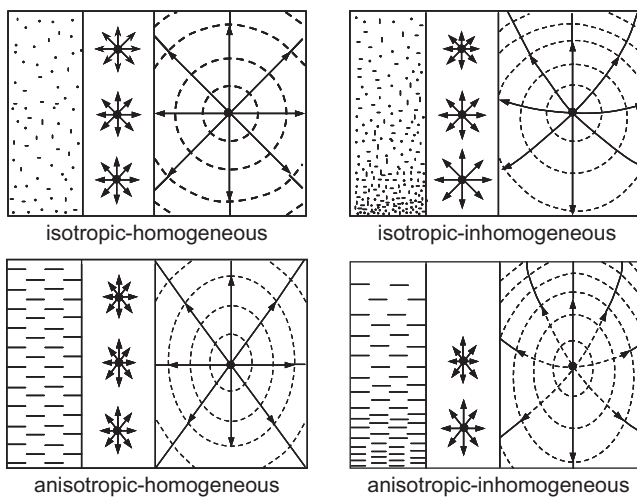


FIGURE 1.8 The categories “homogeneous–inhomogeneous” and “isotropic–anisotropic” after Gassmann (1964).

from a sandstone layer may be homogeneous, whereas a sandstone bed with variation of grain size, shale content, etc. is heterogeneous. The scale is also fundamental for anisotropy. A typical example is a laminated sand; it may be that the individual small layers are isotropic, but a section as resolved by an electrical logging tool “sees” an anisotropy (macroscopic anisotropy, see Section 8.6).

Pore Space Properties

2.1 OVERVIEW—INTRODUCTION

Pore space characterization is based on defined reservoir properties (e.g., porosity and permeability). Pore space properties are important for the description and characterization of pore volume and fluid flow behavior of reservoirs. Laboratory techniques (standard and special core analysis) deliver fundamental properties; thin sections and microscopic or scanning electron microscopic (SEM) investigations are used for description and computer-aided analysis. Sophisticated techniques result in “digitized core images” (Arns et al., 2004; Kayser et al., 2006) and the development of a “virtual rock physics laboratory” (Dvorkin et al., 2008).

The fundamental reservoir properties of the pore space describe:

- volume fractions of the fluids (porosity, saturation, bulk volume of fluids);
- properties controlling fluid distribution in the pore space (capillary pressure, specific internal surface, and wettability);
- properties controlling fluid flow under the influence of a pressure gradient (permeability).

There are relationships between properties: permeability, for example, correlates with porosity.

Important pore geometrical controlling parameters are the pore body size, which defines the average volumetric dimensions of the pores, and the pore throat size, which is the controlling factor in transmissibility/permeability.

2.2 POROSITY

Porosity is a fundamental volumetric rock property: it describes the potential storage volume of fluids (i.e., water, gas, oil) and influences most physical rock properties (e.g., elastic wave velocity, electrical resistivity, and density).

Porosity can be determined directly by various laboratory techniques and indirectly by logging methods.

2.2.1 Definitions

“Porosity is the fraction of rock bulk volume occupied by pore space” (Jorden & Campbell, 1984).

Thus, porosity is defined as the summarized volume of all pores, fractures, cracks, etc., or generalized all fluid (e.g., gas, water, hydrocarbons) or “nonsolid” containing parts of a sample related to the total volume of the sample (Figure 2.1):

$$\phi = \frac{\text{volume of pores}}{\text{bulk volume}} = \frac{\text{bulk volume} - \text{volume of solid minerals}}{\text{bulk volume}} \quad (2.1)$$

Porosity is given as a volume fraction (dimensionless) or as percentage.

The definition above describes the “total porosity”. If the rock contains a part of nonconnected or separated pores (vugs, moldic pores, etc.), then this part does not contribute to any fluid transport within the rock and is “noneffective.” Thus, effective or interconnected porosity is the ratio of the connected pore volume and the total rock volume.

For reservoir description it is important to distinguish between:

- total porosity, the fraction of bulk volume occupied by total pore space;
- effective porosity, the fraction of bulk volume occupied by interconnected pore space.

Amyx et al. (1960) define total porosity as “... the ratio of the total void space in the rock to the bulk volume of the rock; effective porosity is the ratio of the interconnected void space in the rock to the bulk volume of the rock ...”

The following are applied in order to determine porosity:

- direct measurements (laboratory) based on determination of bulk and solid volume, gas expansion, or displacement techniques;
- indirect measurements (logging methods, seismic methods) based on correlation between porosity and properties like density, neutron response, and seismic wave velocity. Porosity can also be derived from NMR measurements (see Section 3).

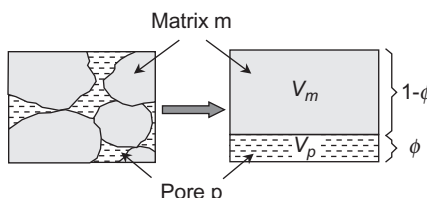


FIGURE 2.1 Definition of porosity.

TABLE 2.1 Summary of Porosity Terms

Porosity Type	Pore Volume	Measurement Technique
Primary porosity	Void volume of a sediment when it was deposited	
Secondary porosity	Void volume that is created by diagenetic processes	
Total porosity (not necessarily connected)	Total void volume. CBW is included in pore volume	Core analysis (disaggregate sample) Density, neutron, NMR logs if dry clay parameters used to derive porosity
Effective porosity (connected)	Void volume contactable by fluids (connected). CBW is included in pore volume	Core analysis (competent sample) Possibly acoustic/sonic log
Effective porosity (log analysis)	Void volume available for storage of hydrocarbons. CBW is excluded from pore volume Unconnected pore volume not necessarily excluded from pore volume. Depends on measurement technique	Porosity logging tools if wet clay parameters used to derive porosity
Effective porosity (usually in reservoir simulations)	Void volume available for storage of producible fluids. CBW is excluded from pore volume Capillary-bound water is also excluded from pore volume	No direct technique to measure this. This definition implies that the effective porosity of a rock is a function of its location within a reservoir

Source: Hook (2003).

In his tutorial “An Introduction to Porosity,” Hook (2003) gave a detailed explanation of porosity terms as they are used in different disciplines (Table 2.1).

Pore size can be classified as shown in Table 2.2 after a compilation of Mann et al. (1977).

Clastic and carbonate reservoir rocks have different pore types; therefore a separate discussion of the two main types is useful.

2.2.2 Porosity of Clastic Rocks

In clastic sediments, pre-diagenetic factors control “primary porosity”: grain size and grain size distribution, grain packing, and particle shape.

TABLE 2.2 Pore Size Classification

Type of Pore	Size (Diameter) d	Type of Pore	Size (Diameter) d
Rough pore	$d > 2 \text{ mm}$	Macropore	$50 \text{ nm} > d > 2 \text{ nm}$
Macrocapillary	$2 \text{ mm} > d > 50 \mu\text{m}$	Mesopore	$2 \text{ nm} > d > 0.8 \text{ nm}$
Capillary	$50 \mu\text{m} > d > 2 \mu\text{m}$	Micropore	$0.8 \text{ nm} > d$
Microcapillary	$2 \mu\text{m} > d > 50 \text{ nm}$		

Source: After a compilation of Mann *et al.* (1977).

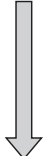
Decreasing porosity  High porosity marine sediments, unconsolidated sediments, sandstone, carbonate (limestone-dolomite), anhydrite, fractured igneous and other initially "dense" rock types

FIGURE 2.2 Tendency of decreasing porosity related to a series of rocks.**TABLE 2.3** Mean Porosity (in %) for Selected Clastic Rocks

Rock Type	Minimum Porosity	Maximum Porosity
St. Peter sandstone	3.6	14.1
Berea sandstone (depth 439–458 m)	4.7	17.1
Bunter sandstone	7.7	26.4
Fontainebleau sandstone	6.8	22.4
Shale, Venezuela		
Depth 89–281 m	31.3	35.8
619–913 m	22.9	28.9
919–1,211 m	17.8	25.6
1,526–1,677 m	12.8	14.6
2,362–2,437 m	10.3	10.4

Source: Data from Schopper (1982).

“Secondary porosity” is the result of mechanical processes (compaction, plastic and brittle deformation, fracturing) and geochemical processes (dissolution, precipitation, volume reductions by mineralogical changes, etc.).

For an overall view, Figure 2.2 shows the tendency of decreasing porosity related to a series of typical rocks.

For selected clastic rocks, Table 2.3 shows some mean porosity data.

TABLE 2.4 Porosity of Artificially Mixed Wet-Packed Unconsolidated Sand

Sorting	Average Porosity	Standard Deviation
Extremely well	0.424	0.008
Very well	0.408	0.006
Well	0.390	0.008
Moderate	0.340	0.010
Poor	0.307	0.018
Very poor	0.279	0.028

Source: Data from Beard and Weyl (1973).

The strong influence of sorting was demonstrated by experiments of artificially mixed wet-packed sand by Beard and Weyl (1973). [Table 2.4](#) shows the decrease of porosity from well-sorted to poorly sorted sediments as a result of pore space filling by fine components.

In sedimentary areas, porosity decreases nonlinearly with depth as a result of *compaction*. The controlling property for the compaction in this process is the mean effective stress. The first empirical formulation is probably that of Athy (1930):

$$\phi(z) = \phi_0 \cdot \exp(-b \cdot z) \quad (2.2)$$

where

ϕ_0 is the porosity at reference depth ($z = 0$)

z is the actual depth

b is a parameter characterizing the compressibility of the sediment.

In a plot, $\log \phi$ versus z , this correlation represents a straight line ([Figure 2.3](#)).

Liu and Roaldset (1994) (also Sclater & Christie, 1980) analyzed porosity versus depth relationships for sandstone and shale from the Northern North Sea using different types of equations. Examples are sandstone:

$$\phi = 0.49 \cdot \exp(-2.7 \cdot 10^{-4} \cdot z) \quad (2.3)$$

$$\phi = 0.728 - 2.719 \cdot 10^{-4} \cdot z + 2.604 \cdot 10^{-8} \cdot z^2 \quad (2.4)$$

shale:

$$\phi = 0.803 \cdot \exp(-5.1 \cdot 10^{-4} \cdot z) \quad (2.5)$$

$$\phi = 0.803 - 2.34 \cdot 10^{-4} \cdot z + 2.604 \cdot 10^{-8} \cdot z^2 \quad (2.6)$$

where the depth z is in meters and the porosity ϕ is a fraction.

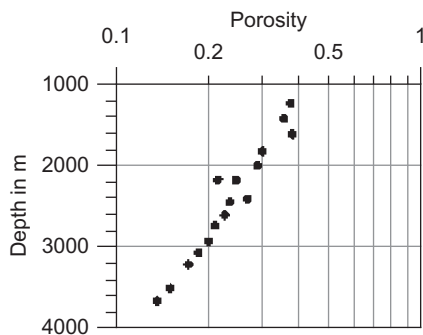


FIGURE 2.3 Plot $\log\phi$ versus z for a sandstone. Data from Nagumo (1965).

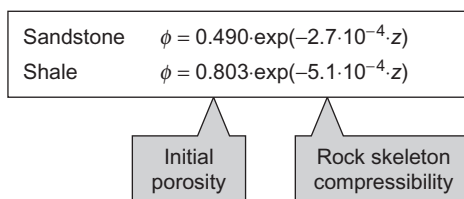


FIGURE 2.4 Porosity as a function of depth and initial porosity.

The two exponential equations allow the following interpretation (Figure 2.4):

- the initial porosity is 0.49 for the sand (this is a loose packing of grains), but for shale, as a result of the high porous structure of the clay component, much higher and in the order of 0.80;
- the rock skeleton of the shale is softer than the sand rock skeleton. Thus, the parameter describing the compressibility is $5.1 \cdot 10^{-4} \text{ m}^{-1}$ for shale and $2.7 \cdot 10^{-4} \text{ m}^{-1}$ for sand.

Figure 2.5 describes the mechanical compaction process in a schematic diagram. Avseth et al. (2005) formulate as rules of thumb for compaction and following cementation: “(1) The depositional porosity of shale is normally higher than that of sand. (2) The porosity gradient with depth is steeper for shale than for sand during mechanical compaction (i.e., at shallow depths). (3) The porosity gradient with depth will be steeper for sand than for shale during chemical compaction (i.e., quartz cementation of sands normally occurs at greater burial depth, beyond 2–3 km).”

The diagram refers to the compaction process. Compaction is the irreversible volume reduction due to different processes mainly by:

- effective pressure due to overburden sediments (compressibility of rock skeleton);

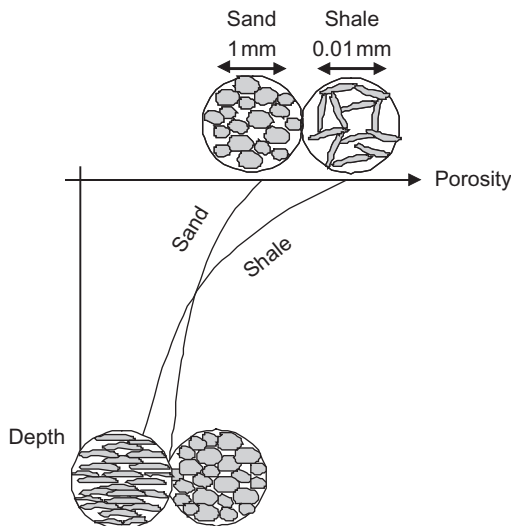


FIGURE 2.5 Compaction process for sand and shale.

- drainage of pore fluids (permeability and time influence);
- grain rearrangement (packing).

Poelchau et al. (1997) compiled porosity-depth curves for sandstone, shale, and limestone from published sources. They give the following ranges for the initial porosity:

- sandstone 0.25–0.55,
- shale 0.50–0.90,
- limestone 0.40–0.95; particularly 0.44–0.55 for grainstone and packstone, 0.70–0.95 for deep sea calcareous ooze.

Rowan et al. (2003) derived porosity-depth profiles from log data of 19 offshore wells. For the three main sediment groups—sand, silt, and shale—they used the shale content V_{sh} from a gammalog as a parameter for classification. The following mean equations result:

$$\text{for sand } (V_{sh} < 0.01) \quad \phi = 0.50 \cdot \exp(-0.29 \cdot z) \quad (2.7)$$

$$\text{for silt } (0.495 < V_{sh} < 0.505) \quad \phi = 0.44 \cdot \exp(-0.38 \cdot z) \quad (2.8)$$

$$\text{for shale } (V_{sh} > 0.9) \quad \phi = 0.40 \cdot \exp(-0.42 \cdot z) \quad (2.9)$$

Baldwin and Butler (1985) derived so-called “solidity versus depth” relationships, where the solidity is the complement to porosity.

With a simple calculation experiment the exponential porosity versus pressure relationship can be derived as follows.

An effective pressure p compresses the porous rock, and porosity ϕ decreases. Assuming that porosity decrease is proportional to the difference

between existing porosity ϕ and porosity at the end of compaction process ϕ_c (“residual porosity,” Revil et al., 2002) results in

$$\left(-\frac{d\phi}{dp} \right) = c(\phi - \phi_c) \quad (2.10)$$

where c is a factor controlled by rock compressibility.

The differential equation

$$\frac{d\phi}{\phi - \phi_c} = -c \cdot dp \quad (2.11)$$

has the solution

$$\phi(p) = \phi_c + (\phi_0 - \phi_c) \cdot \exp(-c \cdot p) \quad (2.12)$$

where

$\phi(p)$ is the actual porosity at effective pressure p

ϕ_c is residual porosity (at $p \rightarrow \infty$)

ϕ_0 is initial porosity at $p = 0$.

If pressure is originated by burial depth z and density ρ of overburden, the [Equation \(2.12\)](#) is

$$\phi(z) = \phi_c + (\phi_0 - \phi_c) \cdot \exp(-c \cdot \rho \cdot g \cdot z) \quad (2.13)$$

with g Earth’s acceleration.

This compaction model demonstrates:

- Athy’s empirical equation results for $\phi_c \rightarrow 0$,
- that the empirical exponent in [Equation \(2.2\)](#) is controlled by the deformation properties and the density of the overburden.

Revil et al. (2002) derived a regression for shale (Oman abyssal plain) ([Figure 2.6](#))

$$\phi = 0.07 + 0.49 \cdot \exp(-6.3 \cdot 10^{-8} \cdot p) \quad (2.14)$$

where p is in Pa. This corresponds exactly to the model-derived type of [Equation \(2.13\)](#) with $\phi_c = 0.07$ and $\phi_0 = 0.56$.

Goult (1998) also derived relationships between porosity and effective stress for shales.

Porosity frequently is modeled by sphere packings. [Figure 2.7](#) shows the model of a clastic sediment (sand, sandstone) as regular sphere packing. In [Figure 2.7](#) the simplest geometry is used: a cubic packing.

The porosity is determined through the porosity definition ([Equation \(2.1\)](#)):

$$\phi_{\text{cubic pack}} = \frac{(2 \cdot R)^3 - \frac{4}{3} \cdot \pi \cdot R^3}{(2 \cdot R)^3} = 1 - \frac{\pi}{6} \approx 0.48 \quad (2.15)$$

This is in remarkable agreement with initial porosities for sand.

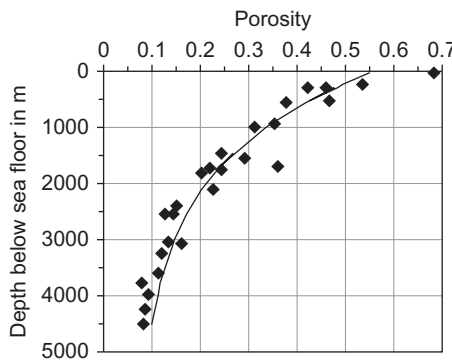


FIGURE 2.6 Compaction of shale after Revil et al. (2002). Field data are from Fowler et al. (1985).

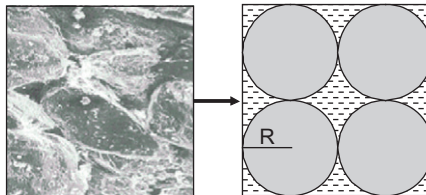


FIGURE 2.7 Model of a cubic sphere pack.

TABLE 2.5 Porosity ϕ and Coordination Number C of Regular Sphere Packings

Geometry	Porosity ϕ	Coordination Number C
Cubic	0.48	6
Orthorhombic (simple hexagonal)	0.40	8
Compact hexagonal, rhombohedral	0.26	12

Modeling of other porosities is possibly by varying the lattice geometry. Table 2.5 gives results in terms of porosity and the so-called “contact-” or “coordination number” K (number of contacts with neighbored spheres).

As a result of idealization and assumptions (one grain size only, grain shape is a sphere, texture is like a crystal lattice) the table shows that sphere packings have:

- only discrete porosity values;
- porosity ranges between 0.26 (minimum) and 0.48 (maximum);
- porosity that is independent of sphere diameter.

The minimum porosity of 0.26 or 26% is especially indicative that these models are very limited with respect to real situations.

2.2.3 Porosity of Carbonate Rocks

Porosity of carbonate rocks covers a broad spectrum of types and magnitudes as a result of diversity of processes. Lucia (1999, 2007) notes that porosity in carbonate reservoirs ranges from 1% to 35%. The porosity at deposition is high for carbonates (initial porosity of limestone 0.40–0.95 particularly 0.44–0.55 for grainstone and packstone, 0.70–0.95 for deep sea calcareous ooze; Poelchau et al., 1997).

The following processes of diagenesis result in porosities significantly smaller or greater than the original porosity.

- Postdiagenetic processes: dissolution, cementation, recrystallization, dolomitization, mineral replacement (unstable aragonite in bioclasts and cements converts to more stable magnesium calcite).
- Leaching of grains by meteoric pore fluids results in enhanced reservoir quality through dissolution or decrease of reservoir quality through cementation.
- Burial compaction, fracturing, and stylolitification create both highly permeable zones and barriers.

The classification developed by Lucia (2007) (see Figure 1.6) refers to the pore space properties and distinguishes between:

- pore space located between grains and crystals (interparticle porosity). Interparticle porosity can be described in terms of pore-size distribution or particle-size distribution and
- all other pore space (vuggy porosity). Vugs are commonly present as dissolved grains, fossil chambers, or large irregular cavities.

Vuggy pore space is further subdivided into:

- separate vugs (vugs are interconnected only through the interparticle pores). Separate vugs are fabric selective in their origin (Lucia, 1999, 2007). Intrafossil and moldic pore space are typical;
- touching vugs (vugs form an interconnected pore system). Touching vugs are typically nonfabric selective in origin. Cavernous, breccia, and solution-enlarged fracture pore types commonly form an interconnected pore system (Lucia, 1999, 2007).

Dolomitization is an important geochemical process, where Mg ions replace Ca ions, forming dolomite from calcite:



Replacement of calcite by dolomite increases porosity by 0.13, creates important reservoir space, and the new intercrystalline pores improve the connectivity of the pore network.

Figure 2.8 characterizes schematically the two fundamental pore systems of carbonates.

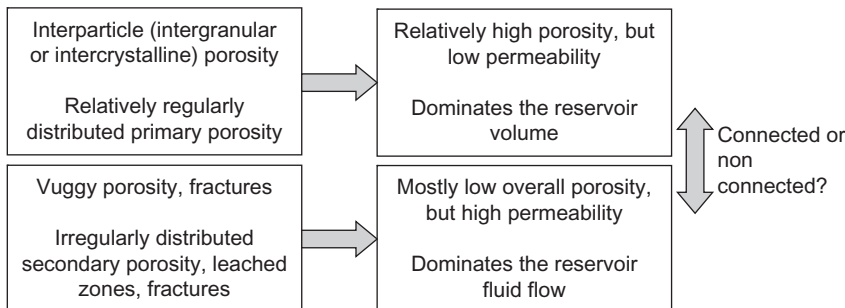


FIGURE 2.8 The two pore networks of carbonates.

Carbonate rocks also show a decrease of porosity under the influence of depth or the overburden pressure, respectively. Brown (1997) analyzed the influence of carbonate mineralogy, shale content, and fabric on the porosity versus depth correlation. For the study, argillaceous limestone, limestone, dolomitic limestone, and dolomite of the Mississippian Madison Group in the Williston Basin were investigated. Figure 2.9 shows the results in a semi-logarithmic plot.

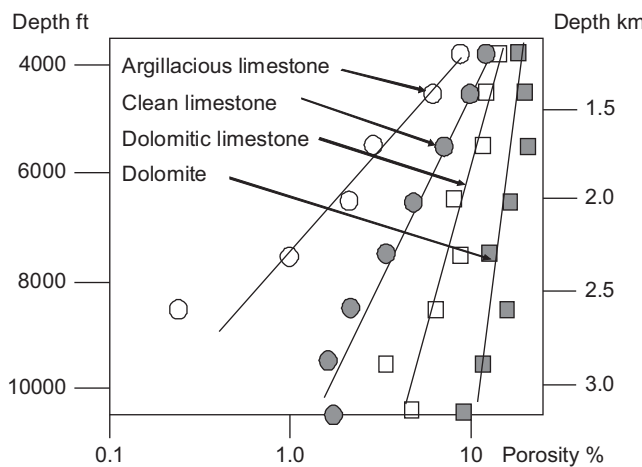


FIGURE 2.9 Porosity versus depth; trends for different lithologies. Data from a figure after Brown (1997).

Argillaceous limestones have lower overall porosity and a faster rate of porosity loss than the clean carbonates at similar depths. Porosity decreases as the clay content of the limestone increases. Figure 2.9 demonstrates:

- that porosity decrease is strongly influenced by mineralogy;

- that clay content increases deformation sensitivity and accelerates porosity loss;
- that (in the example) dolomite shows a higher porosity but a smaller porosity decrease than limestone; the dolomite is more porous but also more rigid than the limestone;
- that straight lines in the semilogarithmic plot indicate in a first approximation an exponential equation.

2.2.4 Fractures, Fractured Rocks

“Fractures are mechanical breaks in rocks; they originate from strains that arise from stress concentrations around flaws, heterogeneities, and physical discontinuities. . . . They occur at a variety of scales, from microscopic to continental.” (Committee on Fracture Characterization and Fluid Flow, US National Committee for Rock Mechanics, 1996).

The effect of fractures on physical rock properties is controlled mainly by:

- fracture geometry (size, aperture, aspect ratio);
- fracture orientation (random or preferred direction);
- roughness of fracture boundaries.

The Committee on Fracture Characterization and Fluid Flow noted that “fracture is a term used for all types of generic discontinuities.” Fracture types can be classified into two groups related to their mode of formation (Bratton et al., 2006):

1. Shear fractures, originated from shear stress parallel to the created fracture. On a big scale, this type corresponds to faults as a result of tectonic events.
2. Tension fractures (extension fractures) originated from tension stress perpendicular to the created fracture. On a big scale, this type corresponds to joints.

Fractures are not only caused by external stress—processes like dolomitization result in volume reduction and create fractures and pore space in the rock. Thermal effects can also create fracturing.

Fractures occur over a broad range of scales. In many cases, the fracture patterns at one scale are similar to patterns at a different scale. This hierarchical similarity is the basis for an upscaling and the quantitative characterization by fractal analysis (Mandelbrot, 1983; Barton & Hsieh, 1989; Turcotte, 1992).

In all types of rocks—igneous, metamorphic, and consolidated sedimentary rocks—fractures may be present. Their origin can be natural or artificial. Fractures have a very strong influence on many rock properties; the occurrence of fractures, for example:

- increases or creates a permeability for fluids;
- decreases dramatically the mechanical strength properties;

- changes elastic wave velocity, electrical resistivity, and thermal conductivity.

If fractures have a preferred orientation, anisotropy of tensorial rock properties result.

Fractures are important for fluid flow in oil, gas, and water production and geothermal processes. In such cases, the fluids are stored mainly in the matrix porosity but produced primarily using fracture permeability (Figure 2.8). Fractures penetrating impermeable shale layers create hydraulic conductivity and can develop a reservoir. Artificial fracturing (hydrofrac) can create new fractures or magnify existing fracture. On the other hand, fractures significantly reduce mechanical rock properties.

Most magmatic (intrusive) and metamorphic rocks have almost no intergranular porosity. Formed by crystallization, the grains intergrow tightly, leaving almost no void space. Typically, granite after formation has a minimal porosity $\phi=0.001$, most of which occurs as small irregular cavities that are remnants of the crystallization process. Tectonic and thermal stresses can create later fractures and cracks—they represent planar discontinuities, occupy a very small volume fraction (low porosity), but can create a connected network and result in permeability.

Volcanic (extrusive) rocks are different. Rapid cooling and pressure decrease can result in porosity. Typical volcanic rocks are porous basalts.

Characterization of fractures is difficult. A volumetric description by fracture porosity in most cases cannot explain the effects. Additional parameters describing geometry and orientation are necessary (e.g., aperture, crack density parameter). Therefore, imaging technologies (acoustic, resistivity) in logging techniques are a very important component for evaluation and detection.

2.3 SPECIFIC INTERNAL SURFACE

Porosity characterizes the volumetric aspect of the pore system. Specific internal surface characterizes the surface area of the pore space or the area of interface solid–fluid. Thus, with the specific internal surface, a second pore-geometrical property is defined and has particular importance for:

- the effects at this interface (e.g., CEC);
- the derivation of model equations for permeability (see Section 2.5.7.2);
- NMR petrophysics (see Chapter 3).

In this section, only the definition and some fundamental properties are discussed.

Pore surface area is normalized by the total sample volume, the pore volume, or the mass and is defined as:

$$S_{\text{total}} = \frac{\text{surface area of the pores}}{\text{total volume}} \quad (2.17)$$

TABLE 2.6 Specific Internal Surface of Some Earth Materials

Material	$S_{\text{mass}} \text{ m}^2 \text{ g}^{-1}$	Material	$S_{\text{mass}} \text{ m}^2 \text{ g}^{-1}$
Quartz spheres 60 μm	0.025	Kaolinite	10–40
Quartz spheres 30 μm	0.05	Illite	30–70
Quartz spheres 2 μm	0.75	Smectite	550–750
Quartz spheres 1 μm	1.5	Gulf Coast shaly sand ($V_{\text{clay}} \approx 15\text{--}30\%$)	100–450
Crushed quartz	3.1		

After Zemanek (1989) and Brooks and Purcell (1952).

$$S_{\text{pore}} = \frac{\text{surface area of the pores}}{\text{pore volume}} \quad (2.18)$$

$$S_{\text{mass}} = \frac{\text{surface area of the pores}}{\text{total mass}} \quad (2.19)$$

$$\text{with the relationships} \quad S_{\text{total}} = S_{\text{pore}} \cdot \phi \quad S_{\text{mass}} = \frac{S_{\text{total}}}{\text{density}} \quad (2.20)$$

Specific internal surface is controlled by:

- size and shape of pores; specific internal surface increases with decreasing particle size;
- microstructure and morphology of the matrix-pore interface.

The magnitude of the specific internal surface depends on the resolution of the method of determination. In most cases, specific internal surface is determined by the BET method (after Brunauer et al., 1938) based on nitrogen gas adsorption with an extremely high resolution (Table 2.6).

2.4 FLUIDS IN THE PORE SPACE—SATURATION AND BULK VOLUME FLUID

The pore space is filled with fluids (normally gas/air, water, oil).¹ If more than one fluid is present, the spatial distribution of the different fluids depends on the physical properties of the rock material, on the fluid properties, and on interactions between the fluids and between fluids and solids (interfacial tension).

¹Under waste site conditions, however, other fluids may also be present.

In this section, only the volumetric or fractional description of different fluids is presented. The factors that control the distribution of immiscible fluids under static conditions are discussed in [Section 2.7](#).

Fluid saturation can be determined as follows:

- from cores, plugs, or samples (direct determination by fluid extraction, capillary pressure measurements);
- indirectly from logs (resistivity, dielectric, neutron measurements, etc.);
- by NMR measurements.

For the description of the volume fraction of a fluid i in a porous rock, the term saturation S_i is used and defined as follows:

$$S_i = \frac{\text{volume of fluid } i}{\text{pore volume}} \quad (2.21)$$

Thus, saturation is the fluid volume, normalized by pore volume. Saturation is given as a fraction or as percentage.

A reservoir with the fluids water, oil, and gas is characterized by three saturation terms and their sum must be 1:

$$S_{\text{water}} + S_{\text{oil}} + S_{\text{gas}} = 1 \quad (2.22)$$

In addition to the parameter “saturation,” the parameter “bulk volume of the fluid” is also used. Bulk volume of a fluid i refers to the volume of that fluid to the rock bulk volume. Bulk volume water is, for example,

$$\text{BVW} = \frac{\text{volume of water}}{\text{rock volume}} = S_w \cdot \phi \quad (2.23)$$

In a (water wet)² porous rock, the water, depending on its interaction with minerals and bonding type, is present as:

- free movable water in the pore space;
- capillary bound water, connected with the grain surface;
- clay-bound water (CBW) with its strong clay–water effects.

The types have different physical properties and effects (e.g., with respect to permeability, electrical resistivity). Therefore, a subdivision into these types is necessary.

The volumetric composition for the two main reservoir rock types is presented in [Figure 2.10](#).

²See [Section 2.6](#).

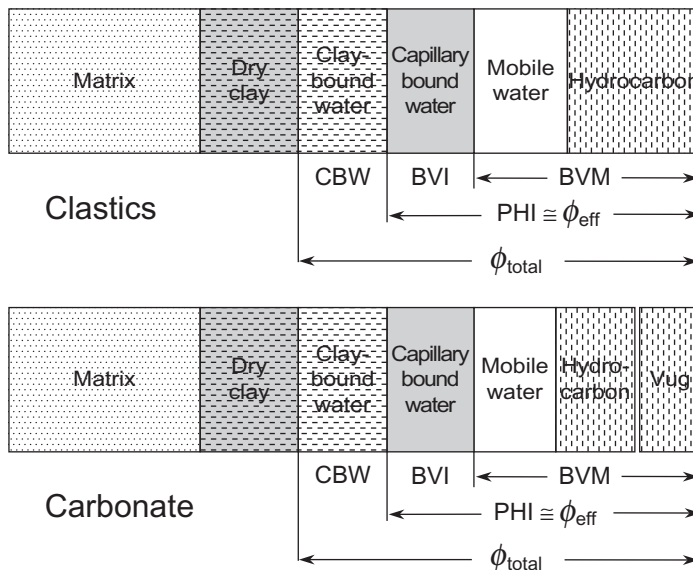


FIGURE 2.10 Volumetric description of a hydrocarbon-bearing clastic and carbonate reservoir. CBW, clay-bound water; BVI, bulk volume irreducible/nonmovable water; BVM, bulk volume movable fluids.

Woodhouse and Warner (2004) proposed a more detailed volumetric model particularly for shaly sands and refer it to the various “porosity methods” of core and log measurements.

Based on experiences with NMR data, Georgi and Chen (2007) recommend a “less rigorous” subdivision in micro, meso and macro pore-space (Figure 2.11) for pore space partitioning.

Schlumberger’s “Carbonate Advisor” (www.slb.com/carbonates) for carbonates defines the cutoffs (see Section 1.4.3.3): microporosity $< 0.5 \mu\text{m}$ $<$ mesoporosity $< 5 \mu\text{m}$ $<$ macroporosity.

2.5 PERMEABILITY

Permeability:

- characterizes the ability of a rock to transmit a fluid; it connects the fluid flow rate with the applied pressure gradient and the fluid viscosity;
- is controlled by the connected passages of the pore space (pore throats);
- is a tensorial property and exhibits, in many cases, anisotropy.

Methods used to determine permeability are:

- direct measurements at samples: cores, core plugs, probe permeameter;

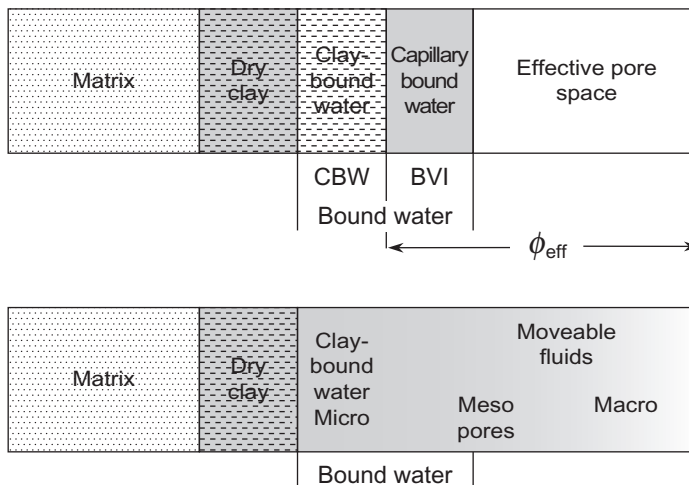


FIGURE 2.11 Generally accepted subdivision of pore volume (upper panel) based on NMR T_2 data. Shown in the lower panel is the less rigorous, micro, meso, and macro pore-space subdivision based on NMR T_2 data (Georgi & Chen, 2007).

- direct tests: well and drillstem tests, wireline formation testers, pump tests;
- indirect methods using grain size parameters (particularly for unconsolidated sediments);
- indirect methods using wireline logs (NMR, Stoneley waves, combined techniques).

2.5.1 Introduction, Definitions

Permeability relates the laminar fluid flow (fluid volume/time) to a macroscopic cross section of a rock, to the viscosity of the fluid, and the fluid pressure gradient. Mobility is the product of permeability and fluid viscosity.

Depending on the fluid composition must be distinguished between:

- absolute permeability (laminar flow of a single nonreactive fluid);
- effective permeability (flow of one fluid in the presence of another fluid, when the fluids are immiscible);
- relative permeability (ratio of effective and absolute permeability).

The term “nonreactive fluids” refers to fluid–rock reactions. Permeability measured in clay-rich rocks, for example, depends strongly on the water salinity. Low-salinity brines cause the clays to swell and reduce permeability (extremely for distilled water).

Figure 2.12 illustrates the principle of laboratory measurement of (absolute) permeability and demonstrates the definition of permeability.

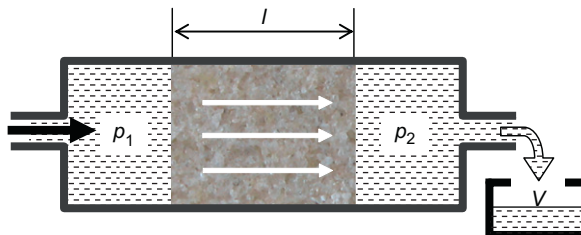


FIGURE 2.12 Permeability measurement—principle.

Fluid flow u is given by Darcy's (1856) law

$$u = \frac{V}{t \cdot A} = - \frac{k}{\eta} \cdot \text{grad } p \quad (2.24)$$

where

u is fluid flow (volume V passing a cross section area A in a time t)

η is dynamic viscosity of the fluid

k is permeability

$\text{grad } p = (p_1 - p_2)/l$ is the macroscopic fluid pressure gradient.³

Permeability results as:

$$k = \eta \cdot \frac{u}{\text{grad } p} \quad (2.25)$$

The permeability has the unit of an area m^2 —in SI units⁴—this explains permeability as a pore geometrical measure. In the oil industry, the Darcy (d) or millidarcy (md) are typical units used with the conversion

$$1 \text{ d} = 0.9869 \cdot 10^{-12} \text{ m}^2 \quad \text{or} \quad 1 \text{ d} \approx 1 \mu\text{m}^2 \quad (2.26)$$

For the laboratory (core) measurement, specific cells (e.g., Hassler cell, see Amyx et al., 1960; Tiab & Donaldson, 2004) are used to measure the fluid flow and control the pressure in order to realize laminar conditions.

Fluid regime is characterized by Reynolds number, Re . The dimensionless Reynolds number is the ratio of the inertial to the viscous forces. Laminar flow occurs at low Reynolds numbers ($\text{Re} < 1-10$), where viscous forces are dominant, and is characterized by smooth, constant fluid motion. Turbulent flow occurs at high Reynolds numbers (>500) and is dominated by inertial forces.

Two effects at the measurements can occur and, if present, must be corrected:

Klinkenberg effect: If gas is used as nonreactive fluid, at low gas pressures the mean free path of gas molecules gets the order of the pore dimensions.

³The “macroscopic” pressure gradient refers to the sample dimension, whereas a “microscopic” pressure gradient refers to the true pore channels length.

⁴Système International d'Unités (SI).

Then gas molecules have a finite velocity at the pore wall, but for liquids, a zero velocity at the wall is assumed. The “gas slippage effect” increases the flow rate and causes an overestimated permeability. Klinkenberg correction uses measurements at different pressures and an extrapolation for a (theoretical) infinite pressure (Cosentino, 2001). It results in the “Klinkenberg corrected permeability,” which is:

- independent of the type of gas,
- approximately the same as for a single phase liquid.

Forchheimer effect: At high flow rates, inertial effects occur and the difference of flow velocity between pore throats and pore bodies causes turbulences—but Darcy’s law requires laminar flow. A plot of fluid flow versus pressure gradient in case of a turbulency deviates from a linear function.

2.5.2 Rock Permeability—An Overview

Permeability of rocks covers orders of magnitude. It ranges from practically impermeable, dense rocks (compact magmatites, dense anhydrite, rock salt), over extremely low permeable shale to carbonates, sand/sandstone and high permeable gravel and karstic limestone (Figure 2.13).

A permeability of 0.1 md is generally considered the minimum for oil production (Lucia, 1999).

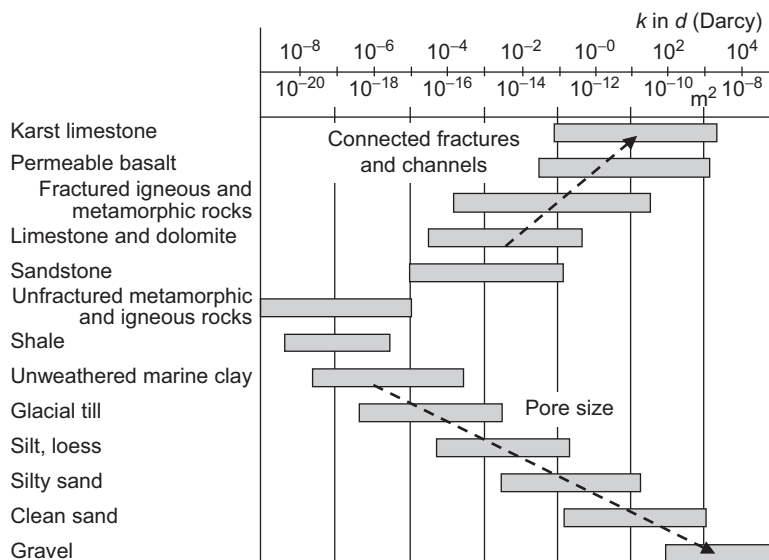


FIGURE 2.13 Permeability: mean magnitude ranges and tendencies. After a figure from Hearst et al., 2000.

TABLE 2.7 Porosity and Permeability Data of Some Sandstone and Carbonate Formations in the World

Field/Formation	Type of Rock	Porosity ϕ	Permeability k in md
Prudhoe Bay, United States	Sandstone	0.22	265
Fort Geraldine Unit, United States		0.23	64
Elk Hills, United States		0.27–0.35	100–2,000
Pullai Field, Malaysia		0.18–0.31	300–3,000
Chincotepec, Mexico		0.05–0.25	0.1–900
Daqing (Lamadian), China		0.246–0.264	200–13,000
Hassi Messaoud, Algeria		0.074	2.5
Ghawar (Ain Dar), Saudi Arabia	Carbonate	0.19	617
Bombay-High, India		0.15–0.20	100–250
Upper and Lower Cretaceous, Denmark		0.15–0.45	0.01–10

Source: Dandekar (2006).

Permeability is a pore space property; therefore the main controlling factors are:

- porosity (connected porosity), and
- pore size and fracture width; permeability is proportional to several powers (≈ 2) of pore size or fracture width.

Ranges in [Figure 2.13](#) illustrate the wide scale of permeability over more than 10 decades and some tendencies:

- for clastic sediments permeability increases with increasing grain size (which controls pore size). Note, for example, the change from shale to gravel;
- as a result of (connected) fractures or karstic large “pores” being preferred flow paths, permeability strongly increases. This is important mainly for carbonates and magmatic rocks.

In the following sections some experimental results demonstrate the main properties that control permeability ([Table 2.7](#)).

2.5.3 Clastic Rocks

Permeability increases with porosity and pore (throat) size. If rock contains clay, permeability can decrease by orders of magnitude.

2.5.3.1 Permeability as a Function of Porosity and Pore Size, Grain Size

In clastic sediments, the correlation between permeability and porosity is one of the most concise tendencies with a high practical importance: permeability–porosity relationships are a frequent type of predictor. Nelson (1994, 2005) published a systematic analysis of such correlations. Any permeability estimate from logs requires a calibration data set that is presented by key wells where comprehensive core and log data are available (Nelson, 1994; Cosentino, 2001).

Figure 2.14 shows the graphic presentation in a plot of logarithmically scaled permeability as function of linear (left) or logarithmically scaled (right) porosity—the so-called “poro–perm plot.”

The two plots allow the derivation of regression equations (k in md, ϕ as fraction):

$$k = 0.04 \cdot \exp(35.77 \cdot \phi) \quad \text{with} \quad R^2 = 0.88 \quad (2.27)$$

$$k = 17885 \cdot \phi^{3.91} \quad \text{with} \quad R^2 = 0.84 \quad (2.28)$$

At the end of this section an example, “Sandstone—part 1,” is given with data from core-laboratory measurements and an Excel spreadsheet on the website <http://www.elsevierdirect.com/companion.jsp?ISBN=9780444537966> (file: Example-Sandstone) in order to derive the permeability versus porosity regression (and other properties) of the investigated sandstone samples.

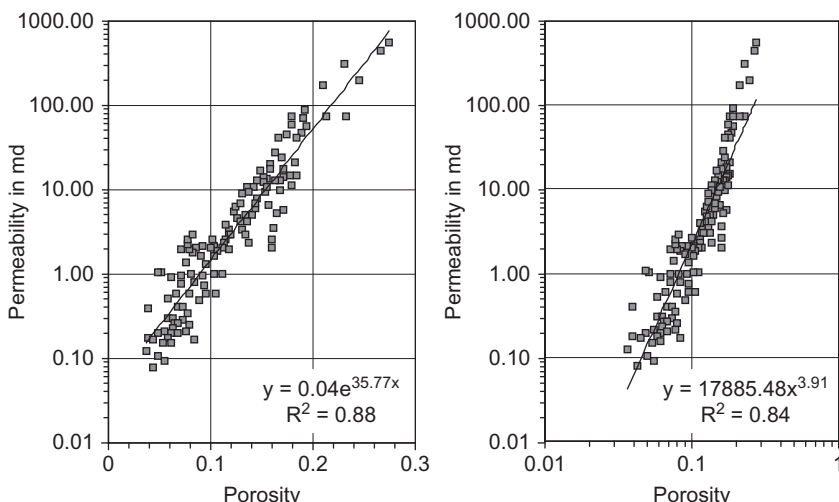


FIGURE 2.14 Permeability versus porosity (Sandstone, Rotliegend) in two different plots.

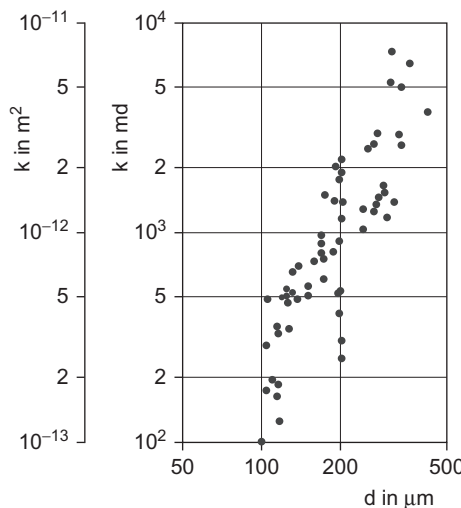


FIGURE 2.15 Permeability versus grain size; Bentheim sandstone, after Engelhard (1960) and Schopper (1982).

Besides porosity, the pore size has a dominant influence on permeability. Figure 2.15 shows permeability versus grain size for Bentheim sandstone with a strong correlation. Regression results in the equation as:

$$\log k = 2.2 \cdot \log d - 2.10 \quad \text{or} \quad k = 0.0079 \cdot d^{2.2} \quad (2.29)$$

where k is in md and d in millimeter.

The two dominant controlling properties, porosity and grain size, can be written as empirical equation⁵

$$k = c_1 \cdot \phi^a \cdot d^2 \quad k = c_2 \cdot \phi^a \cdot r^2 \quad (2.30)$$

where

d is the mean grain size

r is the mean pore radius

a, c_1, c_2 are empirical parameters.

c_1, c_2 depend on the criteria to select representative values of d, r (Nelson, 2005), but also on textural properties like grain shape, sorting and the internal grain arrangement of the sandstone.

⁵Nelson (2005) published the study “Three-Dimensional Perspective,” analyzing the correlations between permeability, porosity, and pore-throat size.

Many empirical equations follow this general form; two examples are presented:

Berg's (1970) equation:

$$k = 5.1 \cdot 10^{-6} \cdot \phi^{5.1} \cdot d^2 \cdot \exp(-1.385 \cdot \psi) \quad (2.31)$$

where

k is the permeability in Darcies (d)

ϕ is the porosity as percentage

d is the median grain diameter in millimeter

ψ is sorting term in phi units $\psi = P_{90} - P_{10}$.

Nelson (1994) recommended this equation for unconsolidated sands and relatively clean quartzose rocks.

van Baaren's (1979) equation:

$$k = 10 \cdot \phi^{3.64+m} \cdot D_d^2 \cdot S_o^{-3.64} \quad (2.32)$$

where

k is permeability in md

ϕ is the porosity as fraction

D_d is dominant grain diameter in micrometer

S_o is sorting index derived from grain size distribution

m Archie's cementation exponent (see Section 8.3).

Both equations are very similar (Nelson, 1994). They show:

- the same exponent for correlation with grain size (2);
- approximately the same exponent for correlation with porosity; for $m = 1.8$ results in van Baaren's equation an exponent of 5.4.

A somewhat different concept of permeability prediction was developed by Pape et al. (1999, 2000). It is based on fractal understanding of pore-space parameters. It "yields a general and petrophysical justified relation linking porosity to permeability."

2.5.3.2 Permeability Description in Hydrogeology

In hydrogeologic practice, a modified version of Darcy's law is frequently applied. Water flow q is referenced to the hydraulic gradient

$$q = -k_f \cdot \text{grad } h \quad (2.33)$$

The property k_f (filtration coefficient, hydraulic conductivity) has the unit of a velocity (m s^{-1}). Between the two properties k and k_f , the following conversion can be used (the correct equation implements water density and viscosity) in a good approximation

$$1 \text{ md} \approx 10^{-8} \text{ m s}^{-1} \quad \text{or} \quad 1 \text{ m s}^{-1} \approx 10^5 \text{ d} \quad (2.34)$$

TABLE 2.8 Hydraulic Conductivity k_f for Unconsolidated Sediments

Rock Type	k_f in m s^{-1}	Converted in d
Gravel, clean	$10^{-2} - 10^{-1}$	$10^3 - 10^4$
Sand, coarse	$\approx 10^{-1}$	$\approx 10^2$
Sand, medium	$10^{-4} - 10^{-3}$	$10^1 - 10^2$
Sand, fine	$10^{-5} - 10^{-4}$	$10^0 - 10^1$
Sand, silty	$10^{-7} - 10^{-5}$	$10^{-2} - 10^0$
Silt, clayey	$10^{-9} - 10^{-6}$	$10^{-4} - 10^{-1}$
Clay	$< 10^{-9}$	$< 10^{-4}$

Source: Höltig (1989).

Höltig (1989) classifies for groundwater practice as

very low permeability $k_f < 10^{-8} \text{ m s}^{-1}$

low permeability $k_f = 10^{-8} - 10^{-6} \text{ m s}^{-1}$

permeable $k_f = 10^{-6} - 10^{-4} \text{ m s}^{-1}$

high permeability $k_f > 10^{-4} \text{ m s}^{-1}$

Table 2.8 shows some data for unconsolidated sediments.

The correlation between hydraulic conductivity k_f (in cm s^{-1}) and grain size d_m (median value in millimeter) for unconsolidated sand is described in an early empirical equation by Hazen (1893).

$$k_f = 100 \cdot d_m^2 \quad (2.35)$$

Terzaghi (1955) implemented porosity ϕ and correlated with the effective grain size d_w

$$k_f = 200 \cdot d_w^2 \left(\frac{\phi}{1 - \phi} \right)^2 \quad (2.36)$$

2.5.3.3 Influence of Shale Content

Permeability of shaly sands is controlled by shale/clay content, type of shale distribution (e.g., laminated, dispersed, structural), porosity, and confining stress. A general impression is given by Figure 2.16.

Fundamental studies by Katsube et al. (1992); Luffel et al. (1993); Best and Katsube (1995); Katsube and Connell (1998); and Katsube et al. (1998) confirm the extremely low permeability values of clay and shale ($< 10^{-3} \text{ md}$).

Best and Katsube (1995) note that “shales generally display a unimodal pore-size distribution” and “have some of the lowest permeability values ($10^{-22} - 10^{-18} \text{ m}^2$ or $10^{-7} - 10^{-3} \text{ md}$) for various rock types.” They also report

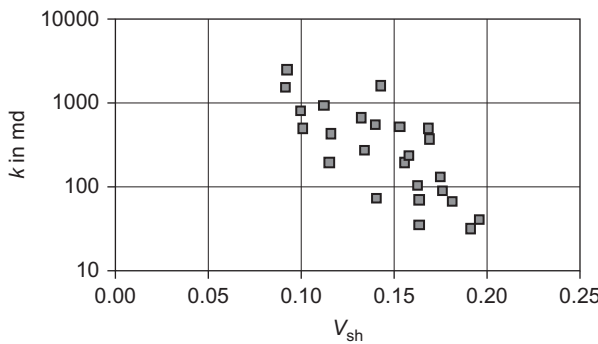


FIGURE 2.16 Permeability as function of shale content (West Sak Reservoir). Data from Vernik (2000).

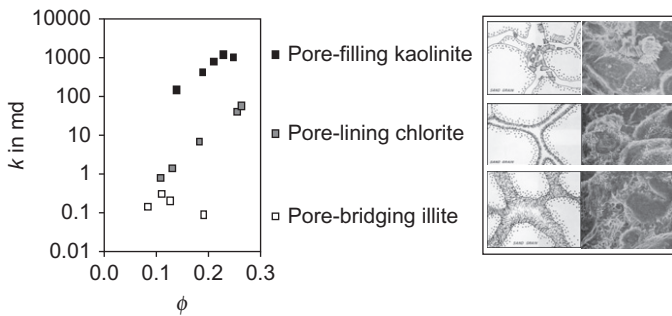


FIGURE 2.17 Permeability versus porosity plot for shaly sands with three different clay types: pore-filling kaolinite, pore-lining chlorite, and pore-bridging illite. Redrawn after Neasham (1977).

that shale permeability decreases as a function of pressure and derive an exponential dependence.

Mesri and Olson (1971) measured the permeability of pure clay (see Revil & Cathles, 1999). Permeabilities show a correlation with the specific internal surface area of the clay minerals: with increasing surface area, a larger amount of water does not take part at the fluid flow and reduces permeability.

The paper of Neasham (1977) allows an insight (Figure 2.17): it demonstrates in a permeability versus porosity plot the influence of clay type and morphology for three types: pore-filling kaolinite, pore-lining chlorite, and pore-bridging illite.

Revil and Cathles (1999) published a systematic analysis of shale permeability and found a high correlation between permeability and porosity. England et al. (1987) derived a relationship between permeability (in md) and porosity (fraction) for shales and mudstones

$$k = 4 \cdot 10^{-15} \cdot \phi^8 \quad (2.37)$$

From an investigation of some 100 sandstone samples, Sen et al. (1990) derived a regression between permeability k in md, and porosity ϕ as fraction and exchange-cation normality Q_v (see Section 8.5):

$$k = 10^{2.65} \left(\frac{\phi^m}{Q_v} \right)^{2.11} \quad R = 0.88 \quad (2.38)$$

Q_v expresses the clay effect; m is Archie's cementation exponent in the order of approximately 2.

Permeability can be directionally dependent. Thus, permeability is a tensorial rock property. In most cases, for sedimentary rocks two permeabilities are used for a characterization:

- k_h for horizontal permeability (flow parallel layering);
- k_v for vertical permeability (flow perpendicular layering).

Sedimentation can create an intrinsic permeability anisotropy (caused by preferential directions of connected pore channels).

Finely laminated sediments show a particular type of macroscopic anisotropy, which is created by an alternating change of permeability between coarse and fine layers or between sand and thin shale layers (laminated shaly sand).

Bang et al. (2000) published experimental data from a North Sea well interval and plotted vertical permeability versus horizontal permeability (Figure 2.18). The reservoir is a "homogeneous sand body" with "generally high porosities (up to 30%)."

Ye et al. (1999) investigated outcrop samples of the Bluejacket Sandstone (Middle Pennsylvania) and correlated permeability anisotropy with the internal

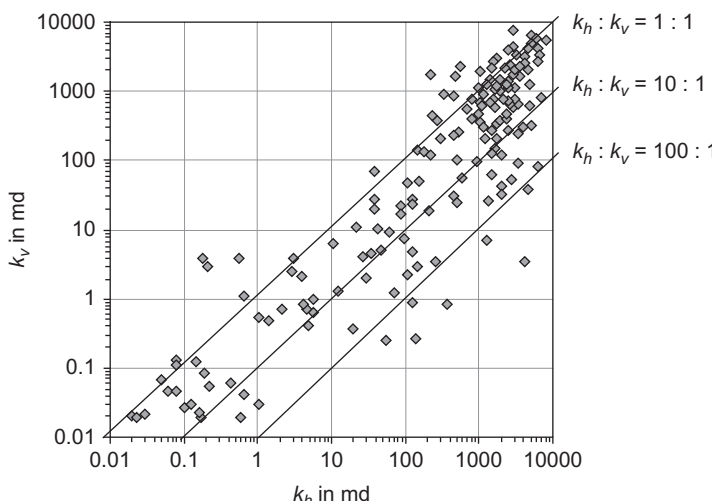


FIGURE 2.18 Vertical permeability k_v versus horizontal permeability k_h . Experimental data after Bang et al. (2000).

facies architecture: meandering channel-fill facies shows strong permeability anisotropy compared with low anisotropy of braided channel-fill facies.

In case of laminated shaly sands, the differences in lamina properties are extreme. Sand layer permeabilities (100–10,000 md) are high, but shale layers with very low permeabilities (0.001–1 md) act as an impermeable barrier for flow perpendicular to layering. For the macroscopic scale in the simplest case, the rock is transversely isotropic, and permeability is described by the two main axis values:

1. k_h permeability parallel stratification or lamination (permeability in horizontal direction);
2. k_v permeability perpendicular stratification or lamination (permeability in vertical direction).

The terms “horizontal” and “vertical” refer to the spatial position of a nondisturbed sedimentation.

2.5.4 Carbonates

The complex pore structure and diversity of carbonates result in problems to derive and correlate permeability with porosity and other parameters. Reservoir properties are controlled by two basic pore networks (Lucia, 1983, 1999, 2007; [Figure 2.8](#)):

1. interparticle pore network (intergranular and intercrystalline porosity);
2. vuggy pore network (pore space larger or within the particles and commonly present as leached particles, fractures, and large irregular cavities).

The effect of vugs on reservoir properties is strongly controlled by the type of interconnection:

- separate vugs (only via/by interparticle pore network, if present);
- touching vugs (direct vug–vug contact).

Non-vuggy rocks controlled by intercrystalline pore type are similar to siliciclastic sediments.

A systematic analysis of carbonate rock pore properties is published in papers by Lucia, particularly in his textbook “Carbonate Reservoir Characterization” (Lucia, 2007).

[Figure 2.19](#) shows permeability versus porosity for non-vuggy carbonates. The average particle size is used as the controlling parameter. Straight lines separate data collectives with respect to particle size. The figure confirms two tendencies as learned from siliciclastic sediments:

1. permeability increases greatly with porosity,
2. permeability also strongly increases with particle size reflecting the pore size.

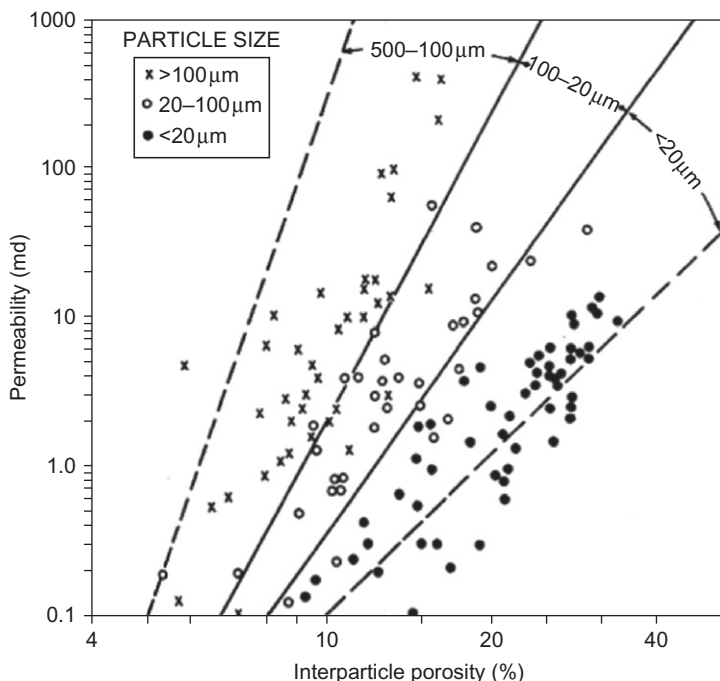


FIGURE 2.19 Permeability (air) versus porosity for various particle-size groups in non-vuggy carbonate rocks (Lucia, 1999, 2007).

Following the rock-fabric classification, Jennings and Lucia (2001) developed a systematic plot presentation for non-vuggy carbonates and subdivided limestone and dolomite into three classes with rock-fabric numbers. The generalized carbonate permeability model provides a relationship between permeability, interparticle porosity, and rock-fabric number

$$\ln(k) = a(\lambda) + b(\lambda) \cdot \ln(\phi_{ip}) \quad \text{or} \quad k = e^{a(\lambda)} \cdot \phi_{ip}^{b(\lambda)} \quad (2.39)$$

where

a, b are the power law parameters, dependent on rock-fabric number

λ is the rock-fabric number

ϕ_{ip} is the interparticle porosity.

Rock-fabric numbers range from 0.5 to 4 and are defined from class-boundary porosity–permeability plots for non-vuggy limestone and dolostone:

- Class 1 (rock-fabric number 0.5–1.5) is composed of grainstones, dolo-grainstones, and large crystalline dolostones;

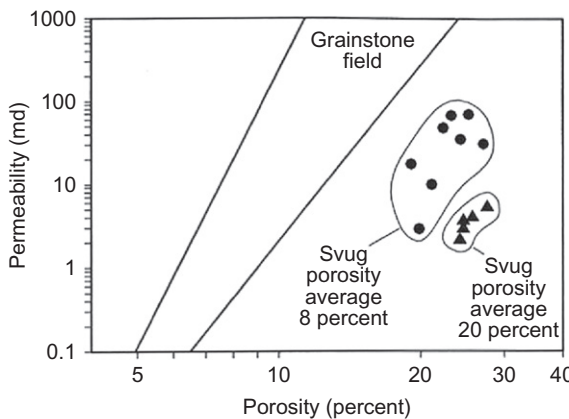


FIGURE 2.20 Effect of separate-vug porosity S_{vug} on permeability (grainstones with molds) (Lucia, 1999).

- Class 2 (rock-fabric number 1.5–2.5) is composed of grain-dominated packstones, fine and medium crystalline, grain-dominated dolopackstones, and medium crystalline, mud-dominated dolostones;
- Class 3 (rock-fabric number 2.5–4.0) includes mud-dominated limestones and fine crystalline, mud-dominated dolostones.

For the power law parameters a , b , Jennings and Lucia (2001) give the following empirical relationships:

$$a(\lambda) = 22.56 - 12.08 \cdot \ln(\lambda) \quad (2.40)$$

$$b(\lambda) = 8.671 - 3.603 \cdot \ln(\lambda) \quad (2.41)$$

when k is in md and ϕ_{ip} is as fraction.

The addition of separate-vug porosity to interparticle porosity:

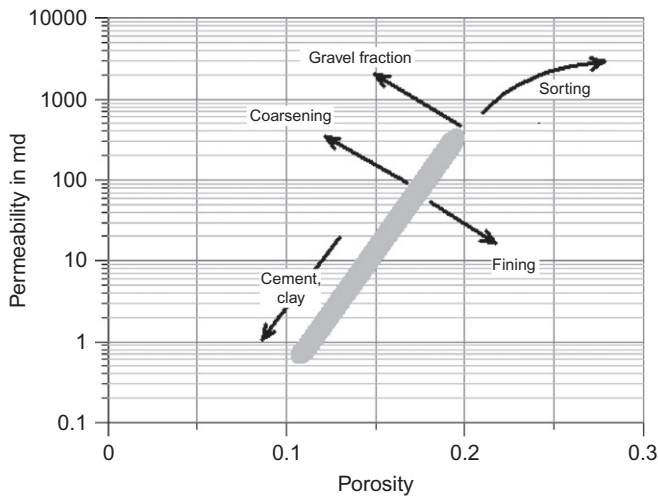
- increases total porosity, but
- does not increase permeability.

Therefore, it is important to determine interparticle porosity by subtracting separate-vug porosity from total porosity and using interparticle porosity to estimate permeability (Lucia, 1983). [Figure 2.20](#) illustrates this effect of separate-vug porosity S_{vug} . Subtracting S_{vug} shifts the dots into the grainstone field.

2.5.5 Summary: Main Influences Controlling Permeability–Porosity Relationships

[Figure 2.21](#) gives schematic porosity–permeability plots for clastic and carbonate rocks, based on figures from Nelson (1994, 2005) and Akbar et al. (1995).

Clastic rocks



Carbonate rocks

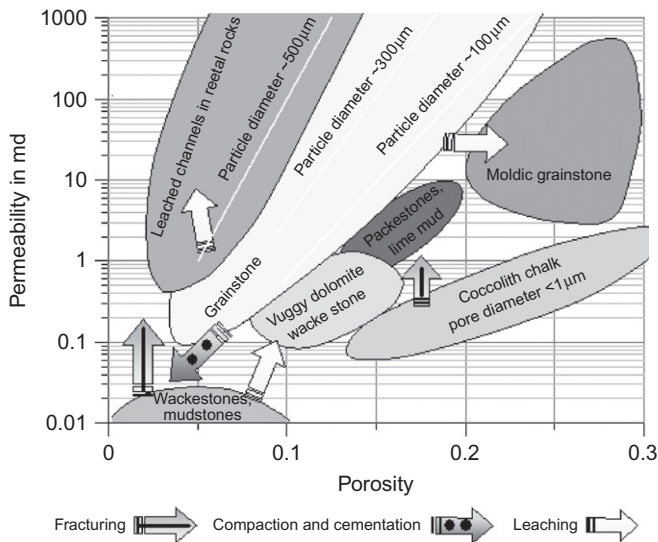
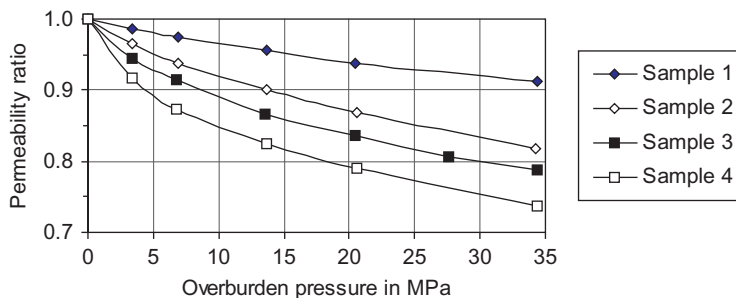


FIGURE 2.21 Schematic poro-perm plots for clastic and carbonate rocks, based on figures from Nelson (1994, 2005) and Akbar et al. (1995), copyright Schlumberger Ltd., used with friendly permission.

2.5.6 Pressure Dependence

Increasing effective pressure compresses the pore space, reduces the pore cross section area, and closes pore throats and fractures. Therefore, permeability decreases with increasing effective pressure. Magnitude of the change



Sample	Description	Permeability at zero overpressure	Porosity at zero overpressure
1	Basal Tuscaloosa, Mississippi	249 md	0.15
2	Basal Tuscaloosa, Mississippi	163 md	0.24
3	Southern California Coast	335 md	0.25
4	Los Angeles Basin California	110 md	0.22

FIGURE 2.22 Permeability ratio (permeability at considered pressure divided by permeability at zero overburden pressure) versus overburden pressure; sandstone. Data from Fatt (1953).

depends on mechanical rock properties: pressure dependence is strong in weak consolidated rocks or fractured rocks, for more competent rocks the pressure dependence decreases. A theoretical model was developed by Sigal (2002).

In general, the decrease of permeability with pressure is nonlinear (Figure 2.22); in the first pressure steps a relatively large change occurs, whereas for higher pressure levels, the relative change is small in most cases.

As an example of the permeability decrease with pressure for crystalline rocks, Figure 2.23 shows results of experiments on samples from the KTB drilling project.

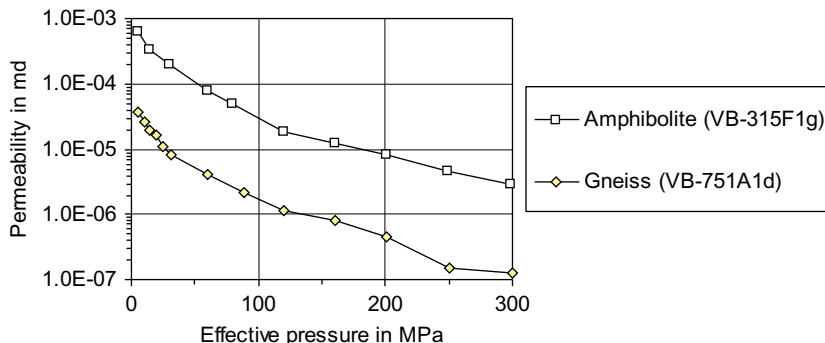


FIGURE 2.23 Permeability versus pressure, amphibolite and gneiss sample from the KTB-project. After Freund and Nover (1995).

For cracked rocks, Walsh (1981) published a model concept; Gavrilenko and Gueguen (1989) have also developed a theory based on a statistical distribution of cracks. Percolation theory is used for the description of interconnection and combined with elastic behavior of cracks for a defined given geometry.

2.5.7 Permeability Models

2.5.7.1 Overview

There are different model concepts used to describe permeability. In most cases, the result is a “theoretical” model-derived equation, but it needs some “empirical” modification in order to express textural and other geological conditioned influences. For practical application, this process is a kind of calibration for the specific formation or rock type (using, e.g., core data).

In the following section the capillary tube model will be discussed more in detail. This simple model:

- gives a description of some main controlling influences,
- helps to formulate the background for empirical modifications,
- creates a link to log-derived parameters (irreducible water saturation $S_{w,irr}$, NMR-derived parameters).

Other model types are based on percolation concepts (Katz & Thompson, 1986; Gueguen & Dienes, 1989), or a fractal description of the pore space (Pape et al., 2000).

2.5.7.2 The Capillary Tube Model (Kozeny–Carman)

The Fundamental Equation

The model concept is applied mainly for clastic sediments. The rock with connected pores is represented by an impermeable cube (macroscopic side length L) with a capillary tube of microscopic length l representing the pore channel (Figure 2.24).

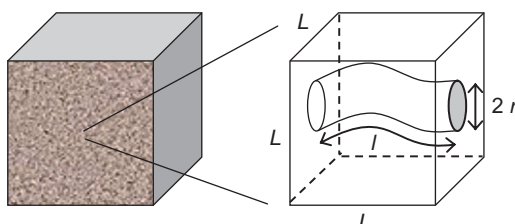


FIGURE 2.24 Simple capillary tube model.

The element with the length L has the cross section $A = L \cdot L$. The model can be considered under two views:

In a “macroscopic view” the fluid flow can be described by Darcy’s law

$$u = \frac{k}{\eta} \cdot \text{grad } p \quad (2.42)$$

Thus, the flowing fluid volume per time is

$$q = u \cdot A = \frac{k}{\eta} A \cdot \text{grad } p = \frac{k}{\eta} A \cdot \frac{\Delta p}{L} \quad (2.43)$$

In a “microscopic view” pore space properties are described by capillary length l and capillary radius r . The tortuosity of the pore channel is

$$\tau = \frac{l}{L} \quad (2.44)$$

The porosity of the model is

$$\phi = \frac{\pi \cdot r^2 \cdot l}{AL} = \frac{\pi \cdot r^2 \cdot \tau}{A} \quad (2.45)$$

The fluid flow in the capillary is given by Hagen–Poiseulle’s law

$$q = \frac{\pi}{8} \cdot \frac{1}{\eta} \cdot r^4 \cdot \frac{\Delta p}{l} \quad (2.46)$$

With the tortuosity the “microgradient” $\Delta p/l$ can be transformed into the “macrogradient”

$$\frac{\Delta p}{l} \cdot \tau = \frac{\Delta p}{L} = \text{grad } p \quad (2.47)$$

Comparison of the two expressions (Equations (2.43) and (2.46)) for volume flow results in

$$q = \frac{k}{\eta} A \cdot \text{grad } p = \frac{\pi}{8} \cdot \frac{1}{\eta} \cdot r^4 \cdot \frac{1}{\tau} \cdot \text{grad } p \quad (2.48)$$

Solved for permeability and implementation of porosity gives

$$k = \frac{1}{8} \cdot \phi \cdot \frac{r^2}{\tau^2} \quad (2.49)$$

The equation shows and explains permeability as a function of:

- porosity: the resulting linear dependence is not in agreement with the stronger dependence derived from experiments;
- pore radius: the dependence on the square of the radius fits the general correlation found by experiments with a dependence of permeability on the square of mean grain or pore size very well;
- tortuosity: this property stands in the model for the complicated path of the pore channel and covers a part of the textural influences; it probably also covers a part of the porosity influence.

For practical derivation of permeability from other physical properties (e.g., well logs) the crucial problem is the effect of pore size and pore channel geometry (pore throat size, tortuosity), whereas porosity in many cases can be derived using standard methods.

Implementation of Specific Surface

The simple geometry of the model opens the way to transform the fundamental problem of permeability dependence on pore radius into the problem dependence on specific internal surface. With this step, a permeability estimate from logs becomes possible.

For the simple capillary model, pore radius can be expressed by specific internal surface. The (microscopic) model results in

$$S_{\text{pore}} = \frac{2\pi \cdot r}{\pi \cdot r^2} = \frac{2}{r} \quad \text{or} \quad r = \frac{2}{S_{\text{pore}}} \quad (2.50)$$

Insertion into [Equation \(2.49\)](#) results in the permeability

$$k = \frac{1}{8} \cdot \phi \cdot \frac{r^2}{\tau^2} = \frac{1}{2} \cdot \phi \cdot \frac{1}{S_{\text{pore}}^2} \cdot \frac{1}{\tau^2} \quad (2.51)$$

Now the controlling effect of the pore dimension is expressed by the specific internal surface of the pore space. There are two ways to implement the effect of specific internal surface (in addition to porosity) in techniques for permeability estimate:

Method 1 Understand irreducible water saturation $S_{w,\text{irr}}$ as a measure of S_{por} . In a water-wet (see [Section 2.6](#)) oil- or gas-bearing formation, irreducible water covers the grain surface with a thin water film. Thus, the water content (determined, e.g., by a resistivity measurement) gives a measure of the pore surface ($S_{\text{por}} \propto S_{w,\text{irr}}$). This is expressed by Timur's empirical equation (Timur, 1968).

$$k = \left[100 \cdot \frac{\phi^{2.25}}{S_{w,\text{irr}}} \right]^2 = 10^4 \cdot \phi^{4.5} \cdot \frac{1}{S_{w,\text{irr}}^2} \quad (2.52)$$

S_{por} ([Equation \(2.51\)](#)) is expressed by $S_{w,\text{irr}}$. However, this technique only works under condition of a reservoir section with $S_{w,\text{irr}}$ (above transition zone).

Method 2 Derivation of S_{por} from an NMR measurement. The Coates equation (Coates et al., 1991) for NMR-derived permeability is (see [Section 3.5.2](#))

$$k = \left[\frac{\phi}{C} \right]^4 \cdot \left[\frac{\text{BVM}}{\text{BVI}} \right]^2 \quad (2.53)$$

where

BVM is bulk volume movable fluids (derived from NMR)

BVI is bulk volume irreducible fluids (derived from NMR)

C is the empirical parameter.

Thus, the ratio BVI/BVM is a measure for the specific internal surface S_{por} .

Modifications for a Better Approximation of the “Real Pore Geometry”

The assumption of a circular shape with constant radius is a very strong idealization for a real pore channel. Therefore, some modifications of the basic model have been developed.

TABLE 2.9 Kozeny Shape Factor F_s

Shape	F_s
Circle	2.00
Ellipse $a/b = 2$	2.13
= 10	2.45
= 50	2.96
Rectangular $a/b = 1$	1.78
= 2	1.94
= 10	2.65
= infinity	3.00
Equilateral triangle	1.67

a. Kozeny’s shape factor F_s and Kozeny constant K_z :

In [Equation \(2.51\)](#), a “shape factor” for different shaped conduits ([Table 2.9](#)) is implemented:

$$k = \frac{1}{F_s \cdot \tau^2} \cdot \phi \cdot \frac{1}{S_{\text{pore}}^2} \quad (2.54)$$

Obviously, the shape has only a minor effect on the predicted permeability (Georgi & Menger, 1994). The factor $F_s \cdot \tau^2$ describes the shape and geometry of the pore channels and is called the Kozeny constant: $K_z = F_s \cdot \tau^2$.

b. Ratio of pore-throat to pore-body radius Γ .

Permeability is controlled by pore-throat radius, but S_{por} by pore-body radius. Therefore, the ratio of pore-throat to pore-body radius Γ is introduced in Equation (2.54):

$$k = \frac{\Gamma^2}{4 \cdot F_s} \cdot \phi \cdot \frac{r^2}{\tau^2} = \frac{\Gamma^2}{F_s} \cdot \phi \cdot \frac{1}{S_{\text{pore}}^2} \cdot \frac{1}{\tau^2} \quad (2.55)$$

c. Definition of a “Reservoir Quality index (RQI)”

Leverett (1939, 1940) equated the term $\sqrt{k/\phi}$ as a rock property. From Equation (2.55)

$$\sqrt{\frac{k}{\phi}} = \frac{\Gamma}{2\sqrt{F_s}} \cdot \frac{r}{\tau} = \frac{\Gamma}{\sqrt{F_s}} \cdot \frac{1}{\tau} \cdot \frac{1}{S_{\text{pore}}} \quad (2.56)$$

The right-hand side of the equation indicates that the term $\sqrt{k/\phi}$ is controlled by specific internal surface or pore size, tortuosity, pore shape, and pore-throat to pore-body ratio. Thus, it covers all textural properties that control permeability except porosity. An RQI can be defined as (Altunbay et al., 1997):

$$\text{RQI} = 0.0314 \sqrt{\frac{k}{\phi}} \quad (2.57)$$

A plot RQI versus ϕ can be used for a quality characterization and a classification in hydraulic units. Georgi and Menger (1994) and Altunbay et al. (1997) have developed an “extended hydraulic unitization” and applied it for carbonates.

2.5.7.3 Flow Through Fractures and Channels

In rocks with intergranular and fracture porosity:

- intergranular pores usually contain a significant volume of fluids, but have a low permeability;
- fractures and channels are important for fluid flow and have a relatively high permeability.

A simple fracture model (Figure 2.25) is considered: a cube with length L . In a single fracture the fluid flow is

$$q = \frac{1}{12 \cdot \eta} \cdot h \cdot w_f^3 \cdot \frac{\Delta p}{L} \quad (2.58)$$

with fracture porosity

$$\phi_{\text{fracture}} = \frac{w_f}{L} \quad (2.59)$$

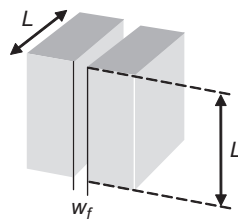


FIGURE 2.25 Simple fracture model.

permeability results for the one-dimensional flow between the two parallel planes as:

$$k_{\text{fracture}} = \frac{1}{12} \cdot \phi_{\text{fracture}} \cdot w_f^2 \quad (2.60)$$

Fracture permeability from this model calculation is controlled by porosity and the square of the fracture dimension. This is comparable to the architecture of [Equation \(2.49\)](#) with square of pore radius.

Witherspoon et al. (1980) introduced a friction factor f to account for the roughness of the fracture surface; therefore, [Equation \(2.60\)](#) becomes

$$k_{\text{fracture}} = \frac{1}{f} \cdot \frac{1}{12} \cdot \phi_{\text{fracture}} \cdot w_f^2 \quad (2.61)$$

2.5.7.4 Modeling—Shale Influence Upon Permeability

[Figure 2.26](#) demonstrates schematically the effects of increasing clay content upon permeability for a dispersed and a laminated distribution.

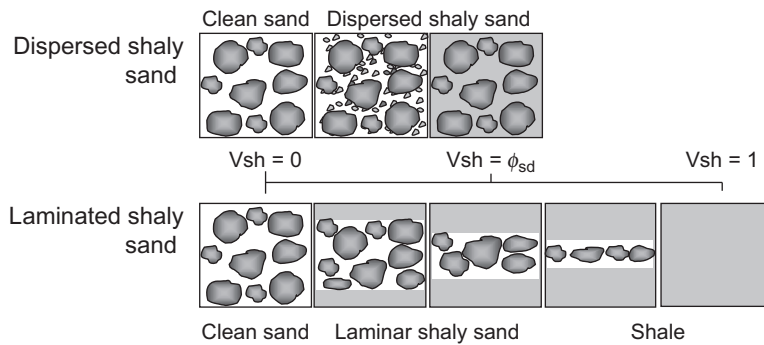


FIGURE 2.26 Permeability in dispersed and laminar shaly sand—schematically.

- For dispersed shaly sand, a relatively monotonic decrease of permeability with increasing clay content can be expected as a result of the decrease of effective pore space.

- For laminated shaly sand, a dramatic decrease of permeability in the vertical direction (k_v) can be expected because the flow is controlled by the low shale permeability, whereas in the horizontal direction, the magnitude of permeability (k_h) is still controlled by the sand fraction for moderate shale content also. This creates permeability anisotropy.

Thus, the two cases must be discussed separately.

The laminated shaly sand in a layered model is composed of two components. The “microscopic” properties related to the individual components (layers) are the microscopic permeabilities k_{sand} , k_{shale} and the volume fraction V_{shale} . The resulting “macroscopic” properties are the permeabilities k_v , k_h .

Relationships between microscopic and macroscopic properties are given with the laws for series and parallel hydraulic conductor circuits and the volume fractions as weighting function

$$k_v = \left(\frac{1 - V_{\text{shale}}}{k_{\text{sand}}} + \frac{V_{\text{shale}}}{k_{\text{shale}}} \right)^{-1} \quad (2.62)$$

$$k_h = (1 - V_{\text{shale}}) \cdot k_{\text{sand}} + V_{\text{shale}} \cdot k_{\text{shale}} \quad (2.63)$$

Therefore, a forward calculation of macroscopic permeabilities in the horizontal and vertical directions (k_h and k_v) needs the microscopic permeabilities (k_{sand} and k_{shale}) and the fractional sediment composition (V_{shale}).

For dispersed shaly sand there are various relationships and models that describe the dependence of permeability on porosity, shale content, and shale properties. Examples are as follows:

1. De Lima (1995) derived an equation describing intrinsic permeability of shaly sands by focusing on the clay-coated sand grains:

$$k = a_0 \cdot \left[\frac{\phi^{(m-0.5)}}{1 + \delta \cdot Q_v} \right]^q \quad (2.64)$$

where ϕ is the porosity, m the cementation exponent (Archie), q is an empirical exponent (for regular-shaped pores is $q = 2$), δ is a parameter controlled by the average size of the sand grains and the particular type of clay, Q_v is the cation exchange concentration (see Section 8.5), and a_0 is a “modified sand shape factor.” A comparison with the Kozeny equation shows that a_0 depends on the number of capillaries, tortuosity, average hydraulic radius, shape of the pore channels, and on porosity.

2. Revil and Cathles (1999) start their consideration with a clean sand with porosity ϕ_{sd} , and a permeability, k_{sd} . The clean sand pores are filled with shale, which reduces porosity

$$\phi = \phi_{\text{sd}} - V_c(1 - \phi_{\text{sh}}) \quad (2.65)$$

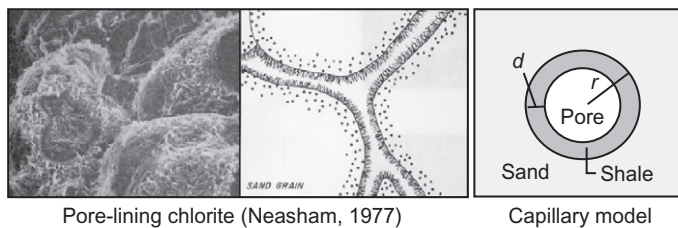


FIGURE 2.27 Capillary tube model for dispersed shaly sand. Clay reduces pore radius from r to $r - d$ (Schön & Georgi, 2003).

where V_c is the clay volume fraction, and ϕ_{sh} is the porosity of the pure clay. This reduced (effective) porosity is correlated with permeability.

3. Schön and Georgi (2003) developed a capillary-based model for dispersed shaly sand that shows an analogy to the Waxman–Smits equation (Section 8.5.3) for electrical properties. This model (Figure 2.27) accounts for the reduction in porosity and decrease in the pore cross-sectional area with the content of clay and the associated immobile water. Starting with Hagen–Poiseulle’s law, the flow rate for a cross section is reduced by a film of clay particles. Permeability for shaly sand can be written as a function of the clean sand permeability k_{sd} and the dispersed shale content V_{sh}

$$k_{\text{shaly sand}} = k_{sd} \left(1 - \alpha \cdot \frac{V_{sh}}{\phi} \right)^2 \quad (2.66)$$

where the factor α is introduced because the cross section reducing shale/clay effect is not completely described by the “dry” shale/clay volume.

Equation (2.66) can be used for regression analyses of experimental data. It is possible to use also other measures for the dispersed clay/shale volume and formulate equivalent equations for permeability. Using natural gamma ray radiation GR as measure of shale content (see Section 5.2.5) results:

$$k_{\text{shaly sand}} = k_{sd} \left(1 - \frac{\alpha}{\phi} \cdot \frac{GR - GR_{\min}}{GR_{\max} - GR_{\min}} \right)^2 \quad (2.67)$$

where k_{sd} is permeability of the clean sand. An example demonstrates the application on real data (Schön & Georgi, 2003).

2.5.8 Multiphase Flow—Effective Permeability

Permeability in Darcy’s law is defined for a single fluid (absolute permeability). If the reservoir contains two or even three nonmiscible fluids (water,

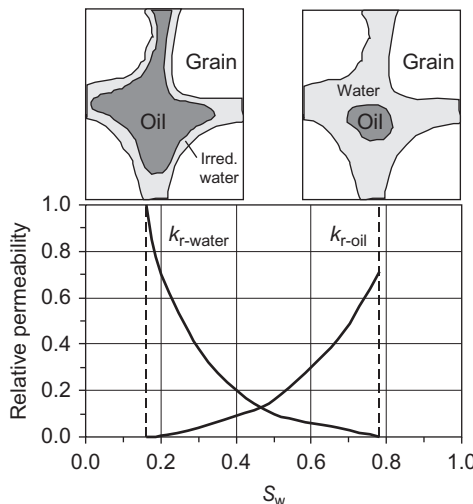


FIGURE 2.28 Relative permeability for water and hydrocarbon (oil or gas) as function of water saturation S_w . The dotted vertical lines indicate the irreducible water saturation (left) and residual oil saturation (right).

oil, gas), then the flow of the individual fluids interferes and the effective permeabilities of the individual fluids are less than absolute permeability.

Effective permeability describes the flow of a fluid through the rock in presence of other pore fluids and depends on the saturation of the considered fluid.

Relative permeability is defined as the ratio of effective permeability and absolute permeability; it varies between 0 and 1.

For effective or relative permeability measurement in modern equipment, fluid saturation frequently is monitored with an X-ray scanner. This controls the phase saturation and saturation distribution along the length of the core sample.

Figure 2.28 shows the relative permeability as a function of actual saturation. Note that the sum of the relative permeabilities of the two phases is less than unity.

2.6 WETTABILITY

Wettability expresses the property for one fluid to adhere to a rock surface in the presence of another immiscible fluid. Therefore, the wettability type controls the relative distribution of fluid within the rock pore space and framework:

- Water-wet: the rock/mineral surface is coated with water, while oil and gas occupy the central position of the largest pores.

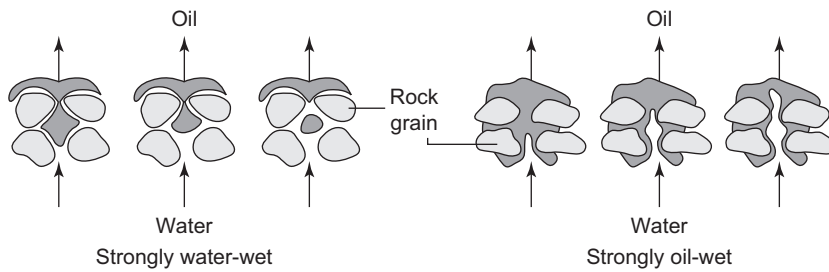


FIGURE 2.29 Wettability types: oil displacement in water and oil-wet reservoirs during water flooding (Cosentino, 2001).

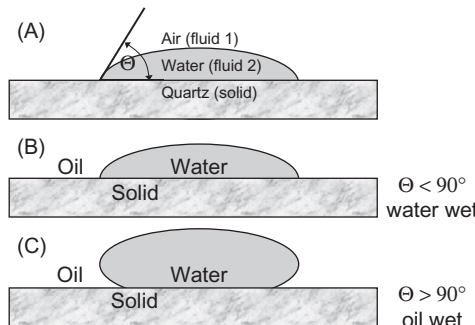


FIGURE 2.30 Wettability: (A) Definition of the angle Θ and interfacial tension terms; (B) water-wet rock (water–oil system); (C) oil-wet rock (water–oil system).

- Oil-wet: the relative positions of oil and water are reversed with respect to the water wet state; the oil coating the rock surface and the water is in the center of the largest pores.
- Intermediate wettability: this term applies to reservoir rocks where there is some tendency for both oil and water to adhere to the pore surface (after Cosentino, 2001) (Figure 2.29).

A detailed discussion of wettability—fundamentals and practical importance—is given with a paper of Abdallah et al. (2007).

Wettability is described by a contact angle Θ (Figure 2.30) and is related to interfacial tension⁶:

$$\cos \Theta = \frac{\sigma_{s1} - \sigma_{s2}}{\sigma_{21}} \quad (2.68)$$

⁶The term “surface tension” is also used. Dandekar (2006) notes that “interfacial tension” may be used for oil–water system, and “surface tension” if gas is present, i.e., for oil–gas and water–gas systems.

where

- σ_{s1} is interfacial tension between solid and fluid 1 (e.g., air)
- σ_{s2} is interfacial tension between solid and fluid 2 (e.g., water)
- σ_{12} is interfacial tension between fluid 1 and fluid 2.

In the oilfield terminology (see also Dandekar, 2006; Tiab & Donaldson, 2004) a rock:

- is strongly water-wet if the contact angle is $\Theta = 0\text{--}70^\circ$,
- has intermediate wettability⁷ if the contact angle is $\Theta = 70\text{--}110^\circ$,
- is strongly oil-wet if the contact angle is $\Theta = 110\text{--}180^\circ$.

Clean sandstone tends to be water-wet, but many sandstone reservoir rocks are intermediate-wet. Carbonates tend to be more oil-wet than clastics. In gas–liquid systems, gas is always the nonwetting phase. Frequently water-wet, for example, are North Sea sandstone reservoirs whereas frequently oil- or mixed-wet are Middle East carbonate reservoirs. Wettability is influenced by saturation history: “Pore surfaces that had been previously contacted by oil may be oil-wet, but those never contacted by oil may be water wet.” (Abdallah et al., 2007).

Laboratory methods for wettability determination are (for details of laboratory technique see Ahmed, 2001; Amyx et al., 1960; Tiab & Donaldson, 1996, 2004):

- Measurement of the contact angle after principle in [Figure 2.30](#).
- Amott method: determination at a core sample. Based on a combination of spontaneous imbibition and forced displacement of the fluids (oil, water) two “displacement ratios” (displacement by oil ratio, displacement by water ratio) are determined.
- USBM (US Bureau of Mines, Texas) wettability index: determination at a core sample. From centrifuge capillary pressure curves (see [Section 2.7](#)) in imbibition and drainage modus, the area under the curves are used to calculate a wettability index I_{USBM} (for more details see e.g., Dandekar, 2006; Tiab & Donaldson, 1996).

For a wettability index determination from NMR logs (see Chapter 3) based on the different relaxation characteristic of wetting and nonwetting fluid, Looyestijn (2008) defined a new index as

$$I_w = \frac{\text{surface wetted by water} - \text{surface wetted by oil}}{\text{total surface}} \quad (2.69)$$

This index is scaled from +1 (fully water-wet) to -1 (fully oil-wet).

⁷Abdallah et al. (2007) note that there is a difference between “intermediate-wetting” (lacking a strong wetting preference) and “mixed-wetting” (variety of wetting preferences).

2.7 FLUID DISTRIBUTION—CAPILLARY PRESSURE IN A RESERVOIR

Capillary pressure p_c is defined as the pressure difference between the non-wetting phase and the wetting phase as a function of the wetting-phase saturation. In reservoir engineering, capillary pressure is an important parameter for the study of vertical saturation distribution.

A petroleum reservoir initially was saturated with water. Migration of oil into the reservoir displaced a part of water. This displacement of the wetting phase (water) by a nonwetting phase (oil) can be simulated in the laboratory experiment of measuring the drainage capillary pressure curve. In reservoir studies the inflow of water must also be modeled. In this case, the imbibition capillary pressure is of interest.

Methods of capillary pressure determination in the laboratory are:

- static methods: mercury injection,
- dynamic methods: centrifuge methods.

2.7.1 Fundamentals

In a reservoir under static conditions (no production and flow influence), gravity and capillary forces are in balance. The fluid distribution in the pore space is controlled by:

- properties of the pore space,
- properties of the fluids,
- interactions between fluids and pore surface and interactions between different fluids.

Figure 2.31 illustrates the fluid distribution in a homogeneous water-wet reservoir (e.g., a sandstone). There are three different regions with respect to the pore fluids:

- Water zone: the rock is 100% water-saturated. Note that the 100% water level is above the FWL (Free Water Level) as a result of the capillary forces; this position correlates with the “displacement pressure” p_d (also called threshold or entry pressure). Displacement pressure is the capillary pressure at the top of the water-saturated zone. It is the minimum pressure required for the nonwetting fluid to displace the wetting fluid (water) and enter the largest pores (Jorden & Campbell, 1984).
- Transition zone (also funicular region): over the transition zone changes of saturation takes place. This region reflects “the most abundant and accessible pore-throat sizes; the steeper the capillary pressure curve in this region, the less uniform the pore throats” (Jorden & Campbell, 1984).

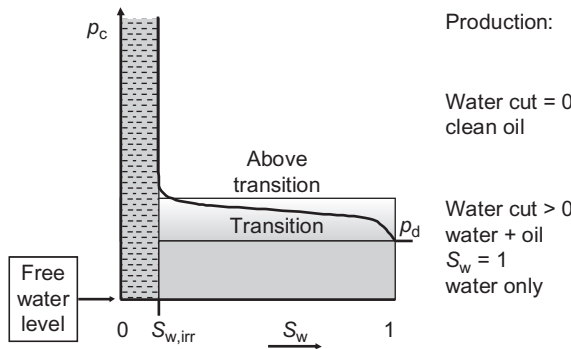


FIGURE 2.31 Fluid distribution in a water-wet homogeneous reservoir. Capillary pressure controls fluid distribution in the reservoir and the fluid production.

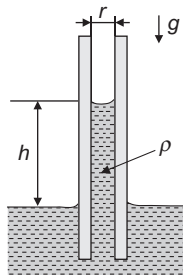


FIGURE 2.32 Capillary tube.

- Pendular region (above transition zone): the wetting fluid (water) is in pendular rings at the grain–grain contacts, on the grain surface, and in the small pores. This part of the water is called capillary bound or irreducible water.

The saturation distribution versus height can be described by the conditions of equilibrium between gravity forces (downward) and capillary forces (upward) as follows:

In a capillary tube (Figure 2.32) at the fluid–solid interface, a surface tension acts and water rises in the tube. This can be formulated as an upward pressure (capillary pressure)

$$p_c = \frac{2 \cdot \sigma \cdot \cos \Theta}{r} \quad (2.70)$$

where

σ is interfacial tension

Θ is the contact angle, expressing wettability

r is the capillary radius.

In equilibrium the capillary pressure equals the pressure by the weight of the rising water column (gravity):

$$p_g = g \cdot \Delta\rho \cdot h \quad (2.71)$$

where

g is Earth's acceleration

$\Delta\rho$ is the density difference between wetting and nonwetting fluid

h is the height above the FWL.

This gives the height above the FWL

$$h = \frac{p_c}{g \cdot \Delta\rho} = \frac{2 \cdot \sigma \cdot \cos \Theta}{g \cdot \Delta\rho \cdot r} \quad (2.72)$$

Thus, the finer the capillary tube, the higher the water will rise.

The vertical equilibrium between capillary forces and gravitational force determines the height of the capillary fringe in an oil reservoir (or any other fluid reservoir).

Equation (2.72) contains two types of properties:

1. reservoir pore geometric properties (in the simple model expressed by radius r),
2. interface properties $\sigma \cdot \cos\Theta$ and difference of fluid densities $\Delta\rho$.

Therefore, a conversion between different fluid systems is possible by changing the interface properties $\sigma \cdot \cos\Theta$ and densities. Also a conversion from laboratory measurements to reservoir conditions is possible.

Table 2.10 gives some data for different fluid systems. A detailed study about the oil–brine interfacial tension and influencing factors (salinity, pH, viscosity) was published by Buckley and Fan (2007).

Figure 2.33 demonstrates the principle of a capillary pressure measurement (drainage, water-wet rock). The piston pressures the nonwetting fluid (oil) into the pores. The process starts (B) if the pressure equals the displacement pressure and the largest pores are filled. The process ends (D) if all pores are filled with oil—only the irreducible water is present.

In real rocks, pores are not tubes but have a complicated shape with throats and bodies of different size (pore size distribution) and a curve results.

Amyx et al. (1960) give a description of the mercury injection technique: “Mercury is normally a nonwetting fluid. The core sample is inserted in the mercury chamber and evacuated. Mercury is forced in the core under pressure. The volume of mercury injected at each pressure determines the nonwetting-phase saturation. This procedure is continued until the core sample is filled with mercury or the injection pressure reaches some predetermined value.”

The incremental mercury volume injected is plotted as function of the injection pressure and delivers the (injection) capillary pressure curve: a mercury withdrawal capillary pressure curve can be obtained by decreasing the pressure in increments and recording the volume of mercury withdrawn.

TABLE 2.10 Capillary Pressure Properties for Different Fluid Systems

System	θ	σ in		$\sigma \cdot \cos\theta$ in	
		Dynes cm^{-1}	$\text{N m}^{-1} = \text{Pa m}$	Dynes cm^{-1}	$\text{N m}^{-1} = \text{Pa m}$
Laboratory					
Air–water	0	72	0.072	72	0.072
Oil–water	30	48	0.048	42	0.042
Air–mercury	40	480	0.480	367	0.367
Air–oil	0	24	0.024	24	0.024
Reservoir					
Water–oil	30	30	0.030	26	0.026
Water–gas	0	50	0.050	50	0.050

After Hartmann and Beaumont (1999) and Darling (2005).

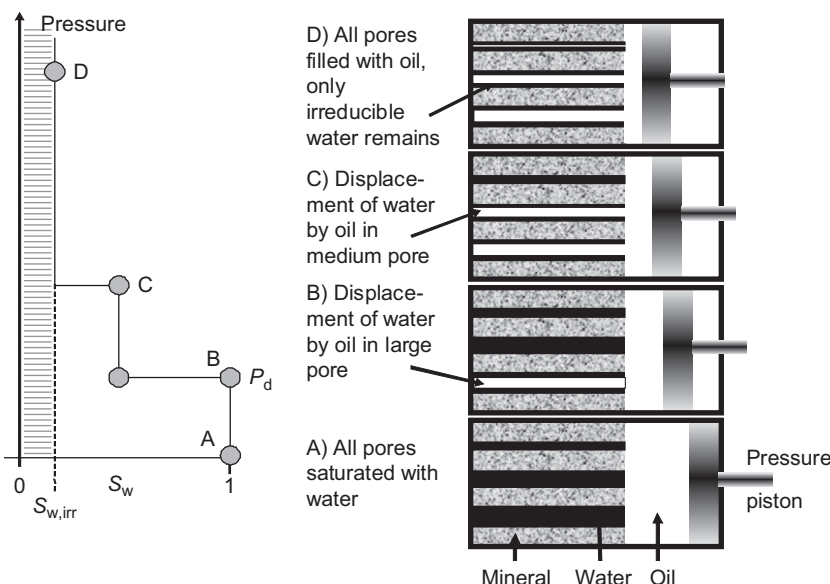


FIGURE 2.33 Principle of a capillary pressure measurement (three pore sizes), after a figure from Sneider (1987); cited by Slatt (2006).

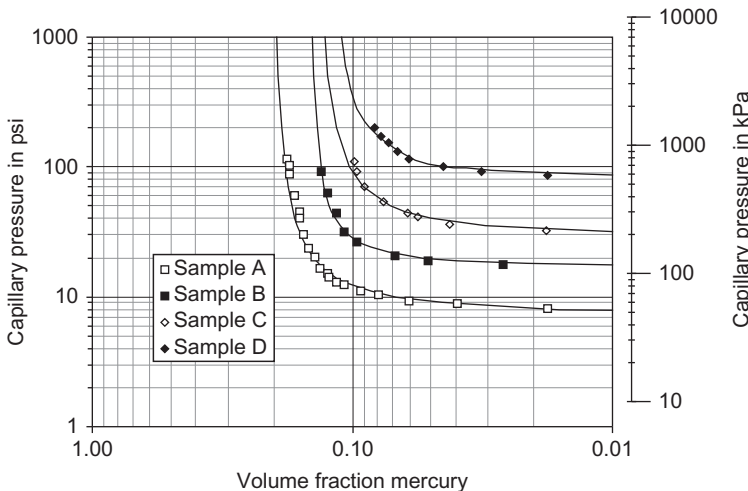


FIGURE 2.34 Capillary pressure curves (mercury air system) from a sandstone formation (Upper Wilcox Sandstone, Texas). Data taken from selected curves from Archie (1950) and Jorden and Campbell (1984).

A third capillary pressure curve is obtained if mercury is reinjected. Withdrawal and reinjection curves give a hysteresis loop (Tiab & Donaldson, 1996).

Capillary pressure is a measure of the porosity accessible through a given pore-throat size. Therefore, pore size distribution, ratio of pore-throat to pore-body radius, and pore shape control the measured real data.

Capillary pressure curve gives information about the pore size distribution (sorting). The shape of the middle part of the capillary pressure is:

- flat for well-sorted pore size; pore-throats have a narrow range of size;
- steep for poorly sorted pore size; pore-throats have a wide range of size.

Figure 2.34 shows some examples for sandstone with about the same porosity but different permeability. This demonstrates the rules resulting from the strong, but opposite dependence of permeability and capillary pressure upon pore radius:

- large pore throat diameter \rightarrow high permeability \rightarrow low capillary pressure,
- small pore throat diameter \rightarrow low permeability \rightarrow high capillary pressure.

Sample A: porosity $\phi = 0.216$, permeability $k = 430$ md

Sample B: porosity $\phi = 0.220$, permeability $k = 116$ md

Sample C: porosity $\phi = 0.196$, permeability $k = 13.4$ md

Sample D: porosity $\phi = 0.197$, permeability $k = 1.2$ md.

Curves are calculated using Thomeer's algorithm (see [Section 2.7.3](#)).

2.7.2 Drainage and Imbibition

There are two modes or directions of saturation change:

1. Drainage is the displacement of a wetting phase by a nonwetting phase—the nonwetting saturation increases. For a water-wet rock, the water saturation decreases.
2. Imbibition is the displacement of a nonwetting phase by a wetting phase—the nonwetting saturation decreases. For a water-wet rock, the water saturation increases.

The drainage curve (Figure 2.35) starts with the 100% water-saturated situation at the displacement pressure p_d . Displacement pressure p_d is the minimum pressure required for the nonwetting fluid (e.g., mercury in the laboratory, oil in the reservoir) to displace the wetting fluid (water) and enter the largest pores. Then, with increasing pressure and depending on the pore size distribution (sorting), the other pores are filled with the nonwetting fluid. The end of this process is reached only if irreducible water $S_{w,irr}$, which cannot be replaced, remains.

For the first imbibition curve (after drainage), the process starts at $S_{w,irr}$ and the wetting fluid (water) displaces the nonwetting fluid. Also in this process there is a remaining part of the displaced fluid—the residual (nonmovable) oil saturation S_{ro} in a reservoir. During the water-drive to produce the

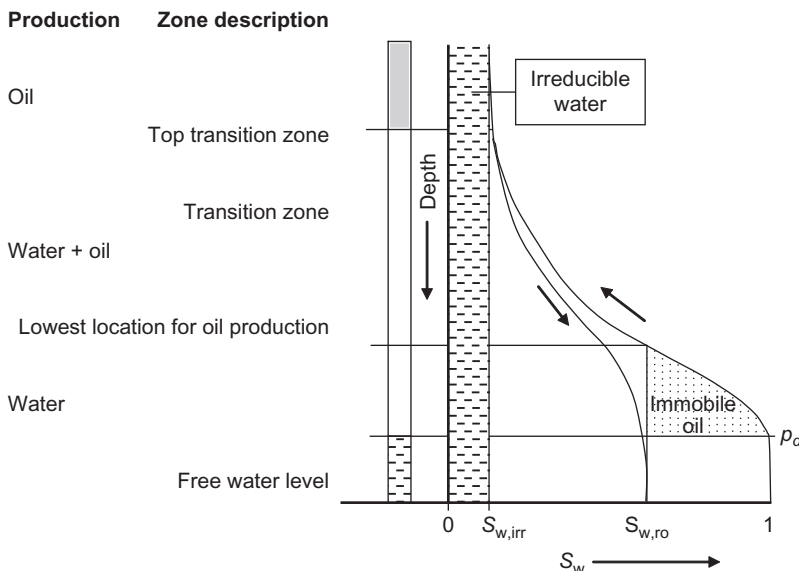


FIGURE 2.35 Drainage and imbibition capillary pressure curve indicating the different fluid production conditions; $S_{w,irr}$ is the residual (irreducible) water saturation and $S_{w,ro} = 1 - S_{ro}$ is the water saturation at residual oil saturation point S_{ro} .

oil, a part of the oil eventually remains trapped as disconnected drops/blobs in the pore space.

The immediate consequences from a capillary curve for fluid production are noted at the left-hand side of the figure.

Summarizing, capillary pressure curve:

- describes the fluid saturation distribution in a reservoir, depending on pore size distribution and wettability of the fluid components;
- represents the fluid distribution as function of pressure. Pressure can be transformed in height above FWL for reservoir conditions;
- gives with the displacement pressure an estimate for the largest pores, which dominantly control the permeability;
- delivers the irreducible water saturation and residual oil saturation;
- gives information about the pore size distribution (sorting).

2.7.3 Capillary Pressure—Description by an Equation

The capillary pressure curve reflects the pore geometry, the properties and the interactions between the different phases. For an analytical description or fitting of the experimentally determined curve, there are various models and equations (for details see references and textbooks like Ahmed, 2001; Amyx, 1960; Tiab & Donaldson, 1996, 2004).

Knowing the function (equation) for capillary pressure versus saturation, the prediction of water saturation distribution above the FWL (saturation height analysis) for the reservoir is possible. Thus, the fluid distribution can be constructed or estimated from core data, if they are representative for the homogeneous section of analysis.

In the technical literature there are different equations and models; some that are frequently used are:

- Leverett (1940): Capillary curves from a specific formation are reduced to a single dimensionless J -function versus saturation curve.
- Brooks–Corey equation and model (Brooks & Corey, 1964; Corey, 1994): This method also uses a dimensionless equation with normalized saturation terms.
- Thomeer (1960): Capillary pressure is approximated by a hyperbola. Introduction of a “pore geometrical factor” as curve parameter.

The dimensionless Leverett function is defined as:

$$J(S_w) = p_c(S_w) \sqrt{\frac{k}{\phi \sigma \cdot \cos \Theta}} \quad (2.73)$$

where

S_w is water saturation

$p_c(S_w)$ is capillary pressure

- k is permeability
- ϕ is porosity
- σ is surface tension
- Θ is the contact angle.

Reservoir rocks with similar pore geometry (but different absolute pore dimensions) result in the same $J(S_w)$ – function.

The connection between water saturation and capillary pressure can be described by the relationship (Darling, 2005)

$$S_w = S_{w,\text{irr}} + a \cdot J^b \quad (2.74)$$

where $S_{w,\text{irr}}$ is the irreducible water saturation and a, b are empirical parameters, derived from the measured data by fitting. For the determination of the parameters a, b a logarithmic plot $(S_w - S_{w,\text{irr}})$ versus J is recommended.⁸

The Brooks–Corey equation and model (Brooks & Corey, 1964; Corey, 1994) describes the capillary pressure of the first imbibition cycle by a dimensionless equation

$$\left(\frac{p_c}{p_d}\right)^{-\lambda} = \frac{S_w - S_{w,\text{irr}}}{1 - S_{w,\text{irr}}} = S_N \quad (2.75)$$

where λ is a rock sorting parameter (pore-size distribution coefficient), and

$$S_N = \frac{S_w - S_{w,\text{irr}}}{1 - S_{w,\text{irr}}} \quad (2.76)$$

is the normalized wetting phase saturation.

For capillary pressure p_c and water saturation $S_{w,\text{irr}}$ results

$$p_c = p_d \left(\frac{S_w - S_{w,\text{irr}}}{1 - S_{w,\text{irr}}} \right)^{-\frac{1}{\lambda}} \quad S_w = (1 - S_{w,\text{irr}}) \left(\frac{p_c}{p_d} \right)^{-\lambda} + S_{w,\text{irr}} \quad (2.77)$$

Reservoir rocks usually have a parameter λ between 0.25 and 4; poorly sorted rocks have low values and well-sorted rocks high values of λ (Murphy, 2004).

Relative permeability curves are also estimated via the Brooks–Corey equations (e.g., see Salazar et al., 2006):

$$\text{wetting phase relative permeability, } k_{rw} = k_{rw}^0 \cdot S_N^{e_w} \quad (2.78)$$

$$\text{nonwetting phase relative permeability, } k_{rnw} = k_{rnw}^0 (1 - S_N)^{e_{nw}} \quad (2.79)$$

⁸For $S_{w,\text{irr}}$ Darling (2005) recommends: “Set $S_{w,\text{irr}}$ equal to 0.01 below the lowest water saturation seen anywhere in the reservoir in cores or logs.”

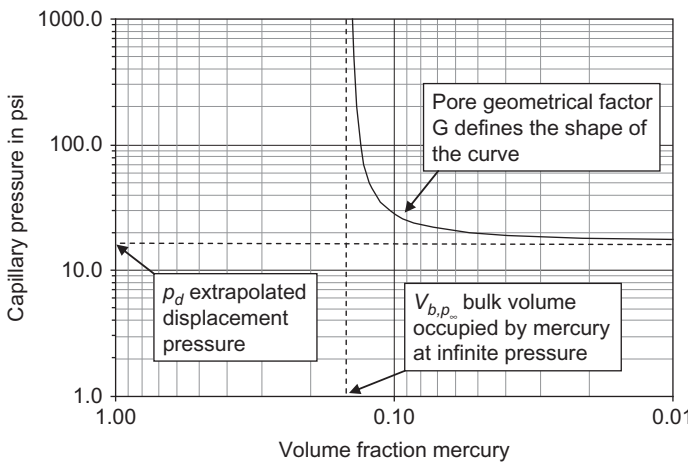


FIGURE 2.36 Capillary pressure curves and analysis by Thomeer's equation.

where k_{rw}^0 and k_{nw}^0 are relative permeability end points, and e_w and e_{nw} are the empirical exponents for each phase.

Thomeer (1960) proposes a logarithmic plot of capillary pressure versus water saturation and approximate data by a hyperbola. Each hyperbola is characterized by a “pore geometrical factor” as curve parameter. The plot shows $\log p_c$ versus $\log V_b$, where V_b is the volume of the nonwetting fluid (mercury), see Figure 2.36.

Capillary pressure curve is described by the equation with the parameter c^2

$$\log\left(\frac{p_c}{p_d}\right) \log\left(\frac{V_{b,pc}}{V_{b,p_\infty}}\right) = -c^2 \quad \text{or} \quad \frac{V_{b,pc}}{V_{b,p_\infty}} = 10^{\frac{-c^2}{\log\left(\frac{p_c}{p_d}\right)}} \quad (2.80)$$

where

p_d is extrapolated displacement pressure

V_{b,p_∞} is bulk volume occupied by the nonwetting fluid (mercury) at infinite pressure.

Frequently the equation is given as

$$\frac{V_{b,pc}}{V_{b,p_\infty}} = e^{\frac{-G}{\log\left(\frac{p_c}{p_d}\right)}} \quad (2.81)$$

where $G = 5.304 \cdot c^2$ is Thomeer's “pore geometrical factor.”

From Thomeer's analysis of the curves in Figure 2.34, the parameters in Table 2.11 result (Jorden & Campbell, 1984).

The Thomeer model is similar to the Brooks–Corey model. The difference between the two is the definition of the normalized saturation.

Methods for a derivation of permeability from the capillary pressure curve are given by Thomeer (1960) and Swanson (1981). Swanson (1981)

TABLE 2.11 Data of Thomeer Analysis of Capillary Pressure Data in Figure 2.34

Sample	ϕ	k in md	$V_{b,p\infty}$	p_d	G
A	0.216	430	0.215	6.7	0.2
B	0.220	116	0.150	16	0.1
C	0.196	13.4	0.145	26	0.2
D	0.197	1.2	0.130	65	0.2

analyzes the p_c versus S_w curve and defines a “point A” in order to find a correlation to permeability.

Other methods and techniques have been developed, for example, by Skelt and Harrison (1995) and Heseldin (1974).

Pittman (1992) derived relationships of porosity and permeability to various parameters derived from mercury injection-capillary pressure curves for sandstone.

In the example at the end of Section 2 capillary pressure data sets for a sandstone are analyzed using Leverett’s and Thomeer’s methods (visit the website <http://www.elsevierdirect.com/companion.jsp?ISBN=9780444537966> and refer Example-Sandstone).

2.7.4 Conversion of Laboratory Capillary Curves to Fluid Distribution in a Reservoir

Laboratory capillary pressure data can be converted into reservoir conditions. Thus, from a small core, the saturation distribution of a reservoir can be constructed if the core represents a pore system that is representative for the investigated reservoir section (homogeneity). This process covers two steps:

Step 1:

Conversion of the properties for the different fluid systems. The conversion is based on [Equation \(2.70\)](#). For two fluid systems (laboratory and reservoir), this immediately results in:

$$p_{c,\text{reservoir}} = p_{c,\text{laboratory}} \frac{[\sigma \cdot \cos \Theta]_{\text{reservoir}}}{[\sigma \cdot \cos \Theta]_{\text{laboratory}}} \quad (2.82)$$

where

$p_{c,\text{reservoir}}$ is the capillary pressure converted to reservoir conditions

$p_{c,\text{laboratory}}$ is the capillary pressure measured under laboratory conditions

TABLE 2.12 Typical Gradients

Fluid	Gradient in psi/ft	Gradient in $\text{Pa m}^{-1} = \text{N m}^{-3}$
Water	0.433–0.450	$(9.8–10.2) \cdot 10^3$
Oil	0.33	$7.5 \cdot 10^3$
gas	0.07	$1.5 \cdot 10^3$
	0.001–0.22	$(0.02–5) \cdot 10^3$

Source: After Hartman and Beaumont (1999).

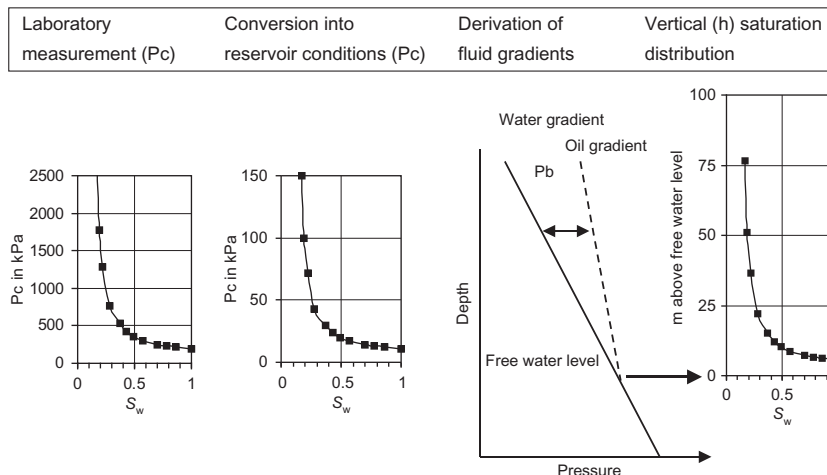


FIGURE 2.37 From laboratory capillary pressure measurement to the saturation versus depth estimate for the reservoir.

$[\sigma \cdot \cos\Theta]_{\text{reservoir}}$ is the fluid system properties for reservoir conditions (see Table 2.10)

$[\sigma \cdot \cos\Theta]_{\text{laboratory}}$ is the fluid system properties for laboratory conditions (see Table 2.10).

Step 2:

Transformation of pressure (in the reservoir system) into height above FWL. The reservoir converted capillary pressure is equivalent the buoyancy pressure in the reservoir. From the water gradient and oil gradient (or gas gradient), the height above the FWL results:

$$h' = \frac{P_{c,\text{reservoir}}}{\text{water gradient} - \text{hydrocarbon gradient}} \quad (2.83)$$

Table 2.12 gives some typical gradients.

[Figure 2.37](#) demonstrates the steps from the laboratory capillary pressure measurement to the saturation versus depth estimate for the reservoir.

These steps are also demonstrated by the example in the next section and on the website <http://www.elsevierdirect.com/companion.jsp?ISBN=9780444537966> (Example-Sandstone).

2.8 EXAMPLE: SANDSTONE—PART 1

2.8.1 Introduction

The data for the sandstone example are taken with friendly permission from the textbook “Well Logging and Formation Evaluation” by Darling (2005).

Log and core data are used to demonstrate subjects of various chapters (pore space properties, electrical properties, nuclear properties). All data and calculations are on the <http://www.elsevierdirect.com/companion.jsp?ISBN=9780444537966> (file: Example-Sandstone).

The used log section represents a sequence of sand, some limestone, and shale. Cored sections show the lithologies in [Table 2.13](#).

2.8.2 Core Data I: Porosity and Permeability—Derivation of a Poro–Perm Regression

From conventional core analysis, porosities and (horizontal) permeabilities are determined ([Table 2.14](#)).

Core data allow the derivation of a porosity–permeability regression.

The power-law results in:

$$k_h = 5.5 \cdot 10^5 \cdot \phi^{4.5} \quad R^2 = 0.98 \quad (2.84)$$

where permeability is in md and porosity is shown as a fraction. The data point of the limestone was eliminated for regression ([Figure 2.38](#)).

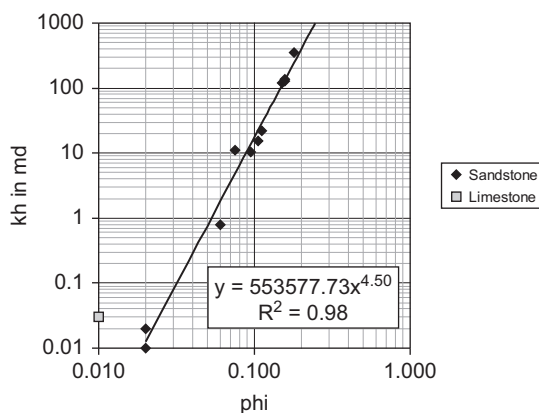
In Section 5.6 this regression is used to derive a permeability log from a porosity log.

TABLE 2.13 Lithologies of the Cored Sections

Depth (m)	Lithology	Depth (m)	Lithology
616.0 – 622.5	Shale	652.0 – 655.5	Silty sandstone
622.5 – 625.0	Sandstone	655.5 – 660.0	Shale
625.0 – 626.5	Limestone	660.0 – 662.0	Sandstone
626.5 – 637.5	Sandstone	662.0 – 664.0	Limestone
637.5 – 639.0	Shale	664.0 – 675.0	Shale
639.0 – 652.0	Sandstone		

TABLE 2.14 Core Data I

Core Description		Porosity and Permeability from Conventional Core Analysis		
Depth in m	Lithology	Depth in m	Plug Porosity	k_h in md
616.0–622.5	Shale	620	0.020	0.01
		622	0.020	0.02
622.5–625.0	Sandstone	624	0.111	22
625.0–626.5	Limestone	626	0.010	0.03
626.5–637.5	Sandstone	628	0.095	10.5
		630	0.156	135.6
		632	0.150	120
		634	0.075	11
		636	0.105	15.3
		638	0.060	0.8
637.5–639.0	Shale	640	0.179	350
		642	0.156	130

**FIGURE 2.38** Regression for porosity–permeability correlation.

2.8.3 Core Data II: Capillary Pressure Curves

At two core plugs 1 and 4 air–brine capillary pressure curves are measured as part of the special core analysis (SCAL). Data are plotted in [Figure 2.39A](#) ([Table 2.15](#)).

[Figure 2.39](#) shows the result of a step-by-step conversion to a plot of water saturation prediction versus depth. The depth of the FWL is at 646 m. In Section 8.9 this result is compared with the result of the determination of water saturation from logs.

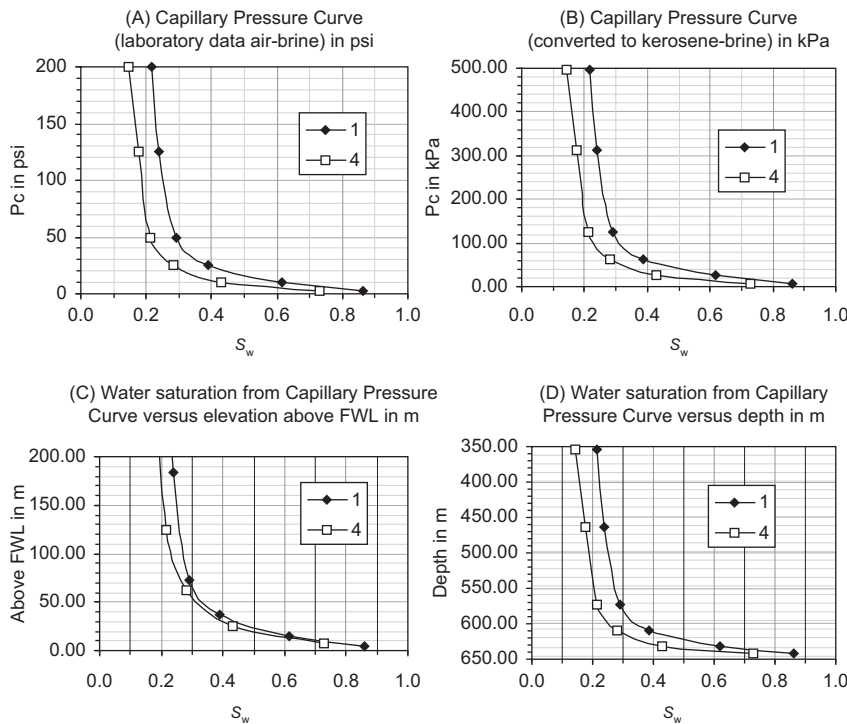


FIGURE 2.39 Capillary pressure curves and their conversion to reservoir conditions.

TABLE 2.15 Core Data II

Sample	Porosity	Permeability in md
1	0.131	67
4	0.179	278

Indications from the two capillary pressure curves (particularly the $S_{w,irr}$) correspond to the different permeability values.

The capillary pressure data set can be analyzed using the Leverett J -function and the Thomeer equation.

Figure 2.40A shows the correlation between the normalized saturation $S_w - S_{w,irr}$ and the J -function; for $S_{w,irr}$ was used 0.05. The resulting equation is

$$S_w = S_{w,irr} + 0.826 \cdot J^{-0.44} \quad (2.85)$$

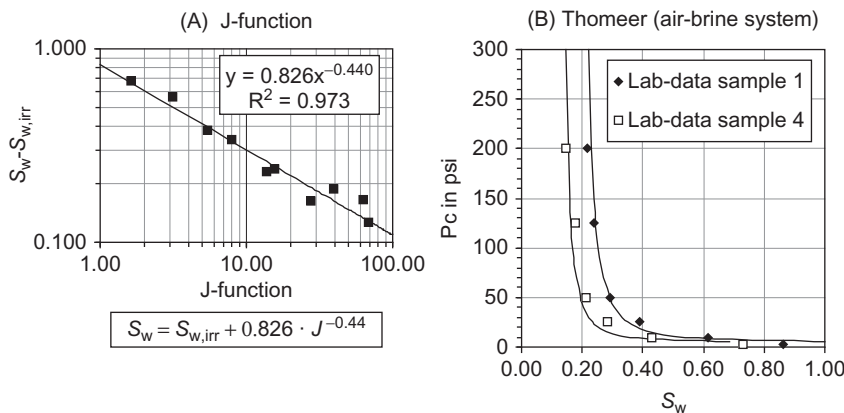


FIGURE 2.40 Analysis of capillary pressure data: (A) Leverett function (dots are both data sets) and (B) Thomeer equation for the two data sets.

TABLE 2.16 Parameters Derived Iteratively

Sample	G	p_d (psi)	V_{b,p_∞}
1	1.5	1	0.12
4	1.5	1	0.08

In Figure 2.40B, the Thomeer analysis is shown. Parameters have been derived iteratively as follows (Table 2.16):

Thus, the Thomeer equations are (p_c in psi):

$$\text{sample 1: } \frac{V_{b,p_c}}{0.12} = e^{\frac{1.5}{\log(p_c)}} \quad \text{sample 2: } \frac{V_{b,p_c}}{0.08} = e^{\frac{1.5}{\log(p_c)}} \quad (2.86)$$

Nuclear Magnetic Resonance— Petrophysical Properties

NMR is not the end all to petrophysics. It is a new tool for understanding and describing the subsurface, both reservoir and non-reservoir rocks, which expands the petrophysical content of our logging data, providing direct estimates of irreducible water, clay bound water, and the permeability.

Georgi and Chen (2007)

3.1 INTRODUCTION

The development and application of nuclear magnetic resonance (NMR) techniques in formation evaluation has originated new insights into the pore space and the pore fluids distribution and behavior. Primarily NMR measurements deliver relaxation data. Figure 3.1 shows as an example the relaxation process as decay of the measured signal calibrated in porosity units for two sandstones with the same porosity. The different decay curves result from different specific internal surface (high S_{por} for fine-grained sand, low S_{por} for coarse-grained sand). Processing techniques result in a partitioning of porosity in free movable (*bulk volume movable*—BVM) and capillary bound (*bulk volume irreducible*—BVI) fraction. This characterizes pore sizes and gives a link to a permeability estimate (see the following sections).

Most nuclei have a magnetic moment and an angular momentum; both are coaxial. NMR measurements in particular use this property of hydrogen nuclei and their ability to interact in a magnetic field like a bar magnet—gyro combination.

Hydrogen nuclei are in fluid molecules of water and hydrocarbons. Therefore, the response of this type of NMR measurements in geosciences applications comes only from the hydrogen nuclei and their physical environment in the pore space—there is no “matrix effect” as is commonly associated with conventional nuclear porosity determinations (see Sections 5.3 and 5.4).

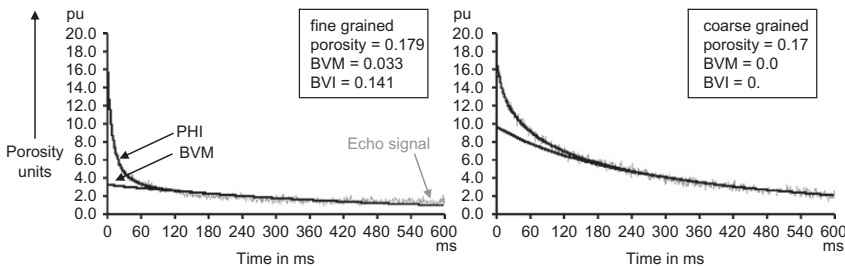


FIGURE 3.1 Comparison of the T_2 decay curves for a fine- and coarse-grained sand with the same porosity. The thin gray curve represents the signal (Georgi, personal communication).

The physical principles of nuclear magnetism are very complex and founded in quantum mechanics. Fundamentals of NMR physics can be found, for example, in the textbooks of Slichter (1980) or Fukushima and Roeder (1981). With respect to the application in reservoir characterization, some more phenomenological concepts can explain the possibilities of this technique. Following the monograph “NMR Logging—Principles and Applications” by Coates et al. (1999), these concepts include:

- nuclear magnetism,
- polarization,
- T_1 and T_2 relaxation time,
- spin echoes and CMPG pulse sequences.

In the following section, some of the fundamentals related to petrophysical properties are compiled. For a more detailed insight, the reader is advised to use the special literature (Coates et al., 1999; Dunn et al., 2002; Kenyon, 1997; Kleinberg & Vinegar, 1996; Vinegar, 1995). A specific “Tutorial nuclear magnetic resonance and formation porosity” was published by Appel (2004).

3.2 PHYSICAL ORIGIN

The phenomenon of NMR is based on the response of atomic nuclei to external magnetic fields. Many nuclei have a net magnetic moment and angular momentum or spin. In the presence of an external magnetic field, the atomic nucleus interacts with the magnetic field. The result is a precession motion around the direction of the external field.¹ Coherent spinning magnetic nuclei produce a measurable signal. It is maximized at resonant frequency.

In principle, an NMR measurement can be made on any nucleus that has an odd number of protons or neutrons or both, such as the nuclei of hydrogen (^1H), carbon (^{13}C), and sodium (^{23}Na). For most of the nuclei found in earth formations, the nuclear magnetic signal induced by external magnetic fields

¹This motion is comparable to a gyroscope which precesses around the earth's gravitational field.

TABLE 3.1 NMR Properties of Various Nuclear Species

Nucleus	Spin	$\gamma/2\pi$ in MHz/T	% Natural Abundance
¹ H	1/2	42.58	99.98
²³ Na	3/2	11.26	100.0
¹³ C	1/2	10.70	1.11
¹⁷ O	5/2	5.77	0.037

Ellis and Singer (2007); Western Atlas (1996).

is small. However, hydrogen, which has only one proton and no neutron, has a relatively large magnetic moment, and produces a relatively strong signal. The large number of atoms in a mole of fluid (following Avogadro's number) results in detectable signals, because in this case, a relatively large number of the unpaired spins do not cancel each other.

The controlling nucleus property is the gyromagnetic ratio γ (Table 3.1). Gyromagnetic ratio is defined as the ratio of the magnetic moment to the angular momentum. It is a measure of the strength of the nuclear magnetism and a constant for a given nucleus. Hydrogen has a high gyromagnetic ratio.

The precessional motion of the spinning nucleus is originated by the magnetic interaction of the magnetic elemental moment and the external field.² Precession has a characteristic frequency called “Larmor frequency” f_L . Larmor frequency is controlled by the gyromagnetic ratio γ as “substantial property” and the external magnetic field strength B_0 as “external field property.”

$$f_L = \left(\frac{\gamma}{2\pi} \right) B_0 \quad (3.1)$$

Table 3.1 shows that besides the protons (H), the Na could be of influence, which is associated with saltwater. However, because the concentration of Na, even in highly mineralized formation water, is small compared to H, the influence is very small.

The conversion for magnetic field strength is: 1 Gauss = 10^{-4} Tesla

3.3 THE PRINCIPLE OF AN NMR MEASUREMENT

The NMR measurement consists of a series of steps called the CPMG (Carr–Purcell–Meiboom–Gill) sequence (Carr & Purcell, 1954; Meiboom & Gill, 1958) in which two magnetic fields are applied:

1. B_0 , an external static field: this field aligns the nuclei and results in a magnetic moment M .

²This effect is used also for proton precession magnetometers.

2. B_1 , a “tipping” field: this is a series of electromagnetic, radio frequency (RF) pulses (with Larmor frequency). It is applied perpendicular to the B_0 field.

The four CPMG steps are as follows.

Step 1: Hydrogen nuclei alignment.

The static field B_0 aligns the elemental magnets in the direction of B_0 . This polarization results in a net magnetization (vector summation of the individual magnetic moments). Polarization does not occur immediately but rather grows with a time constant T_1 and can be described as an exponential law. Magnetization at time t after start of the experiment is

$$M(t) = M_0 \left[1 - \exp\left(-\frac{t}{T_1}\right) \right] \quad (3.2)$$

where M_0 is the final and maximum magnetization in a given magnetic field B_0 .

Step 2: Tipping the aligned protons into transverse plane.

By an oscillating magnetic field B_1 , perpendicular to the direction of B_0 , the aligned protons are tipped from the longitudinal direction (direction of B_0) into the transverse plane. This magnetic field is provided by an RF pulse with resonant frequency (Larmor frequency) and a given duration. The duration determines how far the protons are tipped relative to the B_0 field. The result is a precession with the Larmor frequency in the plane perpendicular to B_0 . Because the protons precess about the axis of the B_0 field, the proton spin axis now describes a cone figure. The maximum NMR signal is received when the protons are tipped by an angle of 90° .

Step 3: Precessing and dephasing.

At the beginning, all the protons precess in unison with the same frequency; they generate a magnetic field that is measured with an antenna. After turning off B_1 , the protons begin to dephase—they lose phase coherence and the resulting net magnetization decreases. This decay with the characteristic relaxation time T_2 has two origins:

1. Dephasing caused by diffusion in an inhomogeneous magnetic field—reversible dephasing effect (this is sometimes referred to as T_2^*).
2. Dephasing caused by molecular interactions—irreversible dephasing effect.

Note that T_1 recovery occurs continually and causes some protons to realign with the B_0 field. However, when subsequent π - or 180° -pulses are applied, as described in Step 4, these protons are randomized relative to their orientation with respect to the B_0 field. This implies that T_2 relaxation time constant must be less than or equal to T_1 relaxation time constant.

Step 4: Refocusing by (partial) reversible dephasing.

The application of a π - or 180° -pulse reverses the precession motion. The idea is that the reverse process for the individual protons has the same rate and the effect of inhomogeneities is compensated after one cycle. The rephased

protons generate a signal—the “spin echo.” Because the reversion is not perfect (irreversible parts of dephasing by molecular processes), the echo signal is smaller than the initial signal. Therefore, step by step, the coherent fraction of the magnetization decreases, and the measured signal becomes smaller, i.e., a relaxation is observed. This procedure of a π -pulse can be applied several times. The time between two π -pulses is the inter-echo time TE. The decay of the amplitude of the echo signals is called transverse relaxation time T_2 because dephasing occurs in the plane transverse to the field B_0 . The decay curve connects the echo amplitudes and is controlled by the irreversible components of the decay.

If after several refocusinges, protons have lost their coherence, the CPMG pulse sequence is finished and the protons return to their equilibrium position. At the end of a CPMG sequence, the protons are completely randomized; to undergo a new sequence, they must be polarized again.

For practical application, the following acquisition parameters are important (Figures 3.2 and 3.3):

- *TE—inter-echo time:* the time between the π -pulses and identical to the time between two echoes.

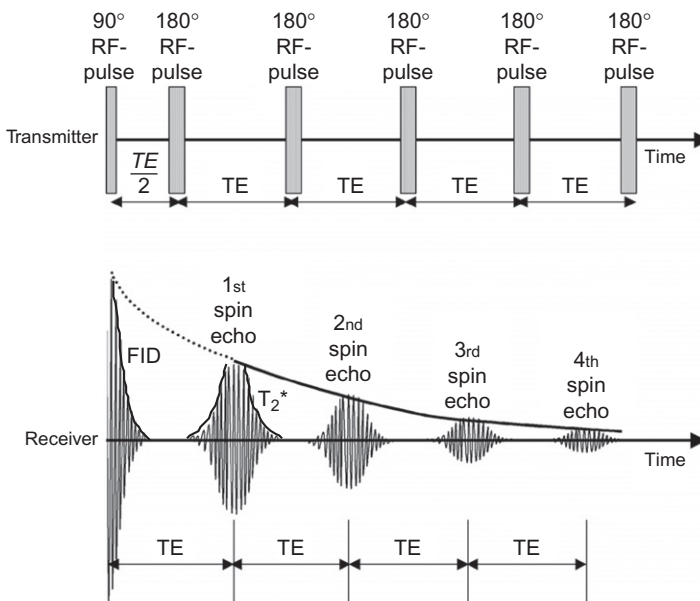


FIGURE 3.2 Carr–Purcell–Meiboom–Gill (CPMG) sequence: Timing of the RF pulses transmitted into the formation, and free induction decay (FID) and spin echoes detected by the receiver. The envelope of the spin echo maxima decays exponentially with the time constant T_2 . The extrapolation of the spin echo envelope to time zero or the initial amplitude of the FID signal yield the net magnetization. After calibration, the net magnetization is a direct measure of formation porosity (Appel, 2004).

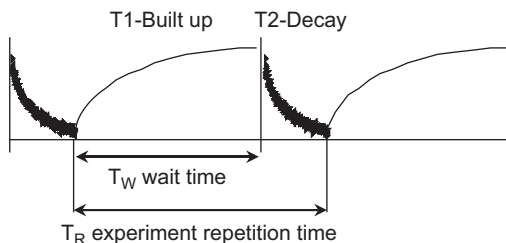


FIGURE 3.3 T_1 built up and T_2 decay of a CMPG sequence with definition of the two acquisition parameters T_W (wait time) and T_R (experiment repetition time).

- T_W —wait time: the time between the last CMPG π -pulse and the first CMPG pulse, the $\pi/2$ pulse, of the next experiment at the same frequency. This is the time allowed for the T_1 recovery process. Generally one chooses T_W to be equal to three times the longest T_1 of the slowest polarizing fluid in the pore space.
- T_R or T_X —experiment repetition time: the time for one sequence from the beginning of one pulse sequence to the start of the next pulse sequence.

In most logging tools, the wait time, T_W , and the inter-echo time, TE , are the key acquisition parameters to probe the hydrocarbon fluid properties (Georgi & Chen, 2007).

The relaxation (and built-up) process can be described by an exponential function with the two relaxation time terms:

- T_1 —longitudinal, or spin—lattice relaxation time;
- T_2 —transverse, or spin—spin relaxation time.

3.4 NMR RELAXATION MECHANISMS OF FLUIDS IN PORES AND FLUID-SURFACE EFFECTS

3.4.1 Overview

The primary NMR information gives:

- the initial signal amplitude, which is proportional to the number of hydrogen nuclei of the fluids in the measurement volume. Therefore, the amplitude of the received NMR signal can be scaled directly in porosity units by calibration;
- the exponential amplitude decay, expressed by the relaxation time spectrum.

Fluids and their interactions in rock pores control the relaxation process by three independent mechanisms:

1. Bulk fluid processes (affects both T_1 and T_2 relaxation): this process is controlled by type and properties of the fluid in the pores.

2. Surface relaxation (affects both T_1 and T_2 relaxation): this process is controlled by pore-size distribution and surface relaxivity.
3. Diffusion in the presence of magnetic field gradients (affects T_2 relaxation only): this molecular diffusion process is controlled by type and properties of the fluid in the pores.

Because the processes act in parallel, the resulting relaxation time is given by the sum of relaxation rates. For transverse relaxation, all three mechanisms contribute

$$\frac{1}{T_2} = \frac{1}{T_{2,\text{bulk}}} + \frac{1}{T_{2,\text{surface}}} + \frac{1}{T_{2,\text{diffusion}}} \quad (3.3)$$

For longitudinal relaxation only bulk and surface relaxation contribute; longitudinal relaxation is unaffected by diffusion in a gradient field (Kenyon, 1997):

$$\frac{1}{T_1} = \frac{1}{T_{1,\text{bulk}}} + \frac{1}{T_{1,\text{surface}}} \quad (3.4)$$

where

T_1 is the overall longitudinal relaxation time as measured and determined by inversion recovery or other NMR acquisition

$T_{1,\text{bulk}}$ is the bulk longitudinal relaxation time of the pore fluid (no container effects, $T_{1,\text{surface}} \rightarrow 0$)

$T_{1,\text{surface}}$ is the longitudinal relaxation time of the pore fluid resulting from surface relaxation

T_2 is the overall transverse relaxation time as measured by a CPMG sequence

$T_{2,\text{bulk}}$ is the bulk transverse relaxation time of the pore fluid (no container effects, $T_{2,\text{surface}} \rightarrow 0$)

$T_{2,\text{surface}}$ is the transverse relaxation time of the pore fluid resulting from surface relaxation

$T_{2,\text{diffusion}}$ is the transverse relaxation time of the pore fluid as induced by diffusion in the magnetic field gradient.

T_1 and T_2 are controlled by molecular processes. For water-saturated rocks, it is frequently the case that $T_1 \approx T_2$. It varies if oil or gas are present (Kenyon, 1997; see [Section 3.4.2](#)).

The relative contribution of the three relaxation mechanisms depends on the type of fluid in the pores (water, oil, or gas), the sizes of the pores, the strength of the surface relaxation, and the wettability of the rock surface. Some general rules are formulated by Kleinberg and Vinegar (1996) as follows:

- For the water in a water-wet rock, the surface relaxation will usually dominate. A bulk relaxation correction must be made when there are iron, manganese, chromium, nickel, or other paramagnetic ions in the mud filtrate.

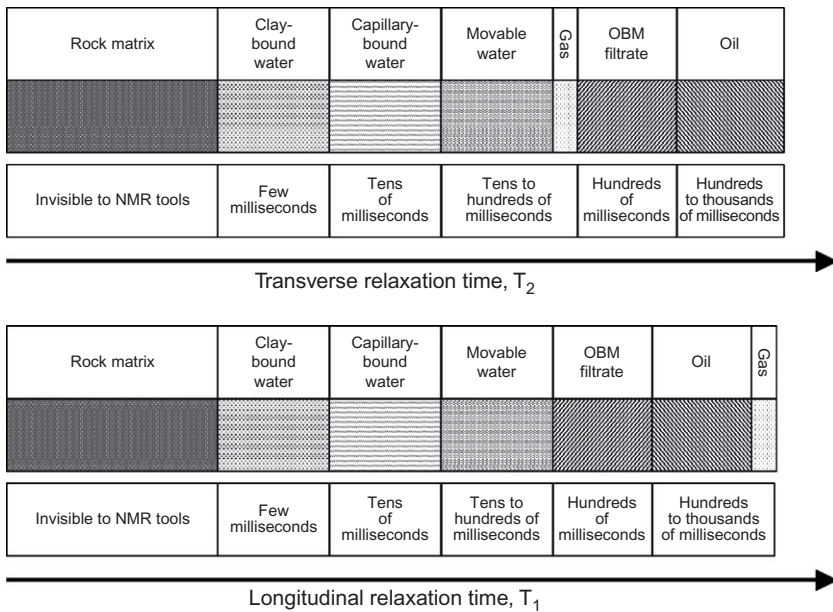


FIGURE 3.4 Approximate relaxation time response of the various formation fluid components. Due to the fast Brownian motion of gas molecules, the NMR signal originating from hydrogen in gas features a significantly shorter transverse relaxation time (T_2) compared to its longitudinal relaxation time (T_1). The depicted situation assumes a logging tool with a narrow distribution of magnetic field gradients (Appel, 2004).

- Water in vugs will relax at its bulk rate, modified by diffusion effects.
- Similarly, oil in water-wet rock will relax at its bulk rate with a diffusion effect.
- The T_1 of gas will be controlled by bulk relaxation, while T_2 is controlled by diffusion relaxation.

Figure 3.4 gives a first overview to the magnitude of relaxation time for approximate relaxation time response of the various formation fluid components after Appel (2004). It may be noted that the labels are based mainly on empirical results and a more phenomenological consideration. The detailed analysis must consider the processes of NMR related to physical properties of interface regions and fluids.

Figure 3.5 demonstrates the bulk and surface contributions of transverse relaxation in a water-filled pore. The following sections describe briefly the three mechanisms.

3.4.2 Bulk Relaxation

Bulk relaxation is the intrinsic relaxation property of a fluid. Bulk relaxation time for fluids is in the order of tens of milliseconds to seconds. To obtain a

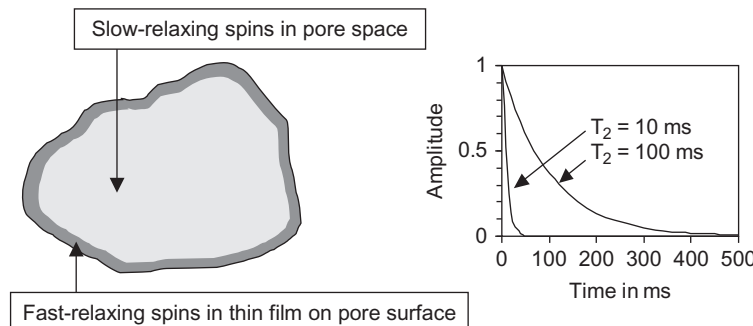


FIGURE 3.5 Bulk and surface contributions of transverse relaxation in a water-filled pore. The diagram on the right shows relaxation curves calculated for $T_2 = 10$ ms (surface relaxation) and $T_2 = 100$ ms (bulk relaxation).

TABLE 3.2 NMR Properties of Reservoir Fluids

Fluid	T_1 in ms	T_2 in ms	Typical T_1/T_2	HI	Ref.
Brine	1–500	1–500	2	1	C
	1–500	0.67–200		1	A
Oil	3,000–4,000	300–1,000	4	1	C
	5,000	460		1	A
Gas	4,000–5,000	30–60	80	0.2–0.4	C
	4,400	40		0.38	A

A: Akkurt *et al.* (1995, 1996); Vinegar *et al.* (1996); Kleinberg *et al.* (1994); C, Coates *et al.* (1999).

correct measurement, the fluid must be placed in a large container to eliminate the effects of surface relaxation; measurement is made using a homogeneous magnetic field. Even then, one must be careful because dissolved oxygen (paramagnetic) can significantly shorten the T_2 relaxation from the nominal three seconds at room temperature and pressure.³ Table 3.2 gives some data.

Bulk relaxation time is controlled by fluid composition, viscosity, density, and temperature, as demonstrated by the following relationships (Coates *et al.*, 1999; Kleinberg *et al.*, 1994; Vinegar *et al.*, 1996).

³Paramagnetic chromium ions in chromium lignosulfate mud filtrates can also reduce the bulk relaxation time of water (Kleinberg and Vinegar, 1996).

Bulk relaxation of water is dependent on viscosity and temperature:

$$T_{1,\text{bulk}} \cong T_{2,\text{bulk}} = 3 \left(\frac{T}{298 \cdot \eta} \right) = 0.01007 \left(\frac{T}{\eta} \right) \quad (3.5)$$

where T is the absolute temperature in Kelvin and η the viscosity in cp.

Bulk relaxation of crude oil is influenced by viscosity (increase of viscosity shortens relaxation time, and different proton mobility results in a broadening of T_2 distribution (Coates et al., 1999):

$$T_{1,\text{bulk}} \cong T_{2,\text{bulk}} = 0.00713 \left(\frac{T}{\eta} \right) \quad (3.6)$$

where T is the absolute temperature in Kelvin and η the viscosity in cp.

The bulk relaxation time $T_{1,\text{bulk}}$ of gas (mostly methane CH_4) is a function of the composition, temperature, and pressure. The pressure of gas controls the density; this results in the equation

$$T_{1,\text{bulk}} \cong 2.5 \cdot 10^4 \left(\frac{\rho_g}{T^{1.17}} \right) \quad (3.7)$$

where T is the absolute temperature in Kelvin and ρ_g is the gas density in g cm^{-3} .

The relaxation T_2 of gas is controlled by the dominant diffusion effects. Therefore, there is no relationship between the two relaxation times (Kleinberg & Vinegar, 1996).

3.4.3 Surface Relaxation

Surface relaxation is a fluid–solid interface effect. The “bonding” of fluid molecules at the surface originates a faster relaxation of the protons, thus a shorter relaxation time compared with bulk relaxation. This effect is controlled by:

- the specific internal surface S_{por} or surface-to-volume ratio (Section 2.3);
- the specific interface property, expressed by surface relaxivity ς_{surf} .

$$\frac{1}{T_{\text{surface}}} = \varsigma_{\text{surf}} \cdot S_{\text{por}} \quad (3.8)$$

Surface relaxivity is a measure of a surface’s ability to cause protons to relax, i.e., lose their phase coherence due to magnetic interactions at the fluid–solid interface. It is dominated by paramagnetic ions on the grain surfaces (Kleinberg et al., 1994). In general, surface relaxation falls in the range $\varsigma_{\text{surf}} \approx 0.003\text{--}0.03 \text{ cm s}^{-1}$ for clastics. It is smaller for carbonates (Coates et al., 1999; Kenyon, 1997; Fehr, 2007; Western Atlas, 1996). Kleinberg and Vinegar (1996) explain this different behavior as follows: “Sandstones generally have an iron content of about 1%, which makes fluid proton relaxation

TABLE 3.3 Some Clay Properties

Clay Type	Specific Internal Surface Area in $\text{m}^2 \text{ g}^{-1}$ (Measured)	CEC in meq/100 g	T_2 in ms	Water Content in %
Montmorillonite	616	76	0.3–1	19–54
Illite	93	15	1–2	9–16
Kaolinite	18	2	8–16	12–20

Source: After Prammer *et al.* (1996).

fairly efficient. Carbonates tend to have lower rates of fluid relaxation than sandstones.”

Because the decay rates are related to the surface-to-volume ratio or internal pore surface (and pore size), the following rules can be derived:

- short T_2 indicates small pores, large surface-to-volume ratio, and low permeability;
- long T_2 indicates large pores, small surface-to-volume ratio, and high permeability.

It must be noted, however, that there is no possibility to derive the spatial distribution of different pore sizes in the volume of investigation. Thus, a sandstone, composed of a mixture of small and large grains (poorly sorted) and a laminated sand with alternating layers of fine- and coarse-grained sands of the similar grain-size distribution for the laminated section, produces the same NMR signal and T_2 distribution. The same situation exists for shaly sands of two very dissimilar distributions: laminated and dispersed shaly sands (see Section 8.5). Therefore, resolution of anisotropy effects (e.g., permeability) for NMR alone cannot be expected, and specific “anisotropy indicators” such as orthogonal resistivity systems or high-resolution imaging tools should be used.

Clay bound water (CBW) creates the shortest relaxation time. This “clay mineral—bound water effect” is controlled by clay mineral properties. Therefore, relaxation time correlates with other “interface properties” of clay minerals such as specific internal surface and CEC (Table 3.3). Thus, T_2 could be used as a CEC indicator (see, for example, Martin & Dacy, 2004).

3.4.4 Diffusion-Induced Relaxation

When a significant gradient exists in the static magnetic field, *molecular diffusion* causes additional dephasing and, therefore, increases the T_2 relaxation rate (diffusion has no influence on T_1 relaxation). This dephasing is caused by

the molecule moving into a region in which the magnetic field strength is different, and, thus, in which the precession rate is different. Gas, gas condensate, light oil, water, and some medium-viscosity oils show such a diffusion-induced relaxation in a gradient magnetic field. The longer the inter-echo spacing in the CPMG sequence, the more pronounced the diffusion effect.

Gradients in the static magnetic field have two possible sources:

1. Magnetic configuration of the tool.
2. Magnetic susceptibility contrast between different grains, the grain material, and pore-filling fluids in porous rocks.

The diffusion-induced relaxation rate is

$$\frac{1}{T_{2,\text{diffusion}}} = \frac{D}{12} (\gamma \cdot G \cdot \text{TE})^2 \quad (3.9)$$

where

D is the molecular diffusion coefficient

γ is the gyromagnetic ratio of a proton

G is the field-strength gradient (G cm^{-1})

TE is the inter-echo spacing used in the CPMG sequence.

[Table 3.4](#) gives some data for the diffusion coefficient of water, oil, and gas.

The following rules are for the diffusion coefficient:

1. Diffusion coefficient of oil is less than that of water, but diffusion coefficient of gas is much larger than that of water.
2. Diffusion coefficient for gas, oil, and water increases with temperature.
3. Diffusion coefficient for gas decreases with increasing pressure (gas density increases with pressure).

TABLE 3.4 Diffusion Coefficient for Reservoir Fluids in $10^{-5} \text{ cm}^2 \text{ s}^{-1}$

Pressure	Temperature	Diffusion Coefficient in $10^{-5} \text{ cm}^2 \text{ s}^{-1}$			
		Water	Oil, $\eta = 5 \text{ cP}$	Oil, $\eta = 39 \text{ cP}$	Gas
14.7 psi	72°F	2.1	0.26	0.03	38,000
5,000 psi	72°F	2.1	0.26	0.03	107
5,000 psi	212°F	8.7	2.44	0.87	183
10,000 psi	72°F	2.1	0.26	0.03	82
10,000 psi	212°F	8.7	2.44	0.87	123
Typical Gulf of Mexico reservoirs		7.7		7.9	100
(Akkurt et al., 1996)					

Western Atlas (1996), Akkurt et al. (1996).

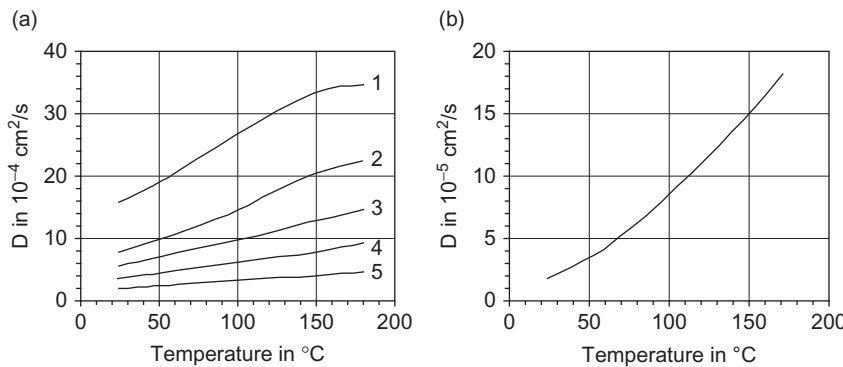


FIGURE 3.6 Diffusion coefficient versus temperature (plotted using graphs from Kleinberg & Vinegar, 1996): (a) Methane, curve parameter is gas pressure: 1—1,600 psi = 11.0 MPa, 2—3,000 psi = 20.7 MPa, 4—4,500 psi = 31.0 MPa, 5—8,300 psi = 57.2 MPa, 6—22,800 psi = 157 MPa. (b) Water (note the different scale for D).

4. Diffusion coefficient for oil varies depending on molecular compositions, which influences viscosity.

The diffusion coefficient of a liquid-phase reservoir fluid depends on temperature T (in K) and viscosity η in cp (Vinegar, 1995; [Figure 3.6b](#)).

$$D = C \frac{T}{298 \cdot \eta} \quad (3.10)$$

where the empirical factor C is approximately 1.2 for oil and 3 for water (Chen et al., 2000).

The diffusion coefficient of methane is very high and depends on pressure (controlling density) and temperature ([Figure 3.6a](#)). Relaxation time T_2 of gas is therefore completely controlled by the diffusion mechanism (Kleinberg & Vinegar, 1996).

For this consideration “unrestricted diffusion” is assumed; pore walls and oil–water interfaces can reduce the distance that a proton can diffuse; this situation is called “restricted diffusion” (see, for example, Coates et al., 1995).

3.4.5 Description of Relaxation as a Multi-exponential Decay—Data Inversion

The observed T_2 decay is the sum of T_2 signals from independently relaxing protons under different conditions in the pores:

- Shortest T_2 typically is related to clay bound water.
- Medium T_2 is related to capillary bound water.
- Long T_2 is related to free movable, producible fluids.

Porous rocks generally contain a variety of pore sizes. The measured signal represents the superposition of all decaying signals as a spectrum. The simple decay function must be reformulated as a multi-exponential relaxation decay function:

$$M(t) = \sum_{i=1}^n M_i(0)e^{-t/T_{2i}} \quad (3.11)$$

where

$M(t)$ is the measured magnetization at time t

$M_i(0)$ is the initial magnetization from the i th component of relaxation

T_{2i} is the decay time constant of the i th component (transverse relaxation).

Decomposition of the T_2 decay data into a series of exponential decay functions is a highly unstable inversion process. One reason that the inversion is complicated is that the exponential decay functions are not orthogonal and hence removing or adding another term affects all terms in the inversion. An alternative model to the multi-exponential decay model was proposed by Miller et al. (1998). Their formulation is based on gamma functions, which form an orthogonal basis for the inversion of the T_2 decay data. Test results derived from 60 echo trains show that the solution is stable even with noisy data (Carmona et al., 2010).

By inversion, the measured NMR signal is decomposed into its constituting components and plotted as a T_2 distribution (Figure 3.7). The result of

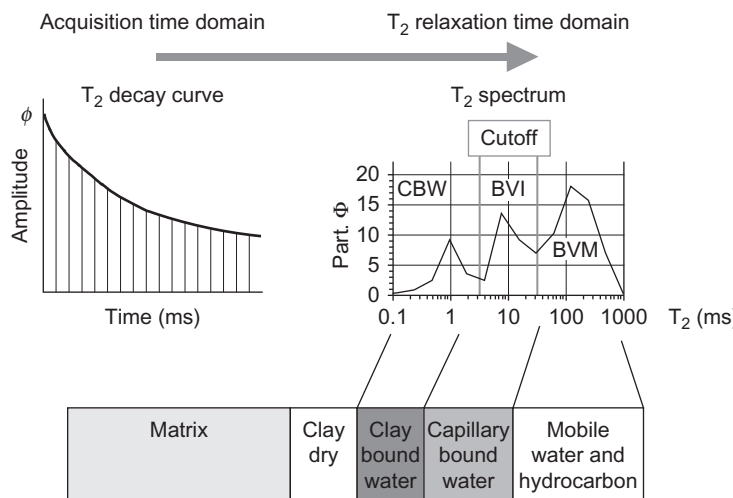


FIGURE 3.7 NMR data processing—principle. Measured data are in a time domain. The inversion process results in a partitioning of the individual relaxation contributions (bulk volumes) with the three regions clay bound water (CBW), capillary bound water (BVI), and free movable water (BVM). Regions are separated by cutoffs.

this process is a partitioning of the relaxation curve into the individual relaxation contributions from different fluid types and pore-size distributions. The amplitude of the received NMR signal is scaled directly in porosity units.

The T_2 spectrum is the primary result for following petrophysical interpretation directed on (Westphal et al., 2005):

- *Porosity*: Porosity is proportional to the strength of the NMR echo train at $t = 0$. This value corresponds to the area under the T_2 distribution curve.
- *T_2 distribution*: The T_2 distribution is composed by the individual constituents and related to three main effects: bulk relaxation, surface relaxation, and diffusion relaxation. Inversion allows the separate interpretation of the three effects.
- *BVI versus BVM*: The BVI (bulk volume irreducible fluid) and BVM (bulk volume of movable fluid) can be estimated by partitioning the T_2 distribution and “can also be interpreted as pore-size distribution” (Chen & Georgi, 1997; Kenyon, 1992; Straley et al., 1995).
- *Permeability*: Permeability is not measured directly with NMR but is estimated on the basis of T_1 and/or T_2 , porosity and pore size (BVM, BVI).

The regions between CBW, BVI, and BVM are separated by “cutoffs,” which depend on the specific internal surface and the surface relaxation. Recommended values are:

- *Cutoff CBW/BVI*: 3 ms (1–5 ms, depends on clay minerals).
- *Cutoff BVI/BVM*: for faster decaying clastics about 33 ms, for slower decaying carbonates about 90 ms.

These values are empirical and used to “differentiate different pore sizes and quantify the amount of water bound by capillary pressures >50 psi in the rock” (Western Atlas, 1996).

Carbonates in particular exhibit a broad variation of T_2 cutoff values as a result of the diversity of pore geometries. Westphal et al. (2005) investigated a series of carbonate rock types and recommend:

- If the predominant pore types are infilled pores or isolated pores like intraparticle pores resulting in lower permeability, a T_2 cutoff value of $T_2 < 45$ ms should be used.
- If low connectivity of interparticle pores predominates, a T_2 cutoff value of 45–60 ms will deliver the best results.
- If connected porosity originating from interparticle pore space or postdepositional diagenetic processes such as dolomitization or dissolution increasing porosity and connectivity predominated, a T_2 cutoff value of 60–110 ms will provide the best results.
- For carbonates with no visual porosity, a T_2 cutoff value of 120–190 ms is suitable.
- For carbonates with very large moldic and/or vuggy pores, the T_2 cutoff value should be at >200 ms.

3.5 APPLICATIONS

The analysis of NMR measurements delivers information about porosity, pore-filling fluids, and petrophysical properties related to the relaxation processes. The influence of the many petrophysical properties represents both a challenge and an opportunity for petrophysics. Some of the influences are additive and difficult to isolate. Fortunately, however, one can control many of the NMR data by using acquisition parameters (e.g., TE and TW), which allow an isolation of some of petrophysical effects (Akkurt et al., 1995; Chen et al., 2006; Vinegar et al., 1996).

3.5.1 Porosity and Pore Volume Partitioning

With the inversion, the relaxation curve is transformed into a porosity distribution with respect to the individual relaxation times. Association of relaxation times with different pore sizes and water volumes allows the determination of:

- total porosity (total area under the curve) $\phi = \text{PHI}$;
- volume of clay bound water (CBW);
- volume of irreducible (capillary bound) water (BVI);
- volume of free movable fluids (BVM).⁴ The movable fluid can be any combination of water, oil, and/or gas.

The observed effects are controlled by the density of proton distribution. Porosity calibration of most tools is based on the known volume of water. For other fluids—particularly gas—a normalization using a “hydrogen index,” HI, is therefore recommended. Hydrogen index is defined as (Appel 2004; Zhang et al., 1998) “the ratio between the amount of hydrogen in the sample and the amount of hydrogen in pure water at standard conditions (STP):

$$\text{HI} = \frac{\text{amount of hydrogen in sample}}{\text{amount of hydrogen in pure water at STP}} = \frac{\text{moles H cm}^{-3}}{0.111} = \frac{\rho_{\text{fl}} \cdot N_{\text{H}} / M}{0.111} \quad (3.12)$$

where

ρ_{fl} is the mass density of the fluid in g cm^{-3}

N_{H} is the number of hydrogen atoms in the molecule

M is the molecular weight of the fluid.

The denominator, 0.111, represents the moles of hydrogen in one cubic centimeter of water at standard conditions. Consequently, the numerator is

⁴Also referred to as free fluid index or FFI.

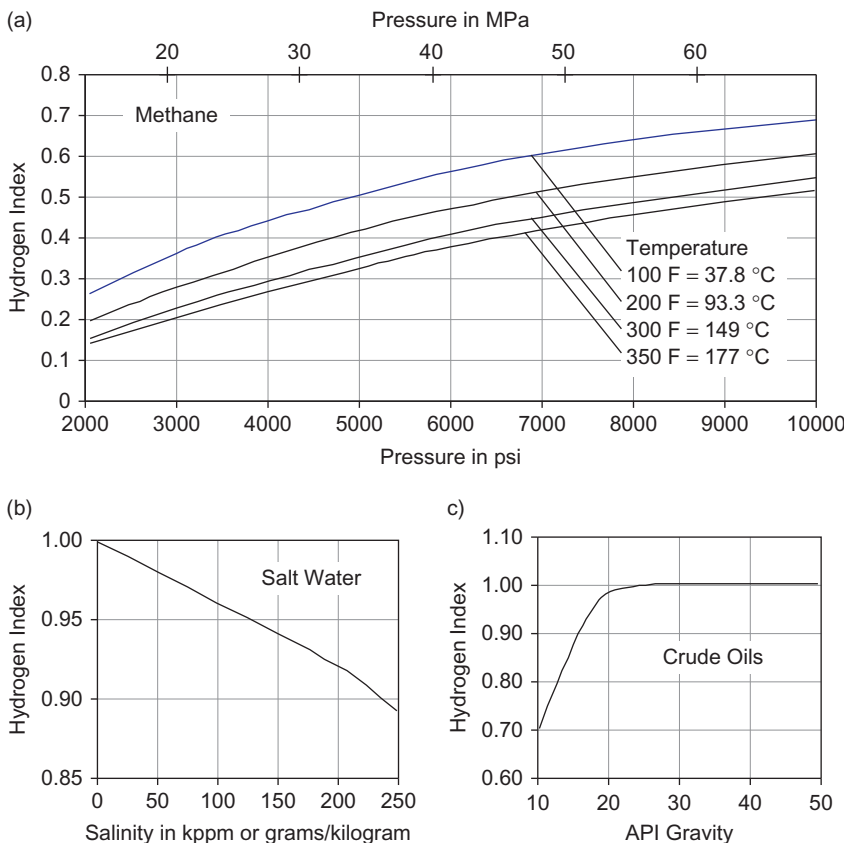


FIGURE 3.8 Hydrogen index for different fluids, compiled after Kleinberg and Vinegar (1996) and Akkurt et al. (1996): (a) Hydrogen index of methane versus pressure; curve parameter is the temperature. (b) Hydrogen index of water versus salinity. (c) Hydrogen index of crude oils versus API gravity (Kleinberg and Vinegar note that the apparent decrease of HI below 17° API is caused primarily by components in the crude oil relaxing faster than 1 ms).

the number of moles of hydrogen in the same volume of the bulk sample at the conditions of the measurement.”

Figure 3.8 shows the hydrogen index for different fluids (compiled after figures from Kleinberg & Vinegar, 1996; Akkurt et al., 1996).

Oil field brines exhibit a wide variation in salinity; at low salinity HI is approximately 1, but at high salinity HI can be reduced by as much as 10% (Dunn et al., 2002; see Figure 3.8b).

For low-density oil (high API gravity, see Section 4.2.2), Kleinberg and Vinegar (1996) found a hydrogen index of approximately 1. Below 20 API gravity the hydrogen index decreases (Figure 3.8c). These considerations are

TABLE 3.5 Hydrogen Index, HI, of Methane Gas as Function of Temperature and Pressure

Pressure	Temperature		
	72°F (22°C)	140°F (60°C)	212°F (100°C)
1,000 psi	0.12	0.10	0.08
5,000 psi	0.53	0.45	0.40
10,000 psi	0.69	0.63	0.59

Western Atlas (1996).

related to dead oils. For live oils, the dissolved gas can reduce the density and a hydrogen index <1 (Dunn et al., 2002) results.

The hydrogen index of gas (Figure 3.8a) is less than that of water and oil because proton density is smaller. In addition to Figure 3.8a, some data are given in Table 3.5.

3.5.2 Permeability, Pore Size, and Capillary Pressure Estimate

Surface relaxation term of T_2 directly depends on the surface-to-volume ratio of the pore or specific internal surface area S_{por} (Equation (3.8)). As discussed in Chapter 2, internal surface area S_{por} is related to pore size, permeability, and capillary pressure. On this basis, an estimate of these pore properties is possible. However, it must be noted that the NMR-derived pore geometric properties and the properties like permeability and capillary pressure are controlled by two different pore size measures:

1. NMR-derived properties are referred to the specific internal surface area, which is controlled by the pore-body size.
2. Permeability is controlled by the pore-throat size and connectivity of the pores; capillary pressure measures the volume of porosity accessible through a given pore-throat size.

Therefore, derived relationships implement the fundamental problem of a correlation between pore-body size and pore-throat size. Such a correlation often exists in clastic sediments but requires core “calibration.” For complex pore systems in carbonates, this is still a problem.

Two permeability models are used to derive permeability from NMR measurements. For both models it is assumed that the volume investigated by NMR measurement is completely water filled. In well logging applications, this is given because the volume investigated by NMR is so shallow that it is completely flushed by drilling fluid; if other fluids are present, a hydrogen index correction must be applied.

The two models are:

1. Coates model (Coates & Denoo, 1988; Coates et al., 1991):

$$k_{\text{Coates}} = \left(\frac{\phi}{C}\right)^m \left(\frac{\text{BVM}}{\text{BVI}}\right)^n \quad (3.13)$$

where

ϕ is the porosity in percent

BVM is bulk volume fluid movable

BVI is bulk volume fluid nonmovable (irreducible)

the parameters m and n are empirical and approximately equal to 4 and 2, respectively

C is also an empirical parameter generally between 6 and 15.

Again, the parameter should be calibrated by comparing core-based permeability. Frequently the equation is written as follows:

$$k_{\text{Coates}} = \left(\frac{\phi}{10}\right)^4 \left(\frac{\text{BVM}}{\text{BVI}}\right)^2 \quad (3.14)$$

2. Schlumberger-Doll Research (SDR) model (Kenyon et al., 1986):

$$k_{\text{SDR}} = b \cdot \phi^4 \cdot T_{2,\text{gm}}^2 \quad (3.15)$$

where $T_{2,\text{gm}}$ is the geometric mean of the T_2 distribution and b is an empirical parameter.

Both concepts:

- have a strong dependence on porosity (permeability is proportional porosity with an exponent in the order of 4; compare Section 2.5.3);
- rely on empirical parameters that, ideally, are determined by calibration with core data.

Calibration parameters in both equations are necessary mainly to account for the relation between pore-throat radius (controlling permeability) and pore-body radius (controlling NMR measurement) for the specific rock type.

Georgi et al. (1997) and Kasap et al. (1999) describe the calibration of NMR-derived permeability using Coates equation: When core (conventional or rotary sidewall) or wireline formation test data are available, the optimum value for the parameter C can be determined by an error minimization (deviation between core permeability and NMR-derived permeability). [Figure 3.9](#) demonstrates this technique.

In carbonate formations, probably as a consequence of the complicated pore systems with micro- and macroporosity, it has proven difficult to compute accurate permeabilities.

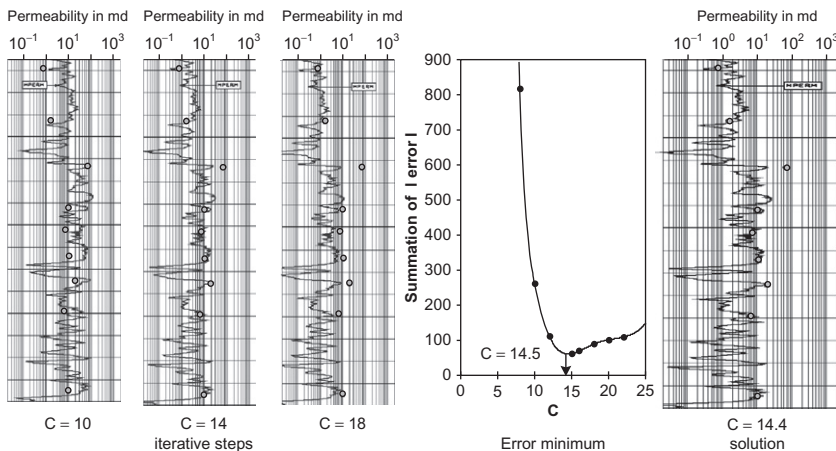


FIGURE 3.9 Optimization of the parameter C in the equation for permeability estimate from NMR measurements (Equation (3.13)) with results of direct permeability measurements (Reservoir Characterization Instrument (RCI)—pressure transient measurements) after Kasap et al. (1999). The left three plots show calculated curves with different parameters C and measured permeability data (dots). The graph in the center presents a summation of absolute errors between predicted and measured data as function of the used value for C ; curve has a minimum error at $C = 14.5$ and gives the optimal input for final solution (right plot) (Georgi et al., 1997; Kasap et al., 1999).

Chang et al. (1997) modified the SDR model based on experimental data by introducing an empirical vug cutoff, $T_{2,\text{cutoff}}$ such that any porosity corresponding to $T_2 \geq 750 \text{ ms}$ is regarded as an isolated vug and, consequently, is excluded from the porosity and geometric mean T_{gm} calculation in the process of estimating permeability:

$$k_{\text{sdr}} = b \cdot \phi_{<750 \text{ ms}}^4 \cdot T_{\text{gm}, <750 \text{ ms}}^2 \quad (3.16)$$

Chen et al. (2006) and Di Rosa et al. (2006, 2008) proposed an approach that generalizes the Coates equation by introducing a coefficient p to account for poorly to well connected vugs, where $p = 1$ corresponds to the pore system containing all regularly connected pores and vugs and the $p = 0$ end point effectively states that all of the apparent BVM is “immobile”:

$$k = \left(\frac{\phi}{C} \right)^m \left(\frac{p \cdot \text{BVM}}{\text{BVI} + (1-p)\text{BVM}} \right)^n \quad (3.17)$$

where BVI and BVM are computed with the same $T_{2,\text{cutoff}}$ as if there were no vugs. Partially connected vugs have $0 < p < 1$.

As noted in Section 3.4.3, NMR is not able to deliver a directional dependent permeability; all input data for permeability estimate are scalars and carry no tensorial information. Therefore, for derivation of k_v and k_h , the combination with methods that deliver such an anisotropy indication is

necessary; Schön et al. (2001) recommended a combination with resistivity measurements using orthogonal induction systems.

From measured NMR relaxation curves, pore size can be derived, which primarily is controlled by the pore-body size.

Kenyon (1992) and Marshall et al. (1995) compared the relaxation time distribution with thin-section images and results of mercury injection measurements and discusses the differences:

- Mercury pressure is controlled by pore-throat or constriction size.
- NMR relaxation is controlled by pore-body size (which controls specific surface).
- Optical microscopy cannot resolve micropores.

The petrophysical background for a relationship between capillary pressure and surface relaxation time is given by three equations.

The fundamental equation for capillary pressure (Equation (2.74)) with the pore throat r_t as controlling pore geometrical parameter:

$$p_c = \frac{2 \cdot \sigma \cdot \cos \Theta}{r_t} \quad (3.18)$$

The equation for surface relaxation (Equation (3.8)) with specific internal surface as controlling pore geometric parameter:

$$\frac{1}{T_2} = \zeta_{\text{surf}} \cdot S_{\text{por}} = \zeta_{\text{surf}} \frac{S}{V} \quad (3.19)$$

The relationship between pore-throat radius and specific internal surface (implementing the ratio of pore-throat radius and pore-body radius). The basic equations for capillary channel models are valid only for a cylindrical capillary with constant radius. If the radius is changing, the constrictivity of the pore system must be considered.

Thus, the relationship is controlled by interface tension terms, pore geometry, and surface relaxivity. Summarized, the equation can be written as

$$p_c = \kappa \frac{1}{T_2} \quad (3.20)$$

where the parameter κ covers these influences. Volotkin et al. (2001) used Equation (3.20) for an analysis of sandstone measurements and derived a mean value of $\kappa = 3 \text{ psi s}$, where capillary pressure was measured in a mercury-air system (injection).

3.5.3 Fluid (Hydrocarbon) Typing

NMR-based fluid typing techniques are based on differences of T_1 and T_2 relaxation time, diffusion coefficient (D_0), and hydrogen index (HI) for different fluids. The relevant NMR properties of bulk fluids are compiled in

Tables 3.2 and 3.4. Techniques are described, for example, by Vinegar et al. (1996), Chen et al. (2000), and by Freedman and Heaton (2004).

Two fundamental methods of hydrocarbon typing have been developed:

1. The dual-wait-time (dual-TW)
2. The dual-interecho-time (dual-TE) methods.

Experiment wait time, TW, and inter-echo time, TE, are two acquisition parameters that can usually be controlled during data acquisition. The dual-TW method is based on the T_1 contrast between water and light hydrocarbons, while the dual-TE method exploits the difference in diffusion contrast of water, oil, and gas.

The two fundamental techniques for hydrocarbon typing can be characterized as follows (Chen et al., 2000):

- *Dual-TW technique* (Akkurt et al., 1995, 1996, 1998): Dual-wait-time, dual-TW, uses the T_1 contrast between the nonwetting light hydrocarbons and the wetting phase (water). The long wait time is chosen such that both oil and water signals are fully polarized before the next experiment. The short wait time is chosen such that the wetting phase (water) signal is fully polarized but the oil signal is only partially polarized. The echo difference signal obtained by subtracting partially polarized echo signal from the fully polarized echo signal represents the oil signal only.
- *Dual-TE technique* (Akkurt et al., 1998; Coates et al., 1995; Looyestijn, 1996): Dual-interecho-time, dual-TE, responds to viscosity contrast, and therefore diffusivity, between reservoir fluids. It separates especially based on the diffusivity difference between water and medium-viscosity oil or between liquid and gas.

Chen et al. (2000) combined dual-TW with multiple TE approaches to maximize the advantages of both T_1 and T_2 contrasts and determine the viscosity of the hydrocarbon fluids.

Density

4.1 DEFINITION AND UNITS

Density ρ is defined as the quotient of mass m and volume V of a material:

$$\rho = \frac{m}{V} \quad (4.1)$$

The SI unit for density is kg m^{-3} . Conversions give the relationships to other used units:

$$1 \text{ g cm}^{-3} = 10^3 \text{ kg m}^{-3}$$

$$1 \text{ kg m}^{-3} = 62.43 \cdot 10^{-3} \text{ lb ft}^{-3} = 8.345 \cdot 10^{-3} \text{ lb gal}^{-1} \text{ (US)}$$

$$1 \text{ kg m}^{-3} = 0.0361 \cdot 10^{-3} \text{ lb in}^{-3}$$

Due to the heterogeneity of rocks, it is necessary to distinguish between different densities that are related to different rock components:

- ρ —bulk density: the mean density of the considered rock volume (including pores, etc.); for example, density of sandstone.
- ρ_i —density of any individual mineral rock component i ; for example, density of quartz.
- ρ_{ma} —mean density of the solid matrix material (mineral or mixture of minerals), also called grain density; for example, density of a carbonate matrix (without pore fluid).
- ρ_{fl} —mean density of the pore (or fracture) fluid; for example, density of water ρ_w .

Bulk density of a composite material (rock) consisting of n components is

$$\rho = \sum_{i=1}^n \rho_i \cdot V_i \quad (4.2)$$

where ρ_i is the density and V_i is the volume fraction of component i .

For a porous rock, the volume fraction for the pore space is given by the total porosity ϕ and [Equation \(4.2\)](#) is

$$\rho = (1 - \phi) \cdot \rho_{\text{ma}} + \phi \cdot \rho_{\text{fl}} \quad (4.3)$$

If the pore fluid is composed by different fluids (water, oil, gas), saturation must be implemented:

$$\rho = (1 - \phi) \cdot \rho_{\text{ma}} + \phi \cdot (S_{\text{water}} \cdot \rho_{\text{water}} + S_{\text{oil}} \cdot \rho_{\text{oil}} + S_{\text{gas}} \cdot \rho_{\text{gas}}) \quad (4.4)$$

4.2 DENSITY OF ROCK CONSTITUENTS

4.2.1 Density of Minerals

The density of minerals is controlled by their elemental composition and internal bonding and structure ([Table 4.1](#)). Compilations of mineral densities are published by Clark (1966), Dortman (1976), Olhoeft and Johnson (1989), Rösler and Lange (1972), Serra (1984), and Wohlenberg (1982).

The density range is for:

- the most abundant rock-forming minerals between $2.2 \cdot 10^3$ and $3.5 \cdot 10^3 \text{ kg m}^{-3}$
- ore minerals between $4.0 \cdot 10^3$ and $8.0 \cdot 10^3 \text{ kg m}^{-3}$.

4.2.2 Density of Pore Fluids

The density of liquids and gases is controlled by:

- chemical composition (including soluble components);
- temperature and pressure (density increases with increasing pressure and decreasing temperature).

For liquid substances, Schlumberger (2000) gives the following mean density values:

Fresh water $1.000 \cdot 10^3 \text{ kg m}^{-3}$

Salt water (200,000 ppm) $1.146 \cdot 10^3 \text{ kg m}^{-3}$

Oil $0.85 \cdot 10^3 \text{ kg m}^{-3}$

Some detailed data are given in [Table 4.2](#).

For water at 23.9°C (75°F) and atmospheric pressure, the relationship between NaCl concentration C (weight fraction) and density can be approximated (Schlumberger, 1989a) as:

$$\rho_{\text{water}} = 1 + 0.73C \quad (4.5)$$

A detailed description of the relationships of fluid density, temperature, pressure, and NaCl concentration (weight fraction) was published by Batzle and Wang (1992). [Figure 4.1a](#) shows a graphic presentation of selected curves (the original paper also gives the regression equations).

TABLE 4.1 Mineral Densities

Mineral	$\rho 10^3 \text{ kg m}^{-3}$	Mineral	$\rho 10^3 \text{ kg m}^{-3}$	Mineral	$\rho 10^3 \text{ kg m}^{-3}$
Actinolite	3.200	Fluorite	3.179	Montmorillonite	2.608
Albite	2.620	Forsterite	3.213	Muscovite	2.831
Almandine	4.318	Galena	7.598	Natrolite	2.245
Andalusite	3.145	Glauconite	2.300	Nepheline	2.623
Anhydrite	2.963	Graphite	2.267	Orthoclase	2.570
Anorthite	2.760	Gypsum	2.305	Phlogopite	2.784
Apatite	3.180	Glaucophane	3.200	Polyhalite	2.780
Aragonite	2.931	Halite	2.163	Pseudobrockite	4.390
Arsenopyrite	6.162	Hedenbergite	3.632	Pyrite	5.011
Augite	3.300	Hematite	5.275	CaAl-pyroxene	3.360
Barite	4.480	Hornblende	3.080	Pyrrhotite	4.610
Beryl	2.641	Illite	2.660	Quartz	2.648
Biotite	2.900	Ilmenite	4.788	Realgar	3.590
Calcite	2.710	Jacobsite	4.990	Rutile	4.245
Cassiterite	6.993	Kainite	2.130	Serpentine	2.600
Chalkopyrite	4.200	Kaolinite	2.594	Siderite	3.944
Chlorite	2.800	Kieserite	2.573	Sillimanite	3.241
Chromite	5.086	Kyanite	3.675	Sphalerite	4.089
Cordierite	2.508	Labradorite	2.710	Spinel	3.583
Danburite	3.000	Langbeinite	2.830	Sylvite	1.987
Diamond	3.515	Leucite	2.469	Talc	2.784
Diaspore	3.378	Maghemite	4.880	Titanomagnetite	4.776
Diopside	3.277	Magnesite	3.010	Tremolite	2.977
Dolomite	2.866	Magnetite	5.200	Trona	2.170
Enstatite	3.209	Malachite	4.031	Vermiculite	2.300
Epidote	3.587	Marcasite	4.870	Wollastonite	2.909
Fayalite	4.393	Microcline	2.560	Wustite	5.722

Selected data from Olhoeft and Johnson (1989).

See also Appendix A.

TABLE 4.2 Fluid Densities

Fluid	Density in 10^3 kg m^{-3}	Fluid	Density in 10^3 kg m^{-3}
Water		Oil	
Pure, distilled	1.000	10° API, STP	1.00
30,000 ppm NaCl	1.022	30° API, STP	0.88
50,000 ppm NaCl	1.037	50° API, STP	0.78
100,000 ppm NaCl	1.073	70° API, STP	0.70
200,000 ppm NaCl	1.146	Gas	
300,000 ppm NaCl	1.219	Average natural gas, STP 93°C (200°F); 48 MPa (7000 psi)	0.000773; 0.252

Gearhart Industries (1978).

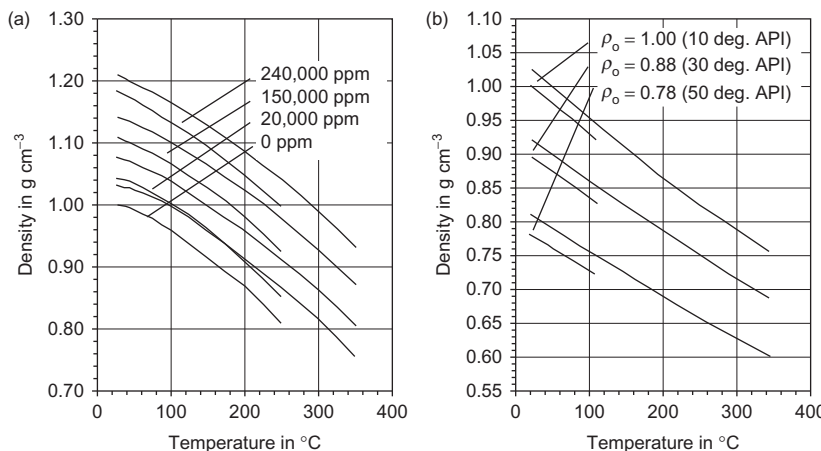


FIGURE 4.1 Fluid density as a function of temperature and pressure, plotted after figures from Batzle and Wang (1992). (a) Brine density as a function of temperature, pressure, and salinity; the upper curve is for 98.1 MPa = 14,228 psi, the lower curve for 9.81 MPa = 1,423 psi. (b) Oil density as a function of temperature, pressure, and composition; the upper curve is for 50 MPa = 7,252 psi, the lower curve for 0.1 MPa = 14.5 psi.

Baker Atlas (1985) recommends for “typical downhole temperatures and pressures ($25 < p$ [psi]/[T (°F)]—80] < 55 ” a relationship for brine density ρ_{brine} (in g cm^{-3}) as a function of salinity S , temperature T , and pressure p :

$$\rho_{\text{brine}} = 1.066 + 7.4 \cdot 10^{-4} \cdot S - 2.5 \cdot 10^{-7} (T + 473)^2 + \frac{p}{1.9 \cdot 10^5} \quad (4.6)$$

where S is in kppm by weight, T in °F, and p in psi.

Converted into SI units, this results in

$$\rho_{\text{brine}} = 1.066 + 7.4 \cdot 10^{-7} \cdot S - 8.1 \cdot 10^{-7} (T + 281)^2 + 7.64 \cdot 10^{-10} \cdot p \quad (4.7)$$

where S is in ppm by weight, T in °C, and p in Pa.

In frozen rocks or soils, the material between the matrix components is ice. The mean density value of ice is $\rho_{\text{ice}} = 0.914 \cdot 10^3 \text{ kg m}^{-3}$ (Clark, 1966).

Natural oils range from light liquids of low carbon number to very heavy tars, bitumen, and kerogen (which may be denser than water). Under room conditions, oil densities can range from under $0.5 \cdot 10^3 \text{ kg m}^{-3}$ to greater than 10^3 kg m^{-3} , with most produced oils in the 0.7 – $0.8 \cdot 10^3 \text{ kg m}^{-3}$ range (Batzle & Wang, 1992).

Batzle and Wang (1992) published polynomial relations for oil to describe the pressure and temperature dependence at a constant composition. The pressure dependence is relatively small, whereas the effect of temperature is stronger. [Figure 4.1b](#) shows selected curves.

For crude oils the American Petroleum Institute (API) oil gravity number is a widely used classification; it is defined as:

$$\text{API} = \frac{141.5}{\rho_{\text{oil}}} - 131.5 \quad (4.8)$$

where ρ_{oil} is the oil density (in $\text{g cm}^{-3} = 10^3 \text{ kg m}^{-3}$) measured at 15.6°C (60°F) and atmospheric pressure.

Gas density is controlled very strongly by gas pressure. Gas mixture density is characterized frequently by a specific gravity G . G is the ratio of the gas density to air density at 15.6°C (60°F) and atmospheric pressure. [Figure 4.2](#) shows the density of methane as a function of temperature and pressure.

4.3 DENSITY OF ROCKS

Bulk density of rocks follows exactly [Equation \(4.2\)](#) and depends on:

- the mineral composition (mineral densities and volume fractions);
- porosity (pores, fractures) and density of pore fluids.

This explains the general rule of density variation:

- Igneous rocks show an increase of density from felsic (acid) to mafic (basic) types;

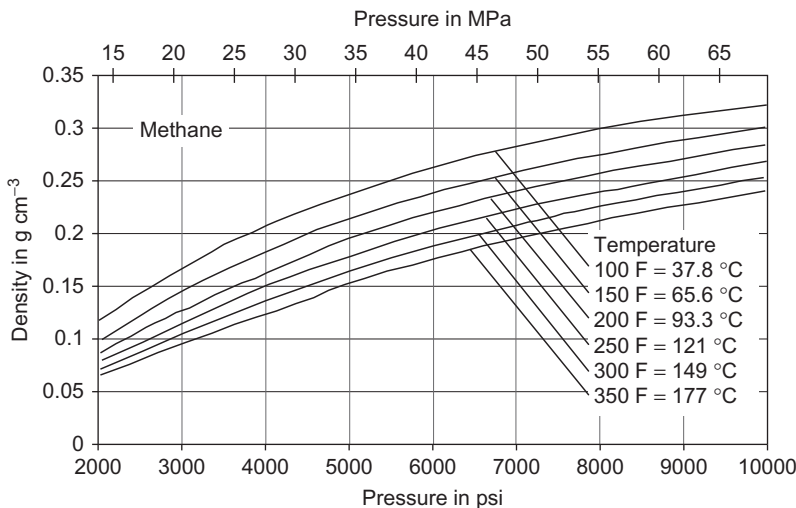


FIGURE 4.2 Density of methane as a function of pressure and temperature plotted after a figure from Akkurt et al. (1996).

- Porous rocks show a density decrease with increasing porosity and decreasing water saturation.

This is demonstrated more in detail by [Figures 4.3–4.5](#).

[Figure 4.3](#) shows the mean range of density for igneous and metamorphic rocks.

In igneous rocks in particular, density increases from felsic (acid) to mafic (basic) types. Each rock type shows a range of density values.¹ In comparison with most sedimentary rocks, this range is relatively small and is mainly a result of a variation of the particular rock composition and a very small influence of pore or fracture volume.

The density of metamorphic rocks is strongly influenced by the composition and density of the initial rock material (the “educt”), the degree of metamorphism, and thermodynamic conditions and processes.

A more detailed relationship between mineral content and rock density for igneous rocks is given in [Figure 4.3](#). The upper part shows the range of densities for rock types from granite to peridotite. The lower part shows the mineral compositions. Densities were calculated (circles) at the “border of composition” (vertical lines) using the mean mineral densities (in parentheses). These calculations agree with measured value range.

¹Olhoeft and Johnson (1989) have analyzed the statistical distribution of density and present histograms for selected types.

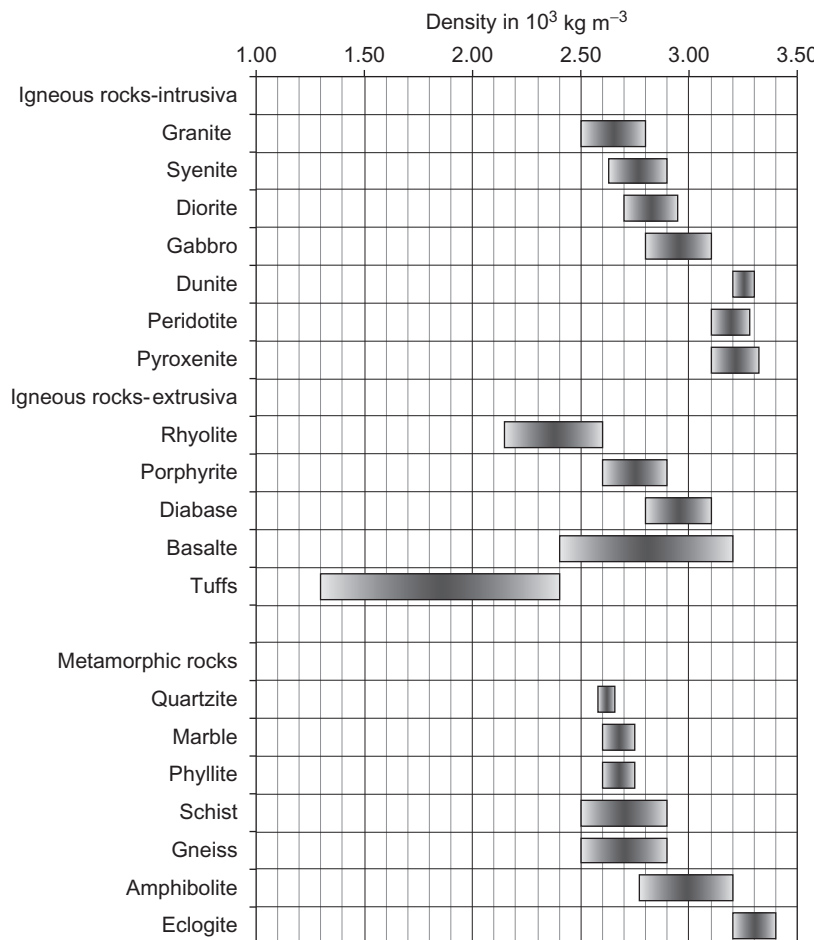


FIGURE 4.3 Mean range of density for igneous and metamorphic rocks.

Figure 4.5 gives an overview about the density of sedimentary rocks. In sedimentary rocks, there are two main groups with respect to density controlling factors:

1. Pore-free sediments (salt, anhydrite, dense carbonate)
2. Porous sediments (the most abundant group, the typical sedimentary rock).

Density of pore-free sediments is determined by their mineral composition; some of them are monomineralic rocks (especially salts). As a result of nearly constant composition, this group is characterized by narrow ranges of density values.

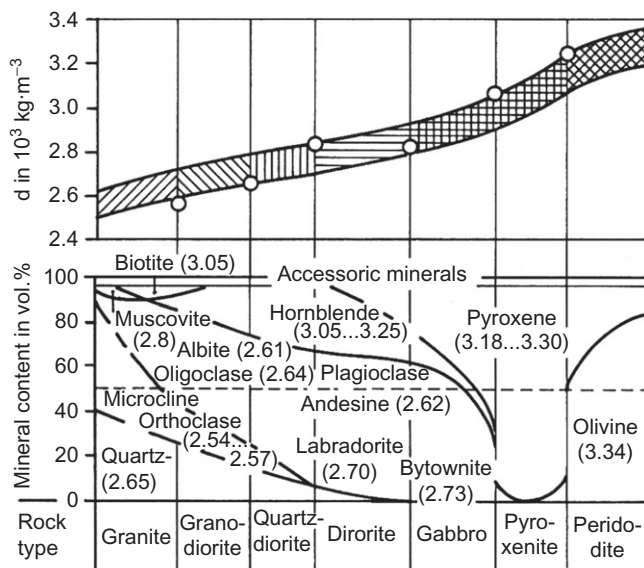


FIGURE 4.4 Correlation between mineral content and density (in 10^3 kg m^{-3}) of magmatic rocks (after Dortman, 1976). (A) Upper part: density range and calculated values (circles). (B) Lower part: mineral content; the mineral density values used for calculations are in parentheses.

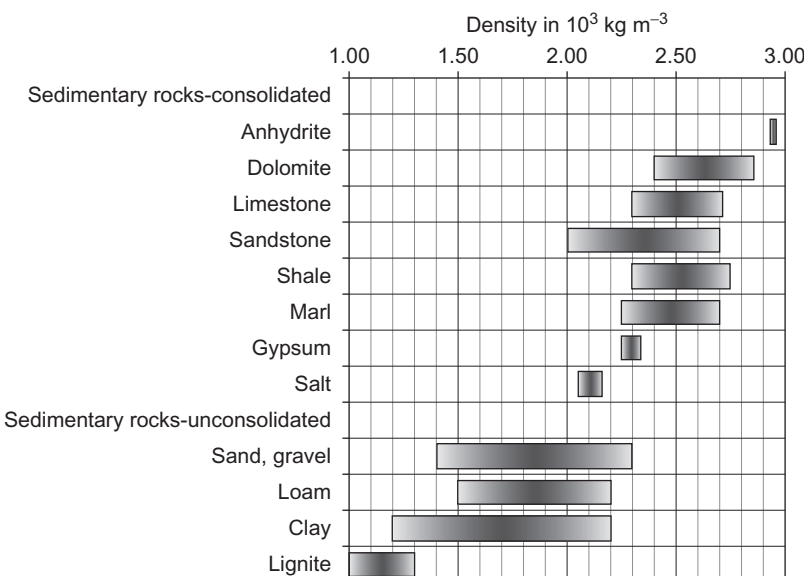


FIGURE 4.5 Mean range of density for sedimentary rocks.

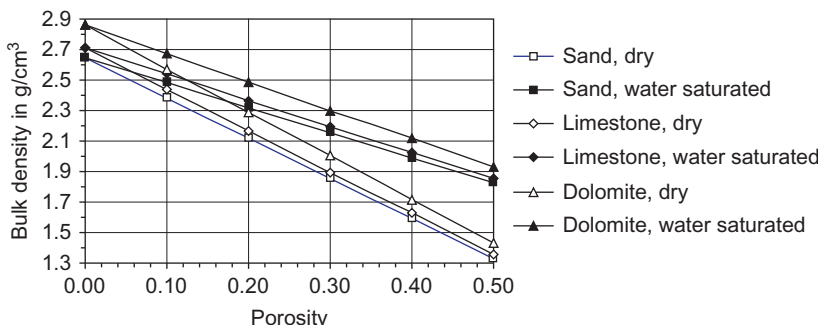


FIGURE 4.6 Relationship between bulk density and porosity for sandstone ($\rho_{\text{ma}} = 2.65 \text{ g cm}^{-3}$), limestone ($\rho_{\text{ma}} = 2.71 \text{ g cm}^{-3}$), and dolomite ($\rho_{\text{ma}} = 2.86 \text{ g cm}^{-3}$). Open signatures indicate dry rocks ($\rho_{\text{fl}} = 0.00 \text{ g cm}^{-3}$); filled signatures indicate water-saturated rocks ($\rho_{\text{fl}} = 1.00 \text{ g cm}^{-3}$).

The density of porous sediments is controlled by:

- the mineral composition (matrix density, also called grain density);
- the porosity;
- the composition of pore content (saturation).

As a result of the distinct difference between the mean matrix density range (about $2.5\text{--}2.9 \cdot 10^3 \text{ kg m}^{-3}$) and the mean density range of pore fluid (liquids about $0.8\text{--}1.2 \cdot 10^3 \text{ kg m}^{-3}$; gases $< 0.4 \cdot 10^3 \text{ kg m}^{-3}$), there is a strong correlation between rock bulk density ρ and porosity ϕ , given in [Equation \(4.3\)](#).

For a sedimentary rock type, there is generally a broad range of density values that reflects variations of porosity and saturation. The highest values represent dense (low porosity) members of the type, whereas the lower values result from porosity increase and/or increase of gas content in the pores.

For reservoir rocks in particular (sandstone, carbonate), the measurement of density ρ (using a gamma–gamma measurement, see [Section 5.3](#)) is applied for a porosity calculation. Rearrangement of [Equation \(4.3\)](#) results in

$$\phi = \frac{\rho_{\text{ma}} - \rho}{\rho_{\text{ma}} - \rho_{\text{fl}}} \quad (4.9)$$

For a porosity determination, the measured bulk density ρ , the matrix density ρ_{ma} , and the fluid density ρ_{fl} are necessary inputs. [Figure 4.6](#) shows the relationship between bulk density and porosity for sandstone, limestone, and dolomite for the dry and the water-saturated rock.

The strong correlation between porosity and bulk density results in a density increase with pressure or depth, which is the result of a decrease of porosity with depth (see [Section 2.2.2](#)).

Nuclear/Radioactive Properties

5.1 FUNDAMENTALS

Nuclear properties are related to the atomic structure of matter: an atom consists of a nucleus and a number of orbiting electrons e^- . Electrons occupy shells (K, L, M, etc.). The nucleus is a combination of electrically neutral neutrons n and positively charged protons p^+ . [Table 5.1](#) gives some fundamental properties of these components.

The number of protons in a nucleus is the atomic number Z . An electrically neutral atom with the atomic number Z also has Z orbiting electrons. The sum of protons and neutrons in the nucleus is the mass number A .

The nomenclature for elements is ${}_Z^A$ chemical symbol A . For example, helium is ${}_2^4\text{He}$.

Each nuclide has a unique set of discrete energy levels or states. A stable nucleus exists at the lowest energy level (ground state). In a higher energy level it is in an excited state and unstable. It releases the excess energy by radiation in order to reach the stable state. The time required for this decay process can range from a fraction of a second to millions of years, depending on the element. The decay process follows the equation:

$$N(t) = N_0 \cdot \exp(-C_d \cdot t) = N_0 \cdot \exp\left(-0.693 \cdot \frac{t}{t_{1/2}}\right) \quad (5.1)$$

where

N_0 is the number of parent nuclei at the start of counting

$N(t)$ is the number of parent nuclei at a time t after the start of counting

C_d is the decay constant of the considered element

$t_{1/2}$ is the “half-life time” of the considered element.

TABLE 5.1 Atomic Properties

	Mass	Electrical Charge
Proton p^+	$1.67 \cdot 10^{-27}$ kg	$+1.602 \cdot 10^{-19}$ C
Neutron n	$1.67 \cdot 10^{-27}$ kg	Neutral, ± 0
Electron e^-	$9.11 \cdot 10^{-31}$ kg	$-1.602 \cdot 10^{-19}$ C

Nuclear processes are statistically determined and can be described by Poisson's distribution. For Poisson's distribution, the standard deviation σ is related to the number of measured counts n :

$$\sigma = \sqrt{n} \quad (5.2)$$

For practical measurements, this has the consequence that the uncertainty of a measurement is controlled by the absolute number of counts; thus it depends on the intensity of radiation and the counting time. Consequently, there are limits or restrictions on the logging speed of nuclear tools.

5.2 NATURAL RADIOACTIVITY

There are three types of natural radioactivity:

1. Alpha radiation (positively charged particle radiation)
2. Beta radiation (negatively charged particle radiation)
3. Gamma radiation (electromagnetic radiation, photons).

The depth of penetration of the radiation is extremely small for both alpha and beta particles. For practical applications (well logging), gamma radiation is used.

The energy E of the gamma radiation is given in electron volts (eV) or as frequency f in Hz:

$$E = h \cdot f = 4.1357 \cdot 10^{-15} \cdot f \quad (5.3)$$

where h is Planck's constant: $h = 4.1357 \cdot 10^{-15}$ eV s = $6.6261 \cdot 10^{-34}$ Js.

5.2.1 Origin of Natural Gamma Radiation in Rocks

Elements frequently have a variety of isotopic forms. If these isotopes are unstable, then they decay to a more stable form and emit radiation. Only three radioactive decay processes, producing measurable quantities of gamma rays, occur in natural rocks:

1. Uranium–radium series (half-life time of $4.4 \cdot 10^9$ years)

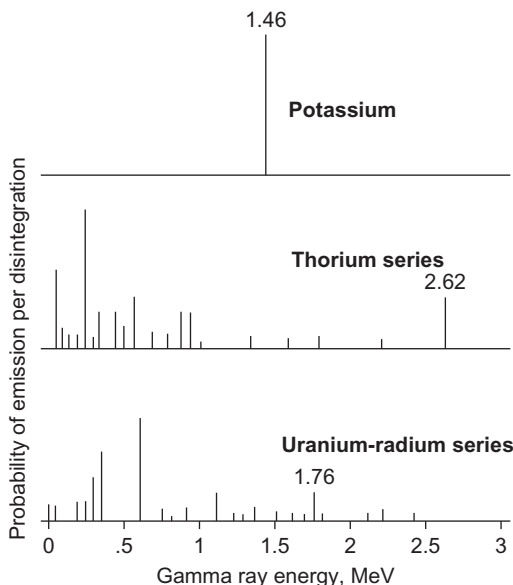


FIGURE 5.1 Prominent gamma-ray energies in megaelectron volt (MeV) from the uranium series, thorium series, and potassium decay. The height of the vertical lines is proportional to the relative intensity of the gamma ray (Ellis and Singer, 2007).

2. Thorium series (half-life time of $1.4 \cdot 10^9$ years)
3. Potassium K⁴⁰ (half-life time of $1.3 \cdot 10^9$ years).

Uranium U-238 (₉₂U²³⁸) and thorium Th-232 (₉₀Th²³²) decay in a series of steps and end with the stable lead Pb-206 (₈₂Pb²⁰⁶) and Pb-208 (₈₂Pb²⁰⁸), respectively. The series of steps result in a spectrum that presents the probability of transitions (decay steps) for discrete energy levels. Both spectra have characteristic peaks: 1.76 MeV for uranium and 2.62 MeV for thorium.

The element potassium contains 0.0119% of the radioactive isotope ⁴⁰K. The decay delivers a monoenergetic gamma radiation¹ with an energy of 1.46 MeV. The stable end product is argon (₁₈Ar⁴⁰) (Figure 5.1).

5.2.2 Potassium, Uranium, and Thorium in Minerals

Potassium is generally chemically combined in many minerals; there are three main groups of potassium-containing minerals:

1. Clay minerals, where potassium occurs either in the mineral structure or adsorbed to the clay particles; an example is illite ($K_2H_3OAl_2(Si_3Al)O_{10}(H_2O,OH)_2$). The potassium content of various clay minerals is

¹Decay by beta radiation with the end product ⁴⁰Ca is also possible.

different: illite has a high content (3.5–8.3%), whereas kaolinite has a low content.

2. Rock-forming minerals, where potassium is chemically combined in the mineral structure; typical examples are the potassium feldspars (orthoclase $KAlSi_3O_8$, microcline $KAlSi_3O_8$), mica (biotite, muscovite); see [Table 5.2](#).
3. Evaporates, where potassium occurs chemically as salt (sylvite KCl , carnallite $KCl \cdot MgCl_2 \cdot (H_2O)_6$).

“Potassium is considered an element that owes its origin to erosion; it is often reworked and transported for long distances” (Baker Atlas, 1985).

Thorium is generally associated with acid (and intermediate) rocks. It is very stable and will not dissolve in a solution. As a result of alteration, thorium is deposited only with detrital sediments, never with purely chemical sediments (carbonates, aragonite). Therefore, in carbonate reservoirs, thorium becomes a very important clay indicator. It is found in mudstones where it is adsorbed by clay minerals, and with heavy minerals that are often abundant in the silty fraction. Thorium is generally considered a marine element (Baker Atlas, 1985).

Uranium is also generally associated with acid (and intermediate) rocks—their average concentration is about 4.65 ppm. As a result of weathering and alteration it forms—unlike potassium and thorium—soluble salts, which are transported in seawater and river water. The salts are unstable and go into sediments. There are three ways that uranium passes into sediments (Serra, 1984, 2004):

1. Chemical precipitation in an acid-reducing (pH 2.5–4.0) environment
2. Adsorption by organic matter or living plants and animals
3. Chemical reaction in phosphorites.

Acid-reducing conditions are found particularly in stagnant, anoxic waters with a relatively low rate of sedimentation, which typically produce black shales (Rider, 1986).

Controlled by transport and sedimentation processes and the chemical environment, uranium occurs in both detrital and chemical sediments (shale, sandstone, conglomerate, carbonate) and is also common in tuff and phosphates. Carbonates rich in organic matter that form under reducing conditions are often very high in uranium. These “radioactive carbonates” are often productive reservoirs. Uranium is also adsorbed by clay minerals; excessively high uranium content in shales indicates source rock (Baker Atlas, 1985).

Rider (1996) stated that “uranium behaves as an independent constituent: it is not chemically combined in the principal molecules of rocks like potassium, but it is loosely associated with secondary components. For this reason it has a very heterogeneous distribution in sediments.”

TABLE 5.2 K, U, and Th Content of Some Minerals (chemical formula see Appendix A: Physical properties of rock-forming minerals)

Mineral	K in %	U in ppm	Th in ppm	Ref.
Plagioclase	0.54	0.02–5.0	0.01–3.0	BA
	0.54	0.2–5.0	0.5–3.0	Sch
Orthoclase	11.8–14.0	0.2–3.0	0.01–7.0	BA
	11.8 ^a (14 ideal)	0.2–3.0	3–7	Sch
Microcline	10.9	0.2–3.0	0.01–7.0	BA
	10.9 ^a (16 ideal)			Sch
Biotite	6.2–10	1–40	0.5–50	Hu
	6.2–10.1 [8.5]	1–40	0.5–50	Sch
	6.7–8.3		<0.01	BA
Muscovite	7.8–9.8	2–8	0–25	Hu
	7.9–9.8		<0.01	BA
	7.9 (9.8 ideal)	2–8	10–25 ^b	Sch
Illite	3.5–8.3	1–5	10–25	Hu
	4.5	1.5	<2.0	BA
	3.5–8.3 [6.1]	1.5	10–25	Sch
Kaolinite	0–0.6	1–12	6–47	Hu
	0.42	1.5–3	6–19	BA
	0–0.6 ^d [0.35]	1.5–9	6–42	Sch
Chlorite	0–0.3		3–5	Hu
	0–0.35 [0.1]			Sch
Smectite	0–1.5	1–21	6–44	Hu
	0–0.6 [0.22]		10–24	Ri
Montmorillonite	0.16	2–5	14–24	BA
	0–4.9 ^c [1.6]	2–5	10–24	Sch
Bauxite		3–30 [8.0]	8–132 [42]	BA
		3–30	10–132	Sch
Bentonite	<0.5	1–21 [5.0]	6–50	BA
		1–36	4–55	Sch

(Continued)

TABLE 5.2 (Continued)

Mineral	K in %	U in ppm	Th in ppm	Ref.
Glauconite	5.08–5.30			BA
	3.2–5.8 [4.5]		<10	Sch
	3.2–5.8 [4.5]		2–8	Ri
Phosphate		1000–350	1–5	BA
Zircon		300–3000	100–2500	BA
Sphene		100–700	100–600	BA
Epidote		20–50	50–500	BA
Apatite		5–150	20–150	BA
Monazite		500–3000	$(2.5–20) \cdot 10^4$	BA
Sylvite KCl	52.4			Sch
Langbeinite	18.8			Sch
Kainite	15.7			Sch
Carnallite	14.1			Sch

^aCorresponds to beginning alteration.

^bPure muscovite has no Th content. In sedimentary rocks, however, the deposition of muscovite (or micas) is generally accompanied by deposition of finer heavy minerals which are Th- and U-bearing.

^cSome montmorillonites might correspond to imperfectly degraded muscovite or to an incomplete transform in illite by diagenesis.

^dKaolinite sometimes contains more K due to imperfectly degraded feldspars. Authigenic kaolinite does not contain K and Th (Schlumberger, 1982).

Values in [] are averages. Reference key: BA: Baker Atlas (1985); Ri: Rider (1996); Sch: Schlumberger (1982); Hu: Hurst (1990).

Summarizing the major occurrences of the three radioactive components are (Schlumberger, 1982a):

- *Potassium*: micas, feldspars (K), micaceous clays (illite), radioactive evaporates
- *Thorium*: shales, heavy minerals
- *Uranium*: phosphates, organic matter.

Table 5.2 gives a compilation of potassium, uranium, and thorium content of minerals. Some important rock-forming minerals like quartz, calcite, dolomite, and anhydrite are not listed because as minerals they are not associated with potassium, uranium, and thorium.

5.2.3 Potassium, Uranium, and Thorium Content of Rocks

Table 5.3 shows a compilation of potassium, uranium, and thorium content of rocks. It corresponds with the content of the corresponding rock-forming minerals (Table 5.2).

TABLE 5.3 K, U, and Th Content of Some Rocks

Rock Type	K in %	U in ppm	Th in ppm	Ref.
Intrusive				
Granite	2.75–4.26	3.6–4.7	19–20	BA
Granitic rocks (average)	4.11	4.35	15.2	Sch
Granitic rocks	2.3–4.0	2.1–7.0	8.3–40	Do
Biotite granite	3.4	4.0	15	D
Gabbro	0.46–0.58	0.84–0.90	2.70–2.85	Sch
Granodiorite	2–2.5	2.6	9.3–11	BA, Sch
	2.3	2.1	8.3	Do
Diorite	1.1	2.0	8.5	BA, Sch
	1.8	1.8	6.0	Do
Dunite	<0.02	<0.01	<0.01	BA, Sch
Dunite, pyroxenite	0.15	0.03	0.08	D
Peridotite	0.2	0.01	0.05	BA, Sch
Extrusive				
Rhyolite	4.2	5.0		BA
	2–4	2.5–5	6–15	Sch
Trachyte	5.7	2–7	9–25	Sch
Alkali basalt	0.61	0.99	4.6	BA, Sch
Plateau basalt	0.61	0.53	1.96	BA, Sch

(Continued)

TABLE 5.3 (Continued)

Rock Type	K in %	U in ppm	Th in ppm	Ref.
Andesite	1.7	0.8	1.9	Sch
	1.7	1.2	4.0	D
Dacite	2.3	2.5	10.0	D
Liparite	3.7	4.7	19	Do
Metamorphites				
Gneiss—Swiss Alps	0.32–4.7 [3.11]	0.9–24 [4.95]	1.2...25.7 [13.1]	RyCe
Gneiss (KTB, Germany)	2.28 ± 0.17	2.6 ± 1.2	8.2 ± 2.0	B
Eclogite	0.8	0.2	0.4	D
Amphibolite—Swiss Alps	0.11–2.22 [1.23]	0–7.8 [1.65]	0.01–13.7 [3.0]	RyCe
Amphibolite	0.6	0.7	1.8	Do
Metabasite (KTB, Germany)	0.6 ± 0.5	2.5 ± 1.6	2.5 ± 1.6	B
Schist—Swiss Alps	0.39–4.44 [2.23]	0.4–3.7 [2.14]	1.6–17.2 [9.73]	RyCe
Quartzite	0.6	0.8	3.1	D
	0.9	0.6	1.8	R
Marble	0.2	1.1	2.2	D
Sediments				
Carbonate	0.0–2.0 [0.3]	2.8–2.5 [2.2]	0.1–7.0 [1.7]	BA
Limestone	0.3	1.6	1.8	D
	0.3	2.0	1.5	R
Dolomite	0.4	3.7	2.8	D
	0.7	1.0	0.8	R
Marl	0.8	2.8	2.5	D
Anhydrite	0.4	0.1	0.3	R
Salt	0.1	0.02	0.3	R

(Continued)

TABLE 5.3 (Continued)

Rock Type	K in %	U in ppm	Th in ppm	Ref.
Sandstone (range, mean)	0.7–3.8 [1.1]	0.2–0.6 [0.5]	0.7–2.0 [1.7]	BA
Graywacke	1.3	2.0	7.0	R
Shale (200 samples)	2.0	6.0	12.0	BA
Common shales	1.6–4.2 [2.7]	2–13	3–47	BA
Shale	2.7	3.7	12	R
Oil shale (Colorado)	<4.0	up to 500	1–30	BA
Black shale	2.6	20.2	10.9	R
North American Shale Composite (NASC) standard	3.2	2.66	12.3	KGS
Clay, N-Atlantic, Caribbean	2.5	2.1	11	KaHa
Clay, unconsolidated, Pleistocene	1.9–2.5	1.1–3.8	5.7–10.2	
Clay/silt, Tertiary	1.3–3.1	1.2–4.3	1.4–9.3	

Values in [] are averages. Reference key: BA: Baker *Atlas* (1985); Sch: Schlumberger (1982); Do: Dortman (1976); RyCe: Rybach and Cermak (1982); B: Bücker *et al.* (1989); KaHa: Kappelmeyer and Haenel (1974); D: Dobrynin *et al.* (2004); R: Rybach (1976); Yalcin *et al.* (1977); KGS: Kansas Geological Survey (2010).

Figure 5.2 shows the tendencies for natural radioactivity resulting from the contribution of potassium, uranium, and thorium:

- Radioactivity of igneous rocks increases from mafic (basic) to felsic (acid) rocks.
- Radioactivity of sedimentary rocks increases from “clean” to “shaly” rocks, that is, with increasing clay content.

Igneous Rocks

Generally, concentrations of all three elements in common igneous rocks are distinctly higher in acidic than in ultrabasic rocks. Exceptions to this are the alkali feldspathoidal rocks. Higher radioactivity of magmatic rocks is mainly related to the presence of accessory uranium- and thorium-bearing minerals (Kobranova, 1989).

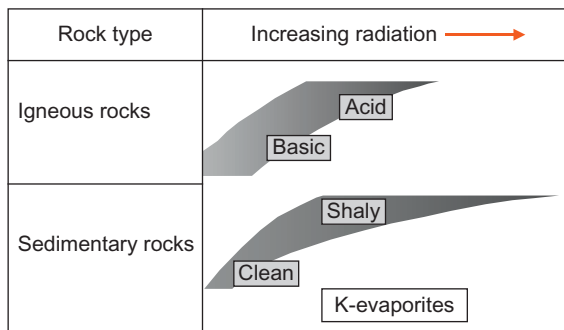


FIGURE 5.2 Natural radioactivity of rocks—general tendencies.

Metamorphic Rocks

The uranium, thorium, and potassium content of metamorphic rocks is a result of the original contents of educt material (igneous or sedimentary) and may have been changed by metamorphic processes. The content is adsorbed and redistributed according to the degree of metamorphic transformation (Rybáček and Čermák, 1982).

Frequently contents of radioactive elements are decreased with increasing metamorphism. Rybáček and Čermák (1982) found that the “depletion of U and Th, caused by progressive metamorphism, is most markedly evident in rocks of the granulite facies. U and Th have the tendency toward upward migration in the earth’s crust because of reactions due to dehydration (middle level of crust) or because of partial melting near the base of the crust (migmatites). K seems to be more or less unaffected by these processes.” The mean Th/U ratios of the metamorphic rocks can deviate from the typical values of intrusive rocks. “This is due to unequal losses of K, Th, and U during metamorphic processes in which the mobility of U plays a great part,” according to Haack (1982).

Sedimentary Rocks

“In sedimentary rocks, the relative mean abundances are less predictable than in igneous rocks. On average, potassium is lower in effective concentrations than uranium or thorium, and thorium contributes about the same level of activity as uranium. As a class, carbonates are the lowest in natural radioactivity of the sedimentary rocks. Generally, shales will have a higher level of natural radioactivity than other sediments; consequently, the gamma-ray sonde is used to distinguish between shales and other sediments” (Hearst and Nelson, 1985).

The correlation between clay content (respectively shaliness) and radiation of sedimentary rocks is important for the reservoir characterization with respect to:

- the distinction between clay and sand layers,

- the determination of the clay content,
- the characterization of “clay types.”

If a spectral gamma measurement is available, the use of thorium and potassium for shale content derivation is recommended. Fertl (1983) noted that the thorium curve of a spectral gammalog allows a quantitative clay volume estimate despite the presence of varying amounts of uranium and potassium (possibly due to mica, especially muscovite, as, for example, in Jurassic sandstones in the North Sea).

Some cases of natural radioactivity of sandstones are discussed in Schlumberger (1982):

- Feldspathic sandstones or arcoses show some K content from feldspar in the sand. Thus, they show a very low Th/K ratio ($<10^{-4}$) and a somewhat lower matrix density than pure quartz ($2.65 \cdot 10^3 \text{ kg m}^{-3}$) due to the low density of feldspar ($(2.52-2.53) \cdot 10^3 \text{ kg m}^{-3}$).
- Micaceous sandstones: micas contain potassium; therefore, the potassium content of micaceous sandstones is higher than that of pure sandstone. The thorium content is also higher due to the heavy thorium-bearing minerals associated with micas. As a result, the Th/K ratio is close to $2.5 \cdot 10^{-4}$. The density of micaceous sandstones is higher than that of pure quartz sandstone due to the higher density of mica ($(2.8-3.1) \cdot 10^3 \text{ kg m}^{-3}$).
- Heavy minerals within sandstones: heavy minerals like zircon, allanite, monazite, and sphene are thorium and uranium bearing. Therefore, in these sandstones, only the thorium and uranium levels are high; the potassium level is very low. Thus, this type of sandstone shows a very high Th/K ratio.

Referring to the occurrence and mechanism of thorium, uranium, and potassium presence in clay minerals and shale, Rider (1996) stated: “To summarize: as shale indicators, thorium may be used in most cases, potassium may be used in many cases, but uranium should not be used at all. This obviously has implications for the simple gamma-ray log: it is not necessarily a good ‘shale indicator.’”

In carbonate series, the integral gamma intensity is very often a poor clay indicator because the measured value is not related to clay content, but to the presence of uranium. Typical cases are:

- Pure carbonate (chemical origin), which has a thorium and potassium level near zero. If the uranium level is also zero, this carbonate was precipitated in an oxidizing environment.
- If there is a variable uranium content, the carbonate can either have been deposited in a reducing environment, or it corresponds to a carbonate with stylolites (which contains impurities such as uranium, organic matter, and even clay minerals), or to phosphate-bearing layers.
- If thorium and potassium are present with uranium, this indicates clay content of the carbonate (clayey carbonate to marl).

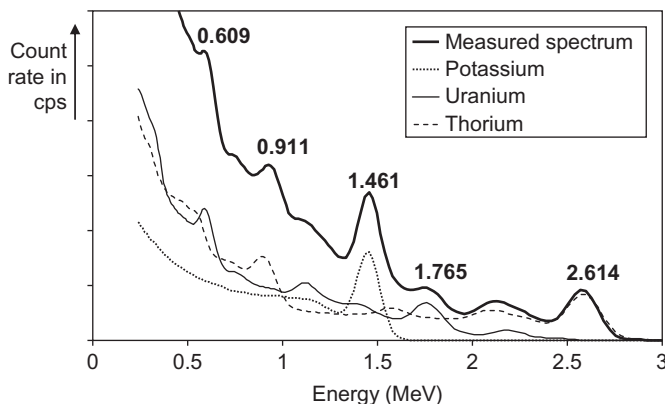


FIGURE 5.3 Natural gamma-ray spectrum with Th, K, and U components from a shale zone (Pemper et al., 2009).

- If potassium is present with or without uranium, it can correspond to a carbonate of algal origin or a carbonate with glauconite (Schlumberger, 1982).

5.2.4 Spectral and Integral Measurements—the API Unit

In the geophysical field practice, two techniques of measurement are applied: spectral measurement and integral measurement. For most applications, the spectral measurement is realized by a data-reduction technique. The whole spectrum is divided into three windows:

1. first window 1.3–1.6 MeV with the prominent K energy (1.46 MeV)
2. second window 1.6–2.4 MeV with the prominent U energy (1.76 MeV)
3. third window 2.4–2.8 MeV with the prominent Th energy (2.61 MeV).

The processing, so-called spectral stripping (see, for example, Ellis, 1987; Hearst and Nelson, 1985), solves a matrix algorithm for the concentration of the three elements (K, U, and Th).

Figure 5.3 shows an example for a spectral measurement in a shale zone.

In many cases an “integral measurement technique” is applied: above a fixed energy level all incoming counts are measured. Therefore, the integral activity is the combined effect of all three contributions

$$I_{\text{API}} = k(a \cdot K + U + b \cdot Th) \quad (5.4)$$

where U , Th are in ppm, and K in percent. k is a constant for a given tool, a is the concentration of U (in ppm) that will give same count rate as 1% K ,

TABLE 5.4 Mean API Values for Gamma Activity

Material	Gamma in API
Quartz, calcite, dolomite (clean)	0
Plagioclase (albite, anorthite)	0
Alcali feldspar (orthoclase, anorthoclase, microcline)	≈220
Muscovite	≈270
Biotite	≈275
Kaolinite	80–130
Illite	250–300
Chlorite	180–250
Montmorillonite	150–200
Sylvite	500+
Carnallite	≈220

Data from Schlumberger (2000).

and b is the concentration of U (in ppm) that will give same count rate as 1 ppm Th (Hearst and Nelson, 1985).²

The measurement scale of the gammalog is the API unit. This reference standard allows consistent comparisons between different gamma-ray counting devices.

The API standard is a calibration test pit at the University of Houston. The American Petroleum (API) facility is constructed of concrete with an admixture of radium to provide uranium decay series, monazite ore as a source of thorium, and mica as a source of potassium. The facility has 4.07% K, 24.2 ppm Th, and 13.1 ppm U (Ellis, 1987). The API standard gives 200 API, equal to twice the mean of an average shale. Table 5.4 gives mean API values for some rock-forming minerals.

5.2.5 Applications

5.2.5.1 Lithologic Profile

In igneous rocks, the general tendency is an increase of radiation from ultra-basic to acid rocks. This is attributed to the higher uranium, thorium, and

²Hearst and Nelson (1985) give for a NaJ detector of dimensions 150 by 80 mm, with a discrimination threshold of 200 keV, a value of $a = 1.05$ and $b = 0.47$.

potassium content of mica and alkali feldspars. Alteration can change the radioactivity.

In sedimentary rocks, clean carbonates and sands normally show the lowest values. Radioactivity increases with the shale content; therefore, the gammalog is one of the most indicative shale indicators. The highest values are from black marine shales.

But there are some important specific cases of high radiation (see Section 5.2.3):

- Sandstone with high content of feldspar, mica, glauconite (“green sand”)
- Carbonate in reducing environment, stylolites, phosphates.

A gammalog allows (qualitative) lithologic profiling. Clean zones (sand, carbonates) and shaly sections can be separated. In geological applications, the gammalog is a tool for

- sedimentological studies by typical curve shapes for channel, coarsening upward, fining upward, and other formations (Rider, 1996);
- well-to-well correlation in sedimentary areas and trend derivation.

5.2.5.2 Shale Content Estimate

A shale content estimate can be derived from a gamma measurement based on the correlation between shale content and radioactive isotope content, which originates natural gamma activity. It is assumed that only shale or clay are responsible for the radiation; no other “radioactive minerals” are present.

For this application, in many cases an integral measurement is used; in order to eliminate the effect of variability of the uranium content, a spectral measurement of the potassium and thorium contribution is recommended.

The analysis consists of two steps:

1. Calculation of a “gamma-ray index” I_{GR} : this is the actual gamma reading normalized by the value for the clean rock (minimum gamma reading) and the shale (maximum gamma reading)

$$I_{GR} = \frac{GR - GR_{cn}}{GR_{sh} - GR_{cn}} \quad (5.5)$$

where

GR_{cn} is the log response in a clean zone—no shale

GR_{sh} is the log response in a shale zone

GR is the log response in the zone of interest.

This normalization of the logs results in $I_{GR} = 0$ for clean rocks and $I_{GR} = 1$ for shale (100% shale).

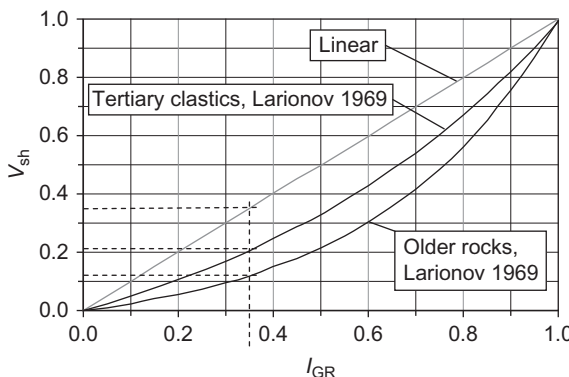


FIGURE 5.4 Relationships between gamma-ray index I_{GR} and shale content V_{sh} ; as an example, $I_{GR} = 0.35$ (dotted line) results in a $V_{sh} = 0.35$ for the linear equation, $V_{sh} = 0.21$ for the Larionov equation/Tertiary clastics, $V_{sh} = 0.12$ for the Larionov equation/Mesozoic and older clastics. On the website <http://www.elsevierdirect.com/companion.jsp>?

ISBN=9780444537966 is the file Nuclear.Vsh-GR with the plotted relationships.

2. Transformation of the gamma-ray index into shale content: for the transformation, empirical equations are recommended for various formations. The following list and Figure 5.4 give a selection. Linear correlation in all cases delivers the highest shale content.

$$V_{sh} = I_{GR} \quad \text{Linear relationship (upper limit)} \quad (5.6)$$

$$V_{sh} = 0.083(2^{3.7I_{GR}} - 1) \quad \text{Tertiary clastics (Larionov, 1969)} \quad (5.7)$$

$$V_{sh} = 0.33(2^{2.0I_{GR}} - 1) \quad \text{Mesozoic and older rocks (Larionov, 1969)} \quad (5.8)$$

5.2.5.3 Clay Mineral Typing

Thorium and potassium are the “mineral significant” radioactive components; clay minerals (and mica and feldspar) are characterized by different typical ratios of the two elements or a different position on a Th/K graph (Figure 5.5A) or in a thorium versus potassium plot (Figure 5.5B). This can be used for an estimate of dominant clay mineral in a formation and also for detection of mica or feldspar.

Figure 5.5C shows an example (Palaeozoic carbonates and mixed carbonates and siliciclastics of the Gipsdalen Group/Barents Sea). Zone 1 shows mixed layer clay and/or illite; Zone 5 shows a glauconitic or feldspathic sandstone with mica and illite.

A critical analysis of the application of Th/K crossplots for identification of clay mineralogy for sandstones was published by Hurst (1990). The main reasons for uncertainties in clay mineralogy are:

- The negligible potassium content of kaolinite and chlorite

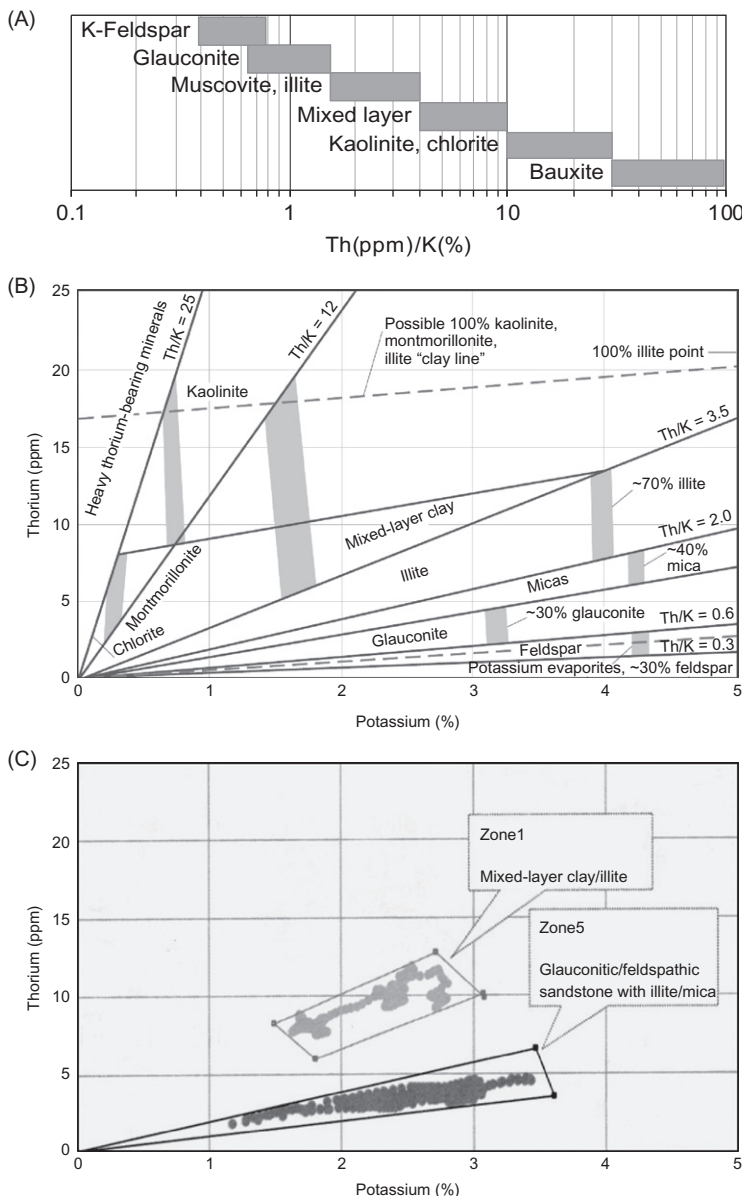


FIGURE 5.5 Th/K plot and K versus Th plot for clay mineral estimate from spectral gammalog. (A) K/Th graph for K feldspar, clay minerals, and mica after Fertl (1979). (B) Th versus K plot (Schlumberger, 2000, with permission). (C) Data from spectral gammalog in two zones in a Th versus K plot with identified clay types (Mohammadlou et al., 2010).

- The tendency of thorium to form discrete authigenic minerals of silt size rather than adsorb onto clay mineral surface
- The inadequate database and insufficient statistical foundation.

5.2.5.4 Source Rock Studies

For source rock studies, the behavior of uranium under different environmental conditions is especially important. As a measure, the Th/U ratio is used (Fertl, 1979):

Th/U>7 → continental, oxidizing

Th/U<7 → marine, gray, ..., green shales

Th/U<2 → marine, black shales, phosphates.

An extremely high adsorption takes place in stagnant, anoxic waters (which typically produce black shales) at a low rate of sediment deposition (e.g., North Sea Jurassic hot shales).

Figure 5.6 shows the strong correlation between the Th/U ratio and organic carbon content for the Devonian black shales. The ratio incorporates lithology variations mainly by the thorium component.

Variations of the natural gamma radioactivity as observed in oil and gas reservoirs are related to the uranium concentration in crude oils (Table 5.5) and the alteration during production (see Fertl, 1983).

Abnormally high gamma values have been detected at the oil/water contact and oil-depleted water-flooded strata (Doering and Smith, 1974; Khusnullin, 1973; King and Bradley, 1977; Fertl, 1983; Lehnert and Just, 1979).

Toulhoat et al. (1989) studied the retention behavior of ions by in situ pumping experiments in low permeability formations (aquifers) and found a clear decrease of uranium content as a result of the pumping procedure.

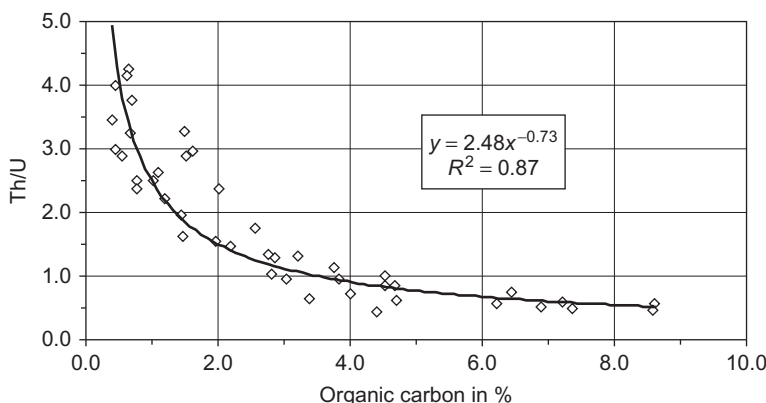


FIGURE 5.6 Th/U ratio versus the organic carbon content for the Devonian black shales (Virginia and Kentucky); data from Fertl (1983).

TABLE 5.5 Uranium Concentration in Several Crude Oils

Location	U in 10^{-3} ppm	Location	U in 10^{-3} ppm
Arkansas	0.5–2.5	Oklahoma	0.32–1.98
Colorado	0.17–0.7	Kansas	0.28–2.6
Montana	0.12	Wyoming	0.24–13.5
New Mexico	0.54	Libya	15.0

Fertl (1983).

5.2.6 Radioactive Heat Generation

Heat is generated as a result of the decay of naturally radioactive elements (potassium, uranium, and thorium) in the earth's crust and contributes significantly to terrestrial heat flow. The mean heat flow at the earth's surface is about 65 mW m^{-2} with the heat flow from the mantle in continental areas being approximately 20 mW m^{-2} . The difference is due to radioactive heat generation in the crustal rocks (Rybáček and Čermák, 1982).

Usually the radiogenic heat production rate is calculated from the potassium, uranium, and thorium content and the rock density using the formula by Rybáček (1976) and Rybáček and Čermák (1982):

$$A = \frac{\rho}{100} (9.52 \cdot U + 2.56 \cdot Th + 3.48 \cdot K) \quad (5.9)$$

where

A is the heat generation in $\mu\text{W m}^{-3}$

ρ is rock density in g cm^{-3}

U, Th are the concentrations of uranium and thorium in ppm

K is the concentration of potassium in %.

In some cases, the unit HGU (heat generation unit) is also used with the following conversion:

$$1 \mu\text{W m}^{-3} = 2.39 \text{ HGU} = 2.39 \cdot 10^{-13} \text{ cal s}^{-1} \text{ cm}^{-3}$$

$$1 \text{ HGU} = 0.418 \cdot 10^{-6} \text{ W m}^{-3} = 10^{-13} \text{ cal s}^{-1} \text{ cm}^{-3}$$

In most igneous rocks, uranium and thorium contribute in a comparable amount, whereas potassium always contributes a substantially smaller amount to total heat production, in proportions of approximately 40% (U); 45% (Th); and 15% (K); (Rybáček and Čermák, 1982). Table 5.6 gives some data.

Table 5.7 shows the potassium, uranium, and thorium content and the heat production rate for some common sedimentary rocks.

TABLE 5.6 Radioactive Heat Generation of Igneous Rocks

Plutonic Rocks	A in $\mu\text{W m}^{-3}$		Volcanic Rocks	A in $\mu\text{W m}^{-3}$	
	Range	Mean		Range	Mean
Granite	0.7–7.65	3.00	Andesite		1.13
Syenite	1.1–5.9	2.84	Basalt	0.2–0.95	0.63
Diorite	0.2–2.45	1.15	Rhyolite	1.9–4.0	3.58
Gabbro	0.1–0.73	0.33	Dacite	0.8–2.9	1.21
Pyroxenite	0.1–0.5	0.23	Porphyrite	0.7–1.7	0.94

Rybäck and Cermak (1982).

TABLE 5.7 Average K, U, and Th Content and Heat Production Rate for Some Sedimentary Rocks

Rock Type	K in %	U in ppm	Th in ppm	Density in g cm^{-3}	A in $\mu\text{W m}^{-3}$
Limestone	0.3	2.0	1.5	2.6	0.62
Dolomite	0.7	1.0	0.8	2.6	0.36
Salt	0.1	0.02	0.01	2.2	0.012
Anhydrite	0.4	0.1	0.3	2.9	0.090
Shale, siltstone	2.7	3.7	12.0	2.4	1.8
Black shale	2.6	20.2	10.9	2.4	5.5
Quartzite	0.9	0.6	1.8	2.4	0.32
Arkose	2.3	1.5	5.0	2.4	0.84
Graywacke	1.3	2.0	7.0	2.4	0.99

Rybäck (1976); see Yalcin et al. (1977).

Determination of radioactive heat generation in general requires a spectral measurement (laboratory, well log, or field measurement). In many cases only a (integral) gammalog is available. Bücker and Rybäck (1996) published a method to determine heat production from integral gamma-ray logs. This method is based on a linear regression between the (integral) gamma-ray GR and heat production A:

$$A = 0.0158(\text{GR} - 0.8) \quad (5.10)$$

TABLE 5.8 Empirical Correlations Between Heat Generation (in $\mu\text{W m}^{-3}$) and Seismic Velocity (in km s^{-1}) and Density (in g cm^{-3})

Equations	Rock Types	Reference
$\ln A = 22.5 - 8.15 \cdot \rho$	Phanerozoic crystalline rocks (Switzerland)	Rybäch and Buntebarth (1984)
$\ln A = 22.54 - 8.145 \cdot \rho$	Granite, trachite, basalt, gabbro (Baikal Region Russia)	Dorofeyeva (1990)
$\ln A = 16.5 - 2.74 \cdot V_p$ at 50 MPa	Phanerozoic crystalline rocks (Switzerland)	Rybäch and Buntebarth (1984)
$\ln A = 13.7 - 2.17 \cdot V_p$ at 100 MPa		Cermak et al. (1990)
$\ln A = 12.4 - 1.93 \cdot V_p$ at 200 MPa		

where

A is the heat generation in $\mu\text{W m}^{-3}$

GR is the gamma intensity in API.

The authors note that the equation is valid for a wide variety of lithologies extending from granite through gneiss, carbonate, and amphibolite to basaltic rocks. In the range 0–350 API and $0.03\text{--}7 \mu\text{W m}^{-3}$, respectively, the error is $<10\%$.

Gegenhuber (2011) developed an improved method to determine heat production from gamma-ray logs implementing mean ratios of K, U, and Th content.

Uranium, thorium, and potassium content varies with rock type and shows increasing radioactive heat generation from basic to acid igneous rocks. This tendency is also reflected in empirical equations correlating heat generation and density and seismic velocity, because both parameters increase from acid to basic types. Examples are given in [Table 5.8](#).

5.3 INTERACTIONS OF GAMMA RADIATION

Methods based on interactions of gamma radiation with rocks use a gamma source and a gamma detector. Depending on the energy of the gamma radiation and the nuclear properties of the target material (rock), two effects are used and two modes of measurement result:

1. Photoelectric effect is applied as a photoelectric cross section (PE) measurement
2. Compton effect is applied as a gamma–gamma–density measurement.

5.3.1 Fundamentals

The gamma photon emitted from a gamma source interacts with the target material and loses a part or all of its energy. In the simplest formulation, this can be expressed for a collimated beam as:

$$\Psi = \Psi_0 \cdot \exp(-\alpha \cdot x) \quad (5.11)$$

where

Ψ is the measured flux after passing the target

Ψ_0 is the measured flux before passing the target

x is the target thickness

α is the absorption coefficient related to the material and the interaction process.

There are three processes of interaction between gamma radiation and matter:

1. Photoelectric effect (low energy)
2. Compton effect (intermediate energy)
3. Pair production (high energy).

The probability of interaction depends not only on the energy of the gamma source but also on the atomic number Z of the target material. [Figure 5.7](#) shows the relative importance of the three effects in a Z versus energy plot. The gray area indicates elements of common rocks.

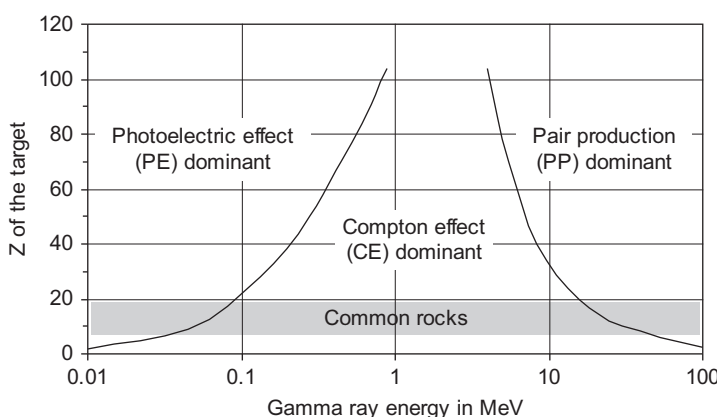


FIGURE 5.7 Relative importance of the three gamma effects in a Z versus energy plot. The lines separate zones for which probability for the neighboring effects are equal (after figures from Baker Atlas, 1985; Hurst and Nelson, 1985).

Photoelectric Effect

An incident low-energy gamma photon (<0.2 MeV) collides with an atom. If the energy of the gamma photon equals or exceeds the discrete “binding energy” of an orbital electron, then

- the gamma photon gives its energy to this orbital electron;
- the electron leaves its orbit and has a kinetic energy $E_{\text{kin}} = \text{gamma-ray energy} - \text{electron binding energy}$.

The probability for the photoelectric effect is controlled by the energy of gamma radiation and the atomic number of the absorbing material Z . For practical applications, two parameters are used:

- Photoelectric cross section index PE in b e^{-1} (barns per electron):

$$\text{PE} = \left(\frac{Z}{10}\right)^{3.6} \quad (5.12)$$

- Volumetric photoelectric cross section U in b cm^{-3} (barns per cubic centimeter):

$$U = \text{PE} \cdot \rho_e \quad (5.13)$$

where ρ_e is the electron density (see [Section 5.3.2](#)).

U is practically independent of porosity; for a mixture of substances U can be calculated as the weighted (by volume fraction) mean of the components.

Compton Effect

An incident intermediate-energy gamma photon (gamma ray) collides with an atom. It scatters at an orbiting electron and transmits only a part of its energy. The energy of the scattered and the kinetic energy of an ejected electron (“Compton or recoil electron”) can be calculated from conservation of energy and momentum (Hearst and Nelson, 1985). The scattering angles are distributed and depend on energy.

Probability of the Compton effect is controlled by the number of electrons in a volume unit of the target material.

Pair Production

An incident high-energy gamma photon (gamma-ray energy >1.022 MeV)³ can be converted into an electron–positron pair when it is near a nucleus.

³1.02 MeV is exactly twice the rest mass of an electron (mc^2).

The photoelectric and Compton effects are applied in geoscience. Both effects result in an attenuation of the gamma radiation, which is expressed in [Equation \(5.12\)](#). The absorption coefficient refers to the effect.

5.3.2 Gamma–Gamma–PE Measurement for Mineral Identification

The photoelectric index (PE) is a supplementary measurement by modern density logging tools. It measures the absorption of low-energy gamma rays by the formation in units of barns per electron. The gamma–gamma measurement in the low energy range ($<100\text{ keV}$) delivers the parameter PE (average photoelectric cross section per electron) with a strong dependence on the (averaged) atomic number Z in the formation, and therefore a sensitive indicator of mineralogy.

If the density ρ_e is also measured (see next section), the parameter U (average photoelectric cross section per cm^3) can be calculated. Definitions of the two parameters are given by [Equations \(5.12\) and \(5.13\)](#).

[Table 5.9](#) shows several important properties for individual rock-forming minerals. The averaged charge-to-mass ratio, Z/A , the photoelectric capture cross section, PE, and U , can be quite different for various minerals.

Particularly of interest is the difference for the main reservoir rock-forming minerals quartz ($\text{PE} = 1.81\text{ barns electron}^{-1}$; $U = 4.8\text{ barns cm}^{-3}$), calcite ($\text{PE} = 5.08\text{ barns electron}^{-1}$; $U = 13.8\text{ barns cm}^{-3}$), and dolomite ($\text{PE} = 3.14\text{ barns electron}^{-1}$; $U = 9.0\text{ barns cm}^{-3}$). This gives a possibility of a mineral composition estimate and is implemented in crossplot techniques (see Section 11.2).

The extremely high value of barite ($\text{PE} = 267\text{ barns electron}^{-1}$; $U = 1066\text{ barns cm}^{-3}$) influences the measurement when the mud contains barite.

5.3.3 Gamma–Gamma–Density Measurement and Porosity Estimate

Gamma–gamma tools in the Compton energy region ($0.5\text{--}5\text{ MeV}$) measure a material response controlled by the number of orbiting electrons per unit volume. Commonly used nuclear sources are cesium (0.66 MeV) and cobalt (1.17 and 1.33 MeV).

The number of atoms per unit volume is

$$n_a = N_A \cdot (\rho_b / A) \quad (5.14)$$

where N_A is Avogadro's number, A the atomic mass number, and ρ_b the bulk density.

TABLE 5.9 Material Properties for Gamma–Gamma Interactions

Substance	Bulk Density ρ_b in g/cm ³	Log Density ρ_e in g/cm ³	Z/A	PE in b/e	U in b/cm ³
Minerals					
Quartz	2.65	2.64	0.499	1.81	4.8
Calcite	2.71	2.71	0.500	5.08	13.8
Dolomite	2.87	2.87	0.499	3.14	9.0
Siderite	3.94	3.89	0.483	14.69	57
Halite	2.16	2.03	0.479	4.65	9.5
Gypsum	2.31	2.33	0.511	3.99	9.4
Anhydrite	2.96	2.98	0.499	5.06	15
Barite	4.48	4.09	0.466	266.8	1066
Orthoclase	2.56	2.53	0.496	2.86	7.2
Albite	2.62	2.59	0.496	1.68	4.4
Muscovite	2.83	2.82	0.497	2.40	6.7
Biotite	3.01	2.99	0.493	6.27	19
Montmorillonite	2.06	2.02	0.502	2.04	4.0
Kaolinite	2.59	2.61	0.504	1.49	4.4
Illite	2.64	2.63	0.499	3.45	8.7
Chlorite	2.88	2.88	0.497	6.30	17
Fluids					
Water (fresh)	1.00	1.11	0.555	0.36	0.40
Oil (medium gravity)	0.80	0.79	0.57	0.125	0.11

Baker Atlas (1985) and Schlumberger (2000).

The number of electrons per unit volume is

$$n_e = Z \cdot n_a = N_A \cdot (Z/A) \cdot \rho_b \quad (5.15)$$

The “electron density” ρ_e , which controls the Compton effect, is defined as:

$$\rho_e = 2 \cdot \rho_b \cdot \frac{Z}{A} \quad (5.16)$$

The bulk density ρ_b directly results in

$$\rho_b = \frac{\rho_e}{2 \cdot Z/A} \quad (5.17)$$

Thus, ρ_b is related to the (measured) electron density ρ_e and the averaged ratio Z/A of the target material (rock). For most rock-forming minerals, the ratio Z/A is a nearly constant 0.5 (see Table 5.9):

$$Z/A \approx 0.5 \quad (5.18)$$

Under this condition, $\rho_b \approx \rho_e$, and the tool can be calibrated directly in bulk *density* units.

If the ratio deviates from the value $Z/A = 0.5$, a correction must be applied. This is also the case particularly for the presence of water with $Z/A = 0.55$. The correction results from a volumetric weighted contribution of the two main components matrix and water:

$$\rho_b = \frac{\rho_e}{1(1 - \phi) + 1.11 \cdot \phi} = \frac{\rho_e}{1 + 0.11 \cdot \phi} \quad (5.19)$$

where ϕ is the porosity.

From bulk density the porosity (total porosity) can be derived:

$$\phi = \frac{\rho_{\text{solid}} - \rho_b}{\rho_{\text{solid}} - \rho_{\text{fluid}}} \quad (5.20)$$

Thus, for a porosity calculation from a density measurement, the knowledge of solid matrix material density ρ_{solid} (also called “matrix density” ρ_{ma}) and fluid density ρ_{fluid} are necessary. An information about matrix mineralogy can be received from geological input, crossplot techniques (see Section 11), and PE measurement.

5.4 INTERACTIONS OF NEUTRON RADIATION

5.4.1 Fundamentals

Fundamentals of neutron logs are presented, for example, by Alger et al. (1971) and Allen et al. (1972), and in a series of tutorials in *Petrophysics* (SPWLA) by Ellis et al. (2003, 2004) and Gilchrist (2009).

Neutrons with a mass of $1.67482 \cdot 10^{-27}$ kg have no electric charge and therefore a high penetration potential (Bassiouni, 1994). Neutrons of different energies interact with atomic nuclei in different ways.

Neutrons are classified using their energy:

- Fast neutrons: energy > 500 keV
- Intermediate neutrons: energy 1–500 keV
- Slow neutrons: energy < 1 keV subdivided into:
 - epithermal neutrons with energy 0.1–1 keV,
 - thermal neutrons with energy < 0.1 eV.

For neutron measurements, a source–detector system is used. Neutron sources are:

1. Spontaneous fission of ^{252}Cf : most of the neutrons that have energies between 250 keV and 2 MeV are relatively low. This source is not in common use in logging (Hearst and Nelson, 1985).
2. Chemical or $\alpha - n$ sources (e.g., Am–Be): a mixture of an α -emitter (Am) and beryllium reacts and produces neutrons with an energy between 1 and 12 MeV; the average energy is about 4.2 MeV (Ellis et al., 2003). This source is widely used for practical applications.
3. Neutron generator: a deuterium–tritium reaction powered by an accelerator produces neutrons with an energy of 14.1 MeV. Neutron generators have some advantages compared with the other sources: they can be switched off and on, they produce a high and exactly defined energy, and they can be used in a pulsed mode.

Neutrons interact with nuclei; they transfer and lose their energy in these processes. There are two fundamental types of interaction:

1. Moderating or slowing down interactions (inelastic scattering, elastic scattering)
2. Absorptive interactions if they reach thermal energy (capturing, activation).

The probability of interaction with a single nucleus is described by a cross section σ . A frequently used unit for microscopic cross section σ is the barn ($1 \text{ barn} = 10^{-24} \text{ cm}^2$). When interactions with matter in bulk is considered, it is convenient to express properties as macroscopic cross section Σ :

$$\Sigma = n_a \cdot \sigma \quad (5.21)$$

where n_a is the number of atoms per cm^3 and Σ results in cm^{-1} . The mean free path is defined as $\lambda = \Sigma^{-1}$ (Hearst & Nelson, 1985).

Figure 5.8 illustrates the processes during the life of a neutron and will be described from the high to the low energy level.

Inelastic Scattering

The fast neutron interacts with a nucleus with the atomic number Z and mass number A . The process forms a compound nucleus with atomic number Z and mass number $A + 1$, which is in an excited state. It decays to the ground state (same as the initial target nucleus), emitting:

- a neutron of lower energy;
- a gamma ray of characteristic energy. This energy is characteristic for the target atom and can be used to identify elements. Table 5.10 shows some of the characteristic energies. This effect is used for the carbon/oxygen log (Chase et al., 1985; Oliver et al., 1981).

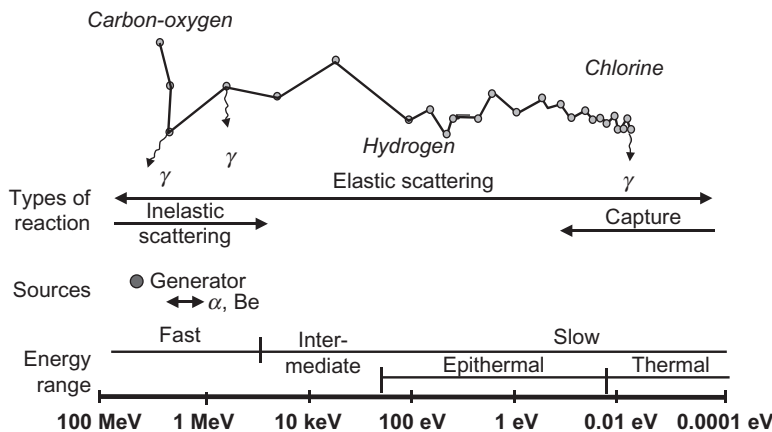


FIGURE 5.8 Neutron phenomena as a function of energy (in MeV). The neutron sources and the energy regions are indicated at the bottom. At the top are the types of reactions and processes plotted (adapted after a figure from Hearst and Nelson, 1985).

TABLE 5.10 Inelastic Scattering and Capturing—Some Characteristic Energies of Emitted Gamma Radiation

Element	Gamma Energy in MeV—Inelastic Scattering	Gamma Energy in MeV—Capturing
H		2.2
O	6.1, 7.0	
C	4.43	
Si	1.78	3.5, 4.9
S	2.2	3.2, 4.9, 5.4
Ca	3.7	2.0, 4.4, 6.4
Al	2.2	7.7
Mg		3.9
Fe		6.0, 7.3, 7.6

Hearst and Nelson (1985).

TABLE 5.11 Averaged Number of Collisions n_{co} Required to Thermalize a 14-MeV Neutron

Element	n_{co} (from 14 MeV)	Element	n_{co} (from 14 MeV)
H	19	Al	290
C	112	Si	297
O	154	Cl	343
Mg	235	Ca	380

(Hearst and Nelson (1985)).

An example of an inelastic scattering spectrum is given in [Figure 5.11](#).

Elastic Scattering

A neutron collides with an atomic nucleus and loses kinetic energy. All of the energy of the incident neutron is converted to the combined kinetic energy of the target nucleus and the neutron after the collision. Thus, this scattering process is a slowing down reaction that can be described as a “billiard ball” interaction. Therefore, elastic scattering shows no induced radiation.

The ratio of the final energy E_f and the initial energy E_0 is (Hearst and Nelson, 1985):

$$\frac{E_f}{E_0} = \frac{A^2 + 2 \cdot A \cdot \cos\Theta + 1}{(A + 1)^2} \quad (5.22)$$

where A is the atomic mass of the target and Θ is the scattering angle.

The maximum energy loss results for $A = 1$ (hydrogen). *Hydrogen* has the same mass as the neutron.⁴ [Table 5.11](#) illustrates this dominant effect of hydrogen by a comparison of the averaged number of collisions required in that element, to thermalize a 14-MeV neutron.

Thus, we can conclude that elastic scattering as the most common interaction is dominated by hydrogen (H). Hydrogen content controls the strength of elastic scattering; this is the background for correlation with water content or “neutron porosity.” But the other elements also interact with neutron radiation; this results in a “matrix effect” for neutron porosity determination.

⁴A neutron loses all its energy in one direct collision (head-on, $\Theta = 0$) with a hydrogen atom (Bassiouni, 1994).

Radiative Capture

For thermalized neutrons, the most probable interaction is radiative capture. Neutrons are captured by a nucleus, forming a compound nucleus in an excited state. It decays to the ground state and emits a gamma radiation with an energy that is characteristic for the host element. Thus, the characteristic properties are:

- the neutron capture cross section in barns;
- the capture gamma energy in MeV. [Table 5.10](#) shows some selected data.

An example for a capture spectrum is given with [Figure 5.11](#).

There are two elements, common in rocks, that have a prominent high capture cross section: boron (759 barns) and chlorine (33 barns). For comparison, silicon has a cross section of 0.16 barn, aluminum of 0.23 barn, and oxygen of 0.0002 barn (Hearst and Nelson, 1985). Both elements are in formation water, although chlorine appears more frequently.

Particularly chlorine results in a capture process producing a time-dependent decay of radiation that is detectable in pulsed neutron capture (PNC) logging. This effect is applied in production logging. The method detects the change of chlorine salinity in the fluid and gives information about changing water saturation. However, with respect to well logging applications, we note that any neutron measurement uninfluenced by water salinity must be realized before neutrons are thermalized (neutron epithermal techniques).

Characteristic Lengths

The complex neutron processes can be described by characteristic lengths. They are a measure of the rectified distance traveled by a neutron in its zig-zag path between the start and end of consideration. A detailed description is given, for example, by Ellis et al. (2003), Ellis and Singer (2007), and Gilchrist (2009):

- Slowing down length L_s is “proportional to the straight-line distance that a neutron covers between the time it is emitted from the source at high energy to the time it reaches a much lower energy. The neutron ‘slows down’ or loses energy because of the elastic scattering interaction. The ratio of the detector counting rates, used to estimate formation porosity, is actually measuring the L_s of the formation” (Ellis et al., 2003).
- Thermal diffusion length L_d is given by the mean-square distance that the neutron travels due to thermal diffusion before absorption.

[Figure 5.9](#) shows the slowing down and diffusion lengths in sandstone, limestone, and dolomite for neutrons from an Am–Be source. The figure demonstrates the strong decrease of both lengths with increasing porosity, but also—particularly for low porosity—the different response of the three rock types (mineralogy or matrix effect).

Slowing down length and diffusion length are inversely proportional to the corresponding cross sections.

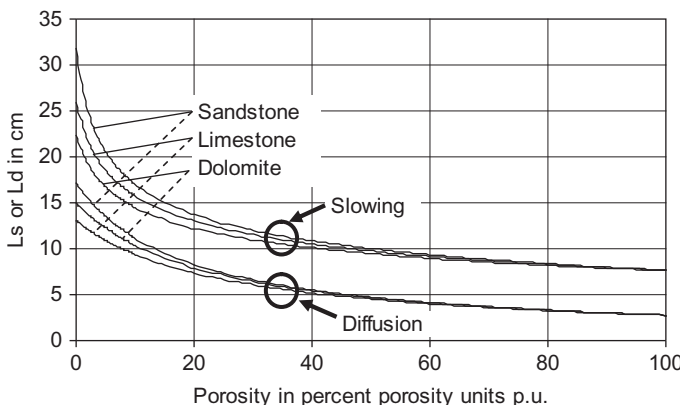


FIGURE 5.9 Slowing down and diffusion lengths in sandstone, limestone, and dolomite for neutrons from an Am–Be source (Gilchrist, 2009).

The migration length L_m is a measure for the combination of the path traveled during the slowing down phase and the distance traveled in the thermal phase before being captured (Ellis, 1987)

$$L_m = \sqrt{L_s^2 + L_d^2} \quad (5.23)$$

5.4.2 Porosity from Neutron Measurements

Traditional commercial neutron tools consist of a neutron source (or neutron generator) and two detectors for the radiation after interaction; formation porosity is determined from the ratio of counts in the two detectors (Gilchrist, 2009).

Because in reservoir rocks, the dominant elastic scattering is controlled mainly by hydrogen, such a system gives information about the “hydrogen concentration”, which is controlled by water or hydrocarbons in the formation. This has created the term “neutron porosity.” The following section will discuss the conditions of neutron-derived porosity.

Figure 5.10 shows a simplified picture of a porous rock with the various solid and fluid components. As a general rule, the different responses indicate that:

- for a water- or oil-saturated rock, the neutron response reflects mainly porosity, whereas gas (with a lower H content/volume) probably has a lower neutron effect;
- the solid minerals in general have a small—but not negligible—fluence (“matrix effect”);
- shale with a high amount of bound water can have a strong effect.

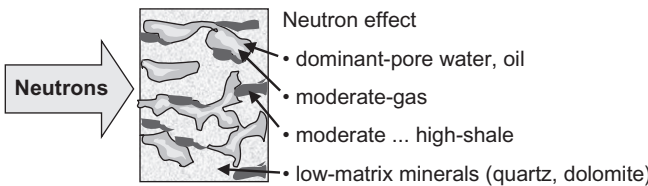


FIGURE 5.10 Simplified picture of a porous rock with the various solid and fluid components for neutron interaction.

For most practical applications, neutron tools are calibrated in a limestone–freshwater calibration facility. The API Calibration Facility at the University of Houston (see API, 1959, Recommended Practice for Standard Calibration and Form for Nuclear Logs) consists of blocks of:

- Carthage marble with a porosity 0.019,
- Indiana limestone with a porosity 0.19,
- Austin limestone with a porosity 0.26.

The fluid is freshwater.

If the neutron tool is calibrated for a limestone matrix and pore fluid freshwater, the measurement:

- in a water-bearing limestone formation: delivers exactly the true porosity;
- in a different formation: corrections are necessary, because different matrix materials (sandstone, dolomite) have a neutron effect that is different in comparison with limestone;
- in a different pore fluid: corrections are necessary, because different fluids (gas, oil) have a neutron effect that is different in comparison with freshwater. Gas in particular has a low H concentration; therefore, the tool reads a low porosity in porous gas zones;
- in a shaly zone: the measurement is influenced by the high amount of H and results in a high neutron porosity reading; a shale correction is necessary.

If the neutron response is expressed as “neutron porosity” ϕ_N , then pure limestone (calcite) has $\phi_N \equiv 0$ and freshwater has $\phi_N \equiv 1$. [Table 5.12](#) gives some more data for fluids and solid rock components.

For any porous rock composed by different mineral components, shale, and fluids, the porosity derived from a limestone–freshwater calibrated device results as:

$$\phi_N = \phi \cdot \phi_{N, \text{fluid}} + (1 - \phi)[(1 - V_{\text{shale}})\phi_{N, \text{matrix}} + V_{\text{shale}} \cdot \phi_{N, \text{shale}}] \quad (5.24)$$

where

ϕ is the rock porosity

ϕ_N is the measured neutron porosity

TABLE 5.12 Neutron Response of Some Rock Components, Expressed as Neutron Porosity ϕ_N

Component	ϕ_N	Component	ϕ_N
Water, fresh	1	Calcite	0
Water, 200,000 ppm NaCl	0.9	Dolomite	0.01–0.02
Oil, average	0.96–1.02	Quartz	–0.02
Gas, average, 15°C, 0.1 MPa	0.0017	Gypsum	0.49
Gas, average, 93°C, 48 MPa	0.54	Shale, average	0.2–0.4

After Serra (2004), Baker Atlas (2002), Schlumberger (2000), and Fricke and Schön (1999).

$\phi_{N,fluid}$ is the neutron response of the fluid

$\phi_{N,matrix}$ is the neutron response of the matrix

$\phi_{N,shale}$ is the neutron response of the shale

V_{shale} is the shale content.

Thus, for an exact porosity calculation from a neutron measurement, the knowledge of the neutron response of the fluid, the neutron response of the matrix, the neutron response of the shale, and the shale content are necessary.

Neutron porosity is an important component for crossplot techniques and combined mineralogy–porosity calculation in order to give an estimate for matrix composition and porosity (see Section 11).

5.4.3 Pulsed Neutron Capture Measurements

Pulsed Neutron Capture (PNC) measurements can be used to determine water saturation in cased producing wells. The decay rate is controlled strongly by chlorine. Therefore, the decay in saltwater (NaCl) is related to water content S_w and makes it possible to distinguish between hydrocarbon and water in cased holes.

The primary measured parameter characterizing the capture process is the time constant τ in ms for the decay of a population of slow neutrons captured by the chlorine (and other substances). The decay time constant τ is connected with the “macroscopic cross section” Σ in capture units:

$$\Sigma = \frac{4550}{\tau} \quad (5.25)$$

The observed (measured) “macroscopic cross section” Σ_{log} is the sum of the contributions from the rock components matrix, shale, and formation fluid:

$$\Sigma_{log} = (1 - \phi - V_{sh})\Sigma_{ma} + V_{sh} \cdot \Sigma_{sh} + \phi(S_w \cdot \Sigma_w + (1 - S_w)\Sigma_{hc}) \quad (5.26)$$

For water saturation, this results in

$$S_w = \frac{\Sigma_{\log} - \Sigma_{ma} - V_{sh}(\Sigma_{sh} - \Sigma_{ma}) - \phi(\Sigma_{hc} - \Sigma_{ma})}{\phi(\Sigma_w - \Sigma_{hc})} \quad (5.27)$$

where

S_w is water saturation

ϕ is porosity

Σ_{\log} is the recorded capture cross section of the formation

Σ_{ma} is the capture cross section of the rock matrix

Σ_{sh} is the capture cross section of the shale

Σ_w is the capture cross section of the formation water

Σ_{hc} is the capture cross section of the hydrocarbon.

In practical applications for water saturation determination, it can often be assumed that the properties ϕ , Σ_{ma} , Σ_{sh} , Σ_{hc} , Σ_w (controlled by salinity) are constant. If this is the case, then the variation of measured Σ_{\log} directly reflects the variation of S_w . If the properties are known (from openhole interpretation), then a quantitative determination of S_w is possible.

Mean values for the magnitude of the cross section are:

- $\Sigma_{ma} \approx 4-10$ cu (capture units)
- $\Sigma_{sh} \approx 10-50$ cu
- $\Sigma_w \approx 70-200$ cu (depends on chlorine content)
- $\Sigma_{hc} \approx 17-22$ cu.

5.5 APPLICATION OF NUCLEAR MEASUREMENTS FOR A MINERAL ANALYSIS

5.5.1 Introduction

Determination of mineral composition (mineralogy) of a rock is of fundamental importance particularly in reservoir characterization. Mineral composition controls “matrix properties” and directly controls the accuracy of derived porosity. But mineral content and composition also give information about the rock-forming processes and resulting rock properties. In carbonatic rocks, mineral composition is related to pore space properties and pore type.

Traditional nuclear measurements (natural gammalog, gamma–gamma log, neutronlog) offer possibilities for an initial classification using defined characteristic values or tendencies. Examples are:

- shale indication from gammalog and a combination gamma–gamma–density and neutronlog;
- carbonate detection (limestone, dolomite) using neutron–density cross-plots (Chapter 11), identification of dolomite and/or limestone supported by photoelectric cross section (PE) measurement;

TABLE 5.13 Occurrence of Elements Detected by Gamma Spectrometry in Rocks and Fluids

Detected Element	Found in
H	Water, hydrocarbons, clay
Ca	Calcite CaCO_3 , dolomite $\text{CaMg}(\text{CO}_3)_2$, anhydrite CaSO_4
Si	Quartz SiO_2 , clay
Cl	Rock salt NaCl
S	Anhydrite CaSO_4
Fe	Pyrite FeS_2 , clay
C	Hydrocarbons, calcite CaCO_3 , dolomite $\text{CaMg}(\text{CO}_3)_2$

Schlumberger, Gamma Ray Spectrometry Tool (1983).

- identification of anhydrite by extremely high density (2.96 g cm^{-3}), supported by PE measurement.

For more detailed and reliable characterization of mineralogical composition, elemental analyses based on spectral nuclear measurement have been developed. The physical processes of nuclear measurements are directly connected with the reaction of certain elements and their components. Thus, nuclear measurements in general are able to deliver “element controlled information.”

In carbonate mineralogy, in some cases calcite and dolomite can be distinguished with the PE. But the PE measurement can have problems if barite is present in the mud or if the formation contains anhydrite. Underestimating the anhydrite content results in an underestimation of grain density, and this leads to an underestimation of total porosity.

Neutron capture spectroscopy can be used to detect Ca, Mg, and S, and therefore to discriminate dolomite $\text{CaMg}(\text{CO}_3)_2$ from calcite CaCO_3 and provide accurate estimates of anhydrite volumes (CaSO_4).

Neutron gamma spectrometric methods using pulsed neutron generators can deliver information about the concentration of various elements from gamma rays produced either in inelastic scattering or in neutron capture events. Elements occurring in different rock components are listed in Table 5.13.

5.5.2 The Principle

Modern methods and tools like “Elemental Capture Spectroscopy Sonde ECS” and “EcoScope” from Schlumberger and the “Formation Lithology

eXplorer (FLeX)" device in combination with the interpretation system "RockView" from Baker Atlas determine certain elemental concentrations and calculate—based on a model assumption—mineral composition. Fundamental papers are written, for example, by Hertzog et al. (1987), Gilchrist et al. (1999, 2000), Barson et al. (2005), Pemper et al. (2006), and Han et al. (2009).

Nuclear spectroscopy methods deliver weight fractions of certain elements (see below), but of course, they cannot deliver a full mineral analysis. Therefore, the link to the rock type requires use of a typical mineral composition (model) in terms of the detectable elements. In practice typical groups are used, such as:

- lithologic fractions of total clay, total carbonate, and quartz, feldspar, and mica (QFM);
- lithologic categories of sand, shale, coal, carbonates, and evaporates.

The delivered concentration of certain elements includes:

- some of the most diagnostic and abundant elements in sedimentary rocks, in particular Si, Ca, Fe, S;
- some diagnostic but not frequently abundant elements like titanium (Ti) and gadolinium (Gd);
- (qualitatively) H and Cl.

In many cases, the transformation from elements to minerals requires an accurate clay content determination followed by an analysis combining the remaining minerals into groups and more detailed composition. The algorithms use mineral standard samples.

5.5.3 Description of the Algorithm Used for the Atlas RockView Analysis

The interpretation is characterized by the following main steps (Pemper et al., 2006):

Elements → general lithology → specific lithology → mineralogy

Measurement of Elemental Concentration

The nuclear logging system uses a pulsed neutron source and measures both inelastic and capture gamma-ray energy spectra. A matrix inversion spectral fit algorithm is used to analyze these spectra in order to separate the total response into its individual elemental components.

The prominent measured elements associated with subsurface rock formations include calcium, silicon, magnesium, carbon, sulfur, aluminum, and

iron. Potassium, thorium, and uranium are measured separately with a natural gamma-ray spectroscopy instrument.

As a result, the tool and data processing measures (detects and quantifies):

- from natural gamma-ray energy spectrum: K, U, Th;
- from capture spectrum: Ca, Si, S, Fe, Ti, Gd, Mn;
- from inelastic spectrum: Si, Mg, Al, C.

Two notes may be added:

1. The final Si content, a very important element, is derived from both capture and inelastic spectra.
2. Some other elements have signals in both capture and inelastic spectra, but sometimes only one of them gives a usable signal. For example, aluminum is present within the capture spectrum, but its low capture cross section makes it difficult to quantify. A similar problem exists for capture magnesium. Both of these elements can be characterized using the inelastic spectrum (Pemper et al., 2006).

Derivation of General Lithology

Lithologies are divided into general categories including sand, shale, coal, carbonates, and evaporites. The tool response is characterized for each element by placing it into formations of known chemical composition. [Figure 5.11](#) shows capture and inelastic spectra for the general basic lithologies.

Some general observations are:

- whereas Ca and C energy peaks are prevalent in the limestone formations, Si stands out in the sandstone,
- Ca, Mg, and C can be observed in the dolomite, and Ca and S can be distinguished in the anhydrite,
- Al energy peaks stand out in shale formations due to the presence of clay and feldspar.

In general, these energy spectra provide a visual display of the physical characteristics that are exploited in the mathematical analysis of gamma-ray spectroscopy. Thus, based upon the chemical composition of the formation, each depth interval is classified into one of five categories: sand, shale, coal, carbonate, evaporate.

Derivation of Specific Lithologies and Mineral Composition

The general categories (sand, shale, coal, carbonate, evaporate) are the basis for more detailed assessment of the specific lithology. A carbonate, for example, is concluded to be calcite or dolomite depending on the amounts of calcium and magnesium. The purpose of the middle step is to provide the

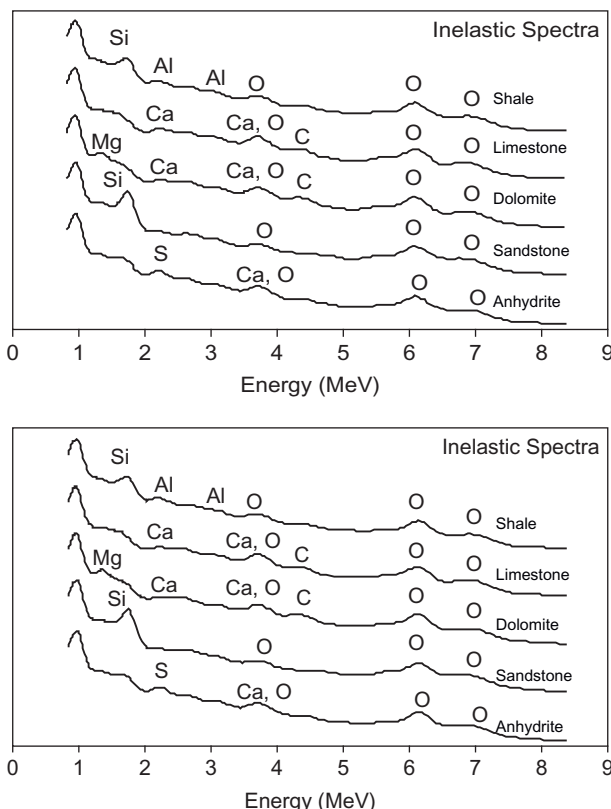


FIGURE 5.11 Capture and inelastic spectra for the general basic lithologies (Pemper et al., 2006).

opportunity to identify and place constraints on the subsequent mineral evaluation of the rock.

If the lithology of the formation can be established based on its chemistry, then the probable mineral composition of the rock matrix can be more readily determined. For specific lithologies, Ternary diagrams of elemental oxides are plotted.

The final step in the interpretation process is to derive mineralogy from the specific lithology. A list containing some of the common sedimentary minerals used for formation evaluation is provided in [Table 5.14](#). Potentially identifiable minerals are quartz, potassium-feldspar, albite, calcite, dolomite, siderite, anhydrite, illite/smectite, kaolinite, glauconite, chlorite, pyrite, and others.

Specific lithologic classification permits placing constraints on the final petrophysical solution. In the case of feldspathic sand, for example, one might wish to predict the presence of illite/smectite, chlorite, and kaolinite

TABLE 5.14 Detectable Elements and Common Sedimentary Minerals

Result of Measurement	Mineral	Formula
Elemental Concentrations:		
K		
Th		
U		
Ca		
Fe		
Gd		
Mg		
S		
Si		
Ti		
Al		
C		
Qualitative Indicators:		
Cl		
H		
O		
	Silicates	
	Quartz	SiO₂
	K feldspar (orthoclase)	KAlSi₃O₈
	Albite (plagioclase)	NaAlSi₃O₈
	Carbonates	
	Calcite	CaCO₃
	Dolomite	CaMg(CO₃)
	Siderite	FeCO₃
	Evaporites	
	Anhydrite	CaSO₄
	Halite	NaCl
	Clay minerals	
	Illite/smectite	K_{1-1.5}Al₄(Si_{7-6.5},Al_{1-1.5})O₂₀(OH)₄
	Chlorite	(Mg,Fe,Al)₆(Si,Al)₄O₁₀(OH)₈
	Kaolinite	Al₄Si₄O₁₀(OH)₈
	Glauconite	K_{0.7}(Mg,Fe₂,Al)(Si₄,Al₁₀)O₂(OH)
	Iron minerals	
	Pyrite	FeS₂
	Hematite	Fe₂O₃

In the mineral formula, immediately detectable elements are shown in bold.

based on various feldspar decomposition models. Similarly, it might be predicted that calcic dolomite, one of the specific lithologies for carbonate, is composed mainly of dolomite with small amounts of calcite and possibly anhydrite (Pemper et al., 2006).

Algorithms are based upon 334 examples of core chemistry and mineralogy from the literature in addition to numerous (463) core samples.

TABLE 5.15 Results (Fractions in %) of RockView Analysis in Comparison with Core Data

Mineral	Core (XRD)	RockView
Anhydrite	7.7	10.2
Calcite	0.0	0.5
Chlorite	1.4	0.0
Dolomite	15.0	17.5
Illite	4.5	5.0
K feldspar	9.9	11.6
Plagioclase	14.1	13.5
Pyrite	0.4	1.1
Quartz	46.2	43.2
Siderite	0.0	0.0
Sum	99.2	102.6

Pemper et al. (2006).

A specific example for practical application is shown in [Table 5.15](#), where the RockView mineralogy is compared with that obtained from core analysis using the X-ray diffraction (XRD) technique

In general, this methodology:

- reduces the uncertainties inherent in interpretations without core sample data;
- gives detailed information about mineral composition and derived properties.

In particular, the method:

- gives a more accurate clay typing and carbonate reservoir characterization;
- in shale gas reservoirs, provides information about the amount and distribution of organic carbon (kerogen) identifying productive zones (gas in place) and discriminating from carbon associated with minerals (Pemper et al., 2009).

Neutron capture spectroscopy is an integrated component of the Schlumberger “Carbonate Advisor” (www.slb.com/carbonates). For carbonates, the measurement of magnesium and sulfur can be used for discrimination of calcite and anhydrite and for anhydrite volume estimate (underestimating anhydrite content results in underestimation of grain density

and underestimation of total porosity). The brochure gives an example and demonstrates that “incorporation of neutron spectrometry in the lithology-porosity analysis identifies anhydrite and improved the porosity estimates, which are up to 2 pu (porosity units) higher than the porosity derived from triple-combo logs alone.”

5.6 EXAMPLE: SANDSTONE—PART 2

The data for the sandstone example are taken from the textbook “Well Logging and Formation Evaluation” by T. Darling (2005).

Log and core data are used to demonstrate subjects of various chapters (pore space properties, electrical properties, nuclear properties). All data and calculations are on the website <http://www.elsevierdirect.com/companion.jsp?ISBN=9780444537966> (file: Example. Sandstone).

The log section from 616 to 645 m represents a sequence of sand, some limestone, and shale. In Section 2.8, core data including porosity are presented. In this section, the application of nuclear logs (gammalog, density log, and neutron log) is discussed.

Figure 5.12 shows gammalog, gamma–gamma–density log, and neutron porosity log (limestone calibrated).

Step 1: Calculation of shale content using gammalog.

Input parameters are (see log): $GR_{\min} = 20$ API $GR_{\max} = 100$ API

Application of linear regression gives the shale content (Equations (4.5) and (4.6))

$$V_{\text{sh}} = I_{\text{GR}} = \frac{GR - GR_{\text{cn}}}{GR_{\text{sh}} - GR_{\text{cn}}} = \frac{GR - 20}{100 - 20} \quad (5.28)$$

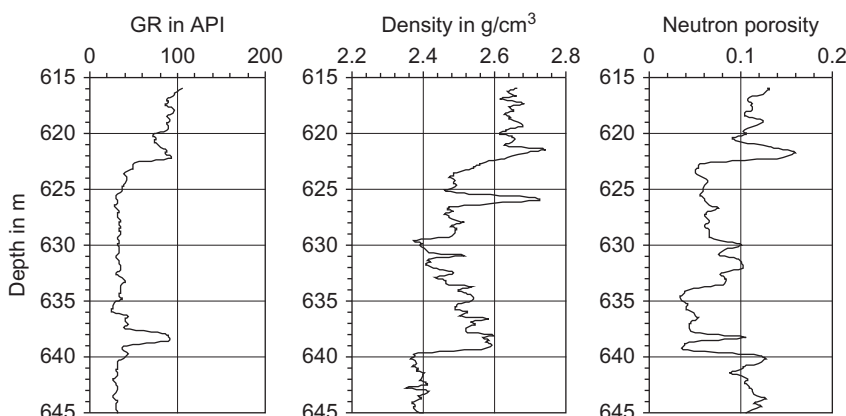


FIGURE 5.12 Gammalog, gamma–gamma–density log, and neutron porosity log (limestone calibrated) for a sandstone-shale section (visit the website <http://www.elsevierdirect.com/companion.jsp?ISBN=9780444537966> and refer Example. Sandstone).

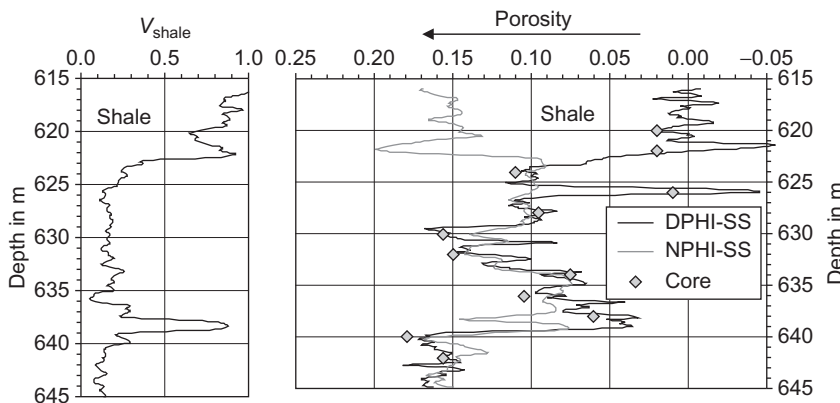


FIGURE 5.13 Sandstone—results of interpretation.

- left: shale content V_{shale} from gammalog,
- right: porosity assuming a sandstone matrix from density log (DPHI-SS) and neutronlog (NPHI-SS); core porosities.

The result is plotted as V_{shale} log in Figure 5.13.

Step 2: Calculation of porosity using gamma—gamma—density and neutron log.

Porosity can be calculated from density log (RHOB = bulk density) under the assumption of a sandstone, and results as:

$$\text{DPHI-SS} = \frac{\rho_{\text{ma}} - \rho_{\text{b}}}{\rho_{\text{ma}} - \rho_{\text{fl}}} = \frac{2.65 - \text{RHOB}}{2.65 - 1.00} \quad (5.29)$$

Input parameters are:

matrix density (sandstone) $\rho_{\text{ma}} = 2.65 \text{ g cm}^{-3}$

fluid density (water) $\rho_{\text{fl}} = 1.00 \text{ g cm}^{-3}$

The result is plotted as DPHI-SS log in Figure 5.13.

The measured neutron porosity NPHI is limestone calibrated. Therefore, a transformation to condition of a sandstone matrix (NPHI-SS) is necessary and, in this case,

$$\text{NPHI-SS} = \text{NPHI} + 0.04 \quad (5.30)$$

This neutron porosity referenced to a sandstone matrix NPHI-SS is also plotted as log. Figure 5.13 shows core porosities in addition to the log-derived porosities.

Logs and core data clearly show that:

- high shale content from gammalog corresponds with separation of the two porosities ($\text{NPHI-SS} > \text{DPHI-SS}$) at 615–622.5 and 638.0–639.0 m;

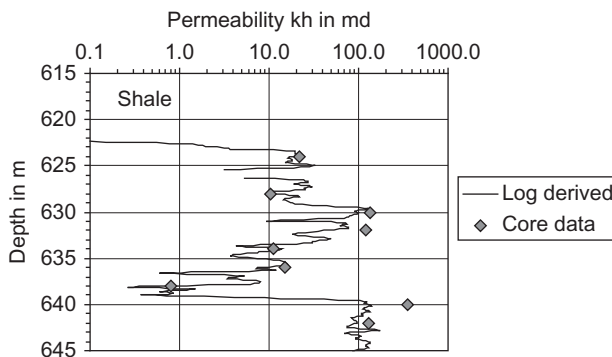


FIGURE 5.14 Permeability log derived from the regression (Equation (2.88)) applied on the porosity log. Log data are compared with core data (Section 2.8).

- for the sandstone reservoir zones 622.5–638.0 and 639.0–645 m, there is a good agreement of the two porosity curves. In Section 8.4 the arithmetic mean is used for a following saturation calculation;
- within the reservoir zones porosity from logs fits well core porosities and confirms the calculation;
- at 625.5–626.5 m log porosities are different with negative value for DPHI-SS. This results from the different matrix of the layer (625.5–626.5 m), which is a limestone with a high density ($\text{RHOB} \approx 2.72 \text{ g cm}^{-3}$). The presence of limestone is also indicated in the core description in Table 2-13;
- in the upper shale zone, density-derived porosity DPHI-SS is closer to core porosity than neutron-derived porosity NPHI-SS (clay-bound water effect).

Step 3: Permeability estimate.

Finally with the porosity–permeability relationship (Equation (2.84)), and the porosity log, a “permeability log” can be calculated and plotted (Figure 5.14). There is a good fit between the curve (log) and the core permeability.

Elastic Properties

6.1 FUNDAMENTALS

6.1.1 Elastic Moduli and Elastic Wave Velocities

The theory of elasticity (see, for example, Landau and Lifshitz, 1965) gives the basis for the description of elastic wave propagation.

Hooke's law describes the relationship between stress and strain of an elastic material. In a general formulation, the stress–strain relationship is a tensorial equation:

$$\sigma_{ik} = C_{iklm}\varepsilon_{lm} \quad (6.1)$$

where

σ_{ik} is the stress tensor

ε_{ik} is the strain tensor

C_{iklm} is the elastic modulus (or stiffness) tensor.

If strain is expressed as a function of stress, the resulting strain–stress relationship is

$$\varepsilon_{ik} = D_{iklm}\sigma_{lm} \quad (6.2)$$

where D_{iklm} is the elastic compliance tensor.

Frequently, an abbreviated notation is applied for the tensor components. The four subscripts of the stiffness and compliance tensor are reduced to two as follows: the pairs $ij(kl)$ are replaced by one index $m(n)$



$ij(kl)$	11	22	33	23, 32	13, 31	12, 21
$m(n)$	1	2	3	4	5	6

For an isotropic material, the number of independent constants reduces to two and the tensor of elasticity has the form

$$\begin{bmatrix} c_{11} & c_{12} & c_{12} & 0 & 0 & 0 \\ c_{12} & c_{11} & c_{12} & 0 & 0 & 0 \\ c_{12} & c_{12} & c_{11} & 0 & 0 & 0 \\ 0 & 0 & 0 & c_{44} & 0 & 0 \\ 0 & 0 & 0 & 0 & c_{44} & 0 \\ 0 & 0 & 0 & 0 & 0 & c_{44} \end{bmatrix} \quad \text{with } c_{12} = c_{11} - 2c_{44} \quad (6.3)$$

The relationship between the components and the Lame parameters λ, μ are

$$c_{11} = \lambda + 2\mu \quad c_{12} = \lambda \quad c_{44} = \mu \quad (6.4)$$

Besides the Lame parameters λ, μ , any pair of two of the following moduli can be used for a description of the elastic properties of an isotropic material:

Young's modulus E , defined as ratio of stress to strain in a uniaxial stress state;

compressional wave modulus M , defined as ratio of stress to strain in a uniaxial strain state;

bulk compressional modulus k , defined as ratio of hydrostatic stress to volumetric strain¹;

shear modulus μ , defined as ratio of shear stress to shear strain;

Poisson's ratio ν , defined as the (negative) ratio of lateral strain to axial strain in a uniaxial stress state.

Note again that for a complete description, only two parameters are necessary. [Table 6.1](#) gives the conversion from one set of parameters to any other.

Corresponding to the two moduli are two independent body waves:

Compressional, longitudinal, or P-wave with the velocity:

$$V_P = \sqrt{\frac{M}{\rho}} = \sqrt{\frac{E}{\rho} \frac{1-\nu}{(1+\nu)(1-2\nu)}} = \sqrt{\frac{\lambda + 2\mu}{\rho}} = \sqrt{\frac{k + (4/3)\mu}{\rho}} \quad (6.5)$$

Shear, transversal, or S-wave with the velocity:

$$V_S = \sqrt{\frac{\mu}{\rho}} = \sqrt{\frac{E}{\rho} \frac{1}{2(1+\nu)}} \quad (6.6)$$

where ρ is the bulk density.

¹Compressibility is the inverse of compressional modulus.

TABLE 6.1 Relationships Between Elastic Moduli in an Isotropic Material

<i>M</i>	<i>E</i>	μ	λ	<i>k</i>	ν
E, ν	$\frac{E \cdot (1 - \nu)}{(1 + \nu) \cdot (1 - 2\nu)}$		$\frac{E}{2 \cdot (1 + \nu)}$	$\frac{E \cdot \nu}{(1 + \nu)(1 - 2\nu)}$	$\frac{E}{3 \cdot (1 - 2\nu)}$
E, μ	$\frac{\mu \cdot (4\mu - E)}{3\mu - E}$			$\mu \cdot \frac{E - 2\mu}{3\mu - E}$	$\frac{\mu \cdot E}{3 \cdot (3\mu - E)}$
E, k	$\frac{3k \cdot (3k + E)}{9k - E}$		$\frac{3kE}{9k - E}$	$\frac{3k \cdot (3k - E)}{9k - E}$	$\frac{3k - E}{6k}$
k, ν	$\frac{3k \cdot (1 - \nu)}{1 + \nu}$	$3k \cdot (1 - 2\nu)$	$\frac{3k(1 - 2\nu)}{2 \cdot (1 + \nu)}$	$3 \cdot \frac{k \cdot \nu}{1 + \nu}$	
k, μ	$k + \frac{4\mu}{3}$	$\frac{9k \cdot \mu}{3k + \mu}$		$k - \frac{2\mu}{3}$	$\frac{3k - 2\mu}{2 \cdot (3k + \mu)}$
k, λ	$3k - 2\lambda$	$9k \cdot \frac{k - \lambda}{3k - \lambda}$	$\frac{3}{2} \cdot (k - \lambda)$		$\frac{\lambda}{3k - \lambda}$
μ, λ	$\lambda + 2\mu$	$\mu \cdot \frac{3\lambda + 2\mu}{\lambda + \mu}$		$\lambda + \frac{2}{3} \cdot \mu$	$\frac{\lambda}{2 \cdot (\lambda + \mu)}$
μ, ν	$2\mu \cdot \frac{1 - \nu}{1 - 2\nu}$	$2\mu \cdot (1 + \nu)$		$\mu \cdot \frac{2\nu}{1 - 2\nu}$	$\frac{2\mu}{3} \cdot \frac{1 + \nu}{1 - 2\nu}$
λ, ν	$\lambda \cdot \frac{1 - \nu}{\nu}$	$\lambda \cdot \frac{(1 + \nu)(1 - 2\nu)}{\nu}$	$\lambda \cdot \frac{1 - 2\nu}{2\nu}$		$\lambda \cdot \frac{1 + \nu}{3\nu}$

See worksheet on the website <http://www.elsevierdirect.com/companion.jsp?ISBN=9780444537966> and refer Conversion elastic parameters.

In seismic and formation evaluation practice, the inverse of the velocity—the “slowness”—is frequently used²:

$$\text{compressional wave slowness } \Delta t_P = DTP = V_P^{-1} \quad (6.7)$$

$$\text{shear wave slowness } \Delta t_S = DTS = V_S^{-1} \quad (6.8)$$

The ratio of the two wave velocities is controlled by Poisson's ratio only (Figure 6.1):

$$\frac{V_P}{V_S} = \sqrt{2 \frac{1 - \nu}{1 - 2\nu}} \quad \text{or} \quad \nu = \frac{1}{2} \frac{(V_P/V_S)^2 - 2}{(V_P/V_S)^2 - 1} \quad (6.9)$$

For the minimum value of Poisson's ratio $\nu = 0$ in a homogeneous, isotropic material, the minimum ratio is $V_P/V_S = \sqrt{2} \approx 1.4$, thus, for real isotropic rocks, it is $V_P/V_S > \sqrt{2}$.

²Note that the slowness is not a time; it is a time divided by the distance!

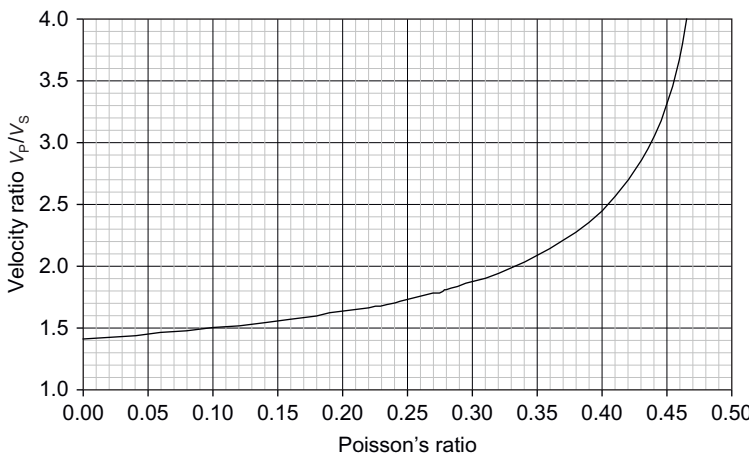


FIGURE 6.1 Conversion between velocity ratio and Poisson's ratio (visit the website <http://www.elsevierdirect.com/companion.jsp?ISBN=9780444537966> and refer Conversions. Elastic parameter).

However, if elastic wave velocities and bulk density are known from measurements, the elastic parameters can be calculated:

$$\mu = \rho \cdot V_S^2 \quad (6.10)$$

$$M = \rho \cdot V_P^2 \quad (6.11)$$

$$E = \rho \cdot V_P^2 \frac{(1 + \nu)(1 - 2\nu)}{1 - \nu} = \rho \cdot V_S^2 \frac{3 \cdot V_P^2 - 4 \cdot V_S^2}{V_P^2 - V_S^2} \quad (6.12)$$

$$\lambda = \rho(V_P^2 - 2 \cdot V_S^2) \quad (6.13)$$

$$k = \rho \left(V_P^2 - \frac{4}{3} V_S^2 \right) \quad (6.14)$$

The transversely isotropic medium is probably the most frequently applied case of anisotropy in earth materials. Gneisses and laminated shale are typical for such an approximation. Fundamental equations for the case of weak anisotropy have been published by Thomsen (1986).

The tensor of elasticity for a transversely isotropic (or hexagonal) medium with the z -axis as the axis of symmetry has five independent elements:

$$\begin{bmatrix} c_{11} & c_{12} & c_{13} & 0 & 0 & 0 \\ c_{12} & c_{11} & c_{13} & 0 & 0 & 0 \\ c_{13} & c_{13} & c_{33} & 0 & 0 & 0 \\ 0 & 0 & 0 & c_{44} & 0 & 0 \\ 0 & 0 & 0 & 0 & c_{44} & 0 \\ 0 & 0 & 0 & 0 & 0 & c_{66} \end{bmatrix} \quad \text{with } c_{12} = c_{11} - 2 \cdot c_{66} \quad (6.15)$$

In this material there are three modes of wave propagation, and their velocities are dependent on the angle θ between the axis of symmetry (z -axis) and the direction of the wave vector (Mavko et al., 1998):

$$\text{quasi-longitudinal mode } V_P = \sqrt{\frac{c_{11} \cdot \sin^2 \theta + c_{33} \cdot \cos^2 \theta + c_{44} + A}{2 \cdot \rho}} \quad (6.16)$$

$$\text{quasi-shear mode } V_{SV} = \sqrt{\frac{c_{11} \cdot \sin^2 \theta + c_{33} \cdot \cos^2 \theta + c_{44} - A}{2 \cdot \rho}} \quad (6.17)$$

$$\text{pure shear mode } V_{SH} = \sqrt{\frac{c_{66} \cdot \sin^2 \theta + c_{44} \cdot \cos^2 \theta}{\rho}} \quad (6.18)$$

$$\text{with } A = \sqrt{[(c_{11} - c_{44})\sin^2 \theta + (c_{33} - c_{44})\cos^2 \theta]^2 + (c_{13} + c_{44})^2 \sin^2 2\theta} \quad (6.19)$$

Pure compressional and shear waves exist only for the propagation in the main axes:

For $\theta = 0^\circ$, the relationship is $A = c_{33} - c_{44}$ and velocities are

$$V_P = \sqrt{\frac{c_{33}}{\rho}} \quad V_{SV} = \sqrt{\frac{c_{44}}{\rho}} \quad V_{SH} = \sqrt{\frac{c_{66}}{\rho}} \quad (6.20)$$

For $\theta = 90^\circ$, the relationship is $A = c_{11} - c_{44}$ and velocities are

$$V_P = \sqrt{\frac{c_{11}}{\rho}} \quad V_{SV} = \sqrt{\frac{c_{44}}{\rho}} \quad V_{SH} = \sqrt{\frac{c_{66}}{\rho}} \quad (6.21)$$

For the transverse isotropic material, Thomsen (1986) defined the following parameters:

$$\varepsilon = \frac{c_{11} - c_{33}}{2 \cdot c_{33}} \quad (\text{"P-wave anisotropy"}) \quad (6.22)$$

$$\gamma = \frac{c_{66} - c_{44}}{2 \cdot c_{44}} \quad (\text{"S-wave anisotropy"}) \quad (6.23)$$

$$\delta = \frac{(c_{13} + c_{44})^2 - (c_{33} - c_{44})^2}{2 \cdot c_{33}(c_{33} - c_{44})} \quad (6.24)$$

For the determination of the five tensor elements, the following five velocities (and the density) can be used: $V_P(0^\circ)$, $V_P(90^\circ)$, $V_P(45^\circ)$, $V_{SH}(90^\circ)$, and $V_{SH}(0^\circ) = V_{SV}(0^\circ)$.

$$c_{11} = \rho \cdot V_P^2(90^\circ) \quad c_{33} = \rho \cdot V_P^2(0^\circ)$$

$$c_{44} = \rho \cdot V_{SH}^2(0^\circ) \quad c_{12} = c_{11} - 2\rho \cdot V_{SH}^2(90^\circ)$$

$$c_{13} = \sqrt{4\rho^2 \cdot V_P^4(45^\circ) - 2\rho \cdot V_P^2(45^\circ)(c_{11} + c_{33} + 2c_{44}) + (c_{11} + c_{44})(c_{33} + c_{44}) - 2c_{44}} \quad (6.25)$$

6.1.2 Elastic Properties—Units and Conversions

Elastic moduli:

SI unit: Pascal (Pa) $1 \text{ Pa} = 1 \text{ N m}^{-2} = 1 \text{ kg m}^{-1} \text{ s}^{-2}$;

frequently used are the gigapascal (1 GPa = 10^9 Pa) or megapascal

(1 MPa = 10^6 Pa)

Conversions: $1 \text{ kp cm}^{-2} = 9.8067 \cdot 10^4 \text{ Pa} \approx 0.1 \text{ MPa}$

$1 \text{ psi} = 6.894 \cdot 10^3 \text{ Pa} = 6.894 \text{ kPa}$ $1 \text{ Pa} = 1.4504 \cdot 10^{-4} \text{ psi}$

Wave velocity:

SI unit: m s^{-1}

Conversions: $1 \text{ m s}^{-1} = 3.2808 \text{ ft s}^{-1}$ $1 \text{ ft s}^{-1} = 0.3048 \text{ m s}^{-1}$

Slowness:

SI unit: $\mu\text{s m}^{-1}$ or $\mu\text{s ft}^{-1}$

Conversions: $1 \mu\text{s m}^{-1} = 0.3048 \mu\text{s ft}^{-1}$ $1 \mu\text{s ft}^{-1} = 3.2808 \mu\text{s m}^{-1}$

(visit the website <http://www.elsevierdirect.com/companion.jsp?ISBN=9780444537966> and refer Conversion. Units)

6.2 ELASTIC PROPERTIES OF THE ROCK CONSTITUENTS

6.2.1 Overview

Elastic properties of rocks are dominated by the properties of the solid rock skeleton including “defects” like pores, fractures, and cracks. These defects have, in most cases, dimensions smaller than the wavelength.

The simplified cartoon of Figure 6.2 illustrates the general tendencies for the basic rock components:

- Solid minerals: minerals, matrix components
- Fluids: liquids (water, oil), air, gas.

For compressional wave velocities, $V_{p,\text{minerals}} > V_{p,\text{water,oil}} > V_{p,\text{gas}}$ and for the corresponding compressional modulus, $k_{\text{minerals}} > k_{\text{water,oil}} > k_{\text{gas}}$.

The shear modulus shows a completely different behavior, because by definition, fluids do not have a shear resistance ($\mu_{\text{fluids}} = 0$). Shear wave

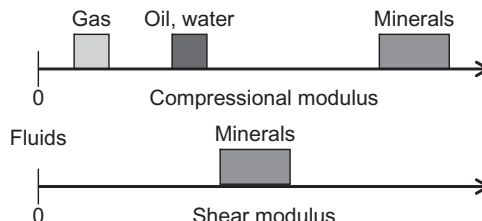


FIGURE 6.2 Compressional and shear modulus for main rock components.

velocity therefore shows only a minor dependence on pore fluids via the density term (see [Section 6.5.3](#)).

Immediately the following tendencies result:

- increasing porosity decreases both compressional and shear wave velocities;
- compressional wave velocity is controlled also by the type of pore fluid (gas, liquid);
- shear wave velocity is not strongly controlled by type of pore fluid.

6.2.2 Solid Components, Minerals

[Table 6.2](#) gives an orientation for the magnitude of wave velocities and parameters of some rock-forming minerals; the data have been taken from various compilations.

We note with respect to:

- the composition of igneous rocks that acid or felsic components have lower elastic moduli and velocities than basic or mafic components;
- the composition of reservoir rocks that there is a significant difference between the three basic types of matrix substances quartz, calcite, and dolomite.

6.2.3 Fluids

6.2.3.1 Overview

Pore fluids (gas, oil, and water) usually have distinct ranges of compressional or bulk modulus (shear modulus of fluids is zero). For orientation, the following ranges are given for compressional bulk modulus k_{fluid} and density ρ_{fluid} :

Gas:	$k_{\text{fluid}} \approx 0.01 - 0.4 \text{ GPa}$	$\rho_{\text{fluid}} \approx 0.1 - 0.5 \cdot 10^3 \text{ kg m}^{-3}$
Oil:	$k_{\text{fluid}} \approx 0.4 - 3.0 \text{ GPa}$	$\rho_{\text{fluid}} \approx 0.7 - 1.1 \cdot 10^3 \text{ kg m}^{-3}$
Water:	$k_{\text{fluid}} \approx 2.0 - 4.0 \text{ GPa}$	$\rho_{\text{fluid}} \approx 0.9 - 1.2 \cdot 10^3 \text{ kg m}^{-3}$

The compressional wave velocity for some fluids is presented in [Table 6.3](#).

A detailed compilation of seismic properties of fluids and relevant empirical equations to describe the effects of pressure and temperature have been published by Batzle and Wang (1992) and Wang (2001). In the following sections, only some selected results are presented; for details, the direct use of the paper of Batzle and Wang (1992) is recommended.

TABLE 6.2 Density, Elastic Moduli, and Wave Velocities of Some Rock-Forming Minerals

Mineral	ρ kg m ⁻³	k GPa	μ GPa	V_p m s ⁻¹	V_s m s ⁻¹	ν	Reference
Quartz	2650	38.2	43.3	6050	4090	0.08	G
	2650	37.0	44.0	6050	4090	0.08	C
	2650	36.5	45.6	6060	4150	0.06	M
Hornblende	3124	87	43	6810	3720	0.29	G
Olivine	3320	130	80	8540	4910	0.24	C
Forsterite	3224	129.6	81.0	8570	5015	0.24	G
	3320	129.8	84.4	8540	5040	0.23	M
Garnets-almandine	4180	176.3	95.2	8510	4770	0.27	M
Garnets-zircon	4560	19.8	19.7	3180	2080	0.13	M
Epidote	3400	106.5	61.1	7430	4240	0.26	M
Pyroxene-diopside	3310	111.2	63.7	7700	4390	0.26	M
Pyroxene-augite	3260	94.1	57.0	7220	4180	0.25	M
"Average" feldspar	2620	37.5	15.0	4680	2390	0.32	M
Anorthite	2760	84	40	7050	3800	0.29	G
Albite	2630	55	29.5	5940	3290	0.28	G
	2630	75.6	25.6	6460	3120	0.35	M
Oligoclase	2640			6240	3390		A
Orthoclase	2570	46.8	27.3	5690	3260		A
Labradorite	2680			6550	3540		A
Microcline	2560			6000	3260		A
Nepheline	2620	45.5	31.5	5750	3450	0.22	G
Biotite	3050	51	27	5350	3000	0.27	G
	3050	59.7	42.3	6170	3730	0.21	M
	3050	41.1	12.4	4350	2020	0.36	M
Muscovite	2790	52	32	5810	3370	0.25	G
	2790	42.9	22.2	5100	2820	0.28	M
	2790	52.0	30.9	5780	3330	0.25	M
	2790	61.5	41.1	6460	3840	0.23	M

(Continued)

TABLE 6.2 (Continued)

Mineral	ρ kg m ⁻³	k GPa	μ GPa	V_p m s ⁻¹	V_s m s ⁻¹	ν	Reference
Kaolinite	1580	1.5	1.4	1440	930	0.14	M
Clay	2580	20.9	6.85				H
"Gulf clays"	2550	25	9	3810	1880	0.34	M
	2600	21	7	3410	1640	0.35	M
Chlorite		95.3	11.4				K
Illite		39.4	11.7				K
Kaolinite		37.9	14.8				K
Calcite	2712	73	32	6540	3430	0.31	G
	2710	76.8	32.0	6640	3440	0.32	M
Dolomite	2860	94	46	7370	4000	0.29	G
	2870	94.9	45.0	7340	3960	0.30	M
Siderite	3960	123.7	51.0	6960	3590	0.32	M
Aragonite	2930	47	38.5	5790	3630	0.18	G
Anhydrite	2970	55	30	5620	3140	0.27	G
	2980	56.1	29.1	5640	3130	0.28	M
Barite	4500	54.9	23.7	4350	2250	0.32	G
Gypsum	2350			5800			M
Apatite	3218			6680	3830	0.26	G
Pyrite	5010	143	128	7920	5060	0.16	G
	4930	147.4	132.5	8100	5180	0.15	M
Halite	2160			4560	2590	0.26	G
Fluorite	3180	86.4	41.8	6680	3620	0.29	M
Sylvite	1990	17.4	9.4	3880	2180	0.27	M
Kerogen	1300	2.9	2.7	2250	1450	0.14	M

Reference key: G, Gebrannde et al. (1982) (k and μ are Hills mean); A, Alexandrov et al. (1966); C, Carmichael (1989); M, data from a compilation by Mavko et al. (1998); H, Helgerud et al. (1999); K, Katahara (1996).

TABLE 6.3 Compressional Wave Velocity for Some Fluids

Fluid	V_p in m s^{-1}	Remarks, Parameters
Air	263	$T = 173^\circ\text{K}$
	332	$T = 273^\circ\text{K}$
	387	$T = 373^\circ\text{K}$
Methane	488	$p = 0.103 \text{ MPa}$
Carbon dioxide	259	
Oil, natural	1035–1370; mean 1280	
Paraffine oil	1420	$T = 307^\circ\text{K}$, $\rho = 835 \text{ kg m}^{-3}$
Gasoline oil	1250	$T = 307^\circ\text{K}$, $\rho = 803 \text{ kg m}^{-3}$
Water	1497	$T = 298^\circ\text{K}$, distilled
	1585	$p = 0.103 \text{ MPa}$; 1000 ppm NaCl
	1638	$p = 0.103 \text{ MPa}$; 1500 ppm NaCl
	1689	$p = 0.103 \text{ MPa}$; 2000 ppm NaCl

After Ebert (1976), Bulatova et al. (1970), Tagiev and Mustafaev (1975), Gregory (1990), Serra (1984), Ellis (1987), Baker Atlas/Western Atlas (1992).

6.2.3.2 Gas

Wang (2001) noted, “Because most gases are extremely compressible under reservoir conditions, in many cases the bulk modulus (incompressibility) of a hydrocarbon gas can be set as 0.01–0.2 GPa in seismic modeling. Errors in gas bulk modulus will yield little uncertainty in the calculated seismic properties in a fluid-saturated rock.”

Bulk modulus and density of gas in a reservoir depend on the pressure, temperature, and the type of gas (Table 6.4).

6.2.3.3 Oil

A relationship published by Batzle and Wang (1992) describes the dependence of oil velocity (in m/s) on API number, temperature T (in $^\circ\text{C}$), and pressure p (in MPa):

$$V_p = 15450(77.1 + \text{API})^{-0.5} - 3.7 \cdot T + 4.64 \cdot p + 0.0115(0.36 \cdot \text{API}^{0.5} - 1)T \cdot p \quad (6.26)$$

Table 6.5 shows some data based on the empirical equations from Batzle and Wang (1992).

TABLE 6.4 Some Values for Hydrocarbon Gas Density and Compressional Modulus

Pressure and Temperature	ρ in 10^3 kg m^{-3}	k in MPa	V_P in m s^{-1}
$T = 373^\circ\text{K}$ (100°C); $p = 25 \text{ MPa}$	0.15–0.35	50–150	550–650
$T = 373^\circ\text{K}$ (100°C); $p = 50 \text{ MPa}$	0.25–0.45	150–350	750–900
$T = 473^\circ\text{K}$ (200°C); $p = 25 \text{ MPa}$	0.12–0.30	50–80	500–600
$T = 473^\circ\text{K}$ (200°C); $p = 50 \text{ MPa}$	0.20–0.40	130–200	550–650

Derived from the relationships (plots) by Batzle and Wang (1992), and calculated compressional wave velocities.

TABLE 6.5 Some Values for Light Oil (50 API) Density and Compressional Modulus

Pressure and Temperature	ρ in 10^3 kg m^{-3}	k in MPa	V_P in m s^{-1}
Dead oil, $T = 373^\circ\text{K}$ (100°C); $p = 25 \text{ MPa}$	0.76	1100	1200
Dead oil, $T = 473^\circ\text{K}$ (200°C); $p = 50 \text{ MPa}$	0.70	800	1070

Derived from the relationships (plots) by Batzle and Wang (1992) and derived velocities.

TABLE 6.6 Some Values for Brine Density and Compressional Modulus

Concentration (Salinity), Pressure and Temperature	ρ in 10^3 kg m^{-3}	k in MPa	V_P in m s^{-1}
Water, fresh, room conditions	1.00	2200	1480
Brine, 3.5 % salinity, room conditions	1.05	2400	1510
Brine $T = 373^\circ\text{K}$ (100°C); $p = 25 \text{ MPa}$	0.97	2600	1635
Brine $T = 473^\circ\text{K}$ (200°C); $p = 50 \text{ MPa}$	0.90	2100	1530

Derived from the relationships (plots) by Batzle and Wang (1992) and derived velocities.

6.2.3.4 Brine

Brine composition can range from almost pure water to saturated saline solution. Bulk modulus, density, and velocity of brine are controlled by the big range of concentration, the temperature, and pressure. Batzle and Wang (1992) derived empirical equations and plots for practical application for these relationships as well. Table 6.6 shows some selected data.

6.3 VELOCITY OF ROCKS—OVERVIEW

Figure 6.3 shows the mean range of the compressional and shear wave velocities for commonly occurring rock types and indicates some typical tendencies and characteristics:

- The velocity of igneous rocks increases from acidic/felsic (granite) to basic/mafic (peridotite) members; the range for an individual rock type

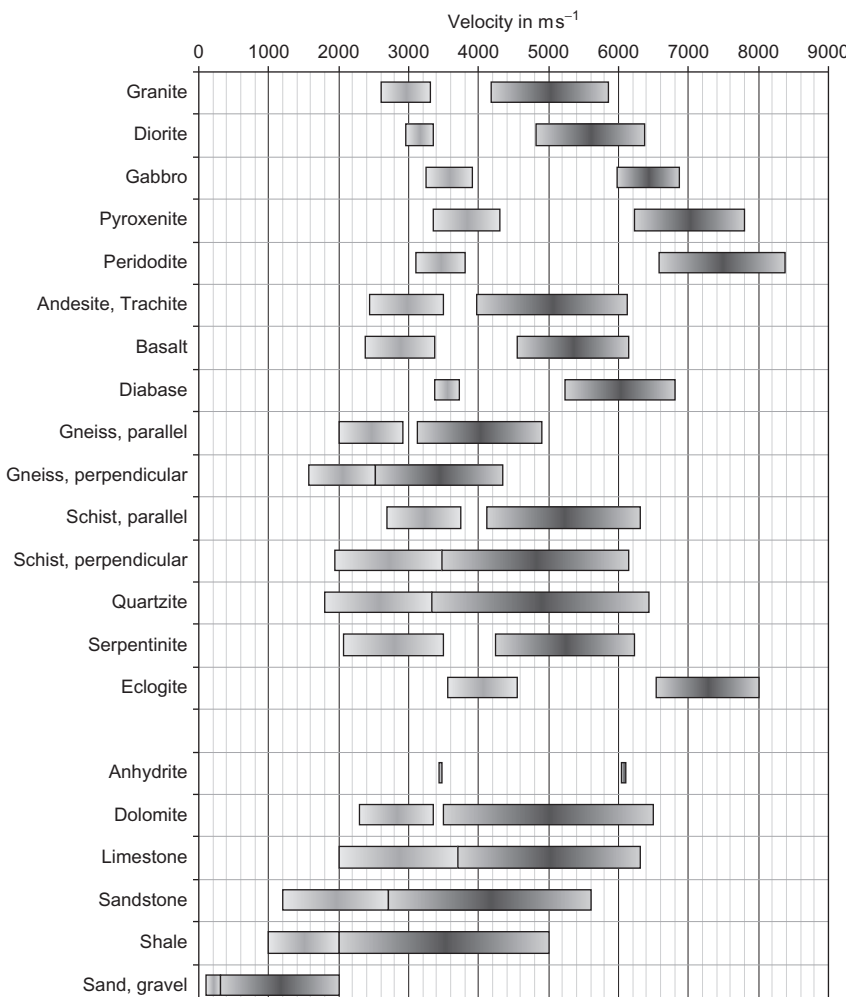


FIGURE 6.3 Range of compressional (higher values) and shear wave (lower values) velocities for commonly occurring rocks.

is the result of variation of rock composition (mineral content) and—if present—fracturing.

- Among the metamorphic rocks, gneiss and schist in particular show an anisotropy with velocity parallel schistosity > velocity perpendicular schistosity.
- Sedimentary porous rocks show a broad range of velocity, where high velocities are typical for those that are relatively dense (low porosity) and low velocities are typical for porous (gas-bearing) members.
- The lowest velocities have (dry) *unconsolidated rocks* as a result of the specific grain—grain contact and high porosity.

There is a broad scatter for porous rocks (influence of porosity, pore fluid, and mineral composition) in particular and a comparable small range for a dense rock with well-defined composition (anhydrite).

The ratio of the two wave velocities V_P/V_S or the Poisson's ratio ν is controlled mainly by rock type and pore fluid. [Figure 6.4](#) gives an overview with some tendencies.

6.4 VELOCITY OF IGNEOUS AND METAMORPHIC ROCKS

Velocity of igneous rocks shows an increase from acid/felsic to basic/mafic rock types. The same tendency shows the density. This gives the background for an empirical correlation between density and velocity, first published by Birch (1961) for magmatic rocks (North American continent and India):

$$V_P = 2.76 \cdot \rho - 0.98 \quad (6.27)$$

where the density ρ is in 10^3 kg m^{-3} ($= \text{g cm}^{-3}$) and V_P in km s^{-1} .

This linear correlation has been applied frequently on various types of igneous and metamorphic rocks. Two examples may demonstrate this.

Volarovic and Bajuk (1977) derived for rocks from Kazakhstan regressions, which show also the pressure influence:

$$V_P = 3.25 \cdot \rho - 3.46 \quad R = 0.85 \quad \text{pressure} = 10^{-1} \text{ MPa} \quad (6.28)$$

$$V_P = 2.72 \cdot \rho - 1.24 \quad R = 0.86 \quad \text{pressure} = 10^2 \text{ MPa} \quad (6.29)$$

$$V_P = 2.44 \cdot \rho - 0.08 \quad R = 0.85 \quad \text{pressure} = 10^3 \text{ MPa} \quad (6.30)$$

Gebrände et al. (1982) analyzed compressional and shear wave velocities for three rock groups:

$$V_P = 4.36 \cdot \rho - 6.73 \pm 0.03 \quad V_S = 1.66 \cdot \rho - 1.48 \pm 0.06 \quad \text{plutonic rocks} \quad (6.31)$$

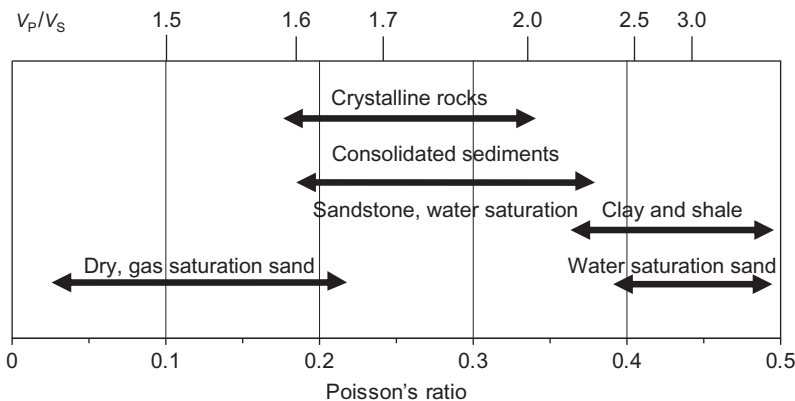


FIGURE 6.4 Average Poisson's ratio for different lithologies, after a figure from Bourbie et al. (1987).

$$V_P = 2.81 \cdot \rho - 2.37 \pm 0.18 \quad V_S = 1.46 \cdot \rho - 1.02 \pm 0.22 \quad \text{volcanic rocks} \quad (6.32)$$

$$V_P = 4.41 \cdot \rho - 6.93 \pm 0.37 \quad V_S = 1.70 \cdot \rho - 1.62 \pm 0.22 \quad \text{metamorphic rocks} \quad (6.33)$$

In some cases, a nonlinear relationship between velocity and density gives a better correlation with experimental results. Christensen and Salisbury (1975) found the following relationship in their investigation of basalts recovered in the Deep Sea Drilling Project:

$$V_P = 2.33 + 0.08 \cdot \rho^{3.63} \quad V_S = 1.33 + 0.011 \cdot \rho^{4.85} \quad (6.34)$$

The pressure for these measurements was 0.5 bar (= 50 kPa).

If igneous or metamorphic rocks are fractured, then:

- velocity decreases compared with the competent rock;
- fracturing creates a higher pressure sensitivity, thus velocity shows a distinct pressure dependence;
- in case of preferred orientation of fractures, anisotropy results.

Velocity decrease with increasing fracturing is not alone a volumetric (fracture, porosity) effect; it is more an effect of the increasing “defects” in the competent rock material and therefore it needs special types of models to describe such effects (see [Section 6.7](#)). [Figure 6.5](#) shows an example and illustrates the velocity decrease for three types of granites with different grain sizes of the rock-forming minerals. The example demonstrates the influence of grain size—or more generally—the structure–textural properties on the character of the velocity versus fracture porosity relationship. For the granites, the change in velocity gets more pronounced with increasing grain size.

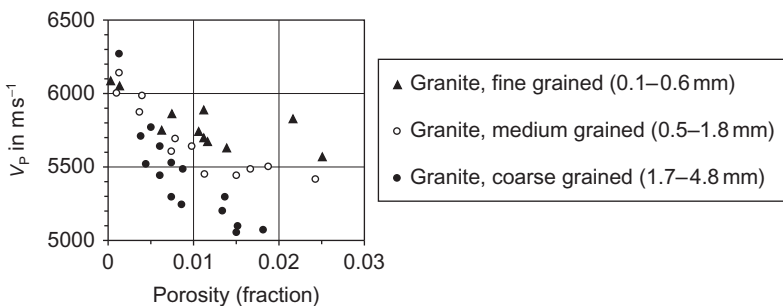


FIGURE 6.5 Dependence of longitudinal wave velocity on crack porosity (volume fraction) and grain size of granitic rocks at a pressure of 1 bar = 0.1 MPa; after Lebedev et al. (1974).

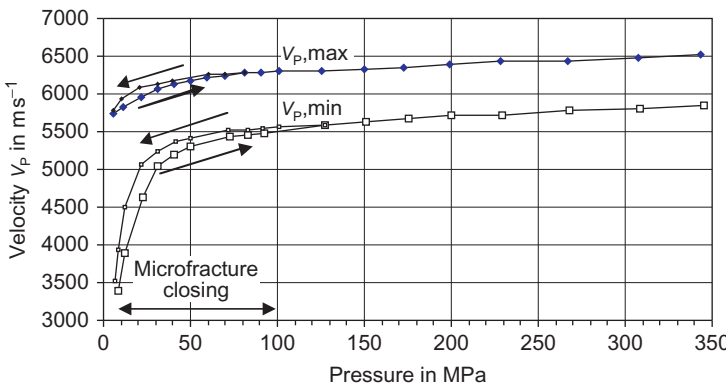


FIGURE 6.6 Compressional wave velocities as a function of hydrostatic pressure (loading and unloading), measured at a gneiss core sample (390C2c, KTB Borehole, depth: 1,757 m) in different directions; data after Zang et al. (1989). v_p max—maximal velocity value in radial direction of the core and v_p min—minimal velocity value in radial direction of the core.

The dependence of velocity on pressure shows the following (Figure 6.6):

- The velocity–pressure relationship is nonlinear: in the higher pressure range, the velocity increase is smaller than in the lower pressure range. Increase of velocity under the influence of pressure in the lower pressure range primarily is due to the closure of large and penny-shaped pores and microjoints. This closure improves the contact between rock-forming minerals. At higher pressure, the compaction of the aggregate is nearly complete. Therefore, further velocity increase is only due to changes in the elastic properties of the mineral substance.
- Velocity change during the loading–unloading cycle is only partially reversible (so-called velocity hysteresis). This fact is one expression for the nonideal elastic behavior of natural rocks.

- Velocity anisotropy (difference of the two curves) is stronger in the low-pressure region and becomes smaller in the high-pressure region. This is caused by the fracture-closing process: anisotropy in the low-pressure range is originated by fracture orientation and intrinsic mineral orientation, but anisotropy in the high-pressure range is only an intrinsic effect.

In magmatic and metamorphic rocks, increasing temperature generally leads to decreasing velocities. The main causes of the velocity change are:

- temperature dependence of the elastic properties of the rock-forming minerals and phase change of minerals;
- temperature dependence of the elastic properties of the pore constituents and change of pore constituents (e.g., pore water) from a liquid to a gaseous state;
- changes in the contact conditions at grains, crack boundaries, etc., resulting from variations of the interface effects and/or from different thermal expansion properties of rock-forming minerals.

For temperatures up to approximately 150°C, the change of fluid properties dominates, but at higher temperatures mineral and contact effects are dominant.

6.5 VELOCITY OF SEDIMENTARY ROCKS

With respect to the velocity and its behavior, there are two types of sedimentary rocks:

1. Dense rocks without pores (anhydrite, salt) with a well-defined velocity that is controlled by the mineral properties and composition.
2. Porous rocks with a velocity range with strong influence of the porosity and pore fluid, but also contact properties of solid rock components (ranging from strong cemented rocks to unconsolidated rocks), and the mineral composition (sandstone, dolomite, limestone, shale influence).

Of particular interest as reservoir rocks is the second group; the diversity of influences originates the variety of relationships and correlations. The following sections focus on these relationships. Dominant are:

- mineralogical composition of the rock matrix;
- consolidation and cementation of the rock matrix;
- porosity, pore shape, and pore content;
- pressure and temperature.

Additionally, fracturing can significantly influence properties of carbonate rocks. Structure and texture lead to different types of anisotropy in the elastic properties.

6.5.1 Influence of Lithology (Mineralogy) and Porosity upon Velocity

The lithologic or mineralogic influence upon velocity is mainly expressed by:

- the difference between clastic (sandstone) and carbonate (dolomite, limestone) rocks;
- the difference between consolidated (sandstone) and unconsolidated (sand) clastic rocks;
- the influence of shale on the velocity.

The decrease of velocity with increasing *porosity* is a general characteristic for all porous rocks.

The influence of the mineral composition on the velocity is expressed by the so-called matrix velocity, which is the extrapolated velocity of a porous rock type for zero porosity (see [Section 6.5.2](#)). For the three main mineral components of reservoir rocks, mean matrix velocities are (compare also [Table 6.2](#) and Appendix A):

quartz (sandstone)	$V_{p,ma} = 5,500 \text{ m s}^{-1}$	$V_{p,ma} = 18,000 \text{ ft s}^{-1}$
calcite (limestone)	$V_{p,ma} = 6,400 \text{ m s}^{-1}$	$V_{p,ma} = 20,400 \text{ ft s}^{-1}$
dolomite (dolomite)	$V_{p,ma} = 7,000 \text{ m s}^{-1}$	$V_{p,ma} = 23,000 \text{ ft s}^{-1}$

Matrix properties are applied for the description of the velocity–porosity dependence using Wyllie's equation ([Section 6.5.2](#)).

6.5.1.1 Clastic Rocks

[Figure 6.7](#) shows results of experimental investigations on sandstone samples with different porosity and different clay content. Both—porosity and clay content—result in a decrease of velocity for compressional and shear wave velocities.

Linear regressions for velocity and slowness result in good correlations (Han et al., 1986):

$$V_P = 5.59 - 6.93 \cdot \phi - 2.18 \cdot C \quad R = 0.985 \quad (6.35)$$

$$V_S = 3.52 - 4.91 \cdot \phi - 1.89 \cdot C \quad R = 0.959 \quad (6.36)$$

$$\Delta t_P = 0.163 + 0.399 \cdot \phi + 0.119 \cdot C \quad R = 0.972 \quad (6.37)$$

$$\Delta t_S = 0.242 + 0.812 \cdot \phi + 0.307 \cdot C \quad R = 0.945 \quad (6.38)$$

where the velocities are in km s^{-1} and the slowness in $\text{s km}^{-1} = 10^3 \mu\text{s m}^{-1}$. Porosity ϕ and clay content C are fractions.

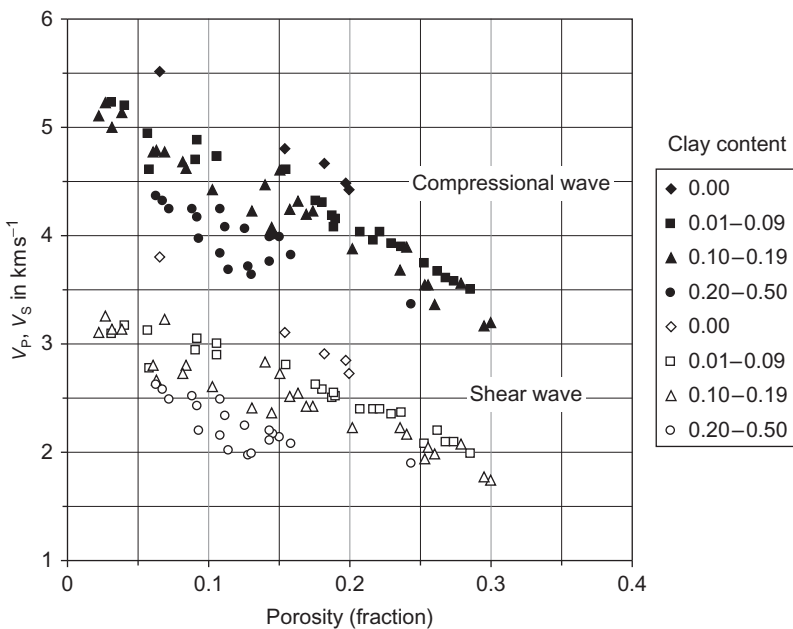


FIGURE 6.7 Compressional and shear wave velocities versus porosity (fraction) for 75 sandstone samples at a confining pressure 40 MPa and a pore pressure 1.0 MPa; data after Han et al. (1986).

Castagna et al. (1985) derived comparable relationships for shaly sands of the Frio Formation:

$$V_p = 5.81 - 9.42 \cdot \phi - 2.21 \cdot C \quad (6.39)$$

$$V_s = 3.89 - 7.07 \cdot \phi - 2.04 \cdot C \quad (6.40)$$

Marion and Jizba (1992) have investigated North Sea shaly sand reservoir rocks (35 MPa pressure) for brine and gas saturation and derived the regressions:

$$\text{gas } V_p = 4.82 - 5.02 \cdot \phi - 0.597 \cdot C \quad V_s = 3.26 - 3.03 \cdot \phi - 0.892 \cdot C \quad (6.41)$$

$$\text{brine } V_p = 5.46 - 6.29 \cdot \phi - 1.10 \cdot C \quad V_s = 3.32 - 3.62 \cdot \phi - 0.952 \cdot C \quad (6.42)$$

Rearrangement of the equations gives

$$\text{gas } V_p = 4.82(1 - 1.04 \cdot \phi - 0.124 \cdot C) \quad V_s = 3.26(1 - 0.930 \cdot \phi - 0.274 \cdot C) \quad (6.43)$$

$$\text{brine } V_P = 5.46(1 - 1.15 \cdot \phi - 0.215 \cdot C) \quad V_S = 3.32(1 - 1.090 \cdot \phi - 0.287 \cdot C) \quad (6.44)$$

Comparison of the factors shows that:

- porosity effect on compressional and shear wave velocities is comparable;
- shear wave velocity is relatively insensitive to change of pore fluid (compare gas and brine);
- the effect of clay is more important for the shear wave velocity.

Kirchberger (2001) analyzed logging data from the Vienna Basin and used the gammalog for characterizing the shale content V_{shale} and the density log for porosity estimate. Shaly sand formations (water bearing) follow a regression:

$$V_P = 5.358 - 5.402 \cdot \phi - 2.926 \cdot V_{\text{shale}} = 5.358(1 - 1.008 \cdot \phi - 0.546 \cdot V_{\text{shale}}) \quad (6.45)$$

$$V_S = 2.802 - 3.935 \cdot \phi - 1.750 \cdot V_{\text{shale}} = 2.802(1 - 1.404 \cdot \phi - 0.625 \cdot V_{\text{shale}}) \quad (6.46)$$

6.5.1.2 Carbonate Rocks

The velocity–porosity relationship of carbonates is complicated as a result of the diversity of *pore types* and the presence of their combination in a specific rock. A systematic analysis was published by Eberli et al. (2003). Figure 6.8 shows a velocity–porosity plot for carbonates with different pore types. Eberli et al. (2003) note “different pore types cluster in the porosity–velocity field, indicating that scattering at equal porosity is caused by the

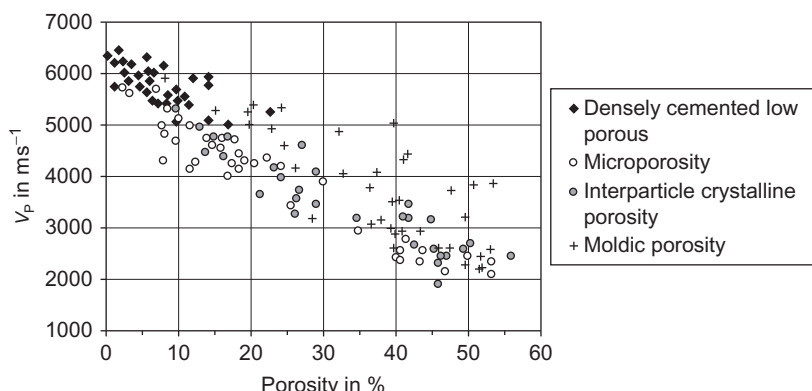


FIGURE 6.8 Velocity–porosity plot for carbonates with different pore types, effective pressure 8 MPa, from Eberli et al. (2003).

specific pore type and their resultant elastic property.” As a general tendency, wave propagation shows for the type:

- “microporosity” and “interparticle crystalline porosity,” good correlation with a character comparable to the clastic sediments;
- “moldic porosity” (and “densely cemented low porosity”), a much broader data scatter and higher velocities.

6.5.1.3 *Unconsolidated Sediments*

Unconsolidated sediments can be classified into:

- noncohesive rocks (e.g., sand, gravel);
- cohesive rocks (e.g., clay, loam).

The differences in the elastic behavior of these two groups are based on various physical conditions at the contacts of the rock particles. For the first group, conditions are controlled by friction effects, whereas for the second group, physio-chemical phenomena are dominant. Similarly to consolidated sedimentary rocks, there exists a significant correlation between velocity and porosity for unconsolidated sediments. Velocity values in unconsolidated sediments are distinctly lower than in consolidated sediments. The compressional wave velocity shows a clear difference for the dry (about $200\text{--}500\text{ m s}^{-1}$) and water-saturated (about $1,600\text{--}2,000\text{ m s}^{-1}$) sediment.

Figure 6.9 gives examples of the velocity versus porosity correlation for dry sediments (A) and for water-saturated marine sediments (B). It is remarkable that the velocity in saturated sediments is comparable to that of water velocity or higher.

Many experimental investigations are published about marine sediments (e.g., Hamilton, 1970, 1971, 1978; Hamilton et al., 1982). As an example for marine sediments (water saturated), Hamilton et al. (1982) derived the following relationships:

$$V_P = 2502 - 2345 \cdot \phi + 140 \cdot \phi^2 \quad \text{continental terrace/shelf and slope} \quad (6.47)$$

$$V_P = 1565 - 59.7 \cdot \phi \quad \text{abyssal hill/turbidite} \quad (6.48)$$

where velocity V_P is in m s^{-1} and porosity ϕ is a fraction.

With increasing clay content, the velocity generally decreases in unconsolidated sediments. This is the result of the low stiffness of the clay-water aggregates in the sediments.

Frozen unconsolidated sediments (permafrost) show a behavior more comparable to consolidated sediments; the ice between grains acts like a cement; thus, the velocity of longitudinal and transverse waves are distinctly higher than in the nonfrozen state. Some data from Canadian Arctic permafrost samples is shown in Table 6.7. Velocity changes in freezing temperatures are discussed also in Pandit and King (1979) and Scott et al. (1990).

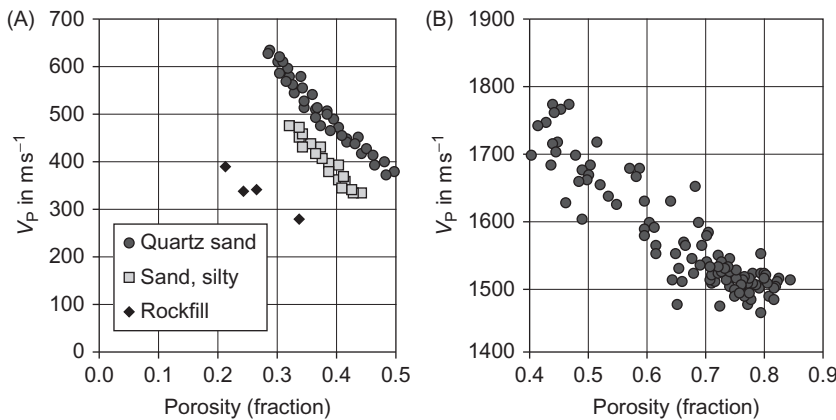


FIGURE 6.9 Compressional wave velocity versus porosity for unconsolidated sediments. (A) Mean curves for the dependence of elastic wave velocities on porosity of dry unconsolidated sediments (Schön, 1964, 1969, 1983). (B) Correlation between compressional wave velocity and porosity of water-saturated marine sediments (Hamilton, 1971).

TABLE 6.7 Seismic Wave Velocities of Permafrost Samples from the Mackenzie River Valley and Canadian Arctic Islands

Sediment	Porosity	T in $^{\circ}\text{C}$	V_P km s^{-1}	V_S km s^{-1}	V_P/V_S
Sand	0.36	-5	4.18	2.42	1.73
	0.36	-15	4.21	2.43	1.73
	0.40	-5	3.88	2.14	1.81
Silt	0.33	-5	3.57	1.90	1.88
	0.33	-15	3.86	2.15	1.80
	0.37	-5	3.38	1.78	1.90
Clay	0.37	-5	2.27	0.91	2.44
	0.37	-15	2.64	1.31	2.02
	0.43	-5	2.27	0.98	2.32

Selected data from Zimmerman and King (1986).

6.5.2 Empirical Velocity–Porosity and Velocity–Density Relationships

In Section 6.5.1.1, the strong correlation between velocity and porosity was demonstrated. Wyllie et al. (1956) derived their famous time-average equation. Written in terms of velocity, the equation is

$$\frac{1}{V_p} = \frac{1 - \phi}{V_{p,ma}} + \frac{\phi}{V_{fl}} \quad (6.49)$$

where

V_p is the compressional wave velocity of the porous rock

$V_{p,ma}$ is the compressional wave velocity of the matrix material

V_{fl} is the compressional wave velocity of the pore fluid (mostly assumed water).

In terms of slowness, the equation is

$$\Delta t_p = (1 - \phi) \Delta t_{p,ma} + \phi \cdot \Delta t_{fl} \quad (6.50)$$

where

Δt_p is the compressional wave slowness of the porous rock

$\Delta t_{p,ma}$ is the compressional wave slowness of the matrix material

Δt_{fl} is the compressional wave slowness of the pore fluid (mostly assumed water).

Rearranging a linear relationship between measured compressional wave slowness (or velocity) and porosity results in the equation:

$$\phi = \frac{\Delta t_p - \Delta t_{p,ma}}{\Delta t_{fl} - \Delta t_{p,ma}} = \frac{\frac{1}{V_p} - \frac{1}{V_{p,ma}}}{\frac{1}{V_{fl}} - \frac{1}{V_{p,ma}}} \quad (6.51)$$

The porosity calculation based on a velocity or slowness measurement needs as input the two “material properties” $\Delta t_{p,ma}$ (or $V_{p,ma}$) and Δt_{fl} (or V_{fl}). Table 6.8 gives some mean values for orientation (see also Appendix A).

It may be noted that the Wyllie equation is heuristic and not a model-derived equation (the addition of travel time for matrix and fluid is physically valid only for wavelengths much smaller than pore or grain size). The equation works best for water-saturated and well-compacted porous rocks, particularly sandstones. Presence of gas can give erroneous results (Asquith and Krygowski, 2004).

Poor consolidation or low effective stress results in high slowness values and therefore an overestimate of porosity. In this case a “compaction correction” is recommended: the slowness in an adjacent shale bed is used as

TABLE 6.8 Mean Input Parameters $\Delta t_{p,ma}$ (Matrix Slowness) and Δt_{fl} (Slowness of Pore Fluid) for Application of Wyllie's Equation

Rock Type	$\Delta t_{p,ma}$ $\mu\text{s ft}^{-1}$	$\Delta t_{p,ma}$ $\mu\text{s m}^{-1}$	Fluid	Δt_{fl} $\mu\text{s ft}^{-1}$	Δt_{fl} $\mu\text{s m}^{-1}$
Sandstone $\phi > 0.1$	55.5	182	Freshwater mud filtrate	189	620
Sandstone $\phi < 0.1$	51.2	168	Saltwater mud filtrate	185	607
Limestone	47.6	156			
Dolomite	43.5	143			

Asquith and Krygowski (2004).

“compaction reference”; if measured slowness is $\Delta t_{shale} > 100 \mu\text{s ft}^{-1}$, the following equation for a compaction-corrected Wyllie porosity is recommended (see for example, Asquith and Krygowski, 2004):

$$\phi_{\text{corrected}} = \phi_{\text{Wyllie}} \frac{1}{C_p} = \frac{\Delta t - \Delta t_{ma}}{\Delta t_{fl} - \Delta t_{ma}} \frac{100}{\Delta t_{shale}} \quad (6.52)$$

In carbonates (see also Figure 6.8), the time-average equation works for most intergranular, interparticle porosities; this pore distribution is somewhat similar to sandstone. In vuggy carbonates, the slowness is dominated by primarily intergranular, interparticle porosity and the resulting porosity tends, in some cases, to be underestimated by the secondary porosity (Asquith and Krygowski, 2004).

The influence of pore type is discussed by Jennings and Lucia (2001) with respect to Wyllie's equation: “In the absence of vuggy pore space, limestones and dolostones typically follow the Wyllie time-average equation, although the scatter can be quite large (Figure 6.10). When grain-mold or intrafossil pore space is present, the data deviates from the Wyllie equation . . .” to lower slowness. This can be described empirically by implementation of separate vug porosity (right axis); see also Lucia (2007).

Raymer et al. (1980) derived the following equation, known as the Raymer–Hunt–Gardner equation, and recommend the application for sandstones with porosity < 0.37

$$V_P = (1 - \phi)^2 V_{P,ma} + \phi \cdot V_{fl} \quad (6.53)$$

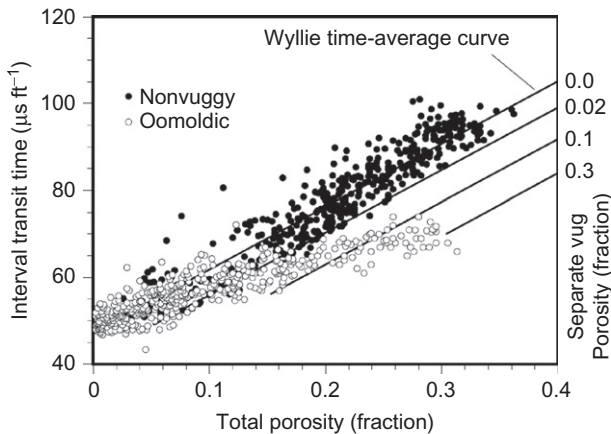


FIGURE 6.10 Interval transit time (slowness) and porosity for nonvuggy limestones in two wells and for oomoldic limestones from three wells compared with the Wyllie time-average curve and separate vug porosity values (Jennings and Lucia, 2001).

TABLE 6.9 Coefficients for the Gardner Equation

Rock Type	<i>d</i>	<i>f</i>	V_p in km s^{-1}
Sandstone	1.66	0.261	1.5–6.0
Limestone	1.50	0.225	3.5–6.4
Dolomite	1.74	0.252	4.5–7.1
Anhydrite	2.19	0.160	4.6–7.4
Shale	1.75	0.265	1.5–5.0

After Castagna (1993), Mavko et al. (1998).
 ρ_b is in g cm^{-3} and V_p is in km s^{-1} .

Porosity is related to density. Gardner et al. (1974) derived an empirical relationship between compressional wave velocity and bulk density that represents an average over many rock types (Mavko et al., 1998):

$$\rho_b \approx 1.741 \cdot V_p^{0.25} \quad \text{where } \rho_b \text{ is in } \text{g cm}^{-3} \text{ and } V_p \text{ is in } \text{km s}^{-1} \quad (6.54)$$

$$\rho_b \approx 0.23 \cdot V_p^{0.25} \quad \text{where } \rho_b \text{ is in } \text{g cm}^{-3} \text{ and } V_p \text{ is in } \text{ft s}^{-1} \quad (6.55)$$

Table 6.9 gives lithology-specific expressions for better approximation by an equation:

$$\rho_b = d \cdot V_p^f \quad (6.56)$$

where *d* and *f* are empirical parameters.

6.5.3 Effect of Pore Fluid and Fluid Saturation

The various pore fluids (water, oil, gas, and mixtures of them) influence elastic wave velocities as a result of effects that are different for compressional and shear waves:

- They influence the elastic properties and density of the pores as a part of the whole “rock” system.
- They can affect the particle contact conditions (e.g., swelling of cement).
- If there are fluid mixtures, they create stress components from interfacial tension and capillary forces.

The complex nature of the effects and their dependence on porosity, pore structure, and physio-chemical properties may be the reason for the difficulty in determining a general description and explanation.

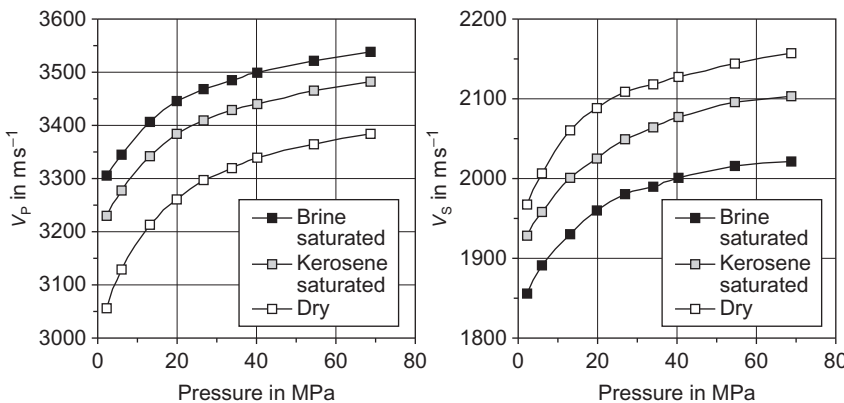


FIGURE 6.11 Compressional and shear wave velocities of Boise sandstone as a function of pressure at different pore fluids; data after King (1966); converted units.

Figure 6.11 shows the effect of three different pore fluids (air, water, and kerosene, but no mixture of them) upon the compressional and shear wave velocities.

The results show three typical features:

1. Velocity increases with pressure (discussed in [Section 6.5.4](#)).
2. Compressional wave velocity increases from air to kerosene to water; thus, it corresponds to the (compressional wave) velocities of these pore fluids.
3. Shear wave velocity shows an opposite order. This happens because fluids have no shear resistance; there is no influence on the rock bulk shear modulus. But the density increases from air to kerosene to water, and this is the only effect on the shear wave velocity and therefore it decreases.³

³This controversial effect of pore fluids on compressional and shear waves can be used as a fluid indicator with the strongest effect as a ratio V_p/V_s ; see [Section 6.8.1](#).

For this consideration is presumed the following:

- Changing pore fluid has no influence on the elastic properties of the rock skeleton. King (1966) measured compressional wave velocity at water-saturation levels lower than at kerosene saturation (and the shear wave velocity for water-saturated sandstone was extremely low) at the Bandera Sandstone. This is an effect of “softening of the matrix” by water–clay interactions (e.g., swelling).
- Pore fluid has no shear resistance. This is not valid for oil with high viscosity. The effect of heavy oil (high viscosity) was investigated, for example, by Wang and Nur (1988); oil results in much higher velocities than in the case of water saturation.

If the pore fluid is composed of two (or more) components (e.g., partial water saturation), interactions between the individual pore constituents and between pore constituents and solid skeleton (e.g., capillary tension, surface-boundary effects) are of influence upon velocities. The different influences on the elastic properties result in different types of velocity-saturation functions. The theoretical description of the velocity versus saturation behavior is one of the most difficult problems in petrophysics.

Figure 6.12 illustrates some typical features of the behavior of velocities at partial water saturation:

- compressional wave velocity shows only very small changes with increasing saturation up to about 80–85%; then the velocity abruptly increases;
- shear wave velocity shows only a small decrease with increasing water content.

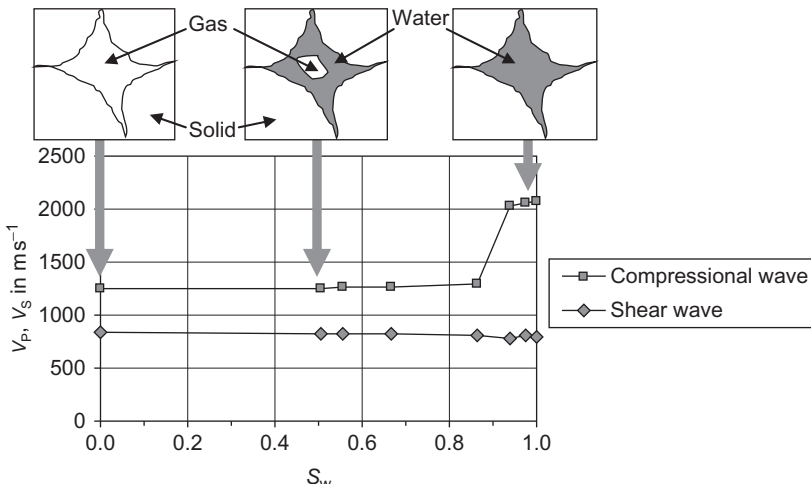


FIGURE 6.12 Influence of gas and water saturation on compressional and shear wave velocities; experimental data from Domenico (1976).

The phenomenon can be explained as follows: the compressibility of the pore-filling mixture (gas and water) is determined up to a high fraction of water (about 80–90%) by the very high compressibility of the gas—a small gas bubble in the pore realizes the small deformation when a wave passes the rock. With total water saturation, the compression modulus “jumps” to the value of the water.

The region where a velocity increase starts depends on the pore size distribution. The Ottawa sand in Figure 6.12 is well sorted. If the rock has a broad spectrum of pore sizes, then also for lower water saturation (approximately 40% or 50%), the small pores are totally water saturated and increases the compressional wave velocity. Thus, the shape of the velocity–saturation function is controlled by pore size distribution and capillary pressure.

The shear modulus of the sediment is not influenced by the pore filling because its shear modulus is zero. The small decrease of shear wave velocity is caused by the increase of density with increasing water saturation.

Lebedev et al. (2009) published a study of velocity (compressional and shear waves) measurement under different saturation conditions. Fluid distribution during the experiment was observed by X-ray computer tomography.

6.5.4 Pressure Influence

Figures 6.11 and 6.13 show some properties of the velocity–pressure behavior of a porous sedimentary rock. In general, there is a characteristic nonlinear dependence of velocity on depth or pressure. In most cases, wave velocities increase strongly with increasing pressure at low levels and less at high pressure.

The increase of the velocity with increasing pressure in sedimentary rocks is caused by:

- decrease of porosity;
- improvement of grain–grain contact conditions;
- closure of fractures, cracks, and other “defects.”

These effects are related to changes of the properties of the rock skeleton.⁴ Therefore, the pressure acting on the rock skeleton (“effective pressure”) is the controlling parameter:

$$p_{\text{eff}} = p - \alpha \cdot p_{\text{pore}} \quad (6.57)$$

⁴The change of the elastic properties of the minerals themselves can be ignored in most cases.

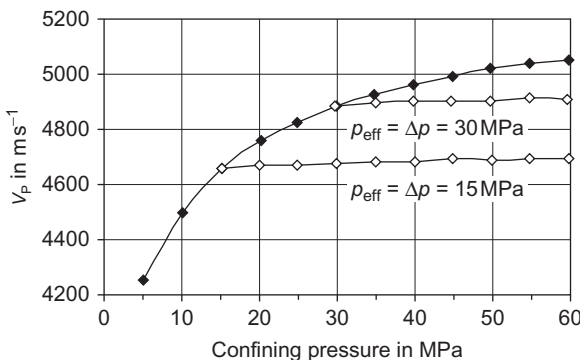


FIGURE 6.13 Compressional wave velocity as a function of confining pressure under different conditions of pore pressure, water-saturated sample of a low porous conglomerate, data from He and Schmitt (2006).

where

p is the total external pressure

p_{pore} is the pore pressure (acting against total pressure and results in a kind of “unloading” of rock skeleton)

α is a parameter depending on material compressibility (Biot–Willis parameter $\alpha = 1 - (k_{\text{skeleton}}/k_{\text{solid}})$ with the (dry) rock skeleton modulus k_{skeleton} and the modulus of the solid matrix material k_{solid}).

The value for α is 0.83, given by Dobrynin (1963). Nur and Wang (1988) note that α is found to be close to 1 for both compressional and shear waves, although significantly smaller values are common in low porosity rocks. If $\alpha = 1$, then [Equation \(6.57\)](#) expresses the differential pressure Δp :

$$p_{\text{eff}} = \Delta p = p - p_{\text{pore}} \quad (6.58)$$

[Equation \(6.58\)](#) demonstrates that a high pore pressure plays the same role as a low external stress, causing the compressional wave velocity to be reduced. This is used in the estimation of abnormal pore pressures from logs or seismic velocities (e.g., Japsen et al., 2006). Since the expected trend in a homogeneous formation would be a monotonous increase of velocity with depth (because the effective stress increases with depth), an overpressured zone shows up as a low velocity zone breaking the expected trend.

Power or exponential laws are most commonly used for an analytical description of the nonlinear velocity versus pressure relationship as an empirical equation. In a generalized form, the power law can be written as follows:

$$V = V_0 \left(\frac{p_{\text{eff}}}{p_0} \right)^m \quad (6.59)$$

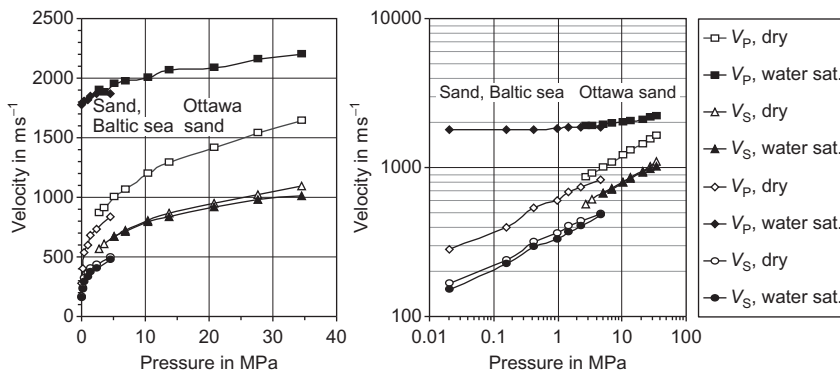


FIGURE 6.14 Velocity as a function of pressure for dry and water-saturated unconsolidated sand. Lower pressure range (20–4,600 kPa): sand, Baltic sea; Schön (1969, 1996). Higher pressure range (2,760–34,500 kPa): Ottawa sand, data from Domenico (1977); converted units.

where

p_{eff} is the actual effective pressure

p_0 is a reference pressure (e.g., at the begin of the experiment)

V_0 is the velocity at the reference pressure.

The exponent m is mostly in the order of $m \approx 1/6 - 1/4$. An exponent $m = 1/6$ results from Hertz's theory (see [Section 6.7.2](#)) for spherical grain contacts under pressure; thus, this shape of equation is preferred for sediments with a granular structure (sand, sandstone).

[Figure 6.14](#) shows as an example the velocity of dry and water-saturated sand as a function of pressure. In a logarithmic plot (right figure), the power law results in a straight line with the exponent as the slope for the dry compressional and the dry and water-saturated shear wave velocity; they are all “rock skeleton controlled.” The compressional wave at water saturation is significantly higher (in the range of water velocity) and less pressure dependent—this wave is “pore fluid controlled.”

A modification is recommended for water-bearing porous rocks in particular:

$$V = a + b \left(\frac{p_{\text{eff}}}{p_0} \right)^m \quad (6.60)$$

or as velocity versus depth relationship:

$$V = a + b \cdot z^m \quad (6.61)$$

where a, b, m are also empirical parameters.

Results of a study for sediments of the Vienna Basin are presented in [Table 6.10](#). Different deformation properties of sandstone and shale, as well

TABLE 6.10 Compressional and Shear Wave Velocities in m s^{-1} as a Function of Depth in m

Lithology	Compressional Wave	R^2	Shear Wave	R^2
Water sand	$V_p = 185 + 143 \cdot z^{0.41}$	0.82	$V_s = 42 + 36 \cdot z^{0.51}$	0.52
Gas sand	$V_p = 227 + 162 \cdot z^{0.38}$	0.79	$V_s = 72 + 58 \cdot z^{0.44}$	0.79
Shale	$V_p = 163 + 129 \cdot z^{0.42}$	0.92	$V_s = 393 + 0.76 \cdot z$	0.86

Kirchberger (2001).

as the fluid properties, result in different velocity versus depth functions. For shear wave velocity of shale, a linear regression gives the best approximation.

In some cases, an exponential law is also applied with the general form:

$$V = a - b \cdot \exp\left(-\frac{p_{\text{eff}}}{p_0}\right) \quad (6.62)$$

where again

p_{eff} is the actual effective pressure

p_0 is a reference pressure (e.g., at the begin of the experiment)

a is the velocity for $p_{\text{eff}} \rightarrow \infty$

$a - b$ is the velocity at $p_{\text{eff}} = 0$.

This equation can also describe the velocity increase as a result of the closure process of fractured rocks (Schön, 1996).

An extended study of the combined influence of effective pressure, porosity, and clay content of sandstones using a multivariate analysis has been published by Eberhart-Phillips et al. (1989). The data consisted of 64 sandstone samples with porosities ranging between 4.6% and 29.4% and a clay content ranging between 0% and 40%. The best fit is

$$V_p = 5.77 - 6.94 \cdot \phi - 1.73 \cdot C^{0.5} + 0.446[p_{\text{eff}} - \exp(16.7 \cdot p_{\text{eff}})] \quad (6.63)$$

with rms error 0.105 km s^{-1}

$$V_s = 3.70 - 4.94 \cdot \phi - 1.57 \cdot C^{0.5} + 0.360[p_{\text{eff}} - \exp(16.7 \cdot p_{\text{eff}})] \quad (6.64)$$

with rms error 0.099 km s^{-1}

where velocities are in km s^{-1} , porosity ϕ and clay content C as fractions, and the pressure p_{eff} in kbar (1 kbar = 100 MPa).

It may be noted that the general tendency of a (nonlinear) increase of velocity with increasing effective pressure is valid as long as the pressure

does not break grains, particles, or sections of the particle contact. Such a breaking can result in a structure collapse and decrease of velocity.

A detailed discussion of velocity–depth trends for sandstone and shale from the North Sea is given by Japsen et al. (2006).

The additional influence of thermally induced microfractures in Aeolian Rotliegend sandstone on the stress dependence of elastic properties was investigated by MacBeth and Schuett (2007).

6.5.5 Temperature Influence

The temperature effects on the dry bulk moduli are very small. The temperature dependence of fluids is more significant and controlled by the composition (Batzle and Wang, 1992; see [Section 6.2.2](#)).

The expected trend, which is in agreement with observations, is that velocities decrease with temperature more in saturated than in dry porous rocks.

6.5.6 Empirical Relationships Between V_P and V_S —Castagna Equation

The ratio V_P/V_S is an important property for seismic applications (see also [Section 6.8](#)). In order to estimate shear wave velocities when only compressional wave velocities are available, Castagna et al. (1985) derived an empirical equation commonly referred to as the “mudrock line”⁵:

$$V_S = 0.8621 \cdot V_P - 1.1724 \quad (6.65)$$

where the velocities are in km s^{-1} .

Numerous researchers have published variants of the Castagna mudrock equation. In 1993, Castagna et al. compiled an analysis of data for different sedimentary rocks. The following consideration gives a part of the results. [Table 6.11](#) lists a selection of the modified equations based on a compilation by Mavko et al. (1998) and [Figure 6.15](#) shows some typical lines in a plot.

For carbonates, Castagna et al. (1993) gives the following regressions:

$$\text{limestone (water saturated)} \quad V_S = -0.055 \cdot V_P^2 + 1.017 \cdot V_P - 1.031 \quad (6.66)$$

$$\text{dolomite (water saturated)} \quad V_S = 0.5832 \cdot V_P - 0.07776 \quad (6.67)$$

All of these correlations are pure empirically and valid only for a specific formation. They result from properties like rock composition, porosity, shale content, etc. with an influence on both wave types in the same direction.

⁵Castagna et al. (1985): “We define mudrock as clastic silicate rock composed primarily of clay- or silt-sized particles” (see also Blatt et al., 1972).

TABLE 6.11 Linear regressions V_s versus V_p for Sandstone and Shale (water-saturated); velocities in km/s

Equation	Remarks	Reference
$V_s = 0.8042 \cdot V_p - 0.8559$	Sandstone	Castagna 1985,
$V_s = 0.7700 \cdot V_p - 0.8674$	Shale	Castagna et al., 1993
$V_s = 0.7936 \cdot V_p - 0.7868$	Sandstone, shaly	Han et al., 1986
	Sandstone	Han et al., 1986
$V_s = 0.8423 \cdot V_p - 1.099$	clay content > 0.25	
$V_s = 0.7535 \cdot V_p - 0.6566$	clay content < 0.25	
	Sandstone	Han et al., 1986
$V_s = 0.756 \cdot V_p - 0.662$	porosity > 0.15	
$V_s = 0.853 \cdot V_p - 1.137$	porosity < 0.15	

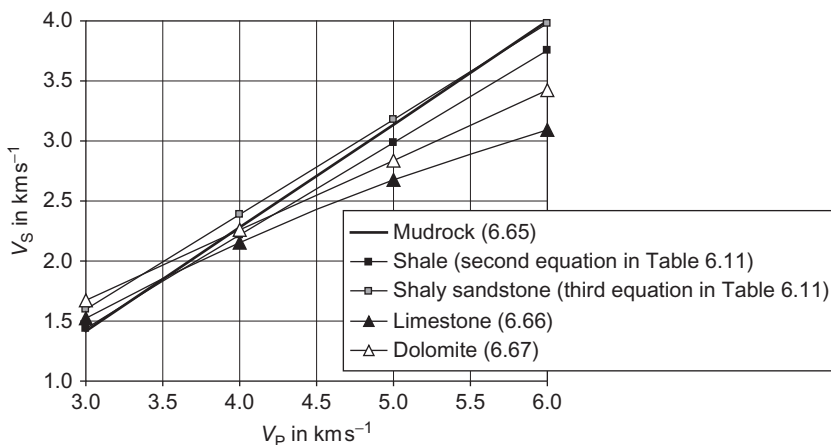


FIGURE 6.15 Empirical regressions V_p versus V_s as Castagna plot; lines represent Equation (6.65), equations in Table 6.11, and equations for carbonates (6.66/limestone and 6.67/dolomite).

A general valid physically based equation is not possible, because the isotropic material is also characterized by two *independent* elastic properties or wave velocities.

6.6 ANISOTROPY

6.6.1 Overview

Implementation of elastic anisotropy is of increasing importance for seismic processing and interpretation. Armstrong et al. (1994) discuss fundamental characteristics and consequences of elastic anisotropy for seismic and acoustic methods. Wang (2002) gives a detailed discussion of elastic anisotropy of sedimentary rocks. Lo et al. (1986) analyzed laboratory measurements at the Berea sandstone, Chicopee shale, and Chelmsford granite.

Layer-induced anisotropy (transversely isotropy) and its consequences for the interpretation of seismic data are the subjects of papers by Helbig (1958, 1992), Backus (1962), White (1983), Thomsen (1986, 1995), Schoenberg and Muir (1989), and Schoenberg (1994).

“Shear wave splitting” is a sensitive indicator of elastic anisotropy and therefore has a special place in rock physics (see, for example, Crampin and Lovell, 1991).

In elastically anisotropic rocks, the velocity of wave propagation depends on the direction of propagation. Obvious anisotropy exists:

- in metamorphic rocks with schistosity and oriented fracturing (typical gneiss);
- in sedimentary rocks with layering or bedding (e.g., laminated shaly sand), but also if fractures are present.

The origins of anisotropy are aligned crystals in igneous rocks, aligned grains in sediments, lamination of sediments (laminated shaly sands), aligned fractures and cracks, and stress-induced anisotropy.

Whereas elastic properties of an isotropic medium are determined by two independent elastic parameters, for an anisotropic material in the simplest case (transversely isotropy), five parameters are necessary. For the transverse isotropy, the elastic properties are equal, for example, in the $x-y$ plane (plane of stratification or schistosity), but vary with the angle from the vertical z -axis.

Figure 6.16 demonstrates—based on Lo et al. (1986)—the petrofabric origin of elastic rock anisotropy. The upper part shows:

- in Berea sandstone, most of the long axes of the quartz grains are parallel to the bedding plane;
- in Chicopee shale, most of the cleavage planes of mica and the long axes of other constituent minerals are parallel to the bedding plane;

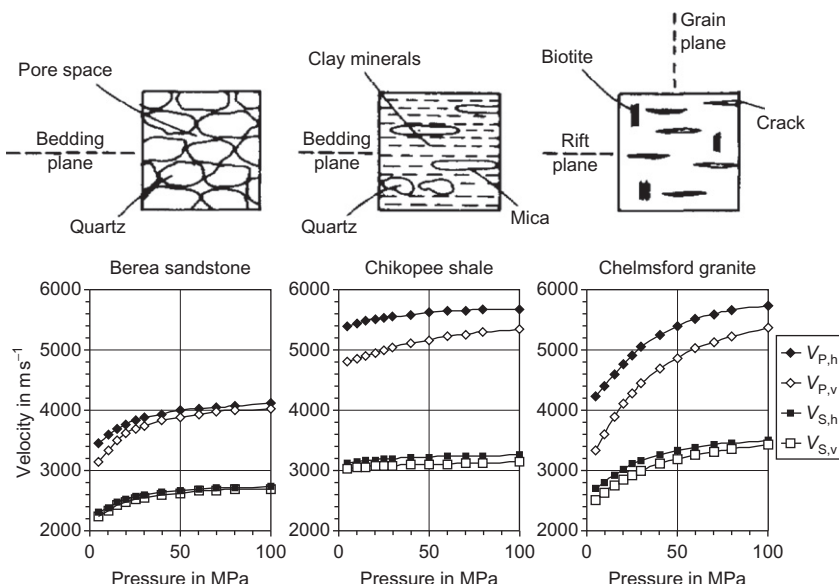


FIGURE 6.16 Anisotropy and its petrofabric origin (compiled from figures and data of Lo et al., 1986). Upper part: schematic petrofabric character of Berea sandstone, Chicopee shale, Chelmsford granite. Lower parts: selected velocities (original symbols in brackets) as function of pressure: compressional wave velocities $V_{p,h}$ (V_{p11}), $V_{p,v}$ (V_{p33}), shear wave velocities $V_{s,h}$ ($V_{s,h1}$), $V_{s,v}$ ($V_{s,3a}$).

- in Chelmsford granite, most of the cracks are parallel to the rift plane and most of the biotite cleavage planes are parallel to the grain plane (Lo et al., 1986).

In the lower part, selected velocities⁶ are plotted as a function of pressure. They clearly indicate:

- the anisotropy for both compressional and shear wave velocities;
- the tendency of decreasing anisotropy with increasing pressure.

As described in [Section 6.1.1](#), Thomsen (1986) defined three parameters ([Equations \(6.22\)–\(6.24\)](#)) for the characterization of weak anisotropy of a transversely isotropic material:

$$\varepsilon = \frac{c_{11} - c_{33}}{2 \cdot c_{33}} \quad \gamma = \frac{c_{66} - c_{44}}{2 \cdot c_{44}} \quad \delta = \frac{(c_{13} + \frac{c_{44}}{2})^2 - (c_{33} - \frac{c_{44}}{2})^2}{2 \cdot c_{33}(c_{33} - \frac{c_{44}}{2})} \quad (6.68)$$

⁶In the original paper, all velocities and tensor components are presented.

where ε and γ describe the anisotropy properties of the compressional and shear waves, respectively. Additionally, a ratio can be defined as:

$$\lambda_{\text{compr}} = \frac{c_{11}}{c_{33}} = 2 \cdot \varepsilon + 1 \quad \lambda_{\text{shear}} = \frac{c_{66}}{c_{44}} = 2 \cdot \gamma + 1 \quad (6.69)$$

If for a transversely isotropic material as the simplest type of anisotropy:

- the vertical axis (x_3) is the axis of symmetry, then the material is called TIV. This is the case, for example, for horizontally layered laminated sediments: elastic properties are uniform horizontally, but vary vertically.
- one horizontal axis (x_1 or x_2) is the axis of symmetry, then the material is called TIH. In the case of vertical fractures, elastic properties are uniform in vertical plane parallel aligned fractures, but vary in perpendicular fractures/crossing fractures (see, for example, Armstrong et al., 1994).

Equations for a TIV system can be transformed into corresponding equations for a TIH system by cyclic transformation.

In the following section, two aspects of anisotropy are discussed briefly:

1. The effect of aligned fractures and cracks and the phenomenon of shear wave splitting, anisotropy of igneous and metamorphic rocks
2. Anisotropy of laminated sediments and correlations between compressional and shear wave anisotropy.

6.6.2 Anisotropy Effect of Fractures, Anisotropy of Igneous and Metamorphic Rocks

In fractured rocks with a preferred direction of fractures, anisotropy results as an effect of the weak parts of the rock (Figure 6.17). For the main directions, four wave velocities can be observed:

- Compressional wave velocity perpendicular to the fracture plane $V_{P\perp}$ is smaller than the compressional wave velocity parallel to this plane $V_{P\parallel}$:
 - low velocity $V_{P\perp}$ is controlled very strongly by the “soft” elastic element of the fractures (a series array of elastic elements);
 - higher velocity $V_{P\parallel}$ is controlled by the competent part of the rock (a parallel array of elastic elements).
- Shear wave velocity must be related to the direction of polarization (particle motion) with respect to the “soft” and “competent” element. It results in:
 - low velocity for the wave propagating vertically (polarization horizontally);
 - low velocity for the wave propagating horizontally (polarization vertically);
 - high velocity for the wave propagating horizontally (polarization horizontally).

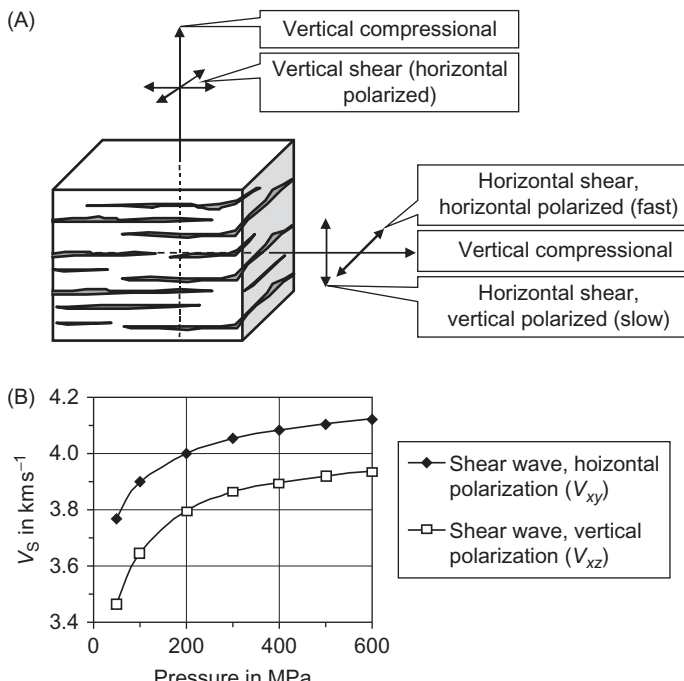


FIGURE 6.17 Shear wave splitting in a transversely isotropic rock. (A) Principle of shear wave splitting and different velocities; short arrows at shear wave indicate particle motion (polarization). (B) Example: Amphibolite (Western Alps/Ivrea zone); anisotropy and shear wave splitting is related to texture and microcracks; foliation is horizontal (data from Siegesmund and Vollbrecht, 1991).

Thus, in the horizontal direction of propagation (or propagation parallel fracturing), there are two shear waves with different directions of polarization and different velocities. This is the phenomenon of “shear wave splitting.”

Thomsen (1995) derived the theoretical background for the calculation of elastic anisotropy due to aligned cracks in porous rocks.

6.6.3 Anisotropy of Laminated Sediments

In sediments, lamination creates macroscopic anisotropy, which results from an alternating change of the elastic properties of thin layers; the effect of the intrinsic or bulk layer anisotropy, particularly for the shale/clay, and fracturing, can be superimposed. Table 6.12 shows some typical values for Thomsen parameters (Equation (6.68)) for sedimentary rocks.

Sams and Andrea (2001) describe the effects of clay in sandstone on elastic properties and present various model calculations. They start with some statements: “The shape and location of clay within sandstones have a large

TABLE 6.12 Typical Values for Thomsen Parameters for Some Sedimentary Rocks

Rock	V_P in m s^{-1}	V_S in m s^{-1}	ρ in g cm^{-3}	ϵ	δ	γ
Sandstone	3368	1829	2.50	0.110	-0.035	0.255
	4869	2911	2.50	0.033	0.040	-0.019
Calcareous sandstone	5460	3219	2.69	0.000	-0.264	-0.007
Shale	3383	2438	2.35	0.065	0.059	0.071
	3901	2682	2.64	0.137	-0.012	0.026
Mudshale	4529	2703	2.52	0.034	0.211	0.046
Clay, shale	3794	2074	2.56	0.189	0.204	0.175
Silty limestone	4972	2899	2.63	0.056	-0.003	0.067
Laminated siltstone	4449	2585	2.57	0.091	0.565	0.046

Thomsen (1986).

impact on the P-wave and S-wave velocities of the rock. They also have large effect on reservoir properties and the interpretation of those properties from seismic data and well logs. Numerical models of different distributions of clay—structural, laminar, and dispersed clay—can lead to an understanding of these effects.” The description of clay effects and the derivation of models are difficult as a result of the following features (Sams and Andrea, 2001):

- Different type of clay distribution (structural, laminated, dispersed)
- Diversity of clay minerals with specific properties
- Intrinsic anisotropic properties of the clay minerals
- Chemical and physical interactions between clay and pore fluid
- Compaction effects.

Published experimental data for clay minerals and shale demonstrate the strong influence of porosity and compaction and show the high anisotropy of this group of rock constituents. If clay minerals are aligned, bulk anisotropy results.

Katahara (1996) published velocity data for kaolinite, illite, and chlorite. Results show a distinct anisotropy for compressional and shear waves. The clay can be described as a transverse isotropic material.

White et al. (1983) published the results of an analysis of Pierre shale elastic anisotropy. A transverse isotropy was assumed and the vertical

TABLE 6.13 Elastic Stiffness Components and Anisotropy Parameters for Jurassic Shale

Confining Pressure in MPa	Elastic Stiffness in GPa					Thomsen's Parameters		
	C_{11}	C_{33}	C_{13}	C_{44}	C_{66}	ε	γ	δ
5	33.5	22.5	14.8	5.0	9.7	0.24	0.47	0.11
10	36.2	24.2	15.3	5.8	10.7	0.25	0.42	0.12
20	39.6	27.0	16.2	6.8	12.0	0.23	0.38	0.12
40	43.2	29.7	17.4	7.8	13.3	0.23	0.35	0.11
60	45.0	31.7	18.1	8.3	13.6	0.21	0.32	0.11
80	46.02	32.91	18.5	8.9	14.2	0.2	0.3	0.09

Hornby (1995).

compressional and shear wave velocities and the anisotropy coefficients have been calculated for depth sections.

The seismic properties of shale and the distinct anisotropy were also investigated by Lo et al. (1986) and Johnston and Christensen (1995). Vernik and Liu (1997) analyzed the elastic properties of North Sea shale for the case of dry and brine-saturated sediments.

Cholach and Schmitt (2003) studied the seismic anisotropy of shales and, for a model, applied the “volume averaging with the orientation distribution function (ODF) and geometric mean averaging. Modeling of the intrinsic anisotropy of shales is based on several assumptions including simplified shale mineralogical composition, the elasticity of the constituent minerals, and the orientations of clay mineral platelets.”

For Jurassic shale (total clay 57–59 vol.%), Hornby (1995) determined the elastic stiffness components and Thomsen's parameters as a function of the confining pressure. Increasing pressure results in a moderate decrease of compressional anisotropy (ε) and a stronger decrease of shear anisotropy (γ) (Table 6.13).

Schön et al. (2005) applied a modular model concept for electrical, hydraulic, and elastic anisotropy studies that allows a joint interpretation of anisotropic formations. The model consideration and analysis of real logging data shows that shear wave velocities depend strongly on the shale distribution and that the difference of the velocity of shear waves with different polarization can be related to the shale distribution (laminar or dispersed, structural). A shear wave-based method can discriminate between laminated

and dispersed shaly zones and provide an estimate of the sand reservoir properties.

6.6.4 Correlations Between Compressional and Shear Wave Anisotropy

In a systematic study, Wang (2002) published experimental results of the elastic properties (all five tensor components) and Thomsen parameters on a total of 256 samples (sandstone, shale, carbonate). A crossplot of γ (shear wave anisotropy) versus ε (compressional wave anisotropy) results in a regression:

$$\gamma = -0.01049 + 0.9560 \cdot \varepsilon \quad R^2 = 0.7463 \quad (6.70)$$

A look on the data distribution suggests some different positions for different lithologies.

In Figure 6.18, data of two groups of shales are plotted and analyzed separately. They give the following regressions.

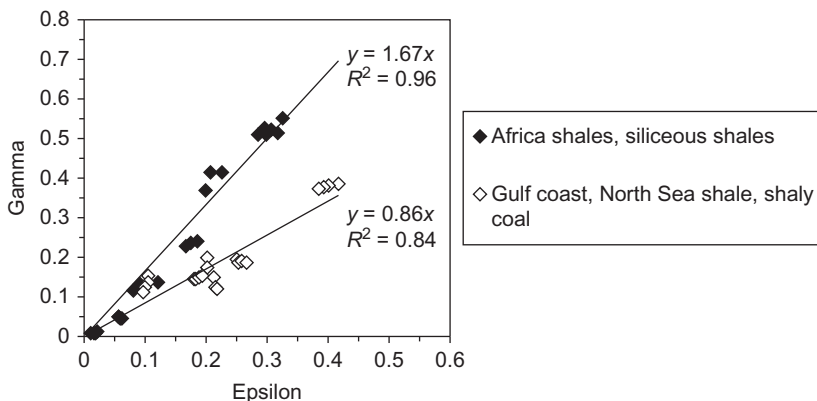


FIGURE 6.18 Crossplot parameter γ (gamma) versus parameter ε (epsilon) for brine-saturated shale (data after Wang, 2002). Data is divided into two groups.

African shales, siliceous shales:

$$\gamma = 1.67 \cdot \varepsilon \quad \varepsilon = 0.60 \cdot \gamma \quad R^2 = 0.96 \quad (6.71)$$

Gulf coast shales, North Sea shales, shaly coal:

$$\gamma = 0.86 \cdot \varepsilon \quad \varepsilon = 1.12 \cdot \gamma \quad R^2 = 0.84 \quad (6.72)$$

Such correlations are pure empirically and valid only for a specific formation. Correlation results from influences (porosity, clay content) on both wave types with the same tendency. A general equation is not possible,

because the anisotropic material is characterized by (at least five) independent elastic properties.

6.7 THEORIES

Wang (2000) states:

The rock–fluid system is so complicated that virtually all the theories for such a system have to make major assumptions to simplify the mathematics.

For a theoretical description, the natural rock as a heterogeneous system with internal structure must be idealized in order to formulate elastic rock properties in terms of volume fractions and properties of the components (minerals and fluids), the rock texture, pressure, etc. In all cases, models are an idealization.

Models can be classified in regards to the type of “geometrical idealization” of the real rock (simple layer models, sphere models, inclusion models). Figure 6.19 gives an overview about some of the frequently used model concepts. In the following sections, some members are presented (principle and possibilities of application). For a more detailed study, textbooks (e.g., Bourbie et al., 1987; Mavko et al., 1998; White 1983;) and the original

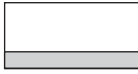
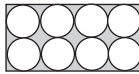
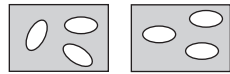
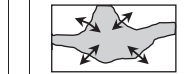
Real rock				
Bound models	Sphere pack models	Inclusion models (Spherical and nonspherical inclusions)	Pore fluid effect models	
 Layer model: Voigt (1910) and Reuss (1926) bounds Hashin–Shtrikman (1962, 1963) bounds	 Hertz (1882) and Mindlin (1949) theory Gassmann (1951) White (1983) Digby (1981) Dvorkin and Nur (1996)	 Random orientation Kuster and Toksöz (1974) Describes granular materials, gives nonlinear pressure dependence of velocities	 Aligned orientation Hudson (1980)	 Gassmann (1951) Biot (1956) Murphy (1982) Mavko and Jizba (1991)
Delivers upper and lower boundary for a given composition		Describes fractured and (low) porous rocks, implements inclusion shape (aspect ratio) and orientation: random orientation (isotropic) or aligned orientation (anisotropic)		Describes influence of changing pore fluid, basic for “fluid replacement techniques”.

FIGURE 6.19 Classification of main types of models for elastic properties.

papers are recommended. Furthermore, in [Section 6.7.7](#), a specific model (“structured model”) is discussed.

In many cases models are derived for porous reservoir rocks, and frequently the equations cover the whole range of a two-component (solid, fluid) mixture from porosity $\phi = 0$ (pure solid, dense) to $\phi = 1$ (pure fluid). Nur et al. (1998) developed a significant threshold with the concept of “critical porosity” for velocity–porosity relationships of porous rocks ([Figure 6.20](#)):

- Real rocks with a frame built up by grains or other solid particles exist only below the critical porosity, and grain contact behavior controls many effects. The elastic properties are “rock skeleton dominated.”
- Above the critical porosity, particles are embedded in the fluid as a suspension. In this region elastic properties are “fluid dominated”; there is no shear resistance and no shear wave. Critical porosities are in the order of approximately $\phi \approx 0.4$.

6.7.1 Bounds for Elastic Moduli: Voigt, Reuss, and Hashin–Shtrikman Bounds

Bound computational models describe the upper and lower limits of elastic parameters of a composite medium. Voigt (1910) gives the upper, and Reuss (1929) gives the lower bound. More narrow bounds are derived by Hashin and Shtrikman (1962a, 1963).

The early work of Voigt (1910) and Reuss (1929) gives an averaging algorithm for the calculation of effective elastic moduli of a composed material ([Figure 6.21](#)). If the material consists of n isotropic components with the

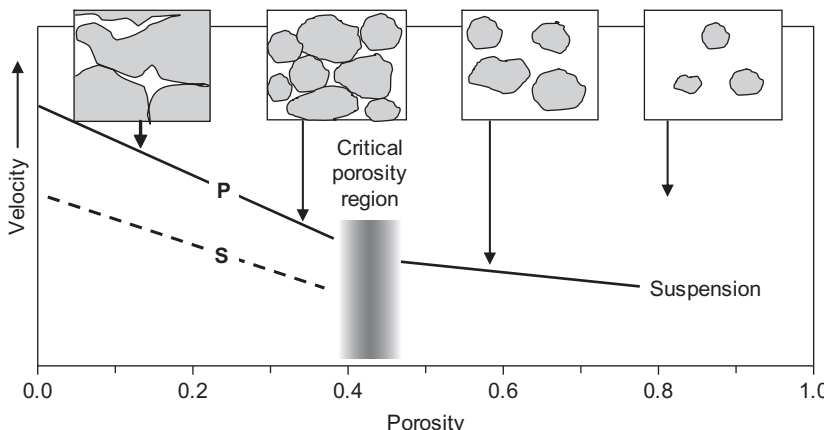


FIGURE 6.20 The critical porosity concept; after a figure from Nur et al. (1998).

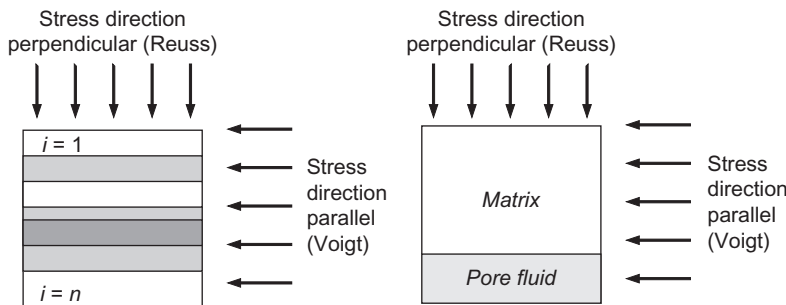


FIGURE 6.21 Voigt and Reuss model for the general case of a rock with n components and a simple porous rock with two components (matrix and pore fluid).

volume fractions V_i and the compression moduli k_i and shear moduli μ_i of the i th component, then the following:

For homogeneous strain, Voigt's average (parallel model) is

$$k_V = \sum_{i=1}^n k_i \cdot V_i \quad \mu_V = \sum_{i=1}^n \mu_i \cdot V_i \quad (6.73)$$

For homogeneous stress, Reuss' average (serial model) is

$$k_R = \left[\sum_{i=1}^n \frac{V_i}{k_i} \right]^{-1} \quad \mu_R = \left[\sum_{i=1}^n \frac{V_i}{\mu_i} \right]^{-1} \quad (6.74)$$

For any mixture, Voigt's average gives the upper bound of the effective elastic modulus and Reuss' average gives the lower bound.

For a porous rock with solid matrix ma and fluid fl as components results

$$k_V = (1 - \phi)k_{ma} + \phi \cdot k_{fl} \quad \mu_V = (1 - \phi)\mu_{ma} \quad (6.75)$$

$$k_R = \left(\frac{(1 - \phi)}{k_{ma}} + \frac{\phi}{k_{fl}} \right)^{-1} \quad \mu_R = 0 \quad (6.76)$$

Shear modulus for the Reuss bound becomes zero because fluid has zero shear modulus ($\mu_{fl} = 0$).

[Figure 6.22](#) gives an example for compressional modulus calculation.

The real measured data are positioned between the two bounds. Therefore, as a representative value, the arithmetic mean of the two bound values is frequently used and called the Voigt–Reuss–Hill average:

$$k_{VRH} = \frac{k_V + k_R}{2} \quad \mu_{VRH} = \frac{\mu_V + \mu_R}{2} \quad (6.77)$$

Mavko et al. (1998) note “the Voigt–Reuss–Hill average is used to estimate the effective elastic moduli of a rock in terms of its constituents and pore space.”

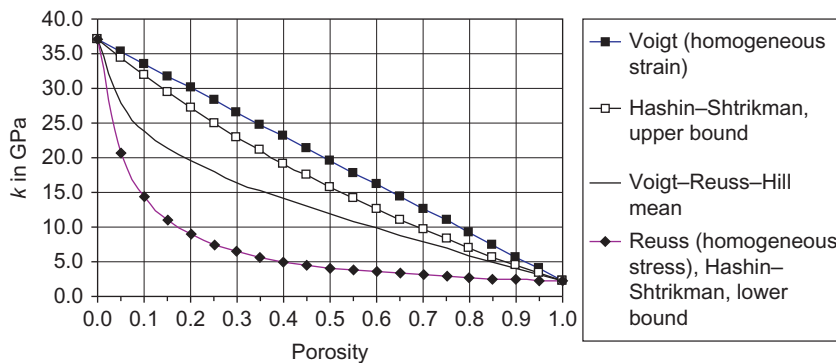


FIGURE 6.22 Voigt, Reuss, Voigt–Reuss–Hill average, and Hashin–Shtrikman bounds for compressional modulus as function of porosity. Input parameters are: quartz $k_{\text{ma}} = 37 \text{ GPa}$, $\mu_{\text{ma}} = 44 \text{ GPa}$, water $k_{\text{fl}} = 2.2 \text{ GPa}$ (for calculations, visit the website <http://www.elsevierdirect.com/companion.jsp?ISBN=9780444537966> and refer Elastic_Mechanical_Bound models).

More narrow boundaries than Voigt and Reuss can be calculated as Hashin–Shtrikman bounds (Hashin and Shtrikman, 1962, 1963). Mavko et al. (1998) present the equations in a comfortable form for a two-component medium:

$$k_{\text{HS}} = k_1 + \frac{V_2}{(k_2 - k_1)^{-1} + V_1(k_1 + \frac{4}{3}\mu_1)^{-1}} \quad (6.78)$$

$$\mu_{\text{HS}} = \mu_1 + \frac{V_2}{(\mu_2 - \mu_1)^{-1} + \frac{2 \cdot V_1(k_1 + 2 \cdot \mu_1)}{5 \cdot \mu_1(k_1 + \frac{4}{3}\mu_1)}} \quad (6.79)$$

where

k_1, k_2 are the bulk moduli of components

μ_1, μ_2 are the shear moduli of components

V_1, V_2 are the volume fractions of components.

The equations give:

- the upper bound when the stiffest material is termed 1;
- the lower bound when the softest material is termed 1.

For a porous rock (component 1 = solid matrix ma, component 2 = fluid fl, porosity = ϕ), the equations result as upper and lower bound:

$$k_{\text{HS,upper}} = k_{\text{ma}} + \frac{\phi}{(k_{\text{fl}} - k_{\text{ma}})^{-1} + (1 - \phi)(k_{\text{ma}} + \frac{4}{3}\mu_{\text{ma}})^{-1}} \quad (6.80)$$

$$k_{\text{HS,lower}} = k_{\text{fl}} + \frac{1 - \phi}{(k_{\text{ma}} - k_{\text{fl}})^{-1} + \phi(k_{\text{fl}})^{-1}} \quad (6.81)$$

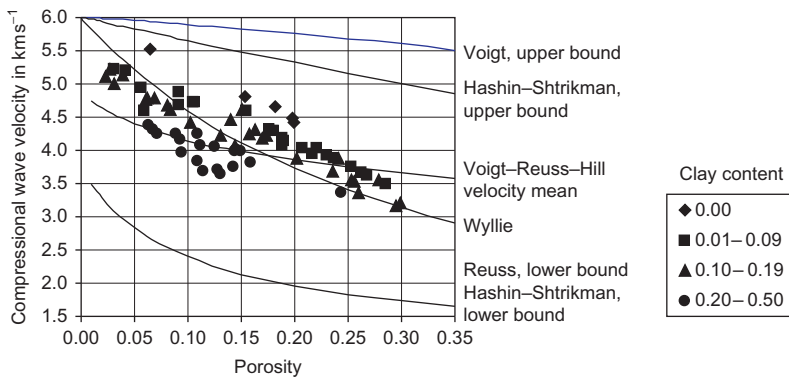


FIGURE 6.23 Calculated compressional wave velocity versus porosity curves for Voigt, Reuss, Hashin–Shtrikman bounds, and velocity mean from Voigt and Reuss bound. Input parameters are: quartz $k_{ma} = 37$ GPa, $\mu_{ma} = 44$ GPa, $\rho_{ma} = 2.65$ g cm $^{-3}$; water $k_{fl} = 2.2$ GPa, $\rho_{fl} = 1.00$ g cm $^{-3}$. The curve for Wyllie's equation (6.49) is also plotted. Data points are the experimental results from Han et al. (1986) as plotted in Figure 6.7.

$$\mu_{HS,upper} = \mu_{ma} + \frac{\phi}{\frac{2(1-\phi)(k_{ma} + 2 \cdot \mu_{ma})}{5 \cdot \mu_{ma} \cdot \left(k_{ma} + \frac{4}{3} \cdot \mu_{ma} \right)} - \frac{1}{\mu_{ma}}} \quad (6.82)$$

$$= \mu_{ma} - \phi \cdot \frac{\mu_{ma}}{1 - \frac{2(1-\phi)(k_{ma} + 2 \cdot \mu_{ma})}{5 \cdot \left(k_{ma} + \frac{4}{3} \cdot \mu_{ma} \right)}} \quad (6.83)$$

$$\mu_{HS,lower} = 0 \quad (6.83)$$

Figure 6.22 shows Voigt, Reuss, and Hashin–Shtrikman bounds for compressional modulus as a function of porosity; input parameters are: for quartz $k_{ma} = 37$ GPa, $\mu_{ma} = 44$ GPa, and for water $k_{fl} = 2.2$ GPa. The lower Hashin–Shtrikman bound is equal to the Reuss bound in case of a porous medium, where one constituent is a fluid (shear modulus zero). Gommensen et al. (2007) therefore implemented a “modified upper Hashin–Shtrikman bound”; this model crosses the Reuss bound at critical porosity.

Figure 6.23 shows a comparison of calculated compressional wave velocities and measured data (same as in Figure 6.7). The curve for Wyllie's Equation (6.49) is also plotted. Despite the scatter of the data, tendency is visible:

- for low porosity data, tend to upper bound prediction; for high porosity to lower bound prediction;
- increasing shale content shift data in the plot in direction of lower bound prediction.

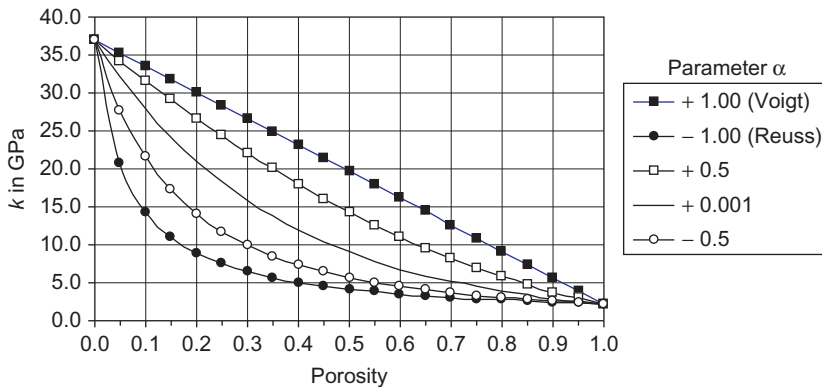


FIGURE 6.24 Voigt (1910), Reuss (1926), and generalized equation (6.85) for compressional modulus as function of porosity. Input parameters are for quartz $k_{\text{ma}} = 37 \text{ GPa}$ and for water $k_{\text{fl}} = 2.2 \text{ GPa}$. Curve parameter is the textural parameter α (for calculations, visit the website <http://www.elsevierdirect.com/companion.jsp?ISBN=9780444537966> and refer Elastic_Mechanical_Bound models).

Another way to get a fit to experimental data is the application of the generalization proposed by Lichtenegger and Rother (1931) for a dielectric number (see Section 8.7.4) on elastic properties. For the general case of n components, the equation is

$$k_{\text{LR}} = \left[\sum_{i=1}^n V_i(k_i^a) \right]^{\frac{1}{a}} \quad \mu_{\text{LR}} = \left[\sum_{i=1}^n V_i(\mu_i^a) \right]^{\frac{1}{a}} \quad (6.84)$$

Equation (6.84) is a generalization of several individual equations; for example:

- the parallel model (Voigt) for $a = 1$;
- the serial model (Reuss) for $a = -1$.

We can understand the exponent α as a “textural parameter.”

For a porous rock, the equation is

$$k_{\text{LR}} = [(1 - \phi)(k_{\text{ma}}^a) + \phi(k_{\text{fluid}}^a)]^{\frac{1}{a}} \quad \mu_{\text{LR}} = [(1 - \phi)(\mu_{\text{ma}}^a) + \phi(\mu_{\text{fl}}^a)]^{\frac{1}{a}} \quad (6.85)$$

Figure 6.24 shows an example of calculated compressional modulus versus porosity for different exponents a . Variation of a fills the space between upper and lower boundary (properties are not defined for $a \equiv 0$).

Figure 6.25 shows a comparison of calculated compressional wave velocities and measured data (same as in Figure 6.7). The curve for Wyllie’s equation (6.49) is also plotted. Despite the scatter of the data, as tendency is visible a shift of the parameter from $a = 0.20$ (clean sandstone) to about $a = 0.05$ (shaly sandstone).

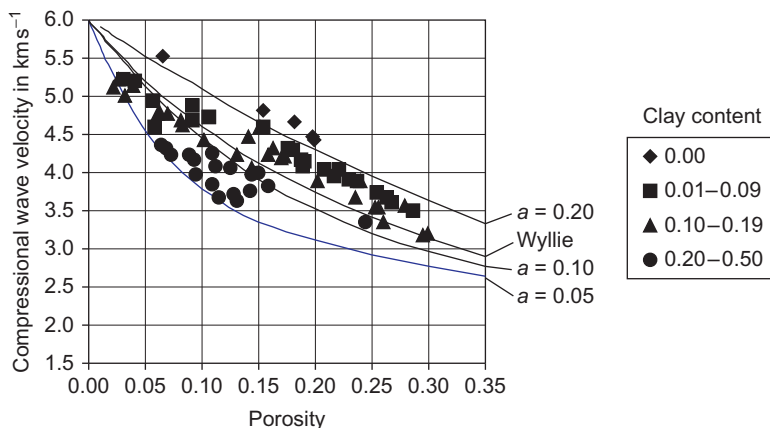


FIGURE 6.25 Calculated compressional wave velocity versus porosity curves for the generalized equation (6.85) (curve parameter $a = 0.20, 0.10, 0.05$). Input parameters are: quartz $k_{\text{ma}} = 37 \text{ GPa}$, $\mu_{\text{ma}} = 44 \text{ GPa}$, $\rho_{\text{ma}} = 2.65 \text{ g cm}^{-3}$; water $k_{\text{fl}} = 2.2 \text{ GPa}$, $\rho_{\text{fl}} = 1.00 \text{ g cm}^{-3}$. The curve for Wyllie's equation (6.49) is also plotted. Data points are the experimental results from Han et al. (1986) as plotted in Figure 6.7.

The examples are calculated for a material with two components (solid matrix material, fluid); all models can be applied on any number of components if volume fractions and elastic moduli of the components are known.

6.7.2 Sphere Pack Models

The concept of a packing of spheres is a fascinating model particularly for unconsolidated rocks (sand, gravel). In most theories it is assumed that:

- grains are spheres of the same diameter;
- centers of the spheres built a lattice system (e.g., cubic, hexagonal).

The derivation is based on:

1. Stress-strain relationships for the contact of spherical particles. The fundamentals of stress-strain behavior due to normal forces at the point of contact were derived in 1881 by G. Hertz (see Landau and Lifshitz, 1965; Love, 1944; White, 1983). Cattaneo (1938) and Mindlin (1949) also introduced tangential forces. A summary discussion is given by Deresiewics (1958).
2. The geometry of the sphere pack model. After the early paper of Hara (1935),⁷ Gassmann (1951) published his classic paper about the elasticity of a hexagonal packing of spheres.

⁷Assuming the cubic packing of spheres as a model to describe the behavior of a carbon-granule microphone.

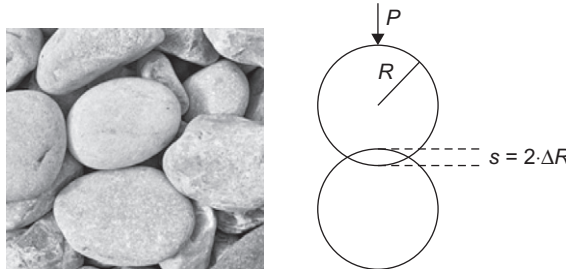


FIGURE 6.26 Deformation at contact of two spheres under normal loading (Hertz's theory).

Further studies are by White and Sengbush (1953) and Brandt (1955). Digby (1981) investigated various packings. Dvorkin and Nur (1996) developed a cemented sand model (see also Mavko et al., 1998).

In the following, the principle is described for a cubic packing. Figure 6.26 shows two spheres of a radius R in contact.

The force P results in a deformation described by displacement of the centers of two neighboring spheres:

$$2 \cdot \Delta R = \left(\frac{9}{2R} \left(\frac{1 - \nu_s^2}{E_s} \right)^2 P^2 \right)^{\frac{1}{3}} \quad (6.86)$$

where E_s, ν_s are Young's modulus and Poisson's ratio, respectively, of the solid sphere material (e.g., quartz). The equation immediately shows the non-linear deformation pressure dependence:

$$\varepsilon = \frac{\Delta R}{R} \propto p^{\frac{2}{3}} \quad (6.87)$$

For the sphere pack, a modulus of deformation results in the proportionality:

$$M_{\text{sphere pack}} \propto p^{\frac{1}{3}} \quad (6.88)$$

and for a velocity, results in the proportionality:

$$V_{\text{sphere pack}} \propto p^{\frac{1}{6}} \quad (6.89)$$

The compressional wave velocity of the cubic packing is (White, 1983):

$$V_p = \left[\frac{3}{8} \left(\frac{E_s}{1 - \nu_s^2} \right)^2 p \right]^{\frac{1}{6}} \left(\frac{6}{\pi \cdot \rho_s} \right)^{\frac{1}{2}} \quad (6.90)$$

The equations show that—in agreement with experimental results for dry sand (see Figure 6.14)—the velocity—pressure or velocity—depth function is nonlinear and follows a power law. The reason for this agreement is the specific deformation behavior at the points of contact of the spherical particles (but not by the specific sphere array). But there is no agreement between the experimental and calculated porosity dependence (compare Schön 1969,

1996). This disagreement is obviously caused by the idealized assumption of the regular lattice array and the uniform sphere size.

For random packing of identical spheres—based on Mindlin's (1949) theory for compressional and shear behavior without a slip at the contact—Mavko et al. (1998) give the the following:

$$\text{effective bulk compressional modulus } k_{\text{eff}} = \left[\frac{1}{18} \left(\frac{C \cdot \mu_s (1 - \phi)}{\pi (1 - \nu_s)} \right)^2 p \right]^{\frac{1}{3}} \quad (6.91)$$

$$\text{effective shear modulus } \mu_{\text{eff}} = \frac{5 - 4 \cdot \nu_s}{5(2 - \nu_s)} \left[\frac{3}{2} \left(\frac{C \cdot \mu_s (1 - \phi)}{\pi (1 - \nu_s)} \right)^2 p \right]^{\frac{1}{3}} \quad (6.92)$$

where

p is the hydrostatic pressure

C is the coordination number (number of contacts to neighbors). The coordination number correlates with the porosity (Table 2-5; Murphy, 1982; see Mavko et al., 1998).

Implementing Equations (6.91) and (6.92) into Equations (6.5) and (6.6) results in compressional and shear wave velocities. For sphere pack models, both wave velocities show identical dependence on porosity and pressure. Thus, the ratio is independent of porosity and pressure and only controlled by Poisson's ratio of the solid material ν_s :

$$\frac{V_p}{V_s} = \sqrt{\frac{10 - 7 \cdot \nu_s}{5 - 4 \cdot \nu_s}} \quad (6.93)$$

This derivation is valid only for a dry model.

6.7.3 Inclusion Models

In inclusion models, the pores or cracks/fractures are considered as voids or inclusions in a solid matrix—comparable to “Swiss cheese.” Such models are preferred for hard rocks with low porosity. Pores, vugs, or cracks are modeled as ellipsoidal inclusions in a solid host material. A variation of the shape of inclusions (from spheres to elliptic cracks or needles) and the properties of the inclusion (empty, gaseous, liquid, solid) opens a broad spectrum of cases.

For the calculation, it is assumed that the following:

- There is no fluid flow between the pores/fractures; this approach simulates very high-frequency saturated rock behavior (Mavko et al., 1998). Therefore Mavko et al. (1998) recommend: “it is better to find the effective moduli for dry cavities and then saturate them with the Gassmann low-frequency relations” (see [Section 6.7.5](#)).

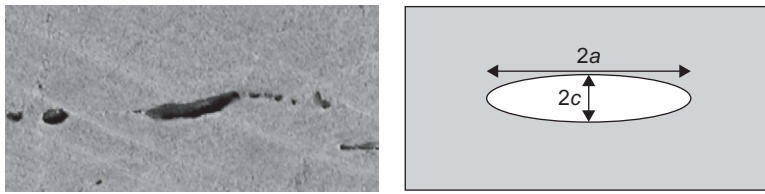


FIGURE 6.27 Definition of aspect ratio $\alpha = c/a$.

- Inclusions are sufficiently far apart from each other and do not interact elastically. An increase of porosity can be realized by a stepwise addition of several inclusions into the result of the foregoing step and use this as new “host material.”

Inclusions are idealized as spheres or ellipsoids (with the extreme shape of disks, needles, etc.). The shape is characterized by the aspect ratio (Figure 6.27). It should be noted that ellipsoidal pores for a given porosity are the “stiffest”; therefore modeled effects of velocity decrease tend to an overestimate of porosity (Cheng, 2008).

6.7.3.1 Kuster and Toksöz (1974)

Kuster and Toksöz (1974; see also Berryman, 1995; Toksöz et al., 1976) developed a theory based on first-order scattering (long wavelength) in a material containing spherical or spheroidal inclusions and calculated the effective moduli k_{KT} and μ_{KT} , where the overall effect of randomly oriented inclusions is isotropic:

$$\frac{k_{KT} - k_s}{k_{KT} + \frac{4}{3}\mu_s} = \frac{\sum_{i=1}^n \phi_i (k_i - k_s) P^{si}}{k_s + \frac{4}{3}\mu_s} \quad \frac{\mu_{KT} - \mu_s}{\mu_{KT} + \varsigma_s} = \frac{\sum_{i=1}^n \phi_i (\mu_i - \mu_s) Q^{si}}{\mu_s + \varsigma_s} \quad (6.94)$$

where

$$\varsigma_s = \frac{\mu_s}{6} \frac{9 \cdot k_s + 8 \cdot \mu_s}{k_s + 2 \cdot \mu_s} \quad (6.95)$$

where

ϕ_i is the volume fraction related to inclusion material i

k_i, μ_i are moduli of inclusion material i

k_s, μ_s are moduli of the solid host material (background).

Factors P^{si}, Q^{si} are related to the shape of the inclusions and refer to background (host) and inclusion properties. They are tabulated by Kuster and Toksöz (1974), Berryman (1995), and Mavko et al. (1998); see Table 6.14.

TABLE 6.14 Parameters P^{si}, Q^{si} for Spheres and Penny-Shaped Cracks with Random Distribution

Inclusion	P^{si}	Q^{si}
Sphere: general	$\frac{k_s + \frac{4}{3}\mu_s}{k_i + \frac{4}{3}\mu_s}$	$\frac{\mu_s + \varsigma_s}{\mu_i + \varsigma_s}$
Sphere: fluid filled	$\frac{k_s + \frac{4}{3}\mu_s}{k_i + \frac{4}{3}\mu_s}$	$\frac{\mu_s}{\varsigma_s} + 1$
Penny-shaped crack: general	$\frac{k_s + \frac{4}{3}\mu_i}{k_i + \frac{4}{3}\mu_i + \pi \cdot \alpha \cdot \beta_s}$	$\frac{1}{5} \left(1 + \frac{8 \cdot \mu_s}{4 \cdot \mu_i + \pi \cdot \alpha(\mu_s + 2 \cdot \beta_s)} + 2 \cdot \frac{k_i + \frac{2}{3}(\mu_i + \mu_s)}{k_i + \frac{4}{3}\mu_i + \pi \cdot \alpha \cdot \beta_s} \right)$
Penny-shaped crack: fluid filled	$\frac{k_s}{k_i + \pi \cdot \alpha \cdot \beta_s}$	$\frac{1}{5} \left(1 + \frac{8 \cdot \mu_s}{\pi \cdot \alpha(\mu_s + 2 \cdot \beta_s)} + 2 \cdot \frac{k_i + \frac{2}{3}\mu_s}{k_i + \pi \cdot \alpha \cdot \beta_s} \right)$
where	$\beta_s = \mu \cdot \frac{3 \cdot k_s + \mu_s}{3 \cdot k_s + 4 \cdot \mu_s}$	$\varsigma_s = \frac{\mu_s}{6} \cdot \frac{9 \cdot k_s + 8 \cdot \mu_s}{k_s + 2 \cdot \mu_s}$

Berryman (1995), Mavko et al. (1998).

For the simple case of one inclusion type (pore, fracture) with volume fraction (porosity) ϕ and a fluid inclusion filling ($\mu_i \rightarrow 0$), Equation (6.94) are

$$\frac{k_{KT} - k_s}{k_{KT} + \frac{4}{3}\mu_s} = \phi \frac{(k_i - k_s)}{k_s + \frac{4}{3}\mu_s} P^{si} \quad \frac{\mu_{KT} - \mu_s}{\mu_{KT} + \varsigma_s} = -\phi \frac{\mu_s}{\mu_s + \varsigma_s} Q^{si} \quad (6.96)$$

Solved for the moduli of the material, the results are

$$k_{KT} = \left(k_s + \phi \frac{\frac{4}{3}\mu_s(k_{fl} - k_s)}{k_s + \frac{4}{3}\mu_s} P^{si} \right) \left(1 - \phi \frac{(k_{fl} - k_s)}{k_s + \frac{4}{3}\mu_s} P^{si} \right)^{-1} \quad (6.97)$$

$$\mu_{KT} = \mu_s \left(1 - \phi \cdot Q^{si} \frac{\varsigma_s}{\mu_s + \varsigma_s} \right) \left(1 + \phi \cdot Q^{si} \frac{\mu_s}{\mu_s + \varsigma_s} \right)^{-1} \quad (6.98)$$

Table 6.14 gives the parameters P^{si}, Q^{si} for spheres and penny-shaped cracks with random distribution (the overall effect is isotropic).

For the simplest case of spherical inclusions, the moduli are

$$k_{KT} = \left(k_s + \phi \frac{\frac{4}{3}\mu_s(k_{fl} - k_s)}{k_{fl} + \frac{4}{3}\mu_s} \right) \left(1 - \phi \frac{k_{fl} - k_s}{k_{fl} + \frac{4}{3}\mu_s} \right)^{-1} \quad (6.99)$$

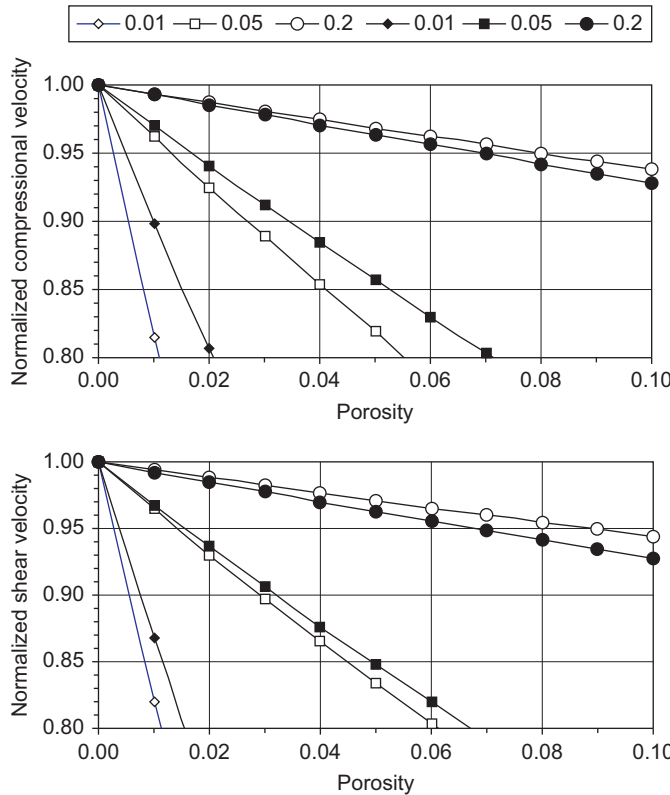


FIGURE 6.28 Normalized compressional and shear velocities as a function of porosity for inclusions filled with water (black symbols) and gas (white symbols), calculated for different aspect ratios (0.01, 0.05, 0.20). Input parameters are: $k_s = 37 \text{ GPa}$, $\mu_s = 44 \text{ GPa}$, $k_{\text{water}} = 2.2 \text{ GPa}$, $k_{\text{gas}} = 0.0015 \text{ GPa}$, $\rho_s = 2.65 \text{ g cm}^{-3}$, $\rho_{\text{water}} = 1.00 \text{ g cm}^{-3}$ (for calculations, visit website <http://www.elsevierdirect.com/companion.jsp?ISBN=9780444537966> and refer Elastic_Mechanical_Inclusion_isotropic).

$$\begin{aligned}
 \mu_{KT} &= \mu_s \cdot \frac{(1 - \phi) \cdot (9 \cdot k_s + 8 \cdot \mu_s)}{(9 \cdot k_s + 8 \cdot \mu_s) + 6 \cdot \phi \cdot (k_s + 2 \cdot \mu_s)} \\
 &= \frac{\mu_s \cdot (1 - \phi)}{1 + 6 \cdot \phi \cdot \frac{k_s + 2 \cdot \mu_s}{9 \cdot k_s + 8 \cdot \mu_s}}
 \end{aligned} \tag{6.100}$$

Figure 6.28 shows as an example of the calculation of normalized velocities versus volume concentration (porosity) of inclusions of different aspect ratios filled with water and gas. The “normalized velocity” is the ratio of calculated velocity and velocity for $\phi \rightarrow 0$ (velocity of host material without inclusion).

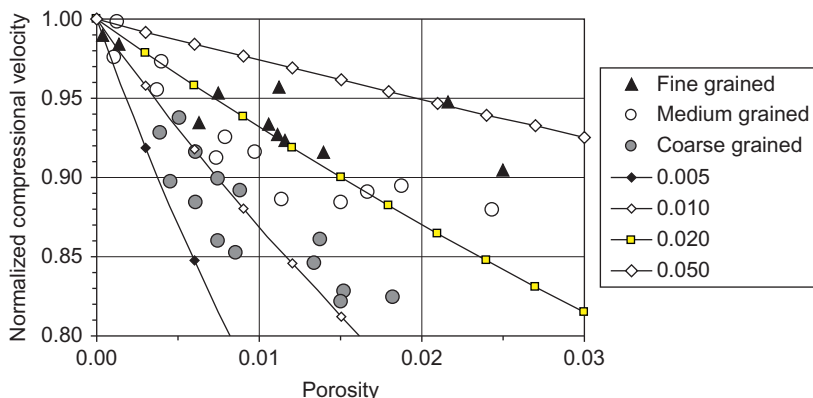


FIGURE 6.29 Normalized compressional velocity as a function of porosity for inclusions filled with water and gas, calculated for different aspect ratios (0.005, 0.01, 0.02, 0.05). Input parameters are: $k_s = 37 \text{ GPa}$, $\mu_s = 44 \text{ GPa}$, $k_{\text{gas}} = 0.0015 \text{ GPa}$, $\rho_s = 2.65 \text{ g cm}^{-3}$, $\rho_{\text{gas}} = 0.001 \text{ g cm}^{-3}$. Points are experimental data for granite after Lebedev et al. (1974; see Figure 6.5), normalized with $6,150 \text{ m s}^{-1}$.

Toksöz et al. (1976) commented on the results as follows:

- “... for a given concentration, the thinner (smaller aspect ratio) pore affects both compressional and shear velocities much more than the spherical pores ...;
- saturating fluids have greater effects on compressional velocities than on shear ...;
- relative effects of a given fluid on compressional and shear velocities depend upon the aspect ratio of the pores ...;
- effects of saturating fluids on velocity are still more complicated since the saturant also affects the density of the composite medium ... At small aspect ratios, both compressional and shear velocities are lower for the gas-saturated case ...”

Figure 6.29 shows a comparison with experimental data from Lebedev et al. (1974). Measured compressional wave velocities are normalized with a velocity for the compact solid material of $6,150 \text{ m s}^{-1}$.

Forward-calculated curves cover the experimental data and indicate that textural properties are connected with the aspect ratio between 0.005 and 0.050 as model input.

6.7.3.2 Budiansky and O'Connell (1976)

Inclusion solutions are applicable only for very low porosity or low concentration of inclusions. A method to extend these to some higher concentrations is the self-consistent approximation. This is done by mathematically replacing the solid material with the resulting effective medium (self-consistent)

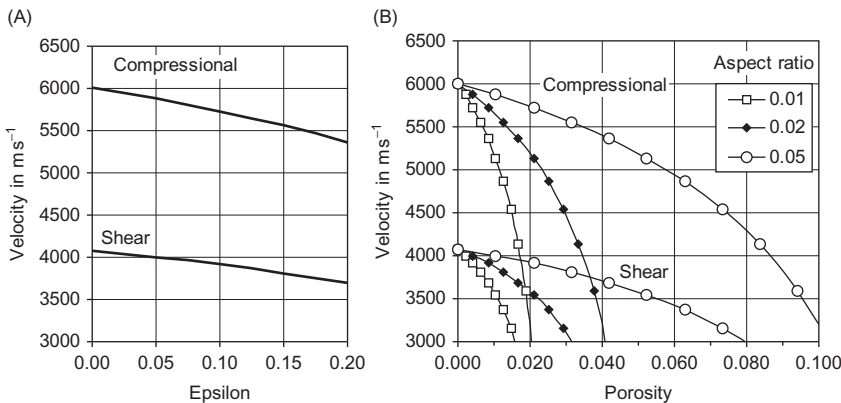


FIGURE 6.30 Velocities for dry penny-shaped inclusions as a function of the parameter ε (A) and as a function of porosity and aspect ratio α (B). Input parameters are: $k_s = 37 \text{ GPa}$, $\mu_s = 44 \text{ GPa}$, $\rho_s = 2.65 \text{ g cm}^{-3}$ (for calculations, visit the website <http://www.elsevierdirect.com/companion.jsp?ISBN=9780444537966> and refer Elastic_Mechanical_Inclusion_isotropic).

stepwise. The method was developed and promoted mainly by Budiansky and O'Connell (1976).

The equations for a penny-shaped cracked medium assume again as an inclusion an ellipsoid with a short axis $2c$ and a long axis $2a$.

For low aspect ratio, the effective bulk and shear moduli for a dry material are:

$$k_{\text{SC}} = k_s \left[1 - \frac{16}{9} \frac{1 - \nu_{\text{SC}}^2}{1 - 2 \cdot \nu_{\text{SC}}} \varepsilon \right] \quad \mu_{\text{SC}} = \mu_s \left[1 - \frac{32}{45} \frac{(1 - \nu_{\text{SC}})(5 - \nu_{\text{SC}})}{2 - \nu_{\text{SC}}} \varepsilon \right] \quad (6.101)$$

where ε is a “crack density parameter,” defined as the number of cracks per unit volume N/V times the crack radius cubed (Mavko et al., 1998):

$$\varepsilon = \frac{N}{V} a^3 \quad (6.102)$$

and the crack porosity is

$$\phi_c = \frac{4 \cdot \pi}{3} \alpha \cdot \varepsilon \quad (6.103)$$

The effective Poisson's ratio ν_{SC} is related to ε and to Poisson's ratio of the (uncracked) host material ν_s

$$\varepsilon = \frac{45}{16} \frac{(\nu - \nu_{\text{SC}})(2 - \nu_{\text{SC}})}{(1 - \nu_{\text{SC}}^2)(10 \cdot \nu_s - 3 \cdot \nu_s \cdot \nu_{\text{SC}} - \nu_{\text{SC}})} \quad (6.104)$$

For a calculation, this equation must be solved first for ν_{SC} for a given ε .

Then, using Equation (6.101), the effective bulk modulus k_{SC} and shear modulus μ_{SC} can be derived.

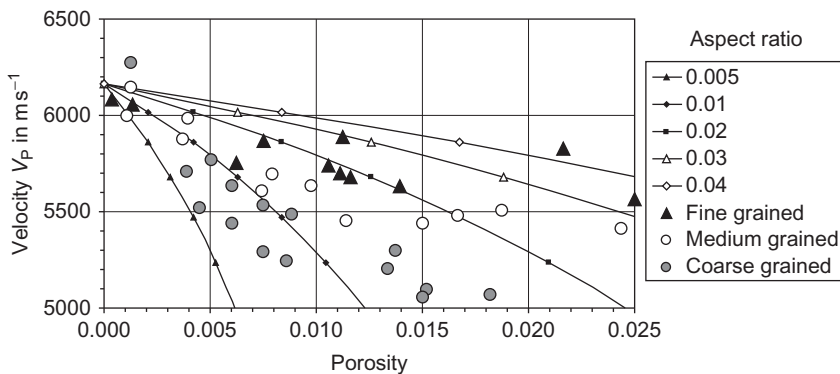


FIGURE 6.31 Compressional wave velocity versus crack porosity. Curves are calculated for penny-shaped inclusions with different aspect ratio α (0.005–0.04); input parameters are: $k_s = 44$ GPa, $\mu_s = 37$ GPa, $\rho_s = 2.65$ g cm $^{-3}$. Points are experimental data for granite after Lebedev et al. (1974; Figure 6.5).

Calculation is simplified by the nearly linear dependence of ν_{SC} on ε (Mavko et al., 1999):

$$\nu_{SC} \approx \nu_s \left(1 - \frac{16}{9} \varepsilon \right) \quad (6.105)$$

All equations express the strong influence of ε (and not primary ϕ_c). Figure 6.30 shows the calculated velocities for dry penny-shaped inclusions as a function of the parameter ε (Figure 6.30A) and as a function of porosity and aspect ratio (Figure 6.30B).

Figure 6.31 shows a comparison of calculated compressional velocities with experimental data from measurements on granite of different grain sizes (Lebedev et al., 1974). Forward-calculated curves cover the experimental data and indicate also for this model that textural properties are connected with the aspect ratio as model input.

Berryman (1995; see also Mavko et al., 1998) gives a more general form of the self-consistent approximation for n components (i is the index of the individual component):

$$\sum_{i=1}^n x_i (k_i - k_{SC}) P^{*i} = 0 \quad \sum_{i=1}^n x_i (\mu_i - \mu_{SC}) Q^{*i} = 0 \quad (6.106)$$

where the superscript $*i$ on P and Q indicates that the factors are for an inclusion of material i in a background medium with self-consistent effective moduli k_{SC}^* and μ_{SC}^* . The equations must be solved by simultaneous iteration (Mavko et al., 1998).

6.7.3.3 Hudson (1980)

Hudson (1980, 1981) modeled the fractured rock as an elastic solid with thin, penny-shaped ellipsoidal cracks or inclusions. Calculation with

TABLE 6.15 First Correction Terms for a Single Crack Set

The Crack Normals Are Aligned Along the 3-Axis (z-Axis); Horizontal Cracks, VTI Medium	The Crack Normals Are Aligned Along the 1,2-Axis (x-,y-Axis); Vertical Cracks, HTI Medium
$c_{11}^1 = -\frac{\lambda_s^2}{\mu_s} \varepsilon \cdot U_3$	$c_{11}^1 = -\frac{(\lambda_s + 2\mu_s)^2}{\mu_s} \varepsilon \cdot U_3$
$c_{13}^1 = -\frac{\lambda_s(\lambda_s + 2\mu_s)}{\mu_s} \varepsilon \cdot U_3$	$c_{13}^1 = -\frac{\lambda_s(\lambda_s + 2\mu_s)}{\mu_s} \varepsilon \cdot U_3$
$c_{33}^1 = -\frac{(\lambda_s + 2\mu_s)^2}{\mu_s} \varepsilon \cdot U_3$	$c_{33}^1 = -\frac{\lambda_s^2}{\mu_s} \varepsilon \cdot U_3$
$c_{44}^1 = -\mu_s \cdot \varepsilon \cdot U_1$	$c_{44}^1 = 0$
$c_{66}^1 = 0$	$c_{66}^1 = -\mu_s \cdot \varepsilon \cdot U_1$

scattering theory analysis of the mean wave field results in the effective moduli in the following form (see also Cheng, 1993; Hudson and Knopoff, 1989; Maultzsch, 2001; Mavko et al., 1998):

$$c_{ij}^{\text{eff}} = c_{ij}^0 + c_{ij}^1 \quad (6.107)$$

where

c_{ij}^0 are the isotropic background moduli
 c_{ij}^1 are the first-order corrections.⁸

While in the Kuster and Toksöz model, randomly distributed cracks are assumed and an isotropic effect results, Hudson's concept results in an anisotropy effect caused by the oriented fractures.

For a single crack set, the first correction terms are given in Table 6.15. Please note that in Equation (6.107), the correction term is added, but Table 6.15 shows that the correction term is negative—thus, elastic properties decrease with fracturing.

λ_s, μ_s are Lame constants of the solid host material (background material); the crack density is

$$\varepsilon = \frac{3 \cdot \phi}{4 \cdot \pi \cdot \alpha} \quad (6.108)$$

⁸Hudson also introduced a second-order correction. Mavko et al. (1998) notes: “The second-order expansion is not a uniformly converging series and predicts increasing moduli with crack density beyond the formal limit. Better results will be obtained by using just the first-order correction rather than inappropriately using the second-order correction.”

where

ϕ is the crack porosity

α is the aspect ratio.

The terms U_1 and U_3 depend on the crack-filling fluid properties. The general equations are (Mavko et al., 1998):

$$U_1 = \frac{16(\lambda_s + 2\mu_s)}{3(3\lambda_s + 4\mu_s)} \frac{1}{1+M} \quad U_3 = \frac{4(\lambda_s + 2\mu_s)}{3(\lambda_s + \mu_s)} \frac{1}{1+K} \quad (6.109)$$

$$\text{with } M = \frac{1}{\pi \cdot \alpha \cdot \mu_s} \frac{\mu_{fl}}{3\lambda_s + 4\mu_s} \quad \text{and} \quad K = \frac{(k_{fl} + \frac{4}{3}\mu_{fl})(\lambda_s + 2\mu_s)}{\pi \cdot \alpha \cdot \mu_s (\lambda_s + \mu_s)} \quad (6.110)$$

where k_{fl} and μ_{fl} are the bulk and shear moduli of the inclusion material, respectively.

For a dry rock, results are $M = 0$ and $K = 0$.

For a fluid-saturated rock (“weak inclusion”), results are

$$M = 0 \quad \text{and} \quad K = k_{fl} \frac{(\lambda_s + 2\mu_s)}{\pi \cdot \alpha \cdot \mu_s (\lambda_s + \mu_s)} \quad (6.111)$$

Hudson (1981) also considers in his model individual fractures isolated with respect to fluid flow. This again is given for high frequencies (ultrasonic). At low frequencies, there is time for wave-induced pore pressure gradients resulting in a fluid flow. For this case, Mavko et al. (1998) recommend that “it is better to find the effective moduli for dry cavities and then saturate them with the Brown and Korringa (1975) low-frequency relations.” Ass’ad et al. (1992) tested Hudson’s model. There is only a small influence of the second-order correction.

[Figure 6.32](#) shows calculated tensor elements as a function of porosity; velocities can be calculated for different wave types and propagation directions using [Equations \(6.20\) and \(6.21\)](#).

The calculated tensor elements allow studies of anisotropy as well as of the velocity ratio V_p/V_s . [Figure 6.33](#) gives an example of forward calculation for the shear wave anisotropy (Thomsen parameter γ) as a function of fracture porosity and aspect ratio. Clearly expressed is the strong influence of aspect ratio on anisotropy. Such studies can help to interpret and understand shear wave splitting effects.

6.7.4 A Simplified “Defect Model” for Fractured Rocks

Fractures, cracks and other defects of the solid mineralic substance change the elastic properties (and other physical properties like electrical, hydraulic, thermal) dramatically. Elastic wave velocities decrease and a strong dependence on pressure results. As demonstrated by experiments and the foregoing

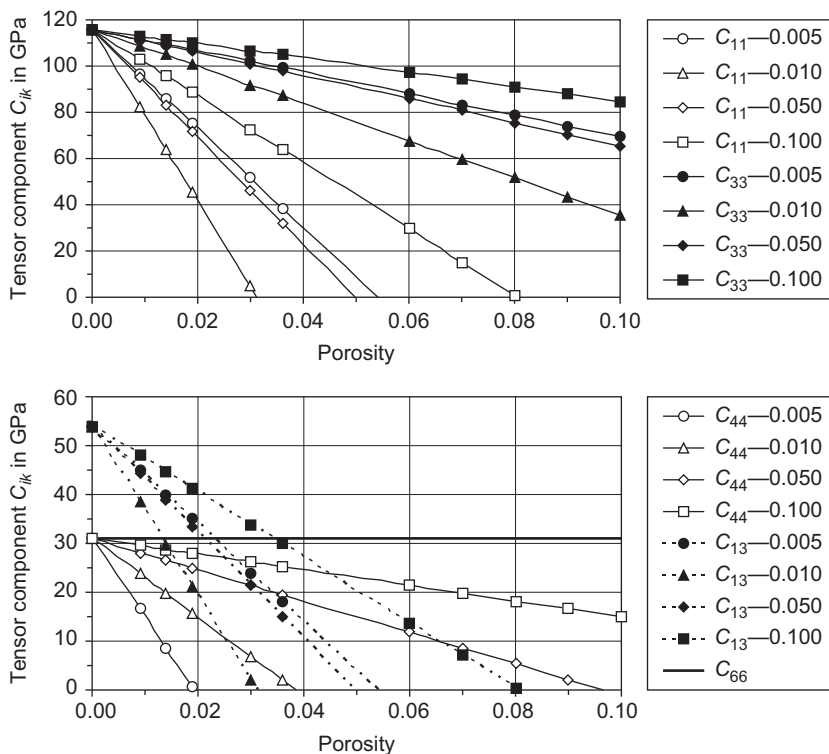


FIGURE 6.32 Hudson's model: calculated elements of the tensor of elasticity as a function of porosity (water-saturated rock). Input parameters are for the solid material (calcite) $\lambda_s = 54$ GPa, $\mu_s = 31$ GPa, and for the fluid $k_f = 2.2$ GPa: the curve parameter is the aspect ratio α . The upper figure shows c_{11} and c_{33} controlling compressional wave velocities in the main axis direction; the lower figure shows c_{44} and c_{66} controlling shear wave velocities in the main axis direction (note: c_{66} is not influenced by the low fracture porosity). Also plotted is the component c_{13} necessary for wave propagation deviating from the main axis direction (for calculations, visit the website <http://www.elsevierdirect.com/companion.jsp?ISBN=9780444537966> and refer Elastic_Mechanical. Inclusion anisotropic).

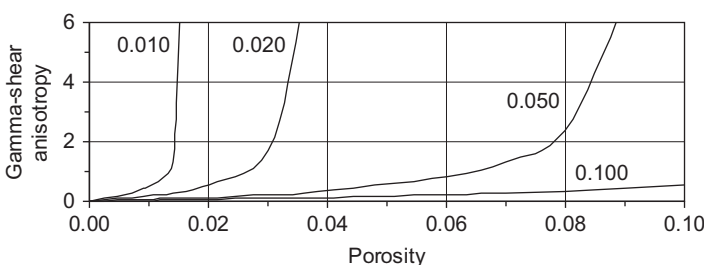


FIGURE 6.33 Hudson's model: calculated shear wave anisotropy (Thomsen parameter γ) as a function of porosity and aspect ratio α (curve parameter). Input parameters are for the solid material (calcite) $\lambda_s = 54$ GPa, $\mu_s = 31$ GPa, and for the fluid (water) $k_f = 2.2$ GPa.

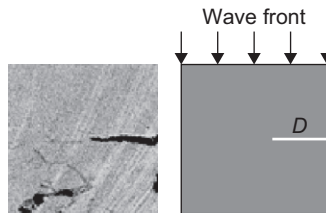


FIGURE 6.34 Simple model for a rock with internal defects (cracks, fractures, etc.) expressed by the parameter D .

sections, the porosity as the ratio of the volume of the defects (cracks, etc.) to the total volume alone cannot express these effects—microcracks with only a small porosity can significantly reduce the velocity (see, for example, Figure 6.5). Other parameters such as aspect ratio and crack density are necessary to describe the physical effects of these defects.

A very simplified model for such a fractured rock is demonstrated below (Schön, 1996). Starting with a cube of solid material, it is assumed that the effect of all defects (fractures, cracks, grain boundaries, intragranular defects, etc.) can be described by one “defect parameter” D (Figure 6.34).

This parameter is like a “cut” of the relative depth D . Neglecting terms of higher order and any effects of the pore fluid, the reduction of the compressional wave modulus results as

$$M_{\text{fractured rock}} = M_s(1 - D) \quad (6.112)$$

where $M_{\text{fractured rock}}$ is the resulting rock modulus and M_s is the modulus for the (defectless) solid matrix material. This relationship is based on the assumption that only the “uncut” part of the rock cross section controls the material rock stiffness.

Three remarks may be added to this simplified relationship.

Remark 1: The simple model has the same basic structure as theories discussed before. But these theories describe the effects in more detail:

The effective bulk and shear moduli for a dry material with penny-shaped cracks after Budiansky and O’Connell (1976; see Equation (6.101)) can be simplified as follows:

$$k_{\text{SC}} = k_s \left[1 - \frac{16}{9} \frac{1 - \nu_{\text{SC}}^2}{1 - 2 \cdot \nu_{\text{SC}}} \varepsilon \right] = k_s [1 - D_k] \quad (6.113)$$

$$\mu_{\text{SC}} = \mu_s \left[1 - \frac{32}{45} \frac{(1 - \nu_{\text{SC}})(5 - \nu_{\text{SC}})}{2 - \nu_{\text{SC}}} \varepsilon \right] = \mu_s [1 - D_\mu] \quad (6.114)$$

where D_k, D_μ refers to the defect effect, related to compressional and shear moduli, respectively.

Hudson's (1980, 1981) equation (see [Equation \(6.107\)](#)) can also be written in this form⁹:

$$c_{ij}^{\text{eff}} = c_{ij}^0 + c_{ij}^1 = c_{ij}^0(1 - D_{ij}) \quad (6.115)$$

Remark 2: Increasing pressure p results in a closure of fractures or—more generally—in a decrease of defects. With an exponential law (see Schön, 1996), the defect parameter as a function of pressure is

$$D(p) = D_0 \cdot \exp(-a \cdot p) \quad (6.116)$$

and velocity results as:

$$V_P(p) \approx V_{\text{solid}} \sqrt{1 - D_0 \cdot \exp(-a \cdot p)} \quad (6.117)$$

where

V_{solid} is the compressional wave velocity of the solid (unfractured) material

D_0 is the initial value of the defect parameter at the pressure $p = 0$
 a expresses the compressional characteristic of the (fractured) rock.

This type of velocity versus pressure relationship was used for an analysis of KTB (Continental Deep Drilling Project) rock samples (Schön, 1996). In this case, two exponential terms of the velocity–pressure function gave reasonable results. The first defect system is connected with the drilling/sampling process and the expansion of the material; the second, with the in situ stress and material conditions.

Remark 3: The same model can also be applied to other properties (e.g., thermal conductivity, strength, and for relationships between them (see Sections 7.5.8 and 11.3).

6.7.5 Gassmann and Biot Model—Modeling of Fluid Effects

The Gassmann model (Gassmann, 1951) estimates the elastic properties of a porous rock at one fluid state, and predicts the properties for another fluid state. Thus, it allows a “fluid substitution” or “fluid replacement.” This fluid substitution is an important part of the seismic rock physics analysis.

In the technical literature, some tutorial papers are published, for example, Wang (2001) and Smith et al. (2003). Kumar (2006) has given a tutorial connected with a MATLAB program.

6.7.5.1 Gassmann's Static Model

Gassmann (1951) developed a model for porous rocks that allows the prediction of velocities if rocks are saturated with one fluid (e.g., water) from velocities if rocks are saturated with a different second fluid (e.g., gas) and vice versa.

⁹Note that c_{ij}^1 are negative.

Gassmann's theory assumes (Dewar and Pickford, 2001) the following:

- The rock is macroscopically homogeneous and isotropic: This assumption ensures that wavelength > grain and pore size (this is given in most cases of seismic field and laboratory measurements). The statistical isotropic porous material with homogeneous mineral moduli makes no assumptions with respect to any pore geometry.
- Within the interconnected pores, there is a fluid pressure equilibrium and no pore pressure gradient as a result of passing waves. Thus, the low frequency allows an equilibration of the pore pressure within the pore space. Therefore, Gassmann's equation works best for seismic frequencies (<100 Hz) and high permeability (Mavko et al., 1998).
- Pores are filled with nonviscous, frictionless fluids. This also contributes to pore pressure equilibrium and results in a fluid independent shear modulus of the porous rock.
- The rock-fluid system is closed (undrained), that is, no fluid can flow in or out of the considered volume during wave passage.
- The pore fluid does not interact with the solid material or rock frame. Gassmann's model does not implement any change of the "rock skeleton or frame modulus" by changing fluids (e.g., softening in case of swelling clay cement by replacement of oil by water with reactive chemical composition or in general as a result of changing surface energy).
- A passing wave results in the motion (displacement) of the whole rock section, but there is no relative motion between solid rock skeleton and fluid. This exactly is given only for zero frequency (static solution); for high frequencies, a relative motion can result in dispersion.

Changing pore fluid influences velocity of elastic waves as a result of changing elastic moduli and changing density. The effects can be described as follows:

1. density follows the equation

$$\rho = (1 - \phi)\rho_s + \phi \cdot \rho_{fl} \quad (6.118)$$

2. shear modulus is independent on the fluid type

$$\mu_{dry} = \mu_{sat} = \bar{\mu} \quad (6.119)$$

3. compressional bulk modulus is strongly dependent on fluid compressional modulus and the key parameter in Gassmann's model. [Figure 6.35](#) explains the principle of the derivation for the two cases.

The left side describes the "dry case": the pores are empty and therefore pore fluid has zero bulk modulus and does not contribute to the compression resistance (pore fluid also has zero shear modulus). This situation is given approximately for air-filled rock at standard room temperature and pressure

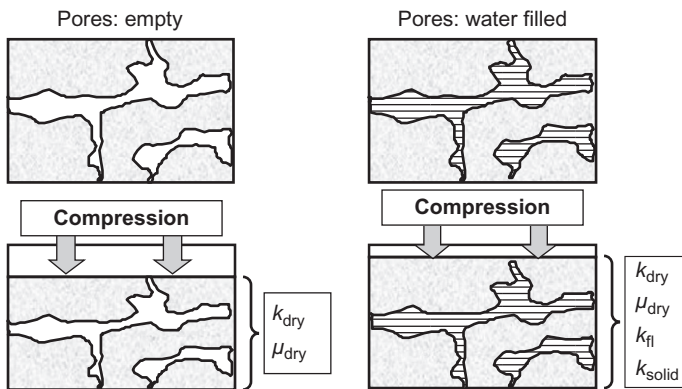


FIGURE 6.35 Derivation of Gassmann's equation. Left side: dry porous rock under the influence of a compression. Right side: fluid-saturated porous rock under the influence of a compression.

(Mavko et al., 1998). The deformation behavior is characterized by the two-frame or rock skeleton moduli $\bar{k}, \bar{\mu}$:

- the effective bulk modulus for the dry rock $k_{\text{dry}} = \bar{k}$
- the effective shear modulus for the dry rock $\mu_{\text{dry}} = \bar{\mu}$.

The right side describes the “fluid-saturated case.” The deformation behavior is characterized by two moduli:

1. The effective bulk modulus for the saturated rock $k_{\text{sat}} > k_{\text{dry}} = \bar{k}$
2. The effective shear modulus for the saturated rock, which is identical to the effective shear modulus for the dry rock $\mu_{\text{sat}} = \mu_{\text{dry}} = \bar{\mu}$, because the pore fluid does not contribute to the shear moduli.

The effective bulk modulus for the saturated rock k_{sat} results from the combined effect of the deformation of the rock skeleton, the solid components, and the fluid (the fluid contributes to the compression resistance).

The derivation considers the coupled contributions to the total volume change and the participating pressure components (effective pressure and pore pressure). The resulting bulk modulus for the saturated rock is therefore greater than for the dry rock (note that in the figure the deformation is therefore smaller) and can be expressed by the following equation, where the second term gives the “modulus magnification” as a result of pore fluid effects and interactions with solid components:

$$k_{\text{sat}} = k_{\text{dry}} + \frac{\left(1 - \frac{k_{\text{dry}}}{k_s}\right)^2}{\frac{\phi}{k_{\text{fl}}} + \frac{1 - \phi}{k_s} - \frac{k_{\text{dry}}}{k_s^2}} \quad (6.120)$$

or

$$\frac{k_{\text{sat}}}{k_s - k_{\text{sat}}} = \frac{k_{\text{dry}}}{k_s - k_{\text{dry}}} + \frac{k_{\text{fl}}}{\phi(k_s - k_{\text{fl}})} \quad (6.121)$$

where

k_{sat} is the effective bulk modulus of the rock with pore fluid

k_{dry} is the effective bulk modulus of the drained or dry rock (“framework”)¹⁰

k_s is the bulk modulus of the solid rock component

k_{fl} is the bulk modulus of the pore fluid

ϕ is the porosity.

The two moduli and the density give the velocities:

$$V_p = \sqrt{\frac{k + \frac{4}{3}\mu}{\rho}} = \sqrt{\frac{\frac{k_{\text{dry}} + \left(1 - \frac{k_{\text{dry}}}{k_s}\right)^2}{\phi} + \frac{4}{3}\mu_{\text{dry}}}{\frac{k_{\text{fl}}}{k_s} + \frac{1 - \phi}{k_s} - \frac{k_{\text{dry}}}{k_s^2} + \frac{(1 - \phi)\rho_s + \phi \cdot \rho_{\text{fl}}}{(1 - \phi)\rho_s + \phi \cdot \rho_{\text{fl}}}}} \quad (6.122)$$

$$V_s = \sqrt{\frac{\mu}{\rho}} = \sqrt{\frac{\mu_{\text{dry}}}{(1 - \phi)\rho_s + \phi \cdot \rho_{\text{fl}}}} \quad (6.123)$$

The process of a fluid substitution for a porous rock with porosity ϕ in practice has the following steps.

Step 1: Compile the material properties of the components:

Moduli: k_s (solid mineral component), $k_{\text{fl},1}$ (fluid 1), $k_{\text{fl},2}$ (fluid 2)

Densities: ρ_s (solid mineral component), $\rho_{\text{fl},1}$ (fluid 1), $\rho_{\text{fl},2}$ (fluid 2).

Step 2: Read from measurements the velocities at saturation with fluid 1 ($V_{p,1}$, $V_{s,1}$) and the porosity ϕ .

Then calculate the effective bulk moduli $k_{\text{sat},1}, \mu_{\text{sat},1}$ (use Equations 6.122 and 6.123).

Step 3: Calculate $k_{\text{dry}} = \bar{k}$ (using Equation (6.120))

¹⁰The modulus is frequently given as \bar{k} .

Step 4: Calculate effective bulk modulus for the replaced fluid saturation 2 (use Equation 6.120).

Step 5: Calculate density for fluid saturation 2 with $\rho = (1 - \phi)\rho_s + \phi \cdot \rho_{fl,2}$

Step 6: Calculate velocities for the rock with fluid saturation 2 with the new parameters using Equations (6.122) and (6.123).

On the website <http://www.elsevierdirect.com/companion.jsp?ISBN=9780444537966> is an Excel spreadsheet for fluid substitution (Elastic_Mechanical. Fluid replacement). An example is given at the end of this chapter in Section 6.10 (also on the website <http://www.elsevierdirect.com/companion.jsp?ISBN=9780444537966>).

An extension of Gassmann's model for anisotropic rocks was published by Brown and Korringa (1975) and Carcione (2001).

6.7.5.2 Biot's Dynamic Model (Frequency Effects)

Gassmann's model assumes no relative motion between the rock skeleton and the fluid (no pressure gradient) during the pass of a wave ("low-frequency case"). Biot's model (Biot, 1956a, 1956b; 1962) considers a relative fluid motion of rock skeleton versus fluid. With this step combined with Gassmann's material parameters, fluid viscosity η and hydraulic permeability k must be implemented. The implementation of viscous flow results in:

- frequency dependence of velocities;
- viscous wave attenuation.

A central parameter of Biot's concept is the "characteristic frequency:"

$$f_c = \frac{\phi \cdot \eta}{2\pi \cdot \rho_{fl} \cdot k} \quad (6.124)$$

which separates a low-frequency range ($f < f_c$) and a high frequency range ($f > f_c$). Low-frequency solution is identical to Gassmann's result. Table 6.16 gives some values for Biot's characteristic frequency.

Geertsma and Smith (1961) derived an approximate solution for velocity equations in Biot's model and expressed deformation properties in terms of compressional moduli for practical purpose (see also Bourbie et al., 1987).

Compressional wave velocity as a function of frequency f is

$$\frac{V_p^2 = V_{p\infty}^4 + V_{p0}^4 \left(\frac{f_c}{f}\right)^2}{V_{p\infty}^2 + V_{p0}^2 \left(\frac{f_c}{f}\right)^2} \quad (6.125)$$

where

V_{P0} is the low-frequency solution after Gassmann (Equation (6.122))
 $V_{P\infty}$ is the high frequency solution.

$$V_{P\infty} = \sqrt{\frac{k_{\text{dry}} + \frac{4}{3} \cdot \mu_{\text{dry}} + \frac{\frac{\phi}{a} \cdot \rho_{\text{fl}} + \left(1 - \frac{k_{\text{dry}}}{k_s}\right) \cdot \left(1 - \frac{k_{\text{dry}}}{k_s}\right) \cdot \left(1 - \frac{k_{\text{dry}}}{k_s} - 2 \cdot \frac{\phi}{a}\right)}{\left(1 - \frac{k_{\text{dry}}}{k_s} - \phi\right) \cdot \frac{1}{k_s} + \frac{\phi}{k_{\text{fl}}}}}{(1 - \phi) \cdot \rho_s + \phi \cdot \rho_{\text{fl}} \cdot (1 - a^{-1})}} \quad (6.126)$$

and the shear wave velocity is

$$V_{S\infty} = \sqrt{\frac{\mu_{\text{dry}}}{(1 - \phi) \cdot \rho_s + \phi \cdot \rho_{\text{fl}} \cdot (1 - a^{-1})}} \quad (6.127)$$

where a is a tortuosity term.¹¹

TABLE 6.16 Some Values for Biot's Characteristic Frequency

Sample	ϕ	k in md	Characteristic Frequency f_c in Hz		
			Water $\eta = 1 \text{ cP}$	Normal Oil $\eta = 10-50 \text{ cP}$	Heavy Oil $\eta = 100-500 \text{ cP}$
Fontainbleau sandstone	0.05	0.10	$80 \cdot 10^6$	$(0.8-4.0) \cdot 10^9$	$(8-40) \cdot 10^9$
Fontainbleau sandstone	0.20	1000	$30 \cdot 10^3$	$(0.3-1.5) \cdot 10^3$	$(3-15) \cdot 10^3$
Tight sand	0.08	0.02	$1.0 \cdot 10^9$	$(10-50) \cdot 10^9$	$(100-500) \cdot 10^9$
Cordova Cream limestone	0.245	9	$4.5 \cdot 10^6$	$(45-230) \cdot 10^6$	$(0.45-2.3) \cdot 10^9$
Sintered glass	0.283	1000	$42 \cdot 10^3$	$(0.42-2.1) \cdot 10^6$	$(4.2-21) \cdot 10^9$

From Bourbie et al. (1987)

ϕ , porosity as volume fraction; k , permeability in md; η , viscosity in centiPoise cP.

6.7.5.3 Some Further Developments of the Gassmann–Biot Concept

An extended overview of the various theoretical concepts and their applications is given by Mavko et al. (1998). The different types of fluid motion in the pore

¹¹For $a \rightarrow \infty$ (no fluid movement possible) is $V_{\infty} \rightarrow V_0$.

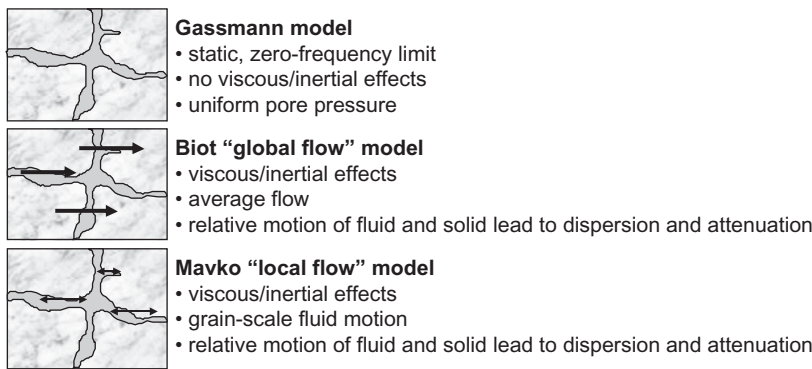


FIGURE 6.36 Schematic sketch of some developments of the Gassmann–Biot concept (adapted after Mavko/Stanford University).

space are discussed and developed with particular emphasis. Gassmann's model considers no fluid flow (static case), whereas Biot's model assumes a “global flow.” Murphy (1982, 1984) and Mavko and Jizba (1991) derived a “local squirt flow model” with unequal pore pressure for velocity and attenuation. Figure 6.36 shows a schematic sketch of some of these concepts.

6.7.6 The Problem of Multiphase Pore Fluids

Typical values of bulk modulus for single fluids in the pore space are (see also Section 6.2.3)

$$k_{\text{gas}} = k_{\text{g}} = 0.02 \text{ GPa}, k_{\text{oil}} = k_{\text{o}} = 0.80 \text{ GPa}, k_{\text{water}} = k_{\text{w}} = 2.2 \text{ GPa}$$

There is an especially big difference between gas and oil/water. In the case of a multiphase fluid in the pore (partial saturation), the effective modulus k_{fl} is controlled by:

- the elastic properties of the components and their volume fractions (saturation);
- the distribution of the fluid phases in the pore space; this is controlled by pore size distribution and wettability, and this is therefore connected with capillary pressure.

The simplest case is a uniform distribution of the phases. In this case (isostress), the Reuss average can be applied:

$$\frac{1}{k_{\text{fl}}} = \sum_i \frac{S_i}{k_i} \quad (6.128)$$

where S_i is the volume fraction (saturation) and k_i is the bulk modulus of fluid i .

For a gas–oil–water mixture, the equation results as:

$$\frac{1}{k_{\text{fl}}} = \frac{S_w}{k_w} + \frac{S_o}{k_o} + \frac{S_g}{k_g} \quad (6.129)$$

With this averaging method, the modulus of the mixture is dominated by the phase with the lowest modulus (highest compressibility). For a water–gas or oil–gas mixture (gas and water or oil, respectively, are evenly distributed in each pore), it results in a “jump” from the k_g level to k_w level immediately at $S_w \rightarrow 1$.

A “patchy saturation” is given when fluids are not uniformly mixed. Effective modulus values cannot be estimated from Reuss averaging (lowest level); an upper limit is given by Voigt’s averaging:

$$k_{\text{fl}} = \sum_i S_i \cdot k_i \quad (6.130)$$

or for a gas–oil–water mixture:

$$k_{\text{fl}} = S_w \cdot k_w + S_o \cdot k_o + S_g \cdot k_g \quad (6.131)$$

Voigt and Reuss equations in general describe the upper and lower limit of the compressional modulus for a mixture (Section 6.7.1).

Domenico (1976) notes that Voigt’s averaging gives the best estimate when patch sizes are large with respect to the seismic wavelength.

Endres and Knight (1989) calculated the effect of various geometrical distributions of water and gas in the pore space upon the velocity-saturation characteristic. Pores are assumed to be spheres and ellipsoids with four different saturation regimes. For calculation, the model of Kuster and Toksöz (1974) was used. Results demonstrate the strong influence of saturation distribution related to various pores on the overall elasticity. This general model concept was applied also by Sengupta and Mavko (2003).

Research by Brie et al. (1995) took a somewhat different approach, deriving an equation that fills the region between Reuss’s (Equation (6.129)) and Voigt’s (Equation (6.130)) boundary by introducing an average mixing exponent e :

$$k_{\text{fluid mixture}} = (k_w - k_g)S_w^e + k_g \quad (6.132)$$

Figure 6.37 shows a plot of fluid bulk modulus versus water saturation with mixing coefficient e as the parameter.

6.7.7 Model with Internal Structure and Bonding Properties

6.7.7.1 The Concept of a “Structured Model”

For porous rocks—particularly sandstones—a model was developed (Schön, 1996) in order to describe various influences on physical properties and the relationships between them. In addition to the properties of the components

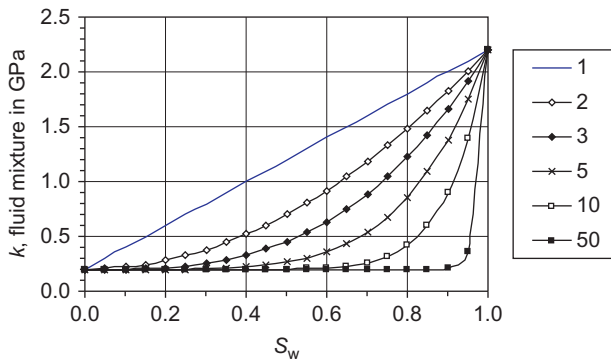


FIGURE 6.37 Fluid bulk modulus versus water saturation with mixing coefficient e as the parameter; $k_{\text{gas}} = 0.02 \text{ GPa}$, $k_{\text{water}} = 2.2 \text{ GPa}$.

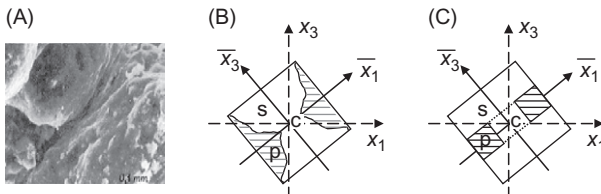


FIGURE 6.38 A model for porous rocks including a variable internal structure—principle of derivation (Schön, 1996).

and the porosity, simplified measures for the internal structure and texture are also implemented.

Figure 6.38 demonstrates the concept. Starting with a homogeneous section of a real porous rock (Figure 6.38A), a stepwise idealization gives the model for calculations. Three different parts of the rock are defined:

1. Solid matrix material (subscript s)
2. Pore fluid (subscript p)
3. Contact region (subscript c) with properties that may be different from those of the solid matrix material as a result of a different substance (cement) and/or the particular shape of the contact.

These three parts are shown in Figure 6.38B as a rock element and referenced to two Cartesian coordinate systems:

1. The “macrosystem” $x_1 - x_2 - x_3$: The x_3 -axis is vertical (up). This system refers to measurements of bulk properties.
2. The “microsystem” $\bar{x}_1 - \bar{x}_2 - \bar{x}_3$: This system is related to the microscopic structure of the two rock particles and their pore space. The

$\bar{x}_1 - \bar{x}_2$ plane is the plane of the particle contact and the \bar{x}_3 -axis is the normal direction upwards on this plane.

Microsystem related to macrosystem is described by a statistically defined angle α (between x_3 and \bar{x}_3). This angle is a measure for the internal structure of the rock and is therefore called “structure angle.”

For further consideration, the rock element is idealized as a model with rectangular cross section (Figure 6.38C). Thus, finally the model consists of a rectangular block with a surrounding pore channel and a special contact region, and has a spatial orientation.

The following influences can be simulated in a very simplified manner:

- by variation of the material properties for the solid block and the pore channels, the influence of matrix and pore fluid properties is implemented;
- by the variation of properties of the contact region, a consideration of different kinds of “bonding” (e.g., cementation) and of the pressure influence is possible;
- by variation of the relative volume of the block and pore channel porosity changes;
- by variation of the cross section of the block, “grain shape” and of the pore channel, “pore shape” varies. Absolute dimensions simulate the “grain size,”
- by variation of the angle α , the internal structure (texture) is modified; the model has the geometry of a transverse isotropic material.

Figure 6.39 shows the model with the pore channel and the signature for the geometrical description in the microsystem. The following parameters are used to describe the “pore and grain geometry”:

$$\text{grain size} = 2 \cdot a \quad \text{pore size} = 2 \cdot b$$

$$\text{grain aspect ratio } \alpha_{\text{grain}} = \frac{\text{grain dimension in } x_3 - \text{direction}}{\text{grain dimension in } x_1 - x_2 - \text{direction}}$$

$$\text{pore aspect ratio } \alpha_{\text{pore}} = \frac{\text{pore dimension in } x_3 - \text{direction}}{\text{pore dimension in } x_1 - x_2 - \text{direction}}$$

The porosity of the model is

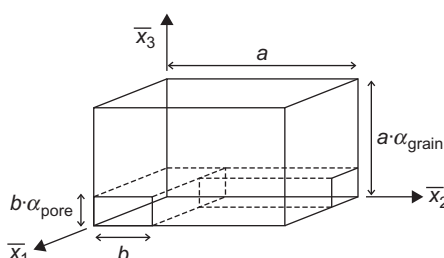


FIGURE 6.39 Geometry of the model element in coordinates of the microsystem.

$$\phi = \frac{\text{volume pore space}}{\text{total model volume}} = \frac{b^2 \cdot \alpha_{\text{pore}}(a + a - b)}{a^3 \cdot \alpha_{\text{grain}}} = \frac{\alpha_{\text{pore}}}{\alpha_{\text{grain}}} \left(\frac{b}{a}\right)^2 \left(2 - \frac{b}{a}\right) \quad (6.133)$$

Any calculation of physical bulk properties follows two steps:

1. Calculation of properties with respect to the microsystem
2. Transformation of the properties into the macrosystem.

6.7.7.2 General Equation for Velocities

For the calculation of the elastic properties in the microsystem, the porous rock is considered as a parallel and series arrangement of springs with the properties of the matrix and the contact region. For simplification, it is assumed that the solid part of the model is divided into one half of pure solid matrix material (modulus M_s) and one half of the contact region material (modulus M_c). All calculations are simplified for linear terms.

It is assumed that the pore space is empty (dry rock). The contribution of the pore fluid can be implemented in a second step using the Biot–Gassmann theory.

For the velocities (compressional and shear) results (Schön, 1996):

$$V = \left\{ \left[\frac{M_s}{\rho_s} \right] \left[2 \left(1 + \frac{M_s}{M_c} \right)^{-1} \right] \left[\frac{G}{1 - \phi} \right] [s_{ik}(\alpha, f)] \right\}^{\frac{1}{2}} \\ = f_1(s) f_2 \left(\frac{M_s}{M_c}, p \right) f_3(G, \phi) f_4(\alpha, f) \quad (6.134)$$

where

M_s is the compressional wave modulus of the solid matrix material

M_c is the compressional wave modulus of the contact region

ρ_s is the density of the solid matrix

ϕ is the porosity

G is a geometric parameter that contains only geometric properties of the grain and pore, and is related to the porosity:

$$G = \left[1 - \frac{\alpha_{\text{pore}}}{\alpha_{\text{grain}}} \frac{b}{a} \left(1 - \left(1 - \frac{b}{a} \right)^{-2} \right) \right]^{-1} \quad (6.135)$$

$S_{ik}(\alpha, f)$ is the element of a “structure tensor.”

The elements of the tensor S_{ik} depend only on the structure angle α and on a bonding parameter f defined as the ratio of the compressional and shear deformation properties of the matrix and contact region (see Equation

(6.145)). The tensor S_{ik} has the symmetry of a transversely isotropic medium:

$$S_{ik} = \begin{bmatrix} s_{11} & s_{11} - 2s_{66} & s_{13} & 0 & 0 & 0 \\ s_{11} - 2s_{66} & s_{11} & s_{13} & 0 & 0 & 0 \\ s_{13} & s_{13} & s_{33} & 0 & 0 & 0 \\ 0 & 0 & 0 & s_{44} & 0 & 0 \\ 0 & 0 & 0 & 0 & s_{44} & 0 \\ 0 & 0 & 0 & 0 & 0 & s_{66} \end{bmatrix} \quad (6.136)$$

The velocity in Equation (6.134) is given as a product of four factors. Each factor contains a special ““group of influences””:

1. The first factor contains only the solid matrix properties and is identical to the compressional wave velocity for the pore-free matrix.
2. The second factor contains the influence of the contact region with its different properties related to the matrix material; this influence is expressed by the ratio of the two moduli. The term also contains the pressure dependence of the velocity controlled by a strong pressure dependence of the contact elasticity (modulus M_c).
3. The third factor contains the influence of porosity ϕ and model- (or grain-) shape G .
4. The fourth factor is an element of the structure tensor (Equation (6.136)) and depends on the internal structure (expressed by the angle α) and the parameter f , which is controlled by the ““bonding properties”” of the contact. Compressional and shear waves with propagation in vertical and horizontal directions differ only in this last term. Which component must be used depends on the wave type of interest:
 - a. Compressional wave, horizontal $\rightarrow s_{11}$
 - b. Compressional wave, vertical $\rightarrow s_{33}$
 - c. Shear wave, horizontal propagation, vertical polarization and shear wave vertical propagation, horizontal polarization $\rightarrow s_{44}$
 - d. Shear wave, horizontal propagation, horizontal polarization $\rightarrow s_{66}$.

It follows immediately that for a dry rock the velocity ratios (e.g., V_p/V_s , elastic anisotropy parameters) depend only on structural and bonding properties.

In the following sections, the factors are discussed with respect to the influence on velocity.

6.7.7.3 Discussion of the ““Porosity Factor””

The factor

$$\frac{V}{V_1} = \left\{ \frac{G}{1 - \phi} \right\}^{\frac{1}{2}} = \left\{ (1 - \phi) \left[1 - \frac{\alpha_{\text{pore}}}{\alpha_{\text{grain}}} \frac{b}{a} \left(1 - \left(1 - \frac{b}{a} \right)^{-2} \right) \right] \right\}^{-\frac{1}{2}} \quad (6.137)$$

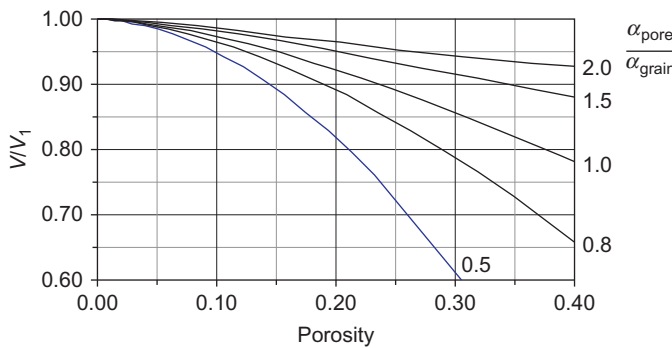


FIGURE 6.40 Porosity-controlled change of velocity V/V_1 for different ratios $\alpha_{\text{pore}}/\alpha_{\text{grain}}$ (for calculations, visit the website <http://www.elsevierdirect.com/companion.jsp?ISBN=9780444537966> and refer Elastic_Mechanical_Structured model).

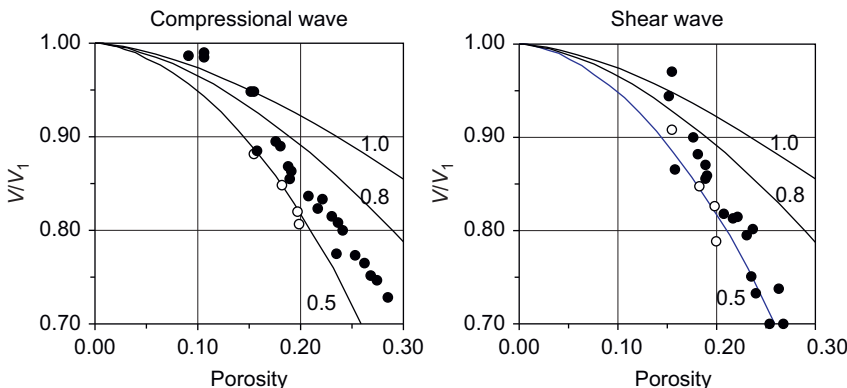


FIGURE 6.41 Model-calculated dependence of wave velocity on porosity (curve parameter is the ratio $\alpha_{\text{pore}}/\alpha_{\text{grain}}$) compared with experimental data from Han et al. (1986) after fluid replacement from water saturated to dry. White-filled circles represent samples with $V_{\text{shale}} = 0$ and black-filled circles represent samples with $0 > V_{\text{shale}} > 0.1$. Left side: compressional wave velocity, calculated with $V_{\text{P1}} = 5.4 \text{ km s}^{-1}$ (for $V_{\text{shale}} = 0$) and $V_{\text{P1}} = 4.7 \text{ km s}^{-1}$ (for $0 > V_{\text{shale}} > 0.1$). Right side: shear wave velocity, calculated with $V_{\text{S1}} = 3.3 \text{ km s}^{-1}$ (for $V_{\text{shale}} = 0$) and $V_{\text{S1}} = 2.8 \text{ km s}^{-1}$ (for $0 > V_{\text{shale}} > 0.1$).

contains the influence of the grain/pore geometry and is related to the porosity (Equation (6.133)) by the model parameters. The term V_1 summarizes all other velocity influences. Figure 6.40 shows this “porosity factor” as a function of the porosity for different grain/pore geometries.

The ratio $\alpha_{\text{pore}}/\alpha_{\text{grain}}$ strongly controls the shape of the velocity–porosity curve. The relative increase of the pore aspect ratio decreases the contact cross section and decreases the velocities.

In Figure 6.41, the calculated change of velocity with porosity is compared with the experimental results from Han et al. (1986) in Figure 6.7. For

a direct comparison, the velocities from experiments are converted to dry status by Gassmann's equation. Clean and shaly sandstone shows different values for V_1 and for the ratio $\alpha_{\text{pore}}/\alpha_{\text{grain}}$.

6.7.7.4 Discussion of the "Contact Elasticity Factor"

The factor

$$\left[2 \left(1 + \frac{M_s}{M_c} \right)^{-1} \right]^{\frac{1}{2}} \quad (6.138)$$

describes the influence of the elastic properties of the contact between the solid components (grain–grain contact, cementation, etc.). For $M_c \rightarrow M_s$ the factor becomes 1. The velocity equation can be written as follows:

$$V = \left\{ \left[\frac{M_s}{\rho_s} \right] \left[2 \left(1 + \frac{M_s}{M_c} \right)^{-1} \right] \left[\frac{G}{1 - \phi} \right] [s_{ik}(\alpha, f)] \right\}^{\frac{1}{2}} = V_2 \left[2 \left(1 + \frac{M_s}{M_c} \right)^{-1} \right]^{\frac{1}{2}} \quad (6.139)$$

where V_2 contains all other influences.

The factor (6.138) also covers the pressure influence on the rock skeleton elastic properties. Hertz's theory applied on the grain–grain contact results in a power law:

$$M_c = M_{\text{co}} \left(\frac{p}{p_{\text{reference}}} \right)^m \quad (6.140)$$

where p is the (variable) effective pressure and $p_{\text{reference}}$ is a reference pressure (mostly pressure at the beginning of an experiment). The modulus M_{co} depends on the contact material properties and m describes the exponent of the nonlinear stress–strain behavior of the contact region.¹² Thus, the pressure dependence has the form

$$\begin{aligned} V &= V_2 \left[2 \left(1 + \frac{M_s}{M_{\text{co}}} \left(\frac{p}{p_{\text{reference}}} \right)^{-m} \right)^{-1} \right]^{\frac{1}{2}} \\ &= V_2 \left[0.5 \left(1 + \frac{M_s}{M_{\text{co}}} \left(\frac{p}{p_{\text{reference}}} \right)^{-m} \right) \right]^{-\frac{1}{2}} \end{aligned} \quad (6.141)$$

The following two examples in Figure 6.42 demonstrate the application.

¹²Hertz's theory gives $m = 1/3$.

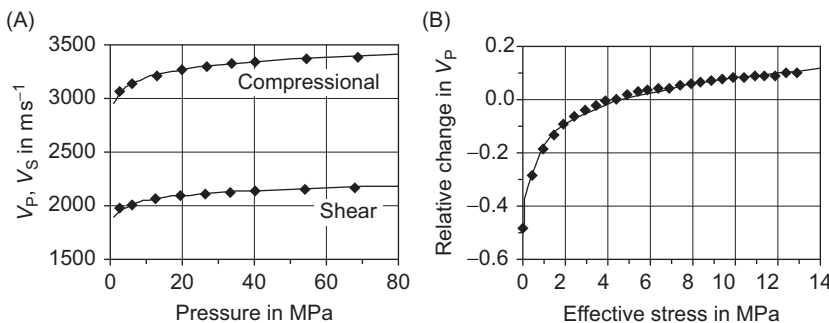


FIGURE 6.42 Velocity versus effective pressure—comparison of experimental and calculated dependence (for calculations, visit the website <http://www.elsevierdirect.com/companion.jsp?ISBN=9780444537966> and refer Elastic_Mechanical_Structured model). Points are measured data; curves are calculated by the Equation (6.142). (A) Boise sandstone (dry). (B) Dry core samples, (A) Gullfaks field. data from King (1966); (B) data from Duffant and Landro (2007).

The best approximation in Figure 6.42A is given by the equations:

$$V_p = 3900[0.5(1 + 2.5 \cdot p^{-0.1})]^{-0.5} \quad V_s = 2500[0.5(1 + 2.5 \cdot p^{-0.1})]^{-0.5} \quad (6.142)$$

where pressure is in MPa and velocities in m s^{-1} . Note that both velocities are controlled by identical contact parameters (2.5). Thus, the “contact modulus” equals the “solid material modulus” divided by 2.5 and the pressure dependence follows an exponent of $m = 0.10$.

In a second example (Figure 6.42B), experimental data published by Duffant and Landro (2007) are used. Experimental data represent the velocity change with pressure (reference pressure is about 5 MPa). The velocity change is defined as $[V(p)/V(p = 5 \text{ MPa})] - 1$. The digitized experimental data are fitted with the following model-derived equation:

$$\frac{V_p(p)}{V_p(p = 4.7 \text{ MPa})} = [1 + 2.8 \cdot p_{\text{eff}}^{-0.33}]^{-0.5} \quad (6.143)$$

Thus, the “contact modulus” equals the “solid material modulus” divided by 2.8 and the pressure dependence follows with the exponent $m = 0.33 = 1/3$, exactly Hertz’s contact elasticity for a spherical contact.

6.7.7.5 Discussion of the Tensor Term (Structure and Bonding Influence)

The basic velocity equation for this consideration is written as follows:

$$V = V_3 \{s_{ik}(\alpha, f)\}^{\frac{1}{2}} \quad (6.144)$$

where V_3 covers all other influences.

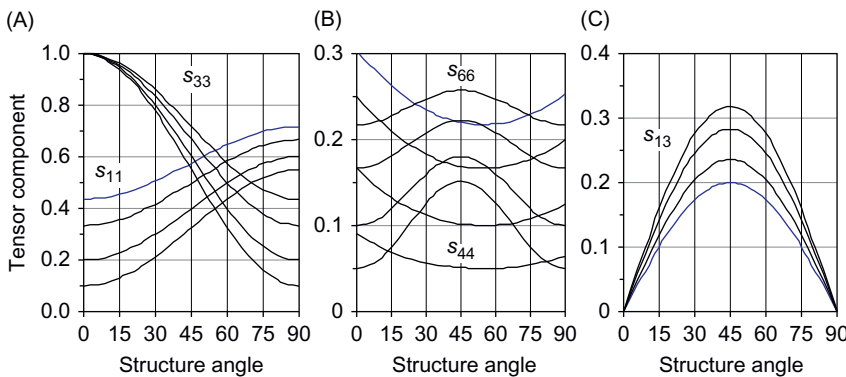


FIGURE 6.43 Components of the structure tensor as a function of the structure angle α and the contact property f . Curves are calculated for (from top to bottom): $f = 2.3, f = 3.0, f = 5.0, f = 10$ (for calculations, visit the website <http://www.elsevierdirect.com/companion.jsp?ISBN=9780444537966> and refer Elastic_Mechanical_ Structured model).

The elements of the tensor S_{ik} depend on the structure angle α and on a parameter f (for details, see Schön, 1989, 1996). The parameter f is defined as the ratio of the compressional and shear deformation properties of matrix (s) and contact region (c):

$$f = \frac{M_s}{\mu_s} \frac{1 + \frac{\mu_s}{\mu_c}}{1 + \frac{M_s}{M_c}} \quad (6.145)$$

For the bonding parameter f , there are two extreme situations:

1. For a completely cemented material, contact properties and solid matrix properties are equal. In this case is $f = (M_s/\mu_s) \approx 2.2-2.5$. This represents the low limit for f .
2. For a “soft” cemented or for unconsolidated porous rock, contact modulus for tangential stress μ_c decreases much more than the modulus for normal stress M_c at the contact. The extreme case is a normal stiffness and a tangential sliding at the contact. Therefore, in such formations, $(M_s/M_c) < (\mu_s/\mu_c)$. This results in higher values for the parameter f , that is, $f > 2.2$.

Thus, the following rule results: increasing cementation and bonding quality is related to decreasing parameter f .

Figure 6.43 shows the elements of the tensor as function of the structure angle α and for bonding factors f . Figure 6.43A and B gives the elements that are relevant for velocities in the main axis directions (A, compressional; B, shear components).

This fourth term in the velocity equation contains only structure and bonding properties. Therefore, any velocity ratio is controlled by structure and bonding properties. In the following considerations, such ratios are studied and applied for an analysis of velocity measurements. Model calculations

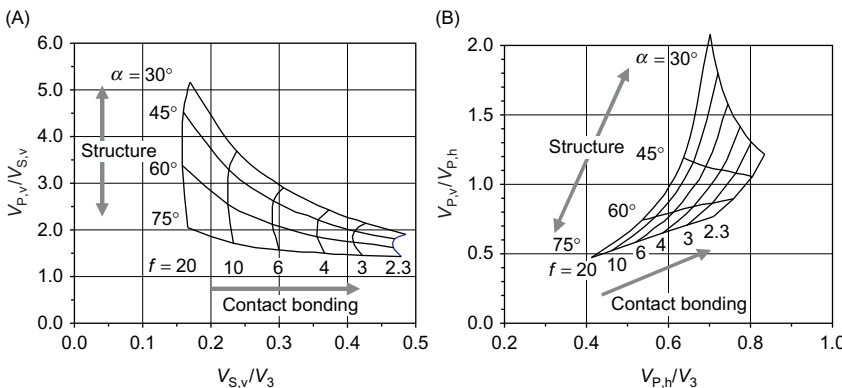


FIGURE 6.44 Forward-calculated crossplots of velocity ratios. (A) Velocity ratio $V_{P,v}/V_{S,v} = \sqrt{s_{33}/s_{44}}$ for vertical wave propagation versus shear wave velocity $V_{S,v}$ normalized by the factor V_3 . (B) Velocity anisotropy ratio $V_{P,v}/V_{P,h} = \sqrt{s_{33}/s_{11}}$ for compressional wave propagation versus horizontal compressional wave velocity $V_{P,h}$ normalized by the factor V_3 (for calculations, visit the website <http://www.elsevierdirect.com/companion.jsp?ISBN=9780444537966> and refer Elastic_Mechanical Structured model).

are presented as crossplots with the two parameters α (structure) and f (bonding). Figure 6.44 shows two examples:

1. Crossplot of velocity ratio $V_{P,v}/V_{S,v} = \sqrt{s_{33}/s_{44}}$ for vertical wave propagation versus the normalized shear wave velocity $V_{S,v}/V_3 = \sqrt{s_{44}}$.
2. Crossplot of velocity anisotropy ratio $V_{P,v}/V_{P,h} = \sqrt{s_{33}/s_{11}}$ for compressional wave propagation versus normalized horizontal compressional wave velocity $V_{P,h}/V_3 = \sqrt{s_{11}}$.

Two examples may demonstrate possibilities of an application for data interpretation.

Example 1:

Han et al. (1986) investigated compressional and shear wave velocities as a function of pressure. Results of four selected samples are plotted in a V_p/V_S versus V_S plot (Figure 6.45). From high to low velocities, the hydrostatic pressure during the measurement increases stepwise (5, 10, 20, 30, 40 MPa; marked by symbols). For the calculated grid, a value $V_3 = 6.5 \text{ km s}^{-1}$ was assumed. Comparison of plot and measured data allows the following interpretation:

- individual samples are characterized by specific structure and bonding properties and their change under pressure;
- hydrostatic pressure creates a dominant variation of the contact bonding; with increasing pressure, the contact bonding becomes better and the parameter f decreases;
- there is a significant difference in the velocity and the velocity ratio between clean (samples 1 and 5) and shaly sandstones (samples 50 and 58) caused by a significant difference in the contact or bonding properties.

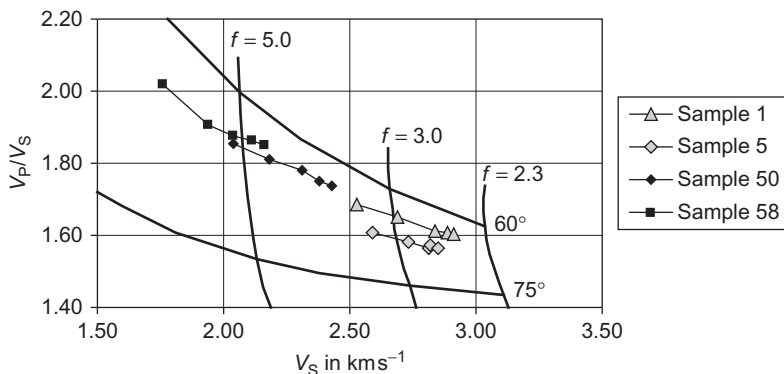


FIGURE 6.45 Ratio V_p/V_s for the interpretation of measurements at sandstones. Curve grid calculated for different α and f . It was assumed empirically $V_3 = 6.5 \text{ km/s}^{-1}$. Points are measured results after Han et al. (1986): Sample 1: porosity at 5 MPa 18.5%; clay content 0%; Sample 5: porosity at 5 MPa 19.9%; clay content 0%; Sample 50: porosity at 5 MPa 17.7%; clay content 11%; Sample 58: porosity at 5 MPa 15.4%; clay content 27%; Hydrostatic pressure increases (left to right) in steps: 5, 10, 20, 30, 40 MPa. Points are measured results after Han et al. (1986).

Example 2 :

Scott (2007) published results of a hydrostatic compression experiment on Ekofisk chalk. [Figure 6.46A](#) shows normalized compressional wave velocities in vertical and horizontal direction versus strain. Three stages of deformation are indicated: elastic, pore collapse, and compaction.

Obviously the elastic wave velocities are affected by these processes and stages. The designed plots can be used to interpret measured velocity data during the deformation process. Digitized data from [Figure 6.46B](#) as data path in a forward modeled grid of $V_{p,v}/V_{p,h} = \sqrt{s_{33}/s_{11}}$ versus the normalized horizontal velocity $V_{p,h}$. In this case of normalized velocity (or velocity at the start of the experiment), a factor of $V_3 = 1.8$ was applied (empirically).

The data path clearly shows three phases in the velocity picture:

- *First phase:* The structure angle is nearly constant; increasing pressure results in an increase of bonding (parameter f decreases). This corresponds with the “elastic” part in [Figure 6.46A](#).
- *Second phase:* This phase has the pathway of a loop; there is a change of structure and bonding, where bonding has a reverse tendency (material becomes softer)—this corresponds to the “pore collapse” in [Figure 6.46A](#).
- *Third phase:* Structure is stabilized with respect to stress field; increasing stress results in stronger bonding (parameter f decreases at constant angle α). This is typical for the “compaction.”

With this background of interpretation, a direct plot of the two velocities is also possible and helpful ([Figure 6.46C](#)).

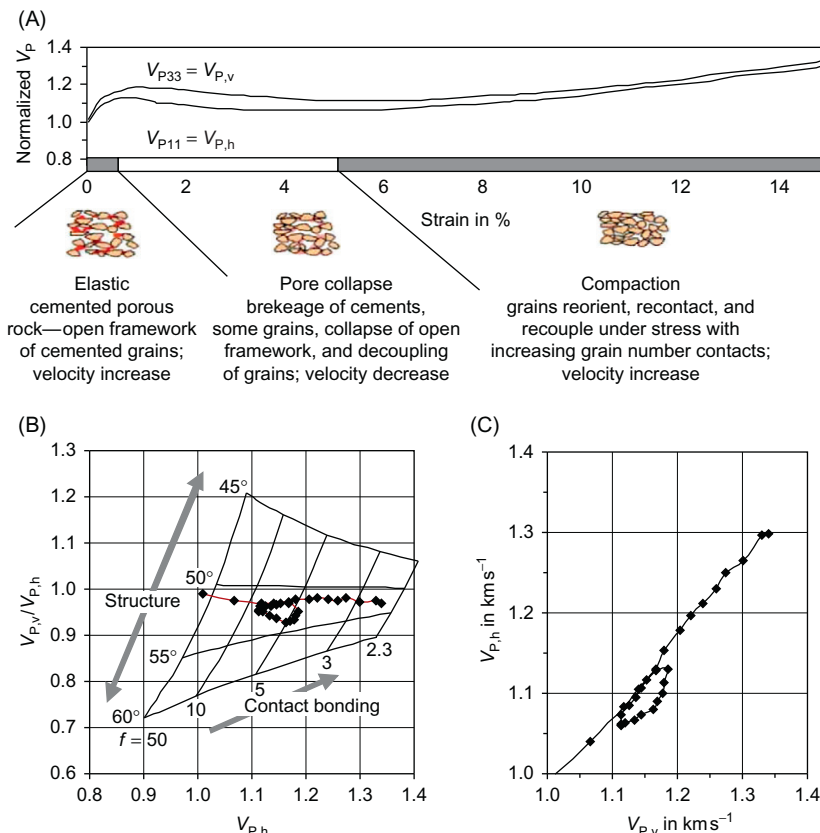


FIGURE 6.46 Analysis of a compression experiment on Ekofisk chalk (Scott, 2007): (A) Hydrostatic compression experiment on Ekofisk chalk, figure after Scott, 2007, modified. (B) Analysis of the data with the structured model: ratio $V_{p,v}/V_{p,h} = V_{p11}/V_{p33}$ versus normalized velocity $V_{p,h}$. Points are experimental data; grid is calculated with $V_3 = 1.8 \text{ km s}^{-1}$. (C) Directly plotted data as $V_{p,h}$ versus $V_{p,v}$ plot.

Comparable loops are also detected by analysis of velocity measurements at gneisses and plagiogranites during strength experiments (Schön, 1996).

6.7.7.6 Outlook

All calculations in this section are for dry rock. The model in this case delivers the “rock skeleton properties” with their dependence on porosity, pressure, texture, and structure.

Gassmann’s equations allow a transformation for the case of any pore fluid.

The structured model can also be applied on other properties (resistivity, thermal conductivity, etc.) and on the calculation of relationships between

them (Schön, 1996). In Section 7.5.2, the model is applied to geomechanical strength parameters.

6.8 RESERVOIR PROPERTIES FROM SEISMIC PARAMETERS

In addition to porosity (calculated using, for example, Wyllie's equation), modern seismic techniques offer possibilities for:

- a lithology estimate,
- fluid identification, and
- reservoir fluid pressure calculation.

From the broad and permanently expanding spectrum of parameters and attributes, only a selection can be presented in order to demonstrate some basic idea. This demonstration began with Wyllie's [equation \(6.50\)](#), which allows the derivation of porosity from P-wave velocity or slowness.

Reflection coefficient or acoustic impedance processing gave the initial knowledge about pore fluid (gas–water) and/or rock type (sand–shale) effects upon these.

Implementation of shear wave parameters into seismic processing and the philosophy of the AVO (amplitude versus offset) technique has been created and has developed different powerful techniques. Petrophysical results are mostly presented as crossplots to visualize both fluid and rock matrix properties.

In the following sections, some petrophysical aspects will be discussed.

6.8.1 AVO—Basic Principle and Link to Physical Properties

AVO techniques use the partitioning of elastic wave energy at a boundary for extraction of information about fluid and lithology. This is controlled by the elastic properties of the two materials and the angle of the incident wave; it results in an offset-dependent reflectivity (amplitude), observed as "AVO." An AVO tutorial was published by Castagna (1993).

At a boundary between two materials of different elastic properties, an incident wave is reflected and refracted. There are two situations with respect to the angle of incidence θ : normal incidence or non-normal incidence.

For normal incidence ($\theta = 0$), an incident compressional or P-wave is reflected as P-wave.¹³ The reflection coefficient is defined as:

$$R_{PP} = \frac{V_{P,2} \cdot \rho_2 - V_{P,1} \cdot \rho_1}{V_{P,2} \cdot \rho_2 + V_{P,1} \cdot \rho_1} = \frac{I_{P,2} - I_{P,1}}{I_{P,2} + I_{P,1}} \quad (6.146)$$

where

$V_{P,1}, V_{P,2}$ are the compressional wave velocities of the two materials

¹³The same relationships are valid for shear waves at normal incidence.

ρ_1, ρ_2 are the densities of the two materials

$I_{P,1} = V_{P,1} \cdot \rho_1, I_{P,2} = V_{P,2} \cdot \rho_2$ are the impedances of the two materials.

At non-normal incidence ($0 < \theta < 90^\circ$), an incident P-wave energy results in a mode conversion and produces both P- and S-reflected and transmitted waves. The angles of the reflected (and transmitted) waves are determined by Snell's law. The amplitudes of the reflected and transmitted waves are given by the Zoeppritz equations (1919). For practical applications, approximations of the Zoeppritz equations are frequently used such as by Aki and Richards (1980) or Shuey (1985).

Shuey's equation (Shuey, 1985) gives the reflection coefficient of the P-wave as a function of the angle of incidence:

$$R_{PP}(\theta) = A + B \cdot \sin^2 \theta + C(\tan^2 \theta - \sin^2 \theta) \quad (6.147)$$

where

$$A = R_{PP} = \frac{I_{P,2} - I_{P,1}}{I_{P,2} + I_{P,1}} \quad B = R_{PP} \left[D - 2(1 + D) \frac{1 - 2\nu}{1 - \nu} \right] + \frac{\Delta\nu}{(1 - \nu)^2} \quad (6.148)$$

$$C = \frac{1}{2} \frac{\Delta V_P}{V_P} \quad D = \frac{\Delta V_P / V_P}{\Delta V_P / V_P + \Delta \rho / \rho} \quad (6.149)$$

$$\text{with } \Delta V_P = V_{P,2} - V_{P,1} \quad V_P = \frac{V_{P,1} + V_{P,2}}{2}$$

$$\Delta\nu = \nu_2 - \nu_1 \quad \nu = \frac{\nu_1 + \nu_2}{2}$$

$$\Delta\rho = \rho_2 - \rho_1 \quad \rho = \frac{\rho_1 + \rho_2}{2}$$

where ν_1, ν_2 are the Poisson's ratios of the two media.

In Equation (6.147):

- the first term is the normal incidence reflection coefficient (Equation (6.146));
- the second term predominates at intermediate angles;
- the third term is dominant as the critical angle is approached (Castagna, 1993).

For $\theta < 30^\circ$, the following approximation is frequently used:

$$R_{PP}(\theta) \approx A + B \cdot \sin^2 \theta \quad (6.150)$$

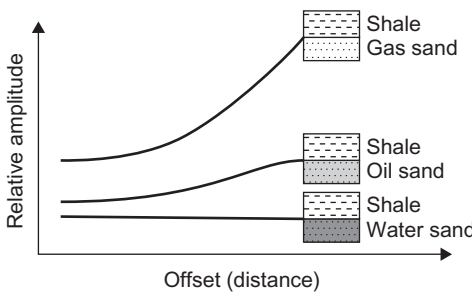


FIGURE 6.47 Typical amplitude-offset patterns (adapted after Yu, 1985).

If reflection coefficients $R_{PP}(\theta)$ or amplitudes are plotted versus the squared sine of the angle of incidence $\sin^2\theta$, a linearized plot results. Linear regression of data points delivers the two AVO attributes:

1. Intercept A : The intercept gives the normal incident reflection coefficient R_{PP} and is controlled by the contrast of the two P-wave impedances.
2. Gradient (slope) B : The gradient is also controlled by the different Poisson's ratios ν_1, ν_2 (or different ratios $V_{P,1}/V_{S,1}$ and $V_{P,2}/V_{S,2}$) and carries a “fluid properties information.”

Figure 6.47 gives a first impression of the AVO effect for different boundary situations. It “shows three distinctive trends clearly differentiated:

1. the reflected amplitudes from a shale to gas–sand interface obtain a high level at near offsets, then increase significantly toward far offsets;
2. for a shale to oil–sand interface, amplitudes are much lower than those from a shale to gas–sand interface and they increase only slightly at far offsets;
3. for a shale to water–sand interface, the trend has the lowest amplitude level and is almost flat” (Yu, 1985).

Indications can be used to spot various fluid contacts, to delineate the size of reservoirs and for a monitoring. Yu (1985) notes: “... however, in practice it is sometimes difficult to differentiate between oil–sand and water–sand because the separation level in offset amplitude is small.”

Equations (6.148)–(6.150) allow a forward calculation of the expected AVO effect. Figure 6.48 shows an example. The negative and positive amplitudes refer to the different position of the reservoir with respect to the shale layer. The input properties for the three components are in Table 6.17.

6.8.2 A Closer Look at Acoustic Impedance and Poisson's Ratio (or Ratio V_P/V_S)

The two petrophysical attributes derived from AVO analyses, intercept and slope, are controlled by the contrast of acoustic impedance (or velocity and

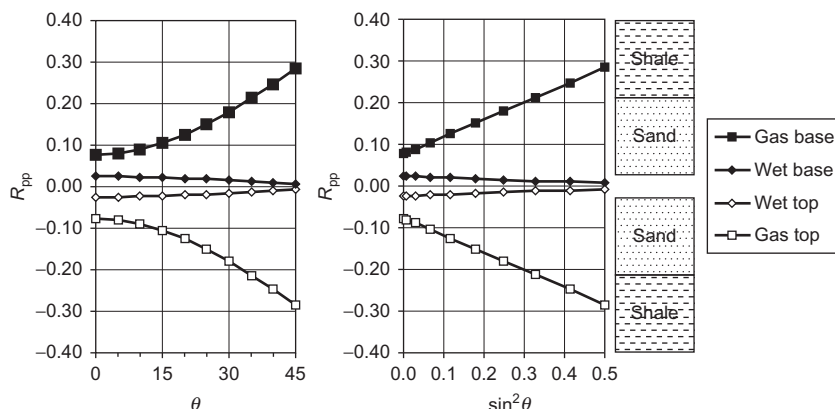


FIGURE 6.48 Forward calculation of the reflection coefficient as a function of the angle of incidence (θ) and as a function of the linearized term ($\sin^2\theta$) using Shuey's approximation. “Top” and “base” refer to the position of the sand reservoir with respect to the position of the shale layer (below or above) (for calculations, visit the website <http://www.elsevierdirect.com/companion.jsp?ISBN=9780444537966> and refer Elastic_Mechanical. Shuey AVO).

TABLE 6.17 Input Data for AVO Forward Calculation

Model Component	V_P in m s^{-1}	ν	ρ in g cm^{-3}
Wet sand	2131	0.4	2.10
Gas sand	1967	0.1	2.05
Shale	2177	0.4	2.16

density) and Poisson's ratio (or ratio V_P/V_S). Figure 6.49 shows the position of gas–sand, water–sand, and shale in a V_P/V_S versus acoustic impedance AI plot.

Ødegaard and Avseth (2004) developed such crossplots to a “rock physics template (RPT)” as a toolbox for lithology and pore fluid interpretation. Figure 6.50 shows a crossplot based on a figure from Ødegaard and Avseth (2004). It demonstrates:

- the difference between sand and shale,
- the change of properties from pore fluid gas to water,
- the influence of porosity,

Influence of pressure and grain cementation is indicated with arrows.

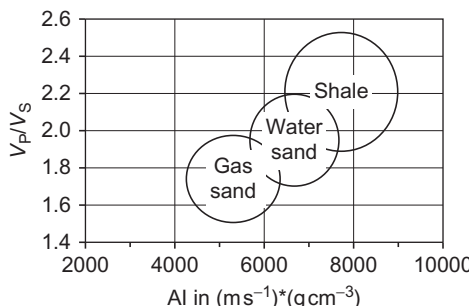


FIGURE 6.49 Position of gas sand, water sand and shale in a V_p/V_s versus acoustic impedance AI plot.

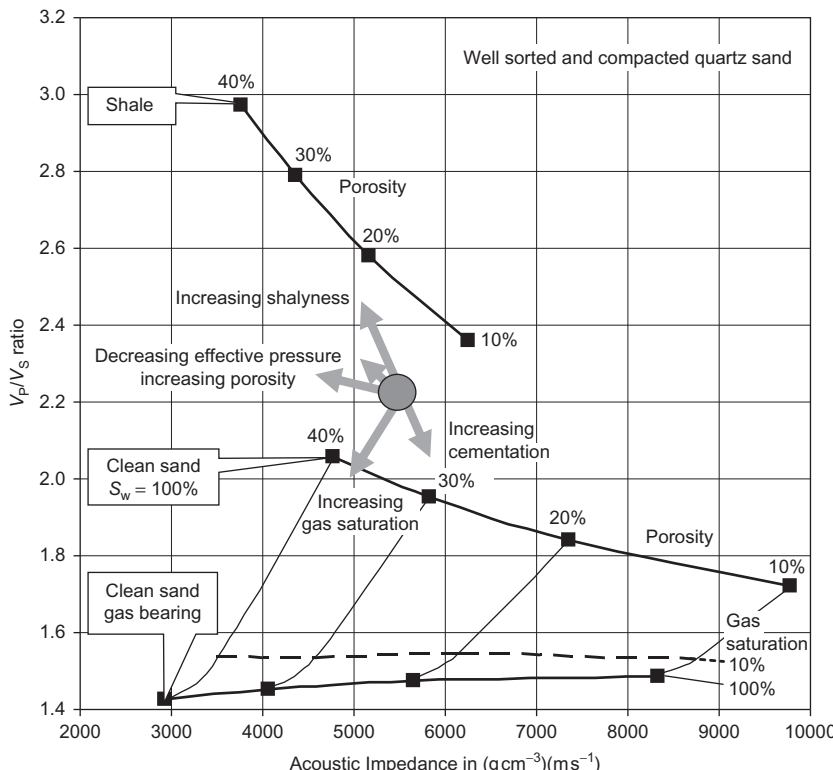


FIGURE 6.50 Crossplot V_p/V_s versus acoustic impedance AI, drawn after a figure “RPT” from Ødegaard and Avseth (2004). “The theoretical trends are shown for idealized silici-clastic lithologies. The effects of changing reservoir parameters on a point of the crossplot is here shown by arrows” (Ødegaard and Avseth, 2004).

The following directions of changing reservoir parameters are remarkable (Veeken, 2007):

- increase in gas saturation will reduce acoustic impedance AI and ratio V_P/V_S ,
- increase in cement volume will increase acoustic impedance AI and reduce ratio V_P/V_S ,
- increase in porosity will decrease acoustic impedance AI and increase ratio V_P/V_S ,
- increase in shaliness will reduce acoustic impedance AI but increase ratio V_P/V_S ,
- changing formation pressure does not have much influence, but it will reduce acoustic impedance AI and increase the ratio V_P/V_S .

Veeken (2007) notes that “the RPT plot is area or basin dependent and velocity–porosity trends are calculated for the expected lithologies and various depth of burial (compaction). A distinction needs to be made between silici-clastic and carbonate systems.”

Chi and Han (2009) conclude: “... using the crossplots of elastic properties with the RPT, we can clearly delineate the lithology and fluid content. The prior information such as well log, core, and geological modeling can help construct the RPT and includes the effects of pressure, temperature, and fluid property.”

6.8.3 The Attributes Lambda Rho and Mu Rho

In addition to Shuey’s method, the “Fatti methodology” (Fatti et al., 1994; see also Burianik, 2000) solves the problem for P and S reflectivities. The P and S impedances of the materials (geological layers) can be calculated from P and S reflectivities by inversion.

From P and S impedances, the attributes $\lambda \cdot \rho$ (lambda rho) and $\mu \cdot \rho$ (mu rho) can be derived as follows:

$$\text{shear impedance is } I_S = V_S \cdot \rho = \sqrt{\frac{\mu}{\rho}} \rho = \sqrt{\mu \cdot \rho} \quad (6.151)$$

$$\text{parameter } \mu \cdot \rho \text{ (“mu rho”) results in } \mu \cdot \rho = I_S^2 \quad (6.152)$$

$$\text{Compressional impedance is } I_P = V_P \cdot \rho = \sqrt{\frac{\lambda + 2\mu}{\rho}} \rho = \sqrt{\lambda \cdot \rho + 2 \cdot \mu \cdot \rho} \quad (6.153)$$

$$\text{Parameter } \lambda \cdot \rho \text{ ("lambda rho") results in } \lambda \cdot \rho = I_p^2 - 2 \cdot I_s^2 \quad (6.154)$$

The petrophysical information of these parameters is discussed more in detail by Goodway et al. (1997) and starts with the note that:

- the modulus λ —or incompressibility—is sensitive to pore fluid;
- the modulus μ —or rigidity—is sensitive to rock matrix.

6.9 ATTENUATION OF ELASTIC WAVES

6.9.1 Definition and Units

Elastic waves lose energy during their propagation in a material and the amplitude decreases with distance from the source. This decrease has two causes:

1. Geometrical spread of the wavefront (divergence)
2. Absorption or attenuation by conversion of elastic energy in other types of energy (e.g., heat) and energy loss as a result of scattering in heterogeneous materials.

The amplitude $A(x)$ at a distance x from the source can be described for propagation in a homogeneous isotropic medium as:

$$A(x) = A(x_0) \left(\frac{x_0}{x} \right)^n \exp[-\alpha(x - x_0)] \quad (6.155)$$

where $A(x_0)$ is the amplitude at a reference distance x_0 (or at the source).

The term $(x_0/x)^n$ describes the amplitude decrease resulting from geometrical divergence. The exponent n depends on the geometry of the wave propagation. For a plane wave $n = 0$ (no divergence).

The term $\exp[-\alpha(x - x_0)]$ describes the amplitude decrease as a result of attenuation. α is the attenuation exponent. For a plane wave (or after elimination of divergence term)

$$\alpha = \frac{1}{x_2 - x_1} \ln \left(\frac{A(x_1)}{A(x_2)} \right) \quad (6.156)$$

α is in m^{-1} or nepers m^{-1} . The frequently used unit dB/m (decibel/m) results from the definition

$$\alpha = \frac{1}{x_2 - x_1} 20 \log \left(\frac{A(x_1)}{A(x_2)} \right) \quad (6.157)$$

Conversions between the two measures are:

$$\begin{aligned} \alpha \text{ (in } \text{dB m}^{-1} \text{)} &= 8.686 \cdot \alpha \text{ (in nepers } \text{m}^{-1} \text{ or } \text{m}^{-1} \text{)} \\ \alpha \text{ (in nepers } \text{m}^{-1} \text{ or } \text{m}^{-1} \text{)} &= 0.115 \cdot \alpha \text{ (in } \text{dB m}^{-1} \text{).} \end{aligned}$$

In many cases, as a measure of elastic energy loss, the dimensionless quality factor Q (Knopoff, 1964, 1965) and its inverse Q^{-1} (dissipation factor) is used:

$$Q^{-1} = \alpha \frac{V}{\pi \cdot f} \quad (6.158)$$

where V is velocity and f is the frequency.

Q^{-1} is attenuation normalized by wavelength. This definition with [Equation \(6.158\)](#) is correct, if small changes of phase velocity can be ignored or for low loss assumption. In general, for a viscoelastic medium, the relationship is (see, for example, Bourbie et al., 1987; Johnston and Toksöz, 1981):

$$Q^{-1} = \alpha \frac{V}{\pi \cdot f - \frac{\alpha^2 \cdot V^2}{4 \cdot \pi \cdot f}} \quad (6.159)$$

For low loss, the term $(\alpha^2 \cdot V^2)/(4 \cdot \pi \cdot f)$ is negligible and [Equation \(6.158\)](#) results.

If α is a linear function of frequency in the first approximation, then Q^{-1} is independent of frequency. It can be used as a dimensionless parameter to describe the attenuation properties of rocks without reference to the particular frequency under consideration. Thus, there are two measures for attenuation:

α is the fractional loss of amplitude per unit distance

Q^{-1} is the fractional loss of amplitude per wavelength or per oscillation.

6.9.2 Attenuation of Elastic Wave Energy in Rocks—Overview

Attenuation of elastic wave energy in rocks is a complex process of different mechanisms. The mechanisms are frequently connected with processes that occur at “defects” of the solid rock components (grain–grain contacts, fractures, etc.), at inhomogeneities (pores, fractures), scattering, and with fluid motion in pores and fractures.

As result of these processes and interactions, inelastic properties of the rock-forming components alone cannot explain attenuation. Main rock components can be characterized briefly by the following features:

- Solid components (minerals) have low attenuation properties; in a first approximation, attenuation increases linearly with frequency. Peselnick and Zietz (1959) give $Q \approx 1900$ or $Q^{-1} \approx 5 \cdot 10^{-4}$ as an example for the mineral calcite.
- Among the fluid components, gas has a high attenuation. Gases and fluids show attenuation properties that are influenced by the composition and thermodynamic conditions (temperature and pressure). Viscous effects

TABLE 6.18 Attenuation Coefficient (at 50 Hz) and Velocity for Some Rock Types

Rock	Velocity V_p in km s^{-1}	Attenuation α_p in m^{-1}
Granite	5.0–5.1	$(0.21–0.38) \cdot 10^{-3}$
Basalt	5.5	$0.41 \cdot 10^{-3}$
Diorite	5.8	$0.2 \cdot 10^{-3}$
Limestone	5.9–6.0	$(0.04–0.37) \cdot 10^{-3}$
Sandstone	4.0–4.3	$(0.7–1.8) \cdot 10^{-3}$
Shale	2.15–3.3	$(0.68–2.32) \cdot 10^{-3}$

After Ellis and Singer (2007).

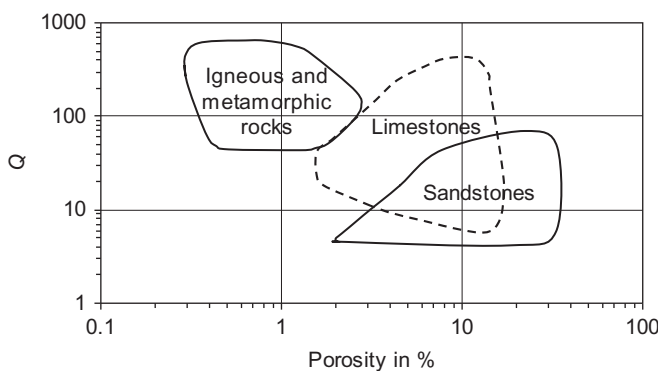


FIGURE 6.51 Q as a function of porosity and rock type, Johnston et al. (1979).

result as first approximation in an increase of attenuation with the square of frequency. Johnston (1981) reports the following data:

- air (dry) $Q \approx 582$ or $Q^{-1} \approx 17 \cdot 10^{-4}$ (frequency 100 kHz);
- water (salt content 36 ppm) $Q \approx 63,000$ or $Q^{-1} \approx 0.16 \cdot 10^{-4}$ (frequency 150 kHz).

Data in Table 6.18 give an overview for the magnitude of the attenuation coefficient of some typical rocks. The table also contains velocity data.

Figure 6.51 presents a compilation of Q data as a function of porosity and rock type after Johnston et al. (1979) with the general trend of Q inversely proportional to porosity.

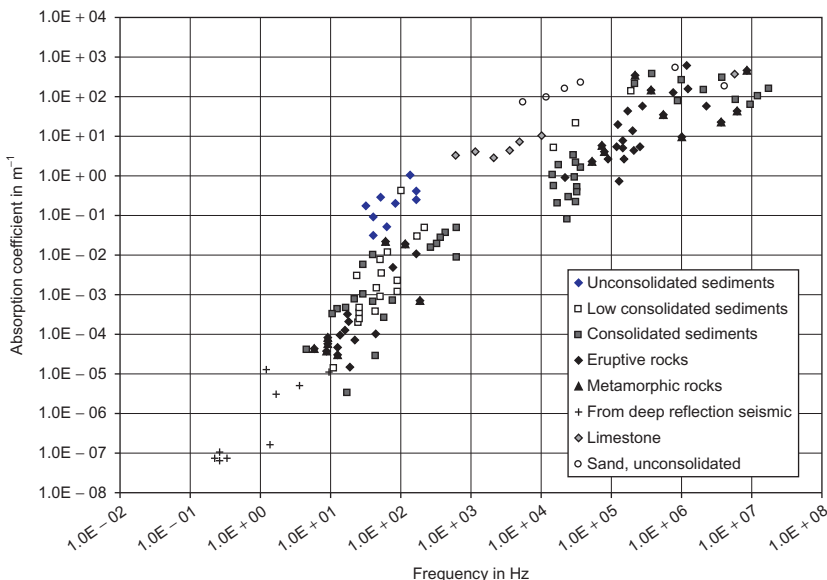


FIGURE 6.52 Attenuation coefficient of various rock types as a function of frequency (drawn on the basis of a figure after Attewell and Ramana (1966), Militzer et al. (1986), Schön (1996)).

Figure 6.52 shows the general frequency dependence of the attenuation coefficient determined at various frequencies of seismic measurements as well as the influence of the rock type. Despite the great scatter of the value, two characteristics can be detected:

1. Attenuation coefficient is a frequency-dependent parameter. It increases with increasing frequency (low-pass filter effect). As a first approximation, there is a proportionality $\alpha \propto f$. Berzon (1977) gives the following mean values:
 - a. $\alpha \approx (10^{-7} - 10^{-6}) \cdot f$ mantle and core
 - b. $\alpha \approx 10^{-5} \cdot f$ unweathered igneous rocks
 - c. $\alpha \approx 10^{-3} \cdot f$ dry, unconsolidated rocks at the earth's surface.
 - d. The linear frequency dependence of α corresponds to a frequency-independent Q^{-1} .
2. Attenuation decreases with increasing rock cementation and depth. Thus, as a general rule of thumb, velocity and attenuation show an opposite behavior with respect to their dependence on many factors of influence (e.g., porosity, pressure, consolidation).

Experimental data, particularly laboratory experiments, show that α is nearly linearly dependent on frequency over a broad frequency range

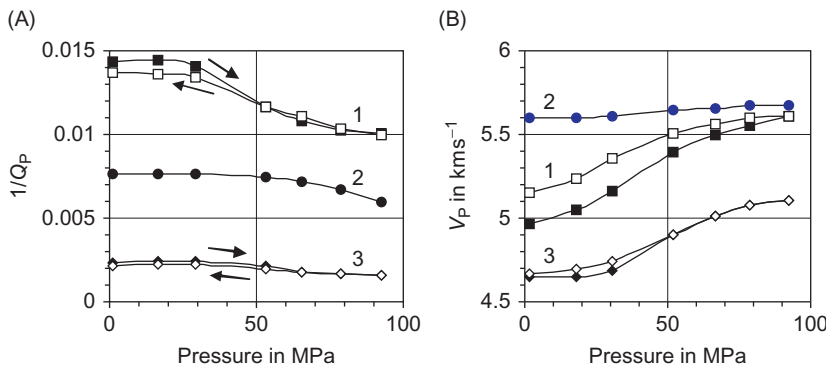


FIGURE 6.53 Dependence of Q_p^{-1} and velocity V_p on hydrostatic pressure; frequency = 32 kHz; after Merkulova et al. (1972). 1—quartzite (thermal cracked), 2—quartzite, 3—granite.

(10^{-2} – 10^7 Hz), especially for dry rocks (Attewell and Ramana, 1966; Berzon, 1977; Bulatova et al., 1970; McDonal et al., 1958; Silaeva and Samina, 1969).

6.9.3 Attenuation of Seismic Waves in Igneous Rocks

Fractures and microcracks act in most cases with an opposite effect on elastic and inelastic properties. Figure 6.53 shows some examples.

Three features may be emphasized:

1. Rocks with a small pressure dependence of velocity also show a small pressure dependence of attenuation (sample 2); rocks with a strong dependence of velocity on pressure also show a strong dependence of attenuation (samples 1 and 3).
2. The fractional changes in attenuation are greater than those of velocity for the same sample and pressure difference.
3. The pressure dependence of attenuation (and velocity) is nonlinear. In some cases, attenuation and velocity show the phenomenon of “hysteresis.”

6.9.4 Attenuation of Seismic Waves in Sedimentary Rocks

The study of elastic wave attenuation particularly in sedimentary rocks carries information about rock properties and is important for the design of seismic investigations. The mechanisms and relationships to extract information from attenuation parameters are not yet fully understood and still a problem.

Table 6.19 gives some data from in situ measurements of Q_p .

TABLE 6.19 Selected Data from in situ Measurements of Q_P

Type of Rocks	f in Hz	Q_P
Gulf coast sediments		
Loam, sand, clay (0–3 m depth)	50–400	2
Sand and shale (3–30 m depth)		181
Sandy clay (30–150 m depth)		75
Clay, sand (150–300 m depth)		136
Limestone and chalk (Texas)	≤ 80	>273
Hunton limestone, dry	$(2.8–10.6) \cdot 10^3$	65
Solenhofen limestone	$(3–15) \cdot 10^6$	112
Pierre shale (0–255 m depth)	50–450	32
Berea sandstone, water saturated	$(0.2–0.8) \cdot 10^6$	10
Navajo sandstone, water saturated	$(0.2–0.8) \cdot 10^6$	7
Amherst sandstone, dry	$(0.93–12.8) \cdot 10^3$	52

After a Compilation from Bourbie et al. (1987).

Attenuation in sedimentary rocks:

- is nearly linearly dependent on frequency (Johnston, 1981);
- increases with porosity (Klimentos and McCann, 1990);
- is strongly influenced by effective pressure and shows a nonlinear decrease with increasing pressure (Winkler and Nur, 1982);
- is influenced by different pore fluids and saturation (Murphy, 1982, 1984);
- increases with presence of clay minerals (Klimentos and McCann, 1990).

The following section gives examples of typical influences.

Klimentos and McCann (1990) investigated compressional wave attenuation properties of 42 sandstones of different porosity and clay contents in a frequency range of 0.5–1.5 MHz. The confining pressure was 40 MPa (equivalent to about 1500 m depth of burial). Experimental data follow a regression:

$$\alpha_p = 3.15 \cdot \phi + 24.1 \cdot C - 0.132 \quad \text{correlation coefficient} = 0.88 \quad (6.160)$$

where

α_p is in dB cm⁻¹ at 1 MHz

ϕ is porosity as volume fraction

C is clay content as volume fraction.

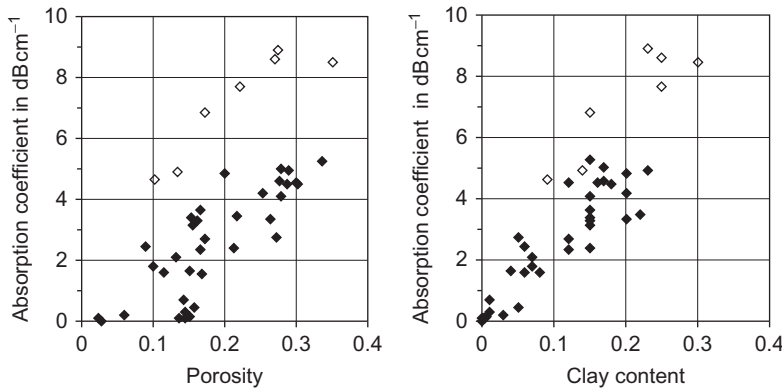


FIGURE 6.54 Compressional wave attenuation coefficient in dB/cm as a function of porosity and clay content; pressure 40 MPa, frequency 1 MHz (data taken from Klimentos & McCann, 1990).

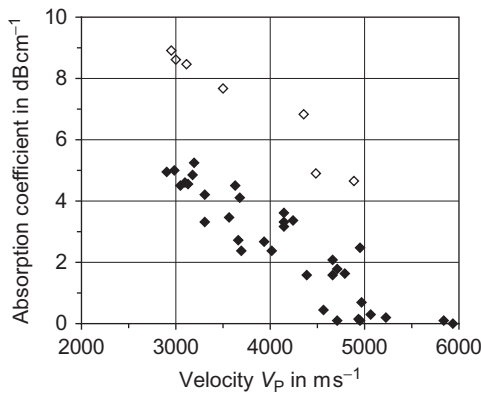


FIGURE 6.55 Compressional wave attenuation coefficient in dB cm^{-1} versus velocity in ms^{-1} ; pressure 40 MPa, frequency 1 MHz (data taken from Klimentos and McCann, 1990).

Figure 6.54 shows a plot of the experimental data; obviously there are two groups of sandstones with respect to the correlation.

The paper of Klimentos and McCann (1990) also gives the velocities. Figure 6.55 shows a correlation of attenuation versus velocity. The two groups are also clearly visible in this plot.

Increasing pressure results in a decrease of attenuation as a result of compaction and improvement of grain–grain contacts and energy transfer. Tao et al. (1995) published results of ultrasonic laboratory investigations at dry and brine-saturated sandstones. One example is presented in Figure 6.56: it demonstrates the general nonlinear pressure dependence of the property Q^{-1}

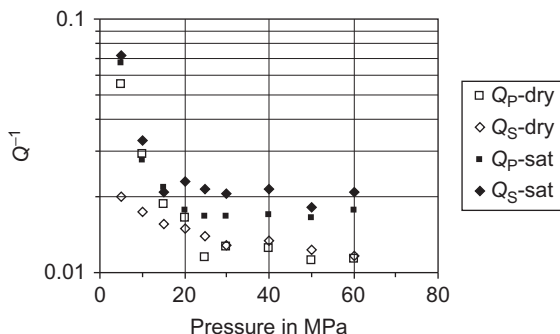


FIGURE 6.56 Q^{-1} as a function of pressure for dry and brine-saturated sandstone (ultrasonic measurements, spectral ratio method), data taken from Tao et al. (1995).

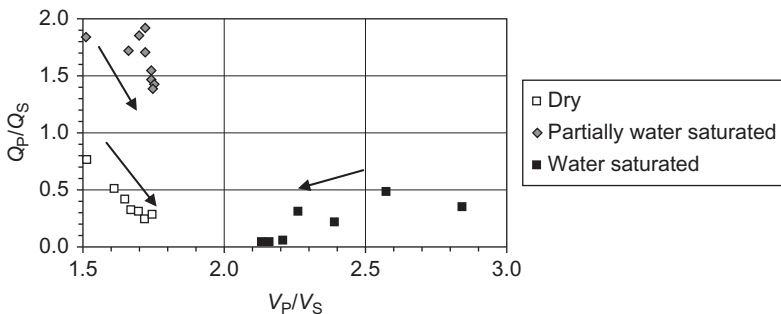


FIGURE 6.57 Attenuation and velocity data for Massilon sandstone plotted Q_P/Q_S versus V_P/V_S . Arrows indicate directions of increasing effective pressure (from 0 to 34.5 MPa), after Winkler and Nur (1982).

as a function of pressure and also shows the different behavior of compressional and shear waves and the influence of pore fluid.

The two ratios Q_P/Q_S and V_P/V_S reflect different physical properties. Experimental data show a tendency for some correlations and remarkable differences between velocity and attenuation properties. In a fundamental paper, Winkler and Nur (1982) discuss the relationship between these two ratios.

Figure 6.57 shows a separation between dry, partly, and fully saturated Massilon sandstone in a Q_P/Q_S versus V_P/V_S plot. Winkler and Nur (1982) note that “ Q_P/Q_S is much more sensitive to degree of saturation than is V_P/V_S .” The data for dry and partially saturated rock in particular are not significantly separated by V_P/V_S , but Q_P/Q_S shows a distinct difference. However, V_P/V_S clearly indicates fully saturated rocks. Winkler and Nur (1982) therefore conclude that “by combining both velocity and attenuation

data, it may be possible to obtain a more precise estimate of degree of saturation than with V_p/V_s alone.”

A systematic study of compressional and shear wave attenuation in limestones was published by Assefa et al. (1999). Limestones contain a complex porosity system with interparticle macropores and micropores within the ooids, calcite cement, and mud matrix. The authors found that “ultrasonic attenuation reaches a maximum value in those limestones in which the dual porosity system is most fully developed.”

6.9.5 Attenuation Mechanisms

In order to explain the attenuation process (and the connected velocity dispersion), numerous theories and mechanisms have been developed and proposed. An overview is given by Winkler and Murphy (1995). Contributing mechanisms depend mainly on rock type, pore fluids, and frequency. Therefore, Winkler and Murphy (1995) conclude that “each mechanism can dominate under certain experimental conditions of frequency, saturation, and strain amplitude.”

The following list is only a selection of some such mechanisms:

- Attenuation originated by matrix inelasticity, including frictional dissipation or loss due to relative motion at grain boundaries and crack surfaces (Johnston and Toksöz, 1981; Tao et al., 1995; Walsh, 1966). This type is dominant in dry rocks.
- Attenuation due to fluid flow in the pore space and dissipation due to the relative motion of the rock skeleton with respect to fluid (Biot, 1956). This mechanism is also called “macroscopic or global flow.”
- Squirting mechanism or local scale fluid motion (Mavko and Nur, 1979; O’Connell and Budiansky, 1974; Wang and Nur, 1988). This flow type is “a microscopic flow which is not coherent over macroscopic length scales” (Winkler and Murphy, 1995).
- Scattering in heterogeneous materials, where the length scale of heterogeneities is in the same order as the wavelength. Therefore, it is a mechanism of high frequency wave propagation. The attenuation increases with the fourth power of frequency (Winkler and Murphy, 1995).

6.10 EXAMPLE OF ELASTIC PROPERTIES: SANDSTONE (GAS BEARING)

The example is a section of a gas-bearing sandstone (Mesozoic). The following logs are selected ([Figure 6.58](#)):

- Natural gammalog GR in API
- Porosity derived from density (with gas correction)
- Deep resistivity log RESD in Ohm m

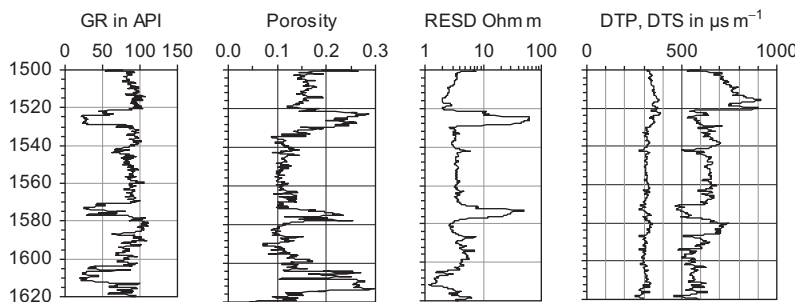


FIGURE 6.58 Selected logs in a sandstone-shale section (gas bearing).

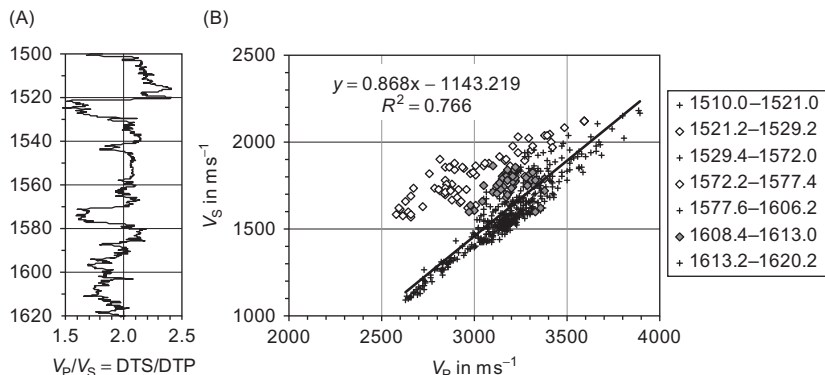


FIGURE 6.59 Velocities in the selected parts: (A) Ratio $V_p/V_s = DTS/DTP$ as a function of depth. (B) Crossplot V_s versus V_p for the sections; the shale sections are crosses, water-bearing sandstones are gray filled, and gas-bearing zones are white filled symbols.

- Acousticlog/Soniclog with compressional (DTP) and shear (DTS) slowness in $\mu\text{s m}^{-1}$.

Gammalog shows three sandstone reservoirs: Reservoir A at 1,521–1,529 m; Reservoir B at 1,572–1,577 m; and Reservoir C at 1,606–1613 m.

Deep resistivity indicates hydrocarbons for Reservoirs A and B, but water for Reservoir C. Reservoirs A and B also differ from Reservoir C with respect to the slowness values (and their ratio).

Figure 6.59 shows a detailed presentation of the elastic wave velocities: the ratio $V_p/V_s = DTS/DTP$ as a function of depth is plotted on the left. Reservoirs A and B show a low value as a result of the gas influence (mainly on V_p).

On the right is a crossplot V_s versus V_p for the different parts of the section. The shale parts are crosses, the water-bearing sandstone are gray filled

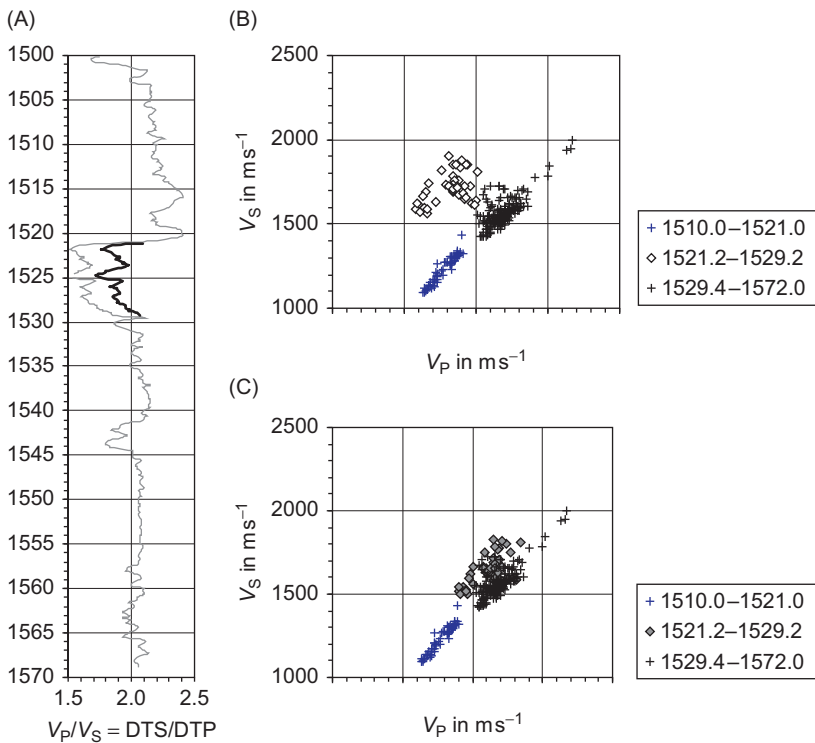


FIGURE 6.60 Fluid replacement for Reservoir A (1,521.2–1,529.2 m): (A) Ratio $V_p/V_s = DTSP/DTP$ as a function of depth. The gray curve is the original curve (same as in Figure 6.59); the black curve is the result of fluid replacement. (B) Crossplot V_s versus V_p for 1,500–1,570 m (original). The shale sections are crosses and gas-bearing zones are white-filled symbols. (C) Crossplot V_s versus V_p for 1,500–1,570 m. The shale sections are crosses. Reservoir A (1,521.2–1,529.2 m) is transformed from gas to water by fluid replacement and is now gray filled to indicate water-bearing sandstone.

and the gas-bearing zones are white-filled symbols. Gas-bearing zones are clearly outside of the general tendency.

Shale parts and the water-bearing reservoir represent a cloud of points. The regression

$$V_s = 0.868 \cdot V_p - 1143.2 \quad R^2 = 0.77 \quad (6.161)$$

is the Castagna equation for this formation, where the velocities are in m s^{-1} (compare Section 6.5.6).

For Reservoir A, a fluid substitution was calculated (Figure 6.60; visit the website <http://www.elsevierdirect.com/companion.jsp?ISBN=9780444537966> and refer Fluid-substitution. example). Inputs are the porosity (from density

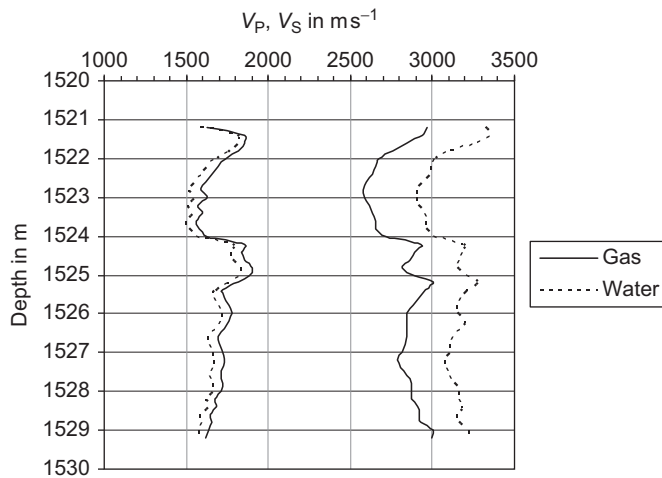


FIGURE 6.61 Compressional and shear wave velocities for Reservoir A in original measured situation (gas) and calculated prediction for water saturation (fluid replacement) (visit the website <http://www.elsevierdirect.com/companion.jsp?ISBN=9780444537966> and refer Elastic_Mechanical. Fluid replacement. example).

log/gas corrected) and the two measured velocities V_P and V_S for the gas-bearing section. For the material properties, the following were used:

- quartz: $\rho_s = 2.65 \text{ g cm}^{-3}$, $k_s = 40 \text{ GPa}$;
- fluid original (gas): $\rho_{fl,1} = 0.3 \text{ g cm}^{-3}$, $k_{fl,1} = 0.13 \text{ GPa}$;
- fluid replaced (water): $\rho_{fl,1} = 1.0 \text{ g cm}^{-3}$, $k_{fl,1} = 2.20 \text{ GPa}$.

On the left side of the figure, the ratio $V_P/V_S = DTSP/DTP$ is plotted as a function of depth, where the gray curve is the original curve (same as in Figure 6.59) and the black curve is the result of fluid replacement. The two crossplots demonstrate the fluid replacement (gas \rightarrow water).

For this part, Figure 6.61 shows the compressional and shear wave velocities from the original measurement (gas) and after fluid replacement (water). Significant changes from gas to water are:

- the strong increase of compressional wave velocity as a result of water compressional modulus;
- the low decrease of shear wave velocity resulting from density increase.

Geomechanical Properties

“Engineering recognizes geophysics as a tool which can often give important information about a site as effectively and more cheaply than a very large number of boreholes.”

D. H. Griffith and R.F. King (1965)

7.1 OVERVIEW, INTRODUCTION

Rock deformation and failure or strength behavior are fundamental problems in geomechanics. Stress distribution and rock properties control the corresponding processes. A discussion of some fundamental topics is given in a special section, “Geomechanics,” of *The Leading Edge* (Sayers and Schutjens, 2007). Petroleum-related rock mechanics is presented in a textbook by Fjaer et al. (1989).

Examples of geomechanical problems are:

- deformation and failure processes originated by tectonic stress, earthquakes, etc.;
- landslides and rockfall;
- deformation of the underground (settlement) and subsurface constructions (tunnel, cavern) caused by the pressure of construction in civil engineering;
- slope and dam stability (failure problems);
- wellbore stability and fracturing;
- reservoir compaction during production and subsidence.

Figure 7.1 illustrates main geomechanical processes in terms of related properties (rock mechanical and geophysical properties) and their change during the process.

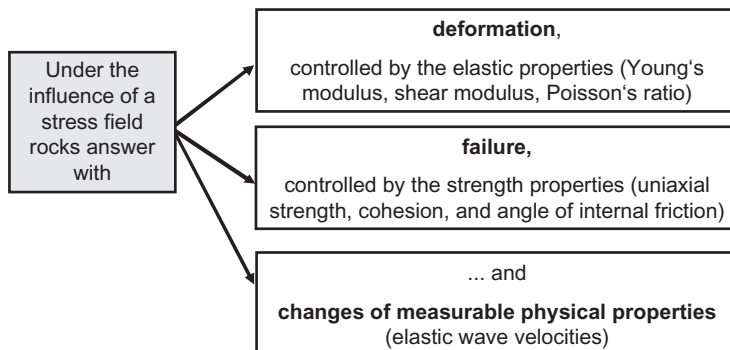


FIGURE 7.1 The physical problem of geomechanical properties evaluation in terms of geophysical parameters.

There are two different types of response on a stress field:

1. The geomechanical response (deformation and/or a failure).
2. The geophysical response as change of the magnitude of a measured parameter (e.g., velocity or resistivity).

The problem combines stress and deformation/failure via geomechanical and geophysical rock properties.

In general, stress is the combined effect of a natural stress field (overburden pressure, pore pressure, tectonic stress) and—maybe—additional artificial components by load, excavation, fluid pressure, etc.

Geomechanical rock properties are a specific group of petrophysical parameters, directly measured in rock mechanics laboratories or by specific field tests. But they are also more or less strongly correlated to other petrophysical parameters (e.g., velocities of elastic waves) and therefore an “indirect” derivation from geophysical measurements is the subject of research and application.

With respect to this application of geophysical methods, we can distinguish between the following:

- a general description or classification of the rock material related to its geotechnical behavior (e.g., rock type, degree of fracturing, and density);
- a determination of geomechanical properties (e.g., modulus of deformation and strength properties).

7.2 CLASSIFICATION PARAMETERS

In engineering, different parameters are used to characterize the “rock quality.” Frequently they are derived from the occurrence of joints and cracks. Johnson and DeGraff (1988) noted: “The engineering use of rock—whether

TABLE 7.1 Rock Quality and RQD Index

Rock Quality	RQD Index in %
Very poor	0–25
Poor	25–50
Fair	50–75
Good	75–90
Excellent	390–100

Carmichael (1989).

as foundation material, in excavations and tunnels, or in maintaining stable slopes—involves rock masses in which the presence of discontinuities often determines the engineering character to a greater degree than do the physical properties of the intact rock . . .”.

Hoek (2010) gives a detailed description of methods and criteria of rock mass classification.

A frequently used parameter is the rock quality designation (RQD) index, developed by Deere et al. (1967). The RQD index is defined as the ratio of core that has competent core sticks >10 cm (or >4 in.) for selected structural domains, or for specific length of core (Barton, 2007; Carmichael, 1989). The RQD is given as a ratio or percentage. Table 7.1 gives a rock quality classification based on the RQD index.

A more complex rock quality parameter Q was defined by Barton et al. (1974); see also Barton (2007):

$$Q = \text{RQD} \frac{J_r \cdot J_w}{J_a \cdot J_n} \frac{1}{\text{SRF}} \quad (7.1)$$

where

RQD is the rock quality designation

J_a is a parameter depending on degree of joint alteration and clay filling

J_n is a parameter depending on the number of joint sets

J_r is a parameter depending on joint roughness

J_w is a parameter depending on amount of water inflow or pressure

SRF is the stress reduction factor (e.g., due to faulting).

Bieniawski (1989) developed a rock classification system called “rock mass rating (RMR).” Six parameters are used to classify a rock mass: uniaxial compression strength, RQD, spacing of discontinuities, condition of discontinuities, orientation of discontinuities, and groundwater conditions.

Verypoor	Poor	Fair	Good	Excellent
RQD				
0%	20%	40%	60%	80%
				100%
Cracks per meter	20	14	10.2	6.7
Meancore length in cm	5	7	10	15
Velocity V_P in m s^{-1}	3000	3500	4000	4500
Dynamic Young's modulus in GPa	18.8	22.7	30.3	39.7
				51.3
				63.5

FIGURE 7.2 Rock classification parameters (RQD index, number of cracks per meter, mean compact core length in meters, compressional wave velocity, and dynamic Young's modulus; unweathered igneous and metamorphic rocks (redrawn after Sjogren et al., 1979; Barton, 2007).

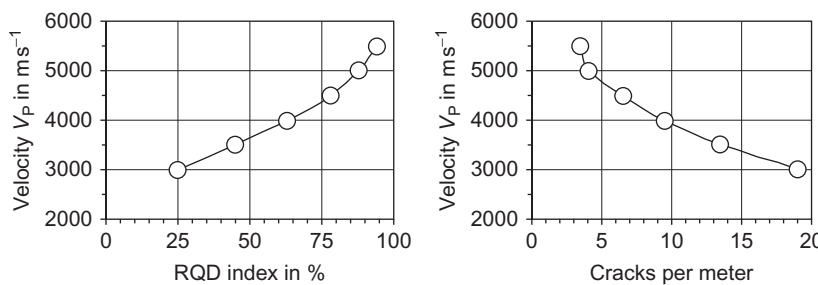


FIGURE 7.3 Compressional wave velocity versus rock classification parameters (number of cracks per meter and RQD index; unweathered igneous and metamorphic rocks; data from Sjogren et al., 1979).

Sjogren et al. (1979) presented a rock classification in connection with measured compressional wave velocities at unweathered igneous and metamorphic rocks. Figure 7.2 shows as scales:

- the RQD index,
- the number of cracks per meter,
- the mean compact core length in m,
- the compressional wave velocity,
- the dynamic Young's modulus.

Figure 7.3 shows the correlation between number of cracks per meter, RQD (in %), and compressional wave velocity in a graphic presentation.

To obtain such a correlation, geophysical—particularly seismic—parameters for classification of rocks with respect to their general geotechnical constitution are recommended.

7.3 FUNDAMENTAL GEOMECHANICAL PROPERTIES AND PROCESSES

7.3.1 Stress and Strain

Stress as the force acting on a given area can have normal and shear components. Normal stress acts perpendicular to a plane, shear stress acts along the face of the plane. In a given stress field, the principal axes are defined as orthogonal directions with pure normal stress components (shear components are zero).

A rock under the influence of stress responds through various kinds of deformation or strain. As a result, changes of linear dimension (length), volume, and shape occur. Deformation can be elastic (reversible) and nonelastic (viscous, plastic, irreversible).

In the simplest case, the vertical (total) stress component is given by the weight of the overburden:

$$\sigma_{\text{vertical}} = g \int_0^z \rho(z) dz \quad (7.2)$$

where g is the earth gravity acceleration, z is the depth, $\rho(z)$ is the density at depth z .

The horizontal stress component is

$$\sigma_{\text{horizontal}} = \frac{\nu}{1 - \nu} \sigma_{\text{vertical}} \quad (7.3)$$

where ν is Poisson's ratio.

In porous rocks, the presence of a total stress tensor $\sigma_{\text{total},ij}$ and a pore pressure σ_{pore} leads to the concept of effective pressure:

$$\sigma_{\text{effective},ij} = \sigma_{ij} = \sigma_{\text{total},ij} - \alpha \cdot \sigma_{\text{pore}} \cdot \delta_{ij} \quad (7.4)$$

where

α is the Biot—Willis effective stress parameter (see Section 6.5.4; Sayers and Schutjes, 2007).

δ_{ij} is the Kronecker delta.

Most petrophysical properties are controlled by the effective pressure (velocity, permeability, porosity etc.; see previous sections).

Deformation and failure behavior are described by different parameters and criteria based on the principal effective stress components $\sigma_{11}, \sigma_{22}, \sigma_{33}$.

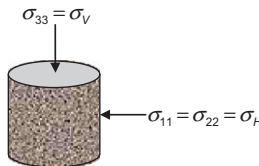


FIGURE 7.4 Cylindrical sample under equal horizontal stress components $\sigma_{11} = \sigma_{22} = \sigma_H$ but different vertical stress component $\sigma_{33} = \sigma_V$.

Figure 7.4 shows a cylindrical sample with equal horizontal stress components $\sigma_{11} = \sigma_{22} = \sigma_H$ but different vertical stress component $\sigma_{33} = \sigma_V$.

Different parameters are used for the description of stress effects:

$$\text{mean effective stress } \sigma_{\text{mean}} = P = \frac{1}{3}(\sigma_{11} + \sigma_{22} + \sigma_{33}) \quad (7.5)$$

$$\text{shear stress } Q = \sqrt{3 \cdot I_2} \quad (7.6)$$

where $I_2 = 1/6[(\sigma_{11} - \sigma_{22})^2 + (\sigma_{22} - \sigma_{33})^2 + (\sigma_{33} - \sigma_{11})^2]$ is the second invariant of the effective stress tensor.

For $\sigma_{11} = \sigma_{22} = \sigma_H$ and $\sigma_{33} = \sigma_V$ results

$$\sigma_{\text{mean}} = P = \frac{1}{3}(\sigma_V + 2 \cdot \sigma_H) = \frac{1}{3}(\sigma_{33} + 2 \cdot \sigma_{11}) \quad (7.7)$$

$$Q = \sigma_V - \sigma_H = \sigma_{33} - \sigma_{11} \quad (7.8)$$

For the description of the deformation process, the “stress path” K is frequently used. It is defined as the ratio of change in effective minimum horizontal stress to the change in effective vertical (overburden) stress:

$$K = \frac{\Delta\sigma_{11}}{\Delta\sigma_{33}} \quad (7.9)$$

7.3.2 The Stress–Strain Curve of a Rock

Figure 7.5 gives some fundamental insights into the mechanical properties and stress–strain curves. The curves show deformation in axial and radial directions of a cylindrical rock sample under the influence of axial stress:

1. At the beginning of the experiment, preexisting cracks are (partially) closed in the axial direction.
2. Further deformation in many cases can be approximated as a linear function of stress (this part is preferred for definition and determination of static moduli).

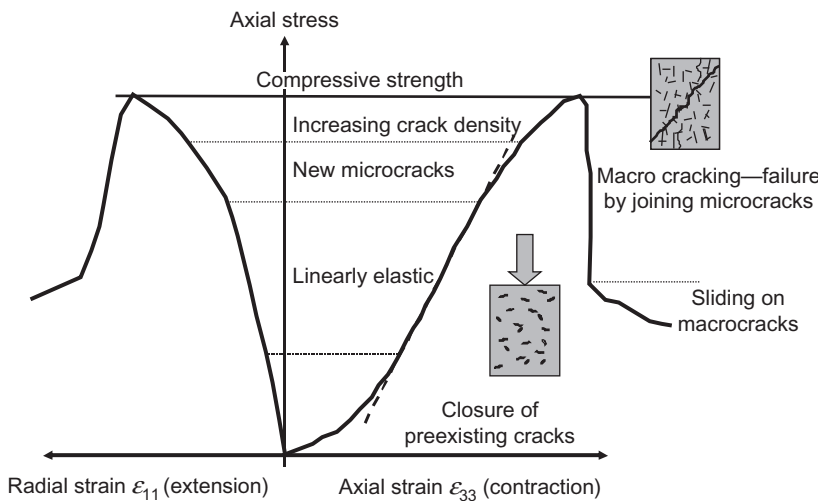


FIGURE 7.5 Stress-strain curve—schematic.

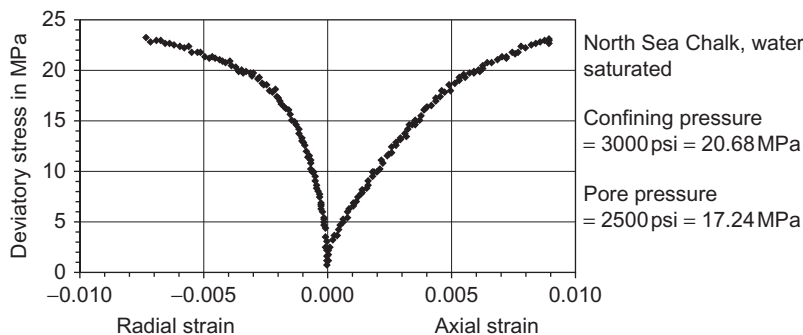


FIGURE 7.6 Stress-strain curves for a water-saturated North Sea Chalk; redrawn from a figure from STIM-LAB, www.stimlab.com. Static Young's modulus 460,000 psi = 3.17 GPa, static Poisson's ratio = 0.20, dynamic Young's modulus = 500,000 psi = 3.45 GPa, dynamic Poisson's ratio = 0.42.

3. Depending on rock properties in the higher range, new cracks are formed until the sample fails at compressive strength.
4. A sliding process begins after the failure at compressive strength.

Figure 7.6 gives a real example from a measurement at water-saturated North Sea Chalk.

Figure 7.6 indicates some fundamental features and key properties:

- The stress-strain curve is, in general, nonlinear, and the deformation process is controlled by various mechanisms.

- The ratio of axial stress and resulting axial strain gives a deformation modulus characterizing the deformation behavior.
- Samples show an axial and a radial deformation; relative change of diameter divided by relative change of axial length in stress direction is Poisson's ratio; it represents a second property characterizing the deformation behavior.

The figures lead also to the two groups of parameters characterizing mechanical properties:

1. Deformation parameters
2. Strength parameters.

7.3.3 Deformation Properties

Deformation properties are derived from a static compression test. Young's modulus is defined as ratio of an axial stress and the resulting axial strain:

$$E = \frac{\sigma}{\varepsilon} \quad (7.10)$$

The stress-strain diagram in most cases shows a nonlinear shape. Therefore, in general, the modulus is stress-dependent and defined as:

$$E(\sigma) = \frac{d\sigma}{d\varepsilon} \quad (7.11)$$

In engineering applications, Young's modulus (modulus of elasticity) is often derived from the linear portion of the stress-strain curve.

Poisson's ratio is defined as the relative change of the radius divided by the relative change of axial length in stress direction:

$$\nu = \frac{\Delta r/r}{\Delta h/h} \quad (7.12)$$

The transformation into other moduli (e.g. compressional modulus, Lame's numbers) follows the equations given in Table 6.1 (visit the website <http://www.elsevierdirect.com/companion.jsp?ISBN=9780444537966> and refer Conversion elastic parameters).

Figure 7.7 gives the average and the range for static Young's modulus and Poisson's ratio for common rock types.

7.3.4 Failure/Strength Properties

Strength characterizes the amount of applied stress at rock failure—the stress condition may be compressive, tensile, or shear and defines the different measures of rock strength. Lockner (1995) published a systematic description of the physical processes of rock failure that includes a bibliography of fundamental papers.

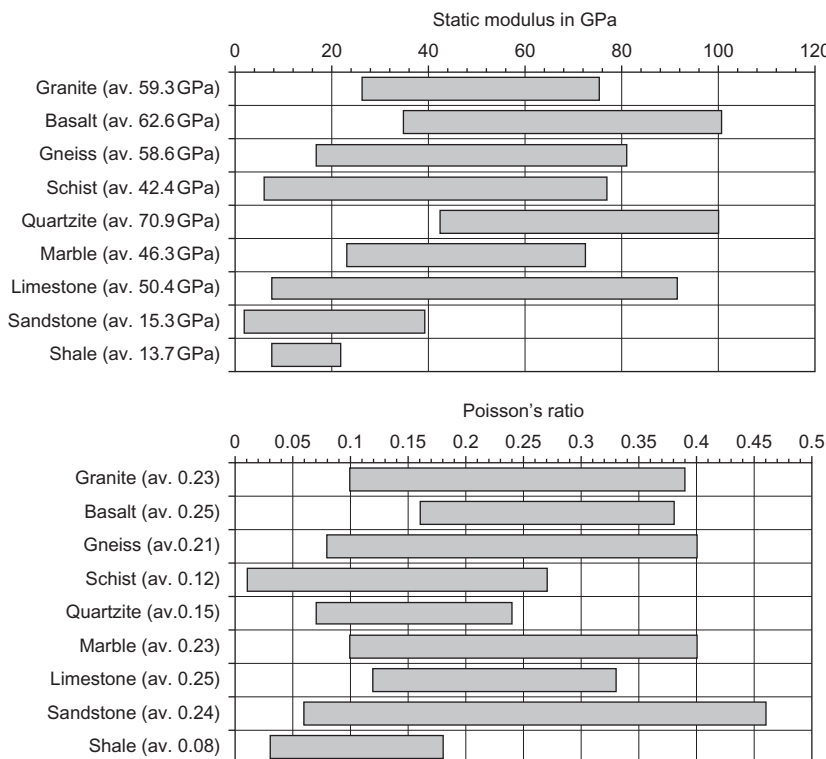


FIGURE 7.7 Average and the range for static Young's modulus and Poisson's ratio for common rock types (after tables from Johnson and DeGraff, 1989).

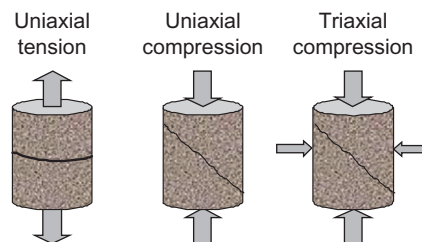


FIGURE 7.8 Three modes of a failure test; arrows indicate applied stresses.

There are three fundamental modes of a failure test shown in [Figure 7.8](#).

The simplest and frequently used failure criterion was formulated by Coulomb in 1773: a shear stress τ tending to cause a failure across a plane is resisted by

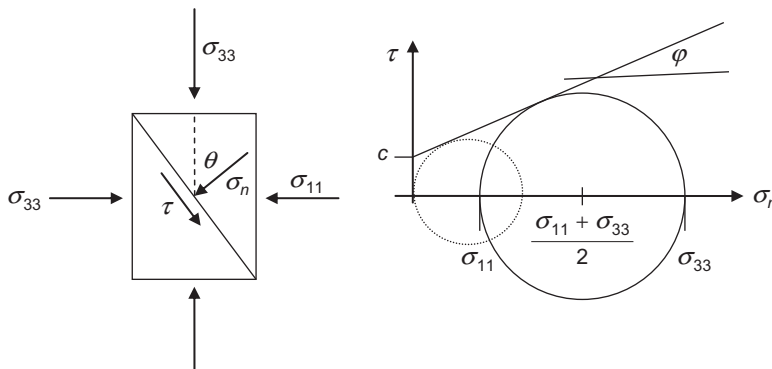


FIGURE 7.9 Mohr's diagram τ versus σ and Mohr's circle with a cylindrical sample under the influence of horizontal stress $\sigma_{11} = \sigma_{22}$ and vertical stress σ_{33} .

- the cohesion c of the material;
- the normal stress σ_n across the plane times the coefficient of internal friction μ (or the angle of internal friction ϕ , where $\mu = \tan \phi$):

$$\tau = c + \tan \phi \cdot \sigma_n \quad (7.13)$$

Failure process and strength properties are illustrated best by Mohr's circle. [Figure 7.9](#) demonstrates the principle:

- On a cylindrical sample under a constant lateral or radial stress $\sigma_{11} = \sigma_{22}$, an axial stress σ_{33} increases until the sample fails (rupture).
- Rupture is connected with a weak shear plane with the angle θ .

Stress normal to the shear plane is

$$\sigma_n = \frac{\sigma_{11} + \sigma_{33}}{2} + \frac{\sigma_{11} - \sigma_{33}}{2} \cos(2\theta) \quad (7.14)$$

Shear stress parallel to the shear plane is

$$\tau = \frac{\sigma_{33} - \sigma_{11}}{2} \sin(2\theta) \quad (7.15)$$

The equations represent in a $\tau - \sigma_n$ plot a circle, called Mohr's circle ([Figure 7.9](#)).

A series of experiments results in a number of circles ([Figure 7.10](#)). The envelope:

- indicates stress conditions of failure (all positions outside the envelope);
- can be approximated in many cases as a straight line and delivers the cohesion c as the intercept with the vertical axis and the angle of internal friction ϕ as slope.

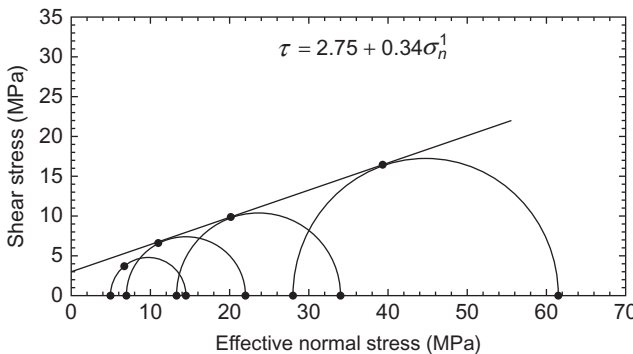


FIGURE 7.10 Mohr's circles and associated failure envelope for intact samples of Muderong Shale (Dewhurst and Hennig, 2003).

Cohesion c and angle of internal friction ϕ are combined as failure criterion in Coulomb's law, which describes the maximum shear stress τ at a given normal stress σ_n (Equation (7.13)):

$$\tau = c + \tan \phi \cdot \sigma_n \quad (7.16)$$

Coulomb's criterion results in the relationship between principal stresses and rock properties (Goodman, 1988; Kezdi, 1969):

$$\sigma_{33} = \sigma_{11} \cdot \tan^2 \left(45 + \frac{\phi}{2} \right) + 2 \cdot c \cdot \tan \left(45 + \frac{\phi}{2} \right) \quad (7.17)$$

The uniaxial compression strength results for $\sigma_{11} \rightarrow 0$

$$\sigma_{33} = \sigma_c = 2 \cdot c \cdot \tan \left(45 + \frac{\phi}{2} \right) \quad (7.18)$$

Figure 7.10 shows as an example Mohr's diagram for the Muderong shale, a relatively weak material with a cohesive strength of 2.75 MPa and a friction coefficient of 0.34. The envelope delivers the equation (Dewhurst and Hennig, 2003):

$$\tau = 2.75 + 0.34 \cdot \sigma_n \quad (7.19)$$

Table 7.2 gives some strength data from a compilation by Goodman (1988).

The influence of mineral composition upon strength properties for one rock type is demonstrated in **Table 7.3**.

Uniaxial compression strength (also unconfined compression strength, UCS) is the most used practical property for an overall classification (**Table 7.4**).

For the uniaxial compression strength, **Figure 7.11** and **Table 7.5** show some values from the literature; data in the table also demonstrate the different magnitudes for the same rock group from different locations.

TABLE 7.2 Some Data for Cohesion (Shear Strength Intercept) and Angle of Internal Friction

Rock	Porosity ϕ	Cohesion c in MPa	Angle Internal Friction ϕ	Range of Confining Pressure in MPa
Berea sandstone	0.182	27.2	27.8	0–200
Bartlesville sandstone		8.0	37.2	0–203
Pottsville sandstone	0.140	14.9	45.2	0–68.9
Muddy shale	0.047	38.4	14.4	0–200
Stockton shale		0.34	22.0	0.8–4.1
Edmonton bentonitic shale	0.44	0.3	7.5	0.1–3.1
Georgia marble	0.003	21.2	25.3	5.6–68.9
Indiana limestone	0.194	6.72	42.0	0–9.6
Hasmark dolomite	0.035	22.8	35.5	0.8–5.9
Blaine anhydrite		43.4	29.4	0–203
Stone Mountain granite	0.002	55.1	51.0	0–68.9
Nevada Test Site basalt	0.046	66.2	31.0	3.4–34.5
Schistose gneiss				
90° to schistosity	0.005	46.9	28.0	0–69
30° to schistosity	0.019	14.8	27.6	0–69

From a Compilation by Goodman (1988).

TABLE 7.3 Cohesion and Angle of Internal Friction for Dolomite-Anhydrite Rocks (Piora Dolomite/Gotthard, Switzerland)

Anhydrite Content in %	Cohesion c in MPa	Angle Internal Friction ϕ
100–80	8.31	32.6
80–60	8.62	31.8
60–40	4.76	37.4
20–0	0	43.8

Range of confining pressure 13–80 MPa; Heiland and Borm (2000).

TABLE 7.4 Engineering Rock Classification

Rock Class	Type	Uniaxial Compression Strength in MPa
A	Very high strength	>220
B	High strength	110–220
C	Medium strength	55–110
D	Low strength	28–55
E	Very low strength	<28

Carmichael (1989).

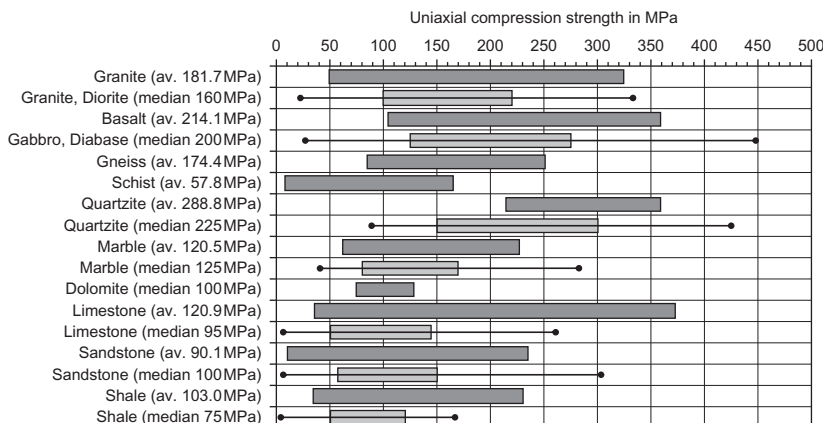


FIGURE 7.11 Average and range of uniaxial compression strength for common rock types. The dark gray boxes represent the range according to tables from Johnson and DeGraff (1989). The light gray boxes and the line with dots are data after Lockner (1995) and Lama and Vutukuri (1978): Boxes represent the range of median value $\pm 25\%$; error bars represent the full range of the data (with the exception of some outliers).

The strength properties of rocks are controlled mainly by:

- the type and mechanical quality of the bonding between the solid components or particles (solid crystal bonds for igneous rocks, cementation for clastic consolidated sediments, cohesion for clay, and friction for cohesionless sediments like sand and gravel);
- the presence, distribution, and orientation of “defects” such as fractures, and fissures;
- the internal rock structure (lamination, schistosity, anisotropy).

TABLE 7.5 Mean Values for the Uniaxial Compression Strength of Some Rocks

Rock	Uniaxial Compression Strength in MPa	Reference
Granite	100–250	R
Granite (Westerly)	229	J
Syenite	100–340	R
Quartzite	290–300	R
Quartzite, Cheshire	460	J
Diabase, Frederick	487	J
Marble	60–190	R
Marble	50–250	F
Marble, Tennessee	152	J
Marble, Carrara	89	J
Marble, Carrara; porosity = 0.69 ± 0.23	93.6 ± 15.3	H
Greywacke, Thuringia, Germany; porosity = 0.4–1.5%	34–123	M
Sandstone	35–150	R
Sandstone	1–250	F
Berea sandstone	74	F
St. Peter sandstone	37	F
Wildmoore sandstone	7	F
Weak reservoir sandstone (North Sea)	1	F
Sandstone, Gosford; porosity = 12.7 ± 2.4	44.1 ± 6.7	H
Sandstone, Saxonia, Germany; porosity = 19–29%	23.5–75.0	M
Shale	2–250	F
Pierre shale	7.5–13.9	F
Limestone	90–120	R
Limestone	5–250	F

(Continued)

TABLE 7.5 (Continued)

Rock	Uniaxial Compression Strength in MPa	Reference
Bedford limestone	51	F
Limestone, Solenhofen	224	J
Limestone, Harz, Germany; porosity = $\phi = 0.4\text{--}3.2\%$	37–181	M
Dolomite	40–350	F
Rock salt	35	R
Sand	0.004–0.012	K
Silt, clay—soft	0.05	K
medium	0.05–0.1	K
hard	0.1–0.4	K
Clay	0.2–0.5	F

Reference key: F, Fjaer *et al.* (2009); K, Kezdi (1969); J, Jaeger and Cook (1976); H, Howarth *et al.* (1989); M, Müller (1978); R, Rshewski and Novik (1971).

7.4 CORRELATION BETWEEN STATIC AND DYNAMIC MODULI

The two types of investigation, static rock mechanical tests and dynamic seismic or ultrasonic measurements, deliver mechanical moduli, which are frequently called “static” (E_{stat}) and “dynamic” (E_{dyn}) moduli, respectively.

The modulus is independent on the duration of stress application only for an ideal elastic material—and there is no difference in the moduli from a “long-term” static and an extremely “short-term” dynamic test. For rocks in general we find $E_{\text{dyn}} > E_{\text{stat}}$.

For this discrepancy between the static and dynamic moduli, a couple of mechanisms are responsible:

1. The magnitudes of stress and strain generated by ultrasonic or seismic wave propagation are extremely small compared to stress and strain associated with the static testing technique.
2. During static deformation, nonelastic components also occur (e.g., due to mobilization of microcracks and grain boundaries). However, ultrasonic (and seismic) measurements are mainly affected by the elastic response.

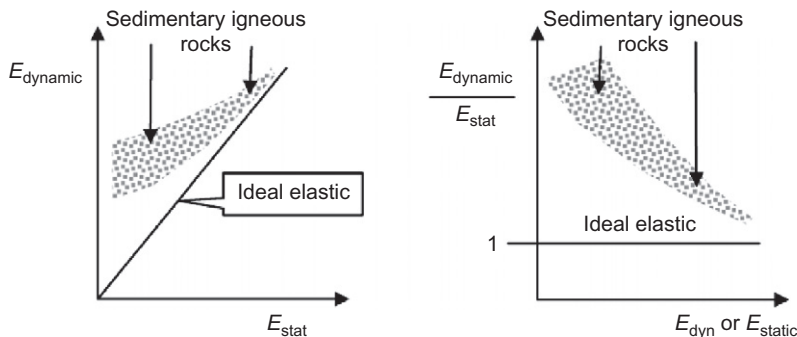


FIGURE 7.12 Dynamic versus static modulus (left) and the ratio of the two moduli versus static or dynamic modulus (right) schematic.

Figure 7.12 shows the expected tendency. The difference between static and dynamic moduli decreases in two ways:

1. From rock types with low moduli (or velocity) to rock types with high moduli (or velocity)
2. From unconsolidated sediments to compact, nonfractured rocks.

Two examples may confirm these tendencies: Figure 7.13 gives a summary picture of measurements on a microcline-granite:

- Both moduli decrease with increasing crack porosity, but the static modulus E_{stat} shows a stronger decrease than the dynamic modulus E_{dyn} (A).
- Therefore, the ratio $E_{\text{dyn}}/E_{\text{stat}}$ increases with increasing crack porosity (B).
- Relatively compact (slightly fractured) rocks have high moduli and low ratio $E_{\text{dyn}}/E_{\text{stat}}$ (near 1), but fractured rocks have low moduli and high ratio $E_{\text{dyn}}/E_{\text{stat}} > 1$ (C).

Figure 7.13C confirms the predicted trends of Figure 7.12 with experimental data. E_{stat} versus E_{dyn} is plotted in Figure 7.13D and shows a linear correlation as first approximation for this particular rock type:

$$E_{\text{stat}} = 1.137 \cdot E_{\text{dyn}} - 9.685 \quad (7.20)$$

where E is in GPa, and the regression coefficient is 0.98.

King (1983) derived from measurements on 152 specimens of igneous and metamorphic rocks from the Canadian Shield:

$$E_{\text{stat}} = 1.263 \cdot E_{\text{dyn}} - 29.5 \quad (7.21)$$

where E is in GPa and the regression coefficient is 0.90.

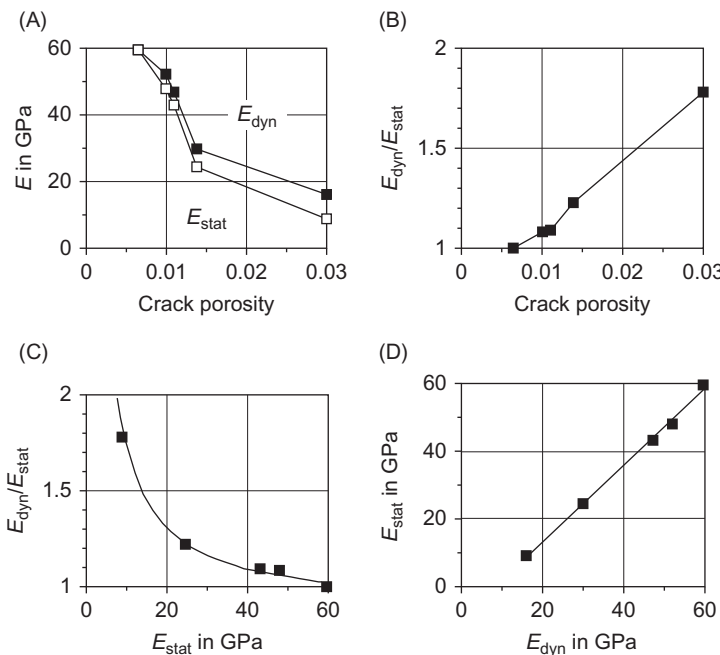


FIGURE 7.13 Static and dynamic determined Young's modulus for microcline-granite (data after Belikov et al., 1970). (A) E_{stat} and E_{dyn} as function of the crack porosity ϕ_c . (B) Ratio $E_{\text{dyn}}/E_{\text{stat}}$ as function of the crack porosity ϕ_c . (C) Ratio $E_{\text{dyn}}/E_{\text{stat}}$ as function of the static modulus E_{stat} . (D) Correlation between E_{dyn} and E_{stat} .

The correlation between the ratio of dynamically and statically determined moduli and pressure was studied by Cheng and Johnston (1981) for various rock types (Navajo and Berea sandstone, Westerly granite, Ammonia Tanks tuff). In this case, the bulk compressional moduli have been compared. With increasing pressure, the material becomes more compact, fractures are closed, and the discrepancy between the two moduli becomes smaller. Figure 7.14 shows two selected examples. A comparable result for Boise sandstone was published by King (1970).

Despite the fundamental difference in the mechanism, empirical correlations have been used successfully to predict static moduli from elastic wave velocities or dynamic moduli. These correlations are valid for the type of rock used to establish the correlation. Some further examples are presented in the following.

Bastos et al. (1998) investigated correlations between static and dynamic moduli in limestone core samples from an offshore Brazilian field. The samples are from three wells at depths of ~ 2350 – 2550 m. The cores (diameter of 5 cm; length of 12.5 cm) were placed in a triaxial cell for simultaneous

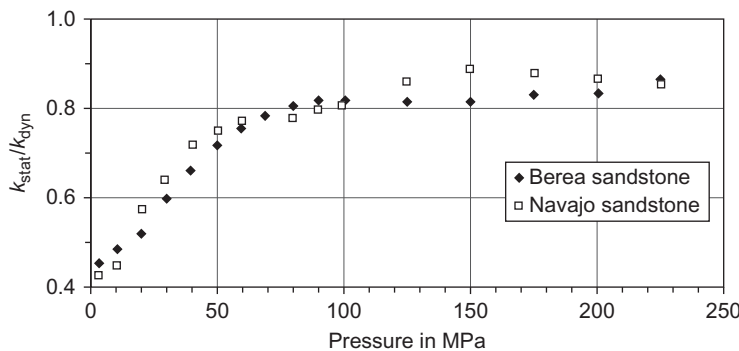


FIGURE 7.14 Ratio of static and dynamic compressional bulk modulus $k_{\text{stat}}/k_{\text{dyn}}$ as a function of pressure for Navajo and Berea sandstone (data after Cheng and Johnston, 1981).

static and dynamic (500 kHz) measurements. The results are the regressions (all moduli in GPa):

$$E_{\text{stat}} = 0.675 \cdot E_{\text{dyn}} - 3.84 \quad R^2 = 0.95 \quad (7.22)$$

$$k_{\text{stat}} = 0.992 \cdot k_{\text{dyn}} - 8.82 \quad R^2 = 0.89 \quad (7.23)$$

$$\mu_{\text{stat}} = 0.621 \cdot \mu_{\text{dyn}} - 0.95 \quad R^2 = 0.94 \quad (7.24)$$

McCann and Entwistle (1992) also used linear regressions. The dynamic modulus was determined from full waveform acoustic logs, and the static modulus was determined on samples in the laboratory. Data and samples are from a number of boreholes in Great Britain (Jurassic sediments) and granite from Scotland. The relationship for all specimens is

$$E_{\text{stat}} = 0.69 \cdot E_{\text{dyn}} + 6.40 \quad R^2 = 0.75 \quad (7.25)$$

As a result of experimental investigations of 300 igneous and metamorphic rock samples from Sweden, Starzec (1999) found a correlation:

$$E_{\text{stat}} = 0.48 \cdot E_{\text{dyn}} - 3.26 \quad R^2 = 0.82 \quad (7.26)$$

For shale from the North Sea, Horsrud (2001) gives a detailed analysis and derived the empirical correlation between compressional wave velocity (dynamic) and static Young's modulus E_{stat} and static shear modulus μ_{stat} :

$$E_{\text{stat}} = 0.076 \cdot V_{\text{P}}^{3.23} \quad \mu_{\text{stat}} = 0.03 \cdot V_{\text{P}}^{3.30} \quad R^2 = 0.99 \quad (7.27)$$

where $E_{\text{stat}}, \mu_{\text{stat}}$ are in GPa, and V_{P} is in km s^{-1} .

The differences between dynamic and static moduli are extreme for unconsolidated rocks, mainly as a result of the deformability of the rock skeleton and the low static moduli. Gorjainov and Ljachowickij (1979) have determined the dynamic and static Young's modulus from shallow seismic

TABLE 7.6 Static and Dynamic Young's Modulus for Unconsolidated Rocks

Rock Type	Description	E_{stat} in MPa	E_{dyn} in MPa
Cohesionless	Gravel	100–200	300–800
	Sand, loose	40–100	150–300
	Sand, dense	80–200	200–500
Cohesive	Clay, hard	10–50	50–500
	Clay, soft	3–6	30–80

After Schön (1983, 1996), Militzer et al. (1986), Fröhlich (1975), Fröhlich and Schwinge (1978).

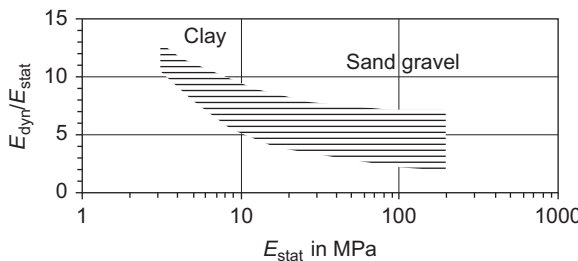


FIGURE 7.15 Tendency of the ratio $E_{\text{dyn}}/E_{\text{stat}}$ for unconsolidated sediments.

measurements and soil mechanic tests for a depth of up to 10 m and also applied a linear regression

$$E_{\text{stat}} = 0.085 \cdot E_{\text{dyn}} + 3.0 \quad \text{sand, wet} \quad (7.28)$$

$$E_{\text{stat}} = 0.033 \cdot E_{\text{dyn}} + 6.5 \quad \text{clay} \quad (7.29)$$

where the moduli are in MPa for the unconsolidated rocks.

Table 7.6 gives an overview of the mean ranges of the two Young's moduli. Mean values for the ratio $E_{\text{dyn}}/E_{\text{stat}}$ for unconsolidated rocks are as great as 5 for cohesionless and 20 for cohesive rocks. McCann and Entwistle (1992) reported values of 100–200 for soft mudrocks and alluvial materials.

Figure 7.15 shows the tendency of the ratio $E_{\text{dyn}}/E_{\text{stat}}$ for unconsolidated sediments.

In view of the magnitude of the data scatter, these and comparable relationships yield only a very raw approximation. For a general and practical application, they are not transferable but must be derived in each case for the individual rock type.

It can be expected that correlations between dynamic properties derived from shear wave velocities give a better correlation, because shear wave velocities, particularly for unconsolidated rocks, are controlled by the “skeleton properties of the rock.” These “skeleton properties” predominantly control the static mechanical properties.

7.5 CORRELATION BETWEEN SEISMIC VELOCITY AND STRENGTH PROPERTIES

Correlation between strength properties and seismic velocities within a rock type is based on some dominant influences changing both properties in a comparable direction:

- increasing fracturing or porosity decreases both properties;
- increasing cementation increases both properties.

A correlation can be expected for a specific rock type but not as a “general formula.”

Figure 7.16 gives a first impression of the correlation between elastic and strength properties.

7.5.1 Some Experimental Results and Empirical Relationships

McNally (1987) studied the correlation between the uniaxial compression strength (142 samples) and the compressional wave slowness (measured with

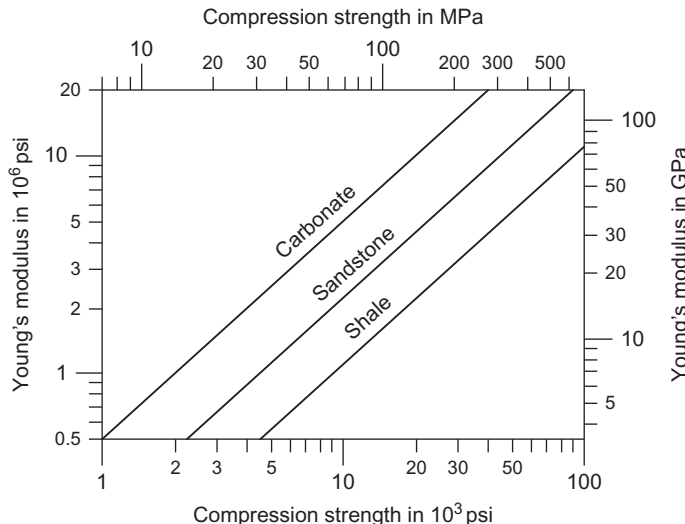


FIGURE 7.16 Correlation between Young's modulus and compression strength for three formation types after Bigelow and Howell (1995), Coates and Denoo (1988) (original scales are in psi; they have also been converted to SI units).

a sonic logging tool) of fine- to medium-grained sandstone from the German Creek formation (Queensland, Australia). There is—for this particular geological situation—a good correlation (Figure 7.17) that is probably controlled by variation of porosity and grain-contact quality. The resulting regression is originally with uniaxial compression strength in MPa and Δt in $\mu\text{s ft}^{-1}$

$$\sigma_c = 1277 \cdot \exp(-0.0367 \cdot \Delta t) \quad \text{with } R^2 = 0.83 \quad (7.30)$$

In Figure 7.17, data are converted into velocities (m s^{-1}) and redrawn as a plot of uniaxial compression strength versus compressional wave velocity. Two regressions are calculated:

$$\text{linear regression } \sigma_c = 0.050 \cdot V_p - 114.5 \quad \text{with } R^2 = 0.88 \quad (7.31)$$

$$\text{power law } \sigma_c = 3 \cdot 10^{-11} \cdot V_p^{3.45} \quad \text{with } R^2 = 0.86 \quad (7.32)$$

Jizba (1991) investigated correlations between compressional and shear wave velocity and uniaxial compression strength. Figure 7.18 shows an example for a tight sandstone confirming the general tendency for both wave types. The author noted that scatter in these data is attributed to confining pressure and clay content.

Horsrud (2001) derived the following empirical correlation especially for shale (North Sea)

$$\sigma_c = 0.77 \cdot V_p^{2.93} \quad R^2 = 0.99 \quad (7.33)$$

where σ_c is in MPa and V_p in km s^{-1} .

Table 7.7 gives some more empirical relationships between uniaxial compression strength (in MPa) and compressional velocity (in m s^{-1}) from the literature.

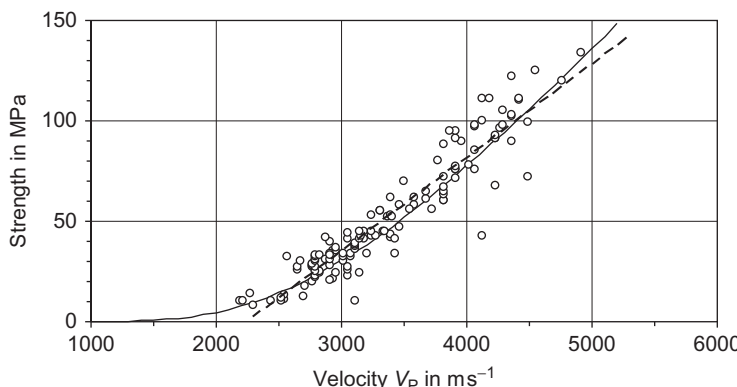


FIGURE 7.17 Uniaxial compression strength versus compressional wave velocity; sandstone from the German Creek formation, Queensland, Australia. Points are experimental data after McNally (1987); curves follow the two regression equations.

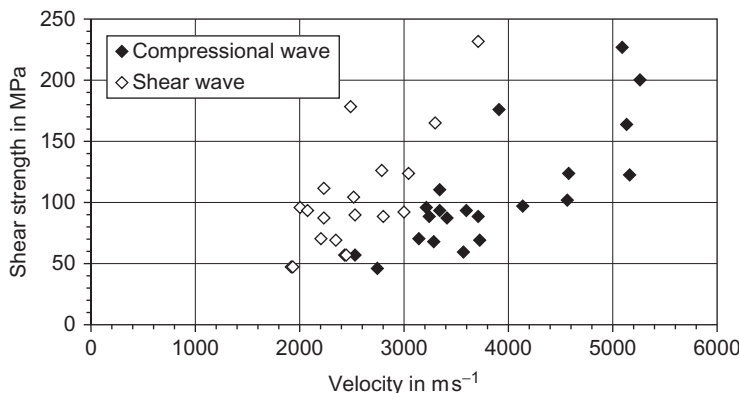


FIGURE 7.18 Shear strength versus velocity of compressional and shear wave; room-dry tight gas sandstone (data from Jizba, 1991).

TABLE 7.7 Empirical Relationships Between Uniaxial Compression Strength (in MPa) and Compressional Velocity (in m s^{-1})

Rock type	Equation	Regression Coefficient	Reference
Sandstone	$\sigma_c = 0.035 \cdot V_p - 31.5$		F
Sandstone	$\sigma_c = 0.050 \cdot V_p - 114.5$	0.88	N
Sandstone	$\sigma_c = 3 \cdot 10^{-11} \cdot V_p^{3.45}$	0.88	N
Sandstone, marble	$\sigma_c = 0.018 \cdot V_p - 16.26$	0.70	HO
Limestone (Voronesh region/Russia)	$\log \sigma_c = 0.358 \cdot V_p + 0.283$	0.86	GR
Limestone (Ural/Russia)	$\log \sigma_c = 0.212 \cdot V_p + 1.874$	0.80	GR
Limestone (Germany)	$\sigma_c = 2.45 \cdot V_p^{1.82}$		MS
Gabbro, Peridotite	$\log \sigma_c = 0.280 \cdot V_p + 1.550$	0.86	GR
Schist	$\log \sigma_c = 0.444 \cdot V_p + 0.003$	0.86	GR
Sandy and shaly rocks	$\sigma_c = -0.98 \cdot V_p + 0.68 \cdot V_p^2 + 0.98$	0.99	GL
Shale	$\sigma_c = 0.77 \cdot V_p^{2.93}$		H

Reference key: F, Freyburg (1972); N, analysis of data from McNally (1987); HO, data from Howarth et al. (1989); H, Horsrud (2001); GR, Golubev and Rabinovich (1976); MS, Militzer and Stoll (1973); GL, Gorjainov and Ljachovickij (1979).

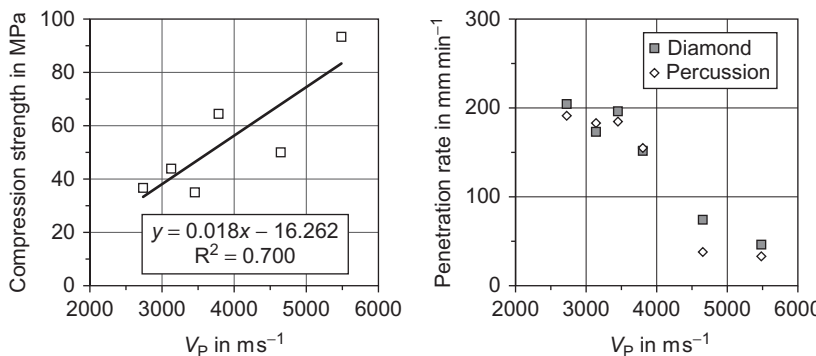


FIGURE 7.19 Correlation between compressional wave velocity (saturated) and uniaxial strength (left) and the penetration rates for diamond and percussion drilling (right); data (averages) from Howarth et al. (1989). Rocks are sandstone and marble.

A compilation of experimental results and relationships was also published by Chang (2004) and Barton (2007) based on data from several authors.

Rock drillability is controlled by strength properties; therefore, correlations between elastic wave velocities and parameters of rock drillability have also been investigated. For example, Somerton et al. (1969) reported that sonic velocity is a good indicator of rock drillability for a given rock type (in this case, limestone and sandstone) and the type of drilling tool.

Howarth et al. (1989) measured various physical properties (density, porosity, velocities, strength, and rock classification properties) on sandstones and marbles as well as the penetration rate for different drilling machines. The authors concluded that statistically significant trends exist between the properties and penetration rates, especially for the elastic wave velocity and penetration rate correlation. Figure 7.19 shows the correlation between the compressional wave velocity (saturated) and uniaxial strength and the penetration rates for diamond and percussion drilling.

7.5.2 Model-Based Relationships

Two model concepts shall be tested in order to explain both correlation and scatter of strength versus velocity relations:

1. The simple defect model (Section 6.7.4) preferred for fractured rocks
2. The structured model (Section 6.7.7) preferred for porous rocks.

The objective of this is not to find a numerically exact solution, but rather a model-based formulation of the relationship.

In Section 6.7.4, a simple defect model for a fractured rock was presented; it can be used for derivation of a relationship between velocities and

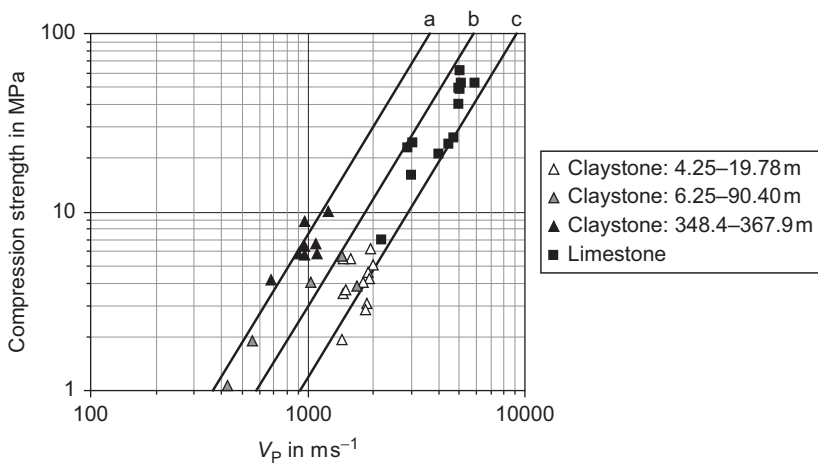


FIGURE 7.20 Comparison of calculated relationship between σ_c and V_p after Equation (7.35) and experimental data: lines are calculated—a for $A_{\sigma,V} = 7.5 \cdot 10^{-6} \text{ MPa (m s}^{-1}\text{)}^{-2}$, b for $A_{\sigma,V} = 3.0 \cdot 10^{-6} \text{ MPa (m s}^{-1}\text{)}^{-2}$, c for $A_{\sigma,V} = 1.2 \cdot 10^{-6} \text{ MPa (m s}^{-1}\text{)}^{-2}$. Experimental data (dots): claystone—data from Wannakao et al., 2009; classified for a shallow (4.25–19 m depth), intermediate (79.25–90.40 m) and deep 348.4–367.9 m section. limestone: Erzgebirge/ Germany (outcrop).

uniaxial compressive strength. Assuming that the strength of a material is controlled by the material section without defects, for the model the simple relation results:

$$\sigma_c = \sigma_{c,\text{solid}}(1 - D) \quad (7.34)$$

where $\sigma_{c,\text{solid}}$ is the strength of the intact matrix material and D the “defect parameter.” A comparison with Equation (6.112) results in a relationship between the strength and the square of the velocity:

$$\sigma_c = V_p^2 \left(\frac{\sigma_{c,\text{solid}}}{V_{p,\text{solid}}^2} \right) = V_p^2 \cdot A_{\sigma,V} \quad (7.35)$$

$A_{\sigma,E} = \sigma_{\text{solid}}/V_{p,\text{solid}}^2$ is controlled by the solid (nonfractured) matrix material properties.

Figure 7.20 shows a comparison between calculated straight lines in a log–log plot and experimental data measured at limestone and claystone samples. There is a reasonable degree of confidence between the calculated dependence and the measured data with $A_{\sigma,V} = 1.2 \cdot 10^{-6} - 3.0 \cdot 10^{-6} \text{ MPa (m s}^{-1}\text{)}^{-2}$ for the limestone samples. For the claystone as a relatively “soft material,” data are classified for a shallow (4.25–19 m depth), intermediate (79.25–90.40 m), and deep 348.4–367.9 m section. The three groups reflect the estimated tendency and correspond to different parameters $A_{\sigma,V}$ in the range between $1.2 \cdot 10^{-6}$ and $7.5 \cdot 10^{-6} \text{ MPa (m s}^{-1}\text{)}^{-2}$.

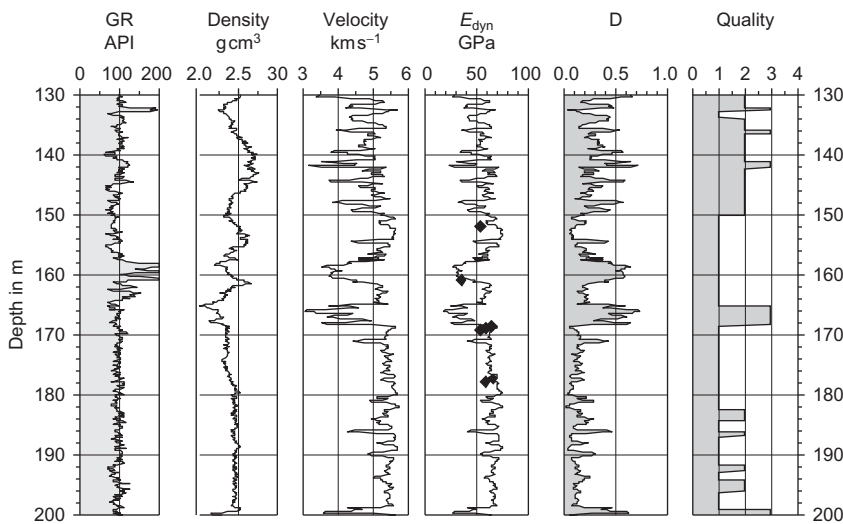


FIGURE 7.21 Geophysical borehole measurements for rock quality classification in an exploration well of the Koralm Tunnel Project. Reference key: Logs and log analysis from Joanneum Research; core analysis and static tests from Technical University of Graz. Tracks 1–3: geophysical logs (gamma, acoustic, density); Track 4: curve represents Young's modulus (dynamic modulus), calculated from acoustic and density logs. Dots represent the static determined values; Track 5: log-derived defect parameter D ; Track 6: rock quality after visual core inspection.

An example for application of geophysical borehole measurements for rock quality classification is shown in Figure 7.21. The section 130–200 m consists mainly of gneiss (Plattengneis) and some layers of pegmatiode and cataclasite. Tracks 1–3 give the geophysical logs (gamma, density, and acoustic log). Track 4 shows dynamic Young's modulus calculated from acoustic and density logs. Because no shear wave was measured, a mean Poisson's ratio of 0.2 was assumed. Dots represent the static Young's modulus, determined in the laboratory. There is a relatively good fit between the two moduli.

Track 5 gives the log-derived defect parameter D , calculated with $V_{P,\text{solid}} = 5800 \text{ m s}^{-1}$ (maximum value). The curve reflects a variation of rock quality. For comparison, the result of a visual geological classification from cores is plotted in Track 6. Sections with the highest quality have a value of 1; with medium quality, a value of 2; and with bad quality, a value of 3.

There is a good match between the two different quality measures. Only in section 157–162 m is there a remarkable difference present: the log-derived high-defect value is not confirmed by bad quality from visual inspection. This conflict results from a change of rock composition. The section is an alternating layering of pegmatiode and cataclasite (indicated also by

the gamma log); thus this part is not represented by the “solid velocity of the gneiss” $V_{P,\text{solid}} = 5800 \text{ m s}^{-1}$.

The example shows the following:

- Geophysical logs (and seismic measurements) can be used at first for a detailed rock quality classification. As a result, typical zones can be defined (particularly zones with probably low rock quality).
- Logs also allow the detection of a change of rock composition (mineral composition),
- Based on these results, selected core investigations and laboratory tests for direct rock property measurements (uniaxial strength test, triaxial test, etc.) are recommended in order to deliver a representative model for geomechanical calculations.

The “structured model” was derived for elastic properties in Section 6.7.7. Strength properties of a sedimentary rock—particularly with a granular structure—are controlled by the mechanical strength behavior at the grain–grain contact. For this contact, Coulomb’s law can be applied

$$\tau = \mu_{\text{contact}} \cdot \sigma_n + c_{\text{contact}} \quad (7.36)$$

where μ_{contact} and c_{contact} refer to the contact region. Shear stress τ and normal stress σ_n are related to the contact plane between the grains. Therefore, the two stresses can be expressed in terms of stress components in the microsystem. Coulomb’s law for the microsystem is now (parameters a, b ; see Section 6.7.7):

$$\sigma_{\bar{1}} = \mu_{\text{contact}} \cdot \sigma_{\bar{3}} + c_{\text{contact}} \frac{(a - b)^2}{a^2} \quad (7.37)$$

The stress components in the microsystem are composed by the components in the macrosystem:

$$\sigma_{\bar{1}} = \sigma_1 \cdot \cos \alpha - \sigma_3 \cdot \sin \alpha \quad \sigma_{\bar{3}} = \sigma_3 \cdot \cos \alpha + \sigma_1 \cdot \sin \alpha \quad (7.38)$$

Insertion leads to

$$\sigma_3 = - \frac{\sigma_1 (\mu_{\text{contact}} \cdot \sin \alpha - \cos \alpha) + c_{\text{contact}} (1 - \frac{b}{a})^2}{\sin \alpha - \mu_{\text{contact}} \cdot \cos \alpha} \quad (7.39)$$

Uniaxial compression strength results for zero radial stress $\sigma_1 = 0$:

$$\sigma_c = \frac{c_{\text{contact}} (1 - b \cdot a^{-1})^2}{\sin \alpha - \mu_{\text{contact}} \cdot \cos \alpha} \quad (7.40)$$

Figure 7.22 shows examples of forward-calculated uniaxial compression strength as a function of porosity; curve parameter is the structure angle. Calculations can be found on the website <http://www.elsevierdirect.com/companion.jsp?ISBN=9780444537966>: Elastic_Mechanical_structured model.

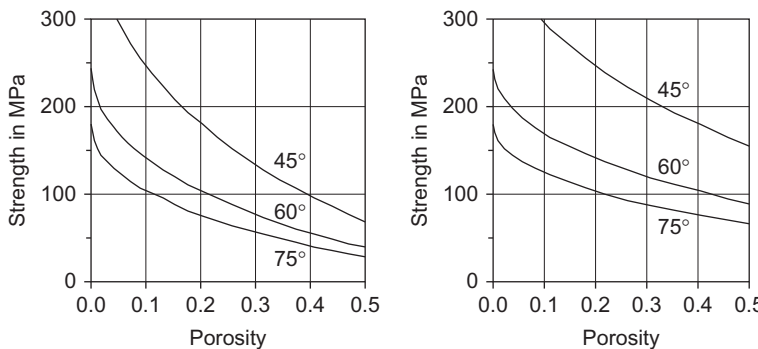


FIGURE 7.22 Forward-calculated uniaxial compression strength as a function of porosity; curve parameter is the structure angle. Input contact properties: $c_{\text{contact}} = 150 \text{ MPa}$; $\mu_{\text{contact}} = 0.5$. The left figure was calculated with $\alpha_{\text{pore}}/\alpha_{\text{grain}} = 1.0$; right figure, with $\alpha_{\text{pore}}/\alpha_{\text{grain}} = 2.0$; for calculations, visit the website <http://www.elsevierdirect.com/companion.jsp?ISBN=9780444537966> and refer Elastic_Mechanical. Structured model.

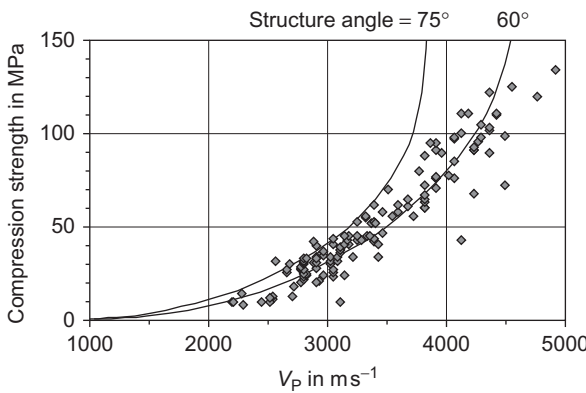


FIGURE 7.23 Uniaxial compression strength versus compressional wave velocity; curves are model calculations; curve parameter is the structure angle. Input parameters are: $\alpha_{\text{pore}}/\alpha_{\text{grain}} = 1.0$, $f = 4.0$, $V_3 = 7,000 \text{ m s}^{-1}$, $\mu_{\text{contact}} = 0.5$, $c_{\text{contact}} = 150 \text{ MPa}$; for calculations, visit the website <http://www.elsevierdirect.com/companion.jsp?ISBN=9780444537966> and refer Elastic_Mechanical. Structured model. Dots are experimental data for a sandstone (German Creek formation, Queensland, Australia, after McNally (1987, same as in Figure 7.17).

The application of the same model for velocity (Section 6.7.7) and strength calculation offers the possibility for the derivation of relationships between the two mechanical properties. Figure 7.23 shows an example. Model calculation is compared with experimental data from Figure 7.17. There is a good fit for an average structure of angle $\alpha \approx 60^\circ$.

In Section 6.7.7.5, the model is used to study changes of velocities and velocity ratios during compression and strength experiments. Velocity ratios in particular indicate different phases of the mechanical process like compaction and pore collapse in terms of structure and bonding.

Electrical Properties

8.1 FUNDAMENTALS

Electrical measurements are an important group of methods in applied geophysics. Resistivity measurements in a well by the Schlumberger brothers were the first commercial type of well logging. Today, the contrast between conductive formation water and insulating hydrocarbons is the basis for a saturation determination following Archie's concept (Archie, 1942).

For a petrophysical characterization of rocks, two electrical parameters are relevant:

1. Specific electrical resistivity
2. Dielectric permittivity.

For most common resistivity measurements, Ohm's law gives the background to determine a resistance RES (in ohms) from a measurement of a flowing current I (in amperes) and the voltage drop U (in volts):

$$\text{RES} = \frac{U}{I} \quad (8.1)$$

Electrical resistance is connected with the material property "specific electrical resistivity" (or its inverse—the conductivity) via a geometry parameter that considers the geometry of the current distribution. For the simple case of a cylindrical sample with current flow parallel to the axis, the relationship is

$$\text{RES} = \rho \frac{l}{A} \quad (8.2)$$

where l is the length and A is the cross section of the sample. Specific electrical resistivity ρ is given in ohm meters (ohm m). In this textbook, the sign R (with a subscript) is used for the specific electrical resistivity following the commonly used notation in well-logging practice.

Two material properties are the subjects of this chapter—the specific electrical resistivity R and the dielectric permittivity ε . The following considerations may give a more general description of the corresponding processes and the connection between them.

The application of an electric field \vec{E} to a rock causes an electrical conduction and a dielectrical polarization process. Both processes result in a current:¹

$$\text{conduction current } \vec{j}_c = C(\omega) \vec{E} \quad (8.3)$$

$$\text{displacement current } \vec{j}_d = \varepsilon(\omega) \frac{\partial \vec{E}}{\partial t} \quad (8.4)$$

where

\vec{E} is the field strength

ε is the dielectric permittivity

j is the current density

C is the conductivity

ω is the angular frequency

t is time.

Frequency-dependent conductivity $C(\omega)$ and frequency-dependent permittivity $\varepsilon(\omega)$ are complex quantities with real and imaginary parts. Thus, complex electrical conductivity is:

$$C(\omega) = C'(\omega) + i \cdot C''(\omega) \quad (8.5)$$

where $C'(\omega)$ is the real and $C''(\omega)$ is the imaginary component. The real part represents the total energy loss (conduction), whereas the imaginary part represents the total storage loss (polarization).²

The phase shift with phase angle ϕ is

$$\tan \phi = \frac{C''}{C'} \quad (8.6)$$

Analog, the complex permittivity, is

$$\varepsilon(\omega) = \varepsilon'(\omega) - i \cdot \varepsilon''(\omega) \quad (8.7)$$

In real materials both properties—conductivity and permittivity—are present. Total current \vec{j} resulting from the applied oscillatory field of the form $E \propto e^{i\omega t}$ is the sum of conduction and displacement current:

$$\vec{j} = \vec{j}_c + \vec{j}_d = C \vec{E} + \varepsilon \frac{\partial \vec{E}}{\partial t} = (C + i \cdot \omega \cdot \varepsilon) \vec{E} \quad (8.8)$$

¹Equation 8.3 is a more general formulation of Ohm's law in terms of current density, field strength, and conductivity.

²The investigation of the complex conductivity as function of frequency is subject of complex resistivity measurements; it is called—particularly in the low-frequency range (<1000 Hz)—“spectral-induced polarization” (see section 8.8).

The simplest description of this behavior is a parallel circuit of a resistor and a capacitor. The conductive and dielectric properties are coupled complex and frequency-dependent properties are:

Frequency-dependent dielectric permittivity

$$\varepsilon(\omega) = \varepsilon(\omega) + \frac{C(\omega)}{i \cdot \omega} = \varepsilon'(\omega) - i \left[\varepsilon''(\omega) + \frac{C(\omega)}{\omega} \right] \quad (8.9)$$

Frequency-dependent conductivity

$$C(\omega) = C(\omega) + i \cdot \omega \cdot \varepsilon = [C(\omega) + \omega \cdot \varepsilon''(\omega)] + i \cdot \omega \cdot \varepsilon'(\omega) \quad (8.10)$$

As a consequence of Equations (8.9) and (8.10):

- the real component of electrical conductivity results for low frequencies ($\omega \rightarrow 0$);
- the real component of dielectric permittivity results for high frequencies ($\omega \rightarrow \infty$).

Units and symbols:

Specific electrical resistivity R is given in ohm meters (ohm m).

Electrical conductivity C is the inverse of specific electrical resistivity and given in Siemens per meter, or S m^{-1} .

Dielectric permittivity is the product of dielectric permittivity of vacuum $\varepsilon_0 = 8.854 \cdot 10^{-12} \text{ F m}^{-1} = 8.854 \cdot 10^{-12} \text{ s}^4 \text{ kg}^{-1} \text{ m}^{-3}$ and (dimensionless) relative dielectric permittivity ε_r

$$\varepsilon = \varepsilon_0 \cdot \varepsilon_r \quad (8.11)$$

Related topics discussed in the following chapters are:

- resistivity or conductivity of rocks (low-frequency phenomenon);
- permittivity of rocks (high-frequency phenomenon);
- frequency-dependent electrical properties and phenomena (spectral-induced polarization, SIP).

8.2 ELECTRICAL PROPERTIES OF ROCK COMPONENTS

8.2.1 Minerals—Solid Components

Table 8.1 shows values of specific electrical resistivity and the permittivity of some minerals. More detailed compilations are published by Olhoeft (1981), Beblo et al. (1982), Melnikov et al. (1975), Parchomenko (1965), Katsube and Collett (1976), and Keller (1989).

Most rock-forming minerals, particularly silicates and carbonates, have very high specific resistivities ($> 10^9$ ohm m); they are practical insulators.

Conductive minerals are sulfides and some oxides. They are rare in the earth's crust. An important member of the conductive group is graphite.

TABLE 8.1 Specific Electrical Resistivity R and Relative Permittivity ϵ_r (at Radiofrequencies) of Selected Minerals

Mineral	R ohm m (O)	ϵ_r (O)	ϵ_r (K)	Mineral	R ohm m (O)	ϵ_r (O)	ϵ_r (K)
Silicates				Sulfates			
Quartz	$2.0 \cdot 10^{14}$	4.5	4.2–5.9	Anhydrite	$1.0 \cdot 10^9$	6.5	
Amphibole, Hornblende	$4.8 \cdot 10^{10}$	8.0		Gypsum	$1.05 \cdot 10^{11}$	6.4	5.0–11.5
Microcline	$1.8 \cdot 10^{11}$	5.48		Apatite	$8.3 \cdot 10^{11}$	11.7	7.4–10.5
Orthoclase	$1.4 \cdot 10^{12}$	5.6		Barite	$1.2 \cdot 10^7$	10.0	7.0–12.2
Albite	$4.8 \cdot 10^8$	6.95	5.3–5.5	Halides			
Anorthite	$7.7 \cdot 10^9$	6.9	7.0–7.2	Halite	$5.0 \cdot 10^{13}$	5.9	5.7–6.2
Labradorite	$6.3 \cdot 10^8$	5.87		Sylvite			4.4–6.2
Muscovite	$2.2 \cdot 10^{12}$	7.6	6.2–8.0	Fluorite	$7.7 \cdot 10^{13}$	6.76	6.79
Biotite	$8.3 \cdot 10^{10}$	6.3	6.2–9.3	Oxides, sulfides			
Chlorite	$1.6 \cdot 10^9$	9.0		Hematite	$1.0 \cdot 10^2$	25.0	25.0
Kaolinite	$3.2 \cdot 10^7$	11.8		Magnetite	$1.0 \cdot 10^{-4}$		
Carbonates				Pyrite	$1.0 \cdot 10^{-3}$		33.7–81.0
Calcite	$9.0 \cdot 10^{13}$	6.35	7.8–8.5	Galena	$1.0 \cdot 10^{-3}$		17.9
Dolomite	$4.3 \cdot 10^{13}$	7.46	6.8–8.0	Sphalerite	$2.6 \cdot 10^{11}$	7.5	
Aragonite	$3.4 \cdot 10^{12}$	8.67					
Siderite	$8.3 \cdot 10^9$	9.3		Graphite	$1.4 \cdot 10^{-5}$		

Reference key: O, Olhoeft (1981) (converted data from conductivity); K, Keller (1989); Hearst and Nelson (1985).

A special type of mineral substance is clay; the electrical conductivity of clay is discussed in [Section 8.5](#).

The relative permittivities of most abundant rock-forming minerals are in the range 4–10. Some minerals have higher values, such as the sulfide and oxide groups.

The variations of magnitude of the electrical properties within one type or group are attributed to impurities and crystalline structures, which also produce electrical anisotropy (Hearst and Nelson, 1985).

8.2.2 Pore Fluids

Among the pore fluids, water is the only effective conductor. In many cases, the ionic conduction of the pore water is the dominant conduction mechanism in a porous or fractured rock, and the specific electrical resistivity is controlled mainly by:

- the chemical composition, concentration, and temperature of the brine or electrolyte;
- the volume fraction (porosity, saturation) and distribution of the electrolyte in the rock.

Gases and oil are essentially nonconductors: the specific electrical resistivity is in the order of $>10^9$ ohm m. Dortman (1976) gives a specific electrical resistivity for oil $R_{\text{oil}} = 10^9 - 10^{16}$ ohm m.

There also exists a distinct difference of the relative permittivity between water ($\epsilon_r \approx 80$) and most other fluids ($\epsilon_r = 1-3$) as shown in [Table 8.9](#).

Thus, with respect to the electrical properties, we have two main types of pore fluids:

1. Water: conducting and high permittivity $\epsilon_r = 80$
2. Oil, gas: nonconducting and low permittivity $\epsilon_r = 1-3$

The specific resistivity of natural waters varies over decades. The highest values are for rainwater; the lowest are for saturated brines in, for example, sedimentary saline facies. [Table 8.2](#) shows some mean values.

[Figure 8.1](#) shows the correlation between specific resistivity, concentration, and temperature for sodium chloride solution (NaCl) in the form of a nomogram.

The temperature dependence of NaCl solutions can be described by an empirical relationship (Arps, 1953):

$$R_{w(T_2)} = R_{w(T_1)} \frac{T_1 + 21.5}{T_2 + 21.5} \quad R_{w(T_2)} = R_{w(T_1)} \frac{T_1 + 6.77}{T_2 + 6.77} \quad (8.12)$$

where T_1 and T_2 , the temperatures in degrees Celsius for the first equation, and in degrees Fahrenheit for the second.

Bigelow (1992) gives the following empirical equation for water resistivity R_w (in ohm m) as a function of NaCl concentration C_{NaCl} (in ppm) and temperature T (in degrees Fahrenheit):

$$R_w = \left(0.0123 + \frac{3647.5}{C_{\text{NaCl}}^{0.955}} \right) \frac{81.77}{T + 6.77} \quad (8.13)$$

If the solutions contain ions other than Na^+ and Cl^- (e.g., K), the so-called multipliers are applied to calculate an equivalent NaCl concentration and its conductivity (see chartbooks; Baker Atlas, 1985; Schlumberger, 1989, 2000).

TABLE 8.2 Range of Resistivity and Conductivity of Natural Water

Water Type	R_w in ohm m Range and Mean in ()	C_w in S m^{-1}
Rainwater	300–2000	0.0005–0.003 (Hö)
Groundwater (fresh)	5–300	0.003–0.2 (Hö)
Seawater	0.18–0.22	4.5–5.5 (Hö)
Mineral/health water	0.5–1.0	1.0–2.0 (Hö)
Tertiary sediments (Europe)	0.7–3.5 (1.4) (K)	0.3–1.4 (0.7)
Mesozoic sediments (Europe)	0.31–47 (2.5) (K)	0.02–3.2 (0.4)
Palaeozoic sediments (Europe)	0.29–7.1 (0.93) (K)	0.14–3.4 (1.1)
Oilfield water		
Chloride waters from oilfields (20°C)	0.049–0.95 (0.16) (K)	1–20 (6.3)
Sulfate waters from oilfields (20°C)	0.43–5.0 (1.20) (K)	0.2–2.3 (0.83)
Bicarbonate waters from oilfields (20°C)	0.24–10 (0.98) (K)	0.1–4 (1.0)

Reference key: Hö, Höltig (1989); K, Keller (1989).

A direct comparison between the resistivity of an NaCl and a KCl solution is shown in [Table 8.3](#). The table also demonstrates that resistivity decreases nearly proportional to the increase of concentration.

8.3 SPECIFIC ELECTRICAL RESISTIVITY OF ROCKS

8.3.1 Overview

The electrical resistivity of rocks varies over many orders of magnitude ([Figure 8.2](#)). It is controlled mainly by factors such as rock type, porosity, connectivity of pores, nature of the fluid, clay content, and metallic (or graphite) content.

A look on the electrical resistivity of the common rock-forming minerals ([Section 8.2.1](#)) shows that most of them are characterized by very high resistivities. Comparable behavior is expected for dry rocks. In porous or fractured water-bearing rock, the electrolytic conductivity of the water and interactions between solid and fluid components create an enhanced electrical conductivity.

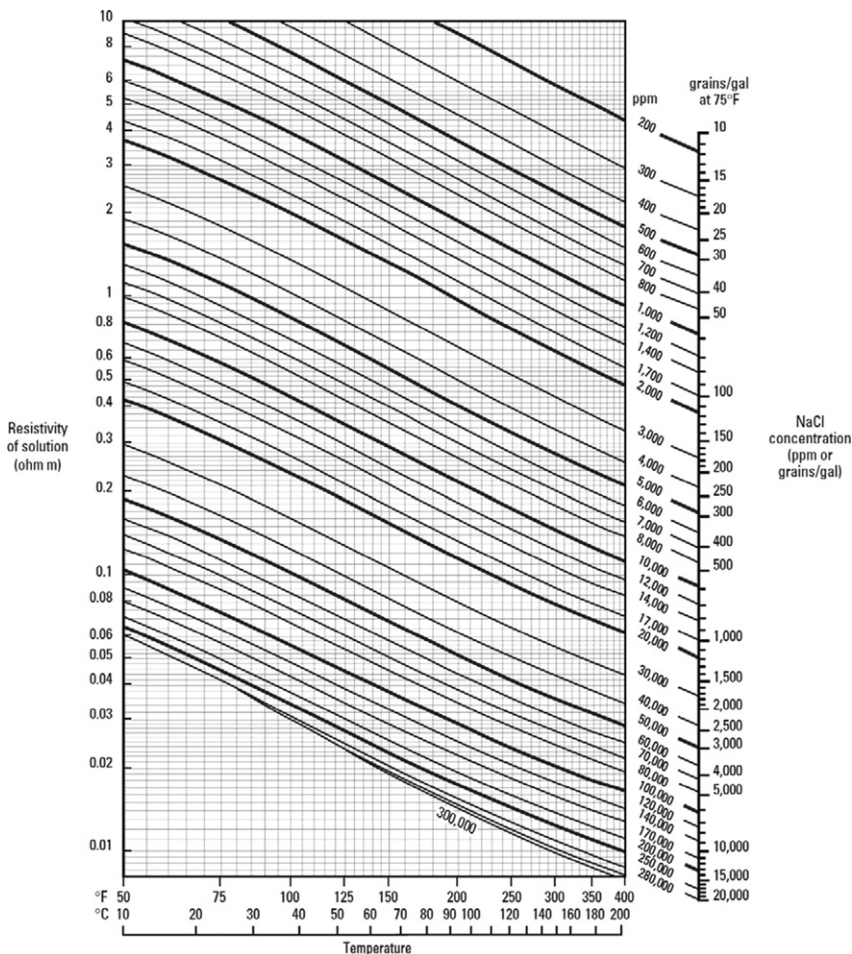


FIGURE 8.1 Correlation between specific electrical resistivity, concentration, and temperature for an NaCl solution; Schlumberger (2000), with friendly permission.

Figure 8.2 gives an overview of the mean ranges of the specific resistivity and relative permittivity of some common rock types. The dominant influence of the pore water on the electrical properties produces a broad range of rock properties for each type, which usually overlaps different types.

The simplified picture notes two tendencies (if the pores or fractures contain water):

1. Resistivity decreases with increasing porosity and fracturing
2. Permittivity increases with increasing porosity and fracturing.

TABLE 8.3 Specific Electrical Resistivity R_w of NaCl and KCl Solutions at 20°C as a Function of the Concentration

NaCl		KCl	
Concentration in mg l ⁻¹	R_w in ohm m	Concentration in mg l ⁻¹	R_w in ohm m
5.85	882	7.456	741
58.5	89.4	74.56	75.1
585	9.34	745.6	7.81
5850	10.3	7456	0.85
58440	0.13	74560	0.10

after Berktold (1982).

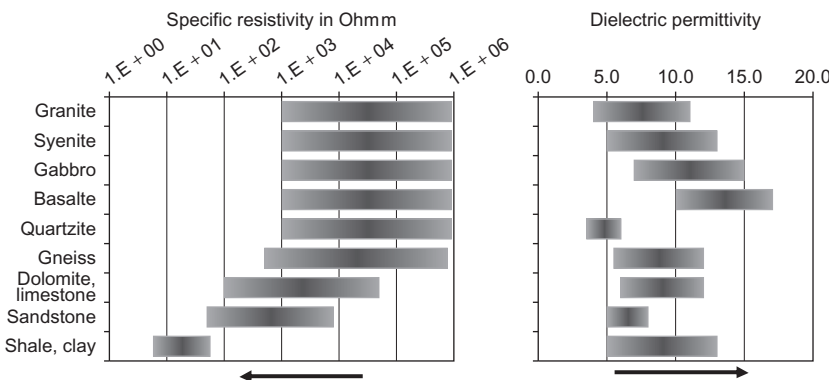


FIGURE 8.2 Mean value ranges and tendencies for specific electrical resistivity and dielectric permittivity; the arrow indicates the effect of water-filled pores and fractures.

In the following sections, the specific electrical resistivity of porous rocks is discussed in more detail. There are two main groups:

1. Rocks with only electrolytic conductivity component of pore water; all other components are insulators ("clean rocks")
2. Rocks with a second conductivity component (in most cases clay or shale).

8.3.2 Specific Electrical Resistivity of Porous Clean Rocks—Archie's Equations

In his historical 1942 paper about electrical conduction in clean sands, G.E. Archie (see also the historical review in the paper of Thomas, 1992)

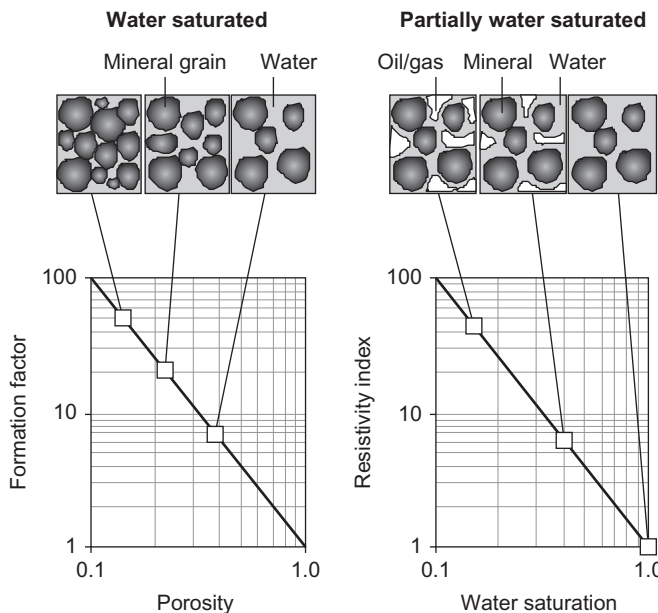


FIGURE 8.3 Archie's equations—a schematic picture. The left figure demonstrates the increase of the formation factor with decreasing porosity for a water-saturated rock. The right figure demonstrates the increase of the resistivity index with decreasing water saturation in a partially water-saturated rock.

suggested that the conductivity of the brine-saturated rock is proportional to brine conductivity and that the specific resistivity of the water-saturated rock R_0 is proportional to the specific electrical resistivity of the brine R_w :

$$R_0 \propto R_w \quad (8.14)$$

This fundamental thesis for Archie's equations is valid, if the brine/water in the connected pores is the only conductor in the rock. Using Figure 8.3, two cases are considered:

1. The porous, clean rock is water saturated
2. The porous, clean rock is partially water saturated.

As a result of the proportionality in case of a water-saturated rock, Archie introduced the “formation resistivity factor F ”:

$$R_0 = F \cdot R_w \quad F = \frac{R_0}{R_w} \quad (8.15)$$

The formation resistivity factor expresses the resistivity magnification relative to the “conductor brine” as a result of the presence of the nonconductive matrix (formation). Because the pores are the only conductor, an inverse correlation of formation factor and connected porosity can be expected.

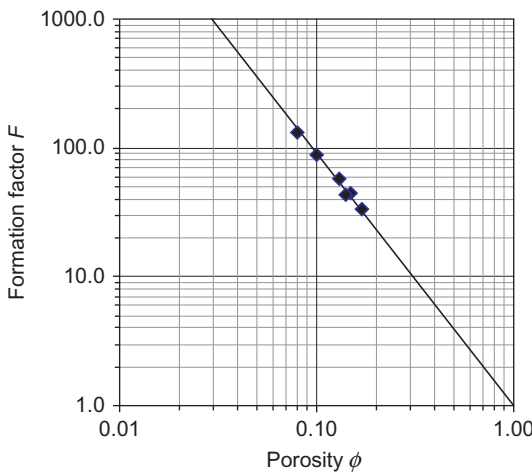


FIGURE 8.4 Formation factor versus porosity; sandstone. Straight line results in $F = 1/\phi^{1.96}$ (visit the website <http://www.elsevierdirect.com/companion.jsp?ISBN=9780444537966> and refer Example-Sandstone. Core analysis).

A graphic presentation of the logarithm of the formation factor versus the logarithm of porosity results approximately (left part of Figure 8.3) in a straight line with the slope m :

$$F = \frac{R_0}{R_w} = \frac{1}{\phi^m} \quad (8.16)$$

where the exponent m is an empirical quantity.

Archie noted that the exponent has a value of about 1.3 for unconsolidated sands and a range between 1.8 and 2.0 for many consolidated sandstones. Therefore, m was called the “cementation exponent.”

Figure 8.4 shows an example for the formation factor versus porosity plot.

Archie’s equation is applied on various rock types. In some cases, the equation is modified with an additional parameter a for a better fit:

$$F = \frac{R_0}{R_w} = \frac{a}{\phi^m} \quad (8.17)$$

In general, the exponent m (and the parameter a) expresses empirically the complicated pore channel geometry with respect to the electrical current flow and is therefore a kind of pore textural property. Table 8.4 summarizes some data for different rock types.

A frequently used version of the Archie equation is the “Humble equation” (see Winsauer et al., 1952) for sand

$$F = \frac{R_0}{R_w} = \frac{0.62}{\phi^{2.15}} \quad (8.18)$$

TABLE 8.4 Mean Values for Archie Parameters

Rock Type	<i>m</i>	Rock Type	<i>m</i>
Unconsolidated sand	1.3	Chalky limestones	1.7–1.8
Very slightly cemented sandstone	1.4–1.5	Crystalline and granular carbonates	1.8–2.0
Slightly cemented sandstone	1.5–1.7	Carbonates with vugs	2.1–2.6
Moderately cemented sandstone	1.8–1.9		
Highly cemented sandstone	2.0–2.2		

Doveton (1986).

and the so-called Shell formula for low porosity carbonates with a porosity-dependent exponent *m*:

$$m = 1.87 + \frac{0.019}{\phi} \quad (8.19)$$

Bigelow (1991) applied this formula for carbonate rocks (Williston Basin, North Dakota, Montana, Saskatchewan) and found a good fit for porosities between 0.04 and 0.25.

Carbonates can be described using Archie's equation if the porosity is intergranular or intercrystalline—then the pore space is a more or less macroscopically homogeneous, and pores are connected.

But in case of more heterogeneous carbonates with moldic or vuggy pore space, it fails. Nonconnected parts of the pore volume do not contribute to the conductivity and result in an extremely high resistivity and formation factor. Systematic studies of these pore types have been published, for example, by Focke and Munn (1987) and Fleury (2002).

Figure 8.5 shows a comparison between the two fundamental pore systems in carbonates:

1. Limestone and dolomite grainstone with intergranular porosity and sucrosic dolomites with intercrystalline porosity show a typical correlation comparable to a sandstone. This results from the randomly distributed connected pore space.
2. Moldic limestones have a high fraction of isolated moldic pores; they contribute to (total) porosity, but not to electrical conductivity.

For (separate) vuggy porosity, Lucia (2007) describes that the exponent is a function of the “vug porosity ratio,” VPR, defined as

$$VPR = \frac{\text{separate-vug porosity}}{\text{total porosity}} = \frac{\phi_{SV}}{\phi_{\text{total}}} \quad (8.20)$$

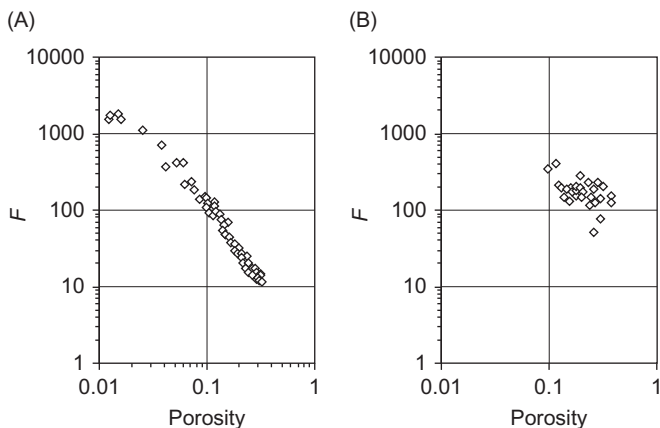


FIGURE 8.5 Formation factor versus (total) porosity for carbonate rocks; data taken from Focke and Munn (1987). (A) Limestone and dolomite grainstone with intergranular porosity and sucrosic dolomites with intercrystalline porosity. (B) Moldic limestones.

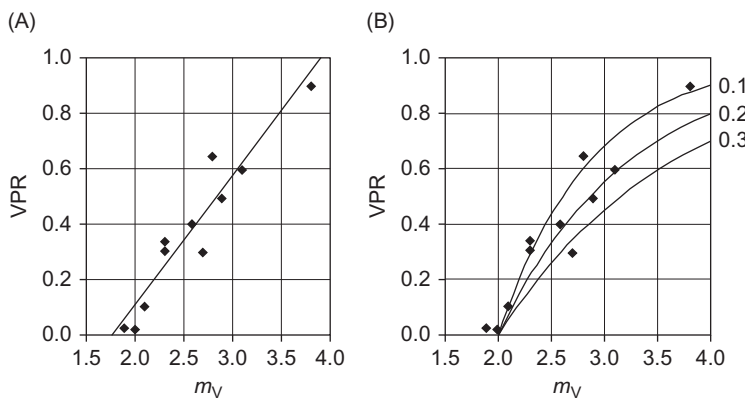


FIGURE 8.6 Archie's exponent for rocks with separate-vug porosity. (A) Correlation between cementation exponent m_V and VPR: points are experimental data; the line is the regression (Equation (8.21)), after Lucia (2007). (B) Alternative calculation using Equation (8.24) for $\phi_{\text{total}} = 0.1, 0.2$, and 0.3 (curve parameter), compared with the experimental data.

Figure 8.6A shows experimental data and the derived equation for the exponent m_V of the vuggy porous rock

$$m_V = 2.14 \left(\frac{\phi_{\text{SV}}}{\phi_{\text{total}}} \right) + 1.76 = 2.14 \cdot \text{VPR} + 1.76 \quad (8.21)$$

An alternative equation can be derived as follows: the connected path for current flow is controlled by the effective porosity:

$$\phi_{\text{eff}} = \phi_{\text{total}} - \phi_{\text{SV}} = \phi_{\text{total}}(1 - \text{VPR}) \quad (8.22)$$

Archie's equation refers to this connected pore space with the exponent m only:

$$F = \phi_{\text{eff}}^{-m} = [\phi_{\text{total}}(1 - \text{VPR})]^{-m} = \phi_{\text{total}}^{-m_V} \quad (8.23)$$

where m_V is the exponent, if we refer formation factor to total porosity of the vuggy porous rock. It results as a relationship between the two exponents:

$$m_V = m \left(1 + \frac{\log(1 - \text{VPR})}{\log \phi_{\text{total}}} \right) \quad (8.24)$$

Figure 8.6B shows a comparison of calculated curves for the assumption of $m = 2$ for the connected porosity and different total porosity of $\phi_{\text{total}} = 0.1, 0.2$, and 0.3 . Curves cover the experimental data.

Lucia (2007) notes that "in presence of fractures and other touching-vug pore types, the m_V value may be < 1.8 ."

Generally, fractured rocks tend to low exponents ($m \approx 1.1 - 1.3$), frequently connected with a high value of the parameter a in Equation (8.17). Pape et al. (1985) derived for the fractured Falkenberg Granite the relationship:

$$F = \frac{4.15}{\phi^{1.08}} \quad (8.25)$$

where the porosity is in the range between 0.005 and 0.07 (0.5–7%).

Lovell and Pezard (1990) investigated basalt cores from the Deep Sea Drilling Program (DSDP) hole 504B and found $a = 6.2$ and $m = 1.05$ for fractured samples.

Unconsolidated rocks show exponents m in the order between 1.1 and 1.4 (Figure 8.7). There is a tendency of decrease with increasing sphericity of the grains (Jackson et al., 1978; Schön, 1996).

If in a porous rock water saturation decreases, then a part of the conductive pore water is replaced by the nonconductive fluid (gas, air, oil), and rock resistivity increases. To describe the saturation effect, Archie normalized the resistivity, measured at any saturation R_t with the resistivity of the total water-saturated rock R_0 and defined as resistivity index:

$$\text{IR} = \frac{R_t}{R_0} \quad (8.26)$$

A logarithmic plot IR versus S_w results approximately again in a straight line (Figure 8.3 and Figure 8.8) with the slope n :

$$\text{IR} = \frac{R_t}{R_0} = \frac{1}{S_w^n} \quad (8.27)$$

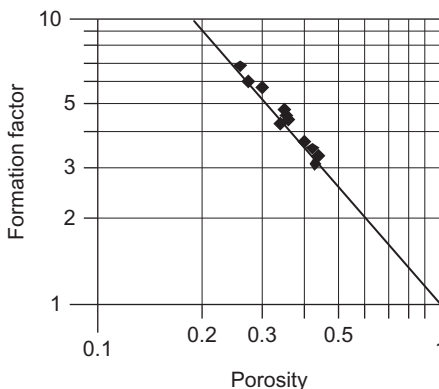


FIGURE 8.7 Formation factor versus porosity for a well-sorted sand; the resulting exponent is $m = 1.4$.

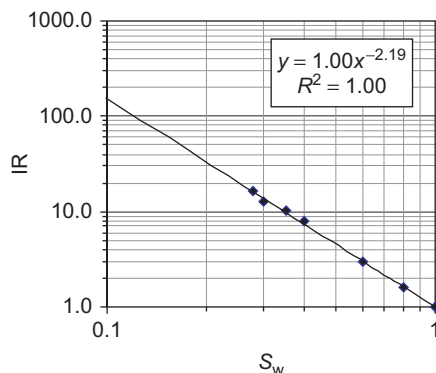


FIGURE 8.8 Resistivity index IR versus water saturation S_w (sandstone); derived exponent is $n = 2.19$; see also Section 8.9; visit the website <http://www.elsevierdirect.com/companion.jsp?ISBN=9780444537966> and refer Example-Sandstone. Core analysis.

where n is the saturation exponent (frequently in the order of 2). This equation gives the fundamental relationship for water saturation calculation from resistivity measurements:

$$S_w = \left(\frac{R_0}{R_t} \right)^{1/n} \quad (8.28)$$

The equation shows that for a saturation calculation from a measured R_t , the resistivity under the condition of water saturation R_0 must be known. R_0 can be calculated, for example, using the [Equations \(8.15\) and \(8.16\)](#) with the input of porosity ϕ (from a separate measurement), the empirical exponent m and the water resistivity R_w :

$$S_w = \left(\frac{R_w}{R_t} \frac{1}{\phi^m} \right)^{1/n} \quad (8.29)$$

Techniques and methods are described in textbooks of formation evaluation and well-log interpretation.

Both exponents m and n express the geometry of the only conductor (brine) in the porous rock and refer to the geometry of the two insulators (mineral grain, hydrocarbon). When $m = n$, the two insulators (mineral, hydrocarbon) are interchangeable in terms of rock resistivity.

The saturation exponent n must be determined experimentally in core laboratories. It is controlled by the distribution of the conducting brine in the pore space, thus depending on the rock texture, wetting properties, and “saturation history” caused by capillary effects.

In water-wet rocks, water adheres to grain surfaces and builds up a more or less continuous phase in the rock. In oil-wet rocks, the nonconducting oil becomes the continuous fluid phase, and the water occurs mostly as isolated droplets. In this case, the resistivity is much higher and the saturation exponent $n > 2$. A discussion of wettability influences on electrical properties is given by Anderson (1986) and Sharma et al. (1991).

Different saturating techniques (imbibition, drainage) and techniques of core preparation also affect the laboratory-determined saturation exponent (see, for example, de Waal et al., 1989; Sharma et al., 1991; Worthington and Pallatt, 1990; Worthington et al., 1989). The application of X-ray and resistivity tomography allows a monitoring of the homogeneous saturation process along the core axis.

In some cases, the resistivity index versus saturation curve is nonlinear on a log–log plot. This phenomenon seems to be related to a bimodal (or multimodal) pore-size distribution, to the presence of microporosity or from rough grain surface coatings (de Waal et al., 1989; Worthington et al., 1989). Worthington and Pallatt (1990) investigated the influence of pore geometry upon the character of the saturation index versus saturation curve and the behavior of n .

In carbonates, the heterogeneity of the pore space again results in more complicated plots IR versus S_w for the saturation exponent. Ellis and Singer (2007) note: “Carbonates are particularly heterogeneous, and are also more likely to be oil-wet, so that for both reasons the relation between resistivity and S_w is likely to be complicated, with n not equal to 2 and also varying with saturation.” For log interpretation of carbonates, Fleury (2002) developed a double or triple porosity model for micritic and oolithic carbonate.

8.3.3 Pressure Dependence of Formation Factor

If water-filled and conducting pore channels are deformed by external pressure on the rock skeleton, then the porosity decreases, the rock resistivity increases, and the formation factor increases.

Palmer and Pallatt (1991) analyzed the formation factor versus pressure relationship for sandstone samples from the North Sea and Alaskan

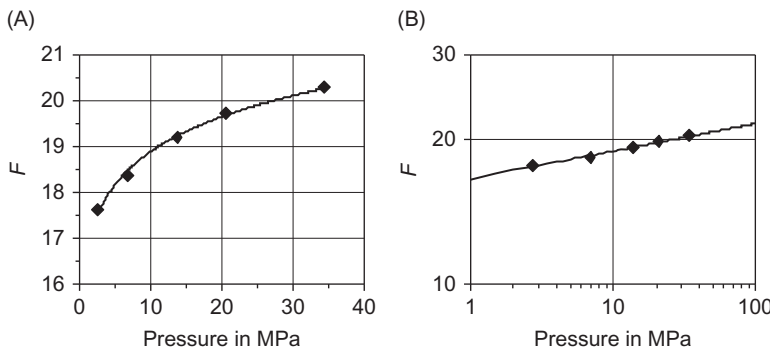


FIGURE 8.9 Formation factor versus overburden pressure dependence. (A) Linear plot, data after Palmer and Pallatt (1991) (pressure converted from psi in MPa). (B) Fitting by a power law using a bilogarithmic plot.

reservoirs. The results show a nonlinear dependency (Figure 8.9A). They fitted the experimental data with an equation relating the actual formation factor $F(p)$ normalized by its value F_{400} at a pressure of 400 psi versus the logarithm of pressure p and found:

$$F(p) = F_{400}(0.621 + 0.143 \cdot \log p) \quad (8.30)$$

Figure 8.9B demonstrates an alternative fit using a power law. A bilogarithmic plot F versus p results in a first approximation to a straight line with the regression:

$$F = 16.6 \cdot p^{0.055} \quad (8.31)$$

or generalized

$$F(p) = F_{p=1} \left(\frac{p}{p=1} \right)^b \quad (8.32)$$

where $F_{p=1}$ is the formation factor at a pressure $p = 1$. The exponent b is the slope of the straight line.

Archer and Jing (1991) investigated both clean and shaly sedimentary rocks. They found a similar nonlinear relationship between formation factor and pressure, as well as a noticeable hysteresis effect occurring between the loading and unloading cycles. This is a result of nonelastic deformation of the rock skeleton.

8.4 CLEAN ROCKS—THEORIES AND MODELS

8.4.1 Introduction

The electrical conductivity as a tensor depends not only on the volume fractions and the electrical conductivity of rock components, but also on their

distribution, geometry, and internal structure. For practical applications, the empirical Archie equations are dominant.

For a model-based description, the following rock types are relevant:

- Clean rocks, where only the water/brine in the pores or fractures conducts the electrical current; the matrix material is an insulator.
- Porous rocks with a “matrix porosity” and any second porosity type like fractures or moldic pores in carbonates; this creates a “dual porosity” system.
- Shaly rocks where in addition to the electrolytic conductivity of the connected pores, a second conductivity component (shale conductivity, excess conductivity or interface conductivity) exists.

The following section is based on the first and second types; shaly rocks are featured separately in a special [Section 8.5](#).

8.4.2 Layer Models

Layer models resolve a rock as a laminated material with layers of different conductivity. Layer thickness represents the volume fraction of the component.

For a current parallel layering (parallel model), results are

$$\text{the conductivity } C_{\parallel} = \sum_i V_i \cdot C_i \quad \text{and the resistivity } R_{\parallel} = \left(\sum_i V_i \cdot R_i^{-1} \right)^{-1} \quad (8.33)$$

For a current perpendicular layering (serial model), results are

$$\text{the conductivity } C_{\perp} = \left(\sum_i V_i \cdot C_i^{-1} \right)^{-1} \quad \text{and the resistivity } R_{\perp} = \sum_i V_i \cdot R_i \quad (8.34)$$

where

V_i is the volume fraction of component i

C_i is the conductivity of component i

R_i is the specific resistivity of component i .

Layer models in case of water-saturated clean porous rocks with one component (mineral) of zero conductivity result for

- parallel layering in $C_{\parallel} = \phi \cdot C_w$ or $R_{\parallel} = \phi^{-1} \cdot R_w$ with a formation factor $F_{\parallel} = \phi^{-1}$
- perpendicular layering in $C_{\perp} = 0$ or $R_{\perp} = \infty$ with a formation factor $F_{\perp} = \infty$.

Thus, this type is not of a practical relevance to model a real homogeneous clean porous rock in terms of electrical conductivity.

A generalization following Lichtenecker and Rother (1931) (see also Section 6.7.1) can be written as

$$C = \left(\sum_i V_i \cdot C_i^\alpha \right)^{\frac{1}{\alpha}} \quad (8.35)$$

This equation represents a summary of several individual equations with the exponent α as a “textural parameter”; for example results

- the parallel model for $\alpha = 1$,
- the serial model for $\alpha = -1$.

For the special case of a water-saturated clean rock (Archie type), the conductivity is

$$C_0 = (\phi \cdot C_w^\alpha)^{\frac{1}{\alpha}} \quad (8.36)$$

or written as formation factor

$$F = \frac{C_w}{C_0} = \phi^{-\frac{1}{\alpha}} \quad (8.37)$$

Thus, Archie’s “cementation exponent” results as $m = 1/\alpha$. The frequently used mean value of $m = 2$ results in $\alpha = 0.5$.

Layer models for laminated shaly rocks have a specific importance (see Section 8.5.2).

8.4.3 Inclusion Models—Spheres

A systematic description and discussion of various mixture theories for rock properties is given by Berryman (1995). Berryman (1995) and Mavko et al. (1998), for example, can be used as reference for theoretical concepts and models (self-consistent effective medium theory, differential effective medium approach). All inclusion models assume a host material with a low concentration of inclusions. Inclusions are of different shape.

For a two-component composite with spherical inclusions in a host material, the so-called Clausius–Mossotti model (see Berryman, 1995) results in

$$\frac{C_{CM} - C_2}{C_{CM} + 2 \cdot C_2} = V_1 \frac{C_1 - C_2}{C_1 + 2 \cdot C_2} \quad (8.38)$$

where

C_{CM} is the conductivity of the composite (Clausius–Mossotti model)

C_1 is the conductivity of the inclusion material

C_2 is the conductivity of the host material

V_1 is the volume fraction of the inclusions.

The application on a rock of Archie type with a nonconducting inclusion representing a mineral grain ($C_1 = C_{\text{ma}} = 0$) with low concentration of grains in the conductive host (water) $V_1 = 1 - \phi$ results in

$$\frac{C_{\text{CM}} - C_w}{C_{\text{CM}} + 2 \cdot C_w} = \frac{1 - \phi}{2} \quad (8.39)$$

with the solution

$$C_{\text{CM}} = C_w \frac{2 \cdot \phi}{3 - \phi} \quad (8.40)$$

Thus, the formation resistivity factor is

$$F = \frac{3 - \phi}{2 \cdot \phi} \quad (8.41)$$

This represents materials like a suspension. A porous rock consisting of insulating matrix substance as host material and fluid as spherical pore inclusion ("Swiss Cheese Model") results in $C_{\text{CM}} = 0$ because inclusions are non-connected. Such a model only works for a host material with conductivity (see next section).

8.4.4 Nonspherical Inclusions

The generalization of the inclusion shape from a sphere to an ellipsoid creates different properties of the composite with respect to the field direction related to the ellipsoid axis system. Therefore, a single ellipsoid or a set of ellipsoids with identical or preferred orientation originates an anisotropy effect. If the inclusions are randomly oriented, then isotropy results.

In this section these two cases are discussed. An application presupposes a conductivity of the host material (matrix porosity or matrix conductivity).

Carbonates in particular frequently have different pore systems. Inclusion models can describe, for example, the effect of spherical (moldic) or elongated (fractures) inclusions in a host material with interparticle porosity. For geometric characterization of the ellipsoidal shape, the aspect ratio (see Figure 6.25) is used. Cheng and Toksöz (1979) report aspect ratios for carbonates in the range $\alpha = 10^{-2} - 10^{-4}$.

8.4.4.1 Oriented Ellipsoidal Inclusions

Bruggeman (1935) and Hanai (1960) derived general relationships for the calculation of the properties for heterogeneous mixtures. The Hanai–Bruggeman equation for conductivity is (see Berryman, 1995)

$$\frac{C_{\text{HB}} - C_{\text{ma}}}{C_w - C_{\text{ma}}} \left(\frac{C_w}{C_{\text{HB}}} \right)^L = \phi \quad (8.42)$$

where

C_{HB} is the rock conductivity

C_w is the water conductivity

C_{ma} is the matrix conductivity

L is the depolarization exponent of the dispersed particles; it is related to the axis directions of the ellipsoid.

In the literature (e.g., Berryman, 1995), references are given for the calculation of the depolarization exponent. There are some extreme values and approximations (see also [Table 8.5](#)):

sphere $L_a = L_b = L_c = 1/3$;

needle $L_c = 0$ (along needle long axis) $L_a = L_b = 1/2$ (along needle short axes);

disk $L_c = 1$ (along short axis) $L_a = L_b = 0$ (along long axes).

For plate-like objects ($a \gg c$), Sen (1980) recommends the approximation

$$L_c = 1 - \frac{\pi c}{2a} = 1 - \frac{\pi}{2} \alpha \quad (8.43)$$

where $\alpha = c/a$ is the aspect ratio.

Applying this for an estimate of L_c (with $L_a + L_b + L_c = 1$) results

$$L_a = L_b = \frac{1 - L_c}{2} = \frac{\pi}{4} \alpha \quad (8.44)$$

[Table 8.5](#) gives some data following Sen's (1980) equation and demonstrates the approximation for a disk with $\alpha \rightarrow 0$:

$$\lim_{\alpha \rightarrow 0} L_a = 0 \quad \lim_{\alpha \rightarrow 0} L_c = 1 \quad (8.45)$$

The depolarization exponent of an inclusion depends on the aspect ratio and is related to the direction of the field with respect to the axis direction of

TABLE 8.5 Aspect Ratio and Depolarization Exponent

$\alpha = c/a$	$L_a = L_b$	L_c
0.1	0.0785	0.8429
0.05	0.0393	0.9215
0.02	0.0157	0.9686
0.01	0.0079	0.9843
0.005	0.0039	0.9921
0.002	0.0016	0.9969
0.001	0.0008	0.9984

the ellipsoid. Therefore, different depolarization factors for different directions lead to anisotropy of conductivity.

This can be applied, for example, on carbonate rocks with a matrix porosity ϕ_{ma} and fracture porosity ϕ_{fr} . If fractures have a preferred orientation, conductivity is a tensor. The tensor simplifies in the event that the axes of the ellipsoid coincide with the axes of the Cartesian coordinate system. For generalization, this tensor can be transformed into any orientation (Moran and Gianzero, 1979).

For a penny-shaped fracture (oblate) with long ellipsoid axes a, b parallel x -, y -axis and a short axis $c \ll a = b$ parallel z -axis the ellipsoid axes $a - b - c$ coincide with the coordinate system $x - y - z$ (main-axis system). Then conductivity components are the solutions of the following equations:

$$C_x = C_y \text{ (x- and y-direction): } \left(\frac{C_{\text{fl,fr}} - C_x}{C_{\text{fl,fr}} - C_{\text{ma}}} \right) \left(\frac{C_{\text{ma}}}{C_x} \right)^{L_a} = 1 - \phi_{\text{fr}} \quad (8.46)$$

$$C_z \text{ (z-direction): } \left(\frac{C_{\text{fl,fr}} - C_z}{C_{\text{fl,fr}} - C_{\text{ma}}} \right) \left(\frac{C_{\text{ma}}}{C_z} \right)^{L_c} = 1 - \phi_{\text{fr}} \quad (8.47)$$

where

ϕ_{fr} is the fracture porosity

$C_{\text{fl,fr}}$ is the conductivity of the fluid in the fracture

$C_{\text{ma}} = C_w \cdot \phi_{\text{ma}}^m \cdot S_{w,\text{ma}}^n$ is the matrix conductivity.

The two equations demonstrate the key function of the depolarization exponent: its dependence on orientation creates the anisotropy.

For graphic presentation, a normalization of the conductivities by matrix conductivity is comfortable:

$$x\text{- and } y\text{-direction: } \left(\frac{\frac{C_{\text{fl,fr}}}{C_{\text{ma}}} - \frac{C_x}{C_{\text{ma}}}}{\frac{C_{\text{fl,fr}}}{C_{\text{ma}}} - 1} \right) \left(\frac{C_{\text{ma}}}{C_x} \right)^{L_a} = 1 - \phi_{\text{fr}} \quad (8.48)$$

$$z\text{-direction: } \left(\frac{\frac{C_{\text{fl,fr}}}{C_{\text{ma}}} - \frac{C_z}{C_{\text{ma}}}}{\frac{C_{\text{fl,fr}}}{C_{\text{ma}}} - 1} \right) \left(\frac{C_{\text{ma}}}{C_z} \right)^{L_c} = 1 - \phi_{\text{fr}} \quad (8.49)$$

Figure 8.10 shows an example. Fractures are oriented in the $x - y$ plane and are water filled ($C_{\text{fl,fr}} = C_w$). Two different aspect ratios are assumed:

$\alpha = 0.10$ —this corresponds to the depolarization exponents $L_a = L_b = 0.079$, $L_c = 0.843$.

$\alpha = 0.01$ —this corresponds to the depolarization exponents $L_a = L_b = 0.008$, $L_c = 0.984$.

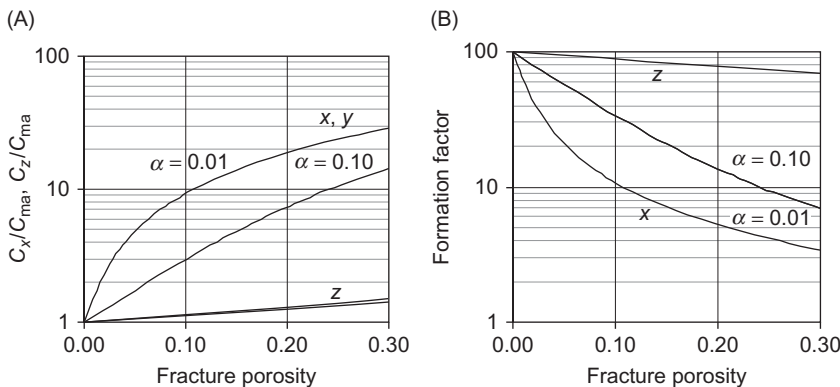


FIGURE 8.10 Fracture porosity effect in a material with matrix porosity of $\phi_{\text{ma}} = 0.10$. Input: $C_w/C_{\text{ma}} = 100$, aspect ratio $\alpha = 0.01$ and $\alpha = 0.10$. (A) ratio of rock and matrix conductivity $C_x/C_{\text{ma}} = C_y/C_{\text{ma}}$ and C_z/C_{ma} versus fracture porosity ϕ_{fr} . (B) Ratio of rock and water resistivity (formation factor of the dual porosity system F) versus fracture porosity ϕ_{fr} . (for calculation, visit the website <http://www.elsevierdirect.com/companion.jsp?ISBN=9780444537966> and refer Electrical Fractured conductivity).

On the left (A) is plotted C_x/C_{ma} and C_z/C_{ma} versus ϕ_{fr} ; on the right (B) is the ratio of rock resistivity and water resistivity (equals the formation factor of the dual porosity system) as function of fracture porosity ϕ_{fr} .

Both plots demonstrate the strong influence of the fractures and the effect of the aspect ratio in the x - (and y -) direction (parallel fracture orientation), but only a small effect in the z -direction (perpendicular fracture orientation).

The discussed rock contains two pore systems: a matrix pore system and a fracture or inclusion pore system. Such “dual porosity systems” were studied, for example, by Watfa and Nurmi (1987) and are common in reservoir engineering (Warren and Root, 1963).

8.4.4.2 Randomly Arranged Inclusions

Randomly arranged inclusions result in an isotropic effect of inclusions. For this case, a generalization of the Clausius–Mossotti relation (Berryman, 1995; Mavko et al., 1998) can be applied:

$$\frac{C_{\text{CM}} - C_{\text{ma}}}{C_{\text{CM}} + 2 \cdot C_{\text{ma}}} = \phi(C_i - C_{\text{ma}})R^{mi} \quad (8.50)$$

where C_{ma} is the matrix conductivity and C_i is the conductivity of the inclusion material.

Solved for the rock conductivity C_{CM} results:

$$C_{\text{CM}} = C_{\text{ma}} \frac{1 + 2 \cdot \phi \cdot R^{mi}(C_i - C_{\text{ma}})}{1 - \phi \cdot R^{mi}(C_i - C_{\text{ma}})} \quad (8.51)$$

where R^{mi} is a function of the depolarization exponents L_a , L_b , L_c .

$$R^{mi} = \frac{1}{9} \sum_{k=a,b,c} \frac{1}{L_k \cdot C_i + (1 - L_k)C_{\text{ma}}} \quad (8.52)$$

TABLE 8.6 Depolarizing Exponents L_a, L_b, L_c and Parameter R^{mi}

Inclusion shape	L_a, L_b, L_c	R^{mi}
Sphere	1/3, 1/3, 1/3	$\frac{1}{C_i + 2 \cdot C_{ma}}$
Needle	0, 1/2, 1/2 (along x-axis)	$\frac{1}{9} \left(\frac{1}{C_{ma}} + \frac{4}{C_i + C_{ma}} \right)$
Disk	1, 0, 0	$\frac{1}{9} \left(\frac{2}{C_{ma}} + \frac{1}{C_i} \right)$

Berryman (1995); $m = ma$ matrix (host) and i , inclusion.

Table 8.6 shows expressions of the parameter R^{mi} for some inclusion shapes.

This model can be applied on carbonates with randomly oriented spherical (moldic) or elongated (fractures) inclusions. Then C_{ma} is the matrix conductivity, which can be expressed as:

$$C_{ma} = C_w \cdot \phi_{ma}^m \cdot S_{w,ma}^n$$

where

ϕ_{ma} is the (interparticle/intraparticle) matrix porosity

$S_{w,ma}$ is water saturation in the matrix pore space

m, n are the Archie exponents.

The porosity ϕ in Equation (8.51) is now the vuggy or moldic porosity ϕ_{vug} , and C_i is the conductivity of the fluid filling the inclusion space (vuggy, moldic) $C_{fl,i}$, which could be water saturated or partially water saturated.

Then Equation (8.51) becomes

$$C_{CM} = C_w \cdot \phi_{ma}^m \cdot S_{w,ma}^n \frac{1 + 2 \cdot \phi_{vug} \cdot R^{mi} \left(C_{fl,i} - C_w \cdot \phi_{ma}^m \cdot S_{w,ma}^n \right)}{1 - \phi_{vug} \cdot R^{mi} \left(C_{fl,i} - C_w \cdot \phi_{ma}^m \cdot S_{w,ma}^n \right)} \quad (8.53)$$

with

$$R^{mi} = \frac{1}{9} \sum_{k=a,b,c} \frac{1}{L_k \cdot C_{fl,i} + (1 - L_k)C_w \cdot \phi_{ma}^m \cdot S_{w,ma}^n} \quad (8.54)$$

8.4.5 Capillary Models

In Section 2.5.7, the capillary model was introduced for the description of permeability. The same model can be applied for calculation of specific rock

resistivity and formation factor. Assuming an electrical current flow in direction of the capillary with the symbols of Figure 2.24 results:

$$R_0 \cdot \frac{L}{L^2} = R_w \frac{l}{\pi \cdot r^2} \quad (8.55)$$

Implementing tortuosity (Equation (2.44)) and porosity (Equation (2.45)) gives the specific electrical resistivity of the water-saturated rock model:

$$R_0 = R_w \frac{T}{\phi} \quad (8.56)$$

and the formation resistivity factor is

$$F = \frac{T}{\phi} \quad (8.57)$$

Thus, the simple model:

- cannot explain the order of the cementation exponent for real rocks (~ 2);
- demonstrates the problem of any correlation between hydraulic and electrical conductivity: the hydraulic conductivity or permeability also depends on the pore (throat) radius, but the electrical conductivity depends only on the summarized conductive cross sections (expressed by porosity).

A sphere-based capillary model was used by Spangenberg (2001) in order to model the influence of gas hydrate content on the electrical properties of porous sediments.

8.5 SHALY ROCKS, SHALY SANDS

“The abnormal conductivity found in shaly reservoir rocks containing an electrolyte is shown to be a consequence of the electrical double layer in the solution adjacent to charged clay surfaces. This increased conductivity results from a higher concentration of ions in the double layer than in the solution in equilibrium with the double layer.”

Winsauer and McCardell (1953)

8.5.1 Introduction: The Shaly Sand Problem

Presence of shale in a reservoir:

- decreases the reservoir quality (porosity, permeability);
- creates an additional electrical conductivity component—any formal application of Archie’s equation results in an overestimate of water saturation.

The electrical properties of clay minerals surrounded by an electrolyte (water) act as a second conductivity component in addition to the electrolytic conductivity of the formation water in the connected pore space. This conductivity contribution of shale/clay depends on:

- shale type (clay mineral);
- shale content (volume fraction) ;
- distribution of shale in the formation (laminar shale, dispersed shale, structural shale).

A parallel conductor system of the two conductivity components is the philosophy of most shaly-sand models.

Worthington (1985) gives a systematic overview to the variety of shaly-sand equations and notes: “A wide variety of procedures are currently in routine use for the evaluation of shaly sands. Each of these can furnish a significantly different reservoir evaluation. Yet, no one method predominates within the industry.”

Figure 8.11 illustrates two basic types of clay occurrence in a rock and the position of shale/clay in an electrical circuit. In a third type, the “structural clay” replaces sand grains by clay agglomerates.

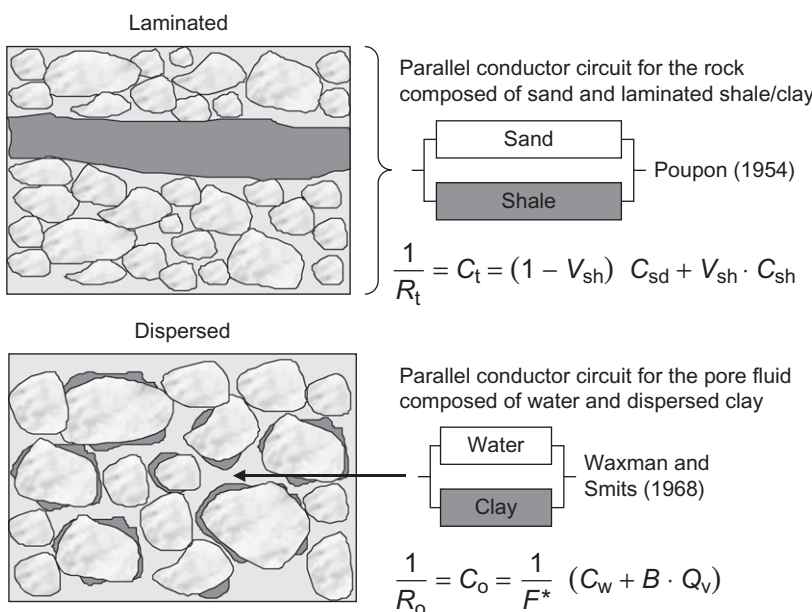


FIGURE 8.11 Two fundamental types of clay presence in a sedimentary rock.

8.5.2 Laminated Shaly Sands—The Poupon Equation

Poupon et al. (1954) derived an equation for the laminated shaly-sand resistivity using the parallel conductor model:

$$C_t = (1 - V_{sh})C_{sd} + V_{sh} \cdot C_{sh} \quad (8.58)$$

$$\frac{1}{R_t} = \frac{1 - V_{sh}}{R_{sd}} + \frac{V_{sh}}{R_{sh}} \quad (8.59)$$

where

V_{sh} is the (laminar) shale content

R_{sh} is the shale resistivity

R_{sd} is the sand resistivity

R_t is the measured rock resistivity

C_{sh} is the shale conductivity

C_{sd} is the sand conductivity

C_t is the measured rock conductivity.

The sand resistivity R_{sd} can be described by Archie's equation. Combination results in

$$\frac{1}{R_t} = \frac{1 - V_{sh}}{R_w} (\phi^m \cdot S_w^n) + \frac{V_{sh}}{R_{sh}} \quad (8.60)$$

Figure 8.12 shows the resistivity R_t as a function of the water saturation S_w at different shale contents V_{sh} calculated using Equation (6.60) (for calculation, visit the website <http://www.elsevierdirect.com/companion.jsp?ISBN=9780444537966> and refer Electrical. Shaly sand equations). The

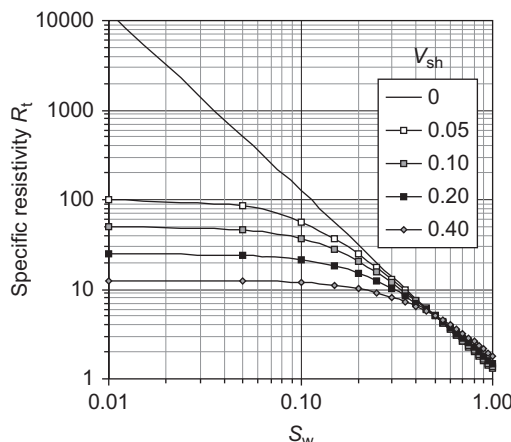


FIGURE 8.12 Resistivity as a function of the water saturation at different shale content calculated using Equation (6.60) (Poupon equation, 1954); input: $R_w = 0.05$ ohm m; $R_{sh} = 5$ ohm m; $\phi = 0.20$; $m = n = 2$.

Excel spreadsheet allows the calculation for variable input parameters and an application for a fast determination of the water saturation from R_t .

The water saturation results as:

$$S_w = \left[R_w \left(\frac{1}{R_t} - \frac{V_{sh}}{R_{sh}} \right) \frac{1}{\phi^m} \frac{1}{1 - V_{sh}} \right]^{1/n} \quad (8.61)$$

For a saturation calculation, the following inputs are necessary:

- The rock resistivity R_t from a resistivity measurement
- The shale resistivity R_{sh} (mostly used is the resistivity of an adjacent shale bed)
- The shale content V_{sh} (e.g., from a gammalog)
- Further for the Archie equation, water resistivity R_w and Archie exponents m, n
- ... and the knowledge: the shale is laminated!

The parallel conductor model assumes a current direction parallel to the plane of lamination. A promotion of this model for current direction parallel and perpendicular to the plane of lamination is applied on the interpretation of measurements with orthogonal induction systems (Section 8.6).

8.5.3 Dispersed Shaly Sand—The Waxman—Smits Equation

In case of dispersed shale, the “shale conductivity” must be added to the pore fluid conductivity. With this idea, Waxman and Smits (1967, 1968) developed the dispersed shaly-sand model. They implemented the fundamental mechanisms of the “shale conductivity” based on cation-exchange processes at the clay mineral—electrolyte (water) interface.

For the simplest case of a water-saturated shaly sand, the conductivity is

$$C_0 = \frac{1}{F^*} (C_w + B \cdot Q_v) \quad (8.62)$$

The Waxman—Smits equation uses the following specific terminology:

C_0 is the conductivity of the shaly sand ($C_0 = R_0^{-1}$), if water saturated

C_t is the conductivity of the shaly sand ($C_t = R_t^{-1}$)

C_w is the conductivity of the formation water ($C_w = R_w^{-1}$)

ϕ is porosity

S_w is water saturation

F^* is the formation factor of the shaly sand

m, n are Archie exponents

B is the equivalent conductivity of sodium clay-exchange cations (in $\text{S cm}^2 \text{ meq}^{-1}$)

CEC is the cation-exchange capacity (in meq g^{-1})

Q_v is the shalyness factor (CEC per unit volume in meq cm^{-3}).

$$Q_v = \text{CEC} \frac{1 - \phi}{\phi} \rho_{\text{mineral}} \quad (8.63)$$

where ρ_{mineral} is the density of the solid mineral substance in g cm^{-3} .

The central physical property of the Waxman–Smits model is the CEC.

Cation exchange is the physical origin of clay–water interface conductance: clay minerals have a negative surface charge. This is the result of substitution of atoms with lower positive valence in the clay lattice. The negative charge of the surface attracts cations such as Na^+ and K^+ . When the clay is immersed in water, cations are released, increasing the conductivity.

CEC measures the ability of clay to release cations (Boyd et al., 1995). The unit for CEC is the milliequivalent per 100 g of dry clay. Table 8.7 shows mean values for CEC of various minerals and demonstrates the correlation to specific internal surface, because CEC is an interface phenomenon.

Figure 8.13 illustrates the correlation between CEC and specific internal surface.

The regression follows an equation:

$$S_m = 520 \cdot \text{CEC}^{1.1} \quad (8.64)$$

where S_m is the specific surface area related to the sample mass (see Section 2.19). The inverse of the factor is the equivalent surface charge density (Patchett, 1975) $\alpha_e \approx 1.9 \cdot 10^{-3} \text{ meq m}^{-2}$.

Doveton (1986) makes an important note: “Since the cations are exchanged primarily at broken bonds on the edges of flakes or by lattice substitutions on cleavage surfaces, the phenomenon tends to be surface area dependent rather than controlled simply by the volume of clay minerals. This

TABLE 8.7 Cation-Exchange Capacity (CEC) and Specific Surface Area for Minerals

Mineral	CEC in meq/100 g	Surface Area $\text{m}^2 \text{ g}^{-1}$
Montmorillonite (smectite)	80–150	82–767
Chlorite	4–40	42
Illite	10–40	97–113
Glauconite	11–20	
Kaolinite	3–15	15–23

After Olhoeft (1981), Keller and Frischknecht (1966), Boyd et al. (1995), Schön (1996).

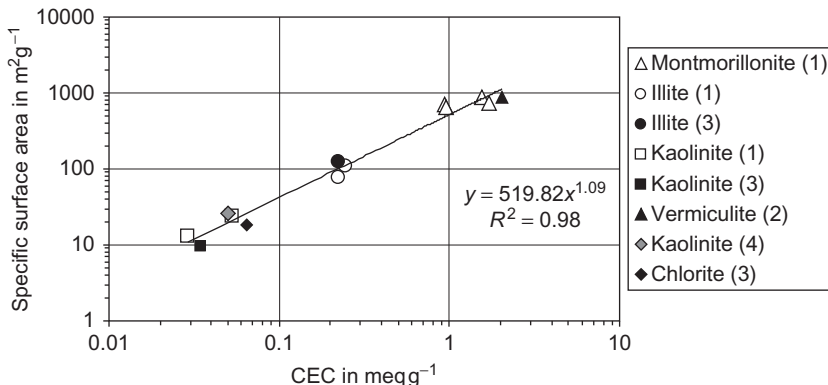


FIGURE 8.13 Correlation between specific surface area (in $\text{m}^2 \text{ g}^{-1}$) and CEC (in meq g^{-1}) for various minerals; after Revil et al. (1997); experimental data from (1) Patchett (1975); (2) Lipsicas (1984); (3) Zundel and Siffert (1985); (4) Lockhart (1980) with permission Geol. Soc. London.

implies that a fine-grained clay has a higher exchange capacity than a coarser-grained form of the same clay volume ...”

The transformation from CEC via the property Q_v into a conductivity is made by the equivalent conductivity term B . The equivalent conductivity of sodium clay-exchange cations is

$$B = \frac{-5.41 + 0.133 \cdot T - 1.253 \cdot 10^{-4} \cdot T^{-2}}{1 + R_w^{1.23}(0.025 \cdot T - 1.07)} \quad (8.65)$$

where T is in degrees Fahrenheit.

$$B = \frac{-1.28 + 0.255 \cdot T - 4.059 \cdot 10^{-4} \cdot T^{-2}}{1 + R_w^{1.23}(0.045 \cdot T - 0.27)} \quad (8.66)$$

where T is in degrees Celsius.

The Waxman–Smits equations for water-saturated and hydrocarbon-bearing shaly rocks follow the concept of a parallel conductor of the two-component electrolyte and dispersed clay contribution.

For water-saturated rocks ($S_w = 1$), the shaly-sand conductivity is given with

$$C_o = \frac{1}{R_o} = \frac{1}{F^*} (C_w + B \cdot Q_v) \quad (8.67)$$

For oil- or gas-bearing rocks ($S_w < 1$), the shaly-sand conductivity is

$$C_t = \frac{1}{R_t} = \frac{S_w^n}{F^*} \left(C_w + \frac{B \cdot Q_v}{S_w} \right) = \frac{\phi^m \cdot S_w^n}{a} \left(C_w + \frac{B \cdot Q_v}{S_w} \right) \quad (8.68)$$

The water saturation results for $n = 2$:

$$S_w = \left[\frac{F^* \cdot R_w}{R_t} + \left(\frac{B \cdot Q_v \cdot R_w}{2} \right)^2 \right]^{\frac{1}{2}} - \left(\frac{B \cdot Q_v \cdot R_w}{2} \right) \quad (8.69)$$

For $n \neq 2$ an iterative algorithm gives S_w .

8.5.4 Dual Water Model

The Dual Water Model (Clavier et al., 1977, 1984) is based on the concept of two types of water in a shaly sand:

1. Free water in the pore space wt
2. Water near the clay surface (bound water) bw.

Conductivities of the two types form a parallel circuit:

$$C_t = \frac{1}{R_t} = \frac{S_{wt}^n}{F^*} \left[C_w + \frac{S_{wb}}{S_{wt}} (C_{wb} - C_w) \right] = \frac{\phi^m \cdot S_{wt}^n}{a} \left[C_w + \frac{S_{wb}}{S_{wt}} (C_{wb} - C_w) \right] \quad (8.70)$$

where

- C_t is rock conductivity
- C_{wt} is free water conductivity
- C_{wb} is bound water conductivity
- S_{wt} is total water saturation
- S_{wb} is bound water saturation.

8.5.5 Simandoux Equation

Based on extensive studies on artificially composed materials (sand and clay), the Simandoux (1963) equation was derived. It represents a structural and dispersed type of shale distribution. The equation was modified by Bardon and Pied (1969):

$$C_t = \frac{\phi^m}{a \cdot R_w} \cdot S_w^n + V_{sh} \cdot C_{sh} \cdot S_w \quad (8.71)$$

For $n = 2$, water saturation results in

$$S_w = \frac{1}{2} \frac{R_w}{\phi^m} \left[\sqrt{4 \frac{\phi^m}{R_w \cdot R_t} + \left(\frac{V_{sh}}{R_{sh}} \right)^2} - \frac{V_{sh}}{R_{sh}} \right] \quad (8.72)$$

8.5.6 Indonesia Equation

This formula was published in 1971 by Poupon and Levaux. The equation is recommended for shaly formations with fairly freshwater:

$$C_t = \frac{C_w}{F} S_w^2 + 2 \sqrt{\frac{C_w \cdot C_{sh}}{F} V_{sh}^{2 - V_{sh}} \cdot S_w^2 + V_{sh}^{2 - V_{sh}} \cdot C_{sh} \cdot S_w^2} \quad (8.73)$$

or in a simplified form for $V_{sh} \leq 0.5$:

$$C_t = \frac{C_w}{F} S_w^2 + 2 \sqrt{\frac{C_w \cdot C_{sh}}{F} V_{sh} \cdot S_w^2 + V_{sh} \cdot C_{sh} \cdot S_w^2} \quad (8.74)$$

8.5.7 Comparison of Some Shaly Sand Equations

Figure 8.14 shows a comparison of the shale effect on the result of water saturation calculation (visit the website <http://www.elsevierdirect.com/companion.jsp?ISBN=9780444537966> and refer Electrical. Shaly sand equations). Input are the measured formation resistivity R_t , the shale content V_{sh} , the shale resistivity R_{sh} , the water resistivity R_w , the porosity ϕ , and the Archie parameters m, n .

The equations and models show the influence of the different input parameters upon the rock conductivity (and in application in formation analysis upon the resulting water saturation). All parameters can be changed to demonstrate the specific effects on the resulting water saturation. Thus, the Excel worksheet can be used for a fast estimate of water saturation under assumption of different shaly-sand models.

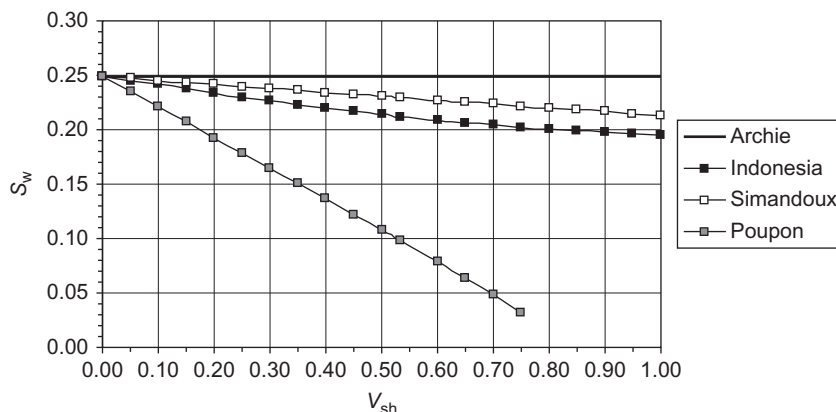


FIGURE 8.14 Water saturation versus shale content calculated for Archie, Poupon, Indonesia, and Simandoux equations if a formation resistivity of $R_t = 10 \text{ ohm m}$, for example, was measured. Parameter: $R_w = 0.03 \text{ ohm m}$, $R_{sh} = 8 \text{ ohm m}$, $\phi = 0.22$, $m = n = 2$; visit the website <http://www.elsevierdirect.com/companion.jsp?ISBN=9780444537966> and refer Electrical. Shaly sand equations.

Figure 8.14 also demonstrates the conclusion that to solve the shaly-sand problem, the following input is necessary (in addition to the inputs for Archie's equation):

- Shale distribution type
- Shale content related to shale distribution type ($V_{\text{sh-lam}}$, $V_{\text{sh-disp}}$, ...)
- Shale properties (C_{sh} , R_{sh} , BQ_v , ...).

There are the following methods and techniques to solve the shaly-sand problem:

1. Shale content (V_{sh}): Preferred are shale content calculations based on gammalog and/or neutron–density combination.
2. Shale distribution type (laminated, dispersed): There are different techniques to estimate shale distribution type: cores and images, Thomas–Stieber analysis (Thomas and Stieber, 1975), “tensorial” conductivity investigation of the formation by measurement of conductivity in an orthogonal axis system (see next section),
3. Shale properties (R_{sh} ; BQ_v , ...): Shale resistivity (R_{sh}) or shale conductivity (C_{sh}) in many practical applications is derived from the resistivity of an “adjacent thick shale bed” or by crossplot techniques. The property for the Waxman–Smits equation BQ_v , CEC is subject of special core analysis measurements.

8.6 LAMINATED SHALY SANDS AND LAMINATED SANDS—MACROSCOPIC ANISOTROPY

8.6.1 Introduction

The simplest and most frequently applied type of anisotropy in geoscience is a transverse isotropic medium (TI). It can be represented by a laminated or layered sediment, if the resolution of the tool cannot resolve the individual laminae. Therefore, this type of anisotropy is called “macroscopic anisotropy.”

The description is frequently given by the properties in the main directions:

- The horizontal direction or parallel direction (parallel to plane of layering)
- The vertical direction or perpendicular direction (normal to plane of layering).

The terms “horizontal” and “vertical” refer to a nondisturbed sedimentation.

Macroscopic anisotropy as the result of laminated sediments has been described by Hagiwara (1994, 1996, 1997), Klein (1996), and Klein et al. (1997). Hagiwara (1994) describes anisotropy as the result of the parallel layering of sand and shale. Klein (1996) and Klein et al. (1997) focused their

investigations on modeling of binary, anisotropic sands; they demonstrated the effects of macroporous and microporous layers of differing water saturation upon resistivity anisotropy. Mollison et al. (1999) and Schön et al. (1999, 2000) derived a modular tensor model to analyze multicomponent induction measurements in anisotropic formations. Kennedy and Herrick (2003) studied the conductivity anisotropy in shale-free sandstone and derived water saturation values of the two sand fractions related to the height above the free water level.

8.6.2 A Modular Concept for Macroscopic Anisotropy

The tensor of electrical resistivity and the tensor of electrical conductivity in the main-axis system of the transversely isotropic rock is defined as follows:

$$R_{ik} = \begin{pmatrix} R_h & 0 & 0 \\ 0 & R_h & 0 \\ 0 & 0 & R_v \end{pmatrix} \quad C_{ik} = \begin{pmatrix} C_h & 0 & 0 \\ 0 & C_h & 0 \\ 0 & 0 & C_v \end{pmatrix} \quad (8.75)$$

For a petrophysical characterization, the dominant feature of a laminated sediment is the composition of such rocks by (at least) two alternating layers (laminae) with different properties. There are the two basic types of sediments:

1. *Laminated shaly sand*: One component is a sand fraction, the other component is a shale layer. Anisotropy is created by the resistivity contrast between sand and shale.
2. *Bimodal laminated sands*: One component is a coarse sand, the other component is a fine sand. Anisotropy is created by the resistivity contrast between two sands with different water saturation (and porosity).

The term “laminated sediment” stands for both types.

The laminated sediment can be described by two types of properties:

1. Microscopic properties related to the individual layers (e.g., resistivity of the sand layer and resistivity of the shale layer).
2. Macroscopic properties related to the response and resolution of the tools (e.g., resistivity of the laminated composite in different directions).

The two types of properties can be combined for practical application as a modular constructed model (Mollison et al., 1999; Schön et al., 1999, 2000). It consists of two modules that are used for a stepwise forward calculation and inversion. The benefits of such a modular concept are:

- the application of the same model for various properties as a basis for a combined interpretation and the derivation of relationships between the different properties;
- the possibility of implementation of well-established algorithms particularly into the parts of the microscopic module (e.g., Archie’s equation).

8.6.3 Forward Calculation

The two types of properties—microscopic and macroscopic—are connected by model equations for the layered sediment:

$$\text{for the horizontal direction } R_h = H \left(\sum_{i=1}^n R_i^{-1} \cdot \Delta h_i \right)^{-1} \quad C_h = \frac{1}{H} \sum_{i=1}^n C_i \cdot \Delta h_i \quad (8.76)$$

$$\text{for the vertical direction } R_v = \frac{1}{H} \left[\sum_{i=1}^n R_i \cdot \Delta h_i \right] \quad C_v = H \cdot \left[\sum_{i=1}^n \frac{\Delta h_i}{C_i} \right]^{-1} \quad (8.77)$$

where individual layers have the thickness Δh_i , the resistivity R_i , and conductivity C_i . The interval has the thickness H and contains n individual layers:

$$H = \sum_{i=1}^n \Delta h_i \quad (8.78)$$

For the simplest case of a two-component laminated sediment (component 1, component 2), the macroscopic properties are

$$R_h = \left(\frac{V_1}{R_1} + \frac{V_2}{R_2} \right)^{-1} \quad C_h = V_1 \cdot C_1 + V_2 \cdot C_2 \quad (8.79)$$

$$R_v = V_1 \cdot R_1 + V_2 \cdot R_2 \quad C_v = \left(\frac{V_1}{C_1} + \frac{V_2}{C_2} \right)^{-1} \quad (8.80)$$

$$\text{with } V_1 + V_2 = 1 \quad (8.81)$$

Anisotropy ratio is

$$\lambda_R = \frac{R_v}{R_h} = (V_1 \cdot R_1 + V_2 \cdot R_2) \left(\frac{V_1}{R_1} + \frac{V_2}{R_2} \right) \quad (8.82)$$

Figure 8.15 demonstrates some general properties for this simplest case of a two-component laminated medium:

- R_v depends linearly on V_1 (series resistor—arithmetic mean), R_h depends nonlinearly on V_1 (parallel resistor—harmonic mean).
- The anisotropy ratio curve is symmetrical and the maximum anisotropy is at $V_1 = V_2 = 0.5$ for the case of isotropic components.

The modular concept can be applied to both types of laminated sediments. In a laminated shaly sand, the resistivity anisotropy is caused mainly by the resistivity contrast between the two components:

- Laminated shale with resistivity R_{sh} (in case of an anisotropic shale, R_{sh} is directionally dependent).
- Sand with resistivity R_{sd} ; the sand component can contain dispersed shale.

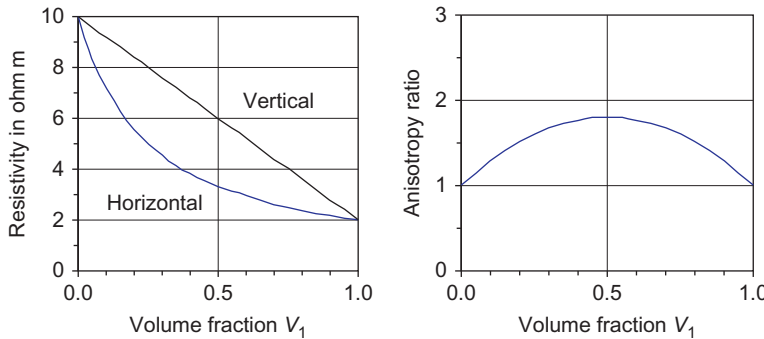


FIGURE 8.15 Results of the forward calculation of macroscopic conductivity, resistivity, and anisotropy for a two-component laminated material as a function of volume fraction of component 1. Individual components are isotropic ($R_1 = 2$ ohm m, $R_2 = 10$ ohm m).

For the case of isotropic sand and isotropic shale, the equations for the shaly-sand composite are

$$R_h = [(1 - V_{sh,lam})/R_{sd} + V_{sh,lam}/R_{sh}]^{-1} \quad C_h = (1 - V_{sh,lam})C_{sd} + V_{sh,lam} \cdot C_{sh} \quad (8.83)$$

$$R_v = (1 - V_{sh,lam})R_{sd} + V_{sh,lam} \cdot R_{sh} \quad C_v = [(1 - V_{sh,lam})/C_{sd} + V_{sh,lam}/C_{sh}]^{-1} \quad (8.84)$$

$$\begin{aligned} \lambda &= 1 + \left(V_{sh,lam} - V_{sh,lam}^2 \right) \left(\frac{C_{sh}}{C_{sd}} + \frac{C_{sd}}{C_{sh}} - 2 \right) \\ &= 1 + \left(V_{sh,lam} - V_{sh,lam}^2 \right) \left(\frac{R_{sh}}{R_{sd}} + \frac{R_{sd}}{R_{sh}} - 2 \right) \end{aligned} \quad (8.85)$$

where

$V_{sh,lam}$ is the volume fraction of laminated shale

R_h , R_v and C_h , C_v are the macroscopic resistivities and conductivities in the horizontal and vertical direction, respectively

R_{sd} , R_{sh} and C_{sd} , C_{sh} are the microscopic resistivities and conductivities of the sand and the laminated shale fraction, respectively.

On the website <http://www.elsevierdirect.com/companion.jsp?ISBN=9780444537966> (file: Electrical. Laminated sediment) is the forward calculation of horizontal and vertical resistivity for:

- laminated shaly sand (resistivity contrast between sand and shale);
- laminated bimodal sand (resistivity contrast between coarse and fine sand).

Resistivities are calculated and plotted as a function of the volume fraction of the components (shale, fine sand).

8.6.4 Inversion (Laminated Shaly Sand)

Following the modular concept, water saturation can be calculated in two modules:

1. *Macroscopic module*: decomposition of the laminated sediment and determination of the sand resistivity.
2. *Microscopic module*: calculation of water saturation for the sand fraction (application of Archie's equation).

Input data from a resistivity measurement are the two macroscopic resistivities R_h , R_v . The unknown properties are the laminated shale content $V_{sh,lm}$ and the two microscopic resistivities R_{sd} , R_{sh} . Thus, there are two input data and three unknown parameters. In this case, two practical solutions are possible depending on which additional a priori information is available.

Solution A: Additional input is the laminated shale content $V_{sh,lm}$ (determined from an independent source, for example, nuclear measurements, Thomas–Stieber technique).

For the two unknown (microscopic) resistivities, the results are

$$R_{sd} = A + \sqrt{A^2 - R_v \cdot R_h} \quad R_{sh} = V_{sh,lm}^{-1} [R_v - (1 - V_{sh,lm}) R_{sd}] \quad (8.86)$$

with

$$A = \frac{R_v + R_h(1 - 2 \cdot V_{sh,lm})}{2(1 - V_{sh,lm})} \quad (8.87)$$

Solution B: Additional input is the shale resistivity R_{sh} (derived from an adjacent thick shale layer).

Then, the sand resistivity and laminated shale content results:

$$R_{sd} = R_h \frac{R_v - R_{sh}}{R_h - R_{sh}} \quad V_{sh,lm} = \frac{R_{sd} - R_v}{R_{sd} - R_{sh}} \quad (8.88)$$

For both cases, the second step is the determination of water saturation for the sand component (application of Archie's equation).

The modular concept can also be applied on bimodal sand; it gives an explanation of a saturation-dependent saturation exponent n (Schön et al., 2000). The concept is widely used for the interpretation of measurements with orthogonal induction systems in well logging.

The example in [Figure 8.16](#) illustrates a low-resistivity pay evaluation in laminated sand-shale sequences in a well from the Gulf Coast (Gulf of Mexico). The 3DEX tool (Baker Atlas) uses three orthogonally orientated coil-receiver pairs to record resistivities on three planes. The borehole was vertical and drilled with oil-based mud. Dips indicate low angle formation dips— $<10^\circ$ mostly dipping east or northeast.

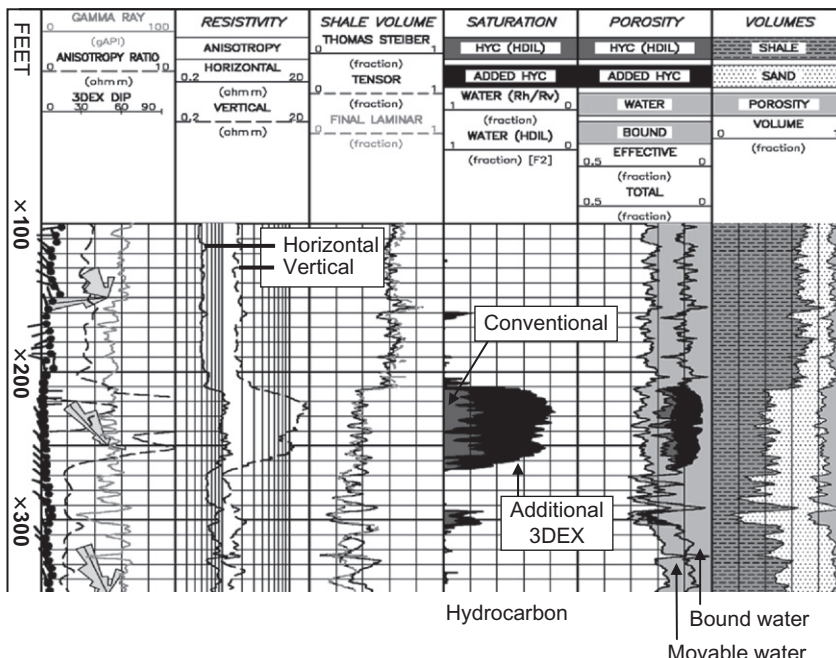


FIGURE 8.16 Low-resistivity pay evaluation in laminated sand-shale sequences based on the 3DEX orthogonal measuring system (courtesy Baker Atlas). The first track from the left (Track 1) depicts the anisotropy ratio curve in dashed black and the gamma ray curve in gray. The black tadpoles represent formation dips recovered from 3DEX; the rose diagrams (grey) reflect formation dips over 100-ft intervals. Track 2 illustrates horizontal resistivity and vertical resistivity (dashed). Track 3 gives a comparison of shale volumes calculated based on the Thomas–Stieber approach and from 3DEX data (dashed). Track 4 shows calculated saturation curves with and without 3DEX data (tensor). Gray areas indicate hydrocarbon saturation based on conventional resistivity, while black areas depict an increase in hydrocarbon saturation due to use of the 3DEX data. Track 5 depicts total porosity and fluid components (movable water, clay-bound water, hydrocarbons). Black indicates additional hydrocarbons due to use of the 3DEX data. Track 6 contains the volumetric information for the shale, sand, and effective porosity.

The sand-shale sequence containing a thinly laminated section at the depth interval x210–x255 can be identified by very high anisotropy ratios >8 (Track 1).

The second track presents the resistivities. In the presented section, the horizontal resistivity is dominated by the lower resistivity shale. The sections with mostly shale are typical for the Gulf Coast: 0.5–0.6 ohm m. In the laminated interval, the horizontal resistivity shows very modest increase to 1.0–1.3 ohm m, while the vertical resistivity is over a decade higher (up to 20 ohm m), indicating the presence of hydrocarbon-bearing sand laminations.

Shale volume calculated using different techniques (Thomas–Stieber approach and 3DEX analysis) is plotted in the third track. They agree well in the upper section including the laminated zone with high anisotropy ratio.

Track 4 compares the saturation-calculation results of a conventional shaly-sand analysis using standard induction log data (which is essentially measuring horizontal resistivity) to a 3DEX- (tensor) based laminated shaly-sand analysis that incorporates vertical resistivity as well. Water saturation in the pay zone has been reduced from 80% to $\sim 25\%$. It means that an additional 40–50 ft of pay has been identified and quantified by having vertical resistivity from 3DEX and using it in the petrophysical analysis.

Track 5 gives the volumetric composition of the pore space. Track 6 represents the lithologic profile including porosity.

8.7 DIELECTRIC PROPERTIES OF ROCKS

8.7.1 Introduction

The dielectric permittivity can be expressed as the product of vacuum permittivity and relative permittivity

$$\varepsilon = \varepsilon_0 \cdot \varepsilon_r \quad (8.89)$$

where

ε_0 is the vacuum permittivity $(8.854 \cdot 10^{-12} \text{ F m}^{-1} = 8.854 \cdot 10^{-12} \text{ A}^2 \text{ s}^4 \text{ kg}^{-1} \text{ m}^{-3})$

ε_r is the relative permittivity.

Figure 8.17 shows the different polarization mechanisms related to frequency dependence of permittivity.

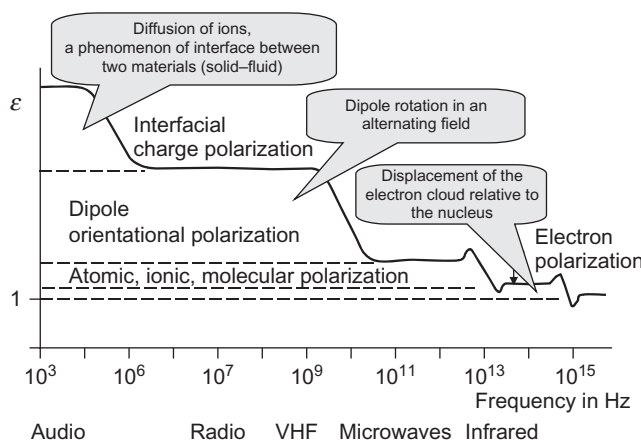


FIGURE 8.17 Polarization mechanisms.

The different mechanisms can be characterized briefly:

1. Electron polarization is created by the distortion of an atom's electron cloud in response to an external electric field in which one side of the atom becomes more positive and the other more negative than normal.
2. Molecular polarization is created by the distortion of an entire molecule in response to an external electric field, in which one part of the molecule becomes more positive than the rest and another part more negative.
3. Ionic polarization is the result of a redistribution of ions within a material due to an external electric field, with positive ions migrating toward the negative side of the field, and negative ions the other side.
4. Dipole orientational polarization is the result of realignment or reorientation of polar molecules (without distortion of shape) in response to an external electric field.
5. Interfacial polarization is based on charge separation and accumulation at local variations in electrical properties during migration of charge in response to an external electric field.

These polarization mechanisms occur in the order listed from high to low frequency, and are simply additive to each other in going from high to low frequency.

From low frequencies with a value of ε_0 to high frequencies with a value of ε_∞ , permittivity decreases through several transitions. In the transition region, the total permittivity changes and an energy dissipation occurs. This transition and the frequency dependence of permittivity can be described by a relaxation model. Debye relaxation and Cole–Cole relaxation are the two fundamental models used to describe the frequency dependence of dielectric constant.

Debye and Hückel (1923) formulated for ideal dielectrics:

$$\varepsilon(\omega) = \varepsilon_\infty + \frac{\varepsilon_0 - \varepsilon_\infty}{1 + i \cdot \omega \cdot \tau} \quad (8.90)$$

where

- ε_0 is the static dielectric permittivity
- ε_∞ is the optic dielectric permittivity
- τ is relaxation time (single process).

Cole and Cole (1941) expanded the equation for multiple relaxations:

$$\varepsilon(\omega) = \varepsilon_\infty + \frac{\varepsilon_0 - \varepsilon_\infty}{1 + (i \cdot \omega \cdot \tau)^{1-\alpha}} \quad (8.91)$$

where α is the Cole–Cole distribution parameter (0–1).

The type of relaxation-time distribution can be easily determined from plots of ε'' versus ω for a broad range of frequencies (the so-called Cole–Cole plot or Argand plot, [Figure 8.18](#)). The Cole–Cole plot for a single relaxation

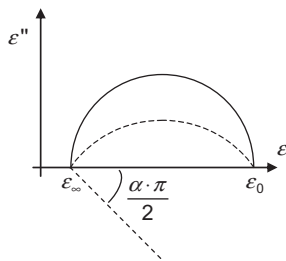


FIGURE 8.18 Real and imaginary part of relative permittivity with conductivity $C = 0$. Solid line: Debye model with single relaxation; Dashed line: Cole–Cole model with relaxation distribution with $\alpha = 0.5$ (after Chelidze and Gueguen, 1999).

time is a semicircle between $\epsilon' = \epsilon_{\infty}$ and $\epsilon' = \epsilon_0$ centered on the ϵ' -axis (Debye model) or below the ϵ' -axis (Cole–Cole model).

Rocks can have very high dielectric permittivity in the low-frequency range. Three mechanisms can create the polarization effects:

1. Maxwell–Wagner or geometrical effect.
2. Metallic-induced polarization: polarization of double layer at metallic conducting grains.
3. Polarization of double layer at insulating grains with fixed charge (e.g., clay).

Maxwell–Wagner effect in heterogeneous materials generally results from a nonuniform charge distribution at the boundary of regions with different electrical properties (e.g., grain boundaries and other discontinuities also within the solid rock matrix). The Maxwell–Wagner effect or geometrical effect enhances the dielectric permittivity due to charge buildup at grain surfaces (acting as an interface with conductivity or permittivity contrast). Grains with a platy shape act as thin capacitors, leading to very high permittivity.

Metallic-induced polarization is responsible for high dielectric permittivity when a polarization layer is generated by surface reactions on conductive grains (e.g., pyrite particles; see Anderson et al., 2006).

The third mechanism is a different double-layer mechanism. It causes polarization in shaly sands at Hz frequencies. Alumino-silicate layers have fixed charges due to lattice defects. Excess mobile positive ions surround the fixed negative charges to form the double layer and can contribute to polarization.

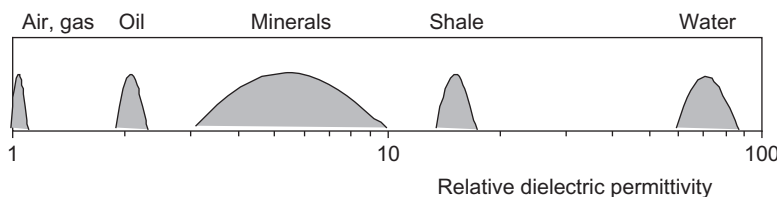
8.7.2 Dielectric Properties of Rock Constituents

In the following sections relative permittivity as a material property is discussed. Table 8.8 gives some relative permittivities for rock-forming components.

TABLE 8.8 Relative Permittivities (at Radio Frequencies) for Rock-Forming Components

Substance	ϵ_r	Substance	ϵ_r
Quartz	4.5–4.7	Gas	1
Calcite	6.4–8.5	Oil	2.2
Dolomite	6.1–7.3	Water	80
Anhydrite	5.7–6.5		
Halite	5.7–6.2	Shale (dry)	13–16

References: Parchomenko (1965), Keller (1989), Gueguen and Palciauskas (1994), Olhoeft (1981, 1985, 1987), Martinez and Byrnes (2001), Cerniak (1964).

**FIGURE 8.19** Permittivity of rock components.**TABLE 8.9** Dielectric Permittivity of Some Pore Fluids, Including Contaminants

Fluid	ϵ	Fluid	ϵ
Air	1.00	Diesel	2.0–2.4
Water	80–81	Trichloethane	7.5
Natural oil	2.0–2.4	Benzene, toluene	2.3–2.4

Schlumberger (1989a, 2000), Baker Atlas (2002), Olhoeft (1992).

The following schematic picture (Figure 8.19) results from these data.

Most rock-forming minerals have a permittivity in the order of $\epsilon_r = 3–10$; higher values show, for example, sulfides and some oxides. The dielectric permittivity of water is about 80 and is temperature dependent. This results in a strong correlation between permittivity and the water content of a rock.

Table 8.9 shows some more data for the permittivity of fluids.

Water with its dipole character has a prominent position within the pore fluids. The influence of concentration on the relative permittivity of water is relatively small compared to the influence on the conductivity. Olhoeft (1981) (see also Hearst and Nelson, 1985) gives an empirical equation for the effect of salt concentration C_{mol}

$$\varepsilon_{r,w} = \varepsilon_{r,\text{pure water}} - 13.00 \cdot C_{\text{mol}} + 1.065 \cdot C_{\text{mol}}^2 - 0.03006 \cdot C_{\text{mol}}^3 \quad (8.92)$$

where C_{mol} is the molal concentration and $\varepsilon_{r,\text{pure water}} \approx 80$.

Permittivity decreases with increasing temperature (Figure 8.20), whereas pressure only changes the value slightly (Hearst and Nelson, 1985). A detailed description of the dielectric permittivity of water—including temperature and concentration dependence—is given by Olhoeft (1981).

If water goes to the solid state (ice), the polarization mechanism changes dramatically; Olhoeft (1979) gives for ice a mean value of $\varepsilon_r = 3.4$. This is reflected in the temperature dependence of the clay permittivity in Figure 8.21.

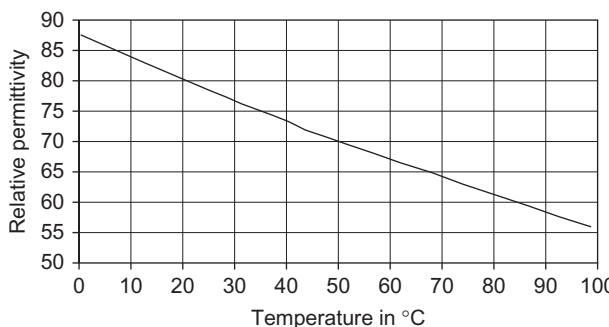


FIGURE 8.20 Temperature dependence of water permittivity (after Eisenberg and Kauzmann, 1969; cited by Gueguen and Palciauskas, 1994).

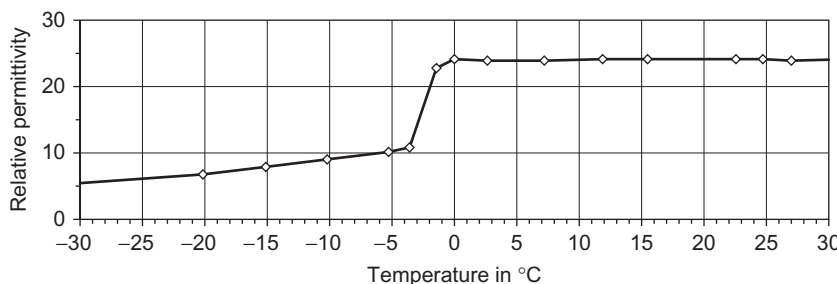


FIGURE 8.21 Temperature dependence of relative permittivity of a clay (Rideau clay, moisture content by volume 40%). Data from Annan and Davis (1978) and Scott et al. (1990).

8.7.3 Dielectric Properties of Rocks—Some Experimental Results

Permittivity of rocks and soils is of particular interest for interpretation of georadar and borehole electromagnetic propagation measurements. [Table 8.10](#) shows some characteristic values. It includes the propagation velocity of electromagnetic wave and the attenuation coefficient. We note the strong influence of water content and water conductivity upon attenuation; this originates limitations for georadar penetration depth.

In general, dielectric permittivity increases with:

- increasing water content
- increasing porosity of the brine-saturated rock ([Figure 8.22](#));
- increasing clay content or increasing CEC ([Figure 8.23](#)).

[Figure 8.22](#) demonstrates some important influences on permittivity for sandstone. [Figure 8.22A](#) shows for two selected samples³ the real part of relative permittivity as function of frequency. With increasing frequency, permittivity decreases and tends toward the asymptotic value at high frequencies (about $5 \cdot 10^8$ Hz = 0.5 GHz).

[Figure 8.22B](#) shows for the highest frequencies ($5 \cdot 10^8$ Hz) the strong correlation between permittivity and porosity for the case of $S_w = 1$. An extrapolation to $\phi \rightarrow 0$ gives $\varepsilon_r \approx 4.5\text{--}5$; this is typical for quartz.

Comparable results for limestone are published by Sengwa and Soni (2006).

The influence of clay content upon dielectric permittivity of a sandstone is shown in [Figure 8.23](#).

TABLE 8.10 Dielectric Permittivity and Properties of Electromagnetic Wave Propagation

Substance	Permittivity ε_r	Propagation Velocity in cm ns^{-1}	Attenuation in dB m^{-1}
Air	1	30	0
Dry sand	4	15	0.01
Water-saturated sand	25	6	0.03–0.3
Clay	5–40	4.7–13	1–300
Peat	60–80	3.4–3.9	0.3
Water (fresh)	80	3.4	0.1
Water (saline)	80	3.4	1000

van Overmeeren (1994).

³In the original paper, five curves are plotted.

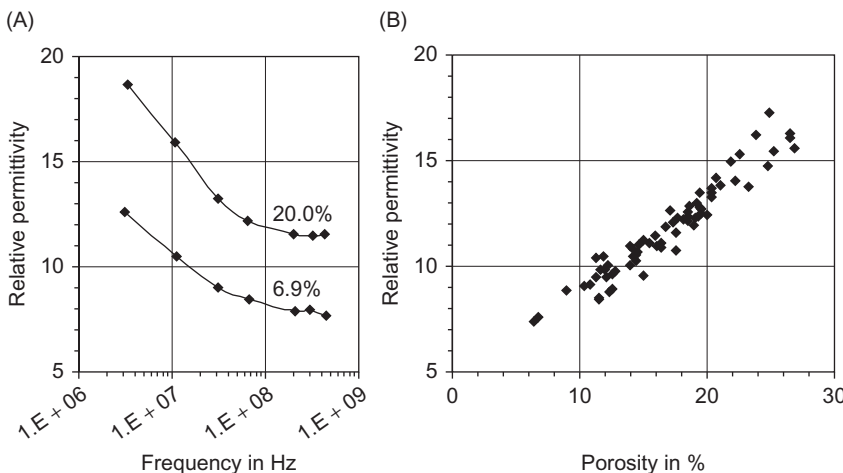


FIGURE 8.22 Permittivity as a function of frequency and porosity for sandstone (freshwater saturated); data taken from Pooley et al. (1978). (A) Real part of relative permittivity as a function of frequency for two samples with different porosity. (B) Real part of relative permittivity as a function of porosity, measured at frequency 0.5 GHz.

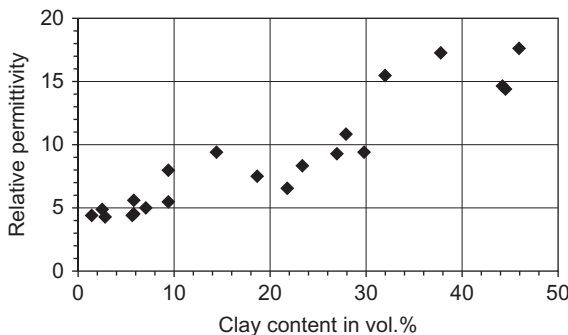


FIGURE 8.23 Correlation between relative dielectric permittivity and clay content for gas-saturated Mesozoic sandstones (West Siberia), frequency 10^6 Hz; after Kobranova (1989).

Garrouch and Sharma (1994) investigated the combined influence of clay content, porosity, and frequency on the dielectric properties of shaly sands in the frequency range between 10 Hz and 10 MHz. The samples are Berea sandstone and Ottawa sand-bentonite packs. They found an increase of dielectric permittivity with:

- increasing porosity of the brine-saturated rock;
- increasing CEC, describing the clay effect and ionic double-layer polarization phenomena at the solid–fluid interface.

A regression analysis suggests an empirical correlation with a proportionality

$$\varepsilon_r \propto \exp(0.15 \cdot \text{CEC} + 0.23 \cdot \phi + 11.1) \quad (8.93)$$

where the porosity ϕ is a fraction and CEC in meq/100 g.

Permittivity increases with increasing water content or water saturation S_w . Knight and Nur (1987) published results of a systematic laboratory study of a tight gas sandstone. Experiments show for the ε_r versus S_w plot of the imbibition-drying cycle a typical “hysteresis.” For the interpretation the authors may be cited: “In the region of $S_w < 0.03$, there is little change in ε_r with S_w ; we interpret this region as corresponding to the presence of a monolayer of water on the surface of the pore space. In the region of $0.03 < S_w < 0.12$, there is a rapid increase in ε_r with increasing S_w ; we interpret this region as the wetting of the pore surfaces by two or three monolayers of water, creating both water-grain and water-gas capacitors. In the region of $S_w > 0.12$, dielectric hysteresis occurs; we interpret this region as corresponding to the filling and emptying of the central volume of the pore space with water, the hysteresis being a result of the changing geometry of the liquid and gas phases.”

8.7.4 Theories and Models

In the literature, various papers describe the dielectric behavior of rocks as composite materials mostly under the aspect of a mixing law in order to model influences like porosity and water saturation. Examples for model consideration strongly directed on reservoir properties are papers by Sherman (1986, 1998), Sen (1980), Garrouch and Sharma (1994), Carcione and Seriani (2000). Toumelin and Torres-Verdin (2009) derived a pore-scaled numerical model.

This section presents an overview of two groups of models:

1. Layer models, modifications, and comparable mixing rules
2. Inclusion models.

8.7.4.1 Layer Models—Series and Parallel

A rock consisting of n components can be idealized in the simplest case as a layer model in following Voigt’s and Reuss’s concept (see Section 6.7.1). The layers represent the individual rock components. The relative thickness of each layer is given by the volume fraction of each rock component.

The relations are:

- for “parallel model” (electrical field parallel to boundary plane between components):

$$\varepsilon_{r,\parallel} = \sum_{i=1}^n V_i \cdot \varepsilon_{r,i} \quad (8.94)$$

- for “series model” (electrical field perpendicular to boundary plane between components:

$$\varepsilon_{r,\perp} = \left[\sum_{i=1}^n V_i \cdot \varepsilon_{r,i}^{-1} \right]^{-1} \quad (8.95)$$

where V_i is the volume fraction and $\varepsilon_{r,i}$ the relative permittivity of the component i .

The two equations represent the upper ($\varepsilon_{r,\parallel}$) and the lower ($\varepsilon_{r,\perp}$) bound of relative permittivity for a rock of a given composition.

For a porous rock with a matrix (ma) and a pore fluid (fl), the equations are:

$$\text{parallel model} \quad \varepsilon_{r,\parallel} = (1 - \phi) \varepsilon_{r,ma} + \phi \cdot \varepsilon_{r,fl} \quad (8.96)$$

$$\text{series model} \quad \varepsilon_{r,\perp} = \left[(1 - \phi) \varepsilon_{r,ma}^{-1} + \phi \cdot \varepsilon_{r,fl}^{-1} \right]^{-1} \quad (8.97)$$

The porosity dependency for the series and the parallel model is plotted in Figure 8.24. Experimentally determined data are situated between the two boundaries (Figure 8.25).

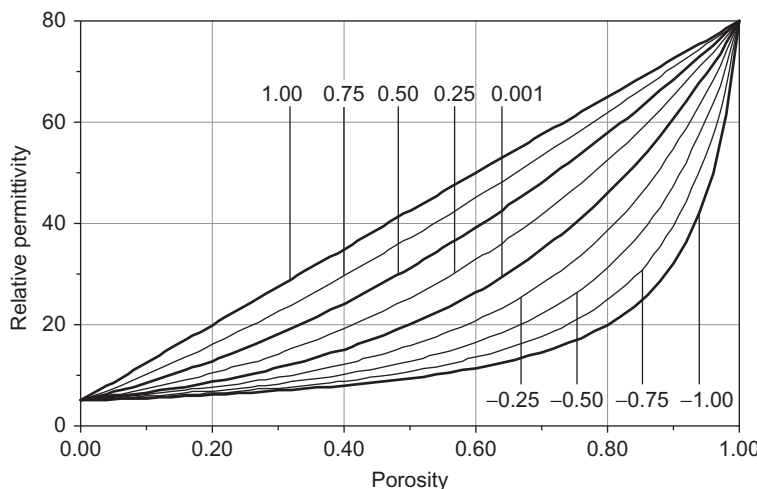


FIGURE 8.24 Relative permittivity versus porosity for a two-component material with matrix (solid) permittivity $\varepsilon_{r,ma} = 5$ and fluid permittivity $\varepsilon_{r,fl} = 80$, calculated with generalized Lichtenegger–Rother equation (curve parameter is the exponent α). Parallel model = curve with exponent $\alpha = 1$ and series model = curve with exponent $\alpha = -1$ (for calculation, visit the website <http://www.elsevierdirect.com/companion.jsp?ISBN=9780444537966> and refer Electrical. Permittivity models).

There are different modifications of the model prediction, to obtain a fit of calculated and measured values:

1. Combination of the two fundamental models as arithmetic mean (in analogy to “Hills value,” Equation (6.77)):

$$\varepsilon_{r,H} = \frac{\varepsilon_{r,\parallel} + \varepsilon_{r,\perp}}{2} \quad (8.98)$$

2. Another way is the application of the Lichtenegger and Rother (1931) generalization for dielectric permittivity to fill the space between the extreme boundaries:

$$\varepsilon_r = \left[\sum_i V_i \left(\varepsilon_{r,i}^\alpha \right) \right]^{\frac{1}{\alpha}} \quad (8.99)$$

Equation (8.99) is a generalization of several individual equations. For example, the parallel model for $\alpha = 1$ and the serial model for $\alpha = -1$. The exponent α is a “textural parameter.”

For a porous rock, the resulting equation is

$$\varepsilon_r = \left[(1 - \phi) \left(\varepsilon_{r,ma}^\alpha \right) + \phi \cdot \left(\varepsilon_{r,fl}^\alpha \right) \right]^{\frac{1}{\alpha}} \quad (8.100)$$

Figure 8.24 shows a calculated plot with $\varepsilon_{r,ma} = 5$ and $\varepsilon_{r,fl} = \varepsilon_{r,water} = 80$; exponent α is the curve parameter. The variation of α fills the space between the maximum and minimum curves.

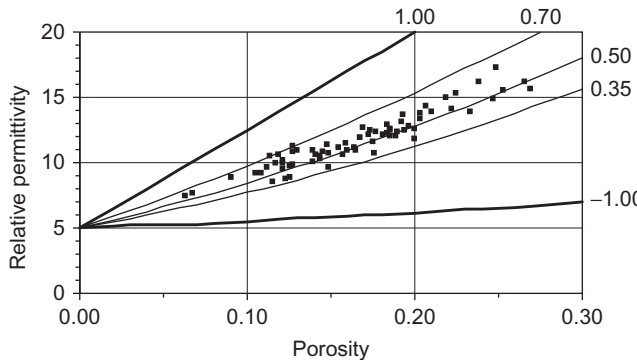


FIGURE 8.25 Relative permittivity versus porosity for a two-component material with matrix (solid) permittivity $\varepsilon_{r,ma} = 5$ and fluid permittivity $\varepsilon_{r,fl} = 80$, calculated with generalized Lichtenegger–Rother equation (curve parameter is the exponent α) and compared with experimental data (dots) for water-saturated sandstone from Pooley et al. (1978). Parallel model = curve with exponent $\alpha = 1$, series model = curve with exponent $\alpha = -1$, and CRIM equation = curve with exponent $\alpha = 0.5$.

Figure 8.25 shows a comparison with experimental data for a water-saturated sandstone (Pooley et al., 1978; see Figure 8.22). Experimental data correspond with calculated curves for an exponent $\alpha = 0.35–0.70$. The complex refractive index method (CRIM) curve (see Section 8.7.4.4) with the exponent $\alpha = 0.5$ gives a good approximation.

8.7.4.2 Inclusion Models—Spherical Inclusions

The earliest mathematical derivation of a mixing formula is credited to Mossotti in 1846; it is usually called the “Clausius–Mossotti approximation” (Olhoeft, 1985):

$$\frac{\varepsilon - \varepsilon_2}{\varepsilon + 2\varepsilon_2} = V_1 \frac{\varepsilon_1 - \varepsilon_2}{\varepsilon_1 + 2\varepsilon_2} \quad (8.101)$$

where

ε is the permittivity of the mixture

ε_2 is the permittivity of the host material

ε_1 is the permittivity of the inclusion material

V_1 is the volume fraction of the inclusion material.

Relative permittivity of a porous material ε_r with fluids as inclusion results in

$$\varepsilon_r = \varepsilon_{r,ma} \frac{2 \cdot \varepsilon_{r,ma} + \varepsilon_{r,fl} - 2\phi(\varepsilon_{r,ma} - \varepsilon_{r,fl})}{2 \cdot \varepsilon_{r,ma} + \varepsilon_{r,fl} + \phi(\varepsilon_{r,ma} - \varepsilon_{r,fl})} \quad (8.102)$$

and with mineral grains as inclusion:

$$\varepsilon_r = \varepsilon_{r,fl} \frac{2 \cdot \varepsilon_{r,fl} + \varepsilon_{r,ma} - 2(1 - \phi)(\varepsilon_{r,fl} - \varepsilon_{r,ma})}{2 \cdot \varepsilon_{r,fl} + \varepsilon_{r,ma} + (1 - \phi)(\varepsilon_{r,fl} - \varepsilon_{r,ma})} \quad (8.103)$$

where

$\varepsilon_{r,ma}$ is the relative permittivity of the mineral component (matrix)

$\varepsilon_{r,fl}$ is the relative permittivity of the fluid component (pore)

ϕ is the volume fraction of the fluid (porosity).

Figure 8.26 shows calculated curves for the parallel and perpendicular model, and for the Clausius–Mossotti model assuming grains or pores as inclusion. With regard to the supposition that there is no influence or distortion of the electrical field of one inclusion by any neighboring inclusion, we can expect that:

- Equation (8.102) is useful mainly for rocks with relatively small porosity.
- Equation (8.103) is useful mainly for high porous sediments (marine sediments).

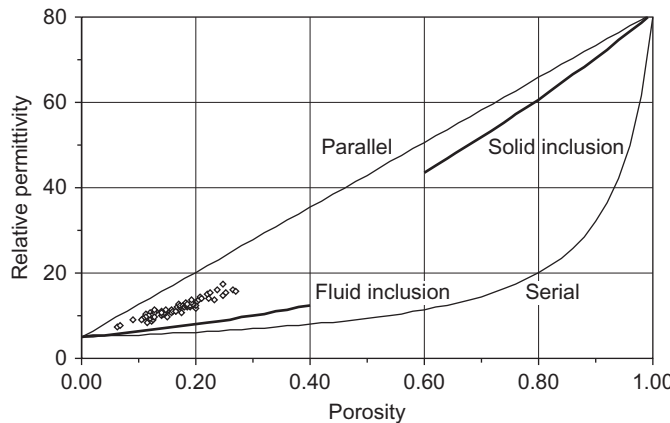


FIGURE 8.26 Relative permittivity versus porosity for a two-component material with matrix (solid) permittivity $\varepsilon_{r,mi} = 5$ and fluid permittivity $\varepsilon_{r,fl} = 80$, calculated with parallel and perpendicular model, and Clausius–Mossotti equation assuming grains or pores as inclusion (for calculation, visit the website <http://www.elsevierdirect.com/companion.jsp?ISBN=9780444537966> and refer Electrical. Permittivity models). Dots are experimental data for water-saturated sandstone from Pooley et al. (1978).

Therefore, in Figure 8.26, the curves are plotted for both cases only up to a volume fraction of the inclusion of 0.4. The calculated curve “fluid inclusion” shows permittivities distinctly below the measured data for the sandstone.

8.7.4.3 Inclusion Models—Nonspherical Inclusions

The generalization of the inclusion shape from a sphere to an ellipsoid creates different properties of the composite with respect to the field direction related to the ellipsoid axis system.

The generalized Hanai–Bruggeman formula (see Berryman, 1995) for ellipsoidal inclusions is

$$\left(\frac{\varepsilon_{HB} - \varepsilon_2}{\varepsilon_1 - \varepsilon_2} \right) \left(\frac{\varepsilon_1}{\varepsilon_{HB}} \right)^L = V_1 \quad (8.104)$$

where

ε_{HB} is the rock permittivity

ε_1 is the host material permittivity

ε_2 is the inclusion material permittivity

V_1 is the volume fraction of the host material

L is the depolarization exponent of the inclusion.

The depolarization exponent represents a kind of a textural parameter and depends on the aspect ratio (see Section 8.4.4). It is related to the direction

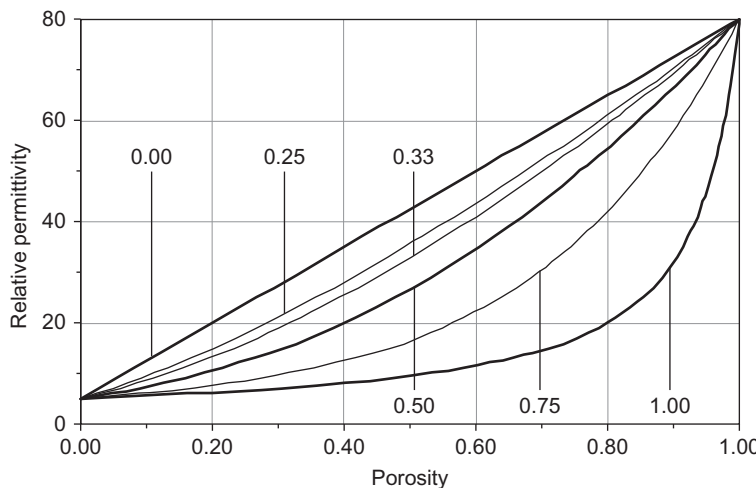


FIGURE 8.27 Permittivity versus porosity for a two-component material with matrix (solid) permittivity $\varepsilon_{r,ma} = 5$ and fluid permittivity $\varepsilon_{r,fl} = \varepsilon_{r,w} = 80$, calculated with the Hanai–Bruggeman equation for different exponents L (for calculation, visit the website <http://www.elsevierdirect.com/companion.jsp?ISBN=9780444537966> and refer Electrical. Permittivity models). The curve for $L = 0.33$ is the same as for the CRIM equation (see Section 8.7.4.4).

of the field with respect to the axis direction of the ellipsoid. Therefore, different depolarization exponents for different directions create anisotropy of permittivity.

For the relative permittivity of a porous rock with matrix and pore fluid, results are

$$\left(\frac{\varepsilon_{r,HB} - \varepsilon_{r,ma}}{\varepsilon_{r,fl} - \varepsilon_{r,ma}} \right) \left(\frac{\varepsilon_{r,fl}}{\varepsilon_{r,HB}} \right)^L = \phi \quad (8.105)$$

Figure 8.27 shows the relative permittivity versus porosity for different exponents L . The variation of L fills the space between maximum and minimum curve:

- For $L = 0$ results the parallel model
- For $L = 1$ results the series model.

Figure 8.28 shows a comparison with experimental data for the water-saturated sandstone (Pooley et al., 1978; see Figure 8.22). Experimental data correspond with calculated curves for exponent $L = 0.25–0.40$. The CRIM curve with exponent $\alpha = 0.33$ also gives a good approximation.

8.7.4.4 The CRIM Formula

The philosophy of Wyllie's time-average formula (see Section 6.52) leads to the CRIM formula (Calvert et al., 1977). The time-average equation is

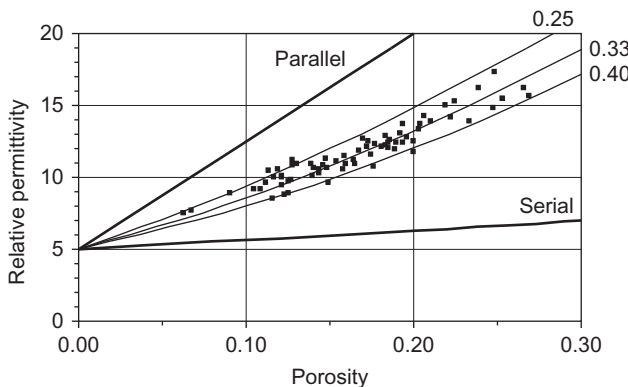


FIGURE 8.28 Permittivity versus porosity for a two-component material with matrix (solid) permittivity $\varepsilon_{r,ma} = 5$ and fluid permittivity $\varepsilon_{r,fl} = 80$, calculated with generalized Hanai–Bruggeman equation for different exponents L ; the curve for $L = 0.33$ is the same as for the CRIM equation (see Section 8.7.4.4) and compared with experimental data for water-saturated sandstone (Pooley et al., 1978).

explained as a summation of the travel time of the signal passing the solid matrix and the pore fluid—both rock components condensed as a layer.

In the case of electromagnetic wave propagation, the time-average formula in terms of slowness⁴ Δt is

$$\Delta t_{\text{CRIM}} = (1 - \phi)\Delta t_{\text{ma}} + \phi \cdot \Delta t_{\text{fl}} \quad (8.106)$$

where Δt_{ma} is the matrix slowness and Δt_{fl} is the fluid slowness for electromagnetic waves.

Electromagnetic wave propagation slowness of a material is related to the relative permittivity and vacuum slowness (inverse of speed of light):

$$\Delta t = \Delta t_{\text{vacuum}} \cdot \sqrt{\varepsilon_r} \quad (8.107)$$

where $\Delta t_{\text{vacuum}} = 1/c_{\text{light}} = (2.998 \cdot 10^8 \text{ m s}^{-1})^{-1} = 3.336 \text{ ns m}^{-1}$.

The relative dielectric permittivity of the composite material therefore results:

$$\varepsilon_{r,\text{CRIM}} = \left((1 - \phi)\sqrt{\varepsilon_{r,ma}} + \phi \cdot \sqrt{\varepsilon_{r,fl}} \right)^2 \quad (8.108)$$

Figure 8.28 shows the result of calculation of relative dielectric permittivity versus porosity for a two-component material with matrix (solid) permittivity $\varepsilon_{r,ma} = 5$ and fluid permittivity $\varepsilon_{r,fl} = 80$, calculated with the CRIM equation (identical curve for $L = 0.33$) compared with experimental data for the water-saturated sandstone (Pooley et al., 1978) with a good fit.

⁴Slowness is the inverse of velocity.

Coutanceau-Monteil and Jacquin (1993) investigated the permittivity of sedimentary rock samples in the frequency range from 20 to 1000 MHz. A comparison of model equations and experimental results shows that the CRIM model fits the data for water- and brine-saturated quarry limestones, whereas the Bruggeman–Hanai equation fits the data for water- and brine-saturated Fontainebleau sandstones fairly well.

A generalization of the CRIM equation for n components gives

$$\varepsilon_{r,CRIM} = \left[\sum_{i=1}^n V_i \cdot \varepsilon_{r,i}^{-\frac{1}{2}} \right]^2 \quad (8.109)$$

Thus, the CRIM equation is identical with the generalized Lichtenecker and Rother (1931) [Equation \(8.100\)](#) with $\alpha = 0.5$.

8.8 COMPLEX RESISTIVITY—SPECTRAL-INDUCED POLARIZATION

8.8.1 Introduction

The phenomenon of induced polarization (IP) was observed by Conrad Schlumberger in a mining region in France circa 1913, and in about 1929, he introduced this technique into hydrocarbon borehole logging (see Seigel et al., 2007). Experimental and theoretical studies by Marshall and Madden (1959), Pelton et al. (1978), Vinegar and Waxman (1984), Olhoeft (1985), Ward (1990), Börner (1991), Börner et al. (1993), Börner and Schön (1995), Vanhala (1997), Titov et al. (2002, 2004), Scott (2006), and others describe characteristics of this phenomenon.

IP is a current-stimulated electrical phenomenon observed as a delayed voltage response in earth materials resulting from a capacitive behavior (Ward, 1990). This delay effect can be described and measured in the time domain and in the frequency domain. The connection between the two domains is given by Fourier transformation. Today's spectral electrical measurements (SIP) are state of the art.

The petrophysical origin of the IP effects is connected with electrochemical processes of the electronic–ionic interaction, interface properties at the grain-fluid boundary region, cation-exchange phenomenon, pore constrictivity, and other effects controlled by rock components, their distribution and interaction ([Figure 8.29](#)).

In the early days, IP was directed mostly on ore mineral exploration. Later, pore space properties and connected effects became more interesting.

Today, frequency-dependent complex resistivity measurements are generally directed on problems of pore space characterization and description of fluid–mineral interactions. Measurements are “sensitive to physico-chemical mineral–water interaction at the grain surfaces. In comparison to conventional

geoelectrics, a complex electrical measurement can also provide—besides conductivity—information on the electrical capacity and the relaxation process in the frequency range below some kHz" (Börner, 2006).

Complex conductivity is a frequency-dependent property with a real and an imaginary component (see [Section 8.1](#); [Equation \(8.5\)](#)). There is presently no universal theory or equation that describes the frequency-dependent complex conductivity. A review of existing theories is given by Dias (2000).

A popular model is the Cole–Cole model (Pelton et al., 1978). Complex conductivity as a function of frequency is given as

$$C(\omega) = C_0 \left[1 + m \left(\frac{(i\omega\tau)^c}{1 + (i\omega\tau)^c(1 - m)} \right) \right] \quad (8.110)$$

where

C_0 is the conductivity at DC ($\omega \rightarrow 0$)

τ is the relaxation time

c is an exponent that typically takes values in the range 0.1–0.6 (Binley et al., 2005), describing the τ -distribution.

The parameter m is

$$m = 1 - \frac{C_0}{C_\infty} \quad (8.111)$$

where C_∞ is the conductivity at high frequency ($\omega \rightarrow \infty$).

The spectrum of the Cole–Cole model shows a maximum phase angle at the frequency

$$\omega_{\text{maximum}} = \frac{1}{\tau(1 - m)^{c/2}} \quad (8.112)$$

At low frequencies (10^{-3} – 10^3 Hz), a main feature observed in many porous rocks is a nearly constant phase angle combined with a steady decrease of the resistivity magnitude with frequency (Börner, 1991, 1995, 2006; Börner et al., 1993; Dissado and Hill, 1984; Jonscher, 1981):

$$C^*(\omega_n) = C_n (i \cdot \omega_n)^{1-p} \quad (8.113)$$

where

C_n is the conductivity magnitude at $\omega = 1$ Hz

ω_n is the normalized angular frequency $\omega_n = \omega/(\omega = 1)$

$1 - p$ is the frequency exponent (in the order of 0–0.5).

The relationship between the frequency exponent ($1 - p$) and the frequency-independent phase angle is

$$\tan \phi = \frac{C''(\omega)}{C'(\omega)} = \tan \left[\frac{\pi}{2} (1 - p) \right] \quad \phi = \frac{\pi}{2} (1 - p) \quad (8.114)$$

Various phenomenological models have been developed to explain the connection of observed electrical effects and rock or pore properties. The following section gives only an overview.

8.8.2 Basic mechanisms

Figure 8.29 shows the three main mechanisms of IP.

Electrode polarization occurs in ore-containing rocks and is originated at the interface of an electronic conductor (ore) and an ionic conductor (electrolyte). Electrode polarization arises from the tendency of the metal to dissolve in the adjacent solutions, producing a dilute solution of metal cations at the interface. When an electric current is driven across the metal–solution interface, the polarization ions near the interface respond to produce an electric field that opposes the flow of current (Snyder et al., 1977).

Electrolytic interface polarization results from different ion mobility and diffusion processes causing a charge buildup in nonmetallic mineralized rocks. A prominent type is the membrane polarization at clay particles in the pore space. Ward (1990) describes the membrane polarization mechanism as follows: polarization arises chiefly in porous rocks in which clay particles partially block ionic solution paths. The diffuse cloud of cations (double layer) in the vicinity of a clay surface is characteristic for clay-electrolyte systems. Under the influence of an electrical potential, positive charge carriers easily pass through the cationic cloud, but negative charge carriers accumulate; an ion-selective membrane, therefore, exists. Upon elimination of the electrical potential, all charges return to equilibrium positions. Consequently, a surplus of both cations and anions occurs at one end of the membrane zone, while a deficiency occurs at the other end.

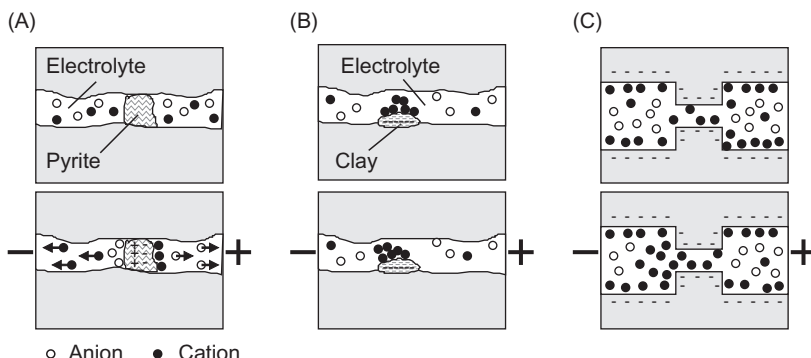


FIGURE 8.29 Models and mechanisms of IP. Top halves of figures without field; lower halves with applied field. (A) Electrode polarization (metallic polarization). (B) Membrane polarization. (C) Polarization by constrictivity of pores.

Polarization by constrictivity of pores results from the effect that pore space is characterized by an alternating change of wide pore bodies and narrow pore throats. Pore space builds up a serial connection of active (ion-selective) and passive (non-ion selective) zones. The zones have different cation and anion transport numbers, which produce local concentration gradients under an external electrical field. The electrical current flow therefore results in a deficiency of anions and surplus of cations at the boundaries of the thick and thin capillaries.

8.8.3 Traditional Parameters of IP Measurements

IP can be characterized by parameters derived in the time domain and in the frequency domain.

In time domain “chargeability” is used for description. In the simplest case it is derived from the following procedure: A primary voltage U_E is applied during an excitation time t_E . After this time, the current is switched off and the decay voltage $U_{IP}(t)$ is measured. Seigel (1959) defined apparent chargeability as the ratio:

$$M = \frac{U_{IP}(t)}{U_E} \quad (8.115)$$

Chargeability is dimensionless, but usually the secondary voltage is in mV and the primary voltage in V. Thus, the chargeability is given in mV/V (sometimes the percentage of this value is also used).

Such a definition of chargeability has an infinite number of possibilities to define the time t . Modern IP methods are directed on a study of the decay curve shape. One way is to integrate under a portion of the decay curve between the decay time t_1 and t_2 and define chargeability as:

$$M_{t_1}^{t_2} = \frac{1}{U_E(t_2 - t_1)} \int_{t_1}^{t_2} U_{IP}(t) dt \quad (8.116)$$

Time-domain instruments digitize the signal at high sampling rates and permit a Fourier analysis into frequency domain in order to study complex resistivity. In frequency domain, the “frequency effect” parameter is used:

$$FE = \frac{R(f_1) - R(f_2)}{R(f_2)} \quad (8.117)$$

where $R(f_1), R(f_2)$ are, respectively, the specific electrical resistivities at frequencies f_1, f_2 with $f_1 < f_2$.

The percent frequency effect is $PFE = FE \cdot 100\%$.

The “metal factor” (Marshall and Madden, 1959) is defined as:

$$MF = 2\pi \cdot 10^5 \frac{R(f_1) - R(f_2)}{R(f_1) \cdot R(f_2)} = 2\pi \cdot 10^5 \frac{FE}{R(f_1)} \quad (8.118)$$

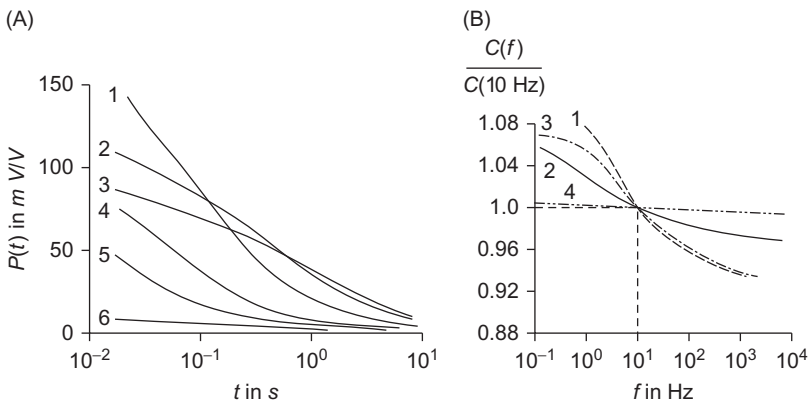


FIGURE 8.30 IP effects of some metallic and nonmetallic minerals, after Collett (1959). Key: (1) graphite, (2) pyrite, (3) chalcopyrite, (4) galena, (5) magnetite, (6) malachite. (A) Decay curves ($P(t) = U_{IP}(T)$) in the time domain (duration of the exciting primary current 21 s). (B) Frequency characteristic (frequency domain); the conductivity at the frequency f is normalized by its value at $f = 10 \text{ Hz}$.

8.8.4 IP in Ore-Containing Rocks

IP measurements for ore prospection have been the first applications of this electrical method. In 1959, Collett published a classic paper with fundamental laboratory data from measurements in both domains.

Figure 8.30A shows the decay curves and Figure 8.30B shows the frequency characteristic for some metallic and nonmetallic minerals mixed with water. The matrix material was an andesite with grain diameter between 0.84 and 2.0 mm. The pore fluid is a 5% 0.01N NaCl solution. The added metallic and nonmetallic mineral content is 3% (by solid volume) with the same grain diameter as the matrix material.

8.8.5 IP in Porous Rocks

In rocks without electronic conducting minerals, IP effects are much lower but mainly influenced by the content and distribution of clay, pore geometric properties, and properties of the electrolyte.

The chargeability of sedimentary rocks was studied in early papers by Vaquier et al. (1957) and Marshall and Madden (1959). These and subsequent investigations are directed mostly on correlations between IP parameters and reservoir properties (clay content, hydrodynamic permeability) and to contamination problems (Börner et al., 1993).

In this section, the relationship of polarization effects to clay properties (shaly sands) and pore space properties (sand) is discussed.

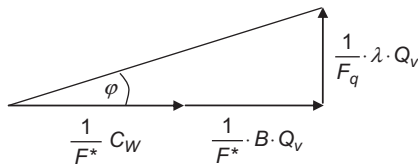


FIGURE 8.31 Complex conductance model for shaly sands (Vinegar and Waxman, 1984) with real or in-phase (x -axis) and imaginary or quadrature (y -axis) component.

8.8.5.1 IP in Shaly Rocks—Vinegar and Waxman (1984) Model

In addition to the Waxman—Smits model (Waxman and Smits, 1968) for the shaly-sand conductivity (in-phase component, see [Section 8.5.3](#)), Vinegar and Waxman (1984) published a complex conductance model implementing a quadrature or imaginary component ([Figure 8.31](#)).

The in-phase conductivity of shaly sands for a brine-saturated shaly sand is (Waxman and Smits, 1968; see [Equation \(8.62\)](#))

$$C_0 = \frac{1}{F^*} (C_w + B Q_v) \quad (8.119)$$

Vinegar and Waxman (1984) describe the quadrature conductivity as follows: “The mechanism for the quadrature conductivity follows a model proposed by Marshall and Madden (1959), where the rock pore is modeled as an alternating series of clay-rich and clay-free zones. The clay-rich zones have high concentrations of fixed negative charge sites that enhance cations relative to anion transport. In the steady-state condition after constant current is applied, the inequality of cation and anion flows causes local concentration excesses and deficiencies to form at clay sites, alternating throughout the pore length. When the applied current is terminated, the diffusion voltages resulting from these concentration gradients decay with time as the ions redistribute themselves to their equilibrium positions.”

There are two mechanisms (see also [Figure 8.29](#)): clay counterion displacements and electrolyte blockage by the clay-site membranes. Both mechanisms are assumed to be proportional to Q_v (Vinegar and Waxman, 1984).

Results for the quadrature conductivity are

$$\text{brine saturated} \quad C_0'' = \frac{1}{F_q} \lambda \cdot Q_v \quad (8.120)$$

$$\text{partially water saturated} \quad C_t'' = \frac{1}{F_q} \lambda \cdot Q_v \cdot S_w^{n-1} \quad (8.121)$$

where

F_q is the quadrature formation factor $F_q = F^* \cdot \phi$

λ is the equivalent quadrature conductance with a weak dependence on salinity.

This offers principally the possibility of a determination of $\lambda \cdot Q_v$ from the quadrature conductivity measurement:

$$\lambda \cdot Q_v = C_0'' \cdot F^* \cdot \phi \quad (8.122)$$

Finally, the complex conductivity is

$$\text{brine saturated } C_0 = \frac{1}{F^*} \cdot \left[(C_w + BQ_v) + i \cdot \frac{1}{\phi} \cdot \lambda \cdot Q_v \right] \quad (8.123)$$

$$\text{partially water saturated } C_t = \frac{S_w^{**}}{F^*} \left[\left(C_w + \frac{BQ_v}{S_w} \right) + i \frac{1}{S_w \cdot \phi} \lambda \cdot Q_v \right] \quad (8.124)$$

Thus, a complex conductivity measurement allows a partitioning of conductivity in the electrolytic part (Archie term) and the shale or interface part.

The frequency-independent phase or loss angle tangent, defined as the ratio of imaginary and real component, is

$$\tan \phi = \frac{C''}{C'} = \frac{\lambda \cdot Q_v}{\phi \cdot S_w \left[C_w + \frac{B \cdot Q_v}{S_w} \right]} \quad (8.125)$$

Vinegar and Waxman (1984) investigated 20 sandstones at five different salinities from 11 formations varying widely in CEC, type of clay and distribution in the rock. Experiments show that the quadrature conductivities and phase angles are approximately independent on frequency in the range 3–1000 Hz.

Vinegar and Waxman (1984) also derived the frequency limits f_{\min}, f_{\max} of the frequency-independent IP spectrum from the diffusion constant of sodium and chloride ions in aqueous solutions ($D = 1.5 \cdot 10^{-5} \text{ cm}^2 \text{ s}^{-1}$) and get magnitudes in the order of $f_{\min} = 0.024 \text{ Hz}$ and $f_{\max} = 2.4 \cdot 10^6 \text{ Hz}$ ($2.4 \cdot 10^8 \text{ Hz}$ if the clay is montmorillonite).

8.8.5.2 Polarization Effects Related to Pore Geometrical Properties

In the low-frequency range of SIP ($< 1000 \text{ Hz}$), the dominant mechanism is the ionic charge associated with the electrical double layer that exists at the mineral–fluid interface (Binley et al., 2005). This is also the case for porous sandstones or sand with a quartz–fluid interface. The effect therefore is related to rock properties like specific internal surface, grain or pore size and in a further step to permeability.

For the frequently applied constant phase angle model (Börner, 1991, 1995; Börner et al., 1993; Dissado and Hill, 1984; Jonscher, 1981), complex conductivity is

$$C^*(\omega_n) = C_n (i \cdot \omega_n)^{1-p} \quad (8.126)$$

with the real and imaginary component (Börner and Schön, 1995):

$$C'(\omega) = C_n' \cdot \omega_n^{1-p} \quad C''(\omega) = C_n'' \cdot \omega_n^{1-p} \quad (8.127)$$

where the frequency-independent factors are

$$C_n' = C_n \cdot \cos \left[\frac{\pi}{2} (1-p) \right] \quad C_n'' = C_n \cdot \sin \left[\frac{\pi}{2} (1-p) \right] \quad (8.128)$$

and the phase angle tangent is

$$\tan \phi = \frac{C''(\omega)}{C'(\omega)} = \frac{C_n''}{C_n'} = \tan \left[\frac{\pi}{2} (1-p) \right] \quad (8.129)$$

Figure 8.32 shows the real and imaginary component of the conductivity for a sandstone versus the frequency in the low-frequency range and demonstrate this frequency behavior.

Investigations on sandstone with no or low shale content show also a kind of interface conductivity that is controlled by the specific internal surface S_{por} . Rink and Schopper (1974) derived this equation (real component) for the electrical conductivity of a water-saturated rock:

$$C_0' = \frac{1}{F} (C_w + f(C_w) S_{\text{por}}) \quad (8.130)$$

where $f(C_w)$ is a function considering the salinity dependence. This term covers in detail the mobility of the counterions, their concentration, and pore space tortuosity (see Börner, 1991; Kulenkampff et al., 1993). Thus, the real part of the interface conductivity is

$$C_{\text{interface}}' = f(C_w) \frac{S_{\text{por}}}{F} \quad (8.131)$$

Experimental results (Börner, 1991; Börner and Schön, 1991; Börner et al., 1996) for the imaginary component of conductivity show a similar

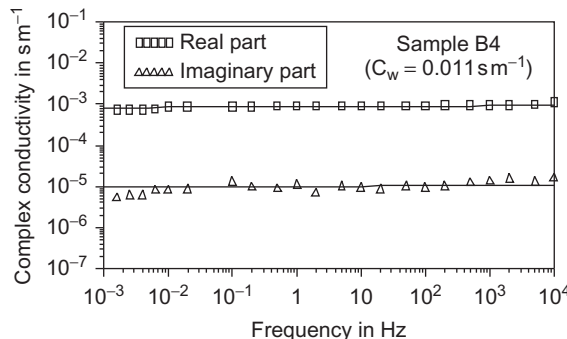


FIGURE 8.32 Complex conductivity versus frequency for a sandstone (Börner, 1991).

dependence on the specific internal surface area to porosity ratio as result of interface effects:

$$C''_{\text{interface}} = C'' = l \cdot f(C_w) \frac{S_{\text{por}}}{F} \quad (8.132)$$

where the factor l is the ratio of the imaginary and real component of the interface conductivity. Thus, the imaginary component of the complex conductivity is only a result of an interface phenomenon—the interfacial effects at and near the grain surface is the source of an internal capacity. This result corresponds to the Vinegar and Waxman (1984) model, where the imaginary component is only a shale-interface effect expressed by Q_v .

The complex conductivity results as:

$$C_0 = \frac{1}{F} \left\{ (C_w + f(C_w)S_{\text{por}}) + i \cdot l \cdot f(C_w)S_{\text{por}} \right\} \quad (8.133)$$

and the phase angle tangent is

$$\tan \phi = \frac{C''}{C'} = \frac{l \cdot f(C_w)S_{\text{por}}}{C_w + f(C_w)S_{\text{por}}} \quad (8.134)$$

The shape of [Equation \(8.133\)](#) is similar to Vinegar and Waxman's (1984) [equation \(8.123\)](#); the cation-exchange terms are replaced by the internal surface controlled terms.

[Figure 8.33](#) confirms these correlations between complex interface conductivity and pore space properties:

- Interface conductivity (real and imaginary component are plotted) of a sandstone increases with increasing pore surface to porosity ratio S_{por} ([Figure 8.33A](#)).
- Interface conductivity (imaginary component is plotted) of a sand decreases with increasing grain diameter d_{10} ([Figure 8.33B](#)).⁵
- Interface conductivity parameter $C_0'' \cdot F^* \cdot \phi$ ([Equation \(8.121\)](#)) increases with increasing cation-exchange parameter Q_v ([Figure 8.33C](#)).

Because surface area to porosity ratio is connected with permeability k (see [Section 2.5.7](#)), a correlation of complex conductivity and permeability can also be expected ([Figure 8.34](#)).

Both parameters (F, C''_n) can be derived from complex electrical measurements and based on the constant phase model.

The constant phase angle model was also applied to other problems of fluid–solid interface reactions in rocks such as:

- characterization of microcrack properties (Börner and Schön, 1995);
- environmental and contamination investigations (Börner, 1992; Weller and Börner, 1996).

⁵Internal surface to porosity ratio is inversely proportional to grain diameter ([Section 2.3](#)).

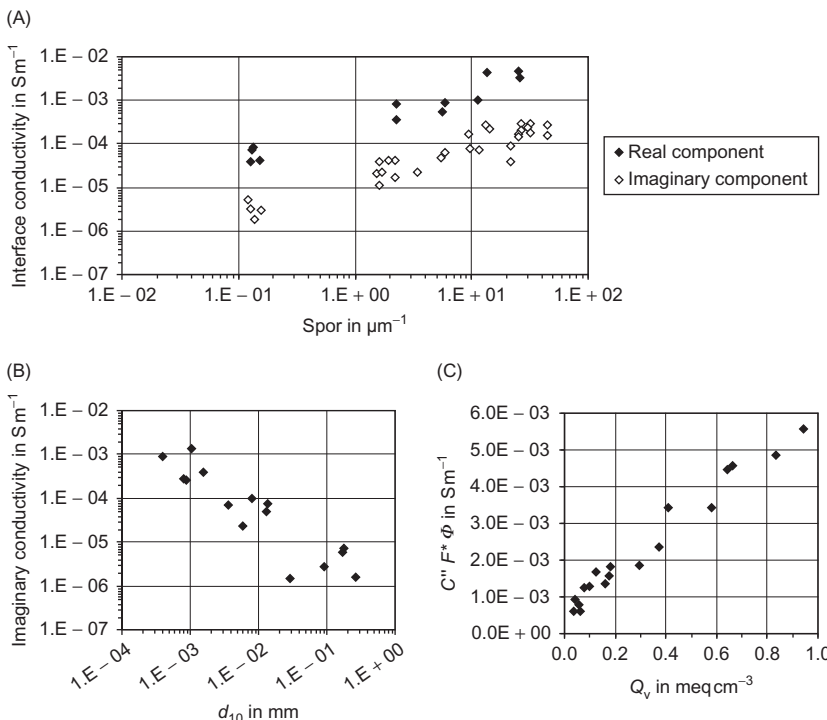


FIGURE 8.33 Complex interface conductivity components in Sm^{-1} (Siemens per meter) versus pore geometrical properties and cation-exchange parameter (replotted, units converted). (A) Complex interface conductivity (real and imaginary component) versus pore surface to porosity ratio S_{por} for sandstones (Börner, 1992). (B) Imaginary conductivity component C_0' versus grain diameter (larger than 10%) d_{10} (Slater and Lesmes, 2002). (C) Imaginary conductivity parameter $C_0'' \cdot F^* \cdot \phi$ versus Q_v (Vinegar and Waxman, 1984).

The constant phase angle behavior changes to a Cole–Cole behavior for the conductivity at frequencies higher than 10 kHz (Kulenkampff and Schopper, 1988; Kulenkampff et al., 1993; Ruffet et al., 1991).

The constant phase angle model does not give the best fit to experimental results in all cases. Based on the Cole–Cole model (Equation (8.95)), Cosenza et al. (2009) found that the position of the maximum phase peak in the phase versus frequency plot shows a proportionality to the grain size and that the exponent is related to the width of the grain-size distribution.

Scott and Barker (2003) investigated the correlation between a “dominant pore-throat diameter” and the frequency at which a peak in the phase angle versus frequency plot occurs in Triassic sandstones. This does not follow the constant phase angle model.

The concept was further developed by Binley et al. (2005) and Scott (2006). Scott (2006) recommended a schematical parallel circuit of electrolytic bulk

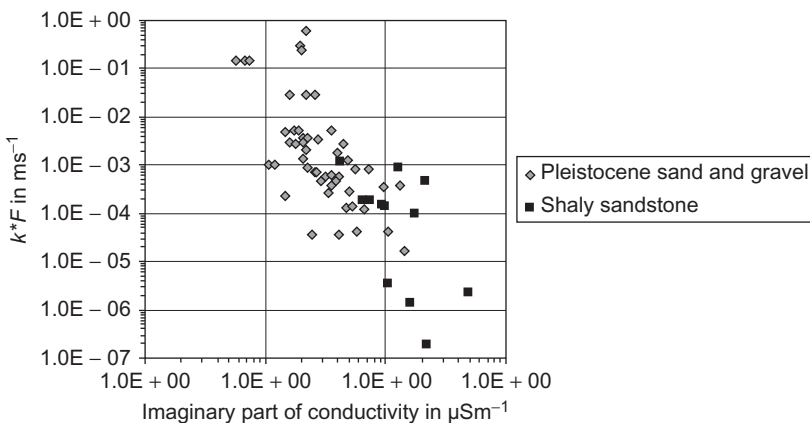


FIGURE 8.34 Product of permeability and formation factor $k \cdot F$ versus imaginary component of conductivity C'' (Börner, 1995). Experimental data for Pleistocene sand/gravel (Germany) and shaly sandstone (different US oil fields; data from Vinegar and Waxman, 1984).

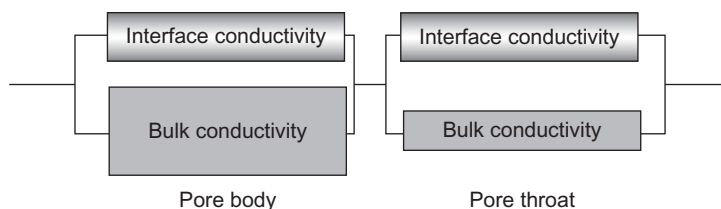


FIGURE 8.35 Model concept for porous rocks with large and narrow pores; in-phase conduction in the bulk pore fluid and complex conduction in parallel along pore surface, modified after Scott (2006).

conductivity and interface conductivity along the electrochemical double layer (Figure 8.35). The difference between the two conductivity components results in the polarization effect:

- The pore-body region has a circuit with a strong bulk conduction.
- The pore-throat region has a similar circuit with a stronger surface conduction (in-phase and quadrature) contribution.

The quadrature component of the conduction from the pore-throat region dominates the overall quadrature conduction for the combined circuit because it is not bypassed by a large in-phase component as in the main pore region.

The theoretical basis for the analysis is the Cole–Cole model. With the model concept, the electrical effect of pore geometry can be characterized by the derived value of relaxation time. Complex electrical measurements show that most of the investigated sandstone samples produce a low-frequency

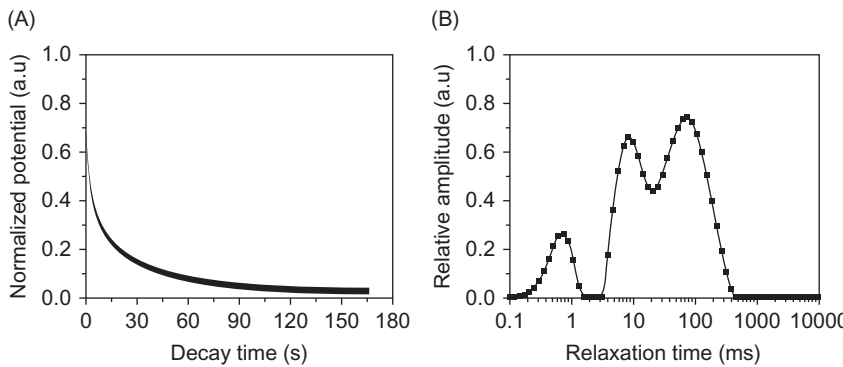


FIGURE 8.36 IP decay curve and relaxation-time spectrum; after Tong et al. (2006).
 (A) normalized decay curve (a.u., arbitrary unit). (B) Relaxation-time spectrum.

phase peak in the range 0.0001–1500 Hz with the tendency that coarse-grained sandstones produce lower-frequency phase peaks than fine-grained sandstones (this phenomenon has also been observed by Lesmes and Morgan, 2001). From the spectral measurements at Permo-Triassic sandstone samples, the quadrature peak relaxation time τ_{peak} was derived and correlated with the dominant pore-throat diameter D_{dominant} (after van Genuchten, 1980):

$$D_{\text{dominant}} = 5.17 \cdot \ln(\tau_{\text{peak}}) + 27.7 \quad R^2 = 0.68 \quad (8.135)$$

where the relaxation time τ_{peak} is in s and D_{dominant} in μm .

Because relaxation time shows a spectrum, it is correlated with the spectrum of pore geometrical properties. On this basis, Tong et al. (2006) used IP measurements on shaly sands for a derivation of capillary pressure curves. Transformation of the normalized decay curve results (comparable NMR processing; see Section 3.5.2) in a relaxation-time spectrum. The relaxation-time spectrum reflects the pore-size distribution but also an information about pore body and pore-throat contributions. **Figure 8.36** shows an example.

8.9 EXAMPLE: SANDSTONE—PART 3

The data for the sandstone example are taken from the textbook “Well Logging and Formation Evaluation” by T. Darling (2005).

In Part 1 (Section 2.8), core data including porosity are discussed; in Part 2 (Section 5.6) porosity is calculated. In this section, Archie’s equation is used for saturation calculation from deep resistivity log (for calculations, visit the website <http://www.elsevierdirect.com/companion.jsp?ISBN=9780444537966> and refer Example-Sandstone. Log Analysis).

Core data deliver the Archie parameters (see also Figures 8.4 and 8.8) $m = 1.96$ and $n = 2.19$. Formation water resistivity is $R_w = 0.03 \text{ ohm m}$.

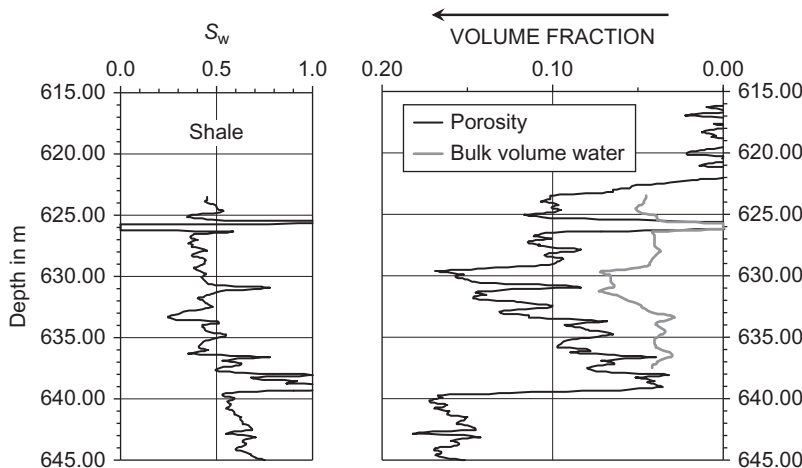


FIGURE 8.37 Water saturation (left) and bulk volume water and porosity (right) calculated from deep resistivity (visit the website <http://www.elsevierdirect.com/companion.jsp?ISBN=9780444537966> and refer Example-Sandstone. Log Analysis).

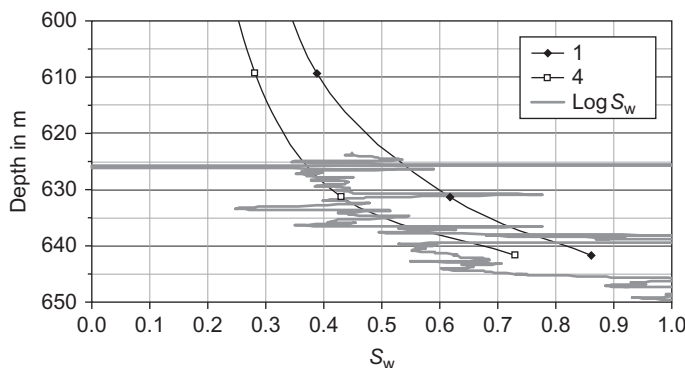


FIGURE 8.38 Comparison of water saturation from log analysis and capillary pressure prediction.

Figure 8.37 shows the calculated water saturation (left) and bulk volume water with porosity (right).

Finally Figure 8.38 shows the comparison of water saturation from log analysis and from capillary pressure prediction (Figure 2.40).

Thermal Properties

9.1 INTRODUCTION

To understand the thermal structure of the earth, knowledge of the thermal properties of the material that constitutes the interior of the earth is indispensable.

Ki-Iti Horai (1971)

Geothermal investigations are related to many questions in geoscience, ranging from studies of the physical state of the earth, tectonics, seismicity, and volcanism to practical problems in mining, drilling, geothermal resources, and geothermal methods used in exploration and environmental geophysics.

Three thermal properties are of fundamental interest in geothermal investigations:

1. specific heat capacity c_p ;
2. thermal conductivity λ ;
3. thermal diffusivity a .

Specific heat capacity characterizes the capability of a material to store heat. Specific heat capacity is given in $\text{J kg}^{-1} \text{K}^{-1} = \text{m}^2 \text{s}^{-2} \text{K}^{-1}$ and is defined as the ratio of the heat input Q to the product of the mass m and the resulting temperature increase ΔT :

$$c_p = \frac{Q}{m \cdot \Delta T} \quad (9.1)$$

where the subscript p indicates specific heat capacity at constant pressure.

Thermal conductivity characterizes the heat flow density q as result of a temperature gradient $\text{grad}T$ (Fourier's law):

$$q = -\lambda \cdot \text{grad} T = -\lambda \cdot \frac{\partial T}{\partial x} \quad (9.2)$$

In general, thermal conductivity is a tensor with the components λ_{ij} and Equation (9.2) is

$$q_i = -\lambda_{ij} \cdot \frac{\partial T}{\partial x_j} \quad (9.3)$$

where ij refers to the directions.

Thermal conductivity λ is given in $\text{W m}^{-1} \text{K}^{-1} = \text{m kg s}^{-3} \text{K}^{-1}$.

Thermal diffusivity a is a measure of penetration of temperature changes into a material; it controls the time-dependent temperature distribution. Diffusivity is connected with specific heat capacity c_p , density ρ , and thermal conductivity λ :

$$a = \frac{\lambda}{c_p \cdot \rho} \quad \text{or in tensorial notation} \quad a_{ij} = \frac{\lambda_{ij}}{c_p \cdot \rho} \quad (9.4)$$

Thermal diffusivity is given in $\text{m}^2 \text{s}^{-1}$.

Table 9.1 gives units and conversions for thermal properties.

Heat transfer is realized by the physical processes of conduction, convection, and radiation. Carslaw and Jaeger (1959) wrote in their classic textbook: “When different parts of a body are at different temperatures, heat flows from the hotter parts to the cooler. There are three distinct methods by which this transference of heat takes place:

1. Conduction, in which the heat passes through the substance of the body itself.
2. Convection, in which heat is transferred by relative motion of portions of the heated body.
3. Radiation, in which heat is transferred direct between distant portions of the body by electromagnetic radiation.” Radiation is usually negligible for processes in the lithosphere.

TABLE 9.1 Units and Conversions for Thermal Properties

Property	SI Unit	cgs Unit	Conversions
λ	$\text{W m}^{-1} \text{K}^{-1}$	$\text{cal cm}^{-1} \text{s}^{-1} \text{C}^{-1}$	$1 \text{ W m}^{-1} \text{K}^{-1} = 2.388 \cdot 10^{-3} \text{ cal cm}^{-1} \text{s}^{-1} \text{C}^{-1}$ $1 \text{ cal cm}^{-1} \text{s}^{-1} \text{C}^{-1} = 418.7 \text{ W m}^{-1} \text{K}^{-1}$
a	$\text{m}^2 \text{s}^{-1}$	$\text{cm}^2 \text{s}^{-1}$	$1 \text{ m}^2 \text{s}^{-1} = 10^4 \text{ cm}^2 \text{s}^{-1}$
c_p	$\text{J kg}^{-1} \text{K}^{-1}$	$\text{cal g}^{-1} \text{C}^{-1}$	$1 \text{ J kg}^{-1} \text{K}^{-1} = 0.2388 \cdot 10^{-3} \text{ cal g}^{-1} \text{C}^{-1}$ $1 \text{ cal g}^{-1} \text{C}^{-1} = 4.187 \text{ kJ kg}^{-1} \text{K}^{-1}$

In some cases, thermal expansion (see [Section 9.3.4](#)) of rocks is also of interest. Thermal expansion behavior is different for the rock-forming minerals; this has significant effects on the structure of rocks and can result in structural damage (Somerton, 1992).

9.2 THERMAL PROPERTIES OF MINERALS AND PORE CONTENTS

9.2.1 Thermal Properties of Minerals

[Table 9.2](#) gives values from various references, mostly from the data collections of Clark (1966), Horai (1971), Horai and Simmons (1969), Melnikov et al. (1975), Cermak and Rybach (1982), Carmichael (1989), Brigaud et al. (1989, 1992), and Clauser and Huenges (1995). Further references are, for example, Dortman (1976), Kobranova (1989), and Somerton (1992).

TABLE 9.2 Thermal Properties of Rock-Forming Minerals

Mineral	λ in $\text{W m}^{-1} \text{K}^{-1}$	c_p in $\text{kJ kg}^{-1} \text{K}^{-1}$
Silica minerals		
Quartz— α	7.69 (CH), 7.69 (CR), 7.7 (B)	0.70 (CR), 0.74 (M)
Quartz—amorphous	1.36 (CH)	
Quartz—mean	6.5 (Ca)	
Ortho—and ring silicates		
Olivine—forsterite	5.03 \pm 0.18 (CH), 6 (M), 5.06 (CR)	0.68 (M),
Olivine—fayalite	3.16(CH), 3 (M), 3.16 (CR)	0.55 (CR), 0.84 (M)
Garnets—almandine	3.31 (CH), 3.3 (M), 3.31 (CR)	
Garnets—grossularite	5.48 \pm 0.21 (CH), 5.48 (CR)	
Zircon	5.54(CH), 5.7(M)	0.61 (CR)
Titanite (sphene)	2.34 (CH), 2.33 (CR)	
Al_2SiO_5 group—andalusite	7.58 (CH), 7.57 (CR)	0.77 (CR)
Al_2SiO_5 group—sillimanite	9.10 (CH), 9.09 (CR)	0.7 (M), 0.74 (CR)
Al_2SiO_5 group—kyanite	14.16 (CH), 14.2 (CR)	0.78 (M), 0.70 (CR)

(Continued)

TABLE 9.2 (Continued)

Mineral	λ in $\text{W m}^{-1} \text{K}^{-1}$	c_p in $\text{kJ kg}^{-1} \text{K}^{-1}$
Epidote	2.83 ± 0.21 (CH), 2.82 (CR)	
Chain silicates		
Pyroxene—enstatite	4.47 ± 0.30 (CH), 4.8 (M), 4.34 (CR)	0.7–0.75 (M), 0.80 (CR)
Pyroxene—diopside, augite	4.66 ± 0.31 (CH), 4.1–5.1(M)	0.67 (M), 0.69 (CR)
Amphibole— hornblende	2.81 ± 0.27 (CH), 2.9–3.0 (M)	0.75 (M)
Sheet silicates		
Mica—muscovite	2.28 ± 0.07 (CH), 2.32 (CR)	0.76 (M)
Mica—biotite	2.02 ± 0.32 (CH), 0.7–1.6 (M)	0.78 (M)
Talc	6.10 ± 0.90 (CH), 6.10 (CR)	0.87 (CR)
Chlorite	5.15 ± 0.77 (CH), 4.2 (M), 5.14 (CR)	0.6 (M)
Serpentine	3.53 ± 1.28 (CH), 1.8–2.9 (M)	0.65
Smectite	1.9 (B)	
Illite	1.9 (B)	
Kaolinite	2.6 (B)	0.93
Mixed—layers	1.9 (B)	
Clay minerals (mean)	2.9 (Q), 1.7 (Ca)	
Framework silicates—feldspar		
Feldspar—mean	2.3 (H), 2.0 (DJ)	
Orthoclase	2.31 (CH), 2.31 (CR), 2.40 (DJ)	0.63–0.75 (M), 0.61 (CR)
Microcline	2.49 ± 0.08 (CH), 2.9 (M), 2.49 (CR)	0.67–0.69 (M), 0.68 (CR)
Albite	2.14 ± 0.19 (CH), 2.31 (CR)	0.71 (CR)
Anorthite	1.69 (CH), 1.68 (CR)	0.71 (CR)
Nepheline	1.73 (CR)	
Oxides		
Magnetite	5.10 (CH), 4.7–5.3 (M), 5.1 (CR)	0.6 (M), 0.60 (CR)
Hematite	11.28 (CH), 11.2–13.9 (M),	0.62 (M), 0.61 (CR)

(Continued)

TABLE 9.2 (Continued)

Mineral	λ	c_p
	in $\text{W m}^{-1} \text{K}^{-1}$	in $\text{kJ kg}^{-1} \text{K}^{-1}$
Ilmenite	2.38 ± 0.18 (CH), 2.2 (M)	0.77 (M)
Spinel	9.48 (CH), 8–13 (M), 9.48 (CR)	0.82 (M)
Rutile	5.12 (CH), 7.0–8.1 (M)	0.74–0.94 (M)
Sulfides		
Pyrite	19.21 (CH), 19.2 (CR)	0.5–0.52 (M), 0.5 (CR)
Pyrrhotite	4.60 (CH)	0.58–0.60 (M)
Galena	2.28 (CH), 2.28 (CR)	0.21 (M), 0.207 (CR)
Sulfates		
Baryte	1.31 (CH), 1.5–1.8 (M), 1.33 (CR)	0.48–0.6 (M), 0.45 (CR)
Anhydrite	4.76 (CH), 4.76 (CR), 5.4 (Ca)	0.55–0.62 (M), 0.52 (CR)
Gypsum	1.26 (CH), 1.0–1.3 (M)	1.07 (M)
Carbonates		
Calcite	3.59 (CH), 3.25–3.9 (M)	0.8–0.83 (M), 0.79 (CR)
Dolomite	5.51 (CH), 5.5 (CR), 5.3 (B)	0.86–0.88 (M), 0.93 (CR)
Aragonite	2.24 (CH), 2.23 (CR)	0.78–0.79 (M), 0.78 (CR)
Magnesite	5.84 (CH), 4.6 (M), 5.83 (CR)	0.88 (M), 0.86 (CR)
Siderite	3.01 (CH), 3.0 (M), 3.0 (B), 3.0 (CR)	0.72–0.76 (M), 0.68 (CR)
Phosphates		
Apatite	1.38 ± 0.01 (CH), 1.4 (M), 1.37 (CR)	0.7 (M)
Halides		
Halite, rocksalt	5.55 ± 0.18 (CH), 5.3–7.2 (D)	0.79–0.84 (M)
Sylvite	6.40 (CH), 6.7–10 (M)	0.55–0.63 (M)
Fluorite	9.51 (CH), 9–10.2 (M), 9.5 (CR)	0.9 (M), 0.85 (CR)
Organic materials	0.25 (Q), 1.0 (B)	

Compiled after data from: B: Brigaud et al. (1989, 1992); C: Clark (1966); Ca: Clauer (2006); Cb: Clauer et al. (2007); CH: Clauer and Huenges (1995); compiled and converted data from Horai (1971); CR: Cermak and Rybach (1982); D: Drury and Jessop (1983); H: Huenges (1989); M: Melnikov et al. (1975); Q: Quiel (1975).

Among the rock-forming minerals, quartz has a high thermal conductivity. Ore minerals and some accessories (rutile, spinel) have extremely high values of thermal conductivity.

Low values are found among the mineral group of mica (biotite), nepheline, and polyhalite. This originates the dependence of thermal conductivity on mineral composition of rocks (see Section 9.3.2).

Griffith et al. (1992) and Rzhevski and Novik (1971) note that there is a difference of the conductivity values between monocrystal, polycrystal, and fused minerals. For quartz in particular, they report a variation between a maximum of $11.7 \text{ W m}^{-1} \text{ K}^{-1}$ (monocrystalline), through $3.6 \text{ W m}^{-1} \text{ K}^{-1}$ (polycrystalline), to $1.39 \text{ W m}^{-1} \text{ K}^{-1}$ (fused). The difference between mono- and polycrystalline results from intergrain contact effects.

The situation in carbonates is comparable: for a model study, Clauser et al. (2007) recommended $2.8 \text{ W m}^{-1} \text{ K}^{-1}$ for calcite and $3.9 \text{ W m}^{-1} \text{ K}^{-1}$ for dolomite, which are distinctly lower as the “crystal” values in [Table 9.2](#).

Thermal conductivity is a temperature-dependent property. The character of this temperature dependence is controlled by the material structure:

- Crystalline solid materials with lattice conductivity are characterized by a decrease of conductivity with temperature based on Debye’s theory.
- Amorphous materials (such as glasses) as well as feldspars are characterized by an increase of thermal conductivity with increasing temperature.

This can be demonstrated by the behavior of quartz (Cermak and Rybach, 1982):

$$\lambda = \frac{1}{0.1450 + 0.578 \cdot 10^{-3} \cdot T} \quad \text{crystalline quartz (0°C to 120°C)} \quad (9.5)$$

$$\lambda = 1.323 + 0.00193 \cdot T - 0.67 \cdot 10^{-5} \cdot T^2 \quad \text{fused quartz (-150°C to 60°C)} \quad (9.6)$$

9.2.2 Thermal Properties of Fluids

[Table 9.3](#) shows thermal properties of some pore fluids. There is a strong difference between the most abundant types—water, oil, and gas.

The table also shows the influence of the temperature upon thermal properties. Kaye and Laby (1968) (see Griffiths et al., 1992) derived the following relationship for thermal conductivity of water:

$$\lambda_{\text{water}} = 0.56 + 0.002 \cdot T - 1.01 \cdot 10^{-5} \cdot T^2 + 6.71 \cdot 10^{-9} \cdot T^3 \quad (9.7)$$

where thermal conductivity λ is in $\text{W m}^{-1} \text{ K}^{-1}$ and temperature T is in $^{\circ}\text{C}$.

The influence of pressure on thermal properties of fluids is relatively small compared with the influence of temperature.

TABLE 9.3 Thermal Properties of Pore Fluids

Medium	T in °C	λ in $\text{W m}^{-1} \text{K}^{-1}$	c_p in $\text{kJ kg}^{-1} \text{K}^{-1}$	a in $\text{m}^2 \text{s}^{-1}$
Air (mean)		0.025		
Gas (mean)		0.027		
Air (dry)	0	0.0243	1.005	$1.87 \cdot 10^{-5}$
	20	0.0257	1.005	$2.12 \cdot 10^{-5}$
	40	0.0271	1.009	$2.49 \cdot 10^{-5}$
	100	0.0314	1.013	$3.38 \cdot 10^{-5}$
Water (mean)		0.50–0.59		
	0	0.5602	4.220	$1.33 \cdot 10^{-7}$
	20	0.5992	4.166	$1.51 \cdot 10^{-7}$
	40	0.6281	4.182	$1.62 \cdot 10^{-7}$
	70	0.6619	4.192	$1.68 \cdot 10^{-7}$
	100	0.6787	4.219	
Oil (mean)	20	0.14–0.15		
Crude oil	20	0.13–0.14	1.88–2.76	
Kerosene	30	0.149		
n-Pentane	20	0.113		
	100	0.081		
Ice	0	2.20	2.040	$1.18 \cdot 10^{-6}$
	-10	2.32	1.997	
	-20	2.43	1.946	
	-40	2.66	1.817	
Snow, dense		0.46		

After data from Woodside and Messmer (1961), Clark (1966), Kappelmeyer and Haenel (1974), Ebert (1976), Gearhart Industries (1978), Kobranova (1989), Baker Atlas (1992), and Schön (1996).

9.3 THERMAL PROPERTIES OF ROCKS—EXPERIMENTAL DATA

9.3.1 Overview

Extensive collections of thermal rock data are compiled, for example, by Clark (1966), Cermak and Rybach (1982), and Clauser and Huenges (1995).

As for other physical rock properties, it is important to note that there is a great variability for the individual rock types. This is attributed to the

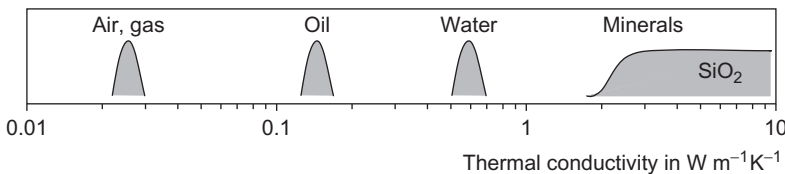


FIGURE 9.1 Schematic picture of thermal conductivity distribution of fluids and rock-forming minerals.

heterogeneity, the diversity in mineral content and rock texture, and fluid content. Clauser and Huenges (1995) made statistical studies for specific rock groups. For a detailed geothermal study, the investigation of local samples is necessary.

A look at the mean values of the thermal conductivity for fluids and minerals (Figure 9.1) shows:

- A distinct difference between thermal conductivity of matrix materials (minerals) and pore-filling materials. Therefore, a decrease of thermal conductivity with increasing porosity and fracturing can be expected.
- A difference between the properties of the individual pore-filling materials. Therefore, a higher thermal conductivity for water-saturated rocks and a lower conductivity for gas-bearing or dry porous rocks can be expected.

Among the rock-forming minerals, the quartz shows a high conductivity (Table 9.2). Therefore, for igneous rocks, high values for felsic or acid and lower values for mafic or basic types are expected. In sedimentary rocks, sandstone has higher conductivity compared with carbonates at comparable porosity as a result of quartz content.

Specific heat capacity of rocks is determined by the rock composition and follows the equation:

$$c_{p,rock} = \sum_i V_i \cdot c_{p,i} \quad (9.8)$$

where $c_{p,i}$ is the specific heat capacity of rock component i and V_i is the corresponding volume fraction.

Specific heat capacity of sedimentary rocks show some higher values than igneous rocks. This is mainly caused by the contribution of pore water with its relatively high specific heat capacity of $\approx 4 \text{ kJ kg}^{-1} \text{ K}^{-1}$.

Vosteen and Schellschmidt (2003) compiled thermal properties of magmatic, metamorphic, and sedimentary rocks of the Eastern Alpine crust. Figure 9.2 shows mean values and ranges of variation of specific heat capacity as a function of temperature.

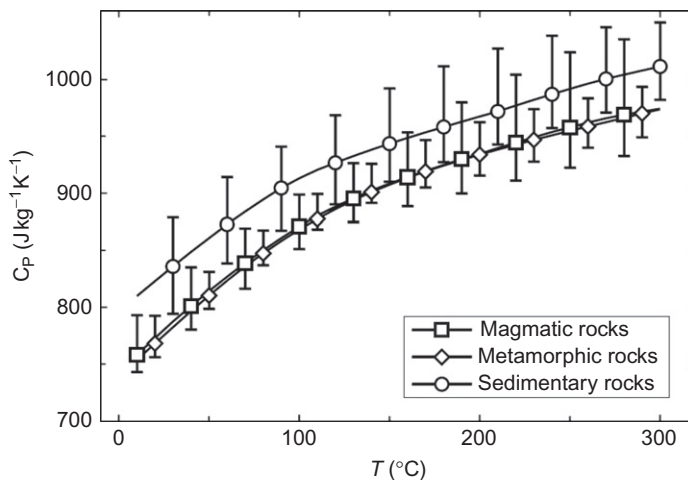


FIGURE 9.2 Mean values and ranges of variation of specific heat capacity as function of temperature (Vosteen and Schellschmidt, 2003).

9.3.2 Magmatic and Metamorphic Rocks

Thermal properties of these two rock groups are controlled mainly by mineral composition and the influence of fractures. Alignment of mineral axes and fractures can create anisotropy; this is characteristic for metamorphic rocks like gneisses (Figure 9.5). Table 9.4 shows a compilation of some data from the literature.

Data confirm the general tendency of an increase of thermal conductivity with increasing quartz content. Roy et al. (1981) derived a correlation between thermal conductivity and quartz content of 100 granite and quartz monzonite samples:

$$\lambda = 2.59 + 2.45 \cdot V_{\text{quartz}} \quad (9.9)$$

where λ is in $\text{W m}^{-1} \text{K}^{-1}$ and V_{quartz} is the volume fraction of quartz.

For most rock types, thermal conductivity decreases with increasing temperature (resulting from the dominant crystalline behavior). This explains the character of some empirical relations. Clauser and Huenges (1995) and Zoth and Hänel (1988) recommend an equation:

$$\lambda(T) = A + \frac{B}{350 + T} \quad (9.10)$$

where $\lambda(T)$ is the thermal conductivity in $\text{W m}^{-1} \text{K}^{-1}$, T is the temperature in $^{\circ}\text{C}$, and the empirical parameters A, B are given in Table 9.5.

TABLE 9.4 Thermal Properties of Igneous and Metamorphic Rocks

Rock	λ in $\text{W m}^{-1} \text{K}^{-1}$			c_p in $\text{kJ kg}^{-1} \text{K}^{-1}$			Reference
	Mean	Range	n	Mean	Range	n	
Granite	3.05	1.25–4.45	356	0.96	0.67–1.55	102	C
	3.43	2.3–3.6	153				J
Granodiorite	2.65	1.35–3.40	89	1.09	0.84–1.26	11	C
	2.63	2.00–3.50	194				J
Syenite	2.31	1.35–5.20	50				C
Diorite	2.91	1.72–4.14	50	1.14	1.13–1.17	3	C
	2.50	2.02–3.33	31				J
Gabbro	2.63	1.62–4.05	71	1.01	0.88–1.13	9	C
	2.57	1.98–3.58	64				
Peridotite		3.78–4.85			0.92–1.09		C
Diabase	2.64	1.55–4.30	115	0.91	0.75–1.00	22	C
Basalte	1.95	1.40–5.33	64	0.88	0.88–0.89	3	C
	1.69	1.12–2.38	72				
Lava	2.50	0.20–4.60	85	1.08	0.67–1.38	5	C
Quarzite	5.26	3.10–7.60	186	1.01	0.71–1.34	8	C
	5.03	2.33–7.45	145				J
Amphibolite	2.46	1.35–3.90	78				C
Gneiss a \perp	1.74	1.2–2.6	55	0.75	0.46–0.92	55	C
Gneiss a \parallel	2.12	1.2–3.1	55				C
Gneiss b \perp	2.65	1.9–3.2	22				
Gneiss b \parallel	3.73	2.5–4.8	8				
Schist \perp	2.91	1.4–3.9	122	0.80	0.67–1.05	18	C
Schist \parallel	3.80	2.2–5.2	122				
Marble	2.56	1.59–4.00	26	0.86	0.75–0.88	8	C

n: number of samples. Reference key: C, Cermak and Rybach (1982) (value ranges and mean values mostly taken from Figure 1 of the paper of Jessop (1990) (data after Roy et al., 1981).

\perp —perpendicular schistosity; \parallel —parallel schistosity.

TABLE 9.5 Empirical Parameters of Equation (9.10)

Rock Type	T in °C	A	B
Acid rocks	0–500	0.64	807
Basic rocks	50–1100	1.18	474
Metamorphic rocks	0–1200	0.75	705
Limestone	0–500	0.13	1073
Mean	0–800	0.70	770

After Clauser and Huenges (1995).

Seipold (2001) gives the following empirical equations for thermal rock conductivity λ as function of temperature T (in K) for magmatic rock types:

$$\text{Granite } \lambda = (0.156 + 5.45 \cdot 10^{-4} \cdot T)^{-1} + 0.763 \cdot 10^{-9} \cdot T^3 \quad (9.11)$$

$$\text{Gneiss } \lambda = (0.191 + 5.25 \cdot 10^{-4} \cdot T)^{-1} + 0.670 \cdot 10^{-9} \cdot T^3 \quad (9.12)$$

$$\text{Amphibolite } \lambda = (0.315 + 3.04 \cdot 10^{-4} \cdot T)^{-1} + 0.326 \cdot 10^{-9} \cdot T^3 \quad (9.13)$$

$$\text{Peridotite } \lambda = T(-42.9 + 0.389 \cdot T)^{-1} + 0.072 \cdot 10^{-9} \cdot T^3 \quad (9.14)$$

In fractured or cracked rocks, thermal conductivity is additionally influenced by the properties of crack filling materials, by fracture porosity, geometry, and distribution.

Fracturing results in pronounced pressure dependence. With increasing pressure, thermal conductivity increases nonlinearly due to closure of cracks, fractures, etc., and the improvement of the contact conditions (at grain–grain and crack boundaries). Figure 9.3 illustrates this nonlinearity of a gneiss sample from the KTB borehole (Continental Deep Drilling Program/Germany). The temperature dependence is also plotted. In comparison with gneiss, the more compact amphibolite sample obviously does not show the typical crack-conditioned behavior at lower pressures.

Among the igneous rocks, volcanicite can have a remarkable porosity. Increasing porosity also decreases thermal conductivity in these rocks. An example is given in Figure 9.4.

Metamorphic rocks—particularly gneisses and schists—frequently show a distinct difference between the thermal conductivity measured parallel and perpendicular schistosity. In addition to the data in Table 9.4, Table 9.6 and Figure 9.5 give some more detailed information.

Figure 9.5 shows the directional dependence of thermal conductivity measured at a gneiss sample. The higher horizontal conductivity results from the dominant contribution of the quartz layers (white bands). A more detailed

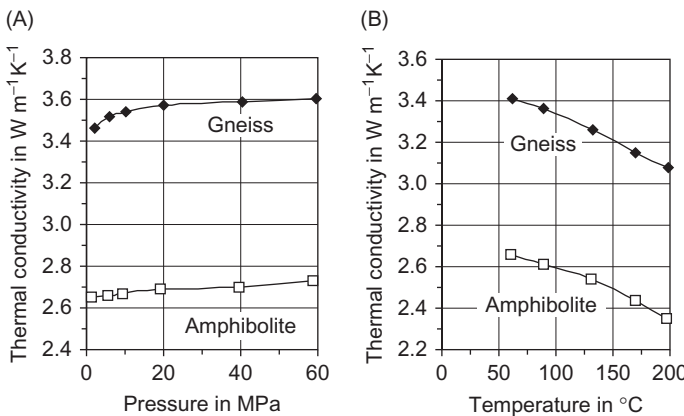


FIGURE 9.3 Thermal conductivity of samples from the KTB borehole; Samples are gneiss from a depth of 1793 m, amphibolite from a depth of 147 m. (A) Conductivity as a function of uniaxial pressure, measured at $T = 54^\circ\text{C}$. (B) Conductivity as a function of temperature, measured at $p = 10 \text{ MPa}$. data from Huenges et al. (1990)

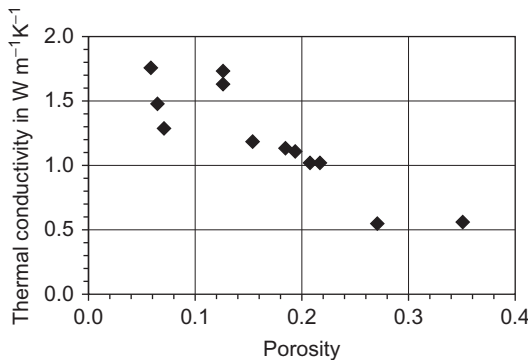


FIGURE 9.4 Thermal conductivity as a function of porosity (dry basalt from Styria/Austria).

investigation of all directions shows that this rock has not only a simple transverse isotropy, but shows also differences in the horizontal directions. Gegenhuber and Schön (2010) have—based on measured data—developed modified models to explain the three-axis anisotropy.

9.3.3 Sedimentary Rocks

9.3.3.1 Overview

Sedimentary rocks are characterized by a broad scatter of thermal properties within a single lithological type. This is originated mainly by the complex influence of mineral composition, texture and grain cementation, porosity, and pore fluids (Table 9.7).

TABLE 9.6 Anisotropy of Thermal Conductivity for Some Metamorphic Rocks

Rock/Location	λ_{\parallel} in $\text{W m}^{-1} \text{K}^{-1}$	λ_{\perp} in $\text{W m}^{-1} \text{K}^{-1}$	$\lambda_{\parallel}/\lambda_{\perp}$	Reference
Gneiss				
Styria/Austria	5.00	3.95	1.25	G
Switzerland, alpine rocks	2.12	1.74	1.22	W
Switzerland, Simplon tunnel	3.73	2.65	1.40	C
Chester, Vermont/USA	3.49	2.61	1.34	C
Schist				
Switzerland, alpine rocks	2.88	2.05	1.40	W
Scotland	3.84	2.86	1.34	R

Reference key: R, Richardson et al. (1976) cited by Cermak and Rybach (1982); C, Clark (1966); W, Wenk and Wenk (1969); G, Gegenhuber and Schön (2010).

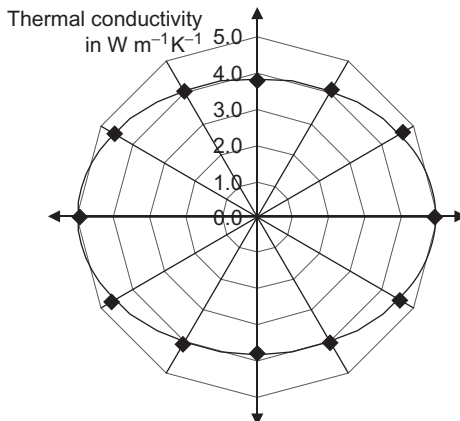
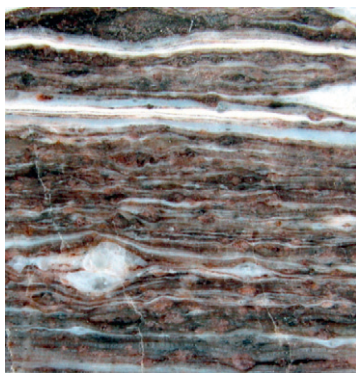


FIGURE 9.5 Anisotropy of thermal conductivity of a gneiss (Stainzer Plattengneis/Austria), originated mainly by the texture of the thin quartz layers (white in the figure); (Gegenhuber and Schön, 2010)

Only pore-free sediments show a relatively small variation, because they do not have the strong influence of porosity and pore fluid, but only some variation of chemical composition and impurities. Typical for this group are salts. **Table 9.8** gives some examples. For Thuringia Rock salt, the anhydrite component increases the mean thermal conductivity.

TABLE 9.7 Thermal Properties of Some Sedimentary Rocks

Rock	λ in $\text{W m}^{-1} \text{K}^{-1}$			c_p in $\text{kJ kg}^{-1} \text{K}^{-1}$			Reference
	Mean	Range	n	Mean	Range	n	
Anhydrite	4.00	1.00–6.05	77	0.88	0.81–0.94	77	CR
	5.43	4.89–5.73					J
		4.90–5.80					B
Dolomite	3.62	1.60–5.50	29	1.00	0.84–1.55	21	CR
	4.68	3.43–5.73	8				J
		3.75–6.30					B
	4.38	3.11–5.01					
Limestone	2.29	0.62–4.40	487	0.93	0.82–1.72	38	CR
	3.44	1.30–6.26	445				J
		1.70–3.30					RM
		2.50–3.10					B
	2.97	2.00–4.41	26				G
		3.01–3.35					
Gypsum	1.29						C
Sandstone	2.47	0.90–6.50	1262	1.64	0.75–3.33	41	CR
	3.72	1.88–4.98	11				J
		1.20–4.20					RM
		2.50–4.20					B
	2.57	1.56–3.86	8				G
					0.82–1.00		F
Berea sandstone) ^a	2.34						F
Bandera sandstone) ^a	1.70						F
Boise sandstone) ^a	1.47						
Graywacke		2.70–3.35					B
Shale	2.07	0.55–4.25	377	1.18	0.88–1.44	17	CR
		0.8–2.1					RM
		0.80–1.25					B
Pierre shale) ^b		1.30–1.70					F

(Continued)

TABLE 9.7 (Continued)

Rock	λ in $\text{W m}^{-1} \text{K}^{-1}$			c_p in $\text{kJ kg}^{-1} \text{K}^{-1}$			Reference
	Mean	Range	n	Mean	Range	n	
Mancos shale) ^b	1.50–2.25						F
Queenston shale) ^b	1.74–1.95						F
Claystone/Siltstone	1.05–1.45						B
Claystone	2.04	0.60–4.00	242				48 CR
Siltstone	2.68	2.47–2.84	3				J
	2.67	2.56–2.78	1				G
Marl	2.21	0.50–4.00	191	1.15	0.78–3.10		CR
Sand	1.44	0.10–2.75	24	2.30	1.97–3.18	8	CR
Sand, tertiary	1.8–2.2						S
Clay	1.53	0.60–2.60		0.85	0.84–1.00	24	CR
Ocean sediments	0.95	0.40–1.70	648				CR
Soil	0.60–0.83						S
Loess	1.6–2.1						S
Peat	0.29	0.60–0.80					S
Coal	0.04–1.50						CR
Coal	<0.5						B

^aDry at 20 °C.^bWater saturated, 35–80 °C, 1–24 MPa, n, number of samples. Reference key: C, Clarke (1966), J, Jessop (1990); S, Schuch (1980); RM, Rybach and Muffler (1981); CR, Cermak and Rybach (1982); B, Blackwell and Steele (1989); G, Gong (2005); F, Fjaer et al. (2008).

9.3.3.2 Influence of Porosity and Pore Fluid

In porous sedimentary rocks, “porosity and moisture content affect the thermal conductivity of rocks to a degree, which can be dominant” (Kappelmeyer and Haenel, 1974). Thermal behavior is strongly influenced by the distinct difference of thermal properties between the solid matrix material (minerals) and the various pore-filling materials.

Fundamental dependencies can be understood by examining Figure 9.1. Generally, thermal conductivity increases with:

- decreasing porosity;
- increasing thermal conductivity of pore content from gas to oil to water (compare curves in Figure 9.6);

TABLE 9.8 Thermal Properties of Some Salts

Rock	λ in $\text{W m}^{-1} \text{K}^{-1}$	Reference
Rock salt, New Mexico, Oklahoma	5.34	C
Rock Salt, Thuringia/Germany		M
Röt-Steinsalz	2.74	
Leine-Steinsalz	2.92	
Staßfurt-Steinsalz (anhydritic)	3.06	
Werra-Steinsalz (anhydritic)	3.22	
Polyhalite, Carlsbad N. Mexico	1.55	C
Polyhalite, Russia	1.55	D

Reference key: C, Clark (1966); D, Dortman (1976); M, Meinke et al. (1967).

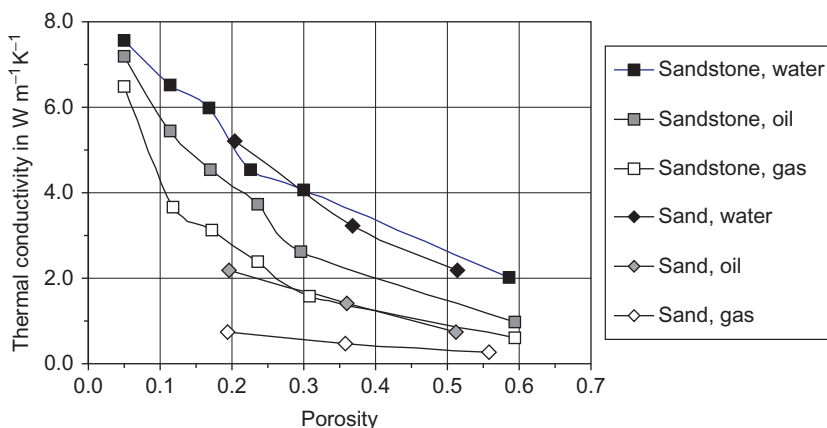


FIGURE 9.6 Thermal conductivity versus porosity for sand and sandstone at different pore fluids. (data taken from Woodside and Messmer, 1961)

- increasing water content;
- increasing thermal conductivity of the solid mineral substance (particularly quartz);
- improvement of grain–grain contact or cementation.

The correlation between porosity and thermal conductivity has been experimentally investigated by several authors. The general tendency as well as the influence of pore-filling material and cementation is seen in the results of Woodside and Messmer (1961) in Figure 9.6 and Table 9.9. The separation between the values for pore-filling materials (air, oil, and water) is

TABLE 9.9 Thermal Conductivity of Various Sandstone Types with Different Pore Fluids

Rock Type	Porosity	Thermal Conductivity in W mK^{-1}			
		Vacuo 0 W mK^{-1}	Air 0.026 W mK^{-1}	<i>n</i> -heptane 0.128 W mK^{-1}	Water 0.628 W mK^{-1}
Berkeley sandstone	0.03	2.906	6.490	7.118	7.411
St. Peter sandstone	0.11	2.495	3.559	5.347	6.364
Tensleep sandstone	0.16	2.621	3.040	4.375	5.866
Berea sandstone	0.22	1.683	2.391	3.739	4.480
Teapot sandstone	0.29	1.093	1.545	2.655	4.049
Tripolite	0.59	0.222	0.528	0.879	2.035

Data after Woodside and Messmer (1961).

clearly visible for unconsolidated sand, whereas for the cemented sandstone, the values are somewhat closer. This is a result of the dominant part of heat transfer via the cemented matrix skeleton.

Rhzewski and Novik (1971) and Griffith et al. (1992) discussed the effect of grain size on thermal conductivity. Decreasing grain size increases the number of grain contacts per unit volume. Decreasing thermal conductivity

- from monocrystalline quartz a reduction of 27% to grain size of 0.10 mm;
- from monocrystalline quartz a reduction of 50% to grain size of 0.05 mm.

was observed.

For granular material, detailed experimental investigations with synthetic quartz sand samples confirm the decrease of thermal conductivity with decreasing grain size (Midtommé and Roaldset, 1998).

Grain–grain contact and cementation control very strong thermal conductivity because the dominant thermal conductor is the rock skeleton. Mann et al. (1977) published thermal properties of typical cements (Table 9.10).

An example for thermal conductivity of carbonate rocks is given in Figure 9.7. The two plots demonstrate also for carbonates:

1. The decrease of thermal conductivity with increasing porosity or decreasing density

2. The higher thermal conductivity for water-saturated rocks compared with dry rocks.

In the two plots of thermal conductivity show only for the lowest density value ($2,521 \text{ kg m}^{-3}$) or highest porosity (0.11) a position of the λ -value outside the general tendency—this is a hint that there likely exists a different mineral composition of this particular sample.

TABLE 9.10 Selected Typical Thermal Properties of Cement

Cement Type	Density in kg m^{-3}	Thermal Conductivity in $\text{W m}^{-1} \text{K}^{-1}$		Specific Heat Capacity in $\text{kJ kg}^{-1} \text{K}^{-1}$	
		At 20°C	At 100°C	At 20°C	At 100°C
Silica cement	2650	7.70	6.00	0.177	0.212
Calcite cement	2721	3.30	2.70	0.199	0.232
Dolomite cem.	2857	5.30	4.05	0.204	0.238
Anhydrite cem.	2978	6.30	4.90	0.175	0.193
Halite cement	2150	5.70	4.85	0.206	0.214
Clay cement	2810	1.80	1.60	0.200	0.220

Mann *et al.* (1977).

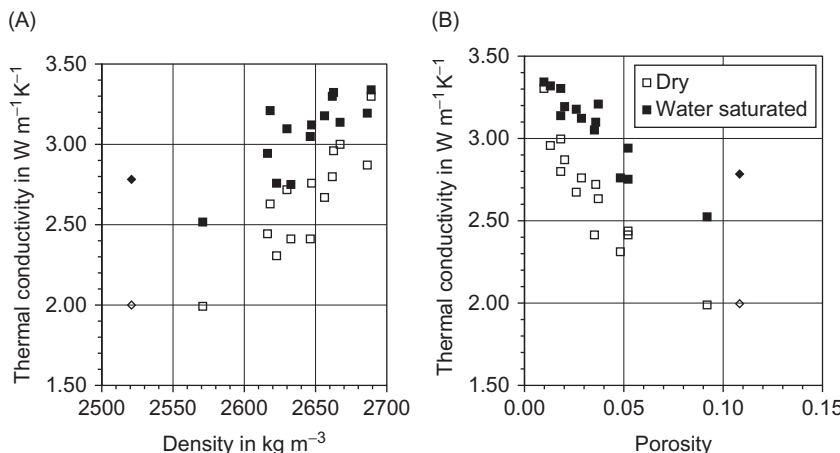


FIGURE 9.7 Analysis of a data set for dry and water-saturated Silurian limestone samples (Gotland) from Poulsen *et al.* (1982). (A) Thermal conductivity versus density. (B) Thermal conductivity versus porosity.

The correlation between thermal conductivity and porosity or thermal conductivity and density, respectively, leads to empirical relationships

$$\lambda = a_1 + b_1 \cdot \rho \quad (9.15)$$

$$\lambda = a_2 - b_2 \cdot \phi \quad (9.16)$$

Analysis of the data from Poulsen et al. (1982) (Figure 9.7), except the value for $\rho = 2,520 \text{ kg m}^{-3}$ and $\phi = 0.11$, results in the regressions:

for dry rock:

$$\lambda = -22.043 + 0.0093 \cdot \rho \quad \text{with} \quad R^2 = 0.77 \quad (9.17)$$

$$\lambda = 3.153 - 14.15 \cdot \phi \quad \text{with} \quad R^2 = 0.84 \quad (9.18)$$

for water-saturated rock:

$$\lambda = -13.343 + 0.0062 \cdot \rho \quad \text{with} \quad R^2 = 0.64 \quad (9.19)$$

$$\lambda = 3.430 - 10.48 \cdot \phi \quad \text{with} \quad R^2 = 0.87 \quad (9.20)$$

Plewa (1976) derived the following regression for Jurassic carbonates from Poland (water saturated):

$$\lambda = 4.12 - 9.82 \cdot \phi \quad (9.21)$$

Hartmann et al. (2005) analyzed core measurements from a well in the German Molasse Basin. Linear regression of experimental data results in the parameters in Table 9.11.

TABLE 9.11 Parameters of Equations (9.15) and (9.16) for Rocks from the German Molasse Basin

Lithology	a_1	b_1	a_2	b_2
All samples, dry	2.715 ± 0.086	-4.167 ± 0.183	2.926 ± 0.103	6.289 ± 0.570
All samples, saturated	2.214 ± 0.192	-2.151 ± 0.452	3.701 ± 0.083	3.304 ± 0.394
Sandy, dry	2.500 ± 0.123	-3.740 ± 0.250	2.818 ± 0.178	5.783 ± 0.898
Sandy, saturated	2.074 ± 0.263	-1.713 ± 0.618	3.828 ± 0.106	3.229 ± 0.541
Carbonate, dry	2.942 ± 0.179	-4.645 ± 0.412	2.939 ± 0.097	6.490 ± 0.489
Carbonate, saturated	1.696 ± 0.230	-1.112 ± 0.540	3.289 ± 0.101	2.352 ± 0.451

Hartmann et al. (2005); thermal conductivity is in $\text{W m}^{-1} \text{K}^{-1}$, porosity as fraction and bulk density in g cm^{-3} .

Based on model equations, Balling et al. (1981) and Lovell (1985) (see Griffith et al., 1992) derived nonlinear equations for the thermal conductivity–porosity correlation:

$$\text{clay, claystone, shale} \quad \lambda = 0.46^\phi \cdot 3.43^{(1-\phi)} \quad (9.22)$$

$$\text{sandstone} \quad \lambda = 0.69^\phi \cdot 4.88^{(1-\phi)} \quad (9.23)$$

$$\text{quartz sand} \quad \lambda = 0.64^\phi \cdot 8.58^{(1-\phi)} \quad (9.24)$$

$$\text{carbonates} \quad \lambda = 0.54^\phi \cdot 3.24^{(1-\phi)} \quad (9.25)$$

where the porosity is a fraction and the thermal conductivity is in $\text{W m}^{-1} \text{K}^{-1}$.

Figure 9.8 shows calculated dependences of thermal conductivity on porosity for the different lithologies.

Especially for clay and claystone, an opposite tendency was also observed. Waples and Tirsgaard (2002) wrote: “Vertical matrix, thermal conductivities of clays, and claystones in onshore Denmark decrease with decreasing porosity, probably because of increasing orientation of highly anisotropic clay platelets during compaction. The relationship between vertical matrix conductivity λ_{vm} and porosity for this data set can be expressed as either:

$$\lambda_{\text{vm}} = 2.544 \cdot \exp(0.943 \cdot \phi) \quad \text{or} \quad \lambda_{\text{vm}} = 2.749 \cdot \exp(0.637 \cdot \phi) \quad (9.26)$$

depending upon the statistical methods used to analyze the data. Using the first equation, the vertical matrix conductivity of the Danish clays and

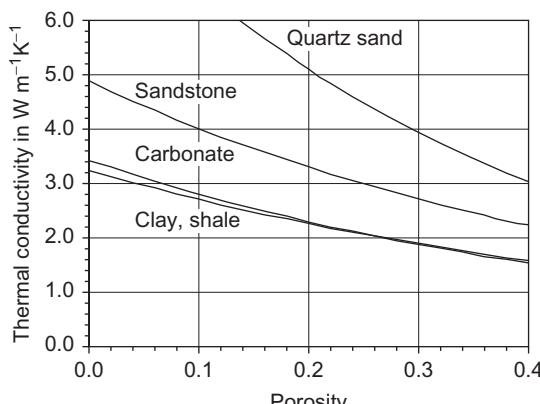


FIGURE 9.8 Thermal conductivity as a function of porosity calculated with the equations for different lithologies. after Griffith et al. (1992)

claystones is found to be about $4.9 \text{ W m}^{-1} \text{ K}^{-1}$ in highly porous sediments, decreasing to $2.54 \text{ W m}^{-1} \text{ K}^{-1}$ when porosity reaches zero. Using the second equation, the vertical matrix conductivity of the Danish clays and claystones is about $4.3 \text{ W m}^{-1} \text{ K}^{-1}$ in highly porous sediments, decreasing to about $2.75 \text{ W m}^{-1} \text{ K}^{-1}$ at zero porosity. Anisotropy varies from an assumed value of 1.02 in highly porous clays to 2.44 at zero porosity using the first equation, and 1.87 at zero porosity using the second equation. These values agree well with measured data. This phenomenon is probably common or universal in fine-grained clay-rich sediments . . . Other specific relationships will probably exist for clay-rich shales and more-pure claystones.”

For soil, specific studies demonstrate the influence of soil density, moisture content, and soil type (Abu-Hamdeh and Reeder, 2000; Clark Jr., 1966; Quiel, 1975; Schuch, 1980). Thermal conductivity of soil is essentially influenced by density, water content (moisture), and composition (particularly organic content). Schuch (1980) may be cited for the general behavior of soils: “The thermal conductivity of dry soils is small ($0.2\text{--}0.8 \text{ W m}^{-1} \text{ K}^{-1}$), reaches a maximum by 20–30 wt% of water content (2 or $3 \text{ W m}^{-1} \text{ K}^{-1}$), decreases for higher contents of water, for example, wet bog, and draws near the value of thermal conductivity of water ($0.6 \text{ W m}^{-1} \text{ K}^{-1}$). This decrease is originated by an increasing porosity in that range and a connected decrease of the heat transfer by the skeleton of the solid parts of the soil.” [Table 9.12](#) shows some data for Central European soils.

A more detailed insight is given by [Figure 9.9](#). The figure demonstrates that thermal conductivity:

- increases with density and with moisture content;
- decreases from sand to loam and clay;
- decreases with organic matter content.

TABLE 9.12 Thermal Conductivity of Some Central European Soils

Soil	Thermal Conductivity in $\text{W m}^{-1} \text{ K}^{-1}$
Raised-bog-peat	0.6–0.7
Low-bog-peat	0.7–0.8
Alluvium loam	1.0–2.5
Loess clay	1.6–2.1
Tertiary sand	1.8–2.2
Horticultural soil	3.3

After Cermak and Rybach (1982).

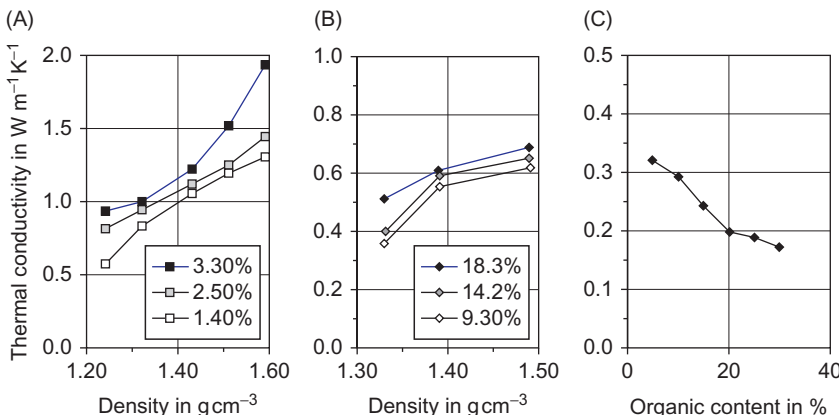


FIGURE 9.9 Thermal conductivity of soil . (A) Thermal conductivity as a function of density at three moisture contents in % (sand). (B) Thermal conductivity as a function of density at three moisture contents in % (clay, loam). (C) Thermal conductivity of clay loam as a function of organic matter content in %. (data after Abu-Hamdeh and Reeder, 2000)

9.3.3.3 Influence of Pressure and Temperature

Increasing effective pressure yields an increasing thermal conductivity in sedimentary rocks primarily due to:

- improved heat transport at grain–grain contacts;
- improved heat transport at closing cracks, microcracks or other defects;
- decrease of porosity.

Therefore, pressure-conditioned variations of the thermal conductivity are more evident in compressible rocks (unconsolidated sediments, consolidated sediments with high porosity) rather than in rocks with zero or low compressibility (dense carbonates, anhydrite). The direct dependence of thermal conductivity on the deformation behavior explains the phenomena of nonlinearity and partial irreversibility (“hysteresis”) of the thermal conductivity versus pressure curve.

A log–log presentation of thermal conductivity versus pressure (Figure 9.10A) frequently results in a linear correlation as a first approximation. This corresponds to a power law of the form

$$\lambda = \lambda_0 \left(\frac{p}{p_0} \right)^m \quad (9.27)$$

where the exponent m is empirical and p_0 is a reference pressure (Schön, 1996).

Figure 9.10B shows examples for temperature dependence of thermal conductivity with a general decrease. For temperature dependence of thermal

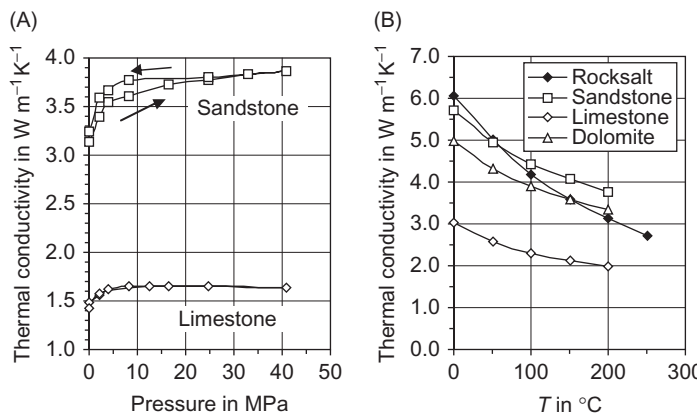


FIGURE 9.10 Thermal conductivity as a function of pressure and temperature (sedimentary rocks). (A) Thermal conductivity versus uniaxial pressure. (B) Thermal conductivity versus temperature. (A) Data from Hurtig and Brugger (1970) and (B) data after Birch and Clarke (1940)

conductivity for sedimentary rocks, empirical equations are derived, for example¹:

$$\text{Zoth and Haenel (1988)} \quad \lambda(T) = A + \frac{B}{350 + T} \quad (9.28)$$

$$\text{Sass et al. (1992)} \quad \lambda(T) = \frac{\lambda_0}{a_1 + T(a_2 - a_3/\lambda_0)} \quad (9.29)$$

where A, B and a_1, a_2, a_3 are empirical constants, T is temperature in $^{\circ}\text{C}$, λ_0 is thermal conductivity at 25°C .

Clauser and Koch (2006) and Clauser et al. (2007) applied the Sass equation and found a good fit for Tertiary sediments (Molasse/Germany) and derived the following empirical constants:

$$a_1 = 0.960 \text{ with a standard deviation} = 0.011$$

$$a_2 = 0.007 \text{ with a standard deviation} = 0.001$$

$$a_3 = 0.014 \text{ with a standard deviation} = 0.003.$$

9.3.4 Some Notes About Thermal Expansion

Thermal expansion describes the linear or volume change of a material as a result of increasing temperature. Thermal expansion of minerals and rocks in general is relatively small, but differences of thermal expansion can result in structural changes or structural damage upon heating (Somerton, 1992). Table 9.13 gives some data for selected and rocks.

¹See eq. 9.10 and Table 9.5.

TABLE 9.13 Linear Thermal Expansion Coefficient in K^{-1} of Some Rock-Forming Minerals Relative to Crystallographic Axes

Mineral	Axis	Expansion Coefficient in K^{-1}	Rock	Expansion Coefficient in K^{-1}
Quartz	$\perp c$	$16 \cdot 10^{-6}$	Berea sandstone	$13 \cdot 10^{-6}$
	$\parallel c$	$10 \cdot 10^{-6}$		
Plagioclase	$\parallel a$	$13 \cdot 10^{-6}$	Bandera sandstone	$20 \cdot 10^{-6}$
	$\perp 010$	$3 \cdot 10^{-6}$		
Calcite	$\perp c$	$29 \cdot 10^{-6}$	Boise sandstone	$17 \cdot 10^{-6}$
	$\parallel c$	$-6 \cdot 10^{-6}$		
Hornblende	$\perp 100$	$7 \cdot 10^{-6}$	Mancos shale Queenston shale	$(13-20) \cdot 10^{-6}$
	$\parallel b$	$11 \cdot 10^{-6}$		$(11-13) \cdot 10^{-6}$
	$\parallel c$	$8 \cdot 10^{-6}$		

Calculated using data from Somerton (1992), Clark (1966) and rocks (Fjaer et al., 2009). Temperature range 100–200°C.

9.4 THEORIES AND MODELS

Several mathematical models have been proposed to predict the conductivity of a rock from a knowledge of its constituents. All depend on a knowledge of conductivity of the minerals, and so all begin with the same disadvantage. Each one employs a different mathematical formulation to account for the distribution of the conductivities within the mineral matrix.

Jessop (1990)

9.4.1 Introduction

Theories and models for rocks as composed materials are directed on specific heat capacity and thermal conductivity. Thermal diffusivity can be derived using Equation (9.4).

Specific heat capacity as a scalar property can be described by a simple averaging relationship

$$c_p = \sum_{i=1}^n V_i \cdot c_{p,i} \quad (9.30)$$

where V_i is the volume fraction of component i and $c_{p,i}$ is the specific heat capacity of component i . The relationship is valid for rocks consisting of n components (minerals, pore fluids).

Thermal conductivity as a tensor depends not only on the volume fraction and thermal conductivity of rock components, but also on their distribution,

TABLE 9.14 Overview to Some Model Concepts for Thermal Conductivity

Bound Models	Inclusion Models (Spherical and Nonspherical Inclusions)	
Layer model: Voigt (1910) and Reuss (1929) bounds	Random orientation	Aligned orientation
Hashin–Shtrikman (1962) bounds	Clausius–Mossotti model: Berryman (1995)	Berryman (1995)
Modifications: Krischer and Esdorn (1956), Lichtenegger and Rother generalization (1931)	Describes fractured and (low) porous rocks, implements inclusion shape (aspect ratio) and orientation: random orientation (isotropic) or aligned orientation (anisotropic)	

on geometry and internal structure, and on the heat transfer conditions at the contacts between them. This complex feature makes the problem of a theoretical treatment more difficult. **Table 9.14** shows an overview to some model concepts for thermal conductivity.

The following sections present an overview of two groups of models related to thermal conductivity:

1. Layer or laminated models, their modifications and comparable mixing rules
2. Inclusion models.

For forward calculation, the model equations are given in excel sheets on the website <http://www.elsevierdirect.com/companion.jsp?ISBN=9780444537966> (files Thermal).

9.4.2 Layer Models—Series and Parallel

A rock consisting of n components can be idealized in the simplest case as a layer model following Voigt's and Reuss's concept (see Section 6.7). Layers represent the individual rock components. The relative thickness of each layer is given by the volume fraction of the rock component (see **Figure 9.11**).

This results in a “parallel model” (heat flow parallel to boundary between components) and a “series model” (heat flow perpendicular to boundary between components). The equations for the general case of n components are

$$\text{parallel model} \quad \lambda_{\parallel} = \sum_{i=1}^n V_i \cdot \lambda_i \quad (9.31)$$

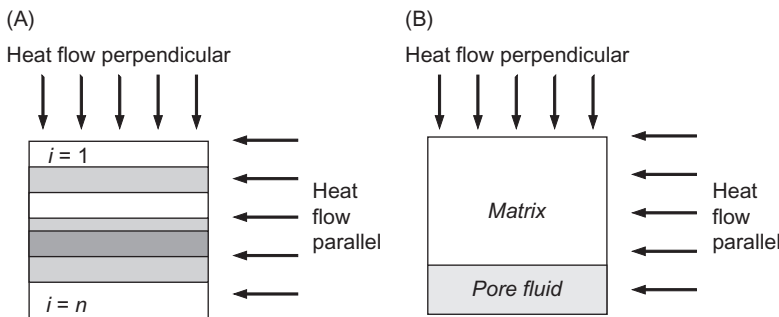


FIGURE 9.11 Layer models for calculation of thermal conductivity: general case (A) and simple porous rock (B).

$$\text{series model } \lambda_{\perp} = \left[\sum_{i=1}^n V_i \cdot \lambda_i^{-1} \right]^{-1} \quad (9.32)$$

where V_i is the volume fraction and λ_i the thermal conductivity of the component i .

The two equations represent the upper (λ_{\parallel}) and the lower (λ_{\perp}) bound of thermal conductivity for a rock of a given composition.

For a porous rock consisting of matrix (ma) and pore fluid (fl), the equations become:

$$\text{parallel model } \lambda_{\parallel} = (1 - \phi) \lambda_{\text{ma}} + \phi \cdot \lambda_{\text{fl}} \quad (9.33)$$

$$\text{series (perpendicular) model } \lambda_{\perp} = [(1 - \phi) \lambda_{\text{ma}}^{-1} + \phi \cdot \lambda_{\text{fl}}^{-1}]^{-1} \quad (9.34)$$

The porosity dependency for the series and the parallel model is plotted in [Figure 9.12](#). For this and most following plots, thermal conductivity of the matrix material is $\lambda_{\text{ma}} = 7.5 \text{ W m}^{-1} \text{ K}^{-1}$ (representing a quartz sandstone) and $\lambda_{\text{ma}} = 4.5 \text{ W m}^{-1} \text{ K}^{-1}$ (representing a carbonate), for the pore fluid water is assumed with $\lambda_{\text{fl}} = 0.6 \text{ W m}^{-1} \text{ K}^{-1}$.

9.4.3 Layer Models—Modifications and Comparable Mixing Rules

Experimental determined data are situated between the two boundaries given by the series and the parallel model. There are different theoretical developments to obtain a better approximation between calculated and measured values:

1. A simple combination of the two fundamental models is their *arithmetic mean*:

$$\lambda_{\text{H}} = \frac{\lambda_{\parallel} + \lambda_{\perp}}{2} \quad (9.35)$$

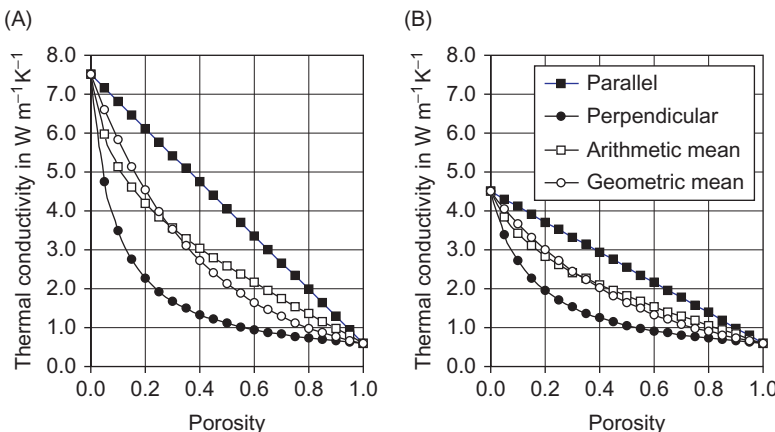


FIGURE 9.12 Layer models—calculated thermal conductivity as a function of porosity. (A) Thermal conductivity of matrix material (quartz) $\lambda_{\text{ma}} = 7.5 \text{ W m}^{-1} \text{ K}^{-1}$, thermal conductivity of pore fluid (water) $\lambda_{\text{fl}} = 0.6 \text{ W m}^{-1} \text{ K}^{-1}$. (B) Thermal conductivity of matrix material (carbonate) $\lambda_{\text{ma}} = 4.5 \text{ W m}^{-1} \text{ K}^{-1}$, thermal conductivity of pore fluid (water) $\lambda_{\text{fl}} = 0.6 \text{ W m}^{-1} \text{ K}^{-1}$ (for calculation, visit the website <http://www.elsevierdirect.com/companion.jsp?ISBN=9780444537966> and refer Thermal. Layered models).

2. Another model with a simple mathematical expression is the *geometric mean*:

$$\lambda_{\text{geom}} = \prod_{i=1}^n (\lambda_i^{V_i}) \quad (9.36)$$

In case of a porous rock, Equation (9.36) becomes:

$$\lambda_{\text{geom}} = \lambda_{\text{ma}}^{1-\phi} \cdot \lambda_{\text{fl}}^\phi \quad (9.37)$$

Figure 9.12 also shows these two mean values.

The fundamental relations for the upper and lower bound (Equations (9.33) and (9.34)) can also be combined in a different way so that the range between the curves of the upper and lower boundaries is “filled” by variation of an additional parameter (a). Krischer and Esdorn (1956) have combined the two fundamental models as follows:

$$\lambda_{\text{KE}} = \left[\frac{a}{\lambda_{\perp}} + \frac{1-a}{\lambda_{\parallel}} \right]^{-1} \quad (9.38)$$

Figure 9.13 shows a calculated plot with the parameter a as curve parameter. This parameter a describes the volume fraction of the series model related to the whole combined model. By variation of a from its minimum value $a = 0$ (identically with the parallel model) to the maximum value $a = 1$ (identically with the series model), the range between the two extremes is described. Authors detected a tendency for this parameter to decrease with

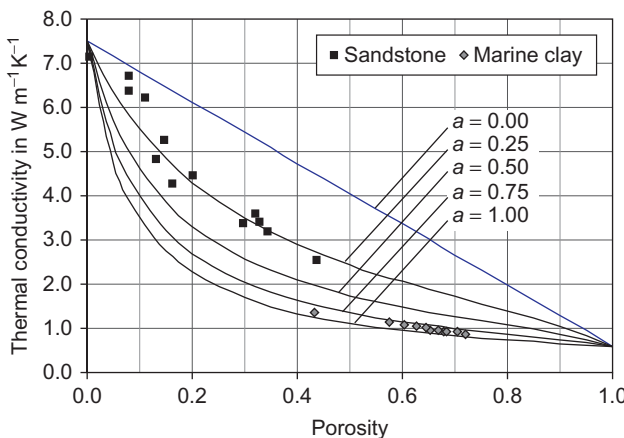


FIGURE 9.13 Mixing rule after Krischer and Esdorn (1956). Curves are calculated with parameter a and the input parameters $\lambda_{\text{min}} = 7.5 \text{ W m}^{-1} \text{ K}^{-1}$ and $\lambda_{\text{fl}} = 0.6 \text{ W m}^{-1} \text{ K}^{-1}$ (for calculation, visit the website <http://www.elsevierdirect.com/companion.jsp?ISBN=9780444537966> and refer Thermal. Layered models). Points are experimental data for clean sandstone/Viking Graben (Brigaud et al., 1992) and marine red clay (Ratcliffe, 1960).

increasing degree of compactness or cementation for construction materials. Figure 9.13 gives a comparison with experimental data for sandstone and marine clay. Obviously the parameter a is a measure of the “cementation” of the sediment—it decreases with increasing contact cementation.

Another way is the application of the Lichtenegger and Rother (1931) generalization (see Section 6.7) on thermal properties. For the general case of n components, the result is

$$\lambda = \left[\sum_{i=1}^n V_i (\lambda_i^\alpha) \right]^{\frac{1}{\alpha}} \quad (9.39)$$

This equation is a generalization of several individual equations. For example, the parallel model is $\alpha = 1$ and the serial model is $\alpha = -1$. The exponent α can be interpreted as a “textural parameter.”

For a porous rock, results are

$$\lambda = [(1 - \phi)(\lambda_{\text{min}}^\alpha) + \phi(\lambda_{\text{fluid}}^\alpha)]^{\frac{1}{\alpha}} \quad (9.40)$$

Figure 9.14 shows as example the calculated thermal conductivity versus porosity for different exponent α . The variation of α fills the space between maximum and minimum curve. Also, for this mixing equation a comparison with experimental data is given (Figure 9.14). The exponent α in this case is controlled by the “cementation”; for sandstone results $\alpha = 0.0$ to 0.5 , and for the marine clay $\alpha \approx -1.0$ to -0.5 .

As an example for application on a polymineralic rock, Table 9.15 shows the comparison of measured and calculated thermal conductivities of three

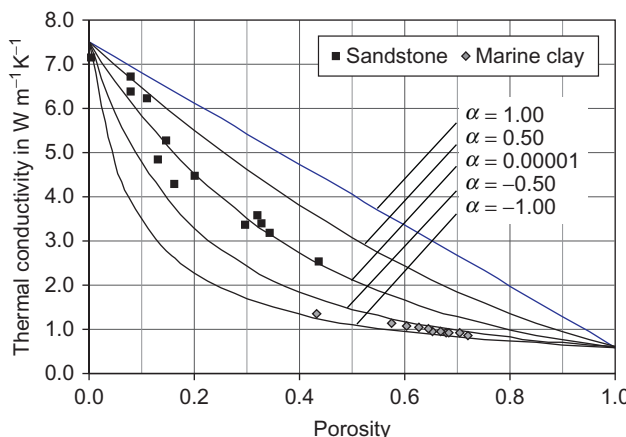


FIGURE 9.14 Mixing rule after generalized Equation (9.40). Curve parameter is α and input parameters are $\lambda_{\text{ma}} = 7.5 \text{ W m}^{-1} \text{ K}^{-1}$ and $\lambda_{\text{fl}} = 0.6 \text{ W m}^{-1} \text{ K}^{-1}$. Points are experimental data for clean sandstone/Viking Graben (Brigaud et al., 1992) and marine red clay (Ratcliffe 1960) (for calculation, visit the website <http://www.elsevierdirect.com/companion.jsp?ISBN=9780444537966> and refer Thermal. Layered models).

granite samples (Kirchberg granite/Saxonia-Germany). Measured data (Seipold, 1990) are compared with:

- calculated conductivities for parallel and perpendicular models;
- Krischer–Esdorn equation with parameter a for best approximation;
- generalized Lichtenecker and Rother equation with exponent α for best approximation (visit the website <http://www.elsevierdirect.com/companion.jsp?ISBN=9780444537966> and refer Thermal. Layered models-10 components).

The measured conductivities are between the calculated extreme for the parallel and perpendicular model. The generalization with the Krischer–Esdorn and Lichtenecker–Rother equation fits the data by adaptation of the parameters a and α , respectively.

9.4.4 Inclusion Models—Spherical Inclusions

A systematic description and discussion of various mixture theories for rock properties is given by Berryman (1995). In this chapter, inclusion models will be discussed briefly.² Early studies of inclusion models going back to Clausius–Mossotti, Maxwell–Garnett and others; theories are directed on different properties (see Berryman, 1995; Parrott and Stuckes, 1975).

²For detailed study of theoretical concepts and models (self-consistent effective medium theory, differential effective medium approach), the reader may be referred to the special literature such as that of Berryman (1994) and Mavko et al. (1998).

TABLE 9.15 Mineral Composition of Granite Samples (Kirchberg granite) and Measured Thermal Conductivity

Sample	E85/23	E85/32	E85/33
Density in kg m^{-3}	2620	2620	2640
Composition			
Quartz (7.70 W mK^{-1})	0.294	0.350	0.516
K-feldspar (2.30 W mK^{-1})	0.304	0.358	0.217
Plagioclase (2.15 W mK^{-1})	0.325	0.258	0.222
Biotite (2.02 W mK^{-1})	0.070	0.029	0.036
Muscovite (2.28 W mK^{-1})	0.002	0.001	0.002
Accessories (3.00 W mK^{-1})	0.004	0.002	0.002
Opaque min. (5.00 W mK^{-1})	0.001	0.002	0.005
Measured thermal conductivity in W mK^{-1}	3.46	3.46	3.83
Calculated Thermal Conductivity in W mK^{-1}			
Parallel	3.83	4.15	5.06
Perpendicular, serial	2.79	2.97	3.51
Krischer–Esdorn equation	3.46	3.46	3.83
with $a =$	0.29	0.51	0.73
Generalized Lichtenegger–Rother equation	3.46	3.46	3.83
with $\alpha =$	0.46	0.02	-0.51

Seipold (1990). In brackets is the thermal conductivity of the mineral for model calculation. Thermal conductivities are calculated for parallel and perpendicular model, the Krischer–Esdorn equation with parameter a for best approximation, and the generalized Lichtenegger and Rother equation with exponent α for best approximation.

For a two-component composite with spherical inclusions (material 1) in a host material (material 2), the result for thermal conductivity is

$$\frac{\lambda_{\text{CM}} - \lambda_2}{\lambda_{\text{CM}} + 2 \cdot \lambda_2} = V_1 \cdot \frac{\lambda_1 - \lambda_2}{\lambda_1 + 2 \cdot \lambda_2} \quad (9.41)$$

where

λ_{CM} is the thermal conductivity of the composite (Clausius–Mossotti model)

λ_1 is the thermal conductivity of the inclusion material

λ_2 is the thermal conductivity of the host material

V_1 is the volume fraction of the inclusions.

For a porous rock consisting of matrix substance as host material and fluid as spherical pore inclusion, the result is

$$\frac{\lambda_{CM} - \lambda_{ma}}{\lambda_{CM} + 2 \cdot \lambda_{ma}} = \phi \frac{\lambda_{fl} - \lambda_{ma}}{\lambda_{fl} + 2 \cdot \lambda_{ma}} \quad (9.42)$$

where

λ_{fl} is the thermal conductivity of the pore fluid

λ_{ma} is the thermal conductivity of the matrix

ϕ is the porosity.

Solved for λ_{CM} results with $\eta = \lambda_{ma}/\lambda_{fl}$:

$$\lambda_{CM} = \lambda_{ma} \frac{(2\eta + 1) - 2 \cdot \phi(\eta - 1)}{(2\eta + 1) + \phi(\eta - 1)} \quad (9.43)$$

The assumption of spherical mineral grains suspended in a fluid gives the relationships:

$$\frac{\lambda_{CM} - \lambda_{fl}}{\lambda_{CM} + 2 \cdot \lambda_{fl}} = (1 - \phi) \frac{\lambda_{ma} - \lambda_{fl}}{\lambda_{ma} + 2 \cdot \lambda_{fl}} \quad (9.44)$$

$$\lambda_{CM} = \lambda_{fl} \frac{3\eta - 2 \cdot \phi(\eta - 1)}{3 + \phi(\eta - 1)} \quad (9.45)$$

With regard to the supposition that there is no influence or distortion of the thermal field of one inclusion by any neighboring inclusion, we can expect that:

- [Equation \(9.43\)](#) is useful mainly for rocks with relatively small porosity;
- [Equation \(9.45\)](#) is useful mainly for high porous sediments (marine sediments).

[Figure 9.15](#) shows a comparison of calculated thermal conductivity as function of porosity with experimental data.

The limitation for both equations is determined by the ratio η . After Beck (1976), [Equation \(9.43\)](#) is applicable up to a porosity of about $\phi = 0.15$, if $\eta \geq 10$. In the case of [Figure 9.15](#), the ratio η is about 12.5.

The applicability of the model is not limited to mixtures of solid matrix material and fluid pore content. It is also useful for a mixture of two different solid components, such as for solid spheres in another solid material or cement. In this case, the porosity must be substituted with the volume fraction of the other material or cement. Kobranova (1989) has applied the inclusion model sequentially to a polymimetic rock. The solid matrix in this particular case consists of 70% quartz, 20% feldspar, and 10% kaolinite. In the first step, a solid material conductivity is calculated for the quartz–feldspar mixture. In the next, this solid material is combined with the kaolinite, and in the final step, this three-component matrix is combined with the pore material.

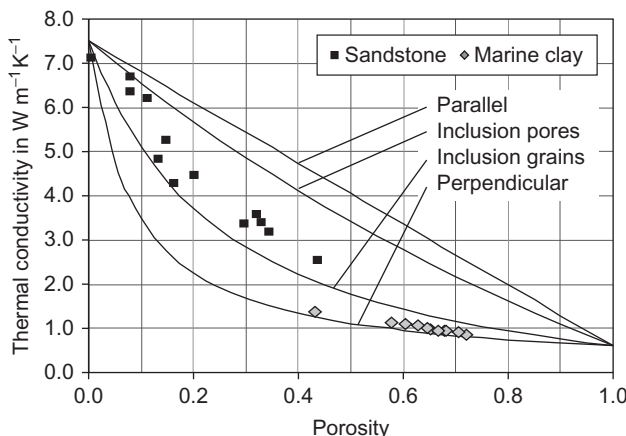


FIGURE 9.15 Spherical inclusion model. Input parameters for calculated curves are $\lambda_{\text{ma}} = 7.5 \text{ W m}^{-1} \text{ K}^{-1}$ and $\lambda_{\text{fi}} = 0.6 \text{ W m}^{-1} \text{ K}^{-1}$. Points are experimental data for clean sandstone/Viking Graben (Brigaud et al., 1992) and marine red clay (Ratcliffe, 1960) (for calculation, visit the website <http://www.elsevierdirect.com/companion.jsp?ISBN=9780444537966> and refer Thermal. Inclusion models).

9.4.5 Inclusion Models—Nonspherical Inclusions

Nonspherical inclusions are used for modeling elongated pores or fractures mostly with the basic shape of an ellipsoid. The ellipsoid as shape requires the implementation of depolarization exponents L_a, L_b, L_c along the principal directions a, b, c of the ellipsoid with the condition:

$$L_a + L_b + L_c = 1 \quad (9.46)$$

The ellipsoidal inclusions can have a preferred axis orientation, and anisotropy results or they are distributed randomly (isotropy).

Aligned Ellipsoids

Aligned ellipsoids can be used for modeling of fractured rocks with a preferred fracture orientation. For aligned ellipsoids, Sen et al. (1981) show that the differential effective medium estimate for an ellipsoidal inclusion in a host material is

$$\left(\frac{\lambda_2 - \lambda_{\text{DEM}}}{\lambda_2 - \lambda_1} \right) \cdot \left(\frac{\lambda_1}{\lambda_{\text{DEM}}} \right)^L = V_1 \quad (9.47)$$

where λ_{DEM} is the rock thermal conductivity, λ_1 the host material conductivity, λ_2 the inclusion material conductivity, and V_1 the volume fraction of the host material. L is the depolarization exponent of the inclusions.

The depolarization exponent implements the directional dependence of the model-calculated thermal conductivity because it is related to the axes of the ellipsoid. References for the exact calculation of the depolarization exponent gives, for example, Berryman (1995). There are also values and approximations for some extreme shapes (see Table 9.17):

sphere $L_a = L_b = L_c = 1/3$

needle $L_c = 0$ (along needle long axis), $L_a = L_b = 1/2$ (along needle short axes)

disk $L_c = 1$ (along short axis), $L_a = L_b = 0$ (along long axes).

Assuming that a fracture system has an orientation, thermal conductivity must be formulated as a tensor. The tensor simplifies for the case that the axes of the ellipsoid coincide with the axes of the Cartesian coordinate system. For generalization, this tensor can be transformed into any orientation by coordinate transformation.

As a first case, it is assumed that there exists a penny-shaped fracture with long ellipsoid axes a, b parallel x, y coordinate axis and a short ellipsoid axis $c \ll a = b$ parallel z coordinate axis. Then, thermal conductivity components are the solutions of the following equations:

$$x\text{- and } y\text{-direction : } \left(\frac{\lambda_{\text{fl,fr}} - \lambda_{\text{DEM},x}}{\lambda_{\text{fl,fr}} - \lambda_{\text{ma}}} \right) \cdot \left(\frac{\lambda_{\text{ma}}}{\lambda_{\text{DEM},x}} \right)^{L_a} = 1 - \phi \quad (9.48)$$

$$z\text{-direction : } \left(\frac{\lambda_{\text{fl,fr}} - \lambda_{\text{DEM},z}}{\lambda_{\text{fl,fr}} - \lambda_{\text{ma}}} \right) \cdot \left(\frac{\lambda_{\text{ma}}}{\lambda_{\text{DEM},z}} \right)^{L_c} = 1 - \phi \quad (9.49)$$

Thus, for any practical application, an estimate of depolarization exponents is necessary. Sen (1981) recommends the following approximation for plate-like objects ($a = b \gg c$):

$$L_c = 1 - \frac{\pi}{2} \cdot \frac{c}{a} = 1 - \frac{\pi}{2} \alpha \quad (9.50)$$

where $\alpha = c/a$ is the aspect ratio.

This can be applied for an estimate of L_c . In a second step, the results are

$$L_a = L_b = \frac{1 - L_c}{2} = \frac{\pi}{4} \alpha \quad (9.51)$$

Table 9.16 gives some data and demonstrates the approximation for a disk with $\alpha \rightarrow 0$:

$$\lim_{\alpha \rightarrow 0} L_a = 0 \quad \text{and} \quad \lim_{\alpha \rightarrow 0} L_c = 1$$

Figure 9.16 shows the calculation for oriented disks with different aspect ratios.

TABLE 9.16 Aspect Ratio and Depolarization Factor

$\alpha = c/a$	$L_a = L_b$	L_c
0.1	0.0785	0.8429
0.05	0.0393	0.9215
0.02	0.0157	0.9686
0.01	0.0079	0.9843
0.005	0.0039	0.9921
0.002	0.0016	0.9969
0.001	0.0008	0.9984

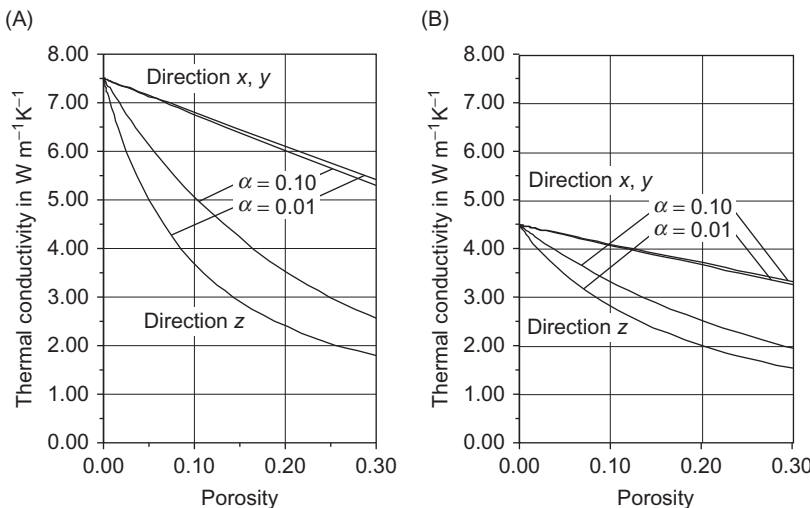


FIGURE 9.16 Thermal conductivity versus fracture porosity calculated with inclusion model (oriented); for calculation, visit the website <http://www.elsevierdirect.com/companion.jsp?ISBN=9780444537966> and refer Thermal. Inclusion models. (A) Thermal conductivity of matrix material (quartz) $\lambda_{ma} = 7.5 \text{ W m}^{-1} \text{ K}^{-1}$, thermal conductivity of pore fluid (water) $\lambda_{fl} = 0.6 \text{ W m}^{-1} \text{ K}^{-1}$. (B) Thermal conductivity of matrix material (carbonate) $\lambda_{ma} = 4.5 \text{ W m}^{-1} \text{ K}^{-1}$, thermal conductivity of pore fluid (water) $\lambda_{fl} = 0.6 \text{ W m}^{-1} \text{ K}^{-1}$. The two curve sets are calculated for different aspect ratio or depolarization factors: aspect ratio $\alpha = 0.01$ ($L_a = L_b = 0.008$ and $L_c = 0.984$) aspect ratio $\alpha = 0.10$ ($L_a = L_b = 0.08$ and $L_c = 0.840$).

The figure demonstrates that thermal conductivity in:

- z -direction decreases strong with the decrease of aspect ratio;
- x - and y -directions increase with the decrease of aspect ratio, but this is only a small effect.

Randomly Arranged Inclusions

Randomly arranged inclusions result in an isotropic effect of inclusions. For this case, a generalization of the Clausius–Mossotti relation (Berryman, 1995; Mavko et al., 1998) can be applied:

$$\frac{\lambda_{CM} - \lambda_m}{\lambda_{CM} + 2 \cdot \lambda_m} = V_i(\lambda_i - \lambda_m)R^{mi} \quad (9.52)$$

where λ_m is the thermal conductivity of the host material, λ_i the thermal conductivity of inclusion material, and V_i the volume fraction of inclusions.

Solved for λ_{CM} , result is

$$\lambda_{CM} = \lambda_m \frac{1 - 2 \cdot V_i \cdot R^{mi}(\lambda_m - \lambda_i)}{1 + V_i \cdot R^{mi}(\lambda_m - \lambda_i)} \quad (9.53)$$

where R^{mi} is a function of the depolarization exponents L_a, L_b, L_c :

$$R^{mi} = \frac{1}{9} \sum_{k=a,b,c} \frac{1}{L_k \cdot \lambda_i + (1 - L_k) \lambda_m} \quad (9.54)$$

Table 9.17 gives expressions of the parameter R^{mi} for some inclusion shapes.

TABLE 9.17 Depolarization Exponents L_a, L_b, L_c and Parameter R^{mi}

Inclusion Shape	Depolarization Exponent for Single or Oriented Inclusion L_a, L_b, L_c	Parameter for Randomly Distributed Inclusions R^{mi}
Sphere	1/3, 1/3, 1/3	$\frac{1}{\lambda_i + 2 \cdot \lambda_m}$
Needle	0, 1/2, 1/2 (needle long axis along x -axis)	$\frac{1}{9} \left(\frac{1}{\lambda_m} + \frac{4}{\lambda_i + \lambda_m} \right)$
Disk	1, 0, 0 (disk short axis along x -axis)	$\frac{1}{19} \left(\frac{2}{\lambda_m} + \frac{1}{\lambda_i} \right)$

After Berryman (1995).
 m, matrix (host); i, inclusion.

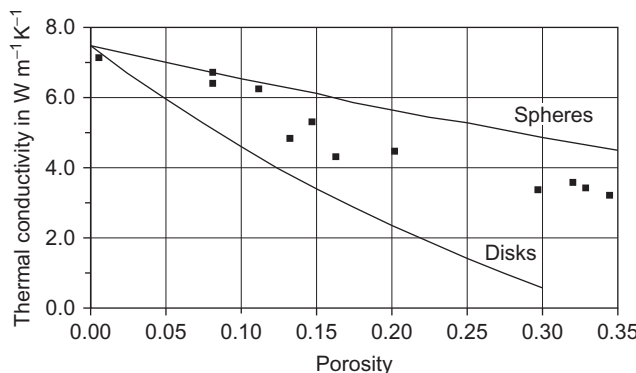


FIGURE 9.17 Thermal conductivity versus porosity. Curves are calculated with the model for randomly distributed spherical and disk inclusions with properties: $\lambda_m = \lambda_{ma} = 7.5 \text{ W m}^{-1} \text{ K}^{-1}$ and $\lambda_i = \lambda_{fl} = 0.6 \text{ W m}^{-1} \text{ K}^{-1}$. Points are experimental data for clean sandstone/Viking Graben (Brigaud et al., 1992) (low porosities only, $\phi < 0.2$); visit the website <http://www.elsevierdirect.com/companion.jsp?ISBN=9780444537966> and refer Thermal.Inclusion models.

For application on porous rocks, thermal conductivity of host material λ_m is the matrix conductivity λ_{ma} , the inclusion conductivity λ_i is the fluid conductivity λ_{fl} , and the volume fraction of inclusions V_i is the porosity ϕ . Figure 9.17 shows a calculation for spheres (same result as Clausius–Mossotti) and disks, compared with experimental data.

In section 11.3.1.3 the inclusion model (non spherical inclusions, random orientation) is used for derivation of a correlation between thermal conductivity and elastic wave velocity.

Magnetic Properties

10.1 FUNDAMENTALS AND UNITS

Magnetic properties describe the behavior of any substance under the influence of a magnetic field. There are two main effects and phenomena:

1. Induced magnetization results when a magnetic field is applied to a material with a magnetic susceptibility.
2. Remanent magnetization exists regardless of the presence of an applied field and occurs within ferri- and ferromagnetic substances, which are characterized by a natural alignment of magnetic moments.

For induced magnetization, the magnetic susceptibility characterizes the magnetic response of a material to an external magnetic field.

The volume susceptibility κ is defined as the ratio of the material magnetization M per unit volume to the external magnetic field strength H :

$$\kappa = \frac{M}{H} \quad (10.1)$$

The volume susceptibility κ is a dimensionless unit.

The mass susceptibility κ_g , measured in units of $\text{m}^3 \text{ kg}^{-1}$, is defined as the ratio of the material magnetization per unit mass to the magnetic field strength, and therefore:

$$\kappa_g = \frac{\kappa}{\rho} \quad (10.2)$$

where ρ is the bulk density.

In general, the susceptibility is a tensor of rank two. Unless otherwise mentioned, the symbol κ means a “mean, quasi-isotropic” susceptibility. For magnetic anisotropy studies, see, for example, Tarling and Hrouda (1993).

TABLE 10.1 Magnetic Units and Conversions

Symbol	SI Unit	CGS Unit	Conversions
H	A m^{-1}	Oe (Oersted)	$1 \text{ A m}^{-1} = 4\pi 10^{-3} \text{ Oe} = 1.257 10^{-2} \text{ Oe}$ $1 \text{ Oe} = 10^3/4\pi \text{ A m}^{-1} = 79.6 \text{ A m}^{-1}$
M	A m^{-1}	Gauss	$1 \text{ Gauss} = 10^3 \text{ A m}^{-1}$ $1 \text{ A m}^{-1} = 10^{-3} \text{ Gauss}$
B	Tesla	Gauss	$1 \text{ Gauss} = 10^{-4} \text{ T}$ $1 \text{ T} = 10^4 \text{ Gauss}$
κ	dimensionless	dimensionless	$\kappa [\text{SI}] = 4\pi \cdot \kappa [\text{cgs}]$ $\kappa [\text{cgs}] = (1/4\pi) \cdot \kappa [\text{SI}]$

In addition to susceptibility, magnetic permeability μ is used to describe magnetic properties. Permeability relates magnetization to magnetic induction B :

$$B = \mu_0(H + M) = \mu_0(1 + \kappa)H = \mu_0 \cdot \mu \cdot H \quad (10.3)$$

where

$\mu_0 = 4\pi 10^{-7} \text{ V s A}^{-1} \text{ m}^{-1}$ is the magnetic permeability for vacuum
 μ is the relative magnetic permeability of the material.

$$\mu = 1 + \kappa \quad (10.4)$$

In SI units, H and M are in A m^{-1} , and B in Tesla ($1 \text{ T} = 1 \text{ V s m}^{-2}$). Table 10.1 shows the SI units with their equivalents in the older CGS system and their respective conversions.

There are three main groups of materials with regard to magnetic properties.

Diamagnetic materials: Diamagnetism is the general property of materials that create a magnetic field in opposition to an externally applied magnetic field in conformity with Lenz's law (Figure 10.1). Diamagnetic materials therefore have a negative (but very low) magnetic susceptibility; for common rock-forming minerals, it is often in the region of -10^{-5} . Diamagnetic susceptibility is independent of temperature. In materials that show ferromagnetism or paramagnetism, the diamagnetism is completely overpowered.

In paramagnetic substances, a magnetic field results in a magnetic moment that has the same direction as the applied field (Figure 10.1). Paramagnetic substances therefore have positive susceptibilities that extend

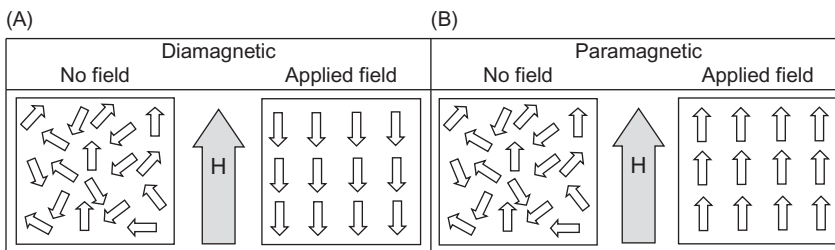


FIGURE 10.1 Diamagnetic and paramagnetic material without magnetic field (A) and with magnetic field (B).

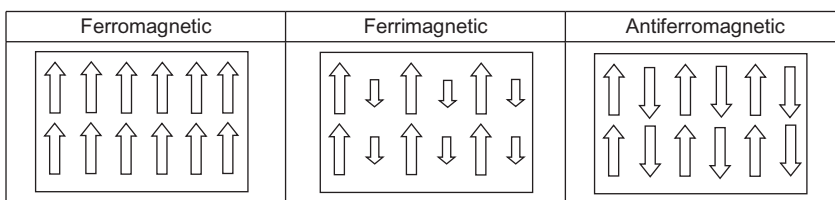


FIGURE 10.2 Ferromagnetic, ferrimagnetic, and antiferromagnetic material.

over a range between 10^{-4} and 10^{-2} (SI) for the common rock-forming minerals (Tarling and Hrouda, 1993). The susceptibility of paramagnetic materials is inversely proportional to absolute temperature (Curie's law or Curie–Weiss's law).

Diamagnetism and paramagnetism exist only in an applied magnetic field; the magnetization is linear in relation to the field strength. If the field is removed as a result of thermal motion, the spins become randomly oriented.

Ferro-, antiferro-, and ferrimagnetic substances show a much higher positive susceptibility than paramagnetic materials and might also have a remanent magnetization. The magnetic behavior is characterized by magnetic volume elements termed “magnetic domains” (single domain, multidomain). The three groups are (Figure 10.2):

1. Ferromagnetic material with parallel orientation of neighboring intrinsic moments and a resulting macroscopic external moment.
2. Antiferromagnetic material with an equal but antiparallel orientation of the intrinsic moments and, therefore, a zero macroscopic external moment.
3. Ferrimagnetic material with antiparallel intrinsic moments of different magnitudes and, therefore, a resulting external moment.

This type of magnetization and susceptibility is temperature dependent. When the temperature is higher than the Curie temperature T_C for

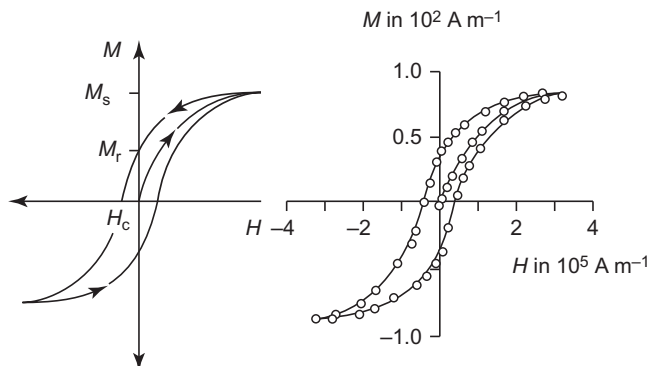


FIGURE 10.3 The magnetic hysteresis curve: (A) schematic, (B) hysteresis curve of a volcanic rock, after Nagata (1961); values are converted to SI units. M_s is saturation magnetization, M_r is remanent magnetization, and H_c is coercive field strength.

ferro-/ferrimagnetics or the Néel temperature T_N for antiferromagnetics, the material has paramagnetic properties. **Table 10.4** gives some values for T_C .

The magnetization depends on the field strength and the “magnetic history” and shows the phenomenon of remanent magnetization (“hysteresis loop,” **Figure 10.3**).

In general, for ferro- and ferrimagnetic substances, the magnetization M is the sum of the induced magnetization M_i and the remanent magnetization M_r :

$$M = M_i + M_r \quad (10.5)$$

The ratio of the remanent magnetization and induced magnetization is called the “Koenigsberger Q -ratio,” a dimensionless quantity defined as:

$$Q = \frac{M_r}{M_i} = \frac{M_r}{\kappa \cdot H} \quad (10.6)$$

where M_r is the magnitude of the (natural) remanent magnetization (per unit volume), κ is the volume susceptibility, and H is the magnitude of the Earth’s magnetic field at the site.

10.2 MAGNETIC PROPERTIES OF ROCK CONSTITUENTS

10.2.1 Magnetic Properties of Minerals

Minerals can also be classified as:

- diamagnetic minerals;
- paramagnetic minerals;
- ferromagnetic minerals, ferrimagnetic minerals, and antiferromagnetic minerals.

TABLE 10.2 Mass Susceptibility κ_g and Volume Susceptibility κ of Some Diamagnetic Minerals

Mineral	κ_g [10^{-8} kg $^{-1}$ m 3]	κ [10^{-6}]	Reference
Anhydrite	-2.11	-59.3	BP
	-0.5 to -2.0	-14 to -60	H
Calcite	-0.48	-13.0	BP
	-0.3 to -1.4	-7.5 to -39	H
Dolomite		-38.0	TH
Quartz	-0.58	-12.4	BP
	-0.5 to -0.6	-13 to -17	H
		-13.4 to -15.4	TH
Fluorite	-0.79	-24.0	BP
Halite	-0.48	-10.4	BP
	-0.48 to -0.75	-10 to -16	H
Orthoclase	-0.58	-12.5	BP
	-0.49 to -0.67	-13 to -17	H
Ice	-1	-9	H

Reference key: BP, Bleil and Petersen (1985); TH, Tarling and Hrouda (1993); H, data compilation from Hunt et al. (1995).

Table 10.2 shows susceptibility values for selected diamagnetic minerals. For more detailed data, see Clark (1966), Lindsley et al. (1966), Melnikov et al. (1975), and Bleil and Petersen (1982).

Table 10.3 shows susceptibility values for paramagnetic minerals.

Ferro-, antiferro-, and ferrimagnetic minerals: The most important and abundant groups are iron and iron-titanium (Fe-Ti) oxides. Iron oxyhydroxides and iron sulfides are significant but not abundant (Bleil and Petersen, 1982).

Fe-Ti-oxides are the dominant magnetic substance, particularly in magmatic rocks; they are components of the ternary system (Figure 10.4), implementing:

- Simple oxide minerals: FeO (wüstite), Fe₃O₄ (magnetite), γ -Fe₂O₃ (maghemite), α -Fe₂O₃ (hematite), FeTiO₃ (ilmenite), Fe₂TiO₄ (ulvöspinel), Fe₂TiO₅ (pseudobrookite), and FeTi₂O₅ (ilmenorutile, ferropseudobrookite).

TABLE 10.3 Mass Susceptibility κ_g and Volume Susceptibility κ of Some Paramagnetic Minerals

Mineral	κ_g [10^{-8} kg $^{-1}$ m 3]	κ [10^{-6}]	Reference
Olivine	5–130, mean 29		BP
	36	990	H
	1–130	1600	D
Amphibole	16–100, mean 49		BP
	16–69	1570	D
Pyroxene	4–94		D
Hornblende	6–100		BP
Smectite	2.7–5		D
Biotite	52		BP
	52–98	1500	H
	5–95	1500–2900	D
Muscovite		226	BP
	0–26, mean 8	122, 165	TH
Illite	15		H
	15	410	D
Montmorillonite	13–14	330–350	H
Chlorite		70, 358, 370, 1550	TH
Bentonite	5.8		D
Siderite	100		D
Dolomite	1.1		D

The range is mostly due to ferrimagnetic impurities. Reference key: BP, Bleil and Petersen (1982); TH, Tarling and Hrouda (1993); H, data compilation from Hunt et al. (1995); D, Dearing (1994).

- Four series (solid solution series) of the system: titanomagnetite, ilmenite-hematite, pseudobrookite, titanomaghemitite.

This system gives “the most basic knowledge of understanding the ferrimagnetic characteristic of general rocks” (Nagata, 1966). The strongest contribution to rock magnetism comes from magnetite, titanomagnetite, and maghemite. A detailed description is given, for example, by Nagata (1961), Stacey and Banerjee (1974), and Bleil and Petersen (1982).

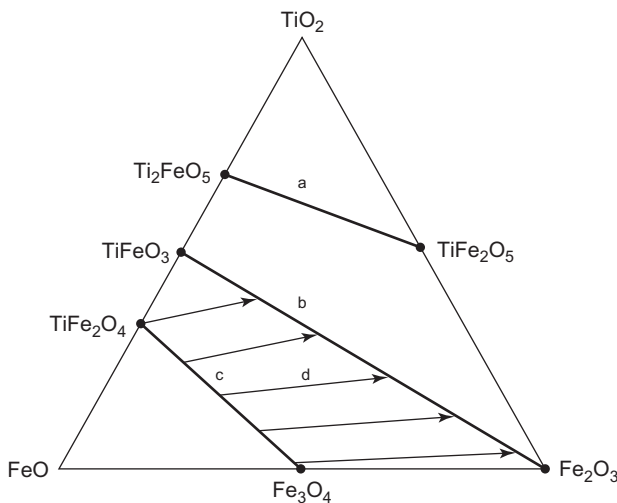


FIGURE 10.4 The ternary system $\text{FeO}-\text{Fe}_2\text{O}_3-\text{TiO}_2$ with typical series: a—pseudobrookite, b—ilmenite—hematite, c—titanomagnetite, d—titanomaghemite. Arrows represent the directions of oxidation.

The series occur in different, preferred rock types:

- Titanomagnetites “are the most common magnetic minerals in igneous rocks. Magnetite occurs in a great variety of igneous, metamorphic, and sedimentary rock types. Typically, it is formed in various types of subsolidus reactions. As a carrier of rock magnetism, magnetite is the most abundant and important oxide mineral. Magnetite occurs on the continents and in the oceanic crust in igneous, sedimentary, and metamorphic rocks.”
- Ulvöspinel is a rare natural crystal present in terrestrial rocks and is almost always intergrown with magnetite. It is frequently observed in lunar samples” (Bleil and Petersen, 1982).
- Ilmenite—hematite yields the following naturally occurring characteristic orientations: Hematite is a carrier of remanent magnetization in sediments (mainly in specular grains and the pigment). In igneous rocks, the primary composition of the series relates to the bulk chemistry of the rock. With decreasing total basicity, the content of ilmenite decreases; subsolidus reactions lead to ilmenite enrichment. This series also occurs in a wide variety of metamorphic rocks.
- Pseudobrookite occurs naturally in igneous and metamorphic rocks.
- Titanomaghemites are the main magnetic constituents in the basaltic oceanic basement, but they also occur in continental igneous rocks (Bleil and Petersen, 1982).

TABLE 10.4 Mass Susceptibility κ_g and Volume Susceptibility κ of Some Ferri- and Ferromagnetic Minerals

Mineral	κ_g [10^{-8} kg $^{-1}$ m 3]	κ [10 $^{-6}$] SI	T_C in °C	Reference
Magnetite		1,200,000–19,200,000 mean 6,000,000	575–585	T
	20,000–110,000	1,000,000–5,700,000		H
Maghemite	40,000–50,000	2,000,000–2,500,000	~600	H
Haematite		500–35,000	675	T
	10–760	500–40,000		H
Ilmenite		300,000–3,500,000 mean 1,800,000	–233	T
	46–80,000	2,200–3,800,000		H
Titanomagnetite	2,500–12,000	130,000–620,000		H
Titanomaghemit	57,000	2,800,000		H
Goethite	26–280	1,100–12,000	~120	H
Ulvöspinel	100	4,800	–153	H
Pyrrhotite	10–30,000	460–1,400,000	320	H

Reference key: T, Telford et al. (1990); H, data compilation from Hunt et al. (1995).

Pyrrhotite (FeS_{1+x}) is ferrimagnetic and a common accessory mineral in rocks and a representative of iron sulfides. Representatives of iron oxyhydr oxides are goethite α -FeOOH and lepidocrocite γ -FeOOH.

Nagata (1966) analyzed samples of eruptive rocks and showed that more than 90% of the magnetically effective substance are parts of the titanomagnetite and the ilmenite–hematite series.

The dependence of susceptibility on magnetic field strength results in the difficulty to give “representative mean values” for ferri- and ferromagnetic minerals. Thus, the values in Table 10.4 are only for general orientation.

10.2.2 Magnetic Properties of Fluids

Most fluids are diamagnetic and have only a very small influence on the magnetic rock properties.

For liquids, Kobranova (1989) gives the following susceptibility values:

$$\text{water } \kappa_{\text{water}} = -0.9 \times 10^{-5} \quad \text{oil } \kappa_{\text{oil}} = -1.04 \times 10^{-5}$$

Potter (2007) reports a mass susceptibility for formation water (Forties Field/North sea) of $\kappa_{g,water} = -0.87 \times 10^{-8} \text{ kg}^{-1} \text{ m}^3$ and for crude oil $\kappa_{g,oil} = -1.02 \times 10^{-8} \text{ kg}^{-1} \text{ m}^3$.

The water mineralization has a small effect because most salts are also diamagnetic.

Ice has a mean susceptibility of $\kappa = -9 \times 10^{-6}$ (Hunt et al., 1995).

Gas components are also diamagnetic, except oxygen, which is paramagnetic. The low value for air therefore is approximately $\kappa_{air} = -0.04 \times 10^{-5}$. For hydrocarbon gases, Kobranova (1989) gives susceptibilities of about $\kappa_{gas} \approx -10^{-8}$.

10.3 MAGNETIC PROPERTIES OF ROCKS

Fundamental publications and comprehensive reviews about rock magnetism are, for example: Hunt et al. (1995), Carmichael (1989), Mooney and Bleifuss (1953), Nagata (1961, 1966), Angenheister and Soffel (1972), Stacey and Banerjee (1974), Bleil and Petersen (1982), Petersen and Bleil (1982), and Tarling and Hrouda (1993). Literature is available on palaeomagnetism and its applications for geology, geophysics, and archaeology, for example, Tarling (1983).

10.3.1 Overview—Rock Magnetization

The magnetic properties of rocks are controlled by those mineral constituents that have a magnetic effect. The fraction of these minerals with respect to the total rock volume may be small. Therefore, two consequences result (Carmichael, 1989):

1. “Magnetic properties can be quite variable within a rock type, depending on chemical inhomogeneity, depositional and/or crystallization, and post-formational conditions.
2. Magnetic properties are not necessarily closely predictable by the lithologic rock type (geologic name). This is because the geologic rock name and the geologic classification are generally given on the basis of the genesis and the gross mineralogy, but a minor fraction of the mineral constituents controls the magnetic properties”.

The most abundant minerals in common rocks are paramagnetic or diamagnetic. The magnetic rock properties are controlled by the ferrimagnetic minerals, although their concentration “in major rock types rarely exceeds 10% vol.” (Bleil and Petersen, 1982). Minerals of the Fe-Ti-system are dominant. In sedimentary rocks, the Fe-hydroxides are also important. Figure 10.5 shows schematically the mineral contribution to the susceptibility of a rock after Tarling and Hrouda (1993). The authors state: “All mineral grains within a rock contribute to its total susceptibility, but their individual

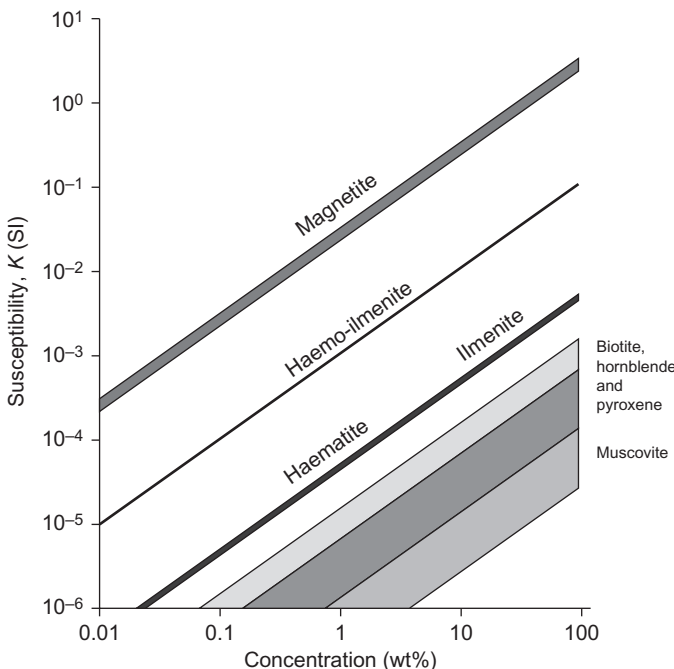


FIGURE 10.5 Mineral contributions to the rock susceptibility (Tarling and Hrouda, 1993).

influence depends on their intrinsic susceptibility, as well as on their concentration.”

10.3.2 Susceptibility Range for Rock Types—Induced Magnetization

Susceptibility has a wide range of values for the individual rock types and more or less distinct tendencies and rules as demonstrated in [Table 10.5](#) and [Figure 10.6](#).

Obviously,

- susceptibility for each rock type varies over orders of magnitude,
- susceptibility of magmatic rocks increases from acid to basic rocks,
- susceptibility of sedimentary rocks increases with increasing clay content.

Gueguen and Palciauskas (1994) give the following general orientation:

Sedimentary rocks $\kappa < 10^{-4}$

Granites and gneisses $\kappa = 10^{-4} - 10^{-3}$

Intrusive basic rocks $\kappa > 10^{-3}$.

TABLE 10.5 Magnetic Susceptibility of Some Selected Rock Types

Rock Type	Volume Susceptibility κ [10 ⁻⁶]	Mass Susceptibility κ_g [10 ⁻⁸ kg ⁻¹ m ³]	Density [10 ³ kg m ⁻³]	Reference
<i>Igneous rocks</i>				
Average acidic igneous rocks	38–82,000	1.4–3,100	2.61	H
	550–120,000	20–4,400	2.79	H
Average basic igneous rocks	170,000	6,500	2.61	H
Andesite	250–180,000	8.4–6,100	2.99	H
Basalt	8,500–79,100			J
Diabase	1,000–160,000	35–5,600	2.91	H
	980–52,780			J
Diorite	630–130,000	22–4,400	2.85	H
Gabbro	1,000–90,000	26–3,000	3.03	H
	5,5300–51,500			J
Granite	0–50,000	0–1,900	2.64	H
	380–33,900			J
Peridotite	96,000–200,000	3,000–6,200	3.15	H
Porphyry	250–38,000	9.2–7,700	2.74	H
	290–6,300			J
Pyroxenite	130,000	4,200	3.17	H
Rhyolite	250–38,000	10–1,500	2.52	H
<i>Sedimentary rocks</i>				
Average sedimentary rocks	0–50,000	0–2,000	2.19	H
Clay	170–250	10–15	1.70	H
Coal	25	1.9	1.35	H
Dolomite	(–10)–940	(–1)–41	2.30	H
	0–900			T

(Continued)

TABLE 10.5 (Continued)

Rock Type	Volume Susceptibility $\kappa [10^{-6}]$	Mass Susceptibility $\kappa_g [10^{-8} \text{ kg}^{-1} \text{ m}^3]$	Density [10^3 kg m^{-3}]	Reference
Limestone	2–25,000	0.1–1,200	2.11	H
	0–3,000	0.5–5		T
Red sediments	10–100	0–931	2.24	H
Sandstone	0–20,900	3–886	2.24	H
Shale	63–18,600		2.10	H
	10–18,000			T
Anhydrite	4–125			K
Rock salt	up to 100			K
Gypsum	1.5–1,250			K
<i>Metamorphic rocks</i>				
Average metamorphic rocks	0–73,000	0–2,600	2.76	H
Amphibole	750	25	2.96	H
Gneiss	0–25,000	0–900	2.80	H
	1,300–25,100			J
Granulite	3,000–30,000	100–1,000	2.63	H
Phyllite	1,600	60	2.74	H
Quartzite	4,400	170	2.60	H
Schist	26–3,000	1–110	2.64	H
	327–3,000	110–630		J
Serpentine	3,100–18,000	0–1,400	2.78	H
Slate	0–38,000		2.79	H

Reference key: H, taken from a data compilation of Hunt *et al.* (1995); J, Jakosky (1950) (converted from cgs); T, Telford *et al.* (1976); K, Kobranova (1989).

Alteration processes can greatly influence magnetic behavior. As an example, Henkel and Guzman (1977) reported martization (oxidation of magnetite to hematite) at an outcropping fracture zone with a negative magnetic anomaly. Other studies, such as of the Svaneke granites (Sweden),

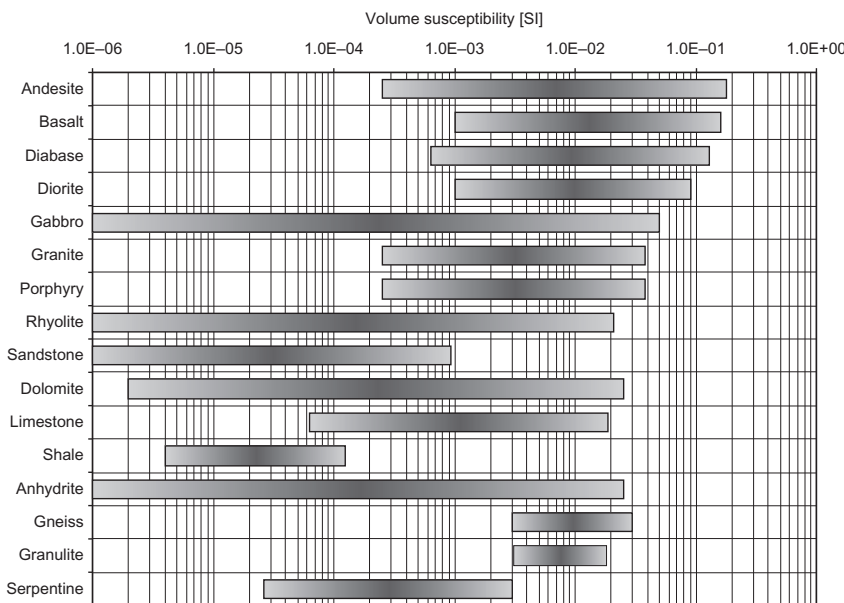


FIGURE 10.6 Volume susceptibility for some rock types, compiled after data from Hunt et al. (1993).

show that the alteration of mafic minerals (hornblende and biotite) into chlorite and magnetite results in increasing susceptibility with an increasing degree of alteration (Platou, 1968).

10.3.3 Correlations Between Susceptibility and Content of Magnetic Substances

The susceptibility of rocks is strongly controlled by the magnetic mineral type and its concentration in the rock. Because “magnetite is the most common and the most magnetic mineral of the iron-titanium oxide series” (Hearst and Nelson, 1985), there is a distinct correlation between rock susceptibility and magnetite content. This can be expressed by a relationship of the general form:

$$\kappa = a \cdot V_{\text{magnetite}}^b \quad (10.7)$$

where $V_{\text{magnetite}}$ is the magnetite volume fraction (mostly in %).

Parameters a and b are empirical values. Normally, b ranges between 1.0 and 1.4 (Grant and West, 1965; see Hearst and Nelson, 1985). [Table 10.6](#) shows some values for the empirical parameters.

TABLE 10.6 Empirical Parameters a, b in [Equation \(10.7\)](#)

Rock Type	a	b	Reference
Rocks, general with 1–80% magnetite	0.0140	1.39	J
Basalt, Minnesota	0.0475	1.08	M
Diabase, Minnesota	0.0336	1.14	M
Granite, Minnesota	0.0244	0.47	M
Gabbro, Minnesota	0.0155	0.36	M
All rocks, Minnesota	0.0363	1.01	M

Volume content in %, properties in SI converted. Reference key: M, Mooney and Bleifuss (1953); J, Jahren (1963).

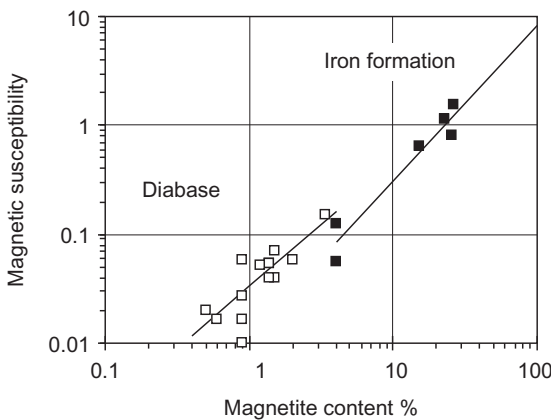


FIGURE 10.7 Correlation between magnetic susceptibility and magnetite content (in %) of rocks and ores from Minnesota (data: Mooney and Bleifuss, 1953).

For example, data from Mooney and Bleifuss (1953) in [Figure 10.7](#) give the correlations:

$$\text{diabase} \quad \kappa = 0.0336 \cdot V_{\text{magnetite}}^{1.14} \quad (10.8)$$

$$\text{iron formation} \quad \kappa = 0.0116 \cdot V_{\text{magnetite}}^{1.43} \quad (10.9)$$

Parasnis (1973) commented about such relations: “Many other relations have also been suggested which make it clear that no universally valid relation between the susceptibility and the Fe_3O_4 content of rocks exist. Furthermore, where a relation does exist, the same susceptibility value may correspond to different Fe_3O_4 contents and vice versa so that a great caution

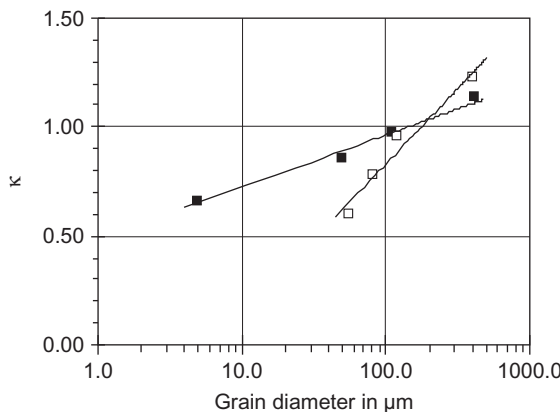


FIGURE 10.8 Susceptibility versus grain diameter of magnetite particles; filled symbols are data after Nagata (1961); open symbols are data after Spravocnik Geofizika (1966).

must be exercised in predicting one from the other. It is therefore advisable to directly determine the susceptibilities of rocks and ores within the area of interest and not rely on formulas of the above type.”

Not only the volume fraction and intrinsic susceptibility of ferro- and ferrimagnetic substances control the rock susceptibility, but also mineral grain size and shape are of influence as a result of domain interactions. Susceptibility decreases with decreasing grain size of magnetic minerals in the rock matrix (Hunt et al., 1995; Nagata, 1961). [Figure 10.8](#) shows two examples.

For disseminated ores with larger grain sizes (multidomain grain size range), susceptibility is influenced by the effect of demagnetization:

$$\kappa_o = V_m \frac{\kappa}{1 + N \cdot \kappa} \quad (10.10)$$

where

κ_o is the bulk susceptibility

κ is the intrinsic susceptibility

V_m is the volume fraction of the magnetic substance

N is the demagnetization factor.

The demagnetization factor is 1/3 for spheres. Carmichael (1989) has published demagnetizing factors for ellipsoids, cylinders, and rectangular prisms of various dimension ratios.

The influence of the internal rock structure on the magnetic properties creates magnetic anisotropy. The susceptibility tensor can be represented by a susceptibility ellipsoid. A detailed description of the magnetic anisotropy of rocks was published by Tarling and Hrouda (1993). Siegesmund et al.

(1993) have studied the fabric-controlled anisotropy of KTB (German Continental Deep Drilling Project) core samples.

10.3.4 Natural Remanent Magnetization

The total magnetization M of any rock is the sum of two vectors:

1. induced magnetization M_i , dependent on the external field
2. remanent magnetization M_r , independent of the external field.

The natural remanent magnetization (NRM) is the field independent and irreversible part of the total magnetization. There are different types and origins of this phenomenon in rocks as follows:

1. *Thermoremanent magnetization (TRM)*: TRM is the remanence acquired by a rock (containing ferrimagnetic substance) when it is cooled from a temperature above its Curie temperature to a lower temperature in the presence of a magnetic field. Generally, most of the magmatic and high-temperature metamorphic rocks are characterized by a distinct TRM higher than the induced magnetization; thus, the Koenigsberger ratio ([Equation \(10.6\)](#)) is $Q > 1$.
2. *Chemical remanent magnetization (CRM)*: CRM occurs during the formation of a magnetic mineral (origin and growing process), for example, as the result of a chemical reaction or phase transition below its Curie temperature under a magnetic field. CRM is therefore related to processes such as oxidation of magnetite to hematite or maghemite, oxidation of titanomagnetite to titanomaghemite, dehydration of iron hydroxide to hematite, precipitation of ferromagnesian minerals (biotite, hornblende, augite), and recrystallization of ferrimagnetic minerals below Curie temperature (Bleil and Petersen, 1982; Hunt et al., 1979). Hunt et al. (1979) remark that CRM is “due to the unusually large volumes of hematite in the form of either pigmentation or specularite … the most probable source of magnetization in red beds.”
3. *Detrital or depositional remanent magnetization (DRM)*: DRM originates from the oriented deposition of previously magnetized mineral grains under the influence of the earth’s magnetic field. The magnetic moments of the particles are aligned to the field direction, so that this direction is “conserved” in the sediment. This is a process that depends on the depositional environment (low turbulence) and also on the sediment type (obvious relations are shown by clays). After deposition, minor changes are possible upon compaction (postdepositional remanent magnetization, or PDRM). The DRM can be important in marine sediments, lake sediments, and varved clays (Carmichael, 1989).

Remanent magnetization is described by the magnitude of M_r (in A m^{-1}) or by the Koenigsberger ratio Q ([Equation \(10.6\)](#)). Q shows a wide scattering

TABLE 10.7 Koenigsberger Ratio Q of Some Selected Rock Types

Rock Type	Q	Reference	Rock Type	Q	Reference
<i>Igneous rocks</i>			<i>Metamorphic rocks</i>		
Average	1–40	H	Granulite	0.003–50	H
Intrusions	0.1–20	H			
<i>Volcanics</i>			<i>Sedimentary rocks</i>		
Granite	0.1–28	H	Average	0.02–10	H
Granite	0.3–1	C	Marine sediments	5	H
Granodiorite	0.1–0.2	H	Red sediments	1.6–6	H
Dolerite	2–3.5	H	Red sediments	2–4	C
Diabase	0.2–4	H	Siltstone	0.02–2	H
Diabase	2–3.5	C	Silty shale	5	H
Gabbro	1–9.5	H	Limestone	0.02–10	C
Oceanic gabbro	0.1–58.4	H			
Basalt	5–10	C			
Seafloor basalt	1–40	C			
Subaerial basalt	1–116	H			
Oceanic basalt	1–160	H			
Seamounts	8–57	H			

Reference key: C, Carmichael (1982), H, taken from a data compilation of Hunt et al. (1995).

of values for a rock type in Table 10.7. Carmichael (1989) gives as average values:

typical igneous rocks $Q = 1–40$,
typical sedimentary rocks $Q = 0.02–10$.

Gueguen and Palciauskas (1994) give the following general orientation for igneous rock types:

acidic intrusive veins $Q = 0–1$,
basic intrusive veins $Q = 1–10$,
basaltic lava $Q = 100$.

Figure 10.9 shows the magnitude of the remanent magnetization M_r versus susceptibility κ for some rock types. The two straight lines indicate a

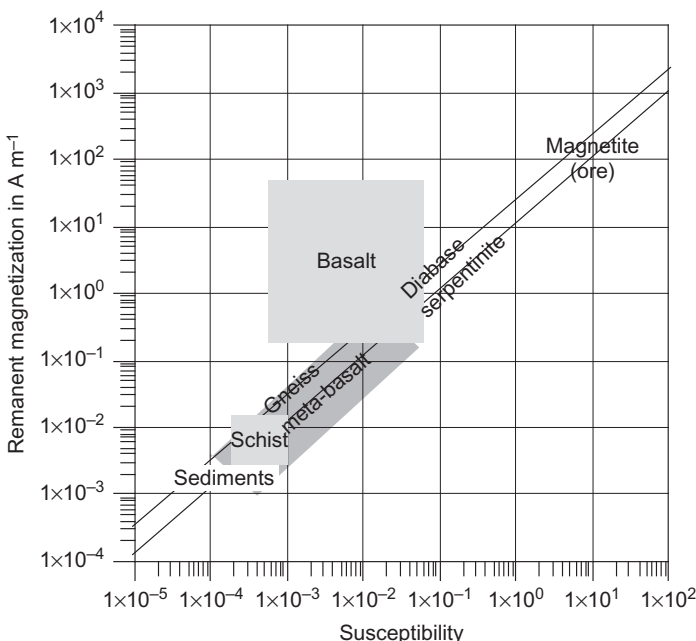


FIGURE 10.9 Remanent magnetization M_r versus susceptibility κ for some rock types. The two straight lines indicate a Koenigsberger ratio $Q = 1$ for the field strength at the pole and the equator, respectively (modified after a figure of Angenheister and Soffel, 1972).

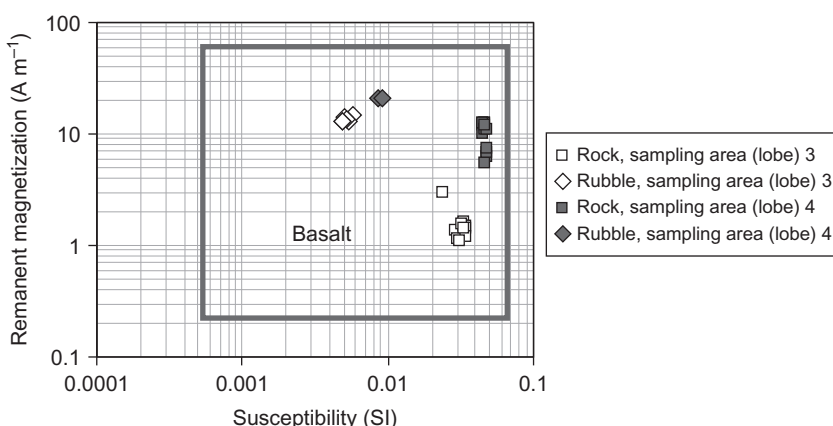


FIGURE 10.10 Remanent magnetization versus susceptibility crossplot; samples from two different lobes at The Barrier (Garibaldi Provincial Park, BC/Canada); Schön (2011).

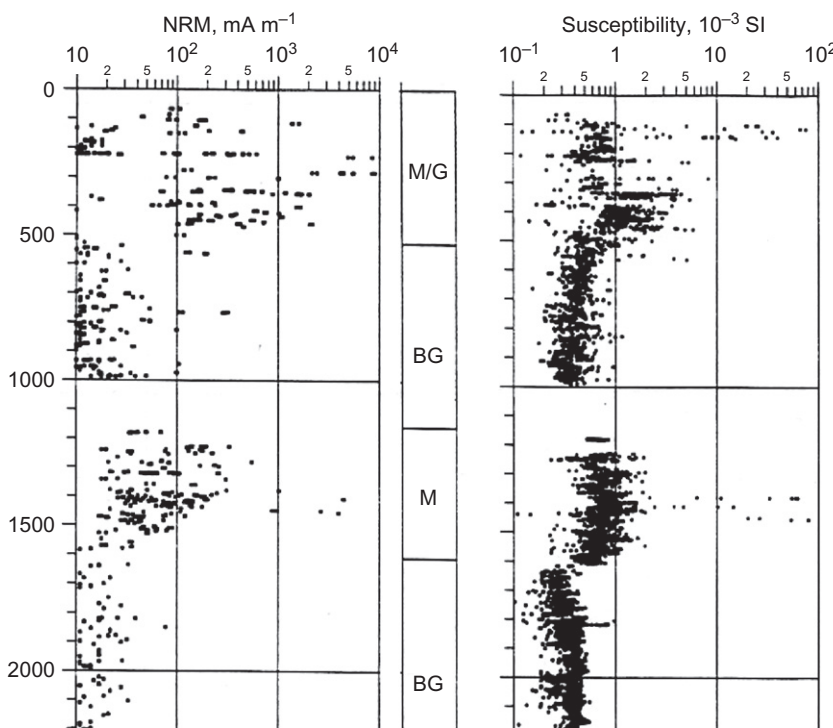


FIGURE 10.11 NRM and susceptibility measured at cores of the KTB (Continental Deep Drilling Program, Germany). Vertical axis: depth in meters; M, metabasite; BG, biotite-gneiss; G, gneiss.

Koenigsberger ratio $Q = 1$ for the field strength at the pole and the equator, respectively. Figure 10.9 demonstrates the high contribution of remanent magnetization particularly for basalt.

Remanent magnetization versus susceptibility crossplots can be used for discrimination of different basalt and lava types as demonstrated in Figure 10.10.

Figure 10.11 shows as a logging example the NRM and susceptibility measured at cores of the KTB (Continental Deep Drilling Program, Germany) with a separation between the main rock types metabasite, biotite-gneiss, and gneiss.

Relationships Between Some Petrophysical Properties

11.1 INTRODUCTION

As shown in the previous chapters, the various physical properties depend on different influences and contributions (Figure 11.1).

The physical basis for the existence of relationships between the various physical properties (e.g., between the velocity of elastic waves and the thermal conductivity) is given by:

- correlations between the properties of the individual rock components (correlations between the elastic and thermal properties of minerals and fluids);
- correlations of the considered properties (e.g., elastic and thermal rock properties) with parameters like porosity and fracturing. Such parameters act as a “connecting bridge” between the properties.

Correlations and relationships can be classified with respect to their application into two groups:

Group 1: Relationships for derivation of specific rock properties (reservoir properties, mechanical properties, etc.) from properties determined by geophysical methods. Examples are seismic or nuclear measurements for estimating porosity, electrical measurements for water saturation calculation, or seismic measurements for derivation of rock mechanical properties. In many cases, a combination of several input properties is applied. This type represents the majority of applications called “petrophysical interpretation” and “formation evaluation.”

Group 2: Relationships for the transformation of a measured (geophysical) property (e.g., velocity of seismic waves) into another (geophysical) property of interest (e.g., thermal conductivity) because it is difficult to measure that property directly in the field.

Correlations of the first type have been discussed in the previous chapters for individual parameters. In the following section, a combined application

Volume fraction and properties of all components, but not on their spatial distribution (texture, structure)	Example: density, nuclear cross sections.
Volume fraction and properties of all components, but also their spatial distribution/texture and interactions at boundaries of the components.	Example: elastic wave velocities, thermal conductivity, strength properties.
Dominant contribution of some specific components or elements. Other components or elements have a second order effect.	Example: for clean rocks, water conductivity is the dominant effect for rock conductivity; for neutron elastic scattering hydrogen is the dominant element.
Contribution of individual components or elements (volume fraction only). Other components or elements have no effect.	Example: all nuclear spectral count rates related to specific elements.
Contribution of individual elements and their "petrophysical environment" (bonding, chemical composition, thermodynamics).	Example: hydrogen nuclei (protons) and their NMR response.

FIGURE 11.1 Petrophysical properties—main influences and dependencies.

of a set of input parameters is discussed: it is directed particularly on properties controlled by porosity and mineral composition, and it gives the basis for combined interpretation techniques especially in log interpretation.

In [Section 11.3](#), correlations between thermal conductivity and seismic wave velocity are discussed. Correlations between elastic wave velocities and mechanical properties have been discussed in [Sections 7.4](#) and [7.5](#).

11.2 RELATIONSHIPS BASED ON LAYERED MODELS— LOG INTERPRETATION FOR POROSITY AND MINERAL COMPOSITION ESTIMATE

11.2.1 Fundamentals

Many problems of petrophysical log interpretation can be formulated as follows:

- Given is a set of measured properties (e.g., density, neutron porosity, and velocity of elastic waves). This data set represents the input.
- Asked for is a set of different petrophysical parameters (e.g., porosity, volume fraction of minerals, and water saturation). This data set represents the output.

The problem can be solved mathematically if the response equations are known for both types and the number of unknowns corresponds to the number of input equations (deterministic case). This method is described as combined interpretation or interpretation of “complex” (multiminerals) lithologies. It is the classic log analysis problem and a type of inversion.

The problem can also be solved conversely: if volumetric rock composition and properties of the individual components (minerals, fluids) are known, the resulting bulk properties (tool answer, measurement) can be calculated via response equations; this is a type of forward modeling.

If volumetric composition and log response are known, then the properties of the components can be derived; this is a parameter estimation problem.

The mathematical formalism becomes comfortable for linear response equations. Then combined interpretation uses volume-based models and techniques with linear volume weighted models. Such linear response equations are valid:

- exactly for scalar properties (e.g., density, nuclear properties);
- as approximation with restrictions for some tensorial properties (e.g., velocity or slowness, using Wyllie's equation, Section 6.5.2).

11.2.2 Determination of Volumetric Rock Composition— Multiple Porosity Methods

Porosity is a key parameter for reservoir studies. In well logging, porosity is derived mostly from nuclear methods (gamma–gamma–density log, neutron log) and acoustic log/sonic log. Porosity determination from logs is an “indirect method.” Additional input parameters (particularly matrix and fluid properties) and the assumption of a “rock model” (mineral composition) are necessary.

Equations for density, neutron porosity, and acoustic response related to porosity have the same linear mathematical structure as shown in the previous sections 5 and 6:

$$\rho = (1 - \phi)\rho_{\text{ma}} + \phi \cdot \rho_{\text{fl}} \quad (11.1)$$

$$\phi_N = (1 - \phi)\phi_{N,\text{ma}} + \phi \cdot \phi_{N,\text{fl}} \quad (11.2)$$

$$\Delta t = (1 - \phi)\Delta t_{\text{ma}} + \phi \cdot \Delta t_{\text{fl}} \quad (11.3)$$

where

ρ is the (measured) bulk density

ϕ_N is the (measured) neutron porosity

Δt is the (measured) slowness

ϕ is the volumetric defined porosity.

The subscript ma indicates matrix properties and fl indicates fluid properties.

Porosity values from each method are as follows:

$$\phi = \frac{\rho_{\text{ma}} - \rho}{\rho_{\text{ma}} - \rho_{\text{fl}}} \quad \phi = \frac{\phi_{N,\text{ma}} - \phi_N}{\phi_{N,\text{ma}} - \phi_{N,\text{fl}}} \quad \phi = \frac{\Delta t_{\text{ma}} - \Delta t}{\Delta t_{\text{ma}} - \Delta t_{\text{fl}}} \quad (11.4)$$

Matrix property and fluid property must be known as input for a porosity calculation.

Application of two or more methods can result in two situations:

1. Resulting porosity values for all methods are identical → porosity is correct and input parameters (particularly matrix properties, input model) are also correct.
2. Resulting porosity values are different for the different methods → porosity is not correctly determined because input parameters (matrix properties, input model) are not correct.

Two techniques—graphic using crossplots and numeric using a mathematical formalism—are presented in order to solve such problems and deliver information about both porosity and mineral composition.

In the following sections, water is considered as the pore fluid (for partial water saturation, see textbooks of log interpretation such as Asquith and Krygowski (2004), Bassiouni (1994), Ellis and Singer (2007), Fricke and Schön (1999), and Serra (1984, 2004)).

11.2.2.1 Crossplots

Crossplots are two-dimensional graphic presentations of the response [equations \(11.1\)–\(11.3\)](#). Crossplots present the variation of any two “porosity-sensitive” properties (density, neutron porosity, slowness). All combinations are possible:

- Neutron–density plot
- Density–slowness plot
- Slowness–neutron plot.

The photoelectric cross section property U or PE (see Section 5.3.2) can also be implemented.

The most frequently applied plot is the neutron–density crossplot. [Figure 11.2](#) shows the principle of a neutron–density crossplot for the three main reservoir rock components: sandstone, limestone, and dolomite. Plots start in the lower left corner with the “matrix point” and go up to the right upper corner with the “water point.” The three lines describe pure limestone, dolomite, and sandstone. Lines are scaled in porosity units.

For practical use, only the part for porosities <0.40 ($<40\%$) is plotted. Crossplots are content present in all chartbooks (e.g., Baker Atlas, 1985; Schlumberger, 2000) where the individual plots are designed for specific tools and different fluid properties (water salinity). [Figure 11.3](#) is such a crossplot for practical application with an example. The deviation from a straight line for the dolomite and sandstone curve is contributed to a better approximation (implementing field data). Plots allow an estimate of mineralogy (lithology) and the determination of a consistent porosity value.

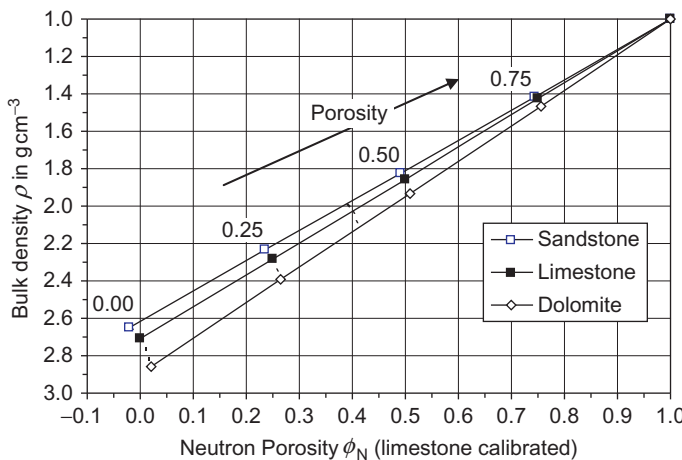


FIGURE 11.2 Calculated neutron–density crossplot: x -axis gives neutron porosity for a limestone calibrated tool; y -axis gives the bulk density. Lines are plotted for sandstone/quartz (matrix density: 2.65 g cm^{-3} , neutron response: -0.02); limestone (matrix density: 2.71 g cm^{-3} , neutron response: ± 0.00); dolomite (matrix density: 2.86 g cm^{-3} , neutron response: $+0.02$); and freshwater (density: 1.00 g cm^{-3} , neutron response: 1.00).

Two tendencies are important:

1. Shale content shifts the points from the sand line to the right (neutron porosity increases), shift apparently toward the dolomite.
2. Gas-bearing zones shift the points to the left (neutron porosity decreases), shift toward low neutron porosity.

Comparable crossplots are available also for slowness and PE factor (Baker Atlas, 1985; Schlumberger, 2000).

The example in Figure 11.3 shows the solution for three data sets.

11.2.2.2 Generalized Numerical Solution

The set of linear response equations (11.1)–(11.3) can be generalized for a rock composed by n different components (solids, fluids).

For any bulk property g following the linear response equation, results:

$$g_m = \sum_{i=1}^n V_i \cdot g_{m,i} \quad \sum_{i=1}^n V_i = 1 \quad (11.5)$$

where

g_m is the bulk property, measured with a method m

$g_{m,i}$ is the property of the component i (related to method m)

V_i is the volume fraction of component i .

This represents a system of $m + 1$ independent linear equations. It can be solved for $n = m + 1$ components (deterministic solution). The calculation

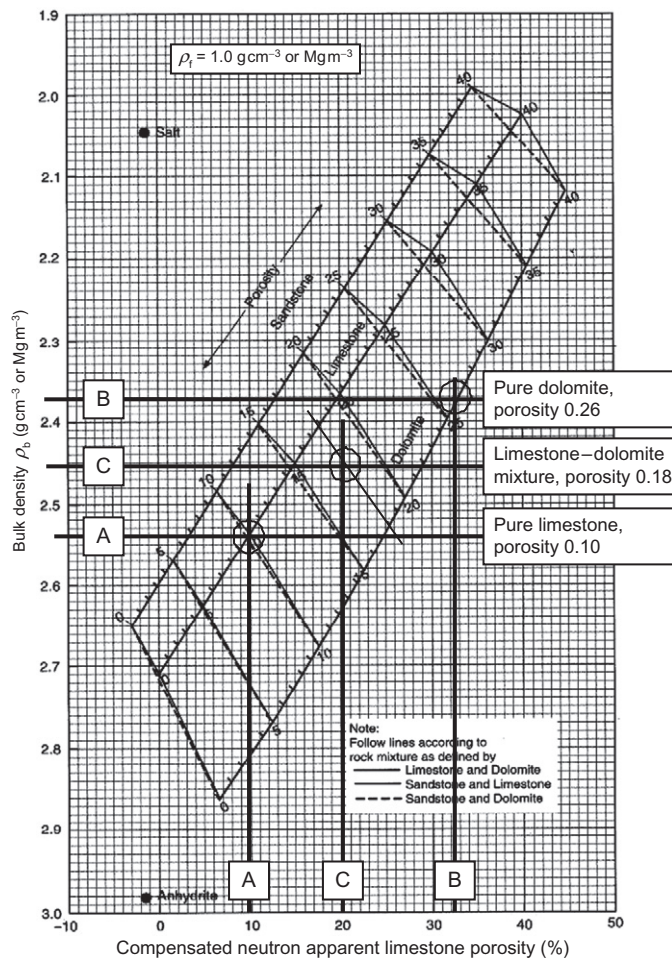


FIGURE 11.3 Neutron–density crossplot (Baker Atlas Log Interpretation Charts, 1985; with friendly permission). Data from three depths of a carbonate section are plotted into the chart. Depth A: measured bulk density $\rho = 2.540 \text{ g cm}^{-3}$ and neutron porosity $\phi_N = 0.100$. The result is a pure limestone with porosity $\phi = 0.10$. Depth B: measured bulk density $\rho = 2.370 \text{ g cm}^{-3}$ and neutron porosity $\phi_N = 0.330$. The result is a pure dolomite with porosity $\phi = 0.26$. Depth C: measured bulk density $\rho = 2.454 \text{ g cm}^{-3}$ and neutron porosity $\phi_N = 0.205$. The result is a mixture of dolomite and limestone with a higher limestone content; porosity $\phi = 0.18$.

of rock composition and porosity is based on this set of linear equations. Equations contain:

- measured magnitude of properties,
- properties of components,
- volume fractions of components.

TABLE 11.1 Rock Composition and Properties of Components

Component	Density in g cm^{-3}	Neutron Porosity	Slowness in $\mu\text{s m}^{-1}$
Quartz	2.65	-0.02	180
Calcite	2.71	0	156
Dolomite	2.87	0.02	143
Water	1.00	1.00	620

The following example demonstrates the technique for density-, neutron-, and acoustic/sonic log measurements applied on a rock with four components.

First the model (rock composition) must be defined. This is one of the most important steps of any interpretation. In practice, the model definition can be supported by geological input, core, or cutting information.

For the example, the model may consist of the components sandstone/quartz, limestone/calcite, dolomite, and pore fluid/water. The properties of the components are summarized in [Table 11.1](#).

The response equations are

$$\rho = 2.71 \cdot V_{\text{calcite}} + 2.87 \cdot V_{\text{dolomite}} + 2.65 \cdot V_{\text{quartz}} + 1.00 \cdot \phi \quad (11.6)$$

$$\phi_N = 0.00 \cdot V_{\text{calcite}} + 0.02 \cdot V_{\text{dolomite}} - 0.02 \cdot V_{\text{quartz}} + 1.00 \cdot \phi \quad (11.7)$$

$$\Delta t = 156 \cdot V_{\text{calcite}} + 143 \cdot V_{\text{dolomite}} + 180 \cdot V_{\text{quartz}} + 620 \cdot \phi \quad (11.8)$$

For the example, the following measured values are used as input:

$$\rho = 2.485 \text{ g cm}^{-3} \quad \phi_N = 0.158 \quad \Delta t = 225 \mu\text{s m}^{-1}$$

Then the equations are

$$2.485 = 2.71 \cdot V_{\text{calcite}} + 2.87 \cdot V_{\text{dolomite}} + 2.65 \cdot V_{\text{quartz}} + 1.00 \cdot \phi \quad (11.9)$$

$$0.158 = 0.00 \cdot V_{\text{calcite}} + 0.02 \cdot V_{\text{dolomite}} - 0.02 \cdot V_{\text{quartz}} + 1.00 \cdot \phi \quad (11.10)$$

$$225 = 156 \cdot V_{\text{calcite}} + 143 \cdot V_{\text{dolomite}} + 180 \cdot V_{\text{quartz}} + 620 \cdot \phi \quad (11.11)$$

Solved for the unknown volume fractions results in:

$$V_{\text{calcite}} = 0.52 \quad V_{\text{dolomite}} = 0.23 \quad V_{\text{quartz}} = 0.10 \quad \phi = 0.15$$

The problem can be solved in a more sophisticated way by using mathematical matrix inversion (see, for example, Doveton, 1986¹) as follows:

The response equations (11.6)–(11.8) are in matrix notation:

$$\begin{bmatrix} \rho \\ \phi_N \\ \Delta t \\ 1 \end{bmatrix} = \begin{bmatrix} 2.71 & 2.87 & 2.65 & 1.00 \\ 0.00 & 0.02 & -0.02 & 1.00 \\ 156 & 143 & 180 & 620 \\ 1.00 & 1.00 & 1.00 & 1.00 \end{bmatrix} \begin{bmatrix} V_{\text{calcite}} \\ V_{\text{dolomite}} \\ V_{\text{quartz}} \\ \phi \end{bmatrix} \quad (11.12)$$

$$\mathbf{M} = \mathbf{R}\mathbf{V} \quad (11.13)$$

where

M is the matrix of measured properties

R is the matrix of responses

V is the matrix of volume fractions.

The solution is

$$\mathbf{V} = \mathbf{R}^{-1}\mathbf{M} \quad (11.14)$$

where \mathbf{R}^{-1} is the inverse matrix.

For the example, results²:

$$\begin{bmatrix} V_{\text{calcite}} \\ V_{\text{dolomite}} \\ V_{\text{quartz}} \\ \phi \end{bmatrix} = \begin{bmatrix} -12.68 & 8.19 & -0.0665 & 45.74 \\ 7.63 & 3.02 & 0.0216 & -24.03 \\ 5.11 & -11.92 & 0.0445 & -20.78 \\ -0.05 & 0.70 & 0.0005 & 0.0651 \end{bmatrix} \begin{bmatrix} \rho \\ \phi_N \\ \Delta t \\ 1 \end{bmatrix} \quad (11.15)$$

with the input data of the example ($\rho = 2.485 \text{ g cm}^{-3}$, $\phi_N = 0.158$, $\Delta t = 225 \mu\text{s m}^{-1}$), now the volume fractions can be calculated directly:

$$\begin{aligned} V_{\text{calcite}} &= -12.68 \cdot 2.485 + 8.19 \cdot 0.158 - 0.0665 \cdot 225 + 45.74 = 0.52 \\ V_{\text{dolomite}} &= 7.63 \cdot 2.485 + 3.02 \cdot 0.158 + 0.0216 \cdot 225 - 24.03 = 0.23 \\ V_{\text{quartz}} &= 5.11 \cdot 2.485 - 11.91 \cdot 0.158 + 0.0445 \cdot 225 - 20.78 = 0.10 \\ \phi &= -0.05 \cdot 2.485 + 0.70 \cdot 0.158 + 0.0005 \cdot 225 + 0.0651 = 0.15 \end{aligned} \quad (11.16)$$

Professional software solutions also include possibilities such as:

- weighting of probability of mineral occurrence;
- weighting factor, which expresses, for example, a more accurate porosity from a density tool than from a sonic or acoustic tool;

¹I highly recommend also reading his incomparable explanation of the principle using the problem of the “classic martini composition.”

²In the example “carbonate profile” (Section 11.2.3), matrix inversion is applied on a two-component carbonate; mathematical tool of inversion is in the website <http://www.elsevierdirect.com/companion.jsp?ISBN=9780444537966> (File: Example-Carbonate).

- statistical tools for better determination of input parameters and matrix solution of the least-squares model with the unity (volume balance) equation as a constraint;
- calculation on a zonal basis with separate models that can be combined for final result.

11.2.3 Example: Carbonate Profile

The example shows a composed carbonate section.³ Data are taken with the friendly permission of AAPG from a case study in the book “Basic Well Log Analysis” from Asquith and Krygowski (2004). All data and calculations are on the website <http://www.elsevierdirect.com/companion.jsp?ISBN=9780444537966> (file: Example-Carbonate).

For the section 9,200–9,250 ft, the following logs are used (Figure 11.4):

GR natural gammalog in API

RHOB bulk density log in g cm^{-3}

NPHI neutron-porosity log (limestone calibrated), decimal fraction.

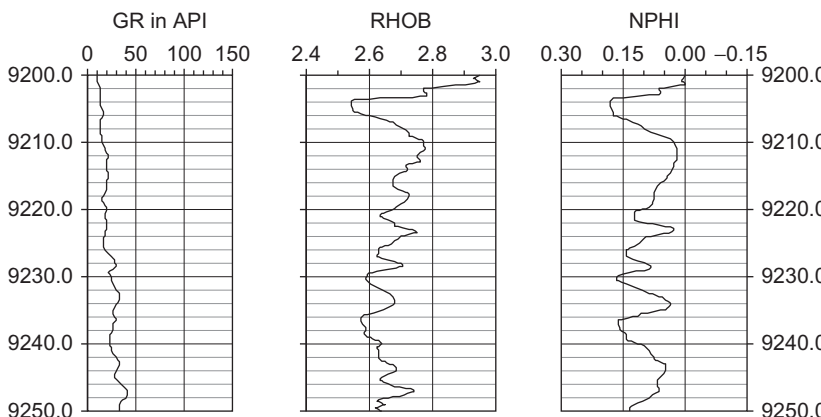


FIGURE 11.4 Log section with gammalog (GR), density log (ρ), and limestone calibrated neutron porosity (ϕ_N); profile composed using data from Asquith and Krygowski (2004).

The profile consists of carbonate rocks with mixed lithology. Cored sections show fractured dolomite; some parts consist of microcrystalline limestone and anhydrite.

Logs show very low gamma radiation. The two “porosity-sensitive logs” (density and neutron porosity) indicate variations in porosity, but measured values may be influenced also by a changing rock composition (dolomite–calcite content).

³Some sections have been taken from the original and used to compose the example.

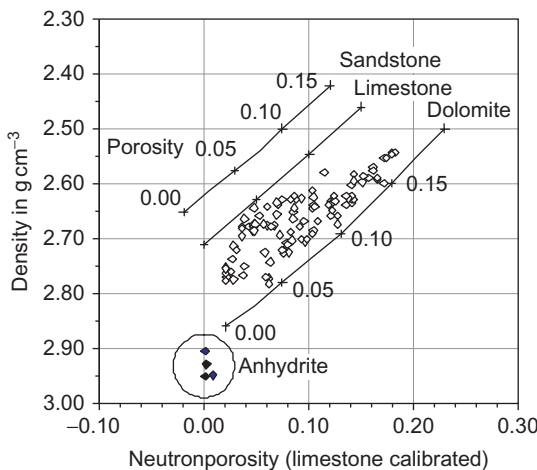


FIGURE 11.5 Neutron–density crossplot.

A better insight into the mineral content gives a neutron–density crossplot (Figure 11.5). The crossplot clearly shows that:

- profile represents a mixture of calcite (limestone) and dolomite;
- there is a tendency of higher porosity in the dolomitic parts;
- some anhydrite is also present; a glance at the density log shows anhydrite with values of $>2.9 \text{ g cm}^{-3}$ in the uppermost part (9,200–9,202 ft).

Therefore, a combined calculation of matrix composition and porosity is necessary. For the defined model (calcite/limestone–dolomite–pore water), the equations in matrix notation are⁴

$$\begin{bmatrix} \text{RHOB} \\ \text{NPHI} \\ 1.00 \end{bmatrix} = \begin{bmatrix} 2.71 & 2.87 & 1.10 \\ 0.00 & 0.02 & 1.00 \\ 1.00 & 1.00 & 1.00 \end{bmatrix} \begin{bmatrix} V_{\text{calcite}} \\ V_{\text{dolomite}} \\ \phi \end{bmatrix} \quad (11.17)$$

and the inverted matrix is

$$\begin{bmatrix} V_{\text{calcite}} \\ V_{\text{dolomite}} \\ \phi \end{bmatrix} = \begin{bmatrix} -5.099 & -9.209 & 14.818 \\ 5.203 & 8.377 & -14.100 \\ -0.104 & 0.833 & 0.282 \end{bmatrix} \begin{bmatrix} \rho \\ \phi_N \\ 1 \end{bmatrix} \quad (11.18)$$

As an example for the depth point, 9,220 ft with the log data $\rho = 2.668 \text{ g cm}^{-3}$ and $\phi_N = 0.095$, the calculation is

⁴For the saline formation water, a fluid density of 1.10 g cm^{-3} was used.

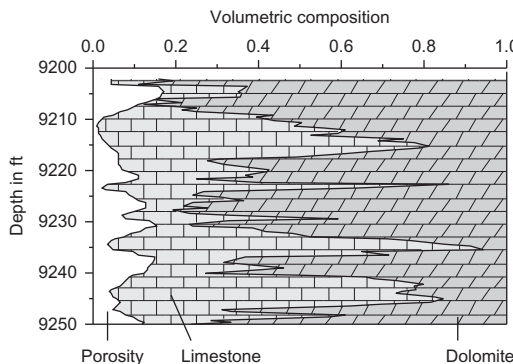


FIGURE 11.6 Result of combined interpretation for limestone, dolomite, and porosity as cumulative plot.

$$V_{\text{calcite}} = -5.099 \cdot 2.668 - 9.209 \cdot 0.095 + 14.818 = 0.339$$

$$V_{\text{dolomite}} = 5.203 \cdot 2.668 + 8.377 \cdot 0.095 - 14.100 = 0.577 \quad (11.19)$$

$$\phi = -0.104 \cdot 2.668 + 0.833 \cdot 0.095 + 0.282 = 0.084$$

The calculation for the whole section is on the website <http://www.elsevierdirect.com/companion.jsp?ISBN=9780444537966> (Example-Carbonate). Figure 11.6 shows the result as volume fraction for limestone, dolomite, and porosity. Note again the tendency that high porosity is connected with the dolomitic parts of the section.

11.3 RELATIONSHIPS BETWEEN THERMAL CONDUCTIVITY AND ELASTIC WAVE VELOCITIES

In addition to reservoir properties and mechanical properties, thermal properties are of increasing interest. Thermal conductivity (see Chapter 9) can be determined in the laboratory, but it is difficult to measure in situ. Therefore, relationships between thermal conductivity and other “measurable” properties (e.g., elastic wave velocities, density) are subjects of research.

In general, there are two ways to derive relationships between different petrophysical properties:

1. Empirical equations (mostly derived from regressions applied on experimental data sets).
2. Theoretical or model-derived relationships based on the application of the same model type on two or more petrophysical properties. Prominent members of this group are relationships using layered models and inclusion models.

Because igneous (and metamorphic) rocks and sedimentary rocks are distinctly different with respect to mineral composition and types of pores and fractures, the two groups are discussed separately.

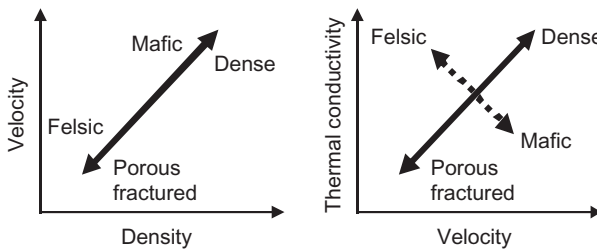


FIGURE 11.7 Expected influence of mineralogy and fracturing/porosity upon velocity, density, and thermal conductivity for igneous rocks.

11.3.1 Igneous and Metamorphic Rocks

11.3.1.1 Empirical Relationships

The following tendencies control the character of expected relationships between elastic wave velocity, thermal conductivity, and also density for igneous and metamorphic rocks:

- Velocity decreases with increasing fracturing or porosity and increases from acid/felsic (granite) to basic/mafic (dunite) types.
- Thermal conductivity decreases with increasing fracturing or porosity but decreases from acid/felsic (granite, high quartz content) to basic/mafic (dunite) types.
- Density decreases with increasing fracturing or porosity and increases from acid/felsic (granite) to basic/mafic (dunite) types.

Figure 11.7 illustrates expected tendencies.

Therefore, the following can be expected:

- A good correlation between velocity and density, because the two influences (fracturing/porosity and mineral composition) act in the same direction.
- Complicated relationships between velocity and thermal conductivity (or density and thermal conductivity) because the mineral influence acts in an opposite direction; this leads to a scatter as a result of variation in fracturing and in mineral composition.

A consideration of specific electrical resistivity and all other parameters show that resistivity is controlled by fracturing/porosity but not directly influenced by mineralogy. Therefore, any correlation will work only for one specific rock type (mineralogy).

Figure 11.8 shows compressional wave velocities, thermal conductivities, and densities for three groups of igneous rocks. For the experimental investigations, prepared samples from a collection “Lithothek” of the Technical University Graz (Austria) are used. Samples are from three rock types: granite, gabbro, and basalt. Compressional wave velocity V_p was determined with an ultrasonic device, and thermal conductivity was determined using

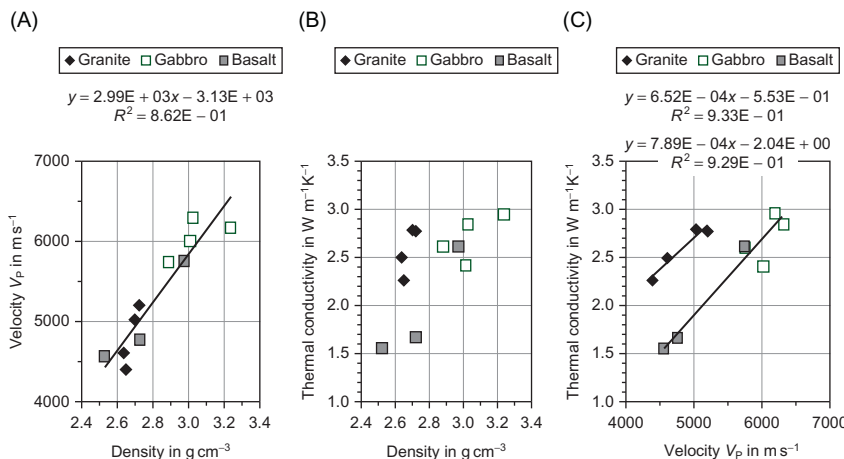


FIGURE 11.8 Correlations between compressional wave velocity, thermal conductivity, and density for three types of igneous rocks.

the thermal conductivity meter from TeKa (Berlin, Germany) with a half-space line source.

Only for the correlation between velocity and density can a regression of Birch's type (see Section 6.4) for all three rock types be derived:

$$V_p = 2990 \cdot \rho - 3130 \quad (11.20)$$

where V_p is in m s^{-1} and ρ in g cm^{-3} .

For the correlation between thermal conductivity and velocity, two regressions for two groups are calculated (Figure 11.8C). The regression equations are

$$\text{for granite } \lambda = 6.52 \cdot 10^{-4} \cdot V_p - 0.553 \quad (11.21)$$

$$\text{for gabbro, basalt } \lambda = 7.89 \cdot 10^{-4} \cdot V_p - 2.04 \quad (11.22)$$

In the next sections, model calculations are used to describe the combined influence of mineral composition (rock type) and fracturing as dominant controlling factors.

11.3.1.2 Model Calculations: The Model with "Defect Parameter"

The defect model (see Section 6.7.4) is a solid mineral block with a "cut." Defects are characterized by their relative length D (defect parameter). For a dry rock in a first approximation, and using only linear terms, the decrease of parameters caused by the defects (fractures, cracks) can be described as follows:

$$\text{elastic moduli: } k_{\text{rock}} = k_{\text{solid}}(1 - D) \quad \mu_{\text{rock}} = \mu_{\text{solid}}(1 - D) \quad (11.23)$$

TABLE 11.2 Factor A_{solid} for Some Minerals

Mineral	V_p in m s^{-1}	λ in $\text{W m}^{-1} \text{K}^{-1}$	A_{solid} in $\text{W s}^2 \text{m}^{-3} \text{K}^{-1}$
Quartz	6050	7.5	$0.21 \cdot 10^{-6}$
Olivine	8550	3.1	$0.04 \cdot 10^{-6}$
Pyroxene	7700	4.5	$0.08 \cdot 10^{-6}$
Hornblende	6810	2.8	$0.06 \cdot 10^{-6}$
Feldspar (mean)	4680	2.0	$0.09 \cdot 10^{-6}$
Muscovite	5810	2.3	$0.07 \cdot 10^{-6}$
Biotite	5350	2.0	$0.07 \cdot 10^{-6}$
Calcite	6640	3.6	$0.08 \cdot 10^{-6}$
Dolomite	7340	5.5	$0.10 \cdot 10^{-6}$
Anhydrite	5640	4.8	$0.15 \cdot 10^{-6}$

$$\text{compressional wave velocity: } V_{P,\text{rock}} = V_{P,\text{solid}} \sqrt{1 - D} \quad (11.24)$$

$$\text{thermal conductivity: } \lambda_{\text{rock}} = \lambda_{\text{solid}}(1 - D) \quad (11.25)$$

For the relationship between thermal conductivity and elastic wave velocity, the simple equation results:

$$\lambda_{\text{rock}} = V_{P,\text{rock}}^2 \left(\frac{\lambda_{\text{solid}}}{V_{P,\text{solid}}^2} \right) = V_{P,\text{solid}}^2 \cdot A_{\text{solid}} \quad (11.26)$$

Thus, thermal conductivity is predicted proportional to the square of velocity.

The factor A_{solid} is controlled only by the solid material properties (minerals). Table 11.2 shows some values for selected minerals. Quartz has a distinctly high magnitude within the most abundant rock-forming minerals, attributed to its high thermal conductivity. Therefore, as tendency for igneous rocks, it can be expected that acid (felsic) types tend toward higher values for the factor A_{solid} than basic (mafic) types.

Figure 11.9 shows forward calculated plots of thermal conductivity versus compressional wave velocity with the factor A_{solid} as curve parameter. The right-hand side figure (Figure 11.9A) is logarithmically scaled and the curves are straight lines with a slope 2.

Figure 11.10 shows the position of the minerals listed in Table 11.2. In this data collection, quartz and anhydrite have a specific position with relatively high values for A_{solid} .

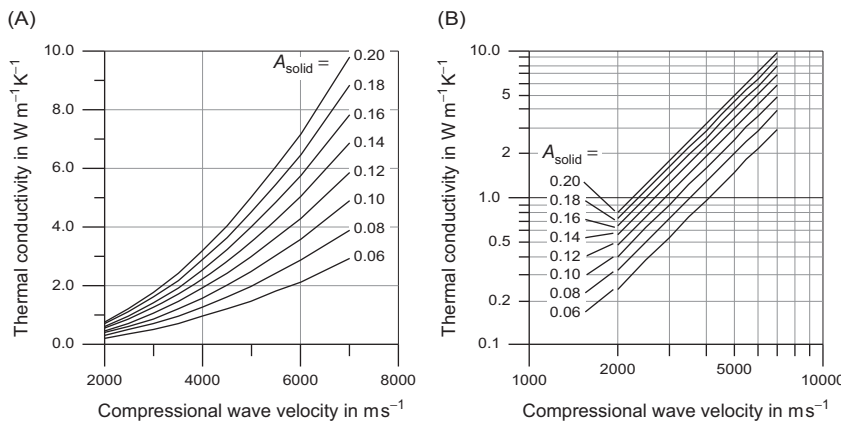


FIGURE 11.9 Calculated plots of thermal conductivity versus compressional wave velocity with the factor A_{solid} (in $10^{-6} \text{ W s}^2 \text{ m}^{-3} \text{ K}^{-1}$) as curve parameter; (A) linear and (B) logarithmically scaled axes (for calculations, visit the website <http://www.elsevierdirect.com/companion.jsp?ISBN=9780444537966> and refer Relationships. Defectmodel).

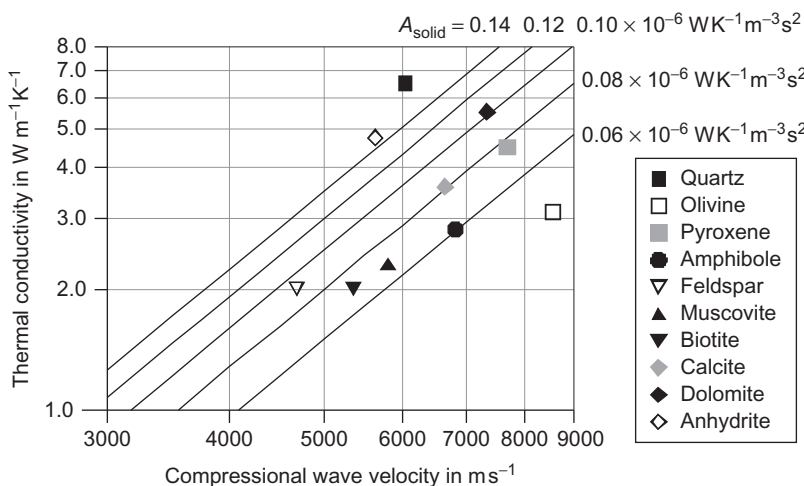


FIGURE 11.10 Thermal conductivity versus compressional wave velocity. Curves are calculated for different values for the parameter $A_{\text{solid}} = (0.06, 0.08, 0.10, 0.12, 0.14) \cdot 10^{-6} \text{ W K}^{-1} \text{ m}^{-3} \text{ s}^2$. The points show the position of the minerals listed in Table 11.2.

The step to rocks is done with Figure 11.11. It shows experimental data for granite, diorite, gabbro, and basalt in such a plot. The simple model reflects the general tendency and separates the data clearly into two groups of different mineral composition represented by the parameter A_{solid} .

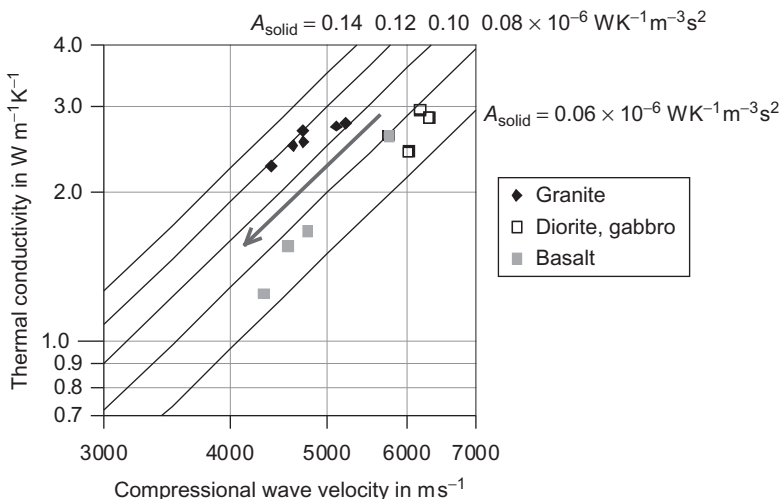


FIGURE 11.11 Thermal conductivity versus compressional wave velocity. Points are experimental data and curves are a calculated relationship for different values for the parameter $A_{\text{solid}} = (0.06, 0.08, 0.10, 0.12, 0.14) \cdot 10^{-6} \text{ W K}^{-1} \text{ m}^{-3} \text{ s}^2$. The arrow indicates the influence of fractures.

The position of the points on the calculated line is a measure of fracturing and other “defects.”

Thus, the relationship between thermal conductivity and compressional wave velocity is controlled by mineral composition (line with parameter A_{solid}) and fracturing or defects (position on the line).

11.3.1.3 Model Calculations: Inclusion Models

Inclusion models can be used for a calculation of thermal conductivity and elastic properties (wave velocities). The two main influences can be implemented by a two-step model:

1. In the first step, the mineral composition is considered from the mineral composition, the properties of the solid mixture as input can be calculated, for example, as Hill’s mean (see Sections 6.7.1 and 9.3.2). Properties represent the “host material” (visit the website <http://www.elsevierdirect.com/companion.jsp?ISBN=9780444537966> and refer Relationships.VR_Hill_mean). Another way—particularly if calculations are compared with experimental data—is the direct input of these parameters (in the following examples this method is used).
2. In the second step, the effects of fractures and cracks are implemented as inclusions and the bulk properties are calculated. Aspect ratio and porosity are additional input parameters or variables (visit the website <http://www.elsevierdirect.com/companion.jsp?ISBN=9780444537966> and refer Relationships. Inclusion model).

TABLE 11.3 Solid Host Material Properties for Model Calculation

Solid Material Property	Granite	Diorite, Gabbro, Basalt
Density ρ in g cm^{-3}	2.66	2.85
Compressional modulus k in GPa	45	72
Shear modulus μ in GPa	30	34
Thermal conductivity λ in $\text{W m}^{-1} \text{K}^{-1}$	3.5	3.0
Derived compressional wave velocity V_p in m s^{-1}	5653	6415

The following equations are applied in the subsequent example for the implementation of fractures and cracks:

- For elastic properties, the equations from O'Connell and Budiansky (1974) and Budiansky and O'Connell (1976) for randomly distributed penny-shaped inclusions (see Section 6.7.3.2).
- For thermal conductivity calculation, the generalization of the Clausius–Mossotti relation (Berryman, 1995; see Section 9.3.5).

Both equations allow the calculation of the velocity and thermal conductivity for dry inclusions⁵ as function of porosity and aspect ratio and also the derivation of relationships between the two properties. Properties of the solid host material are summarized in Table 11.3.

Figure 11.12 presents experimental data compared with calculated curves. The aspect ratio is used as a curve parameter. An optimal fit is given for granite with an aspect ratio $\alpha = 0.20$, and an aspect ratio of $\alpha = 0.27$ for diorite, gabbro, and basalt. Gegenhuber (2011) developed on this basis a petrophysical coded model concept for different rock types.

With the fracture porosity and the density of the solid components, it is possible to derive also relationships between compressional wave velocity and density, and between thermal conductivity and density.

11.3.2 Sedimentary Rocks

The effects of mineral composition, porosity, and saturation are also different for sedimentary rocks with respect to the petrophysical properties density, velocity of elastic waves, and thermal conductivity.

Table 11.4 gives some typical values for quartz, calcite, and dolomite.

⁵For any other pore fluid, the Clausius–Mossotti equation can also be used for thermal conductivity. For elastic wave velocity, a transformation from dry to any other pore fluid is possible using Gassmann's equation in Section 6.7.5.1).

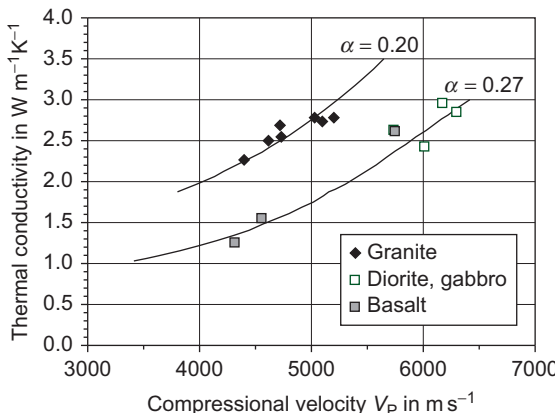


FIGURE 11.12 Thermal conductivity versus compressional wave velocity. Points: experimental data; curves: calculated with inclusion model (for parameter, see Table 11.3). On the website <http://www.elsevierdirect.com/companion.jsp?ISBN=9780444537966> you find an Excel file (Relationships. Inclusion model) for forward calculation of the curves.

TABLE 11.4 Typical Petrophysical Parameter Values for Dominant Minerals in Sedimentary Rocks

Property	Quartz	Calcite	Dolomite
Density in g cm^{-3}	2.65	2.71	2.86
Compressional wave velocity in m s^{-1}	6050	6500	7200
Thermal conductivity in $\text{W m}^{-1} \text{K}^{-1}$	7.5	3.5	5.5

From the table and the results in Sections 4, 6 and 9, one can summarize the following:

- Velocity decreases with increasing porosity and decreasing water saturation, and increases from sandstone to carbonate types.
- Density also decreases with increasing porosity and decreasing water saturation, and increases from sandstone to carbonate types.
- Thermal conductivity decreases with increasing porosity and decreasing water saturation but shows a different behavior with respect to mineral conductivities compared with density and velocity (thermal conductivity decreases from sandstone to carbonate types).

Therefore, a complex relationship between the three parameters is expected as a result of the influence of porosity, saturation, and mineral composition. Shale, a typical component in sedimentary rocks, complicates this situation further.

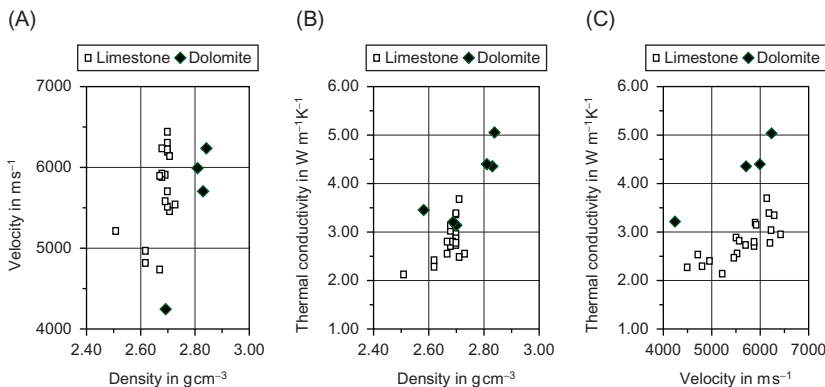


FIGURE 11.13 Correlation between compressional wave velocity, thermal conductivity, and density for two types of dry carbonate rocks (data from Gong, 2005).

TABLE 11.5 Solid Host Material Properties for Model Calculation

Solid Material Property	Calcite/Limestone	Dolomite
Density ρ in g cm^{-3}	2.71	2.86
Compressional modulus k in GPa	75	95
Shear modulus μ in GPa	32	45
Thermal conductivity λ in $\text{W m}^{-1}\text{K}^{-1}$	3.5	5.5
Derived compressional wave velocity V_p in m s^{-1}	6590	7360

Figure 11.13 confirms these characteristics for two rock types (limestone and dolomite).

Using the same model combination as in the previous section, the data from Gong (2005) and own results are analyzed. The properties of the solid host material are summarized in Table 11.5.

In Figure 11.14, experimental data for limestone and dolomite are compared with calculated curves. An optimal fit is given for limestone with an aspect ratio $\alpha = 0.2$ and for dolomite with an aspect ratio $\alpha = 0.1$.

The crosses at calculated curves indicate fracture porosity in steps of 0.05 (or 5%). Limestones are in the range between 0.02 and 0.25, and dolomite between 0.05 and 0.20.

For practical applications, empirical equations are widely used for sedimentary rocks. Well log measurements deliver a variety of petrophysical data (e.g., gamma radiation, elastic wave slowness, density, neutron porosity) and are correlated to thermal conductivity (based on core measurements).

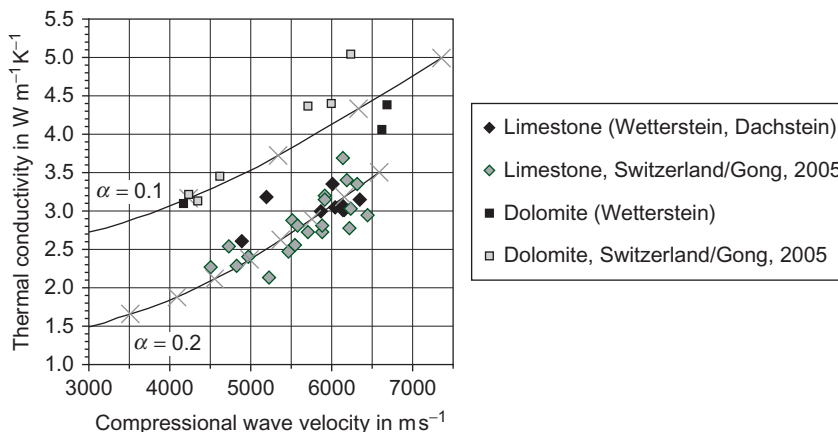


FIGURE 11.14 Thermal conductivity versus compressional wave velocity. Points: experimental data for dry limestone and dolomite; curves: calculated with inclusion model (for input parameters, see Table 11.5). The crosses at calculated curves indicate fracture porosity in steps of 0.05 (or 5%), starting with zero porosity on top.

Vacquier et al. (1988), for example, derived from log data of two oil wells in France an empirical equation (see also Hartmann, 2008):

$$\lambda = a_0 + a_1 \cdot \rho + a_2 \cdot \Delta t + a_3 (1 - \phi_N) + a_4 \cdot V_{sh} \quad (11.27)$$

where thermal conductivity λ is in $\text{W m}^{-1} \text{K}^{-1}$; bulk density ρ (gamma-gamma log) is in kg m^{-3} ; neutron porosity ϕ_N is as fraction; and slowness Δt is in $\mu\text{s m}^{-1}$. V_{sh} is the shale content (fraction) derived from gammalog. Empirical parameters are related to lithology and are given in Table 11.6.

Goss et al. (1975) derived an empirical correlation between thermal conductivity, porosity, and compressional wave velocity. Converted into SI units, results:

$$\lambda = 1.33565 - 0.002554 \cdot \phi + 0.38018 \cdot V_P \quad (11.28)$$

where thermal conductivity λ is in $\text{W m}^{-1} \text{K}^{-1}$; porosity ϕ is in %; and compressional wave velocity V_P is in km s^{-1} .

Thermal conductivity was determined at sandstone, some claystone, siltstone, and carbonate samples from Imperial Valley (California). The authors remark that “the standard deviation for this regression is $\pm 0.4 \text{ mcal cm}^{-1} \text{s} \text{ }^\circ\text{C}$ ($= 0.17 \text{ W m}^{-1} \text{K}^{-1}$), which implies a reliability of $\sim 10\%$ for the predicted thermal conductivity.”

Evans (1977) derived an equation for Jurassic North Sea sediments (39 samples) and implemented additionally the density ρ (in g cm^{-3}):

$$\lambda = -0.049 \cdot \phi - 0.160 \cdot V_P + 3.6 \cdot \rho - 5.50 \quad (11.29)$$

TABLE 11.6 Parameters in Equation (11.27)

Rock Type	a_0	a_1	a_2	a_3	a_4
	$\text{W m}^{-1}\text{K}^{-1}$	$\text{W m}^2 \text{g}^{-1} \text{K}^{-1}$	$10^{-3} \text{W } \mu\text{s}^{-1} \text{K}^{-1}$	$\text{W m}^{-1} \text{K}^{-1}$	$\text{W m}^{-1} \text{K}^{-1}$
Sand	-0.845	1.803	-2.912	1.714	-3.228
Carbonates	2.863	-0.5305	-1.570	1.405	-0.003931
Argillaceous rocks	1.954	-0.3684	-0.3016	3.138	-1.368
Mixture of the three types	9.148	-2.662	-5.115	1.914	-0.5003
Sandy limestone and dolomites	-1.463	0.1000	12.05	1.960	-1.558
Limy and dolomitic shales	1.837	-0.03033	-1.215	1.250	-0.5501
Shaly sands	-3.428	0.7178	3.699	7.038	-1.218

Vacquier *et al.* (1988).

Hartmann et al. (2005) derived multiple regressions for dry and water saturated sandy and carbonaceous sediments from the German Molasse Basin with rms = 0.12–0.15:

Sandy sediments

$$\begin{aligned} \text{dry } \lambda = & - (1.14 \pm 0.47) + (0.512 \pm 0.005)V_P \\ & + (0.615 \pm 0.096)\rho - (0.53 \pm 0.14)\phi \end{aligned} \quad (11.30)$$

$$\begin{aligned} \text{sat. } \lambda = & (1.07 \pm 0.27) + (0.239 \pm 0.002)V_P \\ & + (0.504 \pm 0.053)\rho + (0.042 \pm 0.02)\phi \end{aligned} \quad (11.31)$$

Carbonaceous sediments

$$\begin{aligned} \text{dry } \lambda = & (0.64 \pm 1.06) + (0.371 \pm 0.006)V_P \\ & + (0.209 \pm 0.031)\rho - (2.82 \pm 0.54)\phi \end{aligned} \quad (11.32)$$

$$\begin{aligned} \text{sat. } \lambda = & (0.11 \pm 0.83) + (0.100 \pm 0.005)V_P \\ & + (1.056 \pm 0.172)\rho + (0.66 \pm 0.02)\phi \end{aligned} \quad (11.33)$$

where thermal conductivity λ is in $\text{W m}^{-1} \text{K}^{-1}$, porosity ϕ as fraction, density in g cm^{-3} , and compressional wave velocity V_P is in km s^{-1} .

Brigaud et al. (1992) derived the rock composition (“electrofacies mineralogy and porosity”) from logs and used a four-component (sandstone, carbonate, shale, pore fluid) geometric mean equation for thermal conductivity calculation.

Physical Properties of Rock-Forming Minerals

The following table is compiled from logging parameters summarized in logging chartbooks from Baker Atlas and Schlumberger and used with friendly permission. Parameters:

ρ_b , bulk density in g cm^{-3}

ρ_{\log} , log density (gamma–gamma–density) in g cm^{-3}

Z/A , ratio atomic number/atomic mass number

PE, photoelectric cross section in barns electron^{-1}

$\Delta t_p, \Delta t_s$, slowness for compressional and shear wave in $\mu\text{s ft}^{-1}$ (in $\mu\text{s m}^{-1}$).

Σ , macroscopic cross section in capture units

ϕ_N , neutron porosity in porosity units (%). In the first line, the first raw datum gives the value for epithermal measurement; the second raw, the value for thermal measurement (Baker Atlas). In the second line, the first raw datum gives the value for SNP (sidewall) measurement; the second raw, the value for CNL (compensated neutron) measurement (Schlumberger).

ε , relative dielectric permittivity (Schlumberger, 2000)

λ , thermal conductivity in $\text{W m}^{-1} \text{K}^{-1}$, data from the compilation of Clauser and Huenges (1995).

Minerals	References: First line Baker Atlas—Log Interpretation Charts, 1985 Second line Schlumberger—Log Interpretation Charts, 2000								SLB, 2000	C-H, 1995	
	ρ_b	ρ_{\log}	Z/A	PE	Δt_p	Δt_s	Σ	ϕ_N	ϕ_N	ε	λ
Silicates											
Quartz	2.65	2.64	0.499	1.81	51 (167)	74 (243)	4.26	-1.1	-2.1		7.7
SiO_2		2.64					4.3	-1	-2	4.65	
Opal (3.5% H_2O)	2.16	2.13	0.501	1.75	58 (190)		5.06	3.3	1.9		
$\text{SiO}_2 \cdot (\text{H}_2\text{O})_{0.1228}$		2.13		1.8	58 (190)		5.0	4	2		
Zircon	4.67	4.50	0.469	69.1	96 (315)	147 (482)	5.30	0.2	3.6		5.54
ZrSiO_4		4.50		69			6.9	-1	-3		
Hornblende	3.12	3.12	0.495	5.99	44 (144)	82 (269)	17.6				2.81
$\text{Ca}_2\text{Na}(\text{Mg},\text{Fe},\text{Al},\text{Ti})_3 \text{Si}_8\text{O}_{22}(\text{OH})_2$		3.20			43.8 (144)	81.5 (267)	18	4	8		
Epidote $\text{Ca}_2\text{Al}_2\text{Fe}(\text{SiO}_4)_3\text{OH}$	3.59	3.61	0.495	6.49			21.0				2.83
Forsterite Mg_2SiO_4	3.21	3.23	0.498	1.54	35 (115)	66 (217)	19.7	0.5	-0.6		5.03
Fayalite Fe_2SiO_4	4.39	4.33	0.481	17.17			68.3	2.2	7.2		3.16
Feldspars—alkali											
Orthoclase	2.56	2.53	0.496	2.86			15	-1.5	-1.1	4.4	2.31
KAlSi_3O_8		2.52		2.9	69 (226)		16	-2	-3	6.0	
Anorthoclase	2.59	2.56	0.496	2.86			9.4			4.4	
$(\text{Na},\text{K})\text{AlSi}_3\text{O}_8$		2.59		2.9			16	-2	-2	6.0	
Microcline	2.59	2.57		2.86			13.1				2.49
KAlSi_3O_8		2.53	0.496	2.9			16	-2	-3		

Feldspars—plagioclase

Albite	2.62	2.59	0.496	1.68	47 (154)	98 (322)	7.49	-1.0	-1.3	4.4...6.0	2.14
NaAlSi ₃ O ₈		2.59		1.7	49 (161)	85 (279)	7.5	-1	-2		
Anorthite	2.76	2.74	0.496	3.13	45 (148)		7.28	-1.3	-1.6	4.4...6.0	1.69
CaAl ₂ Si ₂ O		2.74		3.1	45 (148)		7.2	-1	-2		

Micas

Biotite	3.01	2.99	0.493	6.27	51 (167)	224 (735)	30.0	15.8	22.5	4.8...6.0	2.02
K(Mg,Fe) ₃ (AlSi ₃ O ₁₀)(OH) ₂		2.99		6.3	50.8 (167)	224 (735)	30	11	21		
Muscovite	2.83	2.82	0.497	2.40	47 (154)	79 (259)	16.9	13.4	16.5	6.2...7.9	2.28
KAl ₂ (Si ₃ AlO ₁₀)(OH) ₂		2.82		2.4	49 (161)	149 (489)	17	12	20		

Glauconite	2.58	2.54	0.494	6.37			23.4				
(K,Na)(Al,Fe,Mg) ₂ (Al,Si) ₄ O ₁₀ (OH) ₂		2.86		4.8			21				

Clay Minerals

Kaolinite	2.59	2.62	0.504	1.49	212 (696)	328 (1076)	12.8	47.8	45.1	5.8	
Al ₂ O ₃ · 2SiO ₂ · 2H ₂ O		2.41		1.8			14	34	37		
Chlorite	2.88	2.88	0.497	6.30			25.3		5.8		5.15
Mg ₅ (Al,Fe) (OH) ₈ (Al,Si) ₄ O ₁₀		2.76		6.3			25	37	52		
Illite	2.64	2.63	0.499	3.45			15.5	12.7	15.8		
K _{1-1.5} Al ₄ (Si,Al) ₈ O ₂₀ (OH) ₄ (O,OH) ₁₀		2.52		3.5			18	20	30		
Montmorillonite	2.06	2.02	0.502	2.04			14.5	12.6	11.5		
(Na,Ca) _{0.33} (Al,Mg) ₂ Si ₄ O ₁₀ (OH) ₂ · nH ₂ O		2.12		2.0			14	60	60		

(Continued)

Minerals	References: First line Baker Atlas—Log Interpretation Charts, 1985 Second line Schlumberger—Log Interpretation Charts, 2000								SLB, 2000	C-H, 1995	
	ρ_b	ρ_{\log}	Z/A	PE	Δt_p	Δt_s	Σ	ϕ_N	ϕ_N	ε	λ
Carbonate											
Calcite	2.71	2.71	0.508	5.08	46 (151)	89 (292)	7.08	0.0	0.0	7.5	3.59
CaCO_3		2.71		5.1	49.0 (161)	88.4 (290)	7.1	0.0	0.0		
Aragonite CaCO_3	2.93	2.95	0.508	5.08	53 (174)	84 (276)	7.65	0.7	1.0		2.24
Dolomite	2.87	2.87	0.499	3.14	42 (138)	77 (253)	4.7	1.7	0.5	6.8	5.51
$\text{CaMg}(\text{CO}_3)_2$		2.85		3.1	44 (144)	72 (236)	4.7	1	1		
Siderite	3.94	3.89	0.483	14.69	44 (144)	85 (279)	52.3	6.3	12.9	6.8...7.5	3.01
FeCO_3		3.89		15	47 (154)		52	5	12		
Ankerite	2.97	2.96	0.496	9.32			14.9	2.1	5.7		
$\text{Ca}(\text{Fe},\text{Mg})(\text{CO}_3)_2$		2.86		9.3			22	0	1		
Magnesite MgCO_3	2.87	2.87	0.499		44 (144)	75 (246)					5.84
Evaporites, Salt											
Halite	2.16	2.03	0.479	4.65	67 (220)	116 (381)	748	-2.2	-1.8	5.6...6.3	5.55
NaCl		2.04		4.7	67 (220)	120 (394)	754	-2	-3		
Sylvite	1.99	1.87	0.483	8.51	74 (243)	140 (459)	546	-2.7	-4.1	4.6...4.8	6.40
KCl		1.86		8.5			565	-2	-3		
Carnallite	1.60	1.56	0.511	4.09	81 (266)		365	49.1	58.4		
$\text{KMgCl}_3 \cdot 6\text{H}_2\text{O}$		1.57		4.1			369	41	60+		
Kainite	2.15	2.14	0.506	3.50			196				
$\text{KMg}(\text{SO}_4)\text{Cl} \cdot 3\text{H}_2\text{O}$		2.12		3.50			195	40	60+		

Kieserite $\text{MgSO}_4 \cdot \text{H}_2\text{O}$	2.57 2.59	2.59 0.506	0.506 1.83			13.9 14	38 43	
Phosphates								
Chlorapatite $\text{Ca}_5(\text{PO}_4)_3\text{Cl}$	3.18 3.18	3.18 0.495	0.495 6.06			131 130	-1 -1	-1 1.38
Fluorapatite $\text{Ca}_5(\text{PO}_4)_3\text{F}$	3.20 3.21	3.21 0.496	0.496 5.82	45 (148) 42 (138)	80 (262)	10.3 8.5	-0.7 -1	-0.2 -2
Carbonapatite $\text{Ca}_{10}(\text{PO}_4)_6\text{CO}_3\text{H}_2\text{O}$	3.28 3.13	3.31 0.498	0.498 5.58			11.4 9.1	5 5	8
Hydroxyapatite $\text{Ca}_5(\text{PO}_4)_3\text{OH}$	3.16 3.17	3.17 0.498	0.498 5.81	43 (141) 42 (138)	70 (230)	11.5 9.6	5.5 5	6.7 8
Monazite (Ce,La,Y, Th,Nd,Pr)PO ₄	5.27	4.83	0.445			74.5		
Sulfides, Sulfates								
Pyrite FeS_2	5.01 4.99	5.00 0.483	0.483 16.97	38 (125) 17	59 (194) 39.2 (129)	89.8 62 (203)	-2.2 90	-1.9 -2
Marcasite FeS_2	4.88 4.87	4.86 0.483	0.483 16.97			87.7 88	-2 -2	-3 -3
Pyrrhotite Fe_7S_8	4.62 4.53	4.55 0.479	0.479 20.55	65 (213) 21	111 (365)	94.6 94	-2.3 -2	-2.1 -3
Sphalerite ZnS	4.10 3.85	3.94 0.472	0.472 35.93	57 (187) 36	108 (354)	40.9 25		7.8...8.1 -3
Chalkopyrite Cu_2S	4.09 4.07	3.96 0.474	0.474 26.72			98.8 102	-2.0 -2	-1.2 -3

(Continued)

Minerals	References: First line Baker Atlas—Log Interpretation Charts, 1985 Second line Schlumberger—Log Interpretation Charts, 2000								SLB, 2000	C-H, 1995	
	ρ_b	ρ_{\log}	Z/A	PE	Δt_p	Δt_s	Σ	ϕ_N	ϕ_N	ε	λ
Galena	7.60	6.47	0.410	1631			13.2				2.28
PbS		6.39		1630			13	-3	-3		
Sulfur	2.07	2.02		5.43	122 (400)		20.1				
S		2.02		5.4	122 (400)		20	-2	-3		
Anhydrite	2.96	2.98	0.499	5.06	54 (177)	98 (322)	12.3	-1.2	-0.7	6.3	
CaSO_4		2.98		5.1	50 (164)			-1	-2		4.76
Gypsum	2.31	2.33	0.511	3.99	53 (174)		18.8	58.5	57.6	4.1	
$\text{CaSO}_4 \cdot 2\text{H}_2\text{O}$		2.35		4.0	52 (171)			50+	60+		1.26
Barite	4.48	4.09	0.466	266.8	69 (226)	133 (436)	21.0	-1.0	0.2	6.8	
BaSO_4		4.09		267				-1	-2		1.31
Polyhalite	2.78	2.79	0.501	4.32	58 (190)		23.6	16.5	21.6		
$\text{K}_2\text{Mg Ca}_2(\text{SO}_4)_4 \cdot 2\text{H}_2\text{O}$		2.79		4.3			24	14	25		
Coals											
Anthracite	1.60	1.57	0.513	0.16	105 (344)		10.49	46.1	41.4		
$\text{C}_{720}\text{H}_{258}\text{N}_6\text{O}_{16}$		1.47		0.16	105 (344)		8.7	37	38		
Bituminous	1.35	1.33	0.527	0.17	120 (394)		16.36	>60	>60		
$\text{C}_{532}\text{H}_{418}\text{N}_8\text{O}_{41}$		1.24		0.17	120 (394)		14	50+	60+		
Lignite	1.10	1.05	0.525	0.20	160 (525)		12.79	55.6	54.2		
$\text{C}_{480}\text{H}_{412}\text{N}_7\text{O}_{101}$		1.19		0.20	160 (525)		13	47	52		

Graphite C	2.27	2.24	0.500	100 (328)	164 (538)	0.41			155	
Fe-, Mn-, Ti-oxides										
Hematite Fe_2O_3	5.27	5.19	0.476	21.48	46 (151)	72 (236)	101	5.5	12.6	11.28
		5.18		21			101	4	11	
Magnetite Fe_3O_4	5.20	5.10	0.475	22.24	72 (236)	155 (509)	103	4.5	11.2	5.10
		5.08		22	73 (240)		103	3	9	
Limonite $\text{FeO}(\text{OH}) \cdot (\text{H}_2\text{O})_{2.05}$	3.60	3.60	0.505	13.00	57 (187)	103 (338)	71.1	>60	>60	9.9...10.9
		3.59		13	57 (187)	102.6 (337)	71	50+	60+	
Ilmenite FeTiO_3	4.79	4.68	0.474	16.63			164	3.6	9.8	2.38
Rutile TiO_2	4.25	4.13	0.476	10.08	33 (108)	61 (200)	195	3.3	9.4	5.12

Some Conversions

You will find an Excel worksheet on the website <http://www.elsevierdirect.com/companion.jsp?ISBN=9780444537966> for conversions: Conversion units.

Length

$$1 \text{ m} = 3.281 \text{ ft} = 39.37 \text{ in.} \quad 1 \text{ ft} = 0.3048 \text{ m} = 12.00 \text{ in.}$$

$$1 \text{ in.} = 0.0833 \text{ ft} = 0.0254 \text{ m}$$

Velocity

$$1000 \text{ m s}^{-1} = 3280.8 \text{ ft s}^{-1} \quad 1000 \text{ ft s}^{-1} = 304.8 \text{ m s}^{-1}$$

Slowness

$$100 \mu\text{s m}^{-1} = 30.48 \mu\text{s ft}^{-1} \quad 100 \mu\text{s ft}^{-1} = 328.08 \mu\text{s m}^{-1}$$

Density

$$1000 \text{ kg m}^{-3} = 1.000 \text{ g cm}^{-3} = 0.0361 \text{ lb in}^{-3}$$

$$0.100 \text{ lb in}^3 = 2767.8 \text{ kg m}^{-3} = 2.768 \text{ g cm}^{-3}$$

Pressure

$$1000 \text{ Pa} = 0.010 \text{ bar} = 0.00987 \text{ atm} = 0.145 \text{ psi}$$

$$0.010 \text{ atm} = 1013 \text{ Pa} = 0.0101 \text{ bar} = 0.147 \text{ psi}$$

$$1.00 \text{ bar} = 10,000 \text{ Pa} = 0.98693 \text{ atm} = 14,504 \text{ psi}$$

$$1.00 \text{ psi} = 6895 \text{ Pa} = 0.06895 \text{ bar} = 0.06805 \text{ atm}$$

Thermal conductivity

$$1.00 \text{ W m K}^{-1} = 2.388 \text{ mcal cm}^{-1} \text{ s}^{-1} \text{ }^{\circ}\text{C}$$

$$1 \text{ mcal cm}^{-1} \text{ s}^{-1} \text{ }^{\circ}\text{C} = 0.419 \text{ W m}^{-1} \text{ K}^{-1}$$

Specific heat capacity

$$1 \text{ J kg}^{-1} \text{ K}^{-1} = 0.2388 \text{ mcal g}^{-1} \text{ }^{\circ}\text{C} \quad 1.00 \text{ mcal g}^{-1} \text{ }^{\circ}\text{C} = 4.187 \text{ J kg}^{-1} \text{ K}^{-1}$$

Temperature

$$\text{Temperature in K} = (\text{Temperature in } ^{\circ}\text{C}) + 273.16$$

$$\text{Temperature in } ^{\circ}\text{C} = 5/9 * (\text{Temperature in } ^{\circ}\text{F} - 32)$$

$$\text{Temperature in } ^{\circ}\text{F} = 32 + 1.8 * (\text{Temperature in } ^{\circ}\text{C})$$

Files available on the website [http://www.elsevierdirect.com/ companion.jsp? ISBN=9780444537966](http://www.elsevierdirect.com/companion.jsp?ISBN=9780444537966)

Worksheet conversions: There are two worksheets for conversions. Type input data in yellow fields and read converted in white fields.

File	Content
Conversion units	<i>Units:</i> Conversion for temperature, length, volume, mass, density, pressure, velocity and slowness, thermal conductivity, specific heat capacity between SI and other used units.
Conversion elastic parameters	<i>Moduli:</i> Conversion of any combination of two elastic parameters in a different combination for isotropic materials (Table 6.1). In a second worksheet, the moduli are calculated from velocities and density.

Worksheets models and equations: There are worksheets for different models and equations. All worksheets have a similar shape:

- In a green field you will find the relevant equations.
- Input data (e.g., material properties) must be typed into yellow fields. You can also use your own input parameters, of course.
- Variables in the calculation area are in a blue field. Variables are, for example, porosity or aspect ratio. You can also modify the values of the variables.
- The white fields are calculation cells and results.
- In some cases, at the lower end you will find a graphical presentation of calculated data.

If you wish to compare your measured data with model calculations, add your data set to the graphics and modify the input parameters for calculation.

File	Content	Figure in text
<i>Nuclear</i>		
Vsh-GR	<i>Vsh-GR</i> : Relationship between gamma ray index and shale content for different empirical equations.	5.4
<i>Elastic_Mechanical</i>		
Bound models	<p>There are two worksheets:</p> <p><i>Voigt_Reuss_Hashin</i>: For a two-component layered model (solid, fluid), the elastic moduli (compressional modulus, shear modulus) are calculated as function of fluid volume fraction (porosity) based on the model of Voigt (upper bound) and Reuss (lower bound), and the Voigt–Reuss–Hill mean value. The velocities are calculated with density.</p> <p>For the same two-component model, the Hashin–Shtrikman upper and lower bounds are calculated.</p>	6.21
	<i>Generalized equation</i> : For a two-component layered model, (solid, fluid), the elastic compressional modulus is calculated as function of fluid volume fraction (porosity) based on the generalized Lichtenegger–Rother equation.	6.23
Inclusion isotropic	<p>There are two worksheets:</p> <p><i>Kuster_Toksöz</i>: Calculation of normalized compressional and shear wave velocity for a two-component material (solid, fluid) as function of porosity. Two models are used: Inclusions are spheres and inclusions are penny-shaped cracks. Calculations for gas and water filled inclusion.</p> <p><i>Budiansky</i>: Calculation of compressional and shear wave velocity as function of fracture parameter epsilon and porosity. For calculation, penny-shaped random distributed inclusions are assumed.</p>	6.26
		6.28

	Additional input parameter is the aspect ratio.	
Inclusion anisotropic	<i>Hudson's model:</i> Calculation of the components of the tensor of elasticity based on the assumption of a VTI medium (horizontal cracks). Additional input parameter is the aspect ratio.	6.30
Fluid replacement	<p>There are two worksheets:</p> <p><i>Gassmann:</i> The worksheet allows a fluid replacement based on Gassmann's equation. Input: compressional and shear wave velocity measured for rock saturated with fluid 1, porosity, compressional modulus, and density of fluid 1 and fluid 2. Output: compressional and shear wave velocity for the rock saturated with fluid 2.</p> <p><i>Example:</i> The worksheet gives a log example for a fluid replacement gas→water.</p>	6.59
Structured model	<p>There are five worksheets for different velocity influences:</p> <p><i>Porosity:</i> Calculation of the porosity effect upon velocity with the quotient of pore aspect ratio to grain aspect ratio as parameter.</p> <p><i>Pressure:</i> Calculation of pressure effect upon velocity controlled by parameters of the contact elasticity.</p> <p><i>Tensor:</i> Calculation of the components of the "structure tensor" as function of structure angle and contact properties. Derivation of velocity ratios (V_p/V_s) and Thomson's anisotropy parameters for the dry rock.</p> <p><i>Velocity grids:</i> Grids are calculated with the equations from worksheet Tensor. Two sets of parameters are used as input (parameter f, angle α).</p> <p>V_p versus strength: Calculation of the relationship between velocity (in this case compressional wave velocity) and compressional strength.</p>	6.38 6.40 6.41 6.42 7.23

(Continued)

(Continued)

File	Content	Figure in text
Shuey AVO	Using <i>Shuey's equation</i> , R_{pp} is calculated as function of the angle Θ for different cases of wet sand, gas sand, and shale. Input: material parameters of the layers.	6.46
<i>Electrical</i> Fractured conductivity	Calculation of electrical conductivity and formation factor as function of fracture porosity. The rock consists of two pore systems: <ul style="list-style-type: none">• Matrix porosity• Fracture porosity (oriented).	8.11
Laminated sediment	Worksheet gives a forward calculation of the vertical and horizontal resistivity as function of volumetric composition for: <ul style="list-style-type: none">• <i>laminated shaly sand</i> with shale resistivity and sand parameters (water resistivity, porosity, water saturation, Archie exponents) as input;• <i>laminated bimodal sand</i> with parameters for a coarse and a fine sand (water resistivity, porosity, water saturation, Archie exponents) as input.	8.18
Shaly sand equations	There are two worksheets: <i>Poupon equation</i> : Forward calculation of formation resistivity as function of water saturation for different shale content V_{sh} . Calculation based on Poupon's equation for laminated shaly sand. <i>Shaly sand equation</i> : For a given formation resistivity and water resistivity as input, you can calculate the resulting water saturation for the following equations: Poupon, Simandoux, and Indonesia. Inputs are also Archie parameters, porosity, and shale resistivity.	8.13 8.15
Permittivity models	Calculation of relative permittivity as function of porosity (two-component composite) with the input parameters	

	permittivity of solid and of fluid.	
	Worksheet for the following models:	
	• Layered model	8.25
	• Generalized	8.27
	Lichtenecker–Rother	8.28
	• CRIM equation	
	• Inclusion model (Clausius–Mossotti) for sphere	
	• Inclusion model (Hanai–Bruggeman) for ellipsoids with depolarization exponent as parameter.	
<i>Thermal</i> Layered models	There are two worksheets: <i>Two components</i> : Calculation of thermal conductivity of a two-component material (solid, fluid) as function of porosity. The following equations are used: Voigt model (parallel, upper bound), Reuss model (series, lower bound), arithmetic mean, geometric mean, Krischer and Esdorn model with parameter a , generalized Lichtenecker–Rother model with parameter α . <i>Ten components</i> : Worksheet for calculation of thermal conductivity of a material consisting of (maximum) 10 components. Input: volume fraction and conductivity of components. Calculation for following models: Voigt model (parallel, upper bound), Reuss model (series, lower bound), Krischer and Esdorn model with parameter a , generalized Lichtenecker–Rother model with parameter α .	9.12 9.13 9.14 Table 9.14
Inclusion models	There are three worksheets: <i>Spheres</i> : Calculation of thermal conductivity as function of volume fraction for a two-component material under assumption of: • spherical pores as inclusion in a solid host material,	9.15

(Continued)

(Continued)

File	Content	Figure in text
	<ul style="list-style-type: none"> • spherical grains as inclusion in a fluid host material. <p><i>Disk random:</i> Calculation of thermal conductivity as function of volume fraction for a two-component material under assumption of:</p> <ul style="list-style-type: none"> • spherical pores, • disk-shaped random oriented pores as inclusion in a solid host material. <p><i>Ellipsoids oriented:</i> Calculation of thermal conductivity as function of volume fraction for a two-component material under assumption of ellipsoidal inclusions with orientation. Calculations deliver thermal conductivity for x-, y-axis and z-axis. Additional input parameter is aspect ratio.</p>	9.17
<i>Relationships</i>		
VR_Hill_mean	Voigt–Reuss–Hill mean value for elastic properties, velocities, and thermal conductivity is calculated for a 10-component mineral composite. Input: elastic parameters, density, thermal conductivity. Variable: volume fractions.	9.16
Defect model	<p>Based on the defect model, the relationship between thermal conductivity and compressional wave velocity is calculated.</p> <p>The controlling input parameter A_{solid} describes the influence of mineral composition, whereas the defect parameter D controls the effects of fractures, etc. The calculated curves are compared with some experimental data.</p>	11.10
Inclusion model	<p>A correlation between thermal conductivity and compressional wave velocity is calculated based on the application of:</p> <ul style="list-style-type: none"> • the Budiansky and O'Connell model for elastic properties, 	11.13

- the Clausius–Mossotti model for thermal conductivity.

Both models have as input the properties of the components (solid, inclusion), porosity, and aspect ratio.

The calculated curves for two cases are compared with on some experimental data.

Examples:

Examples

Example-Sandstone	The example from the textbook (Darling, 2005) is used to demonstrate core and log data analysis.	2.40
	<i>Core analysis:</i>	
	• Porosity-permeability regression	2.38
	• Capillary pressure analysis	2.39
	• Application of Leverett's and Thomeer's equation	2.40
	• Derivation of Archie parameters	
	<i>Log analysis:</i>	
	• Calculation of V_{shale}	5.12
	• Calculation of porosity	5.13
	• Calculation of water saturation	5.14
	• Permeability estimate.	
Example-Carbonate	The example demonstrates the calculation of mineral fraction (calcite, dolomite) and porosity from neutron log and density log using crossplot and matrix inversion technique. Worksheet <i>crossplot</i> presents the density and neutron data; you can move the plot upward to fit with the chartbook plot. Worksheet <i>analysis</i> gives the calculation for mineral composition and porosity.	11.4
		11.5
		11.6

References

Abdalla, W., Buckley, J.S., Carnegie, A., Herold, J.E.B., Fordham, E., Graue, A., et al., 2007. Fundamentals of wettability. *Oilfield Rev.* Schlumberger 2007, 44–61.

Abu-Hamdeh, N.H., Reeder, R.C., 2000. Soil thermal conductivity: effects of density, moisture, salt concentration, and organic matter. *Soil Sci. Soc. Am. J.* 64, 1285–1290.

Ahmed, T., 2001. *Reservoir Engineering Handbook*. Butterworth-Heinemann, Woburn, MA.

Akbar, M., Vissapraganda, B., Alghamdi, A.I., 2000/2002. A snapshot of carbonate reservoir evaluation. *Oilfield Rev.* Winter, 20–41.

Akbar, M., Petricola, M., Watfa, M., Badri, M., Boyd, A., Charara, M., et al., 1995. Classic interpretation problems: evaluating carbonates. *Oilfield Rev.* Schlumberger January, 38–57.

Aki, K., Richards, P.G., 1980. *Quantitative Seismology: Theory and Methods*. W.H. Freeman and Co., San Francisco, CA.

Akkurt, R., Vinegar, H.J., Tutunjian, P.N., Guillory, A.J., 1995. NMR logging of natural gas reservoirs. *Transactions of the SPWLA 36th Annual Logging Symposium*, paper N.

Akkurt, R., Vinegar, H.J., Tutunjian, P.N., Guillory, A.J., 1996. NMR logging in natural gas reservoirs. *Log Analyst* November–December, 33–42.

Akkurt, R., Mardon, D., Gardner, J.S., Marshall, D.M., Solanet, F., 1998. Enhanced diffusion: expanding the range of NMR direct hydrocarbon-typing applications. *Transactions of the SPWLA 39th Annual Logging Symposium*, paper GG.

Al-Awadi, M., Clark, W.J., Herron, M., Zang, T., Zhao, W., Hurley, N., et al., 2009. Dolomite: perspectives on a perplexing mineral. *Oilfield Rev.* Schlumberger Autumn 2009, 32–45.

Alexandrov, K.S., Belikov, B.P., Rysova, T.V., 1966. Vycislenie uprugich parametrov gornich porod po mineralnomu sostavu. *Izvestia A. N. SSSR Ser. Geol. Moskva* 2, 3–19.

Alger, R.P., Locke, S., Nagel, W.A., Sherman, H., 1971. The dual-spacing neutron log—CNL. In: 46th Annual Fall Meeting SPE, paper SPE 3565.

Allen, L.S., Mills, W.R., Desai, K.P., Caldwell, R.L., 1972. Some features of dual-spaced neutron porosity logging. In: 13th Annual Logging Symposium Transactions, Society of Professional Log Analysts (SPWLA), paper P.

Altunbay, M., Georgi, D., Takezaki, H.M., 1997. Permeability prediction for carbonates: still a challenge? Presented at the Middle East Oil Show and Conference, 15–18 March, Bahrain, paper SPE 37753.

Anderson, W.G., 1986. Wettability literature survey, 3: the effect of wettability on the electrical properties of porous media. *J. Pet. Technol.* 38, 1371–1378.

Amyx, J.W., Bass, D.M., Whiting, R.L., 1960. *Petroleum Reservoir Engineering Physical Properties*. McGraw-Hill, New York, NY.

Anderson, B.I., Barber, T.D., Lüling, M.G., Sen, P.N., 2006. Observations of large dielectric effects on induction logs, or, can source rocks be detected with induction measurements. In: SPWLA 47th Annual Logging Symposium Transactions, June 4–7, paper OOO.

Angenheister, G., Soffel, H., 1972. *Gesteinsmagnetismus und Paläomagnetismus*. Gebr. Borntraeger, Stuttgart.

Annan, A.P., Davis, J.L., 1978. High-frequency electrical methods for the detection of freeze-thaw interfaces. In: Proceedings of 3rd International Conference on Permafrost Geophysics, Nat. Res. Council, Canada, pp. 495–500.

API, 1959. Recommended Practice for Standard Calibration and Form for Nuclear Logs. API—American Petroleum Institute, Houston, TX.

Appel, M., 2004. Tutorial nuclear magnetic resonance and formation porosity. *Petrophysics* 45 (3), 296–307.

Archer, J.S., Jing, X.D., 1991. The influence of reservoir condition measurements of shaly sand electrical properties on equity studies. In: Transactions of 14th European Formation Evaluation Symposium of the SPWLA, London, 1–24, paper L.

Archie, G.E., 1942. Electrical resistivity log as an aid in determining some reservoir characteristics. *Trans. AIME* 31, 350–366.

Archie, G.E., 1950. Introduction to petrophysics of reservoir rocks. *AAPG Bull.* 34, 943–961.

Armstrong, P., Ireson, D., Chmela, B., Dodds, K., Esmersoy, C., Miller, D., et al., 1994. The promise of elastic anisotropy. *Oilfield Rev. Schlumberger* 8, 36–47.

Arns, C.H., Averdunk, H., Baugé, H., Sakellariou, A., Senden, T.J., Sheppard, A.T., et al., 2004. Digital core laboratory: analysis of core fragments from 3D images. In: SPWLA 45th Annual Logging Symposium Transactions, Nordwijk, paper EEE.

Arps, J.J., 1953. The effect of temperature on the density and electrical resistivity of sodium chloride solutions. *J. Pet. Technol.* 195, 17–20, Technical Note.

Assquith, G., Krygowski, D., 2004. Basic Well Log Analysis, second ed., AAPG Methods in Exploration Series 16, Tulsa.

Ass'ad, J., Tatham, R., McDonald, J.A., 1992. A physical model study of microcrack-induced anisotropy. *Geophysics* 57 (12), 1562–1570.

Assefa, S., McCann, C., Sothcott, J., 1999. Attenuation of P- and S-waves in limestones. *Geophys. Prospect.* 47, 359–392.

Athy, L.F., 1930. Density, porosity and compaction of sedimentary rocks. *Bull. Am. Ass. Pet. Geol.* 14, 1–24.

Attewell, P.B., Ramana, Y.V., 1966. Wave attenuation and internal friction as functions of frequency in rocks. *Geophysics* 31, 1049–1056.

Avseth, P., Mukerji, T., Mavko, G., 2005. Quantitative Seismic Interpretation, Applying Rock Physics Tools to Reduce Interpretation Risk. Cambridge University Press, New York, NY.

Backus, G.E., 1962. Long-wave anisotropy produced by horizontal layering. *J. Geophys. Res.* 67, 4427–4440.

Baker Atlas/Baker Hughes, 1985. Log Interpretation Charts. Baker Hughes Inc., Houston, TX.

Baker Atlas/Western Atlas, 1992. Introduction to Wireline Log Analysis. Western Atlas Inc., Houston, TX.

Baker Atlas, 2002. Introduction to Wireline Log Analysis. Baker Hughes Inc., Houston, TX.

Baldwin, B., Butler, C.O., 1985. Compaction curves. *AAPG Bull.* 14, 1–24.

Balling, N., Kristiansen, J.I., Breiner, N., Poulsen, K.D., Rasmussen, R., Saxov, S., 1981. Geothermal Measurements and Subsurface Temperature Modelling in Denmark, *Geologiske Skrifter*. Aarhus University, Aarhus, Denmark, p. 16.

Bang, J., Solstad, A., Mjaaland, S., 2000. Formation electrical anisotropy derived from induction log measurements in a horizontal well. Presented at the 2000 SPE Annual Technical Conference and Exhibition, Dallas, Texas, 1–4 October, paper SPE 62908.

Bardon, C., Pied, B., 1969. Formation water saturation in shaly sands. In: SPWLA 10th Annual Logging Symposium Transactions, Houston, Texas, 25–28 May, paper Z.

Barson, D., Decoster, E., Grau, J., Herron, M., Herron, S., Guru, U.K., et al., 2005. Spectroscopy: the key to rapid, reliable petrophysical answers. *Oilfield Rev.* Schlumberger Summer 2005.

Barton, N., 2007. Rock Quality, Seismic Velocity, Attenuation and Anisotropy. Taylor & Francis Group/Balkema, Leiden, The Netherlands.

Barton, C.C., Hsieh, P.A., 1989. Physical and hydrologic-flow properties of fractures. 28th International Geological Congress Field Trip Guide Book T385, P-36, AGU, Washington.

Barton, N., Lien, R., Lunde, J., 1974. Engineering classification of rock masses for the design of tunnel support. *Rock Mech.* 6 (4), 189–239.

Bassiouni, Z., 1994. Theory, measurement, and interpretation of well logs, H.L. Doherty Memorial Fund of AIME, SPE.

Bastos, A.C., Dillon, L.D., Vasquez, G.F., Soares, J.A., 1998. Core derived acoustic, porosity and permeability correlations for computation pseudo-logs. In: Harvey, P.K., Lovell, M.A. (Eds.), *Core-Log Integration*, 136. Geological Society, London, pp. 141–146, Special Publication.

Batzle, M., Wang, Z., 1992. Seismic properties of pore fluids. *Geophysics* 57, 1396–1408.

Beard, D.C., Weyl, P.K., 1973. Influence of texture on porosity and permeability of unconsolidated sand. *AAPG Bull.* 57, 349–369.

Beblo, M., Schopper, J.R., Haak, V., 1982. Electrical properties. In: Hellwege, K.-H. (Ed.), *Landolt-Börnstein Numerical Data and Functional Relationships in Science and Technology*, New Series, Group V. Geophysics and Space Research, vol. 1, Physical Properties of Rocks, subvol. Springer-Verlag, Berlin, pp. 239–307.

Beck, A.E., 1976. An improved method of computing the thermal conductivity of fluid-filled sedimentary rocks. *Geophysics* 41, 133–144.

Belikov, B.P., Alexandrov, K.S., Rysova, T.W., 1970. *Uprugie Svoistva Porodo-Obrasujscich Mineralov i Gornich Porod*. Izdat. Nauka, Moskva.

Berg, R.R., 1970. Method for determining permeability from reservoir rock properties. *Trans. Gulf Coast Ass. Geol. Soc.* 20, 303–317.

Berktold, A., 1982. Elektrische Leitfähigkeit von Lösungen reiner Salze und von natürlichen Wässern. In: *Landolt-Börnstein Zahlenwerte und Funktionen aus Naturwissenschaft und Technik*, Neue Serie V. Springer-Verlag, Berlin, 1b.

Berryman, J., 1995. Mixture theories for rock properties. In: Arens, T.J. (Ed.), *A Handbook of Physical Constants*. American Geophysical Union, pp. 205–228.

Berzon, J.S., 1977. *Seismiceskaja Razvedka Vertikalno Sloistych sred Fundamenta*. Izdat. Nedra, Moskva.

Best, A.I., 1995. Classification of rocks and their abundances on the earth, rock physics and phase relations—a handbook of physical constants. AGU Reference Shelf 3, American Geophysical Union.

Best, M.E., Katsebe, T.J., 1995. Shale permeability and its significance in hydrocarbon exploration. *Leading Edge*, 165–170.

Bieniawski, Z.T., 1989. *Engineering Rock Mass Classifications*. John Wiley & Sons, New York, NY.

Bigelow, E.L., 1991. Geological log analysis of a carbonate reservoir. In: *SPWLA 14th European Formation Evaluation Symposium Transactions*, London.

Bigelow, E., 1992. *Introduction to Wireline Log Analysis*. Western Atlas Inc., Houston, TX.

Bigelow, E.L., Howell, E.P., 1995. Practical analysis of formation strength properties in both consolidated and unconsolidated reservoirs. In: *SPWLA 36th Annual Logging Symposium Transactions*, 26–29 June, paper TTT.

Binley, A., Slater, L.D., Fukes, M., Cassaini, G., 2005. Relationship between spectral induced polarization and hydraulic properties of saturated and unsaturated sandstone. *Water Resour. Res.* 41, W12417, doi:10.1029/2005WR004202.

Biot, M.A., 1956a. Theory of propagation of elastic waves in a fluid-saturated porous solid (I. Low frequency range). *J. Acoust. Soc. Am.* 28 (2), 168–178.

Biot, M.A., 1956b. Theory of propagation of elastic waves in a fluid-saturated porous solid (II. Higher frequency range). *J. Acoust. Soc. Am.* 28 (2), 179–191.

Biot, M.A., 1962. Generalized theory of acoustic propagation in dissipative media. *J. Acoust. Soc. Am.* 34 (9), 1254–1264.

Birch, F., 1961. The velocity of compressional waves in rocks to 10 kilobars, part II. *J. Geophys. Res.* 66, 2199–2224.

Birch, F., Clarke, H., 1940. The thermal conductivities of rocks and its dependence upon temperature and composition (I., II.). *Am. J. Sci.* 238, 8–9, 529–558 and 613–635.

Blackwell, D.D., Steele, J.L., 1989. Thermal conductivity of sedimentary rocks: measurement and significance. In: Naeser, N.D., McCulloh, T.H. (Eds.), *Thermal History of Sedimentary Basins*. Springer-Verlag, New York, NY.

Blatt, H., Middleton, G.V., Murray, R.C., 1972. *Origin of Sedimentary Rocks*. Prentice Hall Inc.

Bleil, U., Petersen, N., 1982. Magnetic properties of minerals. In: Hellwege, K.-H. (Ed.), *Landolt-Börnstein Numerical Data and Functional Relationships in Science and Technology*, New Series, Group V. Geophysics and Space Research, vol. 1, Physical Properties of Rocks, subvol. B. Springer-Verlag, Berlin, pp. 308–365.

Börner, F., 1991. Untersuchungen zur komplexen elektrischen Leitfähigkeit von Gesteinen im Frequenzbereich von 1 Millihertz bis 10 Kilohertz, Dissertation–Thesis, Bergakademie Freiberg.

Börner, F., 1992. Complex conductivity measurements of reservoir properties. In: *Proceedings of the Third European Core Analysis Symposium*, Paris, pp. 359–386.

Börner, F., 1995. Estimation of hydraulic conductivity from complex electrical measurements. In: SCA Conference San Francisco, paper No. 9523.

Börner, F., 2006. Complex conductivity measurements. In: Kirsch, R. (Ed.), *Groundwater Geophysics*. Springer-Verlag, Berlin.

Börner, F., Gruhne, M., Schön, J., 1993. Contamination indications derived from electrical properties in the low frequency range. *Geophys. Prospect.* 41, 83–98.

Börner, F.D., Schön, J.H., 1991. A relation between the quadrature component of electrical conductivity and the specific surface area of sedimentary rocks. *Log Analyst* 32, 612–613.

Börner, F.D., Schön, J.H., 1995. Low frequency complex conductivity measurements of microcrack properties. *Surv. Geophys.* 16, 121–135.

Börner, F.D., Schopper, F.D., Weller, A., 1996. Evaluation of transport and storage properties in the soil and groundwater zone from induced polarization measurements. *Geophys. Prospect.* 44, 583–602.

Borysenko, A., Clennell, B., Burger, I., Josh, M., Sede, R., Ralston, J., et al., 2009. Monitoring of fluid saturation and oil-water displacement using dielectric and NMR measurements. In: *Transactions on SPWLA 50th Annual Logging Symposium*, June 21–24, paper VVV.

Bourbie, T., Coussy, O., Zinzner, B., 1987. *Acoustics of Porous Media*. Gulf Publishing Company, Houston, TX.

Boyd, A., Darling, H., Tabanou, J., 1995. The lowdown on low-resistivity pay. *Oilfield Rev. Schlumberger Autumn*, 4–10.

Brandt, H., 1955. A study of the speed of sound in porous granular media. *J. Appl. Mech.* 22, 479–486.

Bratton, T., Canh, D.V., Que, N.V., Duc, N.V., Gillespie, P., Hunt, D., et al., 2006. The nature of naturally fractured reservoirs. *Oilfield Rev. Schlumberger Summer*, 4–23.

Brie, A., Pampuri, F., Marsala, A.F., Meazza, O., 1995. Shear sonic interpretation in gas-bearing sands. In: 70th SPE Annual Technical Conference and Exhibition, Dallas, TX, paper SPE30595.

Brigaud, F., Vasseur, G., Caillet, G., 1989. Use of well log data for predicting detailed in situ thermal conductivity profiles at well sites and estimation of lateral changes in main sedimentary units at basin scale. In: Maury, V., Fourmaintraux, D. (Eds.), *Rock at Great Depth*. Balkema, Rotterdam.

Brigaud, F., Vasseur, G., Caillet, G., 1992. Thermal state in the north Viking Graben (North Sea) determined from oil exploration well data. *Geophysics* 57 (1), 69–88.

Brooks, C., Purcell, W., 1952. Surface area measurements on sedimentary rocks. *AIME Pet. Trans.* 195, 289–296.

Brooks, R.J., Corey, A.T., 1964. Hydraulic properties of porous media, *Hydrol. Papers* 3. Colorado State University, Fort Collins, CO.

Brown, A., 1997. Porosity variation in carbonates as a function of depth: Mississippian Madison Group, Williston Basin. In: Kupecz, J.A., Gluyas, J., Bloch, S. (Eds.), *Reservoir Quality Prediction in Sandstones and Carbonates*, AAPG Memoir 69, 29–46.

Brown, R., Korringa, J., 1975. On the dependence of the elastic properties of a porous rock on the compressibility of the pore fluid. *Geophysics* 40, 608–616.

Bruggeman, D.A.G., 1935. Berechnung verschiedener physikalischer Konstanten von heterogenen Substanzen. I: Dielektrizitätskonstanten und Leitfähigkeiten der Mischkörper aus isotropen Substanzen. *Ann. Phys.* 24, 636–679.

Brunauer, S., Emmett, P., Teller, E., 1938. Adsorption of gases on multimolecular layers. *J. Am. Chem. Soc.* 60 (2), 309–319.

Bücker, Ch., Rybach, L., 1996. A simple method to determine heat production from gamma-ray logs. *Mar. Pet. Geol.* 13 (4), 373–375.

Bücker, C., Huenges, E., Lippmann, E., Rauen, A., Wienand, J., Wolter, K.E., 1989. Gammaspektrometrie und Wärmeproduktionsrate, KTB-Report 89-3, Projektleitung KTB im NLFB, 476.

Buckley, J.S., Fan, T., 2007. Crude oil/brine interfacial tensions. *Petrophysics* 48 (3), 175–185.

Budiansky, B., O'Connell, R.J., 1976. Elastic moduli of a cracked solid. *Int. J. Solids Struct.* 12, 81–97.

Bulatova, S.M., Volkova, E.A., Dubrov, E., 1970. Akusticeski Karotas. Izdat. Nedra, Leningrad.

Burianik, M., 2000. Amplitude vs. offset and seismic rock property analysis: a primer. CSEG Record. November, 6–14.

Calvert, T.J., Rau, R.N., Wells, L.E., 1977. Electromagnetic propagation—a new dimension in logging. In: 47th Annual California Regional Meeting SPE, paper SPE 6542.

Carcione, J.M., 2001. *Wave Fields in Real Media: Wave Propagation in Anisotropic Anelastic and Porous Media*. Pergamon Press.

Carcione, M., Seriani, G., 2000. An electromagnetic modelling tool for the detection of hydrocarbons in the subsoil. *Geophys. Prospect.* 48, 231–256.

Carmichael, R.S., 1989. *Practical Handbook of Physical Properties of Rocks and Minerals*. CRC Press, Boca Raton, FL.

Carmona, R., Hernandez, J., Marcos, J., Minetto, C., Arro, R., 2010. Application of RMN using a probabilistic method into the Echoes inversion. *Petroleum World, Latin American Energy, Oil & Gas, Venezuela, Bolivia, Trinidad, Peru*, August 29. <http://www.petroleumworld.com/sf09110101.htm>.

Carr, H.Y., Purcell, E.M., 1954. Effects of diffusion on free precession in nuclear magnetic resonance experiments. *Phys. Rev.* 94, 630–638.

Carlslaw, H.S., Jaeger, J.C., 1959. *Conduction of Heat in Solids*. Clarendon Press, Oxford.

Castagna, J.P., 1993. Amplitude-versus-offset analysis; tutorial and review. In: Castagna, J.P., Backus, M.M. (Eds.), *Offset-Dependent Reflectivity—Theory and Practice of AVO Analysis*. Society of Exploration Geophysicists.

Castagna, J.P., Batzle, M.L., Eastwood, R.L., 1985. Relationships between compressional-wave and shear-wave velocities in clastic silicate rocks. *Geophysics* 50, 571–581.

Castagna, J.P., Batzle, M.L., Kan, T.K., 1993. Rock physics—the link between rock properties and AVO response. In: Castagna, J.P., Backus, M.L. (Eds.), *Offset-Dependent Reflectivity—Theory and Practice of AVO Analysis. Investigations in Geophysics*, 8. pp. 135–171.

Cattaneo, C., 1938. Sul contatto di due corpi elastici. *Accad. Lincei* 27, 342–348, 434–436, 474–478.

Cermak, V., Rybach, L., 1982. Thermal properties. In: Hellwege, K.-H. (Ed.), *Landolt-Börnstein Numerical Data and Functional Relationships in Science and Technology, New Series, Group V. Geophysics and Space Research, vol. 1, Physical Properties of Rocks*, subvol. A. Springer-Verlag, Berlin, pp. 305–371.

Cermak, V., Bodri, L., Rybach, L., Buntebarth, G., 1990. Relationship between seismic velocity and heat production: comparison of two sets of data and test of validity. *Earth Planet. Sci. Lett.* 99 (1990), 48–57.

Cerniak, G.J., 1964. *Dielectriceskie Metody Issledovania Vlashnych Gruntov*. Izdat. Nedra, Moskva.

Chang, Ch., 2004. Empirical rock strength logging in boreholes penetrating sedimentary formations, geology and earth environmental sciences, Chungnam National University. Daejeon 7 (3), 174–183.

Chang, D., Vinegar, H., Morriss, C., Straley, C., 1997. Effective porosity, producible fluids, and permeability in Carbonates from NMR logging. *Log Analysts* 38 (2), 60–72.

Chase, D.M., Schmidt, M.G., Ducheck, M.P., 1985. The Multiparameter Spectroscopy Instrument Continuous Carbon/Oxygen Log—MSI C/O, Canadian Well Logging Society 10th Formation Evaluation Symposium, Calgary, 1985.

Chelidze, T.L., Gueguen, Y., 1999. Electrical spectroscopy of porous rocks: a review—I. Theoretical models. *Geophys. J. Int.* 137, 1–15.

Chen, S., Georgi, D.T., 1997. Permeability from NMR Relaxation Data. Baker Atlas, Houston, TX, 4 p. (unpublished).

Chen, S., Georgi, D.T., Withjack, E.M., Minetto, C., Olima, O., Gamin, H., H., 2000. Estimation of oil viscosity with multiple *TE* dual wait-time MRIL logs. *Petrophysics* 41 (1), 33–40.

Chen, S., Munkholm, M., Shao, W., Jumagaziyev, D., Begova, N., 2006. Application of NMR logging for characterizing movable and immovable fractions of viscose oils in Kazakhstan heavy oil field, 47th Annual SPWLA Logging Symposium Transactions, Paper DD.

Cheng, A., 2008. Future developments in rock physics—a personal view, 17 June, Cambridge GeoSCIENCES.

Cheng, C.H., 1993. Crack models for a transversely anisotropic medium. *J. Geophys. Res.* 98, 675–684.

Cheng, C.H., Johnston, D.H., 1981. Dynamic and static moduli. *Geophys. Res. Lett.* 8 (1), 39–42.

Cheng, C.H., Toksöz, M.N., 1979. Inversion of seismic velocities for the pore aspect ratio spectrum of a rock. *J. Geophys. Res.* 84, 7533–7543.

Chi, X.-G., Han, D., 2009. Lithology and fluid differentiation using a rock physics template. *Leading Edge* January, 60–65.

Cholach, P.Y., Schmitt, D.R., 2006. Seismic anisotropy of shales. *CSEG Record*. September, 39–43.

Chopra, S., Chemingui, N., Miller, R., 2005. An introduction to this special section—carbonates. *Leading Edge* May, 488–489.

Choquette, P.W., Pray, L.C., 1970. Geologic nomenclature and classification of porosity in sedimentary carbonates. *Bull. Am. Assoc. Petrol. Geol.* 54, 207–250.

Christensen, N.J., Salisbury, U.H., 1975. Structure and constitution of the lower oceanic crust. *Rev. Geophys. Space Phys.* 13, 57–86.

Clark Jr., S.P., (Ed.), 1966. *Handbook of Physical Constants*. The Geological Society of America, Inc., New York.

Clauser, C., 2006. Geothermal energy. In: Heinloth, von K. (Ed.), *Landolt-Börnstein Numerical Data and Functional Relationships in Science and Technology*, New Series, Group VIII. Advanced Materials and Technologies, vol. 3, Energy Technologies, subvol. C: Renewable Energies. Springer-Verlag, Berlin, pp. 493–604.

Clauser, C., Huenges, E., 1995. Thermal conductivity of rocks and minerals, in: *Rock Physics and Phase Relations—A Handbook of Physical Constants*, AGU Reference Shelf 3, American Geophysical Union.

Clauser, C., Koch, A., 2006. Erstellung statistisch abgesicherter thermischer und hydraulischer Gesteinseigenschaften für den flachen und tiefen Untergrund in Deutschland, Phase 1—Westliche Molasse und nördlich angrenzendes Süddeutsches Schichtstufenland, Bericht zum BMU-Projekt FKZ 0329985, internet: http://www.geophysik.rwth-aachen.de/html/geothermik_thermostat.htm (download September 2009)

Clauser, C., Hartmann, A., Koch, A., Mottaghy, D., Pechnig, R., Rath, V., 2007. Erstellung statistisch abgesicherter thermischer und hydraulischer Gesteinseigenschaften für den flachen und tiefen Untergrund in Deutschland, Phase 1—Westliche Molasse und nördlich angrenzendes Süddeutsches Schichtstufenland, Final report for BMU-Projekt FKZ 0329985, RWTH Aachen, Archived at the TIB Hannover <http://www.tib-hannover.de>, also at http://www.geophysik.rwth-aachen.de/html/geothermik_thermostat.htm (downloaded Sept. 2009).

Clavier, C., Coates, G., Dumanoir, J., 1977. The theoretical and experimental bases for the “dual water” model for the interpretation of shaly sands, SPE paper No. 6859.

Clavier, C., Coates, G., Dumanoir, J., 1984. The theoretical and experimental bases for the “dual water” model for the interpretation of shaly sands. *Soc. Pet. Eng. J.* 24 (2), 153–168.

Coates, G.R., Denoo, S.A., 1981. Mechanical properties program using borehole analysis and Mohr’s circle, in: *SPWLA 22nd Annual Logging Symposium Transactions*, Mexico City, Mexico, 23–26 June, paper DD.

Coates, G.R., Denoo, S., 1988. The producibility answer product. *Schlumberger Tech. Rev.* 29 (2), 55.

Coates, G.R., Miller, M., Gillen, M., Henderson, G., 1991. The MRIL in Conoco 33-1: an investigation of a new magnetic resonance imaging log. Presented at the *SPWLA 32nd Annual Logging Symposium*, Midland, Texas, 16–19 June, paper DD.

Coates, G.R., Miller, D.L., Mardon, D., Gardener, J.S., 1995. Applying log measurements of restricted diffusion and T_2 to formation evaluation, *Transactions 36th Annual Logging Symposium*, paper P.

Coates, G.R., Xiao, L., Prammer, M., 1999. *NMR Logging—Principles and Applications*. Gulf Publishing Company, Halliburton Energy Services Publication, Houston, TX, H02308.

Cole, K.S., Cole, R.H., 1941. Dispersion and absorption in dielectrics. *J. Chem. Phys.* 9, 341.

Collett, L.S., 1959. Laboratory investigation of overvoltage. In: Wait, J.R. (Ed.), *Overvoltage Research and Geophysical Applications*. Pergamon Press.

Committee on Fracture Characterization and Fluid Flow, U.S. National Committee for Rock Mechanics, 1996.

Corey, A.T., 1994. Mechanics of Immiscible Fluids in Porous Media. Water Resources Publications, Highland Ranch, CO.

Cosentino, L., 2001. *Integrated Reservoir Studies*. Editions Technip, Paris.

Cosenza, P., Ghorbani, A., Camerlynck, C., Reijiba, F., Guerin, R., Tabbagh, A., 2009. Effective medium theories for modelling the relationships between electromagnetic properties and hydrological variables in geomaterials: a review. *Near Surface Geophysics* 7, 563–578.

Coutanceau-Monteil, N., Jacquin, Ch., 1993. Improvements of the coaxial line technique for measuring complex dielectric permittivities of centimetric samples in the 20 to 1,000 MHz range: application to sedimentary rocks. *Log Analyst* Sept-Oct., 21–33.

Crampin, S., Lovell, J.H., 1991. A decade of shear-wave splitting in the Earth's crust: what does it mean? what use can we make of it? and what should we do next? *Geophys. J. Int.* 107 (3), 387–408.

Dandekar, A.Y., 2006. *Petroleum Reservoir Rock and Fluid Properties*. Taylor & Francis, Boca Raton, FL.

Darcy, H., 1856. *Les Fontaines Publiques de la Ville de Dijon*. V. Dalmont, Paris.

Darling, T., 2005. *Well Logging and Formation Evaluation*. Gulf Profess. Publish./Elsevier Inc.

de Lima, O.A.L., 1995. Water saturation and permeability from resistivity, dielectric, and porosity logs. *Geophysics* 60, 1756–1764.

de Waal, J.A., Smits, R.M., de Graaf, J.D., Schipper, B.A., 1989. Measurement and evaluation of resistivity index curves, in *SPWLA 30th Annual Logging Symposium Transactions*, paper II.

Dearing, J.A., 1994. *Environmental Magnetic Susceptibility*. Chi Publishing, Kenniworth.

Debye, P., Hückel, E., 1923. The theory of electrolytes. I. Lowering of freezing point and related phenomena. *Physikalische Zeitschrift* 24, 185–206.

Deere, D.U., Hendron, A.J., Patton, F.D., Cording, E.J., 1967. Design of surface and near surface construction in rock. In: Fairhurst, C. (Ed.), *Failure and breakage of rock*. Proc. 8th U.S. Symp. Rock Mech, New York—Soc. Min. Eng., Am Inst. Min. Metall. Eng., pp. 237–302.

Deresievics, H., 1958. Mechanics of Granular Matter. *Advances in Applied Mechanics*, vol. V. Academic Press, New York, NY, 233–306.

Dewar, J., Pickford, S., 2001. Rock physics for the rest of us—an informal discussion. *CSEG Recorder* May, 49.

Dewhurst, D.N., Hennig, A.L., 2003. Geomechanical properties related to top seal leakage in the Carnarvon Basin, Northwest Shelf, Australia. *Pet. Geosci.* 9, 255–263.

Di Rosa, D., Gyllensten, A., Chen, S., Li, W., Georgi, D.T., Tauk, R., 2006. Use of the NMR diffusivity log to identify and quantify oil and water in carbonate formations, SPE 101396, Abu Dhabi International Petroleum Exhibition and Conference held in Abu Dhabi, U.A.E., 5–8 November.

Di Rosa, D., Gyllensten, A., Chen, S., Li, W., Georgi, D.T., Tauk, R., 2008. Use of the NMR diffusion log to identify and quantify oil and water in carbonate formations. *SPE Reservoir Evaluation & Engineering* April, 238–245.

Dias, C.A., 2000. Developments in a model to describe low-frequency electrical polarization of rocks. *Geophysics* 65 (2), 437–451.

Digby, P.J., 1981. The effective elastic moduli of porous granular rocks. *J. Appl. Mech. ASME* 48, 803–808.

Dissado, L.A., Hill, R.M., 1984. Anomalous low-frequency dispersion. *J. Chem. Soc. Farad. Trans.* 80, 291–319.

Dobrynin, W.M., 1963. *Izmenenie fiziceskich svoistv pescanikov pod deistviem vsestoronnego davlenija*. Trudy MINChGP, vyp. 41, Gostop Moscow.

Dobrynin, W.M., Vendelstejn, B.J., Koshevnikov, D.A., 2004. *Petrofizika, Izdatelstvo Neft i Gaz*, Moskva.

Doering, M.A., Smith, D.P., 1974. Locating extraneous water sources with the gamma ray log. *SPE Fall Meeting*, paper SPE 5116.

Domenico, S.N., 1976. Effect of brine gas mixture on velocity in unconsolidated sand reservoir. *Geophysics* 41, 882–894.

Domenico, S.N., 1977. Elastic properties of unconsolidated porous sand reservoirs. *Geophysics* 42, 1339–1368.

Dorofeyeva, R.P., 1990. *Teplogeneracia gornich porod i radiogennoe teplo Pribaikala i Sabaikala*. Fizika Semli 1, 82–90.

Dortman., N.B., 1976. *Fiziceskie Svoistva Gornich Porod i Polesnich Iskopamych*. Izdat. Nedra, Moskva.

Doveton, J.H., 1986. *Log Analysis of Subsurface Geology*. John Wiley & Sons, New York, NY.

Drury, M.J., Jessop, A.M., 1983. The estimation of rock thermal conductivity from mineral content—an assesment of techniques. *Zbl. Geol. Paläont. Teil. 1*, 35–48.

Duffant, K., Landrø, M., 2007. Vp/Vs ratio versus differential stress and rock consolidation—a comparison between rock models and time-lapse AVO data. *Geophysics* 72/5, C81–C94.

Dunham R.J., 1962. Classification of carbonate rocks according to depositional texture. In: Ham, W. E. (Ed.), *Classification of carbonate rocks—a symposium*. AAPG Memoirs 1, 108–121.

Dunn, K.-J., D.J. Bergman, D.J., Latoracca, G.A., 2002. Nuclear Magnetic Resonance—Petrophysical and Logging Applications, *Handbook of Geophysical Exploration*, vol. 32. Pergamon Press/Elsevier Science, Amsterdam.

Dvorkin, J., Nur, A., 1996. Elasticity of high-porous sandstones: theory for two North Sea data-sets. *Geophysics* 61, 1363–1370.

Dvorkin, J., Armbruster, M., Baldwin, Ch., Fang, Q., Derzi, N., Gomez, C., et al., 2008. The future of rock physics: computational methods vs. lab testing. *First Break* 26, 63–68.

Eberhart-Phillips, D., Han, D., Zoback, M., 1989. Empirical relationships among seismic velocity, effective pressure, porosity, and clay content in sandstone. *Geophysics* 54 (1), 82–89.

Eberli, G.P., Baechle, G.T., Anselmetti, F.S., 2003. Factors controlling elastic properties in carbonate sediments and rocks. *Leading Edge* July, 654–660.

Ebert, H. (Ed.), 1976. *Physikalisches Taschenbuch*, Vieweg und Sohn, Braunschweig.

Eisenberg, D., Kauzman, W., 1969. *The Structure and Properties of Water*. Oxford University Press.

Ellis, D.V., 1987. *Well Logging for Earth Scientists*. Elsevier Science, New York, NY.

Ellis, D.V., Singer, J.M., 2007. *Well Logging for Earth Scientists*. Springer-Verlag, Dordrecht.

Ellis, D., Case, Ch.R., Chiaramonte, J.M., 2003. Tutorial: porosity from neutron logs I: measurement. *Petrophysics* 44 (6), 383–395.

Ellis, D., Case, Ch.R., Chiaramonte, J.M., 2004. Tutorial: porosity from neutron logs II: interpretation. *Petrophysics* 45 (1), 73–86.

Endres, A.L., Knight, R., 1989. The effect of microscopic fluid distribution on elastic wave velocities. *Log Analyst* Nov-Dec, 437–445.

Engelhardt, W.V., 1960. *Der Porenraum der Sedimente*, Berlin, Göttingen. Springer-Verlag, Heidelberg.

England, W.A., Mackenzie, A.S., Mann, D.M., Quigley, D.M., 1987. The movement and entrapment of petroleum fluids in the subsurface. *J. Geol. Soc. London* 144, 327–347.

Evans, T., 1977. Thermal properties of North Sea rocks. *Log Analyst* 18 (2), 3–12.

Fatt, I., 1953. The effect of overburden pressure on relative permeability. *Pet. Trans. AIME* 198, 325–326.

Fatti, J.L., Smith, G.C., Vail, P.V., Strauss, P.J., Levitt, P.R., 1994. Detection of gas in sandstone reservoirs using AVO analysis: a 3-D seismic case history using the Geostack Technique. *Geophysics* 59, 1362–1376.

Fehr, A., 2007. NMR- and SIP-Messungen an Gesteinsproben, Diplomarbeit RWTH Aachen.

Fertl, F., 1979. Gamma ray spectral data assists in complex formation evaluation. *Log Analyst* September–October, 3–37.

Fertl, W.H., 1983. Gamma ray spectral logging: A new evaluation frontier (part I to VII): World Oil, series March 1983 to November 1983.

Fertl, W.H., 1987. Log-derived evaluation of shaly clastic reservoirs. *J. Pet. Technol.* February, 175–186.

Fjaer, E., Holt, R.M., Horsrud, P., Raaen, A.M., Rines, R., 2008. Petroleum Related Rock Mechanics. second ed. Elsevier Science, Amsterdam.

Fleury, M., 2002. Resistivity in carbonates: new insights, SPE Annual Technical Conference and Exhibition, San Antonio, Texas, 29 Sept.–2 Oct., paper SPE 77719.

Focke, J.W., Munn, D., 1987. Cementation exponents in Middle Eastern carbonate reservoirs. SPE Formation Evaluation June, 155–167, paper SPE 13735.

Fowler, S.R., White, R.S., Louden, K.E., 1985. Sediment dewatering in the Makran accretionary prism. *Earth Planet. Sci. Lett.* 75, 427–438.

Freedman, R., Heaton, N., 2004. Fluid characterization using nuclear magnetic resonance logging. *Petrophysics* 45 (3), 241–250.

Freund, D., Nover, G., 1995. Hydrostatic pressure tests for the permeability-formation factor relation on crystalline rocks from the KTB drilling project. *Surveys in Geophysics* 16 (1), 47–62.

Freyburg, E., 1972. Der untere und mittlere Buntsandstein SW-Thüringens in seinen gesteintechnischen Eigenschaften. *Ber. Dts. Ges. Geol. Wiss.* A. 17 (6), 911–919.

Fricke, S., Schön, J., 1999. Praktische Bohrlochgeophysik, Ferd. Enke Verlag Stuttgart.

Fröhlich, L., 1975. Einsatzmöglichkeiten und Ergebnisse einer geophysikalischen Komplexmethodik zur Strukturuntersuchung und Kennwertbestimmung, Diss. Univ. Leipzig (unpublished).

Fröhlich, L., Schwinge, G., 1978. Geophysikalische Messungen zur Lösung ingenieur-geologischer Bauwerksüberwachung für Wasserspeicher im Lockergesteinsbereich. *Zeitschr. F. Geol. Wiss.* 6 (8), 1017–1024.

Fukushima, E., Roeder, S.B.W., 1981. Experimental Pulse NMR. A Nuts and Bolts Approach. Addison Wesley.

Gardner, G.H.F., Gardner, L.W., Gregory, A.R., 1974. Formation velocity and density—the diagnostic basis for stratigraphic traps. *Geophysics* 39, 770–780.

Garrouch, A.A., Sharma, M.M., 1994. The influence of clay content, salinity, stress, and wettability on the dielectric properties of brine-saturated rocks: 10 Hz to 10 MHz. *Geophysics* 59 (6), 909–917.

Gassmann, F., 1951a. Elastic waves through a packing of spheres. *Geophysics* 16, 673–685.

Gassmann, F., 1951b. Über die Elastizität poröser Medien. *Vierteljahrsschr. d. Naturforsch. Ges. Zürich* 96, 1–22.

Gassmann, F., 1964. Introduction to seismic travel time methods in anisotropic media. *Pure Appl. Geophys.* 58 (II), 63–113.

Gavrilenko, P., Gueguen, Y., 1989. Pressure dependence of permeability: a model for cracked rocks. *Geophys. J. Int.* 98, 159–172.

Gearhart Industries, 1978. Formation evaluation data handbook. Edition Forth Worth, USA.

Gebrände, H., Kern, H., Rummel, F., 1982. Elasticity and inelasticity. In: Hellwege, K.-H. (Ed.), *Landolt-Börnstein Numerical Data and Functional Relationships in Science and Technology, New Series, Group V. Geophysics and Space Research, vol. 1, Physical Properties of Rocks, subvol. B*. Springer-Verlag, Berlin, pp. 1–233.

Geertsma, I., Smith, D.C., 1961. Some aspects of elastic wave propagation in fluid saturated porous solids. *Geophysics* 26, 169–181.

Gegenhuber, N., 2011a. An improved method to determine heat production from gamma-ray logs. Extended abstracts 73rd EAEG 2011 Conference & Exhibition, 23–26 May 2011, Vienna.

Gegenhuber, N., 2011b. Compressional wave velocity-thermal conductivity correlation: from the laboratory to logs. Extended abstracts 73rd EAEG 2011 Conference & Exhibition, 23–26 May 2011, Vienna.

Gegenhuber, N.M., Schön, J.H., 2010. Anisotropy of thermal conductivity of a gneiss—experiments and models, EGU general assembly. EGU 2010-1535, Vienna.

Georgi, D.T., Chen, S., 2007. NMR Contributions to Petrophysics, Manuscript #992. Presented at 2007 Petrotech Conference, New Delhi, India, January 15–19, 2007.

Georgi, D.T., Menger, S.K., 1994. Reservoir quality, porosity and permeability relationships. *Trans. 14. Mintrop-Seminar (Beilage)*, DGMK und Ruhr-Universität Bochum 163/1–163/35.

Georgi, D.T., Kasap, E., Altunbay, M., Tang, X., Cheng, A., 1997. Permeability profiles—key to reservoir management. *In Depth*, Baker Atlas June 10, 1–12.

Gilchrist, W.A., 2009. Tutorial: compensated neutron log response issues. *Petrophysics* 50 (5), 416–426.

Gilchrist, W.A., Prati, E., Pemper, R., Mickael, M.W., Trcka, D., 1999. Introduction of a New Through-Tubing Multifunction Pulsed Neutron Instrument. In: *Trans. SPE 74th Annual Technical Conference and Exhibition*, Houston, 1999, paper SPE 56803.

Gilchrist, W.A., Pemper, R.R., Trcka, D., Frost, E., Wilson, W., 2000. Initial Field Applications of a New 1.7-Inch Pulsed Neutron Instrument, Paper FF, *Trans. SPWLA 41st Annual Logging Symposium*, Dallas, 2000.

Golubev, A., Rabinovich, G.J., 1976. Resultaty primenienia apparatury akusticeskogo karotasa dlja predelenija prochnostykh svoistv gornych porod na mestorosdeniach tverdykh iskopaemykh. *Prikl. Geofiz.* Moskva 73, 109–116.

Gommensen, L., Fabricius, I.L., Mukerji, T., Mavko, G., Pedersen, J.M., 2007. Elastic behaviour of North Sea chalk: a well-log study. *Geophys. Prospect.* 55, 307–322.

Gong, G., 2005. Physical properties of alpine rocks: a laboratory investigation, Thesis University of Geneva, These No. 3658.

Goodman, R.E., 1988. *Introduction to Rock Mechanics*. John Wiley & Sons, New York, NY.

Goodway, W., Chen, T., Downton, J., 1997. Improved AVO fluid detection and lithology discrimination using Lame petrophysical parameters; “Lambda-Rho”, “Mu-Rho” & “Lambda/Mu fluid stack”, from P and S inversions, CSEG meeting abstracts, pp. 148–151; CSEG Recorder, 22(7), 3–5, and SEG meeting abstracts, pp. 183–186.

Gorjainov, N.N., Ljachovickij, F.M., 1979. *Seismiceskie Metody v Insenernoi Geologii*. Izdat. Nedra, Moskva.

Goss, R., Combs, J., Timur, A., 1975. Prediction of thermal conductivity in rocks from other physical parameters and from standard well logs, in SPWLA 16th Annual Logging Symposium Transactions, New Orleans, Louisiana, 16–19 June, paper MM.

Goult, N.R., 1998. Relationships between porosity and effective stress in shales. *First Break* 16 (12), 413–419.

Grant, I.S., West, G.F., 1965. *Interpretation Theory in Applied Geophysics*. McGraw-Hill, New York, NY.

Gregory, A.R., 1990. Ultrasonic velocity and attenuation measurements in water-based drilling muds, paper presented at ASME ETCE Conference, New Orleans, LA, January.

Griffith, D.H., King, R.F., 1965. *Applied Geophysics for Engineers and Geologists*. Pergamon Press.

Griffiths, C.M., Brereton, N.R., Beausillon, R., Castillo, D., 1992. Thermal conductivity prediction from petrophysical data: a case study. In: Hurst, A., Griffiths, C.M., Worthington, P.F. (Eds.), *Geological Applications of Wireline Logs II*, Geological Society Special Publication No. 65, pp. 299–315.

Gueguen, Y., Dienes, J., 1989. Transport properties of rocks from statistics and percolation. *Math. Geol.* 21 (1), 1–13.

Gueguen, Y., Palciasuskas, V., 1994. *Introduction to the Physics of Rocks*. Princeton University Press, New Jersey, NJ.

Haack, U., 1982. Radioactivity of rocks. In: Hellwege, K.-H. (Ed.), *Landolt-Börnstein Numerical Data and Functional Relationships in Science and Technology*, New Series, Group V. Geophysics and Space Research, vol.1, Physical Properties of Rocks, subvol. B. Springer-Verlag, Berlin, pp. 433–481.

Hagiwara, T., 1994. Response of 2 MHz resistivity devices in thinly laminated formations (anisotropic resistivity and EM log interpretation). Presented at SPE 69th Annual Technical Conference, pp. 667–675, paper 28426.

Hagiwara, T., 1996. A new method to determine horizontal-resistivity in anisotropic formations without prior knowledge of relative dip, in SPWLA 37th Annual Logging Symposium Transactions, New Orleans, LA, paper Q.

Hagiwara, T., 1997. Macroscopic anisotropy approach to analysis of thinly laminated sand/shale sequences: sensitivity analysis of sand resistivity estimate and environmental corrections, paper presented at SPE Annual Technical Conference and Exhibition, San Antonio, Texas, paper SPE 38669.

Hamilton, E.L., 1970. Sound velocity and related properties of marine sediments. North Pacific. *J. Geoph. Res.* 75, 4423–4446.

Hamilton, E.L., 1971. Elastic properties of marine sediments. *J. Geoph. Res.* 76, 579–604.

Hamilton, E.L., 1978. Sound velocity-density relations in sea floor sediments and rocks. *J. Acoust. Soc. Am.* 63, 366–377.

Hamilton, E.L., Bachman, R.T., Berger, W.H., Johnson, T.C., Mayere, L.A., 1982. Acoustic and related properties of calcareous deep-sea sediments, *Journ. Sediment. Pet.* 52, 0733–0753.

Han, D., Nur, A., Morgan, D., 1986. Effects of porosity and clay content on wave velocities in sandstones. *Geophysics* 51 (11), 2093–2107.

Han, X., Pemper, R., Tutt, T., Li, F., 2009. Environmental Corrections and System Calibration for a new Pulsed-Neutron Mineralogy Instrument, SPWLA 50th Annual Logging Symposium, June 21–24, paper S.

Hanai, T., 1960. Theory of the dielectric dispersion due to the interfacial polarization and its application to emulsions. *Kolloidzeitschrift* 171, 23–31.

Hara, G., 1935. Theorie der akustischen Schwingungsausbreitung in gekörnten Substanzen und experimentelle Untersuchungen an Kohlepulver, Elektr. Nachrichtentechnik 12 (7), 191–200.

Hartmann, A., 2008. Inversion of geothermal parameters using borehole and core data, Dissertation (PhD), RWTH Aachen.

Hartmann, A., Rath, V., Clauer, C., 2005. Thermal conductivity from core and well log data. *Int. J. Rock Mech. Min. Sci.* 42 (2005), 1042–1055.

Hartmann, D.J., Beaumont, E.A., 1999. Predicting reservoir system quality and performance. In: Beaumont, E.A., Forster, N.H. (Eds.), AAPG treatise of petroleum geology, exploration for oil and gas traps, Ch. 9 (9-1 to 9-154).

Hashin, Z., Shtrikman, S., 1962a. A variational approach to the theory of elastic behavior of polycrystals. *J. Mech. Phys. Solids* 10, 343–352.

Hashin, Z., Shtrikman, S., 1962a. On some variational principles in anisotropic and nonhomogenous elasticity. *J. Mech. Phys. Solids* 10, 335–342.

Hashin, Z., Shtrikman, S., 1963. A variational approach to the elastic behavior of multiphase materials. *J. Mech. Phys. Solids* 11, 127–140.

Hazen, A., 1893. Some physical properties of sands and gravels with special reference to their use in filtration, 24th Ann. Rept., Mass. State Board of Health, Pub. Doc. 34, pp. 539–556.

He, T., Schmitt, D., 2006. P- and S-wave velocity measurements and pressure sensitivity analysis of AVA response, CSPG-CSEG-CWLS Joint Convention, May, 398–404.

Hearst, J.R., Nelson, P.H., 1985. Well Logging for Physical Properties. McGraw-Hill, New York, NY.

Hearst, J.R., Nelson, P.H., Paillet, F.L., 2000. Well Logging for Physical Properties. second ed. John Wiley & Sons.

Heiland, J., Borm, G., 2000, Triaxiale Hochdruck-Untersuchungen zu Auflockerung und Entfestigung von Gesteinen; Zweijahresbericht GeoForschungsZentrum Potsdam 1998/1999, 109–114.

Helbig, K., 1958. Elastische Wellen in anisotropen Medien, Gerlands Beiträge z. Geophysik 67 (3), 256–288.

Helbig, K., 1992. Coordinate-free representation of the elastic tensor, EAEG 54th Meeting and Technical Exhibition, Paris, 1–5 June, paper A049, 80–81.

Helgerud, M.B., Dvorkin, J., Nur, A., Sakai, A., Collett, T., 1999. Elastic wave velocity in marine sediments with gas hydrates—effective medium modelling. *Geophys. Res. Lett.* 26, 2021–2024.

Henkel, H., Guzman, M., 1977. Magnetic features of fractured zones. *Geoexploration* 15, 173–181.

Hertz, H., 1882. Über die Berührung fester elastischer Körper. *Journal für die reine und angewandte Mathematik*, 92, 156–171.

Hertzog, R., Colson, L., Seeman, B., O'Brien, M., Scott, H., McKeon, D., et al., 1987. Geochemical Logging with Spectrometry Tools, Paper SPE 16792, Trans., SPE 62nd Annual Technical Conference and Exhibition, Dallas, 1987.

Heseldin, G.M., 1974. A method of averaging capillary pressure curves, SPWLA 15th Annual Logging Symposium, paper I.

Hoek, E., 2010. Practical Rock Engineering; http://download.rockscience.com/hoek/pdf/Practical_Rock_Engineering.pdf.

Höltig, B., 1989. Hydrogeologie. Ferd. Enke-Verlag, Stuttgart.

Hook, J.R., 2003. Tutorial—an introduction to porosity. *Petrophysics* 44 (3), 205–S212.

Horai, K., Simmons, G., 1969. Thermal conductivity of rock-forming minerals. *Earth and Planet. Sci. Lett.* 6, 359–368.

Horai, K.-I., 1971. Thermal conductivity of rock-forming minerals. *J. Geophys. Res.* 76 (5), 1278–1308.

Hornby, B.E., 1995. Experimental Determination of the Anisotropic Elastic Properties of Shales, 6 IWSA Workshop, 13th February 1995, pp. 237–269.

Horsrud, P., 2001. Estimating mechanical properties of shale from empirical correlations. *SPE Drill. Comp.* June, 68–73.

Howarth, D.F., Adamson, W.R., Berndt, J.R., 1989. Correlation of model tunnel boring and drilling machine performances with rock properties. *Int. J. Rock Mech. Sci. Geomech.* 23, 171–175.

Huckenholz, H.G., 1982. The rocks of the earth. In: Hellwege, K.-H. (Ed.), *Landolt-Börnstein Numerical Data and Functional Relationships in Science and Technology, New Series, Group V. Geophysics and Space Research, vol.1, Physical Properties of Rocks, subvol. A*. Springer-Verlag, Berlin.

Hudson, J.A., 1980. Overall properties of a cracked solid. *J. Math. Proc. Cambridge Philos. Soc.* 88, 371–384.

Hudson, J.A., 1981. Wave speeds and attenuation of elastic waves in material containing cracks. *Geophys. J. R. Astr. Soc.* 64, 133–150.

Hudson, J.A., Knopoff, L., 1989. Predicting the overall properties of composite materials with small-scale inclusions or cracks. *Pageoph* 131 (4), 551–576.

Huenges, E., 1989. Vergleich der an Kernen gemessenen Wärmeleitfähigkeit mit der aus Modalanalysen berechneten Wärmeleitfähigkeit. *KTB Rep. Han.* 89-5, F1–F9.

Huenges, E., Burkhard, H., Erbas, K., 1990. Thermal conductivity profile of the KTB pilot corehole. *Sci. Drill.* 1, 224–230.

Hunt, C.P., Moskowitz, B.M., Banerjee, S.K., 1995. Magnetic properties of rocks and minerals, rock physics and phase relations—a handbook of physical constants, AGU Reference Shelf 3, 1995 American Geophysical Union.

Hurst, A., 1990. Natural gamma-ray spectrometry in hydrocarbon-bearing sandstones from the Norwegian Continental Shelf, Geological Society, London, Special Publ. 1990, 48, pp. 211–222.

Hurtig, E., Brugger, H., 1970. Wärmeleitfähigkeitsmessungen unter einaxialem Druck. *Tectonophysics* 10 (1-3), 67–77.

Iwere, F.O., Moreno, J.E., Apaydin, O.G., 2002. Vug characterization and pore volume compressibility for numerical simulation of vuggy and fractured carbonate reservoirs, SPE 74341, SPE Internat. Petroleum Conf. And Exhib., Mexico.

Jackson, P.D., Taylor, D., Smith, P.M., 1978. Standard resistivity-porosity-particle shape relationships for marine sands. *Geophysics* 43 (6), 1250–1268.

Jaeger, J.C., Cook, N.G.W., 1976. *Fundamentals of Rock Mechanics*. Chapman & Hall, John Wiley & Sons, New York, NY.

Jahren, C.E., 1963. Magnetic susceptibility of bedded iron-formation. *Geophysics* 28 (5), 756–766.

Jakosky, J.J., 1950. *Exploration Geophysics*. second ed. Trija Publishing Comp., Los Angeles, LA.

Japsen, P., Mukerji, T., Mavko, G., 2006. Constraints on velocity-depth trends from rock physics models. *Geophys. Prospect.* 55, 135–154.

Jennings, J.W., Lucia, F., 2001. Predicting permeability from well logs in carbonates with a link to geology for interwell permeability mapping. Presented at SPE Annual Conference and Exhibition, New Orleans, paper SPE 71336.

Jessop, A.M., 1990. Thermal Geophysics. Elsevier, Amsterdam.

Jizba, D.L., 1991. Mechanical and acoustic properties of sandstones and shales, PhD Thesis Stanford University.

Johnson, R.B., DeGraff, J.V., 1988. Principles of Engineering Geology. John Wiley & Sons, New York, NY.

Johnston, D.H., 1981. Attenuation: a state-of-the-art summary. In: Toksöz, M.N., Johnston, D.H. (Eds.), Seismic Wave Attenuation, SEG reprint series No. 2, 123–139.

Johnston, D.H., Toksöz, M.N., 1981. Chapter 1—definitions and terminology. In: SEG Geophysics reprint series No. 2 Seismic Wave Attenuation, SEG Tulsa/Oklahoma, 1–5.

Johnston, D.H., Toksöz, M.N., Timur, A., 1979. Attenuation of seismic waves in dry and saturated rocks—II. mechanisms. *Geophysics* 44 (4), 691–711.

Johnston, J.E., Christensen, N.I., 1995. Seismic anisotropy of shales. *J. Geophys. Res.* 100 (B4), 5991–6003.

Jonscher, A.K., 1981. Review: a new understanding of the dielectric relaxation of solids. *J. Mat. Sci.* 16, 2037–2060.

Jorden, J.R., Campbell, F.L., 1984. Well logging I—rock properties, borehole environment, mud and temperature logging, Henry L. Doherty Memorial Fund of AIME, SPE: New York, Dallas.

Kansas Geological Survey, 2010. <http://www.kgs.ku.edu/PRS/ReadRocks/GRLog.html>.

Kappelmeyer, O., Haenel, R., 1974. Geothermics. Geoexploration Monographs, Series 1—No. 4 Rosenbach, O., Morelli, C. (Eds.), Gebr. Borntraeger, Berlin, Stuttgart.

Kasap, E., Altunbay, M., Georgi, D.T., 1999. Flow units from integrated WFT and NMR data. In: Schatzinger, R., Jordan, J. (Eds.), Reservoir Characterization—Recent Advances, AAPG Memoir 71, 179–190.

Katahara, K.W., 1996. Clay mineral elastic properties, 66-th SEG-Meeting, Denver, Expanded abstracts II, 1691–1694.

Katsube, T.J., Collett, L.S., 1976. Electromagnetic propagation characteristic of rocks. In: Strens (Ed.), The Physics and Chemistry of Minerals and Rocks. John Wiley & Sons, London, pp. 279–296.

Katsube, T.J., Connell, S., 1998. Shale permeability characteristics. in Current Research 1998-E. Geological Survey of Canada 183–192.

Katsube, T.J., Issler, D.R., Cox, W.C., 1998. Shale permeability and its relation to pore-size distribution. in Current Research 1998-E. Geological Survey of Canada 51–57.

Katsube, T.J., Williamson, M., Best, M.E., 1992. Shale pore structure evolution and its effect on permeability, in: Symposium Volume III of the 33rd Annual Symp. of the SPWLA, The Society of Core Analysts Preprints, Oklahoma City, Oklahoma, 15–17 June, paper SCA-9214, 1–22.

Katz, A.J., Thompson, A.H., 1986. Quantitative prediction of permeability in porous rock. *Phys. Rev. B*. 34, 8179–8181.

Kaye, G.W.C., Laby, T.H., 1968. Tables of Physical and Chemical Constants. Longmans, London.

Kayser, A., Knackstedt, M., Ziauddin, M., 2006. A closer look at pore geometry. *Oilfield Rev.* (Schlumberger) Spring, 4–13.

Keller, G.V., 1989. Electrical properties. In: Carmichael, R.S. (Ed.), Practical Handbook of Physical Properties of Rocks and Minerals. CRC Press, Boca Raton, FL.

Keller, G.V., Frischknecht, F.C., 1966. Electrical Methods in Geophysical Prospecting. Pergamon Press.

Kennedy, D.W., Herrick, D.C., 2003. Conductivity anisotropy in shale-free sandstone, in SPWLA 44th Annual Logging Symposium Transactions, Galveston, Texas, paper T.

Kenyon, W.E., 1992. Nuclear magnetic resonance as a petrophysical measurement. *Nucl. Geophys.* 6 (2), 153–171.

Kenyon, W.E., 1997. Petrophysical principles of applications of NMR logging. *Log Analyst* 38 (2), 21–43.

Kenyon, W.E., Day, P.I., Straley, C., Willemsen, J.F., 1986. A three-part study of NMR longitudinal relaxation studies of water saturated sandstones. *SPE Form. Eval.* September, 626–636, SPE 15643.

Kezdi, A., 1969. *Bodenmechanik*. Verlag Bauwesen, Berlin.

Khusnulin, M.K., 1973. Application of gamma method for determination of waterflooded strata. *Geol. Neft i Gaza* 12, 63–67.

King, M.S., 1966. Wave velocities as a function of overburden pressure and pore fluids. *Geophysics* 21, 739–754.

King, M.S., 1970. Static and dynamic elastic moduli of rocks under pressure. In: Somerton, W.H. (Ed.), *Rock Mechanics: Theory and Practice*. AIME, New York, NY, pp. 329–351, chapter 19.

King, M.S., 1983. Static and dynamic elastic properties of rocks from the Canadian Shield, *Intern. J. Rock Mech. Min. Sci. Geomech* 20 (5), 237–241.

King, R.L., Bradley, R.W., 1977. Gamma ray log finds bypassed oil zones in six Texas oil fields. *Oil Gas J.* April 4, 1977, 92–99.

Kirchberger, L.A., 2001. Investigation of elastic parameters at chosen well locations in the Vienna Basin, Diploma Thesis, Montanuniversität Leoben/Austria, unpublished.

Klein, J.D., 1996. Saturation effects on electrical anisotropy. *Log Analyst* Jan-Feb, 47–49.

Klein, J.D., Martin, P.R., Allen, D.F., 1997. The petrophysics of electrically anisotropic reservoirs. *Log Analyst* May-June, 25–36.

Kleinberg, R.L., Vinegar, H.J., 1996. NMR properties of reservoir fluids. *Log Analyst* November-December, 20–32.

Kleinberg, R.L., Kenyon, W.E., Mitra, P.P., 1994. Mechanism of NMR relaxation of fluids in rocks. *J. Magn. Reson. Ser. A* 108, 206–214.

Klimentos, T., McCann, C., 1990. Relationships among compressional wave attenuation, porosity, clay content, and permeability in sandstones. *Geophysics* 55 (8), 998–1014.

Knight, R.J., Nur, A., 1987. Geometrical Effects in the Dielectric Response of Partially Saturated Sandstones. *Log Analyst* Nov.-Dec., 513–519.

Knopoff, L., 1964. *Q. Rev. Geophys.* 2, 625–660.

Knopoff, L., 1965. Attenuation of elastic waves in the earth. In: Mason, W.S. (Ed.), *Physical Acoustics*. Academic Press, New York, NY, pp. 287–324.

Kobranova, V.N., 1989. *Petrophysics*. MIR Publ., Springer-Verlag, Moscow.

Krischer, O., Esdorn, H., 1956. Die Wärmeübertragung in feuchten, porigen Stoffen verschiedener Struktur. *Forsch. a. d. Gebiet d. Ingenieurwesens* 22 (1), 1–8.

Kulenkampff, J., Schopper, J.R., 1988. Low frequency complex conductivity—a means for separating volume and interlayer conductivity, *Transactions 12th Europ. Formation Evaluation Symposium*, Oslo.

Kulenkampff, J., Börner, F., Schopper, J.R., 1993. Broad band complex conductivity laboratory measurements enhancing the evaluation of reservoir properties, *Transactions 15th Europ. Formation Evaluation Symposium*, Stavanger 1993.

Kumar, D., 2006. A tutorial on Gassmann fluid substitution: formulation, algorithm, and Matlab code. *Geohorizons* January, 4–12.

Kuster, G.M., Toksöz, M.N., 1974. Velocity and attenuation of seismic waves in two-phase media, part I: theoretical formulations. *Geophysics* 39, 587–606.

Lama, R.D., Vutukuri, V.S., 1978. Handbook on Mechanical Properties of Rocks. Trans Tech Publications, Clausthal, Germany, 481 pp.

Landau, L., Lifshitz, E.M., 1965. Lehrbuch der Theoretischen Physik. Bd. VII. Akademie Verlag, Berlin.

Larionov, W.W., 1969. Borehole Radiometry. Izdat. Nedra, Moscow.

Lebedev, M., Toms-Stewart, J., Clenell, B., Perkvukhina, M., Shulakova, V., Paterson, L., et al., 2009. Direct laboratory observation of patchy saturation and its effects on ultrasonic velocities. *Leading Edge* January, 24–27.

Lebedev, T.S., Sapoval V.V.J., Korcin V.A., 1974. Untersuchungen der Geschwindigkeit von elastischen Wellen in Gesteinen unter den thermodynamischen Bedingungen der tiefen Erdkruste. *Veröffentl. des Zentralinst. Phys. d. Erde*, Nr. 22, Akad. d. Wiss. d. DDR, Potsdam, pp. 17–34.

Lehnert, K., Just, G., 1979. Sekundäre Gamma-Anomalien in gasproduzierenden Bohrungen. *Zeitschrift f. Geol. Wiss.* 7 (44), 503–511.

Lesmes, D.P., Morgan, F.D., 2001. Dielectric spectroscopy of sedimentary rocks. *J. Geophys. Res.* 106, 13329–13346.

Leverett, M.C., 1939. Flow of oil-water mixtures through unconsolidated sands. *Trans. AIME* 132, 149–171.

Leverett, M.C., 1940. Capillary behavior in porous solids. *Trans. AIME* 142, 152–169.

Lichtenegger, K., Rother, K., 1931. Die Herleitung des logarithmischen Mischungsgesetzes aus allgemeinen Prinzipien der stationären Strömung. *Phys. Z.* 32, 255–266.

Lindsley, D.A., Andreasen, G.E., Balsley, J.R., 1966. Magnetic properties of rocks and minerals. In: *Handbook of Physical Constants*, Mem. Geol. Soc. America 97, 543–552.

Lippmann, E., Bücker, Ch., Huenges, E., Rauen, A., Wienand, J., Wolter, K.E., 1989. Gesteinsphysik im Feldlabor: Messungen und Ergebnisse, KTB-Report 89-3; Projektleitung KTB im NLFB, pp. 120–129.

Lipsicas, M., 1984. Molecular and surface interactions in clay intercalates. In: Johnson, D.L., Sen, P.N. (Eds.), *Physics and Chemistry of Porous Media*. American Institute of Physics, New York, NY, pp. 191–202.

Liu, G., Roaldset, E., 1994. A new decompaction model and its application to the northern North Sea. *First Break* 12, 81–89.

Lo, T., Coyner, K.B., Toksöz, M.N., 1986. Experimental determination of elastic anisotropy of Berea sandstone, Chicopee shale, and Chelmsford granite. *Geophysics* 51, 164–171.

Lockhart, N.C., 1980. Electrical properties and the surface characteristics and structure of clays. *J. Coll. Inter. Sci.* 74, 520–529.

Lockner, D.L., 1995. Rock failure, rock physics and phase relations—a handbook of physical constants, AGU Reference Shelf 3, American Geophysical Union.

Looyestijn, W.J., 1996. Determination of oil saturation from diffusion NMR logs, *Transactions 37th SPWLA Annual Logging Symposium*, paper SS.

Looyestijn, W.J., 2008. Wettability index determination from NMR logs. *Petrophysics* April, 130–145.

Love, A.E.H., 1944. *A Treatise on the Mathematical Theory of Elasticity*, fourth ed., Dover, New York.

Lovell, M.A., 1985. Thermal conductivities of marine sediments. *Q. J. Eng. Geol.* 18 (3), 437–441.

Lovell, M.A., Pezard, P.A., 1990. Electrical properties of basalts from DSDP Hole 504B: a key to the evaluation of pore space morphology. In: Hurst, A., et al., (Eds.), *Geological Applications of Wireline Logs*. Geological Society, London, pp. 339–345.

Lucia, F.J., 1983. Petrophysical parameters estimated from visual descriptions of carbonate rocks: a field classification of carbonate pore space, SPE: 88-96, paper presented at the 1981 SPE Ann. Conf. and Exhib. San Antonio (SPE 10073).

Lucia, F.J., 1999. Carbonate Reservoir Characterization. Springer-Verlag, Berlin.

Lucia, F.J., 2007. Carbonate Reservoir Characterization, second ed. Springer-Verlag, Berlin.

Luffel, D.L., Hopkins, C.W., Schettler, P.D., 1993. Matrix permeability measurement of gas productive shales. Presented at the 68th Annual Conference and Exhibition of the SPE, paper SPE 26633.

MacBeth, C., Schuett, H., 2007. The stress-dependent elastic properties of thermally induced microfractures in aeolian Rotliegend sandstone. *Geophys. Prospect.* 55, 323–332.

Mandelbrot, B.B., 1983. Fractal Geometry of Nature. Freeman, New York, NY.

Mann, U., Hantschel, T., Schaefer, R.G., Krooss, B., Leythaeuser, D., Littke, R., et al., 1977. Petroleum migration: mechanisms, pathways, efficiencies and numerical simulations. In: Welte, D.H., Horsfield, B., Baker, D. (Eds.), *Petroleum and Basin Evolution*. Springer-Verlag, Berlin.

Marion, D., Jizba, D., 1992. Acoustic properties and their dependence on porosity, mineralogy, and saturation: application to field-scale measurements. In: Worthington, P.F., Chardaire-Riviere, C. (Eds.), *Advances in core evaluation—reservoir management*. Proc. 3rd Core Analysis Symposium, Paris.

Marshall, D.J., Madden, T.R., 1959. Induced polarization, a study of its causes. *Geophysics* 24, 790–816.

Marshall, D., Gardner, J.S., Mardon, D., Coates, G.R., 1995. Method for correlation NMR relaxometry and mercury injection data. In: Society of Core Analysts—1995 SCA Symposium, paper 9511.

Martin, P., Dacy, J., 2004. Effective Q_v by NMR core tests. In: SPWLA 45th Annual Logging Symposium, June 6–9, paper HH.

Martinez, A., Byrnes, A.P., 2001. Modeling dielectric-constant values of geologic materials: an aid to ground-penetrating radar data collection and interpretation. Kansas Geological Survey, *Current Research in Earth Sciences, Bulletin* 247, part I.

Maultsch, S., 2001. Investigations into the effect of fluid fill and anisotropy on the AVO signatures of reservoir rocks, Diplomarbeit TU Berlin.

Mavko, G., Nur, A., 1979. Wave attenuation in partially saturated rocks. *Geophysics* 44, 161–178.

Mavko, G., Jizba, D., 1991. Estimating grain-scale fluid effects on velocity dispersion in rocks. *Geophysics* 56, 1940–1949.

Mavko, G., Mukerji, T., Dvorkin, J., 1998. *The Rock Physics Handbook*. Cambridge University Press.

McCann, D.M., Entwistle, D.C., 1992. Determination of Young's modulus of the rock mass from geophysical well logs. In: Hurst, A., Griffiths, C.M., Worthington, P.F. (Eds.), *Geological Applications of Wireline Logs II*, 65. Geological Society Special Publication, pp. 317–325.

McDonal, F.J., Angona, F.A., Mills, R.L., Sengbush, R.L., van Norstrand, R.G., White, J.E., 1958. Attenuation of shear and compressional waves in Pierre shale. *Geophysics* 23, 421–439.

McNally, G.H., 1987. Estimation of coal measures rock strength using sonic and neutron logs. *Geoexploration* 24, 381–395.

Meiboom, S., Gill, D., 1958. Modified spin-echo method for measuring nuclear relaxation times. *Rev. Sci. Instrum.* 29, 688–691.

Meinke, W., Hurtig, E., Weiner, J., 1967. Temperaturverteilung, Wärmeleitfähigkeit und Wärmefluß im Thüringer Becken. *Geophys. Geol.*, Leipzig 11, 40–71.

Melnikov, N.W., Rshewski, W.W., Prodotjakonov, M.M., 1975. *Spravocnik (kadastr.) Fiziceskich Svoistv Gornich Porod*. Izdat. Nedra, Moskva.

Merkulova, W.M., 1972. Pogloscenie ultrasvukovych voln v gornych porodach v oblasti castot 10–160 kHz. *Izvestija A. N. SSSR Fiz. Sem.* 22, 20–25.

Mesri, G., Olson, R.E., 1971. Mechanisms controlling the permeability of clays. *Clays Clay Miner.* 19, 151–158.

Midtommé, K., Roaldset, E., 1998. The effect of grain size on thermal conductivity of quartz sands and silts. *Pet. Geosci.* 4, 165–172.

Militzer, H., Stoll, R., 1973. Einige Beiträge der Geophysik zur Primärdatenerfassung im Bergbau. *Neue Bergbautechnik* 3 (1), 21–25.

Militzer, H., Schön, J., Stötzner, U., 1986. *Angewandte Geophysik im Ingenieur- und Bergbau*. Ferd. Enke Verlag Stuttgart und VEB Deutscher Verlag für Grundstoffindustrie, Leipzig.

Miller, A., Chen, S., Georgi, D.T., Vozoff, K., 1998. A new method for estimating T_2 distributions from NMR measurements. *Magn. Reson. Imaging* 16 (5–6), 617–619.

Mindlin, R.D., 1949. Compliance of elastic bodies in contact. *J. Appl. Mech. Trans. ASME* 71, 259–268.

Mohammadalou, M., Mork, M.B.E., Langeland, H., 2010. Quantification of shale volume from borehole logs calibrated by SEM analysis: a case study. *First Break* 28 (2010), 47–55.

Mollison, R.A., Schön, J., Fanini, O., Gupta, P., Kriegshäuser, B., Meyer, W.H., 1999. A model for hydrocarbon saturation determination from an orthogonal tensor relationship in thinly laminated anisotropic reservoirs. In: *SPWLA 40th Annual Logging Symposium Transactions*, Oslo, Norway, 30 May–3 June, paper OO.

Mooney, H.M., Bleifuss, R., 1953. Magnetic susceptibility measurements in Minnesota. 2. Analysis of field results. *Geophysics* 18 (2), 383–393.

Moran, J.H., Gianzero, S., 1979. Effects of formation anisotropy on resistivity-logging measurements. *Geophysics* 44 (7), 1266–1286.

Müller, B., 1978. Beziehungen zwischen chemischer Zusammensetzung, gesteintechnischen Eigenschaften und dem Trennflächengefüge in Karbonatgesteinen. *Zeitschr. Geol. Wissenschaften* 6 (7), 897–914.

Murphy, D.P., 2004. Capillary pressure seminar (handout). Seminar held at the 45th SPWLA Annual Logging Symposium, Noordwijk, Holland, 6–9 June.

Murphy, F.W., 1982. Effects of partial water saturation on attenuation in sandstones. *J. Acoust. Soc. Am.* 71, 1458–1468.

Murphy, F.W., 1984. Acoustic measures of partial gas saturation in tight sandstones. *J. Geophys. Res.* 89 (11), 549–559.

Nagata, T., 1961. *Rock Magnetism*. Maruzen Co., Tokyo.

Nagata, T., 1966. Magnetic properties of rocks and minerals. In: Flügge, S. (Ed.), *Handbuch der Physik Bd. XLIX/1 (Geophysik III/1)*. Springer-Verlag, Berlin, pp. 248–301.

Nagumo, S., 1965. Compaction of sedimentary rock. A consideration by the theory of porous media. *Bull. Earthquake Res. Inst.* 43, 339–348.

Neasham, J.W., 1977. The morphology of dispersed clay in sandstone reservoirs and its effect on sandstone shalyness, pore space and fluid flow properties. Presented at the SPE Annual Technical Conference and Exhibition, 9–12 October, Denver, Colorado, paper SPE 6858.

Nelson, P.H., 1994. Permeability-porosity relationships in sedimentary rocks. *Log Analyst* May–June, 38–61.

Nelson, P.H., 2005. Permeability, porosity, and pore-throat size—a three-dimensional perspective. *Petrophysics* December, 452–455.

Nur, A., Wang, Z., 1988. Seismic and acoustic velocities in reservoir rocks, vol. 1, SEG Geophysics reprint series No. 10, Introduction.

Nur, A., Mavko, G., Dvorkin, J., Galmudi, D., 1998. Critical porosity: a key to relating physical properties to porosity in rocks. *Leading Edge* 17, 357–362.

O'Connell, R.J., Budiansky, B., 1974. Seismic velocities in dry and saturated cracked solids. *J. Geophys. Res.* 79, 4626–4627.

Ødegaard, E., Avseth, P., 2004. Well log and seismic data analysis using rock physics templates. *First Break* 23 (October), 37–43.

Olhoeft, G.R., 1979. Electrical properties. Initial Report on the Petrophysics Laboratory, U.S. Geol. Survey, Circ. 789.

Olhoeft, G.R., 1981. Electrical properties of rocks. In: Touloukain, Y.S., Judd, W.R., Roy, R.F. (Eds.), *Physical Properties of Rocks and Minerals*. McGraw-Hill, New York, NY.

Olhoeft, G.R., 1985. Low frequency electrical properties. *Geophysics* 50, 2492–2503.

Olhoeft, G.R., 1987. Electrical properties from 10⁻³ to 10⁺⁹ Hz—physics and chemistry. In: Proc. 2nd Int. Symp. Physics and Chemistry of Porous Media. Schlumberger-Doll, Ridgefield, pp. 281–298.

Olhoeft, G.R., 1992. Geophysical detection of hydrocarbon and anorganic chemical contamination. In: Proc. Symposium on the Application of Geophysics to Engineering and Environmental Problems, 26–29 April, pp. 587–595.

Olhoeft, G.R., Johnson, G.R., 1989. Densities of rocks and minerals. In: Carmichael (Ed.), *Practical Handbook of Physical Properties of Rocks and Minerals*, Section II. CRC Press, Boca Raton, FL.

Oliver, D.W., Frost, E., Fertl, W.H., 1981. Continuous Carbon/Oxygen (C/O) Logging—Instrumentation, Interpretive Concepts and Field Applications. In: *Trans. SPWLA 22nd Annual Logging Symposium*, Mexico City, 1981, paper TT.

Palmer, T., Pallatt, N., 1991. The effect of overburden pressure on formation factor for shaly sands. In: *Trans. 14th European Formation Evaluation Symposium*, London, paper M.

Pandit, B.I., King, M.S., 1979. A study of the effects of pore-water salinity on some physical properties of sedimentary rocks at permafrost temperatures. *Can. J. Earth Sci.* 16, 1566–1580.

Pape, H., Riepe, L., Schopper, J.R., 1985. Petrophysical detection of microfissures in granites. In: *SPWLA 26th Annual Logging Symposium Transactions*, Dallas, Texas, paper P.

Pape, H., Clauer, Ch., Iffland, J., 1999. Permeability prediction based on fractal pore-space geometry. *Geophysics* 64 (5), 1447–1460.

Pape, H., Clauer, Ch., Iffland, J., 2000. Variation of permeability with porosity in sandstone diagenesis interpreted with a fractal pore space model. *Pure Appl. Geophys.* 157, 603–619.

Parasnis, D.S., 1973. *Mining Geophysics*. Elsevier, Amsterdam.

Parchomenko, E.J., 1965. *Elektriceskie svoistva gornich porod*. Izdat. Nauka, Moskva.

Parrot, J.E., Stuckes, A.D., 1977. Thermal conductivity of solids. *Phys. Today* 30 (2), Pion, London, 1975.

Patchett, J.G., 1975. An investigation of shale conductivity. In: *SPWLA Ann. Symposium*, New Orleans, paper U.

Pelton, W.H., Ward, S.H., Hallof, P.G., Sill, W.R., Nelson, P.H., 1978. Mineral discrimination and removal of inductive coupling with multifrequency IP. *Geophysics* 43, 588–609.

Pemper, R., Sommer, A., Guo, P., Jacobi, D., Longo, J., Bliven, S., et al., 2006. A new pulsed neutron sonde for derivation of formation lithology and mineralogy. In: *SPE 102770*, paper presented at 2006 SPE Annual Technical Conference and Exhibition, San Antonio.

Pemper, R., Han, X., Mendez, F., Jacobi, D., LeCompte, B., Bratovic, M., et al., 2009. The direct measurement of carbon in wells containing oil and natural gas using pulsed neutron mineralogy tool. In: SPE 124234, paper presented at 2009 SPE Annual Technical Conference and Exhibition, New Orleans.

Peselnick, L., Zietz, J., 1959. Internal friction of fine-grained limestones at ultrasonic frequencies. *Geophysics* 24, 285–296.

Petersen, N., Bleil, U., 1982. Magnetic properties of rocks. In: Hellwege, K.-H. (Ed.), Landolt-Börnstein Numerical Data and Functional Relationships in Science and Technology, New Series, Group V. Geophysics and Space Research, vol. 1, Physical Properties of Rocks, subvol. B. Springer-Verlag, Berlin, pp. 366–432.

Pittman, E.D., 1992. Relationship of porosity and permeability to various parameters derived from mercury injection-capillary pressure curves for sandstone. *Am. Assoc. Pet. Geol. Bull.* 76 (2), 191–198.

Platou, S.W., 1968. On the petrophysical properties of granitic rocks. *Geol. Fören. Stockholm Förhandlingar* 90, 427–433.

Plewa, S., 1976. Correlation between thermal conductivity and other physical parameters of rocks. In: Adam, A. (Ed.), Geoelectric and geothermal studies KAPG Geophysical monograph. Akad. Kiado, Budapest, pp. 48–52.

Poelchau, H.S., Baker, D.R., Hantschel, T., Horsfield, B., Wygrala, B., 1997. Basin simulation and design of the conceptual basin model. In: Welte, D.H., Horsfield, B., Baker, D.R. (Eds.), Petroleum and Basin Evolutions. Springer-Verlag, New York, NY, pp. 3–70.

Pooley, I.Ph., Nooteboom, I.I., De Waal, P.J., 1978. Use of V.H.F. dielectric measurements for formation analysis. *Log Analyst* 3, 8–30.

Potter, D.K., 2007. Magnetic susceptibility as a rapid, non-destructive technique for improved petrophysical parameter prediction. *Petrophysics* 48 (3), 191–201.

Poulsen, K.D., Saxov, S., Balling, N., Kristiansen, J.I., 1982. Thermal conductivity measurements on Silurian limestones from the Island of Gotland, Sweden. *Geol. Fören. Stockholm Förhandlingar* 103 (Pt. 3), 349–356.

Poupon, A., Levaux, J., 1971. Evaluation of water saturation in shaly formations: In: SPWLA 12th Logging Annual Symposium Transactions, paper O1-2, also in Shaly Sand Reprint Volume, SPWLA, pp. IV, 81–95.

Poupon, A., Loy, M.E., Tixier, M.P., 1954. A contribution to electrical log interpretation in shaly sands. *Trans. AIME* 201, 138–145.

Prammer, M.G., Drack, D.E., Bouton, J.C., Gardner, J.S., 1996. Measurement of clay-bound water and total porosity by magnetic resonance logging. *Log Analyst* November–December, 61–69.

Quiel, F., 1975. Thermal-IR in geology. *Photogram. Eng. Remote Sens.* 341–346.

Ratcliffe, E.H., 1960. The thermal conductivities of ocean sediments. *J. Geophys. Res.* 65 (5), 1535–1541.

Raymer, D.S., Hunt, E.R., Gardner, J.S., 1980. An improved sonic transit time-to-porosity transform. In: Proc. SPWLA 21st Ann. Meeting, paper P.

Reuss, A., 1929. Berechnung der Fließgrenze von Mischkristallen. *Angew. Mathem. Mech.* 9, 49–58.

Revil, A., Cathles III, L.M., 1999. Permeability of shaly sands. *Water Resour. Res.* 35, 651–662.

Revil, A., Pezard, P.A., Darot, M., 1997. Electrical conductivity, spontaneous potential and ionic diffusion in porous media. In: Lovell, M.A., Harvey, P.K. (Eds.), Geological Society Special Publication 122, pp. 253–275.

Revil, A., Grauls, D., Brevart, O., 2002. Mechanical compaction of sand/clay mixtures. *J. Geophys. Res.* 107 (B11), 2293, ECV11-1–ECV11-15.

Rhzewski, V., Novik, G., 1971. The Physics of Rocks. Mir Publishers, Moscow (translated from Russian by Chatterjee, A.K.).

Rider, M.H., 1986. The Geological Interpretation of Well Logs. Blackie, Glasgow, London.

Rider, M.H., 1996. The Geological Interpretation of Well Logs, second ed. Whittles Publishing, Caithness, England.

Rink, M., Schopper, J.R., 1974. Interface conductivity and its implication to electric logging. In: SPWLA 15th Annual Logging Symposium Transactions, Houston, Texas, paper J.

Rösler, H.J., Lange, H., 1972. Geochemical Tables. Elsevier, Amsterdam.

Rowan E.L., Hayba, D.O., Nelson, Ph.H., Burns, W.M., Houseknecht, D.W., 2003. Sandstone and shale compaction curves derived from sonic and gamma ray logs in offshore wells, North Slope, Alaska—parameters for basin modeling. U.S. Geological Survey, Open-File Report 03-329.

Roy, R.F., Beck, A.E., Touloukian, Y.S., 1981. Thermophysical properties of rocks. In: Touloukian, Y.S., Ho, C.Y. (Eds.), Physical Properties of Rocks and Minerals, vol. II-2. McGraw-Hill/CINDAS Data Series on Material Properties.

Ruffet, C., Gueguen, Y., Darot, M., 1991. Complex conductivity measurements and fractal nature of porosity. *Geophysics* 56, 758–768.

Rybach, L., 1976. Radioactive heat production; a physical property determined by the chemistry of rocks. In: Strens, R.G.J. (Ed.), The Physics and Chemistry of Minerals and Rocks. John Wiley & Sons, London, pp. 309–318.

Rybach, L., Buntebarth, G., 1984. The variation of heat generation, density and seismic velocity with rock type in the continental lithosphere. *Tectonophysics* 103, 335–344.

Rybach, L., Cermak, V., 1982. Radioactive heat generation in rocks, Chapter 4.4. In: Hellwege, K.-H. (Ed.), Landolt-Börnstein Numerical Data and Functional Relationships in Science and Technology, New Series, Group V. Geophysics and Space Research, vol. 1, Physical Properties of Rocks, subvol. B. Springer-Verlag, Berlin, pp. 433–481.

Rybach, L., Muffler, L.J.P., 1981. Geothermal Systems: Principles and Case Histories. John Wiley & Sons, Chichester.

Rzhevski, W.W., Jamscikov, W.S., 1973. Akusticeskie Metody Issledovania i Kontrolja Gornich Porod v Massive. Izdat. Nauka, Moskva.

Rzhevski, W.W., Novik, G.J., 1978. Osnovy Fiziki Gornich Porod. Izdat. Nauka, Moskva.

Salazar, J.M., Torres-Verdin, C., Alpak, F., Habashy, T.M., Klien, J.D., 2006. Estimation of permeability from borehole array induction measurements: application to the petrophysical appraisal of tight gas sands. *Petrophysics* December, 527–544.

Sams, M.S., Andrea, M., 2001. The effect of clay distribution on the elastic properties of sandstone. *Geophys. Prospect.* 49, 128–150.

Sass, J.H., Lachenbruch, A.H., Moses, T.H., 1992. Heat flow from a scientific research well at Cajon Pass, California. *J. Geophys. Res.* 97 (B4), 5017–5030.

Sayers, C.M., Schutjens, P.M.T.M., 2007. An introduction to reservoir geomechanics. *Leading Edge* May, 597–601.

Schlumberger, 1982a. Natural Gamma Ray Spectrometry, Essentials of N.G.S. Interpretation.

Schlumberger, 1982b. Well Evaluation Developments—Continental Europe, Schlumberger.

Schlumberger, 1983. Gamma Ray Spectrometry Tool, Schlumberger ATL & Marketing Brochure.

Schlumberger, 1989a. Log Interpretation Charts. Schlumberger Ed. Serv.

Schlumberger, 1989b. Log Interpretation Principles/Applications. Schlumberger Ed. Serv.

Schlumberger, 2000. Log Interpretation Charts. Schlumberger Ed. Serv.

Schlumberger, 2008. "Carbonate Advisor" Brochure (www.slb.com/carbonates).

Schoenberg, M., 1994. Transversely isotropic media equivalent to thin isotropic layers. *Geophys. Prospect.* 42, 885–915.

Schoenberg, M., Muir, F., 1989. A calculus for finely layered anisotropic media. *Geophysics* 54 (5), 581–589.

Schön, J., 1964. Modellseismische Untersuchungen im Hinblick auf die Schallgeschwindigkeit in Lockergesteinen. *Freiberger Forschungshefte*, C 173. Verlag Grundstoffindustrie, Leipzig.

Schön, J., 1969. Die Ausbreitungsgeschwindigkeit elastischer Wellen in Lockerböden und ihre Beziehung zu bodenmechanischen Kennwerten. *Freiberger Forschungshefte*, C 250. Verlag Grundstoffindustrie, Leipzig.

Schön, J., 1983. Petrophysik. Akademie Verlag, Berlin, Ferd. Enke Verlag Stuttgart.

Schön, J.H., 1996. Physical Properties of Rocks: Fundamentals and Principles of Petrophysics (Handbook of Geophysical Exploration Series). Pergamon Press, London.

Schön, J.H., Georgi, D.T., 2003. Dispersed shale, shaly-sand permeability—a hydraulic analog to the Waxman-Smits equation. Presented at the SPWLA 44th Annual Logging Symposium, 22–25 June, paper S.

Schön, J.H., Mollison, R.A., Georgi, D.T., 1999. Macroscopic electrical anisotropy of laminated reservoirs: a tensor resistivity saturation model. Presented at the SPE Annual Technical Conference and Exhibition, paper SPE 56509.

Schön, J.H., Georgi, D., Fanini, O., 2000. Anisotropic reservoir characterization (laminated sands) using orthogonal resistivity, NMR, and formation test data, paper B-16, *Trans. Petrophysics meets Geophysics*, 2000, Paris, 6–8 November.

Schön, J.H., Georgi, D.T., Fanini, O., 2001. Imparting directional dependence on log-derived permeability. In: *SPE Ann. Techn. Conf.* New Orleans, October, SPE Paper 71721.

Schön, J., Georgi, D., Tang, X., 2005. Elastic wave anisotropy and shale distribution. In: *SPWLA 46th Annual Logging Symposium*, New Orleans, paper Q.

Schön, P., 2011. Instability and Failure Mechanisms of the Barrier, Southwest British Columbia—Master Thesis. Simon Fraser University, Burnaby, BC Canada.

Schopper, J.R. 1982. Porosity and permeability. In: Hellwege, K.-H. (Ed.), *Landoft-Börnstein Numerical Data and Functional Relationships in Science and Technology*, New Series, Group V. Geophysics and Space Research, vol. 1, Physical Properties of Rocks, subvol. A. Springer-Verlag, Berlin.

Schuch, M., 1980. In: Göttlich, K. (Ed.), *Physik des Torfes und der Moorböden*. Moor- und Torfkunde, Stuttgart.

Slater, J.C., Christie, P.A.F., 1980. Continental stretching: an explanation of the post mid-Cretaceous subsidence of the central North Sea basin. *J. Geophys. Res.* 85, 3711–3739.

Scott, J.B.T., 2006. The origin of the observed low-frequency electrical polarization in sandstones. *Geophysics* 71 (5), 235–238.

Scott, J.B.T., Barker, R.D., 2003. Determining pore-throat size in Permo-Triassic sandstones from low-frequency electrical spectroscopy. *Geophys. Res. Lett.* 30 (9), 1450.

Scott, T.E., 2007. The effects of stress paths on acoustic velocities and 4D seismic imaging. *Leading Edge* May, 602–608.

Scott, W.J., Sellmann, P.V., Hunter, J.A., 1990. Geophysics in the study of permafrost. In: St. Ward (ed.), *Geotechnical and environmental geophysics—Investigations in Geophysics* No. 5 SEG, pp. 355–384.

Seigel, H.O., 1959. A theory of induced polarization effects (for step-function excitation). In: Wait, J.R. (Ed.), *Overvoltage Research and Geophysical Applications*. Pergamon Press, pp. 4–21.

Seigel, H., Nabighian, M., Parasnis, D.S., Vozoff, K., 2007. The early history of the induced polarization. *Leading Edge* 26 (3), 312–322.

Seipold, U., 1990. Pressure and temperature dependence of thermal transport properties of granites. *High Temp.–High Press.* 22, 541–548.

Seipold, U., 2001. Der Wärmetransport in kristallinen Gesteinen unter Bedingungen der kontinentalen Kruste, Scientific Technical Report STR01/13, Geoforschungszentrum (GFZ), Potsdam.

Sen, P.N., 1980. The dielectric and conductivity response of sedimentary rocks, Soc. of Petroleum Engineers of AIME, 11p., paper SPE 9379.

Sen, P.N., 1981. Relation of certain geometrical features to the dielectric anomaly of rocks. *Geophysics* 46, 1714–1720.

Sen, P.N., Scala, C., Cohen, M.H., 1981. A self-similar model for sedimentary rocks with application to the dielectric constant for fused glass bead. *Geophysics* 46, 781–796.

Sen, P.N., Straley, C., Kenyon, W.E., Wittingham, M.S., 1990. Surface-to-volume ratio, charge density, nuclear magnetic relaxation, and permeability in clay-bearing sandstones. *Geophysics* 55, 61–69.

Sengupta, M., Mavko, G., 2003. Impact of flow simulation parameters on saturation scales and seismic velocity. *Geophysics* 68 (4), 1267–1280.

Sengwa, R.J., Soni, A., 2006. Low-frequency dielectric dispersion and microwave dielectric properties of dry and water-saturated limestones of the Jodhpur region. *Geophysics* 71 (5), 269–277.

Serra, O., 1984. *Fundamentals of Well-Log Interpretation*. Elsevier, Amsterdam.

Serra, O., 2004. *Well Logging*. Vol. 1: Data Acquisition and Applications; Vol. 2: Well Logging and Reservoir Evaluation. Editions Technip, Paris.

Serra, O., 2007. *Well Logging*. Vol. 3: Well Logging and Reservoir Evaluation. Editions Technip, Paris.

Sharma, M.M., Garrouch, A., Dunlap, H.F., 1991. Effects of wettability, pore geometry, and stress on electrical conduction in fluid saturated rocks. *Log Analyst* September–October, 511–526.

Sherman, M., 1986. A model for the determination of water saturation from dielectric permittivity measurements. In: SPWLA 27th Annual Logging Symposium Transactions, Houston, Texas, June 9–13, paper E.

Sherman, M., 1998. A model for the frequency dependence of the dielectric permittivity of reservoir rocks. *Log Analyst* September–October, 358–367.

Shuey, R.T., 1985. A simplification of Zoeppritz equations. *Geophysics* 50, 609–614.

Siegesmund, S., Vollbrecht, A., 1991. Complete seismic properties obtained from microcrack fabrics and textures in an amphibolite from the Ivrea Zone, Western Alps, Italy. *Tectonophysics* 199, 13–24.

Siegesmund, S., Vollbrecht, A., Chlupac, A., Nover, G., Dürrast, H., Müller, J., et al., 1993. Fabric-controlled anisotropy of petrophysical properties observed in KTB core samples. *Sci. Drill.* 4, 31–54.

Sigal, R.F., 2002. The pressure dependence of permeability. *Petrophysics* March–April, 92–102.

Silaeva, O.O., Samina, O.G., 1969. Pogloscenie Ultrasvuka v Granitach, Izvestija Akad. Nauka SSSR, Ser. Geofiz. 9, 1354–1359.

Simandoux, P., 1963. Dielectric measurements on porous media: application to the measurement of water saturation. In: Shaly Sand Reprint Volume, SPWLA, pp. IV 97–124.

Sjogren, B., Ofsthus, A., Sandberg, I., 1979. Seismic classification of rock mass qualities. *Geophys. Prospect.* 27, 409–442.

Skelt, C., Harrison, B., 1995. An integrated approach to saturation height analysis. Presented at the SPWLA 36th Annual Logging Symposium, 26–29 June, Paris, France, paper NNN.

Slater, L., Lesmes, D.P., 2002. Electrical-hydraulic relationships for unconsolidated sediments. *Water Resour. Res.* 38 (10), 1213.

Slatt, R.M., 2006. Stratigraphic reservoir characterization for petroleum geologists, geophysicists and engineers. In: Cubitt, J. (Ed.), *Handbook of Petroleum Exploration and Production*, vol. 6. Elsevier, New York, NY, p. 2006.

Slichter, C.P., 1980. Principles of Magnetic Resonance. second ed. Springer-Verlag.

Smith, T.M., Sondergeld, C.H., Rai, C.S., 2003. Gassmann fluid substitutions: a tutorial. *Geophysics* 68, 430–440.

Snyder, D.D., Merkel, R.H., William, J.T., 1977. Complex formation resistivity—the forgotten half of the resistivity log. In: SPWLA 18th Annual Logging Symposium Transactions, Houston, Texas, paper Z.

Somerton, W.H., 1992. Thermal Properties and Temperature-Related Behavior of Rock/Fluid Systems: Developments in Petroleum Science 37. Elsevier, Amsterdam.

Somerton, W.H., Esfandiari, F., Singhal, A., 1969. Further studies of the relation of physical properties of rock to rock drillability, Soc. Petr. Eng. AIME, Dallas, Texas, paper SPE 2390.

Spangenberg, E., 2001. Modeling of the influence of gas hydrate content on the electrical properties of porous sediments. *J. Geophys. Res.* 106 (B4), 6535–6548.

Spravocnik Geofizika, 1966. Izdatelstvo Nedra, Moskva.

Stacey, F.C., Banerjee, S.K., 1974. The Physical Principles of Rock Magnetism. Elsevier, Amsterdam.

Starzec, P., 1999. Characterization of the physical properties of rocks. Department of Geology Chalmers University of Technology, Sweden, Publ. A 90.

Stim-Lab/Corelab, 2005. Company paper: Triaxial Testing of Rock, Weakly and Unconsolidated Sands and Proppants, Duncan OK.

Straley, C., Morriss, C.E., Kenyon, W.E., Howard, J., 1995. NMR in partially saturated rocks: laboratory insights on free fluid index and comparison with borehole logs. *Log Analyst* 36, 40–56.

Swanson, B.F., 1981. A simple correlation between permeabilities and mercury capillary pressures. *J. Pet. Technol.* December, 2498–2504.

Tagiev, K.K., Mustafaev, K.A., 1975. Mechanism pogloscenia energii seismiceskikh voln v nefti i vode. *Prikl. Geofiz.* 80, 114–119.

Tao, G., King, M.S., Nabi-Bibhendi, M., 1995. Ultrasonic wave propagation in dry and brine-saturated sandstones as a function of effective stress: laboratory measurements and modeling. *Geophys. Prospect.* 43, 299–327.

Tarling, T.H., 1983. Palaeomagnetism. Chapman & Hall, London.

Tarling, T.H., Hrouda, D.H., 1993. The Magnetic Anisotropy of Rocks. Champan & Hall, London.

Telford, W.M., Geldart, L.P., Sheriff, R.E., Keys, D.S., 1976. Applied Geophysics. Cambridge University Press.

Terzaghi, K.V., 1955. Influence of geological factors on the engineering properties of sediments. *Econ. Geol.* 15, 557–618.

Thomas, E.C., 1992. 50th anniversary of the Archie equation: Archie left more than just an equation. *Log Analyst* May–June, 199–205.

Thomas, E.C., Stieber, S.J., 1975. The distribution of shale in sandstones and its effect upon porosity. In: SPWLA 16th Annual Logging Symposium Transactions, 4–7 June, paper T.

Thomeer, J.H.M., 1960. Introduction of a pore geometrical factor defined by the capillary pressure curve. *J. Pet. Technol.* March, 73–77.

Thomsen, L., 1986. Weak elastic anisotropy. *Geophysics* 51 (10), 1954–1966.

Thomsen, L., 1995. Elastic anisotropy due to aligned cracks in porous rock. *Geophys. Prospect.* 3, 805–829.

Titab, D., Donaldson, E.C., 1996, 2004. *Petrophysics*. Gulf Publishing Company, Houston, TX.

Timur, A., 1968. An investigation of permeability, porosity, and residual water saturation relationships for sandstone reservoirs. *Log Analyst* July–August, 8–17.

Titov, K., Kemna, A.A., Tarasov, V., Levitski, A., 2002. Theoretical and experimental study of time domain-induced polarization in water-saturated sands. *J. Appl. Geophys.* 50, 417–433.

Titov, K., Komarov, V., Tarasov, V., Vereecken, H., 2004. Induced polarization of unsaturated sands determined through time domain measurements. *Vadose Zone J.* 3, 1160–1168.

Toksöz, M.N.C.H., Cheng, Timur, A., 1976. Velocities of seismic waves in porous rocks. *Geophysics* 41 (4), 621–645.

Tong, M., Wang, W., Jiang, Y., 2006. Determining capillary-pressure curve, pore-size distribution, and permeability from induced polarization of shaly sands. *Geophysics* 71 (3), N33–N40.

Toulhoat, T., Bigot, S., Chupeau, J., 1989. In situ fixation of U, Ca, and K pumping through multilayered aquifers in sandstone–clay sequential successions. *Panel Proc. IAEA*, Vienna, March 1989, pp. 77–91.

Toumelin, E., Torres-Verdin, C., 2009. Pore-scale simulation of kHz-GHz electromagnetic dispersion of rocks: effects of rock morphology, pore connectivity, and electrical double layers. In: SPWLA 50th Annual Logging Symposium Transactions, The Woodlands, Texas, 21–24 June, paper RRR.

Turcotte, D.L., 1992. *Fractals and Chaos in Geology and Geophysics*. Cambridge University Press.

Vacquier, V., Mathieu, Y., Legendre, E., Blondin, E., 1988. Experiment on estimating thermal conductivity from oil well logging. *Am. Assoc. Pet. Geol. B.* 72, 758–764.

van Baaren, J.P., 1979. Quick-look permeability estimates using sidewall samples and porosity logs. In: 6th Annual European Logging Symp. Trans., SPWLA.

van Genuchten, M.T., 1980. A closed-form equation for predicting the hydraulic conductivity of unsaturated soils. *Soil Sci. Soc. Am. J.* 44, 829–898.

van Overmeeren, R.A., 1994. Georadar for hydrogeology. *First Break* 12, 401–408.

Vanhala, H., 1997. Mapping oil-contaminated sand and till with the spectral induced polarization (SIP) method. *Geophys. Prospect.* 45, 303–326.

Vaquier, V., Holmes, C.R., Kintzinger, P.R., Lavergne, M., 1957. Prospecting for groundwater by induced electrical polarization. *Geophysics* 22, 660–687.

Veeken, P.C.H., 2007. *Seismic Stratigraphy, Basin Analysis and Reservoir Characterization, Seismic Exploration*—vol. 37. Elsevier, Amsterdam.

Vernik, L., 2000. Permeability prediction in poorly consolidated siliciclastics based on porosity and clay volume logs. *Petrophysics* March–April, 138–147.

Vernik, L., Liu, X., 1997. Velocity anisotropy in shales: a petrophysical study. *Geophysics* 62 (2), 521–532.

Vinegar, H.J. 1995. SPWLA Short course notes on NMR, SPWLA Houston 1995.

Vinegar, H.J., Waxman, M.H., 1984. Induced polarization of shaly sands. *Geophysics* 49, 1267–1287.

Vinegar, H.J., Akkurt, R., Tutunjian, P., 1996. NMR logging of natural gas reservoirs, US Patent 5,497,087.

Voigt, W., 1910. Lehrbuch der Kristallphysik. Teubner-Verlag, Leipzig.

Volarovic, M.P., Bajuk, E.I., 1977. Elastic properties of rocks. In: Volarovic, M.P., Stiller, H., Lebedev, T.S. (Eds.), Issledovanie Fizicheskikh svoistv Mineralnogo Vescchestva Zemli pri Vysokikh Termodynamicheskikh Parametrah. Izdat. Nakova Dumka, Kiev, pp. 43–49.

Volotkin, Y., Looyestijn, W.J., Slijkerman, W.F.J., Hofman, J.P., 2001. A practical approach to obtain primary drainage capillary pressure curves from NMR core and log data. *Petrophysics* July–August, 334–342.

Vosteen, H.D., Schellschmidt, R., 2003. Influence of temperature on thermal conductivity, thermal capacity and thermal diffusivity for different types of rock. *Phys. Chem. Earth* 28, 499–509.

Walsh, J.B., 1966. Seismic wave attenuation in rock due to friction. *J. Geophys. Res.* 71, 2591–2599.

Walsh, J.B., 1981. Effects of pore pressure and confining pressure on fracture permeability. *Int. J. Rock Mech. Min. Sci. Geomech.* 18 (5), 429–435.

Wang, Z., 2000. The Gassmann equation revisited: comparing laboratory data with Gassmann's predictions, *Seismic and Acoustic Velocities in Reservoir Rocks*, vol. 3, Recent Developments, SEG Reprint Series, pp. 1–23.

Wang, Z., 2001. Y2K tutorial, fundamentals of seismic rock physics. *Geophysics* 66 (2), 398–412.

Wang, Z., 2002. Seismic anisotropy in sedimentary rocks, part 2: laboratory data. *Geophysics* 67 (5), 1423–1440.

Wang, Z., Nur, A., 1988. Velocity dispersion and the “local flow” mechanism in rocks. In: 58th Int. SEG meeting, Expand. Abstracts, pp. 928–930.

Wannakao, L., Sriputorn, S., Trirat, J., 2009. Correlations between mechanical and ultrasonic wave properties of claystone from Mae Moh coal mine, *Rock Mechanics*, Fuenkajorn P. (Ed.), ISBN 978 974 533 624 7.

Waples, D.W., Tirsgaard, H., 2002. Changes in matrix thermal conductivity of clays and clays-tones as a function of compaction. *Pet. Geosci.* 8 (4), 365–370.

Ward, St.H., 1990. Resistivity and induced polarization methods. In: Ward, St. (Ed.), *Geotechnical and environmental geophysics—Investigations in Geophysics*, No. 5 SEG, pp. 169–189.

Warren, J.E., Root, P.J., 1963. The behaviour of naturally fractured reservoirs. *Soc. Pet. Eng. J.* September, 245–255.

Watfa, M., Nurmi, R., 1987. Calculation of saturation, secondary porosity and producibility in complex Middle East carbonate reservoirs. In: SPWLA 28th Annual Logging Symposium Transactions, London, England, paper CC.

Waxman, M.H., Smits, L.J., 1967. Electrical conductivities in oil-bearing shaly sands. Presented at 42nd Annual Fall Meeting: Society of Petroleum Engineers, 8, 107–122, paper SPE 1863-A.

Waxman, M.H., Smits, L.J., 1968. Electrical conductivities in oil bearing shaly sands. *SPE J.* 8 (2), 107–122.

Wedepohl, K.H., 1969. *Handbook of Geochemistry*. Springer-Verlag, Berlin.

Weller, A., Börner, F., 1996. Measurements of spectral induced polarization for environmental purposes. *Environ. Geol.* 27, 329–334.

Wenk, H.R., Wenk, E., 1969. Physical constants of alpine rocks (density, porosity, specific heat, thermal diffusivity and conductivity), *Beiträge zur Geologie der Schweiz* Nr. 45, Leemann AG. Zürich, pp. 343–357.

Western Atlas, 1996. NMR Terminology Glossary (this compilation contains many references to original papers).

Westphal, H., Surholt, I., Kiesl, C., Thern, H.F., Kruspe, T., 2005. NMR measurements in carbonate rocks: problems and an approach to a solution. *Pure Applied Geophysics* 162, 549–570.

White, J.E., 1983. *Underground Sound*. Elsevier, Amsterdam.

White, J.E., Sengbush, R.L., 1953. Velocity measurements in near surface formations. *Geophysics* 18, 54–69.

White, J.E., Martineau-Nicoletis, L., Monash, C., 1983. Measured anisotropy in Pierre shale. *Geophys. Prospect.* 31 (5), 709–725.

Winkler, K.W., Murphy III, W.F., 1995. Acoustic velocity and attenuation in porous rocks, rock physics and phase relations—a handbook of physical constants. AGU Reference Shelf 3.

Winkler, K.W., Nur, A., 1982. Seismic attenuation: effects of pore fluids and frictional sliding. *Geophysics* 47, 1–15.

Winsauer, W.O., McCardell, W.M., 1953. Ionic double-layer conductivity in reservoir rock. *Trans. AIME* 198, 129–134.

Winsauer, W.O., Shearin, H.M., Masson, P.H., Williams, M., 1952. Resistivity of brine-saturated sands in relation to pore geometry. *AAPG Bull.* 36, 253–277.

Witherspoon, P.A., Wang, J.S.Y., Iwai, K., Gale, J.E., 1980. Validity of cubic law for fluid flow in a deformable rock fracture. *Water Resour. Res.* 16, 1016.

Wohlenberg, J. 1982. Density. In: Hellwege, K.-H. (Ed.), *Landolt-Börnstein Numerical Data and Functional Relationships in Science and Technology*, New Series, Group V. Geophysics and Space Research, vol. 1, Physical Properties of Rocks, subvol. A. Springer-Verlag, Berlin.

Woodhouse, R., Warner, H.R., 2004. Improved log analysis in shaly sandstones based on S_w and hydrocarbon pore volume routine measurements of preserved cores cut in oil-based mud. *Petrophysics* 45 (3), 281–295.

Woodside, W., Messmer, J.H., 1961. Thermal conductivity of porous media (I. Unconsolidated porous sands, II Consolidated rocks.). *J. Appl. Phys.* 32 (9), 1688–1699.

Worthington, P.F., 1985. The evolution of shaly-sand concepts in reservoir evaluation. *Log Analyst* 26 (1), 23–40.

Worthington, P.F., Pallatt, N., 1990. Effect of variable saturation exponent upon the evaluation of hydrocarbon saturation. Presented at the SPE Annual Technical Conference and Exhibition, New Orleans, LA, September, paper SPE 20538.

Worthington, P.F., Pallatt, N., Toussaint-Jackson, T.J., 1989. Influence of microporosity on the evaluation of hydrocarbon saturation. *SPE Form. Eval.* 4, 203–209.

Wyllie, M.R.J., Gregory, A.R., Gardner, L.W., 1956. Elastic wave velocities in heterogeneous and porous media. *Geophysics* 21, 41–70.

Yalcin, M.N., Littke, R., Sachsenhofer, R.F., 1977. Thermal history of sedimentary basins. In: Welte, D.H., Horsfield, B., Baker, D. (Eds.), *Petroleum and Basin Evolution*. Springer-Verlag, Berlin.

Ye, L.S., Kerr, D., Kexian, Y., 1999. Facies architecture of the bluejacket sandstone in the Eufaula Lake Area, Oklahoma: implications for reservoir characterization of the subsurface Bartlesville sandstone. In: Schatzinger, R., Jordan, J. (Eds.), *Reservoir Characterization—Recent Advances*, AAPG Memoir, 71, 29–44.

Yu, G., 1985. Offset-amplitude variation and controlled-amplitude processing. *Geophysics* 50 (12), 2697–2708.

Zang, A., Wolter, K., Berkhemer, H., 1989. Strain recovery, microcracks and elastic anisotropy of drill cores from KTB deep well. *Sci. Drill.* 1 (3), 115–126.

Zemanek, J., 1989. Low-resistivity hydrocarbon-bearing sand reservoirs. SPE FE December, 515–521.

Zhang, Q., Lo, S.L., Huang, C.C., Hirasaki, G.J., Kobayashi, R., House, W.V., 1998. Some exceptions to default NMR rock and fluid properties. Trans. 39th Annual Logging Symposium, SPWLA, paper FF.

Zimmerman, R.W., King, M.S., 1986. The effect of the extent of freezing on seismic velocities in unconsolidated permafrost. *Geophysics* 51 (6), 1285–1290.

Zoeppritz, K., 1919. Erdbebenwellen VIIB, on the reflection and propagation of seismic waves. *Göttinger Nachr.* I, 66–84.

Zoth, G., Haenel, R., 1988. Appendix. In: Hänel, R., Rybach, L., Stegema, L. (Eds.), *Handbook of Terrestrial Heatflow Density Determination*. Kluwer, Dordrecht.

Zundel, J.P., Siffert, P., 1985. Mechanisme de retention de l' octylbenzene sulfonate de sodium sur les mineraux argileux. *Solid–Liquid Interactions in Porous Media*. Editions Technip, pp. 447–462.

Index

A

Absolute permeability, 33
Acid reducing conditions, 110
Acoustic impedance, 230f
 Poisson's ratio and, 228–231
 sand and, 230f
 shale and, 230f
Actinolite, 99t
Air-mercury, capillary pressure, 62t
Air-oil, capillary pressure, 62t
Air-water, capillary pressure, 62t
Albite, 99t
 electrical resistivity of, 276t
 gamma-gamma interactions, 130t
 thermal properties, 339t
Aligned ellipsoids, 368–371
Alkali basalt, 113t
Alkali feldspar, 3t
 gamma activity, 119t
Allanite, 117
Alluvium loam, 358t
Almandine, 99t
 thermal properties, 339t
Alpha radiation, 108
Aluminosilicates, 8, 312
American Geological Institute, 4–5
American Petroleum Institute
 (API), 101
 Calibration Facility, 119, 137
 units, 118
Amorphous materials, thermal
 conductivity, 342
Amphibole, 3t, 378t
 electrical resistivity of, 276t
 magnetic susceptibility of, 383t
 thermal properties, 339t
Amphibolite, 103f
 thermal conductivity of, 347
Amplitude-offset patterns, 228f
Andalusite, thermal properties, 339t
Angle of internal friction, 256t
 for anhydrite, 256t
 for dolomite, 256t
Anhydrite, 99t, 104f, 140, 377t, 406t
 angle of internal friction, 256t

gamma-gamma interactions, 130t
Gardner equation coefficients, 172t
magnetic susceptibility of, 383t
permittivities, 313t
 thermal properties, 339t, 351t
Anisotropy, 15–16, 181–188
 compressional wave, 187–188
 fractures and, 183–184
 of igneous rocks, 183–184
 of laminated sediments, 184–187
 layer-induced, 181
 macroscopic, 305
 of metamorphic rocks, 183–184
 permeability, 54
 petrofabric origin, 182f
 shear wave, 187–188
 of thermal conductivity, 349t
 gneiss, 349t, 350f
 schist, 349t
 velocity, 164
Anorthite, 99t
 electrical resistivity of, 276t
 thermal properties, 339t
Apatite, 3t, 99t, 111t
 thermal properties, 339t
API. *See* American Petroleum
 Institute
Aragonite, 99t
 electrical resistivity of, 276t
 thermal properties, 339t
Archie's concept, 273
 mean values for, 283t
Archie's equation, 14, 303f
 electrical resistivity and, 280–287
 schematic picture, 281f
Archie's exponent, 284f
Argand plot, 311–312
Argillaceous limestones, 27–28, 413t
Arsenopyrite, 99t
Aspect ratio, 292t, 370t
Atlas RockView Analysis, 141–146
Atomic properties, 108t
Augite, 99t
AVO techniques, 226–228
Avogadro's number, 76–77

B

- Bandera sandstone
 - thermal expansion, 360t
 - thermal properties, 351t
- Barite, 99t
 - gamma-gamma interactions, 130t
- Baryte, thermal properties, 339t
- Basalt, 103f
 - thermal properties, 346t
- Basalt, 253f, 386t, 389t
 - magnetic susceptibility, 383t
- Bauxite, 111t
- Bentheim sandstone, 38
- Bentonite, 111t, 378t
- Benzene, 313t
- Berea sandstone, 20t
 - thermal expansion, 360t
 - thermal properties, 351t
- Beryl, 99t
- Beta radiation, 108
- Bimodal laminated sands, 305
- Biot's characteristic frequency, 212t
- Biot model, 207–213
 - global flow, 213f
- Biotite, 3t, 99t, 111t, 113t, 378t, 406t
 - electrical resistivity of, 276t
 - gamma-gamma interactions, 130t
 - thermal conductivity, 366t
 - thermal properties, 339t
- Black shale, 113t
 - Devonian, 123f
- Bluejacket sandstone, 42–43
- Boise sandstone, 261
 - compressional wave velocity, 173f
 - shear wave velocity, 173f
 - thermal expansion, 360t
 - thermal properties, 351t
- Bonding properties, 214–226
- Bound models, 188f
- Brine
 - compressional modulus, 159t
 - conductor, 281
 - density, 159t
 - elastic properties, 159
- Brine-saturated sandstone, 239f
- Brine-saturated shale, 187f
- Brooks-Corey equation, 65, 66
- Budiansky and O'Connell inclusion models, 200–202
- Bulk density, 97, 131
- Bulk relaxation, 82–84
 - transverse relaxation and, 83f

Bulk volume fluid, 30–32, 336f

- Bulk volume irreducible, 75**
- Bulk volume movable (BVM), 75**
- Bureau of Mines, US, 58
- Burial compaction, 26
- BVM. *See Bulk volume movable*

C

- CaAl-pyroxene, 99t
- Calcite, 10, 99t, 377t, 406t
 - composition, 399t
 - electrical resistivity of, 276t
 - gamma-gamma interactions, 130t
 - permittivities, 313t
 - replacement of, 26
 - thermal expansion, 360t
 - thermal properties, 339t
- Canadian Shield, 260
- Capillary models, clean rock, 295–296
- Capillary pressure, 59–70
 - curves, 48–55, 63f
 - conversion, 72f
 - determination, 59
 - dynamic methods, 59
 - static methods, 59
 - drainage curves, 64f
 - equation, 65–68
 - fluid distribution and, 68–70
 - imbibition curves, 64f
 - measurement, 62f
 - saturation and, 69f
 - NMR for, 92–95
- properties, 62t
 - air-mercury, 62t
 - air-oil, 62t
 - air-water, 62t
 - oil-water, 62t
 - water-gas, 62t
 - water-oil, 62t
 - typical gradients, 69t
- Capillary tube model, 48–52, 48f, 55f
 - fundamental equation, 48–50
- Carbonate Advisor (Schlumberger), 32
- Carbonates, 4, 8–12, 43–45, 89–90, 413t
 - classification of, 11–12
 - pore types, 11f
 - composition, 10–11
 - density of, 411f
 - detection, 139
 - hydrocarbon-bearing, 32f

non-vuggy
permeability in, 44f
porosity in, 44f
permeability, 25f
porosity and, 46f
pore networks of, 27f
porosity of, 25f, 26–28
permeability and, 46f
profile, 401–403
properties of, 13t
radioactive, 110
siliciclastics *v.*, 12
thermal properties, 339t
velocity, 167–168
velocity-porosity plot, 167f
Carnallite, 111t
gamma activity, 119t
Cassiterite, 99t
Castagna equation, 242
sedimentary rock velocity and, 179–181
Castagna plot, empirical
regressions as, 180f
Cation-Exchange Capacity (CEC), 300t
CBW. *See* Clay-bound water
CEC. *See* Cation-Exchange Capacity
Cement, thermal properties of, 355t
Cementation, 364
exponent, 282, 290
Central European soils, 358t
Chalcopyrite, 99t
Chalk
Ekofisk, 224, 225f
North Sea, 251f
Channels, fluid flow through, 52–53
Chargeability, 327, 328
Chemical remanent magnetization (CRM), 388
Chlorine, 135
Chlorite, 9f, 99t, 111t, 378t
electrical resistivity of, 276t
gamma activity, 119t
gamma-gamma interactions, 130t
thermal properties, 339t
Chromite, 99t
Chromium, 82–83
Clastics, 4, 5–8, 36–43
classification of, 5–6
by grain size, 5f
formation of, 5
hydrocarbon-bearing, 32f
permeability, 45f
porosity and, 45f
textural properties of, 6–7
velocity, 165–167
Clausius-Mossotti model, 290–291, 294, 320, 366, 371, 409
Clay, 104f, 113t
Loess, 358t
magnetic susceptibility, 383t
mineral typing, 121–123
permittivity of, 314f
properties, 85t, 86t
thermal, 356–357
Clay-bound water (CBW), 31, 85
Claystone, 5, 6
building blocks of, 9f
dispersed, 4–5
fundamental properties, 7–8
laminated, 5
mineral properties of, 10t
structural, 5
thermal properties, 351t
Clean rocks, 288–296
capillary models, 295–296
inclusion models, 290–291
nonspherical, 291–295
randomly arranged, 294–295
introduction, 288–289
layer model, 289–290
nonspherical inclusions, 291–295
Clinopyroxene, 3t
Coal
magnetic susceptibility, 383t
thermal properties, 351t
Cohesion, 256t
Cole-Cole distribution parameter, 311, 325
Cole-Cole model, 333, 334–335
spectrum of, 325
Committee on Fracture Characterization and Fluid Flow, 28
Compact hexagonal sphere pack, 25t
Compaction, 21, 22–23
burial, 26
of sand, 23f
of shale, 23f, 25f
Compaction reference, 170–171
Complex conductance model, 329f
Complex permittivity, 274
Complex refractive index method (CRIM), 320, 322–324
Complex resistivity, 324–335
Compressibility, 22
Compression strength, Young's modulus and, 264f

Compressional modulus, 154f
 brine, 159t
 oil, 159t

Compressional wave anisotropy, 187–188

Compressional wave attenuation, 238f

Compressional wave slowness, 151, 153
 porosity and, 170

Compressional wave velocity, 158t, 210, 211–212, 248f, 265

Boise sandstone, 173f

clastics, 165–167

crack porosity and, 202f

of cubic packing, 195

depth and, 178t

fluid saturation and, 174f, 243f

of minerals, 156t

normalized, 199f, 200f

porosity and, 166f, 199f, 200f, 219f

porosity curves and, 192f, 194f

pressure and, 176f

shear strength and, 266f

thermal conductivity and, 407f, 410f, 411f, 412f

uniaxial compression strength and, 266t, 267f, 271f

Compton effect, 126, 128

Conductivity. *See also* Thermal conductivity
 hydraulic, 40t
 imaginary part of, 334f
 in-phase, 334f
 interface, 332, 333f
 macroscopic, 307f
 of minerals, 342
 quadrature, 329–330

Contact modulus, 221

Contact number, 25

Convection, 338

Conventional core analysis, 71t

Coordination number, 25

Cordierite, 99t

Cored sections, lithologies of, 70t

Coulomb's criterion, 255

Coulomb's law, 270

CPMG sequence (Carr-Purcell-Meiboom-Gill), 77–78, 79f

Crack density parameter, 201

Crack porosity, 163f
 compressional wave velocity and, 202f

Cracked rocks, 48

Cracks
 penny-shaped, 198t
 single set, 203t

CRIM. *See* Complex refractive index method

Critical porosity concept, 189f

CRM. *See* Chemical remanent magnetization

Crossplots, 396–397
 density-slowness, 396
 neutron-density, 396, 397f, 402f
 slowness-neutron, 396

Crude oil
 thermal properties, 344t
 uranium in, 124t

Crystalline solid materials
 thermal conductivity, 342

Cubic packing
 compressional wave velocity of, 195

Cubic sphere pack, 25f

Cylindrical sample, 250f

D

Danburite, 99t

Darcy's law, 35, 39
 fluid flow and, 49
 permeability in, 55–56

Debye model, 311–312

Deep Sea Drilling Project, 162, 285

Defect model, 204–207

Defect parameters, 206, 405–408

Deformation properties
 geomechanical, 252
 under normal loading, 195f

Density. *See also* Neutron-density
 crossplots
 brine, 159t
 bulk, 97, 131
 of carbonates, 411f
 definition, 97–98
 fluid, 100t
 gamma-gamma measurement, 129–131
 hydrocarbons, 159t
 log, 401f
 mean, 97
 of methane, 102f
 of minerals, 98, 156t
 oil, 159t
 of pore fluids, 98–101
 porosity and, 105
 radioactive heat generation and, 126t
 of rocks, 101–105
 soil, 357
 units, 97–98

Density-slowness crossplots, 396

Dephasing, 78

Depolarization exponent, 292t, 371t

Depolarizing exponent, 295t
Depositional remanent magnetization. *See* Detrital remanent magnetization
Depth, porosity and, 22f
Detrital remanent magnetization (DRM), 388
Devonian black shale, 123f
Diabase, 103f, 386t, 389t
 magnetic susceptibility, 383t
 thermal properties, 346t
 uniaxial compression strength, 258t
Diagenesis, 26
Diamagnetic materials, 374
 mass susceptibility, 377t
 volume susceptibility, 377t
Diamond, 99t
Diaspore, 99t
Dielectric permittivity, 280f, 313t
Dielectric properties, 310–324
 experimental results, 315–317
 introduction, 310–312
 models, 317–324
 inclusion, 320–321
 layer, 317–320
 of rock constituents, 312–314
 theories, 317–324
Diesel, 313t
Diffusion coefficients, 87f
Diffusion-induced relaxation, 85–87
Dikes, 2
Diopside, 99t
Diorite, 103f, 113t
 magnetic susceptibility, 383t
 thermal properties, 346t
Dipole orientational polarization, 311
Dispersed clay, 4–5
Dispersed shaly sand, 53, 299–302
Dolomainstones, 44
Dolomite, 10, 99t, 104f, 377t, 378t, 406t, 413t
 angle of internal friction, 256t
 composition, 399t
 electrical resistivity of, 276t
 gamma-gamma interactions, 130t
 Gardner equation coefficients, 172t
 magnetic susceptibility, 383t
 permeability, 35f
 permittivities, 313t
 porosity, 28, 398f
 thermal properties, 339t, 351t
 uniaxial compression strength, 258t
Dolomitization, 26
Dominant pore-throat diameter, 333
Drainage, 64–65
 capillary pressure curve, 64f
DRM. *See* Detrital remanent magnetization
Dual porosity systems, 294
Dual Water Model, 302
Dunite, 103f, 113t
Dynamic moduli, 259–264
 compressional bulk, 262f
 Young's, 263t

E

Eastern Alpine crust, 344
Eclogite, 103f
EcoScope, 140–141
ECS. *See* Elemental Capture Spectroscopy
 Sonde
Effective permeability, 33, 55–56
Effective pressure, 221f
Effective stress, porosity and, 24
Ekofisk chalk, 224, 225f
Elastic moduli, 149–153
 bounds for, 189–194
 isotropic materials, 151t
 of minerals, 156t
Elastic properties
 of brine, 159
 conversions, 154
 fundamentals, 149–154
 of gases, 158
 of rock constituents, 154–159
 fluids, 155–159
 minerals, 155
 overview, 154–155
 solid components, 155
sandstone, 240–243
theories, 188–226
 bound models, 188f
 classification of, 188f
 inclusion models, 188f
 pore fluid effect models, 188f
 sphere pack models, 188f
 units, 154
Elastic scattering, neutron
 radiation, 134
Elastic stiffness components, 186t
Elastic wave attenuation, 232–240
 coefficient, 234t
 frequency and, 235f
 definition, 232–233
 mechanisms, 240
 overview, 233–236
 seismic

Elastic wave attenuation (*Continued*)

igneous rocks, 236

sedimentary rocks, 236–240

units, 232–233

Elastic wave velocities, 149–153

thermal conductivity and, 403–414

Electrical properties

forward calculation, 306–307

fundamentals, 273–275

of pore fluids, 277–278

of rock components, 275–278

minerals, 275–276

sandstone, 335–336

symbols, 275

units, 275

Electrical resistivity, 273

Archie’s equation, 280–287

fluid saturation and, 298f

overview, 278–280

range of, 278t

specific, 276t, 278–288

Electrode polarization, 326

Electrolytic interface polarization, 326

Electromagnetic wave propagation, 315t

Electrons, 107

polarization, 311

Elemental Capture Spectroscopy Sonde (ECS), 140–141

Elemental concentration, 141–142

detectable, 144t

Enstatite, 99t

Epidote, 99t, 111t

thermal properties, 339t

Evaporites, 4, 8–12

Experiment repetition time, 80

Exponential law, 178

Extended hydraulic unitization, 52

External field property, 77

F

Failure/strength properties, 252–258

modes of, 253f

Fayalite, 99t

Feldspar, 406t

alkali, 3t, 119t

thermal conductivity, 366t

thermal properties, 339t

Feldspathic sandstones, 117

Felsic rocks, 2

Ferrimagnetic material, 375f

mass susceptibility, 380t

volume susceptibility, 380t

Ferromagnetic material, 375f

mass susceptibility, 380t

volume susceptibility, 380t

FLeX. *See* Formation Lithology eXplore

Fluids. *See also* Pore fluids

bulk modulus, 215f

density, 100t

temperature and, 100f

distribution, 59–70

capillary pressure and, 68–70

fundamentals, 59–63

elastic properties of, 155–159

flow, 29

channels, 52–53

Darcy’s law and, 49

fractures, 52–53

magnetic properties, 380–381

magnetic properties of, 380–381

multiphase pore, 213–214

replacement, 242f

saturated case, 209

saturation

capillary pressure and, 336f

compressional wave velocity, 174f, 243f

electrical resistivity and, 298f

sedimentary rock velocity and, 173–175

shear wave velocity, 174f, 243f

thermal properties of, 342–344

typing

NMR for, 95–96

Fluorite, 99t, 377t

thermal properties, 339t

Forchheimer effect, 35

Formation factor, 284f, 286f

overburden pressure dependence, 288f

pressure dependence of, 287–288

Formation Lithology eXplore (FLeX), 140–141

Fosterite, 99t

Fourier transformation, 324

Fourier’s law, 337

Fractal analysis, 28

Fractures, 28–29

anisotropy and, 183–184

characterization of, 29

defect model, 204–207

fluid flow through, 52–53

permeability, 53

porosity, 294f

- shear, 28
- tension, 28
- Frequency-dependent conductivity, 275
- Frequency-dependent dielectric permittivity, 275
- Frequency-independent phase angle, 325–326
- Friction factor, 53
- G**
 - Gabbro, 103f, 113t, 266t, 386t
 - magnetic susceptibility, 383t
 - thermal properties, 346t
 - Galena, 99t
 - thermal properties, 339t
 - Gamma radiation, 108
 - alkali feldspar, 119t
 - biotite, 119t
 - carnallite, 119t
 - characteristic energies, 133t
 - chlorite, 119t
 - energy, 127f
 - fundamentals, 127–129
 - illite, 119t
 - interactions, 126–131
 - kaolinite, 119t
 - mean API values for, 119t
 - montmorillonite, 119t
 - muscovite, 119t
 - natural spectrum, 118f
 - origin of, 108–109
 - plagioclase, 119t
 - quartz, 119t
 - sylvite, 119t
 - Gamma spectrometry, 140t
 - Gamma-gamma interactions, 130t
 - albite, 130t
 - anhydrite, 130t
 - barite, 130t
 - biotite, 130t
 - calcite, 130t
 - chlorite, 130t
 - dolomite, 130t
 - gypsum, 130t
 - halite, 130t
 - illite, 130t
 - kaolinite, 130t
 - montmorillonite, 130t
 - muscovite, 130t
 - orthoclase, 130t
 - quartz, 130t
 - siderite, 130t
 - Gamma-gamma-density measurement, 129–131
 - Gamma-gamma-PE measurement, 129
 - Gammalog, 120, 146f, 401f
 - Gamma-ray index, 120, 121, 121f
 - Gardner equation coefficients, 172t
 - Garnets, thermal properties, 339t
 - Gases, elastic properties of, 158
 - Gassmann-Biot concept, 212–213
 - Gassmann's equation, 15, 207–213
 - Gassmann's model, 213f
 - Gassmann's model, 207–211
 - Geomechanical properties
 - classification, 246–249
 - deformation, 252
 - dynamic moduli, 259–264
 - failure/strength, 252–258
 - fundamental, 249–258
 - strain, 249–250
 - stress, 249–250
 - model-based relationships, 267–271
 - overview, 245–246
 - static moduli, 259–264
 - Geophysical borehole measurements, 269f
 - Geophysical methods, 14
 - German Molasse Basin, 356t
 - Glacial till permeability, 35f
 - Glaucite, 99t, 111t
 - Glaucophane, 99t
 - Gneiss, 103f, 152, 253f
 - magnetic susceptibility of, 383t
 - thermal conductivity of, 347
 - anisotropy of, 349t, 350f
 - thermal properties, 346t
 - Goethite, 380t
 - Grain diameter, 387f
 - Grain packing, 7
 - Grain shape, 7
 - Grain size
 - clastic classification and, 5f
 - parameters, 6–7
 - permeability and, 37–39
 - Grain sorting, 7
 - Grainstones, 44
 - Granite, 103f, 113t, 253f, 386t
 - Kirchberg, 366t
 - magnetic susceptibility, 383t
 - mineral composition of, 366t
 - Svanek, 384–385
 - thermal conductivity of, 347, 366t
 - thermal properties, 346t
 - uniaxial compression strength, 258t

Granodiorite, 113t
 thermal properties, 346t
 Granulite, 389t
 magnetic susceptibility of, 383t
 Graphite, 99t
 Gravel, permeability, 35f
 Graywacke, 113t
 thermal properties, 351t
 uniaxial compression strength, 258t
 Grossularite, thermal properties, 339t
 Gypsum, 99t, 104f
 gamma-gamma interactions, 130t
 magnetic susceptibility of, 383t
 thermal properties, 339t, 351t
 Gyromagnetic ratio, 77

H

Haematite, 380t
 Hagen-Poiseulle's law, 55
 Halite, 99t, 377t
 gamma-gamma interactions, 130t
 permittivities, 313t
 thermal properties, 339t
 Hanai-Bruggeman formula, 321
 Hashin-Shtrikman bounds,
 189–194, 191f
 Hedenbergite, 99t
 Hertz's theory, 177, 195f, 220
 Heterogeneity, 15–16
 Hills value, 319
 Homogeneity, 15
 Hooke's law, 149
 Horizontal permeability, 42
 Hornblende, 99t, 378t, 406t
 electrical resistivity of, 276t
 thermal expansion, 360t
 Hudson inclusion models,
 202–204, 205f
 Humble equation, 282–283
 Hydraulic conductivity, 40t
 Hydrocarbons
 density, 159t
 relative permeability of, 56f
 typing, 95–96
 Hydrogen, 134
 gyromagnetic ratio of, 77
 index, 91f, 92t
 Hydrogen nuclei, 75
 Hydrogeology, permeability and,
 39–40
 Hysteresis, 317
 magnetic, 376f

I
 Ice, 377t, 381
 thermal properties, 344t
 Igneous rocks, 2–3. *See also specific types*
 anisotropy of, 183–184
 classification of, 2–3
 empirical relationships, 404–409
 Koenigsberger ratio of, 389t
 magnetic susceptibility of, 383t
 radioactive heat generation of, 125t
 radioactivity of, 115
 seismic wave attenuation in, 236
 thermal properties of, 346t
 velocity of, 161–164
 Illite, 9f, 99t, 111t, 378t
 gamma activity, 119t
 gamma-gamma interactions, 130t
 properties, 86t
 thermal properties, 339t
 Ilmenite, 3t, 99t, 380t
 thermal properties, 339t
 Ilmenite-hematite, 379
 Imbibition, 64–65
 capillary pressure curve, 64f
 defined, 64
 Inclusion models, 188f, 196–204
 Budiansky and O'Connell, 200–202
 calculations, 408–409
 clean rock, 290–291
 nonspherical, 291–295
 randomly arranged, 294–295
 of dielectric properties, 320–321
 Hudson, 202–204, 205f
 Kuster and Toksöz, 197–200
 nonspherical, 321–322, 368–372
 spherical, 320–321, 365–367
 of thermal properties, 365–372
 Indonesia equation, 303, 303f
 Induced magnetization, 382–385
 Inelastic scattering, 132–133
 In-phase conduction, 334f
 Integral measurements, 118–119
 Inter-echo time, 79
 Interface conductivity, 332, 333f
 Interface properties, 61
 Interfacial polarization, 311
 Interfacial tension, 57–58
 Intermediate rocks, 2
 Intermediate wettability, 57, 58
 Internal structure model, 214–226
 variable, 215f
 Interparticle pore network, 43

Interval transit time, 172f
 Ionic polarization, 311
 Irreducible saturation, 50
 Isotropic materials, 151t

J

Jacobsite, 99t
 Jurassic shale, 186

K

Kainite, 111t
 Kaolinite, 9f, 99t, 111t
 electrical resistivity of, 276t
 gamma activity, 119t
 gamma-gamma interactions, 130t
 properties, 86t
 thermal properties, 339t
 Karst limestone, 35f
 Kerogen, 145
 Kerosene, thermal properties of, 344t
 Kieserite, 99t
 Kirchberg granite, 366t
 Klinkenberg effect, 34–35
 Koenigsberger ratio, 388–389, 389t
 of igneous rocks, 389t
 of metamorphic rocks, 389t
 of sedimentary rocks, 389t
 Kozeny constant, 51–52
 Kozeny equation, 54
 Kozeny shape factor, 51t
 Krischer-Esdorn equation, 365
 KTB borehole, 348f
 Kuster and Toksöz Inclusion models, 197–200
 Kyanite, 99t
 thermal properties, 339t

L

Labradorite, 99t
 electrical resistivity of, 276t
 Lambda rho, 231–232
 Lame parameters, 150
 Lame's numbers, 252
 Laminated clay, 5
 Laminated sands, 304–310
 bimodal, 305
 Laminated sediments, anisotropy of, 184–187
 Laminated shaly sand, 54, 298–299,
 304–310
 inversion, 308–310
 Lamination, 43
 Langbeinite, 99t, 111t

Large crystalline dolostones, 44
 Larmor frequency, 77, 78
 Lava, thermal properties, 346t
 Layer model, 289–290
 of dielectric properties, 317–320
 mixing rules, 362–365
 parallel, 361–362
 petrophysical relationships, 394–403
 series, 361–362
 of thermal properties, 361–362
 Layer-induced anisotropy, 181
 Leaching, 26
 Leucite, 99t
 Leverett function, 65–66, 72
 Lichtenegger-Rother equation, 319f, 365
 Lignite, 104f
 Limestone, 10, 104f, 137, 253f, 266t, 413t
 argillaceous, 27–28
 Gardner equation coefficients, 172t
 initial porosity, 23
 Karst, 35f
 magnetic susceptibility of, 383t
 non-vuggy, 172f
 porosity, 398f
 Silurian, 355f
 thermal properties, 351t
 uniaxial compression strength, 258t
 Linear thermal expansion, 360t
 Lithification, 4
 Lithologic profile, 119–120
 sedimentary rock velocity
 and, 165–169
 Lithothek, 404–405
 Loam, 104f
 alluvium, 358t
 Loess clay, 358t
 Log analysis, 336f
 Longitudinal relaxation, 81, 82f
 Longitudinal wave velocity, crack
 porosity and, 163f
 Low-bog-peat, 358t
 Low-resistivity pay evaluation, 309f

M

Mackenzie River Valley, 169t
 Macropores, 12
 Macroscopic anisotropy, 305
 Macroscopic conductivity, 307f
 Macroscopic module, 308
 Macrosystems, 215
 Mafic rocks, 2
 Maghemite, 99t, 380t

Magmatic rock 1f. *See also specific types*
 mineralogical classification of, 2f
 thermal properties of, 345–348

Magnesite, 99t
 thermal properties, 339t

Magnetic hysteresis, 376f

Magnetic properties
 of fluids, 380–381
 of minerals, 376–380
 of rock constituents, 376–381
 units, 374t

Magnetic susceptibility, 382f, 386f
 content and, 385–388
 grain diameter and, 387f
 of igneous rocks, 383t
 of metamorphic rocks, 383t
 natural remanent magnetization and, 390f
 of sedimentary rocks, 383t

Magnetite, 3t, 99t, 380t, 385
 thermal properties, 339t

Magnetization, 88

Malachite, 99t

Marble, 103f, 253f
 thermal properties, 346t
 uniaxial compression strength, 258t

Marcasite, 99t

Marl, 104f

Mass susceptibility
 of diamagnetic materials, 377t
 of ferrimagnetic materials, 380t
 of ferromagnetic materials, 380t
 paramagnetic substances, 378t

Massilon sandstone, 239–240, 239f

Matrix effect, 75

Matrix point, 396

Mavko local flow model, 213f

Maxwell-Wagner, 312

Mean density, 97

Megaelectron volt (MeV), 109f

Mercury, 61
 pressure, 95

Mesopores, 12

Mesozoic sandstone, 316f

Metal factor, 327–328

Metamorphic rocks, 3. *See also specific types*
 anisotropy of, 183–184
 empirical relationships, 404–409
 Koenigsberger ratio of, 389t
 magnetic susceptibility of, 383t
 radioactivity and, 116
 thermal properties of, 345–348, 346t
 velocity of, 161–164

Methane, 87f
 density of, 102f

MeV. *See* Megaelectron volt

Mica, thermal properties, 339t

Micaceous sandstones, 117

Microcline, 99t, 111t
 electrical resistivity of, 276t
 thermal properties, 339t

Microcrack properties, 332

Micropores, 12

Microsystems, 215

Minerals
 conductivity of, 342
 density of, 98, 156t
 elastic moduli, 156t
 elastic properties of, 155
 electrical properties of, 275–276
 in granite, 366t
 magnetic properties of, 376–380
 potassium in, 109–112
 thermal properties, 339–344
 rock-forming, 339t
 thorium in, 109–112
 uranium in, 109–112
 wave velocities, 156t

Mississippian Madison Group, 27

Mixing rule, 362–365, 365f

Modulus magnification, 209–210

Mohr's circle, 255f

Mohr's diagram, 254f

Molecular diffusion, 85–86

Molecular polarization, 311

Monazite, 111t, 117

Montmorillonite, 8, 9f, 99t, 111t, 378t
 gamma activity, 119t
 gamma-gamma interactions, 130t
 properties, 86t

Mu rho, 231–232

Mudrock line, 179

Multi-exponential decay, 87–89

Multiphase flow, 55–56

Multiphase pore fluids, 213–214

Muscovite, 99t, 111t, 378t, 406t
 electrical resistivity of, 276t
 gamma activity, 119t
 gamma-gamma interactions, 130t
 thermal conductivity, 366t
 thermal properties, 339t

N

Natrolite, 99t

Natural radioactivity, 108–126

Natural remanent magnetization, 388–391
susceptibility and, 390f, 391f

Nepheline, 99t
thermal properties, 339t

Neutron radiation, 131–139
elastic scattering, 134
fundamentals, 131–136
inelastic scattering, 132–133
porosity and, 136–138

Neutron-density crossplots, 396, 397f, 402f

NMR. *See* Nuclear magnetic resonance

Nonreactive fluids, 33

Nonspherical inclusions, 291–295

Non-vuggy carbonates, 44f

Non-vuggy limestone, 172f

Normal loading, deformation under, 195f

North Sea, 42
chalk, 251f

Nuclear magnetic resonance (NMR), 75
applications, 90–96
capillary pressure estimate, 92–95
permeability, 92–95
pore size, 92–95
pore volume partitioning, 90–92
porosity, 90–92
data processing, 88f
fluid typing, 95–96
fundamentals, 76
measurement, 77–80
physical origin, 76–77
of reservoir fluids, 83t

Nuclear measurements, 139–146

Nuclear properties, 107–108

O

Octahedral unit, 8

ODF. *See* Orientation distribution function

Ohm's law, 274

Oil
compressional modulus, 159t
crude
thermal properties, 344t
uranium in, 124t
density, 159t
shale, 113t
thermal properties, 344t

Oil-water, capillary pressure, 62t

Oil-wet, 57

Olivine, 3t, 378t, 406t
thermal properties, 339t

Oman abyssal plain, 24

Ore-containing rocks, spectral-induced polarization in, 328

Orientation distribution function (ODF), 186

Oriented ellipsoidal inclusions, 291–294

Orthoclase, 99t, 111t, 377t
electrical resistivity of, 276t
gamma-gamma interactions, 130t
thermal properties, 339t

Orthopyroxene, 3t

Orthorhombic sphere pack, 25t

P

Pair production, 128–129

Parallel conductor circuits, 297

Parallel model, 317
layer, 361–362

Paramagnetic substances, 374–375
mass susceptibility, 378t
volume susceptibility, 378t

Patchy saturation, 214

Peat
low-bog, 358t
raised-bog, 358t

Pendular region, 60

Penny-shaped cracks, 198t

n-Pentane, thermal properties, 344t

Peridotite, 103f, 113t
magnetic susceptibility, 383t
thermal conductivity of, 347
thermal properties, 346t

Permafrost, 168
seismic velocity, 169t

Permeability, 32–56
absolute, 33
anisotropy, 54
carbonates, 25f
clastics, 45f
in Darcy's law, 55–56
definitions, 33–35
determining, 32–33
dolomite, 35f
effective, 33, 55–56
equations for, 49–50
fracture, 53
glacial till, 35f
grain size and, 37–39
gravel, 35f
horizontal, 42
hydrogeology and, 39–40
limestone, 35f
log, 148f
mean magnitude ranges, 35f

Permeability (*Continued*)

- measurement principle, 34f
- models, 48–55
 - capillary tube model, 48–52, 48f
 - overview, 48
- NMR for, 92–95
- pore size and, 37–39
- pore-throat radius and, 52
- porosity and, 37–39
 - of carbonates, 46f
 - of clastics, 45f
 - main influences on, 45
 - in non-vuggy carbonates, 44f
 - plots, 37f
- pressure and, 47f
- relative, 33
 - curves, 66–67
 - defined, 56
 - for hydrocarbons, 56f
 - for water, 56f
- sand, 35f
- sandstone, 25f, 35f
- sedimentation and, 42
- shale, 35f, 41f
 - influence of, 53–55
- vertical, 42

Permittivity

- anhydrite, 313t
- calcite, 313t
- clay, 314f
- complex, 274
- dielectric, 280f, 313t
- dolomite, 313t
- electrical resistance, 279
- frequency-dependent dielectric, 275
- halite, 313t
- porosity and, 321f, 322f
- quartz, 313t
- water, 314f

Permo-Triassic sandstone, 334–335

Petrophysical relationships

- introduction, 393–394
- layered models, 394–403

Petrophysics, 12–13

Phase angle tangent, 332

Phlogopite, 99t

Phosphate, 111t

- thermal properties, 339t

Photoelectric effect, 126, 128

- gamma-gamma measurement, 129

Phyllite, 103f

- magnetic susceptibility of, 383t

Plagioclase, 3t, 111t

- gamma activity, 119t
- thermal conductivity, 366t
- thermal expansion, 360t

Plutonic rocks, 2

PNC. *See* Pulsed neutron capture

Poisson's ratio, 152f, 162f, 252

- acoustic impedance and, 228–231

Polarization mechanisms, 310f. *See also*

- Spectral-induced polarization
- dipole orientational, 311
- electrode, 326
- electrolytic interface, 326
- electron, 311
- interfacial polarization, 311
- ionic, 311
- molecular, 311
- pore geometrical properties and, 330–335
- water, 314

Polyhalite, 99t

Polymetallic rock, 364–365

Pore constrictivity polarization, 327

Pore fluids

- density of, 98–101
- dielectric permittivity of, 313t
- electrical properties of, 277–278
- multiphase, 213–214
- sedimentary rocks
 - thermal properties, 349–357
 - velocity and, 173–175
 - thermal properties of, 344t

Pore geometrical factor, 65

- polarization effects related to, 330–335

Pore network

- interparticle, 43
- vuggy, 43

Pore radius, 49

Pore size

- NMR for, 92–95
- permeability and, 37–39

Pore space properties

- overview, 17

Pore surface area, 29–30

Pore types, carbonate, 11f

Pore volume partitioning, NMR for, 90–92

Pore-body, 51

Pore-throat, 51

- permeability and, 52

Poro-perm plot, 37

Poro-perm regression, 70

Porosity, 17–29

of artificially mixed wet-packed unconsolidated sand, 21t of carbonates, 25f, 26–28 compressional velocity and, 166f, 199f, 200f compressional wave slowness and, 170 compressional wave velocity and, 219f crack, 163f critical, 189f curves, 192f, 194f definitions, 18–19 density and, 105 depth and, 22f lithologies, 27f profiles, 23 dolomite, 28, 398f dual, 294 effective stress and, 24 exponential, 23 factor, 218–220 fracture, 294f influence of, 349–357 initial limestone, 23 sandstone, 23 shale, 23 limestone, 398f mean, 20t measurements direct, 18 indirect, 18 from neutron measurements, 136–138 NMR for, 90–92 permeability and, 37–39 of carbonates, 46f of clastics, 45f main influences on, 45 in non-vuggy carbonates, 44f plots, 37f relative permittivity and, 321f, 322f residual, 23–24 sandstone, 36t, 105f, 316f secondary, 20 sedimentary rocks thermal properties, 349–357 velocity and, 165–169 separate vugs, 45f shear velocity and, 199f shear wave velocity and, 219f thermal conductivity and, 348f, 356f, 370f, 372f sand, 353f volumetric rock composition and, 395–401 Porous rocks, spectral-induced polarization in, 328–335 Porphyry, magnetic susceptibility, 383t Postdiagenetic processes, 35 Potassium, 109, 121 heat production rate, 125t major occurrences of, 112 in minerals, 109–112 in rocks, 113–118 thorium and, 122f Poupon equation, 298–299, 303f Power law parameters, 45 Precessing, 78 Pressure. *See also* Capillary pressure compressional wave velocity and, 176f dependence, 46–48 permeability and, 47f effective, 221f formation factor and, 287–288 permeability and, 47f sedimentary rock velocity and, 175–179 thermal conductivity and, 359f Prophyrite, 103f Protons, 107 Pseudobrookite, 99t, 379 Pulsed neutron capture (PNC), 135 measurements, 138–139 P-wave velocity, 185 Pyrite, 99t thermal properties, 339t Pyroxene, 378t, 406t thermal properties, 339t Pyroxenite, 103f magnetic susceptibility, 383t Pyrrhotite, 99t, 380t thermal properties, 339t

Q

Quadrature conductivity, 329–330 Quartz, 3t, 99t, 342, 377t, 406t composition, 399t electrical resistivity of, 276t gamma activity, 119t gamma-gamma interactions, 130t permittivities, 313t thermal conductivity, 366t thermal expansion, 360t thermal properties, 339t Quartzite, 103f, 253f magnetic susceptibility of, 383t

Quartzite (*Continued*)
 thermal properties, 346t
 uniaxial compression strength, 258t

R

Radiation
 alpha, 108
 applications, 119–123
 lithologic profile, 119–120
 beta, 108
 gamma, 108
 characteristic energies, 133t
 interactions, 126–131
 natural spectrum, 118f
 origin of, 108–109
 igneous rocks and, 115
 integral measurements, 118–119
 metamorphic rocks and, 116
 neutron, 131–139
 fundamentals, 131–136
 inelastic scattering, 132–133
 spectral measurements, 118–119

Radiative capture, 135

Radioactive carbonates, 110

Radioactive heat generation, 124–126
 density and, 126t
 of igneous rocks, 125t

Radioactivity, 116–118

Raised-bog-peat, 358t

Randomly arranged inclusions, 294–295, 371–372

Raymer-Hunt-Gardner equation, 171–172

Real pore geometry, 51–52

Realgar, 99t

Red sediments, 389t
 magnetic susceptibility of, 383t

Reflection coefficients, 228

Regular sphere packings, 25t

Relative permeability, 33
 curves, 66–67
 defined, 56
 for hydrocarbons, 56f
 for water, 56f

Relaxation process, 80
 bulk, 82–84, 83f
 diffusion-induced, 85–87
 longitudinal, 81, 82f
 multi-exponential decay and, 87–89
 surface, 81
 transverse, 81, 82f, 83f

Relaxation-time spectrum, 335f

Reservoir properties, 14
 fundamental, 17
 NMR, 83t
 pore geometric, 61
 from seismic parameters, 226–232

Reservoir Quality index (RQI), 52

Residual porosity, 23–24

Reversible dephasing, 78

Reynolds numbers, 34

Rhyolite, 103f, 113t
 magnetic susceptibility, 383t

RMR. *See* Rock mass rating

Rocks. *See specific types*

Rock cycle 1f

Rock density, 101–105

Rock magnetization, 381–382

Rock mass rating (RMR), 247

Rock properties
 classification, 15t
 general characteristics, 12–16

Rock quality designation (RQD), 247, 247t
 parameters, 248f

Rock salt
 magnetic susceptibility of, 383t
 thermal properties of, 353t
 uniaxial compression strength, 258t

Rock skeleton, shale, 22

Rock-fabric classification, 44

Rock-fluid system, 188

Rocks
 potassium content of, 113–118
 thorium content of, 113–118
 uranium content of, 113–118

RQD. *See* Rock quality designation

RQI. *See* Reservoir Quality index

Rutile, 99t
 thermal properties, 339t

S

Salt, 104f
 rock
 magnetic susceptibility of, 383t
 thermal properties of, 353t
 Thuringia, 349, 353t
 uniaxial compression strength, 258t
 thermal properties of, 353t

Saltwater, 138

Sand
 acoustic impedance and, 230f
 artificially mixed wet-packed
 unconsolidated
 porosity of, 21t

bimodal laminated, 305
compaction process for, 23f
dispersed shaly, 53
isotropic, 307
laminated, 304–310
 bimodal, 305
 laminated shaly, 54
 inversion, 308–310
permeability, 35f
shaly, 296–304
 complex conductance
 model, 329f
 composite, 307
 equations, 303–304
 problem, 296–297
thermal conductivity
 porosity and, 353f
thermal properties, 351t
unconsolidated, 177f

Sand-shale sequence, 309

Sandstone, 5, 70–73, 104f, 146–148, 253f, 266t
 Bandera
 thermal expansion, 360t
 thermal properties, 351t
 Bentheim, 38
 Berea, 20t
 thermal expansion, 360t
 thermal properties, 351t
 Bluejacket, 42–43
 Boise, 261
 compressional wave velocity, 173f
 shear wave velocity, 173f
 thermal expansion, 360t
 thermal properties, 351t
 brine-saturated, 239f
 complex conductivity and, 331f
 elastic properties of, 240–243
 electrical properties, 335–336
 feldspathic, 117
 Gardner equation coefficients, 172t
 initial porosity, 23
 magnetic susceptibility of, 383t
 Massilon, 239–240, 239f
 Mesozoic, 316f
 micaceous, 117
 permeability, 25f, 35f
 Permo-Triassic, 334–335
 porosity, 36t, 105f, 316f
 thermal conductivity of, 354t
 thermal properties, 351t
 Triassic, 333
 uniaxial compression strength, 258t

Sass equation, 359
Saturation, 30–32
 capillary pressure measurement and, 69f
 determining, 31
 fluid
 capillary pressure and, 336f
 compressional wave velocity, 174f, 243f
 electrical resistivity and, 298f
 sedimentary rock velocity and, 173–175
 shear wave velocity, 174f, 243f
 irreducible, 50

SCAL. *See* Special core analysis

Schist, 103f, 253f
 magnetic susceptibility of, 383t
 thermal conductivity of
 anisotropy of, 349t
 thermal properties, 346t

Seamounts, 389t

Secondary porosity, 20

Sedimentary rocks 1f, 4–12,
 409–414. *See also* specific types
 dominant materials in, 401f
 Koenigsberger ratio of, 389t
 magnetic susceptibility of, 383t
 overview of, 4–5
 radioactivity of, 116–118
 seismic wave attenuation in, 236–240
 thermal properties, 348–359, 351t
 pore fluid and, 349–357
 porosity and, 349–357
 velocity of, 164–181
 carbonates, 167–168
 Castagna equation, 179–181
 clastics, 165–167
 fluid saturation and, 173–175
 lithology and, 165–169
 pore fluid and, 173–175
 porosity and, 165–169
 pressure and, 175–179
 temperature and, 179
 unconsolidated sediments,
 168–169

Sedimentation, permeability and, 42

Seismic parameters, reservoir properties
 from, 226–232

Seismic velocity, 264–271
 empirical relationships, 264–267
 experimental results, 264–267
 permafrost, 169t

- Seismic wave attenuation
 - igneous rocks, 236
 - sedimentary rocks, 236–240
- Separate vugs, 43
 - porosity, 45f
- Series model, 318
 - layer, 361–362
- Serpentine, 99t
 - magnetic susceptibility of, 383t
 - thermal properties, 339t
- Shale, 6, 104f, 113t, 139, 253f
 - acoustic impedance and, 230f
 - brine-saturated, 187f
 - compaction process for, 23f, 25f
 - content estimate, 120–121
 - Devonian black, 123f
 - Gardner equation coefficients, 172t
 - indicator, 117
 - influence of, 40–43
 - initial porosity, 23
 - Jurassic, 186
 - linear regressions, 180t
 - magnetic susceptibility of, 383t
 - permeability, 35f, 41f
 - influence of, 53–55
 - rock skeleton of, 22
 - thermal expansion, 360t
 - thermal properties, 351t
 - uniaxial compression strength, 258t
- Shaly rocks, 296–304
 - spectral-induced polarization in, 329–330
- Shaly sand, 296–304
 - complex conductance model, 329f
 - composite, 307
 - dispersed, 53
 - equations, 303–304
 - laminated, 54, 298–299, 304–310
 - problem, 296–297
- Shear fractures, 28
- Shear modulus, 154f, 208
- Shear strength
 - compressional velocity and, 266f
- Shear velocity
 - normalized, 199f
 - porosity and, 199f
- Shear wave anisotropy, 187–188
 - calculated, 205f
- Shear wave slowness, 151, 153
- Shear wave splitting, 181
 - in transversely isotropic rocks, 184f
- Shear wave velocity, 210
 - Boise sandstone, 173f
 - depth and, 178t
 - fluid saturation and, 174f
 - porosity and, 219f
- Shell formula, 282–283
- Shuey's equation, 227
- Shuey's method, 231
- Siderite, 99t, 378t
 - electrical resistivity of, 276t
 - gamma-gamma interactions, 130t
 - thermal properties, 339t
- Silicic rocks, 2
- Siliciclastics
 - carbonates *v.*, 12
 - properties of, 13t
- Sillimanite, 99t
 - thermal properties, 339t
- Silt, uniaxial compression strength, 258t
- Siltstone, 5
 - thermal properties, 351t
- Silurian limestone, 355f
- Simandoux equation, 302, 303f
- Slate, magnetic susceptibility of, 383t
- Slowness-neutron crossplots, 396
- Smectite, 111t, 378t
 - thermal properties, 339t
- Snell's law, 227
- Sodium chloride, 277, 279f
- Soil
 - Central European, 358t
 - density, 357
 - horticultural, 358t
- Solid components
 - elastic properties of, 155
- Solid material modulus, 221
- Source rock studies, 123
- Special core analysis (SCAL), 71
- Specific heat capacity, 345f
- Specific internal surface, 29–30
- Specific internal surface, 50–51
- Spectral measurements, 118–119
- Spectral-induced polarization, 324–335
 - basic mechanisms of, 326–327
 - decay curve, 335f
 - effects, 328f
 - in ore-containing rocks, 328
 - in porous rocks, 328–335
 - in shaly rocks, 329–330
 - traditional parameters of, 327
- Sphalerite, 99t
- Sphene, 111t

Sphere pack
 compact hexagonal, 25t
 cubic, 25f
 orthorhombic, 25t
 regular, 25t

Sphere pack models, 188f, 194–196

Spin echo, 78–79

Spinel, 99t
 thermal properties, 339t

St. Peter sandstone, 20t
 uniaxial compression strength, 258t

Static magnetic field, 86

Static moduli, 259–264
 compressional bulk, 262f
 Young's, 263t

Stokes' law, 6

Strain, 249–250

Stress, 249–250

Stress-strain curve, 250–252, 251f

Structural clay, 5

Structure tensor, 217
 components of, 222f

Structured model, 214–217

Surface relaxation, 81, 84–85
 transverse relaxation and, 83f

Svaneke granites, 384–385

Syenite, 103f, 113t
 thermal properties, 346t
 uniaxial compression strength, 258t

Sylvite, 99t, 111t
 gamma activity, 119t
 thermal properties, 339t

T

Talc, 99t
 thermal properties, 339t

Temperature. *See also* Thermal properties
 dependence, 164
 dry bulk moduli and, 179
 fluid density and, 100f
 sedimentary rock velocity and, 179
 specific heat capacity and, 345f
 thermal conductivity and, 359f
 water permittivity and, 314f

Tension fractures, 28

Tensor elements, 153–154

Ternary systems, 379f

Tertiary sand, 358t

Tetrahedral unit, 8

Textural parameter, 319

Thermal conductivity
 amorphous materials, 342
 of amphibolite, 347
 anisotropy of, 349t
 gneiss, 349t, 350f
 schist, 349t
 of Central European soils, 358t
 compressional wave velocity and, 407f, 410f, 411f, 412f
 crystalline solid materials, 342
 elastic wave velocities and, 403–414
 of gneiss, 347
 of granite, 347, 366t
 of peridotite, 347
 porosity and, 348f, 356f, 370f, 372f
 sand, 353f
 pressure and, 359f
 of sandstone, 354t
 temperature and, 359f

Thermal diffusivity, 338

Thermal expansion, 359
 linear, 360t

Thermal properties. *See also* Temperature
 of cement, 355t
 clay, 356–357
 conversions, 338t
 of fluids, 342
 of igneous rocks, 346t
 introduction, 337–339
 of magmatic rocks, 345–348
 of metamorphic rocks, 345–348, 346t
 of minerals, 339–344
 rock-forming, 339t
 models, 360–372
 inclusion, 365–372
 layer, 361–362
 of pore fluids, 344t
 of rocks, 343–359
 overview, 343–344
 of salts, 353t
 sandstone, 351t
 of sedimentary rocks, 348–359, 351t
 pore fluids and, 349–357
 porosity and, 349–357
 theories, 360–372
 units, 338t

Thermoremanent magnetization (TRM), 388

Thomas-Stieber technique, 308, 310

Thomeer's equation, 67f, 72

Thomsen parameters, 185t, 204

Thorium, 109, 121
 heat production rate, 125t
 major occurrences of, 112
 in minerals, 109–112

Thorium (*Continued*)
 potassium and, 122f
 in rocks, 113–118
 3DEX, 308, 310
 Thuringia rock salt, 349
 thermal properties of, 353t
 TH systems, 183
 Time-domain instruments, 327
 Tipping field, 78
 Titanite, thermal properties, 339t
 Titanomaghemites, 379, 380t
 Titanomagnetite, 99t, 379, 380t
 TIV systems, 183
 Toluene, 313t
 Tortuosity, 49, 331
 Touching vugs, 43
 Trachyte, 113t
 Transition zone, 59
 Transverse plane, 78
 Transverse relaxation, 81, 82f
 bulk contributions to, 83f
 surface contributions to, 83f
 Transversely isotropic rocks, shear wave
 splitting in, 184f
 Tremolite, 99t
 Triassic sandstone, 333
 Trichloethane, 313t
 TRM. *See* Thermoremanent magnetization
 Trona, 99t
 Tuffs, 103f

U

Ultramafic rocks, 2
 Ulvöspinel, 379, 380t
 Unconsolidated rocks, 161
 Unconsolidated sand, 177f
 Unconsolidated sediments, 263f
 velocity, 168–169
 Uniaxial compression, 255
 strength, 257f
 compressional velocity and,
 266t, 267f, 271f
 mean values, 258t
 Uranium
 behavior of, 110
 in crude oils, 124t
 heat production rate, 125t
 major occurrences of, 112
 in minerals, 109–112
 in rocks, 113–118
 variable content, 117
 Uranium-radium series, 108

V

Variable internal structure, 215f
 Velocity, 160–161. *See also* Compressional
 wave velocity
 anisotropy, 164
 elastic wave, 149–153, 403–414
 general equation for, 217–220
 porosity factor in, 218–220
 igneous, 161–164
 longitudinal wave, 163f
 metamorphic rocks, 161–164
 ratios, 223f
 sedimentary rock, 164–181
 carbonates, 167–168
 Castagna equation, 179–181
 clastics, 165–167
 fluid saturation and, 173–175
 lithology and, 165–169
 pore fluid and, 173–175
 porosity and, 165–169
 pressure and, 175–179
 temperature and, 179
 unconsolidated sediments,
 168–169
 seismic, 264–271
 empirical relationships, 264–267
 experimental results, 264–267
 permafrost, 169t
 shear, 199f
 shear wave, 210
 Boise sandstone, 173f
 depth and, 178t
 for fluid saturation, 243f
 fluid saturation and, 174f
 porosity and, 219f
 S-wave, 185
 Velocity-density relationships, empirical,
 170–172
 Velocity-porosity plot, 167f
 empirical, 170–172
 Venezuelan shale, 20t
 Vermiculite, 99t
 Vertical permeability, 42
 Vienna Basin, 177–178
 Vinegar and Waxman model, 329–330
 Voigt and Russ bounds, 189–194
 Voigt-Reuss-Hill average, 190
 Volcanic rocks, 2, 29
 Volcanite, 347
 Volume susceptibility, 385f
 of diamagnetic materials, 377t
 of ferrimagnetic materials, 380t

- of ferromagnetic materials, 380t
- paramagnetic substances, 378t
- Volumetric rock composition, 395–401
 - crossplots, 396–397
 - generalized numerical solution, 397–401
- Vugs, 12, 26
 - separate, 43
 - porosity, 45f
 - touching, 43
- Vuggy pore network, 43

W

- Wait time, 80
- Water
 - composition, 399t
 - electrical resistance of, 278t
 - permittivity, 314f
 - point, 396
 - polarization, 314
 - relative permeability of, 56f
 - thermal properties, 344t
 - zone, 59
- Water-gas, capillary pressure, 62t
- Water-oil, capillary pressure, 62t
- Water-wet, 56, 58, 287
- Waxman-Smits equation, 299–302, 304

- Wettability, 56–58
 - determination, 58
 - index, 58
 - intermediate, 57, 58
- Williston Basin, 27
- Wollastonite, 99t
- Wustite, 99t
- Wyllie equation, 170
 - application of, 171t
- Wyllie time-average formula, 322–323

X

- X-ray diffraction (XRD), 145
- XRD. *See* X-ray diffraction

Y

- Young's modulus, 252, 261f, 262
 - compression strength and, 246f
 - dynamic, 263t
 - static, 263t

Z

- Zircon, 111t, 117
 - thermal properties, 339t
- Zoeppritz equations, 227